

# Magazine of Civil Engineering

116(8), 2022

ISSN  
2712-8172



**Magazine of Civil Engineering**

ISSN 2712-8172

Online peer-reviewed open-access scientific journal in the field of Civil and Construction Engineering

**Founder and Publisher:** Peter the Great St. Petersburg Polytechnic University

This journal is registered by the Federal Service for Supervision of Communications, Information Technology, and Mass Media (ROSKOMNADZOR) in 2020. Certificate EI No. FS77-77906 issued February 19, 2020.

**Periodicity:** 8 issues per year

Publication in the journal is open and free for all authors and readers.

**Indexing:** Scopus, Web of Science (ESCI, RSCI), DOAJ, Compendex, EBSCO, Google Academia, Index Copernicus, ProQuest, Ulrich's Serials Analysis System, CNKI

**Corresponding address:** 29 Polytechnicheskaya st., Saint Petersburg, 195251, Russia

**Chief science editor:** associate member of RAS, D.S. in Engineering, Vitaly V. Sergeev

**Deputy chief science editors:**

D.S. in Engineering, Galina L. Kozinetc

D.S. in Engineering, Sergey V. Korniyenko

**Executive editor:** Ekaterina A. Linnik

**Translator, editor:** Darya Yu. Alekseeva

**DT publishing specialist:**

Anastasiya A. Kononova

**Contacts:**

E-mail: [mce@spbstu.ru](mailto:mce@spbstu.ru)

Web: <http://www.engstroy.spbstu.ru>

---

Date of issue: 26.12.2022

© Peter the Great St. Petersburg Polytechnic University. All rights reserved.

© Coverpicture – Ilya Smagin

**Editorial board:**

T. Awwad, PhD, professor, Damascus University, Syrian Arab Republic

M.I. Balzannikov, D.Sc., professor, Samara State University of Economics, Russia

A.I. Belostotsky, D.Sc., professor, StaDyO Research & Engineering Centre, Russia

A.I. Borovkov, PhD, professor, Peter the Great St. Petersburg Polytechnic University, Russia

A. Borodinecs, Dr.Sc.Ing., professor, Riga Technical University, Latvia

M. Veljkovic, PhD, professor, Delft University of Technology, The Netherlands

R.D. Garg, PhD, professor, Indian Institute of Technology Roorkee (IIT Roorkee), India

M. Garifullin, PhD, postdoctoral researcher, Tampere University, Finland

T. Gries, Dr.-Ing., professor, RWTH Aachen University, Germany

T.A. Datsyuk, D.Sc., professor, Saint-Petersburg State University of Architecture and Civil Engineering, Russia

V.V. Elistratov, D.Sc., professor, Peter the Great St. Petersburg Polytechnic University, Russia

T. Kärki, Dr.-Ing., professor, Lappeenranta University of Technology, Russia

G.L. Kozinetc, D.Sc., professor, Peter the Great St. Petersburg Polytechnic University, Russia

D.V. Kozlov, D.Sc., professor, National Research Moscow State Civil Engineering University, Russia

S.V. Korniyenko, D.Sc., professor, Volgograd State Technical University, Russia

Yu.G. Lazarev, D.Sc., professor, Peter the Great St. Petersburg Polytechnic University, Russia

M.M. Muhammadiev, D.Sc., professor, Tashkent State Technical University, Republic of Uzbekistan

H. Pasternak, Dr.-Ing.habil., professor, Brandenburgische Technische Universität, Germany

F. Rögner, Dr.-Ing., professor, Technology Arts Science TH Köln, Germany

V.V. Sergeev, D.Sc., professor, Peter the Great St. Petersburg Polytechnic University, Russia

T.Z. Sultanov, D.Sc., professor, Tashkent Institute of Irrigation and Agricultural Mechanization Engineers, Republic of Uzbekistan

M.G. Tyagunov, D.Sc., professor, National Research University "Moscow Power Engineering Institute", Russia

M.P. Fedorov, D.Sc., professor, Peter the Great St. Petersburg Polytechnic University, Russia

D. Heck, Dr.-Ing., professor, Graz University of Technology, Austria

A.G. Shashkin, D.Sc., "PI Georekonstruktsiya", LLC, Russia

V.B. Shtilman, D.Sc., JSC "B.E. Vedeneev VNIIG", Russia

**Contents**

Rizwan, M., Ahmad, N., Naeem Khan, A. Seismic damage mechanism of weak beam-column joint frames	11601
Nizina, T.A., Balykov, A.S., Volodin, V.V., Kyashkin, V.M. Structure and properties of cement systems with additives of calcined clay and carbonate rocks	11602
El-Mir, A., Nehme, S., Assaad, J. Feasibility of concrete mixtures containing coarse and/or fine recycled brick aggregates	11603
Al-Hammood, A.A., Frayyeh, Q.J., Abbas, W.A. Iraqi bentonite as natural pozzolan	11604
Kaldar-ool, A-Kh.B., Opubul, E.K. Stress condition of orthotropic vault structure with cylindrical anisotropy	11605
Arairo, W., Masrouri, F., Abdallah, A., Rosin-Paumier, S., Sraj, O., Khatib, M. Temperature effects on the design parameters of a geothermal pile	11606
Bogdanova, V.V., Kobets, O.I., Buraya, O.N., Ustinov, A.A., Zybina, O.A. Intumescent compounds for fireproofing of polymer pipelines	11607
Golubev, I.A., Vlasov, D.Y., Tsarovtseva, I.M., Mayorova, M.A., Chipizubov, V.V., Shaposhnikov, N.O.	11608
Kachooee, A. An improved lateral restrained local fuse used in concentric braces	11609
Samarin, O.D. Thermal mode of a room with integrated regulation of microclimate systems	11610
Khater, H.M., El Nagar, A.M., Ezzat, M. Processing, characterization and hardening mechanism of one-part geopolymers	11611
Maskalkova, Yu.G., Rzhnevskaya, V.A. Size effect of cube specimen on strength of expanded clay fiber-reinforced concrete	11612
Khalmuradov, R.I., Khudoynazarov, K., Nishanov, U.A. Elastic-plastic deformation of a round plate reinforced with stiffeners	11613
Belash, T.A., Ivanova, T.V., Ivashintsov, D.A. Additional measures protecting buildings from climatic influences	11614
Rodin, A.I., Ermakov, A.A., Kyashkin, V.M., Rodina, N.G., Erofeev, V.T. Porous glass ceramics from siliceous rocks with high operating temperature	11615



Research article

UDC 699.841

DOI: 10.34910/MCE.116.1



## Seismic damage mechanism of weak beam-column joint frames

M. Rizwan<sup>1</sup> , N. Ahmad<sup>2</sup> , A. Naeem Khan<sup>2</sup>

<sup>1</sup> Sarhad University of Science and Information Technology, Peshawar, Pakistan

<sup>2</sup> Department of Civil Engineering, University of Engineering and Technology Peshawar, Peshawar, Pakistan

✉ [rizwan.civil@suit.edu.pk](mailto:rizwan.civil@suit.edu.pk)

**Keywords:** reinforced concrete, structural concrete, special moment resisting frame, building frame, beam-column joints, shake table test, progressive collapse

**Abstract.** The use of old building design codes and improper execution of recent seismic design practices resulted in substandard and vulnerable reinforced concrete building stock, the majority of which is built with weak beam-column joint connections (i.e. joint panels having no transverse reinforcement and built in low strength concrete). In order to understand the seismic response and damage behavior of recent special moment resisting frame (SMRF) structures with the defect of weak beam-column joints, shake table tests were performed on two 1:3 reduced scale two storey and one bay RC frame models. Reference code design and weak beam-column joint frame models were subjected to unidirectional dynamic excitation of increasing intensities using the natural record of 1994 Northridge Earthquake. The input scaled excitation were applied from 5 % to 130 % of the maximum input peak ground acceleration record, to force the test models from elastic to inelastic stage and then to fully plastic incipient collapse stage. The weak beam-column frame experienced flexural cracking of the columns, longitudinal bar-slip in beam members, cover concrete spalling and severe damageability of the joint panels under multiple dynamic excitations. The deficient frame was able to resist only 40 % of the maximum acceleration record as compared to the code design frame, which was able to resist up to 130 %. Based on the experimental observations, a drift-based damage scale was developed for different performance limits states that can be employed for the global performance assessment of deficient weak beam-column joint RC frames.

**Acknowledge:** The authors are thankful to the Earthquake Engineering Center (EEC), Department of Civil Engineering, UET Peshawar, for supporting the experimental research presented herein.

**Citation:** Rizwan, M., Ahmad, N., Naeem Khan, A. Seismic damage mechanism of weak beam-column joint frames. Magazine of Civil Engineering. 2022. 116(8). Article no. 11601. DOI: 10.34910/MCE.116.1

### 1. Introduction

Reinforced concrete construction is on the peak in many urban areas of the world. This type of construction is particularly used for multi-storey buildings, schools, hospitals, and residential type buildings because of the vast availability of constituents of concrete around the world and the ease of construction. Although the design and construction of RC buildings in the developing countries are mostly based on the locally available or adopted international building codes, the proper construction execution of the specified design in the field is still a big challenge. The improper construction practices and use of old seismic code provisions resulted in a widespread substandard and vulnerable building stock [1–2], with recent surveys showing a number of construction/design deficiencies [1, 3]. The commonly available construction/design defects include: substandard quality of concrete (low strength concrete), joint panels without transverse reinforcement, beam column members with reduced flexural reinforcement along with shear reinforcement spacing larger than specified by the code, and non-seismic hooks among others. In all these typical construction or non-seismic design practices, the weak beam-column joint connections i.e. joint panels

having no transverse ties reinforcement and built with low strength concrete, are very common. An RC building with joints having such non-seismic provisions can cause shear failures of the critical panel regions; in turn, such failures can result in partial or full collapse of the structures. It is also worth to mention, majority of these RC buildings in the developing countries are located in high seismic regions and can be subjected to large earthquakes of extreme excitations in the future [4]. RC structures if not built properly can result in catastrophic failure and subsequent human and economic losses due to strong earthquake induced ground motions [5–9].

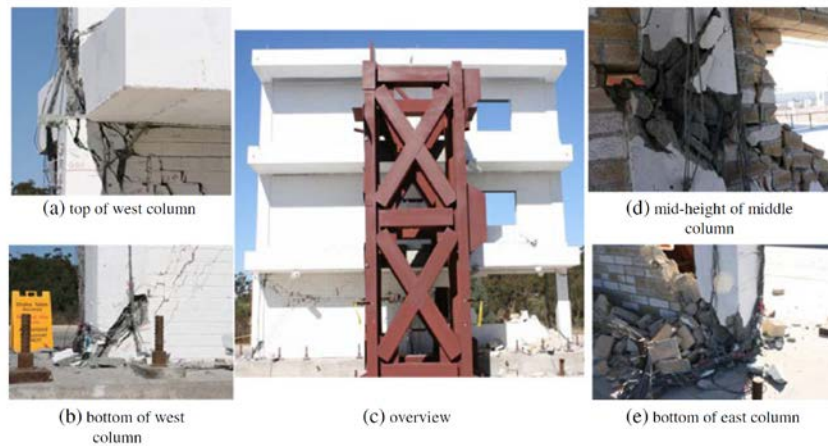
In recent decades, many researchers performed experimental investigations through quasistatic tests on weak beam-column connections and shake table tests on deficient frame structures, in order to assess their seismic performance [10–28]. In most of these experimental studies, either full scale and/or reduced scale beam-column connections and frame structures were employed. In these experimental investigations, different types of substandard and non-seismic parameters and diverse structural configuration were considered, in order to assess the seismic performance and damage mechanism of deficient of RC structures. Quintana et al. [10] tested a 1:2.5 reduced scale three-storey deficient frame structure (Fig. 1 a) on shaking simulator, in order to assess the damage mechanism and to provide benchmark test data for the retrofitting of old type, non-ductile and non-seismic design buildings. The test model was built with plain rebars, without joint transvers reinforcement provisions and with 90° non-seismic hooks. The test models were subjected to increasing PGA excitation of several earthquake records in order to observe the damage behavior of the test frame. During the initial excitations it was observed that the model experienced a lap splice failure at the top storey joints because of the use of plain rebars. At high PGA intensity most of the damage was concentrated at lower storey column bases and extensive damage was observed at beam-column connections; this showed high vulnerability of these deficient RC structures. Stavridis et al. [11] conducted shake table tests on a 2:3 scale three-storey and two-bay RC frame structure (Fig. 1 b) with older code design parameters and non-seismic detailing. The effects of infill panels were also investigated during the experimental program. Increasing inputs excitations were applied to test specimens in order to investigate the damage mechanism with low, moderate and high-level shaking intensities. It was observed during the testing program that at low level intensity, minor cracks were appearing in the infill panels, with the development of plastic hinge formation at column bases, i.e. cracking and joint shear failures at high level excitations. Yavari et al. [12] tested four 1:2.25 scaled two-storey and two-bay RC frames (Fig. 1 c) with non-seismic detailing in the beam and column members and no transverse reinforcement in the beam-column joints. The objectives of the experimental program were to investigate the collapse mechanism and gravity load redistribution with increasing dynamic excitations. Different factors affecting the behavior of these deficient RC frame structures during an earthquake loading including axial load demand on the column members and shear failure pattern of weak beam-column connections were evaluated. It was observed from the experimental study that the collapse of deficient RC frame structures may be a result of the plastic hinging mechanism produced at the base of non-ductile columns ends and critical shear failures of beam-column connections. Sharma et al. [13] conducted shake table test on a 3D, three-storey RC frame model (Fig. 1 d) with design deficiency of having no transverse reinforcement in beam-column connection and poor anchorage provision. The objectives of the testing program were to investigate the effectiveness of a tuned mass damper (TLD) retrofitting scheme and to observe the inelastic behavior of a non-seismic design RC frame structure under increasing dynamic excitations. It was observed from the test results that under increasing dynamic shaking, the model damage behavior is mostly concentrated at the lower storey columns base and beam-column panels. Most of the experimental studies available in the literature were focused on the vulnerability assessment of gravity type/old type RC buildings and/or the performance of a specific retrofitting, strengthening or isolation technique [14–28]. However, experimental shake table investigations on the recent special moment resisting frames (SMRF) structures (seismic code compliant beam and column members), but having weak beam-column joints (no transverse ties reinforcement and built with low strength concrete) and their seismic behavior at the ultimate damage state, are lacking.

In order to assess the ultimate capacity and damage mechanism of frames with weak beam-column joints, shake table tests were performed on representative frames structures. The shake table tests investigations have been performed on two 1:3 reduced scale two-storey RC frame specimens. Model-1 (reference model) was a code compliant model design based on the seismic building code. Whereas, Model-2 had similar characteristics but was provided with no ties in beam-column panel zone along with concrete strength less than the design specification (33 % less) to consider the effects of the most commonly available defects in the existing building stock [1, 3]. The test specimens were subject to multiple excitations using the natural accelerogram of 1994 Northridge Earthquake ranging from 5 % to 130 % of peak ground acceleration. These multiple scaled excitations were used in order to force the test models from elastic stage to inelastic and finally near collapse stage. The damage mechanism of each specimen was observed and reported. Acceleration and displacement response of the structure was recorded and analyzed to obtain the inter-storey drift demand, inter-storey shear and displacement profile of the structure and to develop deformation-based damage scale for seismic assessment of the considered structures.

The objectives of the current experimental program were to understand the dynamic response, damage mechanism at ultimate capacity and to develop drift-based damage scales for RC frame structures with weak beam-column joint connections.



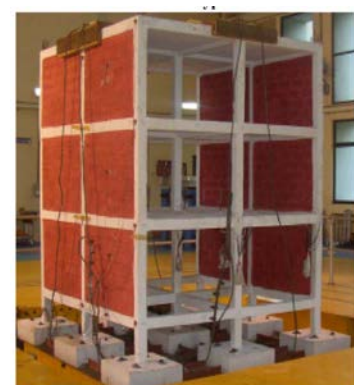
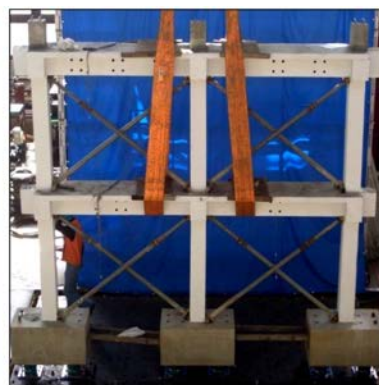
(a) 1:2.5 scale three storey two bays by one bay deficient RC model tested by Quintana et al. [10]



(b) 2:3 scale three storey RC frame tested by Stavridis et al. [11]



(c) 2:2.25 scale two storey and two bay RC frame tested by Yavari et al. [12]



(d) 1:3 scale three storey RC model tested by Sharma et al. [13]

Figure 1. Shake table tests investigations on deficient RC frame models.

## 2. Methods

### 2.1. Experimental Program

#### 2.1.1 Test Specimens

The current research focused on low rise RC frame structures with weak beam-column joints (non-seismic detailing along with low strength concrete), in order to quantify their seismic performance and

observe their damage response. In particular, a RC frame with a two storey structure was considered, typically employed for low rise schools, hospital or apartment type public buildings. The considered structure consisted of a 2 by 1 bay frame, with each bay length of 5487 mm (18 feet) and storey height of 3658 mm (12 feet) for both the stories, as shown in Fig. 2. The representative frame structure was designed according to static force-based procedures (BCP-SP 2007/UBC 97) [29–30], considering high seismic zone of 4.0 (0.40 g design peak ground acceleration) with stiff soil type B (NEHRP classification). The modeling and design were carried out using the design software CSI ETABS considering all load combinations as per the code. For the material properties, 21 MPa (3000 psi) concrete and 414 MPa (60,000 psi) rebar yield strength were considered in the design process. The design model was detailed as per the ACI-318-14 [31] recommendations for the SMRF provisions. Fig. 1 also shows the design details of the prototype structure.

### 2.1.2 Preparation of One-Third Reduced Models

The seismic shake table simulator in Earthquake Engineering Center, Department of Civil Engineering, UET Peshawar, has a table size of 1.5 m x 1.5 m (5 feet by 5 feet) and can operate with loading capacity of about 5 tons (11.01 kips) only in the unidirectional excitation. Due to the size and loading capacity limitations, only the interior critical frame was extracted from the prototype design building and reduced to one-third scale for seismic excitation as shown in Fig. 2. For scaling between the prototype and model dimension, a simple linear model idealization was considered as shown in Table 1. Such simple modeling allowed simplicity and reduced the cost as well as complexities associated with scaling the stress-strain properties of the materials (concrete and reinforcing bar) in the model domain. As shown in Table 1, all the members of the extracted prototype frame, i.e. beam, column and slab, and reinforcing rebar were reduced by a scale factor of  $S_L/3$ . For the constituents of concrete, 8.52 mm (3/8 in) down aggregate size was taken for model preparation, in order to use scaled coarse aggregate, whereas cement and fine aggregate were used with no scaling. As mentioned earlier two types of concrete strength were employed in this study, i.e. 21 MPa (3000 psi) and low strength test model with a 14 MPa (2000 psi) concrete compressive strength. For this purpose, ACI concrete mix design methods were followed for the preparation of concrete constituent mix.

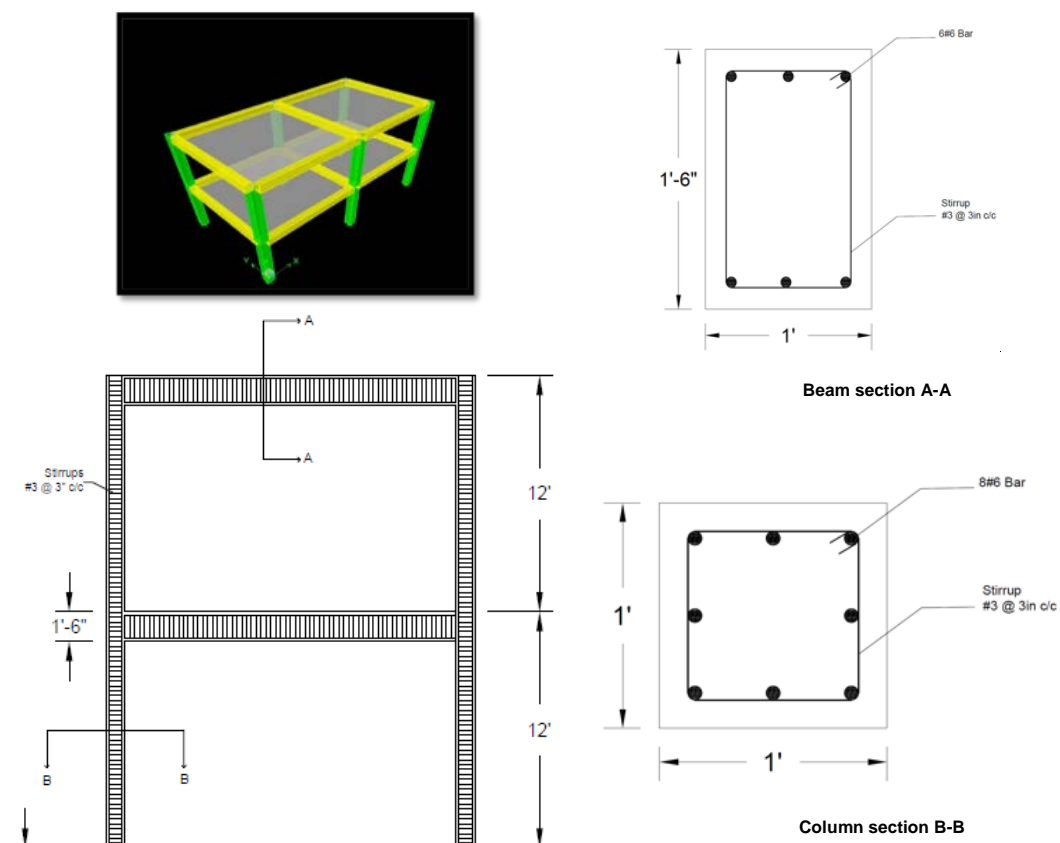
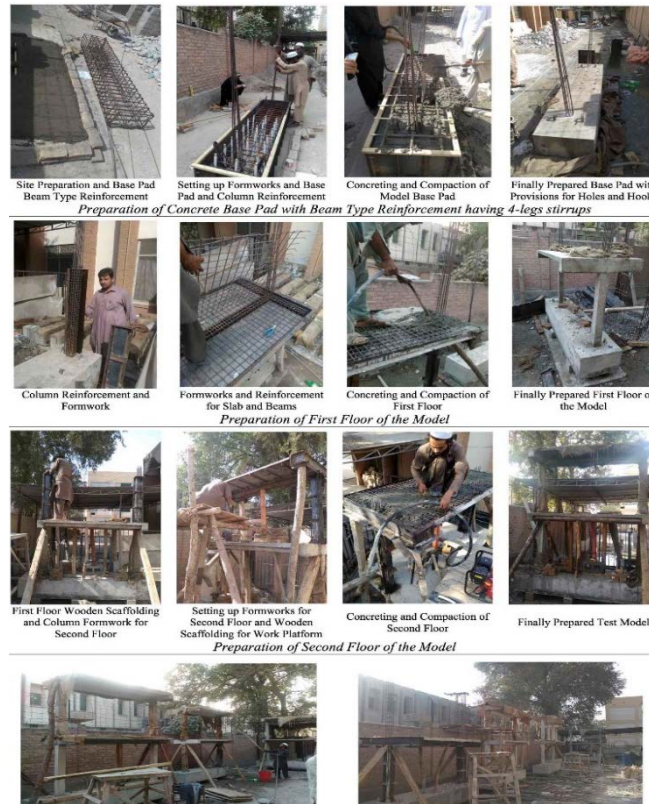


Figure 2. Geometric and design layout of prototype RC frame.

**Table 1. Prototype and reduced models' dimensions and similitude conversion factors.**

Structural Properties		Simple Model Similitude Requirement		
Prototype Frame	Test Models (Scale 1:3)	Physical Quantity	Relationship	Scale Factor
<b>Beams:</b> 304 mm x 459 mm (12 in x 18 in)	<b>Beams:</b> 102 mm x 153 mm (4 in x 6 in)	Length	$S_L = L_p/L_m$	3
<b>Columns:</b> 304 mm x 304 mm (12 in x 12 in)	<b>Columns:</b> 102 mm x 102 mm (4 in x 4 in)	Stress	$S_f = f_p/f_m$	1
<b>Slab:</b> 153 mm (6 in)	<b>Slab:</b> 51 mm (2 in)	Strain	$S_e = \epsilon_p/\epsilon_m$	1
<b>Concrete strength:</b> 21 MPa (3000 psi) 14 MPa (2000 psi)	<b>Concrete strength:</b> 21 MPa (3000 psi) 14 MPa (2000 psi)	Specific Mass	$S_\rho = \rho_p/\rho_m$	1
<b>Aggregate size:</b> 25.4 mm (1 in)	<b>Aggregate size:</b> 9.52 mm (3/8 in)	Displacement	$S_d = d_p/d_m = S_L$	3
<b>Steel strength and dia:</b> 414 MPa (60000 psi) 19 mm (#6 Rebar) 10 mm (#3 Rebar)	<b>Steel strength and dia:</b> 60000 psi (414 MPa) 6.33 mm (#2 Rebar) 3.33 mm (#1 Rebar)	Force	$S_F = F_p/F_m = S_L 2 S_f$	9
		Time	$S_t = t_p/t_m = S_L \sqrt{(S_e S_\rho / S_f)}$	3
		Frequency	$S_\Omega = \Omega_p/\Omega_m = 1/S_t$	1/3
		Velocity	$S_v = v_p/v_m = \sqrt{(S_e S_\rho / S_f)}$	1
		Acceleration	$S_a = a_p/a_m = S_f S_L S_\rho$	1/3

The concrete mix proportion of cement:sand:coarse aggregate, for both design specified strength of 21 MPa (3000 psi) and reduced strength of 14 MPa (2000 psi) are shown in Table 1. Fig. 3 shows the sequence of construction for the 1:3 scaled frame models. Due to scaling and similitude requirements the reduced scale models were subjected to gravity and seismic mass less than the required. To satisfy the condition of mass simulation for the reduced scale test models, additional floor mass was applied following the mass simulation model [10, 32]. On each floor level extra mass of 1200 kg was applied through steel blocks mounted and fixed to the floor by means of fully secured 13 mm (1/2 inch) steel bolts as shown in Fig. 4.



**Figure 3. Test frames construction stages.**

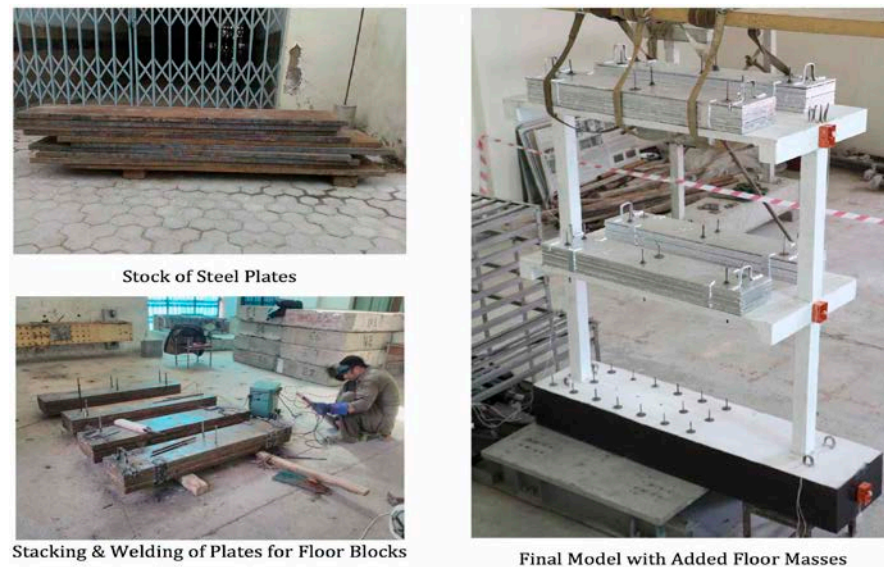


**Figure 4. Added floor mass preparation and setup for artificial mass simulation.**

## 2.2. Shake Table Test of RC frames Specimens

### 2.1.3 Testing setup and model instrumentation

The test model's setup on the shaking simulator and model instrumentation are shown in Fig. 5. The objective of experimental testing was to observe the global response of the test frames, so only external instrumentation was employed in the form of six accelerometers and three linear displacement transducers. The instruments sensitivity, maximum capacity and conversion coefficient are reported in Table 2. On each floor level (mid position of joint panel region) and at the base pad level, three accelerometers were installed on the front and back sides of the test models in order to record floor and base pad accelerations. For recording the displacement at each floor and pad level, three displacement transducers were attached to a fixed steel frame, which was installed in-line with the model in-plane position.

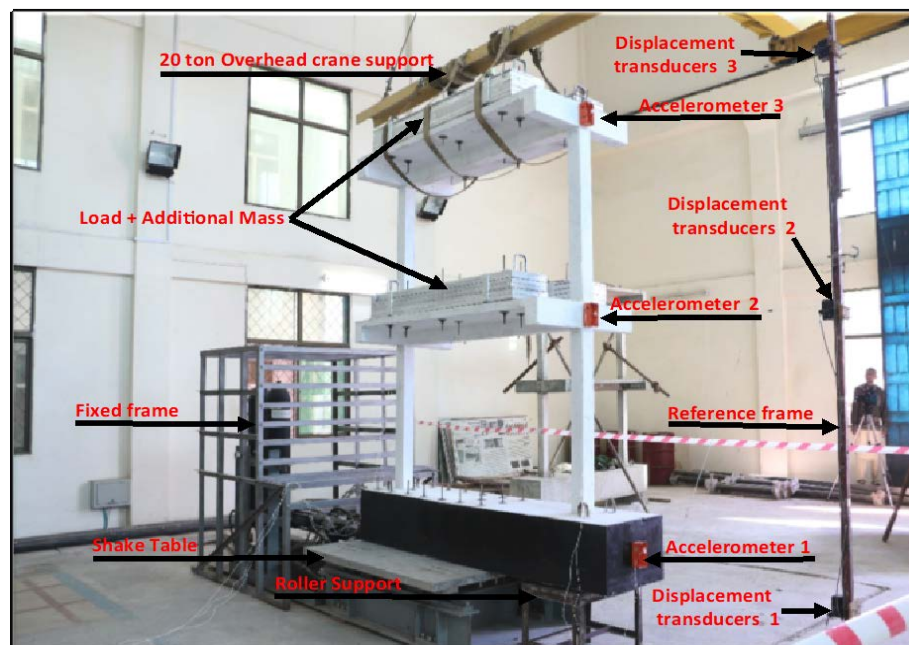


**Figure 5. Test frame instrumentation and shaking setup.**

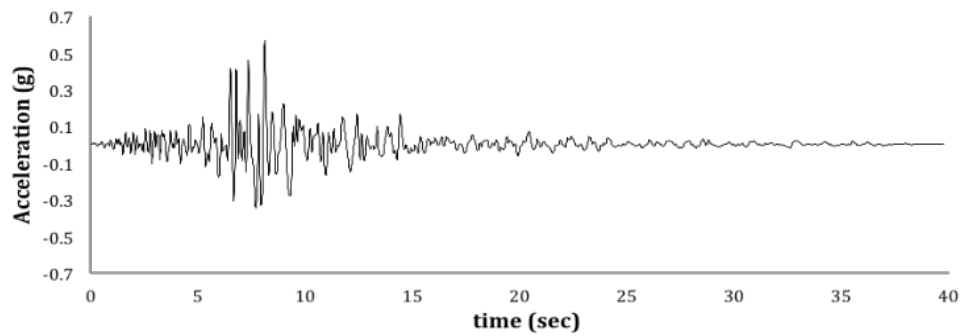


**Figure 6. Input time history record of 1994 Northridge Earthquake.**

#### 2.1.4 Shake table Input Loading Protocols

The test models were tested by the Earthquake Engineering Center (EEC)'s seismic simulator in a unidirectional motion. Table 3 reports the characteristics limit values of the shake table. In order to excite the test models from elastic stage to full ultimate collapse stage, and also to be within the shaking range of shaking simulator, the 1994 Northridge Earthquake natural acceleration record was selected. This selection was made after careful analysis of a number of natural acceleration records to be within the range of shake table limiting acceleration, velocity and displacement limits. Fig. 6 shows the horizontal component of 1994 Northridge Earthquake record acceleration time history. The record was obtained from PEER strong motion data base (090 CDMG Station 24278) and had a peak acceleration, velocity and displacement values of 0.57 g, 518 mm/sec (20.39 in/sec) and 90 mm (3.54 in), respectively. The acceleration record time step was reduced by 1/3 to satisfy the input frequency requirement for the model as mentioned in Table 1. Table 4 and 5 reported the input multiple excitations and test sequence for both code compliant Model-1 and Model-2. Both frame models were excited with incremental excitations of 5 %, 10 %, 20 %, 30 %, 40 %, 50 %, 60 %, 70 %, 80 %, 90 %, 100 % and 130 % depending on the ultimate capacities of the tested frame. The idea of using multiple scaled excitation, i.e. from low to high level, was to deform and force the test structures from elastic to inelastic stage and then to attain full ultimate incipient collapse stage. The EEC's seismic simulator performs a self-adjustment motion called Self-Check, once the input time history is given to the shake table. After the simulator self-check adjustment, the test models were excited with scaled incremental excitations of the maximum acceleration records. After each run the damage mechanism of the test models was observed and documented with snapshots. The test sequence was progressing until the test models reached the near incipient collapse stage, after which the test was concluded. The recorded acceleration and displacement response time histories were obtained for each test run in the form of voltage values.

#### 2.1.5 Recorded Data Processing

The accelerometers and displacement transducers recorded the data in the form of voltage values (mV). To get the time histories values in the form of accelerations (g) and displacements (mm), the recorded raw data needed to be divided by the instruments conversion coefficient as reported in Table 2. Once the recorded data were corrected for the respective instrument coefficient, the raw data were further processed for base line correction and signal filtering. This data processing correction and filtering was done to remove any noise in the actual recorded data. For this purpose, the SeismoSignal (SeismoSoft 2018) data processing software was employed with a linear category base line correction and filter type of Butterworth with frequency range of 0.10 Hz to 25 Hz considered.

**Table 2. Test model instrumentation positions and characteristics.**

Channel	Position	Direction	Maximum Capacity	Parameter	Coefficient	Unit
A1	Pad level	Front	±10g	Acceleration	492.20	mv/g
A2	First Floor	Front		Acceleration	501.10	mv/g
A3	Second Floor	Front		Acceleration	510.10	mv/g
A4	Pad level	Back		Acceleration	508.90	mv/g
A5	First Floor	Back		Acceleration	490.10	mv/g
A6	Second Floor	Back		Acceleration	502.00	mv/g
D7	Pad level	Front	24 inches (610 mm)	Displacement	1000.00	mv/inch
D8	First Floor	Front		Displacement	1000.30	mv/inch
D9	Second Floor	Front		Displacement	1000.20	mv/inch

**Table 3. Earthquake Engineering Centre (EEC)'s seismic simulator (shake table) limits.**

Shaking simulator characteristics	Limits
Excitation direction	Single degree of freedom / unidirectional
Physical dimension	1.5m x 1.5m (5 feet x 5 feet)
Pay load capacity	5 tones
Maximum acceleration	1.1 g
Maximum velocity	±1.1 m/s
Maximum displacement	±125 mm

**Table 4. Input protocol and testing sequence for Model-1.**

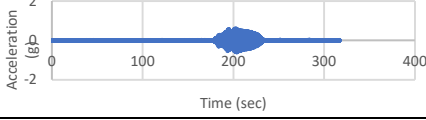
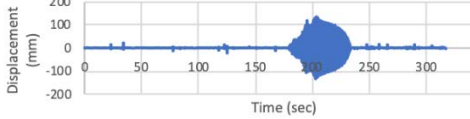
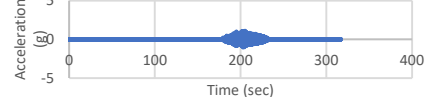
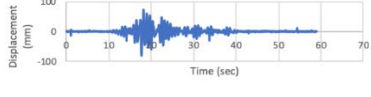
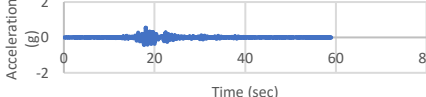
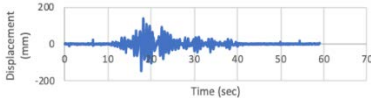
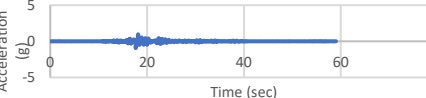
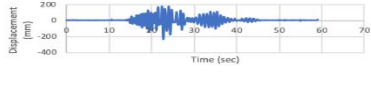
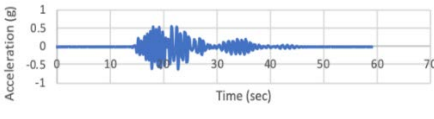
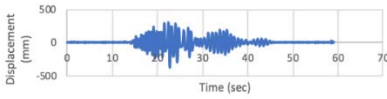
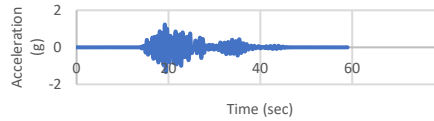
Time History	Run (%)	Observed Input PGA (g)
1994 Northridge Earthquake	Self-Check	0.60
	5% Run	0.033
	10% Run	0.06
	20% Run	0.12
	30% Run	0.16
	40% Run	0.19
	50% Run	0.25
	60% Run	0.31
	70% Run	0.36
	80% Run	0.41
	90% Run	0.49
	100% Run	0.62
	Self-Check 130%	0.62
130% Run	1.06	

**Table 5. Input protocol and testing sequence for Model-2.**

Time History	Run (%)	Observed Input PGA (g)
1994 Northridge Earthquake	Self-Check Run	0.015
	5% Run	0.52
	10% Run	0.25
	20% Run	0.31
	30% Run	0.35
	40% Run	0.73

Once the processed data were obtained, the displacement and acceleration histories were converted from the model domain to the prototype domain using the scaling conversion factors as mentioned in Table 1. Table 6 shows the experimentally obtained, first and second floor level acceleration and displacement time histories for the Model-1. Table 6 shows the time histories records for the selected significant runs in the prototype domain. For obtaining the relative displacements of each floor relative to the base of the pad, the displacement histories of the base pad were subtracted from each floor level displacements. For each test run, the peak values of displacement were obtained and normalized by the height of the storey to obtain the corresponding first and second floor drifts. To calculate the floor inertial forces at each floor level as well as the total base shear force at base of the porotype model, each of the floor accelerations were multiplied by each floor total mass, which included: the additional block mass, self-weight of the slab, self-weight of the beam and half column above and below the floor level. The inertial forces at each floor level were added to obtain the total base shear force at the base of frames.

**Table 6. Model-1 experimental observed displacement and acceleration histories.**

Run	Floor level	Displacement History	Acceleration History
Self-Check Run	Ground floor level		
	First floor level		
100% Run	Ground floor level		
	First floor level		
130% Run	Ground floor level		
	First floor level		

### 3. Results and Discussions

Table 7–8 shows Model-1 and Model-2 maximum roof displacement, maximum drift ratio, maximum base shear force and the observed damage mechanism for the selected significant runs. Fig. 7 shows the test model's comparison at the final run, i.e. incipient collapse stage and joint panel damage mechanisms. The code design Model-1 was initially excited by shake table self-check run which forced the structure to a drift of about 1.88 % and with shaking intensity of 0.60 g. During this first run the model developed significant beam flexural cracks at the first storey level. This flexural cracking was due to the reinforcement rebar yielding and plastic hinge mechanism. Minor vertical cracks were observed in the beam on the ground storey at the beam-column interface, which was due to the beam's longitudinal steel bars slip. This longitudinal beam's bar slip was observed also in full scale special moment resisting beams tested under quasi-static cyclic loading [33, 34]. During this run, there were flexural cracks observed on the ground storey at columns bases and on the first storey at beam ends. The model was then subjected to multiple excitations from 5 % to 100 %, with slight increase in cracking pattern. After this the test model was subjected to 130 % of the maximum acceleration record during which the model experienced shaking intensity of about 1.06 g. During this run the previous damage got significantly aggravated. The test model experienced concrete crushing and core spalling at the base and top ends of the columns on the ground storey due to excessive compressive strain demand on the cover concrete. Minor spalling was also observed at the base of columns on the first storey. Additionally, the model was observed with severe diagonal cracks in the joint panel region on the ground storey and slight diagonal cracks in the joint region on the first storey, which was due to transferring moments from beam-ends to columns' ends.

**Table 7. Observed damage in Model-1.**

Run	Top storey maximum displacement mm (Inch)	Top storey maximum Drift (%)	Maximum Base shear force kN (kips)	Observed damage
Self-Check – 0.60 g	61.45 (2.42)	0.87	151.08 (33.96)	 <p>Flexure Cracks at Base of Columns</p>  <p>Flexure Horizontal &amp; Vertical Cracks in Beam</p>
100% – 0.62 g	133.56 (5.26)	1.88	188.90 (42.47)	 <p>Concrete Crushing at Ground Storey Column Top</p>  <p>Cover Spalling at Ground Storey Column Base</p>
130% – 1.06 g	373.03 (14.69)	5.26	254.73 (57.27)	 <p>Diagonal Cracks in Joint Panel, Ground Storey</p>  <p>Diagonal Cracks in Joint Panel, First Storey</p>

This damage pattern testified to the existence of materials' over-strength in beams that resulted in plastic section moment capacity higher than the yield moment capacity, consequently, increasing demands on the joint region [12, 14].

**Table 8. Observed damage in Model-2.**

Run	Top storey maximum displacement mm (Inch)	Top storey maximum Drift (%)	Maximum Base shear Force kN (kips)	Observed Damage
5%– 0.52g	123.69 (4.87)	1.75	117.92 (26.51)	 Flexural Cracks in Beams and Columns, Ground Storey  Slight Cracks in Joint Panel on Ground Storey
30% – 0.35 g	182.37 (7.18)	2.57	137.48 (30.91)	 Severe Bat-Like Cracks in Joints on First Storey  Damage Progress in Joint Panel on Ground Storey
40% – 0.73 g	338.19 (13.31)	4.77	184.50 (41.48)	 Cover Detachment and Damage in Joint on First Storey  Severe Damage to Joint Panel on Ground Storey

In comparison to Model-1, weak beam-column deficient Model-2 deformed laterally to larger roof drift under similar input excitations and damage to structural members (beam and columns) and beam-column joint panels occurred at comparatively lower excitation demand. Model-2 was able to only resist 40 % of the PGA value (0.73 g) as compared to Model-1. Unlike Model-1, Model-2 experienced damage in joints much earlier and to extreme extent under significantly lower excitations. This is due to the fact of using low strength concrete in SMRFs. This reduces the steel-to-concrete bond strength and allows steel bars slip through concrete, consequently resulting in larger displacement of the model. Unlike Model-1, the damage evolution showed that damage in Model-2 was more limited to the joint region than the columns and beams. Furthermore, the joint panels were damaged under less shear demand (in transferring beam moments to

columns) due to the lower principal tensile strength of the joint panel, since the joint principal strength capacity primarily depends on the strength of core concrete that is related to the compressive strength of concrete [13, 35]. Joint cracks in Model-1 spread over larger area (joint panel core and transverse beams), whereas joint cracks in Model-2 spread primarily within the joint panel core.

 	 	Ground storey Joints Front and back Joints
 	 	First storey Joints Front and back Joints
Model-1 at 130% Run	Model-2 at 40% Run	Final/Incipient collapse Run
1.06 14.69 (373.03) 5.26 57.27 (254.73)	0.73 13.31 (338.19) 4.77 41.48 (184.50)	PGA, g Displacement, in (mm) Drift, % Base shear, kips (kN)

**Figure 7. Comparison of test models at final/incipient collapse stage.**

Most of the global performance assessment studies require development of damage scale that specify strength or deformation limits and expected damage conditions of structure for various performance levels. The present study developed a drift-based damage scale for the considered deficient frame as per the damage levels: slight damage, moderate to heavy damage and critical damage, compatible with FEMA (2003) [36] for building seismic performance limit state, i.e. operational, life safety and collapse prevention. The developed drift-based performance level and corresponding damage for deficient weak beam-column joint frame model are reported in Table 9. As it can be seen from Table 9, the performance limit state for the case of operational level corresponds to drift of about 1.75 % with slight damage at the column bases and beam ends. With the drift demand of about 2.57 %, the test model was in the life safety limit state with moderate to heavy damages at column beam members ends and in the joint panel regions. At a drift demand of about 4.77 % the frame was in the collapse prevention limit state, with heavy non-repairable damages at members end and severe damage at joint panel regions. The drift-based performance levels and damage mechanism can be used for the damage models and fragility functions development in the context of performance based seismic assessment and economic loss estimation studies for deficient RC frames structures.

#### 4. Conclusions

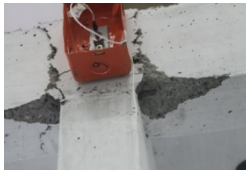
Recent reinforced concrete SMRF structures with weak beam-column joints defects were evaluated through dynamic shake table testing, in order to assess the seismic performance and ultimate damage mechanism of such class of deficient RC structures. The test models consisted of a code design SMRF model and a deficient model without transverse ties reinforcement in the beam column panels and built in low strength concrete. Unidirectional dynamic shake table tests were used to shake the test model under

various scaled excitations in order to observe seismic damage mechanism and develop drift-based performance limit states.

The following are the main conclusions from this experimental research work:

1. The code design SMRF model experienced beam and column plastic hinge formation at the member ends under extreme ground shaking and complied with the code well (1.3 times (1.06 g) more than the input design level shaking).

**Table 9. Drift based performance levels and damage scales for the weak beam-column joint frame.**

Limit State	Damage State	Damage Description	Experimental (Drift %)
LS-1 Operational	Slight Damage	<ul style="list-style-type: none"> <li>- Slight cracks at the base of columns on the ground storey.</li> <li>- Flexural cracks and slight vertical cracks at the beam-ends on both the ground storey and first storey.</li> </ul> 	1.75%
LS-2 Life Safety	Moderate to Heavy Damage	<ul style="list-style-type: none"> <li>- Flexural cracks at the base of columns widened on both the ground storey and first storey.</li> <li>- Flexural and vertical cracks at beam-ends significantly widened in beam on ground storey.</li> <li>- Damage in the joint panels on ground storey aggravated.</li> </ul> 	2.57%
LS-3 Collapse Prevention	Critical Damage to Incipient Collapse	<ul style="list-style-type: none"> <li>- Significant flexural cracks at top end and also at the bottom end of all columns and beam ends on both ground storey and first storey.</li> <li>- Joint regions on both ground storey and first storey with extreme damage and diagonal bat-like cracks.</li> <li>- Bat-like concrete cover wedge detachment from joint regions.</li> <li>- Heavy Concrete crushing and cover spalling at column base and beam ends.</li> </ul> 	4.77%

2. We observed in the current study that beam longitudinal reinforcement was subject to bar slip and bar pullout due to the use of low-strength concrete that resulted in steel-concrete bond failure.

3. Concrete structures in which joints were not provided with confining ties showed joint damageability, while cover and core concrete showed spalling upon being subject to large lateral deformation.

4. The experimental testing on the deficient weak beam-column joint RC frame revealed that such frame building typology exhibited a mixed mechanism of column and beam members hinging followed by severe beam-column joint panel damage. This also resulted in altering the damage mechanism of the structure from beam-sway to column-sway and joint panel mechanism that consequently resulted in lowering the lateral strength and displacement ductility of the structural frames. This can result in significant vulnerability of the considered frame structures. The performance states of this structure type are dictated

by the joint damage state and their reparability issues that the engineers may face following damaging earthquake events.

5. The weak beam-column joint SMRF model was able to only resist 40 % of the PGA value (0.73 g) as compared to reference code design SMRF model, which was able to resist 130 % (1.06 g).

6. The experimental tests showed that the deficient weak beam-column joint frame reached the operational limit state at a drift demand of 1.75 %, life safety limit state at a drift demand of 2.57 %, and was found to be in the incipient collapse state at a drift demand of about 4.77 %.

## References

1. Badrashi, Y.I., Ali, Q., Ashraf, M. Reinforced Concrete Buildings in Pakistan – Housing Report. 159. Earthquake Engineering Research Institute. 2010. Oakland, CA. Pp. 1–16.
2. Ahmad, N., Shahzad, A., Rizwan, M., Khan, A.N., Ali, S.M., Ashraf, M., Naseer, A., Ali, Q., Alam, B. Seismic Performance Assessment of Non-Compliant SMRF Reinforced Concrete Frame: Shake Table Test Study. *Journal of Earthquake Engineering*. 2017. Vol. 21. DOI: 10.1080/13632469.2017.1326426
3. Badrashi, Y.I., Ali, Q., Ashraf, M., Rashid, M. Seismic design characterization of RC special moment resisting frames in Pakistan-field survey to laboratory experiments. *Journal of Engineering and Applied Sciences*. 2016. 35(2). Pp. 25–32.
4. Bilham, R. Earthquakes in India and in the Himalaya: tectonic, Geodesy, and history. *Ann Geophysics* 2004. 47(2/3). Pp. 839–858.
5. Naseer, A., Khan, A.N., Hussain, Z., Ali, Q. Observed Seismic Behavior of Buildings in Northern Pakistan during the 2005 Kashmir Earthquake. *Earthquake Spectra*. 2010. Vol. 26. No. 2. Pp. 425–449. DOI: 10.1193/1.3383119
6. Arslan, M.H., Korkmaz, H.H. What is to be Learned from Damage and Failure of Reinforced Concrete Structures during Recent Earthquakes in Turkey. *Engineering Failure Analysis*. 2007. Vol. 14. No. 1. Pp. 1–22. DOI: 10.1016/j.engfailanal.2006.01.003
7. Erdil, B. Why RC Buildings Failed in the 2011 Van, Turkey, Earthquakes: Construction versus Design Practices. *Journal of Performance of Constructed Facilities*. 2016. Vol. 31. No. 3. DOI: 10.1061/(ASCE)CF.1943-5509.0000980
8. Ruiz-Pinilla, J.G., Adam, J.M., Perez-Carcel, R., Yuste, J., Moragues, J.J. Learning from RC Building Structures Damaged by the Earthquake in Lorca, Spain, in 2011. *Engineering Failure Analysis*. 2011. Vol. 68. 2016. Pp. 76–86. DOI: 10.1016/j.engfailanal.2016.05.013
9. Ates, S., Kahya, V., Yurdakul, M., Adanur, S. Damages on Reinforced Concrete Buildings due to Consecutive Earthquakes in Van. *Soil Dynamics and Earthquake Engineering*. 2013. Vol. 53. Pp. 109–118. DOI: 10.1016/j.soildyn.2013.06.006
10. Quintana-Gallo, P., Pampanin, S., Carr, A.J., Bonelli, P. Shake Table Tests of Under Designed RC Frames for the Seismic Retrofit of Buildings – Design and Similitude Requirements of the Benchmark Specimen. *Proceedings of the New Zealand Society of Earthquake Engineering*. 2010. Paper No. 39. 12 p.
11. Stavridis, A., Koutromanos, I., Shing, P. S. Shake-Table Tests of a Three-Storey Reinforced Concrete Frame with Masonry Infill Walls. *Earthquake Engineering & Structural Dynamics*. 2012. Vol. 41. No. 6. Pp. 1089–1108. DOI: 10.1002/eqe.1174
12. Yavari, S., Elwood, K.J., Wu, C.L., Lin, S.H., Hwang, S.J., Moehle, J.P. Shaking Table Tests on Reinforced Concrete Frames without Seismic Detailing. *ACI Structural Journal*. 2013. Vol. 110. No. 6. Pp. 1000–1012.
13. Sharma, A., Reddy, G. R., and Vaze, K. K. Shake Table Tests on a Non-Seismically Detailed RC Frame Structure. *Structural Engineering and Mechanics*. 2012. Vol. 41. No. 1. Pp. 1–24. DOI: 10.12989/sem.2012.41.1.001
14. Elwood, K.J., Moehle, J.P. Shake Table Tests and Analytical Studies on the Gravity Load Collapse of Reinforced Concrete Frames. PEER Report 2003/01. Pacific Earthquake Engineering Research Center. 2003. University of California, Berkeley, Berkeley, CA. 364 p.
15. Calvi, G.M., Magenes, G., Pampanin, S. Experimental Test on a Three-Story R.C Frame Designed for Gravity Only. *Proceedings of the 12th European Conference on Earthquake Engineering*. 2002. London, UK.
16. Benavent-Climent, A., Morillas, L., Escolano-Margarit, D. Seismic Performance and Damage Evaluation of a Reinforced Concrete Frame with Hysteretic Dampers through Shake-Table Test. *Earthquake Engineering & Structural Dynamics*. 2014. Vol. 43. No. 15. Pp. 2399–2417. DOI: 10.1002/eqe.2459
17. Magliulo, G., Petrone, C., Capozzi, V., Maddaloni, G., Lopez, P., Manfredi, G. Seismic Performance Evaluation of Plasterboard Partitions via Shake Table Test. *Bulletin of Earthquake Engineering*. 2014. Vol. 12. No. 4. Pp. 1657–1677. DOI: 10.1007/s10518-013-9567
18. Koutromanos, I., Kyriakides, M., Stavridis, A.; Billington, S., Shing, P.B. Shake-Table Tests of a 3-Story Masonry-Infilled RC Frame Retrofitted with Composite Materials. *Journal of Structural Engineering, ASCE*. 2013. Vol. 139. No. 8. 2013. Pp. 1340–1351. DOI: 10.1061/(ASCE)ST.1943-541X.0000689 *Earthquake Engineering, V. 11, No. 1, pp. 69–91. DOI: 10.1007/s10518-012-9404-5* ????
19. Garcia, R., Hajirasouliha, I., Pilakoutas, K. Seismic Behaviour of Deficient RC Frames Strengthened with CFRP Composites. *Engineering Structures*. 2010. Vol. 32. No. 10. Pp. 3075–3085. DOI: 10.1016/j.engstruct.2010.05.026
20. Dolce, M., Cardone, D., Ponzo, F. Shaking-Table Tests on Reinforced Concrete Frames with Different Isolation Systems. *Earthquake Engineering and Structural Dynamics*. 2007. Vol. 36. No. 5. Pp. 573–596. DOI: 10.1002/eqe.642
21. Hashemi, A., Mosalam, K.M. Shake-Table Experiment on Reinforced Concrete Structure Containing Masonry Infill Wall. *Earthquake Engineering and Structural Dynamics*. 2006. Vol. 35. No. 14. Pp. 1827–1852. DOI: 10.1002/eqe.612
22. Pinto, A., Varum, H., Molina, J. Experimental Assessment and Retrofit of Full-Scale Models of Existing RC Frames. *Proceedings of the 12th European Conference on Earthquake Engineering*. 2002. London, UK.
23. Hakuto, S., Park, R., Tanaka, H. Seismic Load Tests on Interior and Exterior Beam-Column Joints with Substandard Reinforcing Details. *ACI Structural Journal*. 2002. Vol. 97. No. 1. Jan.-Feb. Pp. 11–25.
24. Zarnic, R., Gostic, S., Crewe, A.J., Taylor, C.A. Shaking Table Tests of 1:4 Reduced-Scale Models of Masonry Infilled Reinforced Concrete Frame Buildings. *Earthquake Engineering & Structural Dynamics*. 2001. Vol. 30. No. 6. DOI: 10.1002/eqe.39
25. Beres, A., Pessiki, S., White, R., Gergely, P. Implications of Experiments on the Seismic Behaviour of Gravity Load Designed RC Beam-to-Column Connections. *Earthquake Spectra*. 1996. Vol. 12. No. 2. Pp. 185–198. DOI: 10.1193/1.1585876

26. Bracci, J., Reinhorn, A., Mander, J. Seismic Retrofit of Reinforced Concrete Buildings Designed for Gravity Loads: Performance of Structural Model. ACI Structural Journal. 1995. Vol. 92. No. 6. Nov.-Dec. Pp. 711–723.
27. Aycardi, L.E., Mander, J.B.; Reinhorn, A.M. Seismic Resistance of Reinforced Concrete Frame Structures Designed Only for Gravity Loads-Experimental Performance of Subassemblages. ACI Structural Journal. 1994. Vol. 91. No. 5. Pp. 552–563.
28. El-Attar, A.G., White, R.N., Gergely, P. Shake Table Test of a 1/6 Scale Two Story Lightly Reinforced Concrete Building. Technical Report NCEER-91 0017I, National Center for Earthquake Engineering Research (NCEER). 1991. Buffalo, NY. 118 p.
29. BCP (Building Code of Pakistan: Seismic Provisions). 2007. Ministry of Housing and Works, Islamabad, Pakistan. 302 p.
30. UBC (Uniform Building Code). International Conference of Building Officials. 1997 Whittier, CA.
31. ACI (American Concrete Institute). Building code requirements for structural concrete. ACI 318. Farmington Hills. 2014. MI: ACI.
32. Morcarz, P., Krawinkler, H. Theory and Application of Experimental Model Analysis in Earthquake Engineering. 1981. Technical Report Report No. 50, CA, 1981, 272 pp.
33. Ahmad, N., Rashid, M., Waqas, A. Quasi-static cyclic tests on special moment resisting beams. Technical Report, Earthquake Engineering Center. 2016. UET Peshawar, Khyber Pakhtunkhwa, Pakistan.
34. Rashid, M. 2016 "Earthquake Induced Damages in Modern Reinforced Concrete Special Moment Resisting Frames: Repair-ability and Cost Implications" MSc Thesis, Civil Engineering Department University of Engineering and Technology Peshawar, Pakistan.
35. Pampanin, S., Calvi, G.M., Moratti, M. "Seismic Behavior of R.C. Beam-Column Joints Designed for Gravity Only. Proceedings of the 12<sup>th</sup> European Conference on Earthquake Engineering. 2002. Paper No. 726, London, UK. Pp. 1–10.
36. FEMA. "NEHRP Recommended Provisions for Seismic Regulations for New Buildings." FEMA 450, Federal Emergency Management Agency. 2003. Washington, DC.

**Information about authors:**

**Muhammad Rizwan, PhD**

E-mail: [rizwan.civil@suit.edu.pk](mailto:rizwan.civil@suit.edu.pk)

**Naveed Ahmad, PhD**

ORCID: <https://orcid.org/0000-0003-1275-8380>

E-mail: [naveed.ahmad@uetpeshawar.edu.pk](mailto:naveed.ahmad@uetpeshawar.edu.pk)

**Akhtar Naeem Khan, PhD**

E-mail: [drakhtarnaem@uetpeshawar.edu.pk](mailto:drakhtarnaem@uetpeshawar.edu.pk)

*Received 27.03.2020. Approved after reviewing 28.06.2022. Accepted 01.07.2022.*



Research article

UDC 691.54; 691.3

DOI: 10.34910/MCE.116.2



## Structure and properties of cement systems with additives of calcined clay and carbonate rocks

T.A. Nizina , A.S. Balykov , V.V. Volodin , V.M. Kyashkin 

National Research Mordovia State University, Saransk, Republic of Mordovia, Russia

✉ [artbalrun@yandex.ru](mailto:artbalrun@yandex.ru)

**Keywords:** cements, additives, calcined clay, carbonate rocks, mixtures, hydration, microstructure, X-ray diffraction, calcium compounds, hardening, compressive strength, optimization

**Abstract.** Currently, one of the primary areas of technical progress in the field of construction is creating modern high performance concretes based on modified cement binders using various chemical and mineral additives that allow effective control of the structure formation and properties of material. The stock of the conventional additives for cement systems is failing to meet the increasing demand, which is related to territorial limitations and high cost of the most popular and efficient mineral modifiers (silica fume, metakaolin, fly ash, granulated slag, etc.). In this respect, thermally activated polymineral clays used as individual mineral additives and in complexes with carbonate rocks are promising for many regions of the Russian Federation, including the Republic of Mordovia. The paper presents results of studying the patterns in which mineral additives obtained on the basis of local raw materials of the Republic of Mordovia (calcined polymineral clay, dolomite and thermally activated mixture of clay and limestone) influence the technological characteristics of plasticized cement paste, phase composition and physical-mechanical properties of cement stone. Optimal dosages of mineral additives of calcined clay and thermally activated mixture of clay and limestone were identified: they did not exceed 19 and 12 % by binder weight, respectively. These dosages improved strength characteristics of cement systems in comparison with the control composition without the additives. X-ray powder diffraction established that using the developed mineral additives based on calcined polymineral clay and carbonate rocks increased hydration rate of Portland cement and allowed a targeted guidance of the cement stone phase composition: optimizing the ettringite concentration, reducing the number of the weakest and corrosion-exposed Portlandite crystals, increasing the density and strength of the bulk of calcium hydrosilicates by shifting the balance towards an increased content of highly dispersive low basic phases of C–S–H(I) type instead of high basic C–S–H(II) compounds. All of these factors determined the chemical efficiency of these mineral modifiers in cement systems.

**Citation:** Nizina, T.A., Balykov, A.S., Volodin, V.V., Kyashkin, V.M. Structure and properties of cement systems with additives of calcined clay and carbonate rocks. Magazine of Civil Engineering. 2022. 116(8). Article no. 11602. DOI: 10.34910/MCE.116.2

### 1. Introduction

The late 20<sup>th</sup> century and early 21<sup>st</sup> century were marked by revolutionary changes in concrete technology [1–6], which was and is one of the main building materials. The most important achievements in the field of cement concretes were those that broadened the understanding of processes taking place at the micro-level and promoting improved primary characteristics of the material – strength, deformability, corrosion resistance, etc. [7, 8]. Among them were scientific justification of cement hydration processes and development of scientific bases for modifying cement systems with chemical and mineral additives that

allowed for efficient control over concrete structure formation at all stages of technology ensuring the high quality of products and structures based on it [9–16].

Out of many types of mineral modifiers for the compositions of high-strength cement systems, highly dispersive pozzolanic additives have increased efficiency. These additives contain amorphous silica or alumina and have high reactive activity: condensed silica fume, high-dispersive fly ash of heat power plants with a minimal content of non-combusted residues, blast-furnace granulated slag, etc. [9, 10, 17–20]. It was confirmed by the results of the authors' studies [21–24].

One of the most efficient pozzolanic additives is metakaolin [25–32] representing a product of thermal treatment of mono-mineral kaolinite clays  $\text{Al}_2(\text{OH})_4[\text{Si}_2\text{O}_5]$  or  $\text{Al}_2\text{O}_3 \cdot 2\text{SiO}_2 \cdot 2\text{H}_2\text{O}$  within the range of 650–800 °C. Removal of about 14 wt. % of chemically bonded water results in the destruction of the initial crystalline structure and formation of the amorphous phase (metakaolinite). Calcination at a higher temperature (900–1000 °C) promotes the mullite formation by transformation the crystalline grid of metakaolinite with the detachment of  $\gamma\text{-Al}_2\text{O}_3$ . At the same time, it should be noted that the high cost of the resulting enriched raw materials, the large specific surface requiring the use of plasticizers, and the growing needs of the paper and medical industries that are also kaolin consumers cause a low degree of its application in the cement industry. Moreover, the kaolin reserves are limited both spatially and quantitatively. According to [33], only 3 % of the global kaolin reserves are found in Russia that occupies about 1/9 of the land area of the whole world.

In this connection, it is important to create an efficient substitute for deficient and expensive imported mineral modifiers with cheaper additives based on common local raw materials. In this respect, thermally activated polymineral clays used as individual mineral additives and in complex with other modifiers are the most promising for many regions of the Russian Federation, including the Republic of Mordovia.

The papers [34–40] were defined the optimal parameters for baking polymineral clays based on the evaluation of their reactivity depending on the chemical and mineralogical composition of raw materials. It has been found that the initial products of dehydration and thermal destruction of clay minerals with a partially restructured (meta-stable) crystalline grid are of increased activity. A transition to an active form of most clay minerals (kaolinite, montmorillonite, illite, bentonite, etc.) was reached within 400–800 °C.

Apart from active mineral additives, an important component of modern concretes is relatively chemically inert additives (fillers) of carbonate rocks such as limestones, dolomitic limestones, and dolomites [41]. However, the lack of reactivity of such additives is doubtful, which was proved by researchers [42] who studied hydration of  $\text{C}_3\text{S}$  in the presence of a superplasticizer and  $\text{CaCO}_3$  using calorimetry. As a result of the application of highly dispersive limestone the additional centers of crystallization of new formations in cement systems was installed. The papers [43–46] showed that the efficiency of additives of carbonate rocks is increased in the presence of aluminosilicate components that, in addition to tricalcium aluminate contained in cement, can be such aluminum-containing mineral additives, for example, as slags, fly ashes, thermally activated clays, etc. In this connection, a relevant trend is the combined use of thermally activated clays and carbonate rocks in the formulations of modified cement composites.

Thus, according to the results of literature review, it has been found that the resources of currently used additives for cement systems do not meet the increasing demand, which is related to territorial limitation and high cost of the most popular and efficient mineral modifiers (silica fume, metakaolin, fly ash, blast-furnace granulated slag). Currently, most studies in the area of aluminosilicate modifiers carried out by foreign and national scientists are dedicated to the efficiency of the calcination product of kaolinite monomineral clays (metakaolin). At the same time, such sedimentary rocks as polymineral low-kaolinite clays, widely distributed in many regions of the Russian Federation, are not considered as components of complex additives for cement systems. Of particular interest at present is the use of thermally activated mixtures of polymineral clays and carbonate rocks (limestones, dolomites) as complex additives in the formulations of cement systems. The highest attention in creating efficient complex modifiers based on calcined clays and carbonate rocks must be paid to studying their physical-chemical and technological compatibility between each other, with Portland cements, superplasticizers, other components of the formulation with identification of synergistic effects. It is also required to have detailed studies of the effects of the chemical and mineral compositions of both clays and carbonate rocks on the structure formation of cement stone and properties of modified cement concretes of various types.

The aim of the current research was to establish the patterns of influence of mineral additives based on calcined polymineral clay and carbonate rocks of the Republic of Mordovia on the structure formation and physical-mechanical properties of plasticized cement systems with the identification of the most effective modifiers. To achieve this aim, the following tasks were solved:

- mineralogical (phase) composition of the initial clay and carbonate rocks was established;

- the effect of dosages of mineral additives based on calcined clay and carbonate rocks on the mobility of plasticized cement paste was studied;
- the influence of mineral additives based on thermally activated clay and carbonate rocks on the phase composition and physical-mechanical properties of cement stone was studied;
- interrelations and regularities in the “composition – structure – property” system were revealed, which allow optimizing the formulations of modified cement compositions to achieve the required levels of technological and physical-mechanical characteristics.

## 2. Materials and methods

### 2.1. Materials

The primary component of binder in the formulations of cement systems was Portland cement CEM I 42.5 R (PC) manufactured by Mordovtsement PJSC (Russian State Standard GOST 31108). Melflux 5581 F polycarboxylate superplasticizer was used as modifier using in complexes with the following types of mineral additives:

1. thermally activated clay of the Nikitsky deposit (TCN) (temperature and time of calcination: 700 °C and 2 hours;  $S_{ss} = 7800 \text{ cm}^2/\text{g}$  (grinding for 1 hour)) located in the north-western part of Saransk, the Republic of Mordovia, the Russian Federation;
2. dolomite of the Yelnikovskiy deposit (DY) ( $S_{ss} = 4450 \text{ cm}^2/\text{g}$  (grinding for 3 hours)) located near the village of Budayevo, Yelnikovskiy district, the Republic of Mordovia, the Russian Federation;
3. thermally activated mixture of Nikitsky clay and limestone of the Atemarsky deposit (TM(CN+LA)) (clay to limestone ratio = 2/1; temperature and time of calcination: 700 °C and 2 hours) located near the village of Atemarsky, Lyambirskiy district, the Republic of Mordovia, the Russian Federation.

This ratio of clay and carbonate rock (2/1) in the thermally activated mixture was adopted as the most optimal taking into account its correspondence to the proportion of the chemical reaction of the interaction of 1 mol of alumina metakaolin with 1 mol of calcium carbonate in the presence of excess of calcium ions in a water solution with the formation of 1 mol of calcium hydromonocarboaluminate as described in [47].

### 2.2. Methods

The first stage included the study of the mineralogical (phase) composition of Nikitsky clay, Yelnikovskiy dolomite, and Atemarsky limestone.

The phase composition analysis of clay and carbonate rocks was done using X-ray powder diffraction (X-ray phase analysis). X-ray structural measurements were conducted using an Empyrean automated diffractometer by PANalytical (Netherlands) with a vertical goniometer in the radiation of a copper anode with a nickel filter ensuring suppression of the background and spectral line  $K_{\beta}$  together with the monochromator on the secondary beam. Shooting was done in the geometry according to Bragg-Brentano ( $\theta-2\theta$  scanning) using a spectral doublet  $\text{Cu } K_{\alpha 1,2}$  with weighted average wavelength  $\lambda = 1.5406 \text{ \AA}$ . X-ray powder diffraction patterns were obtained using PIXcel<sup>3D</sup> two-coordinate semiconductor detector operating in the linear detector mode.

Qualitative phase analysis was done in semi-automatic mode using the HighScore Plus software linked with the base of the International Center for Diffraction Data ICDD PDF-2. Matches between the position and intensity of specimen reflexes and the card of a respective standard were searched. In the case of automatic selection of a large number of standard phases by the software from the PDF-2 library, the results were additionally specified in manual mode.

To specify the concentration and primary structural characteristics of the identified phases of the Nikitsky deposit clay, full-profile Rietveld analysis was used (quantitative X-ray phase analysis). The method was to calculate the theoretical model of the diffraction pattern using the structural models of phase components of the analyzed powder and reduce the calculated profile of the model diffraction pattern to the profile of the experimental diffraction pattern when varying profile and structural parameters and evaluating the level of discrepancy by the least square method. In order to find the relative concentration of crystalline phases of Atemarsky limestone and Yelnikovskiy dolomite, the method of corundum numbers was used.

The second stage found the effects of dosages of mineral additives (MA) of the thermally activated Nikitsky clay, Yelnikovskiy dolomite and Atemarsky limestone on the flowability of plasticized cement paste and physical-mechanical properties of cement stone (average density in normal humidity conditions at the age of 28 days, compressive strength at the age of 1, 7 and 28 days). The study was carried out for cement

systems with the Melflux superplasticizer dosage of 1 % by weight of binder (Portland cement (PC) + mineral additive (MA)) and water-binder ratio  $W/B = W/(PC + MA) = 0.21$  with varying content of used mineral modifiers in compositions within 0–20 % of binder weight (PC + MA) with increment of 5 % (Table 1).

Analysis of changes in the flowability of the plasticized cement paste depending on the content of mineral additives was done using a mini-cone (ring of the Vicat apparatus under the Russian State Standard GOST 310.3). The optimal dosage of the mineral modifier was deemed to be the amount that ensures the required consistency of cement paste defined by the mini-cone spread diameter of at least 250–255 mm.

The compression strength of cement stone was measured using Wille Geotechnik® press (13-PD/401 model). The primary parameters were configured and obtained experimental results were recorded using the GEOSYS 8.7.8 software.

**Table 1. The researched compositions of cement systems.**

Composition number	Portland cement	Type of mineral additives		
		TCN	DY	TM(CN+LA)
% by weight of binder (Portland cement + mineral additive)				
1	95	5	–	–
2	90	10	–	–
3	85	15	–	–
4	80	20	–	–
5	95	–	5	–
6	90	–	10	–
7	85	–	15	–
8	80	–	20	–
9	95	–	–	5
10	90	–	–	10
11	85	–	–	15
12	80	–	–	20
Control	100	–	–	–

The third stage included the study of the effects of mineral additives based on thermally activated Nikitsky clay, Yelnikovsky dolomite, and Atemarsky limestone on the phase composition of cement stone aged 28 days using the X-ray phase analysis method. As study subjects, in addition to the non-modified composite of control composition, cement systems were selected, which had the dosage of mineral additives TCN, DY and TM (CN+LA) of 20 % of binder weight (PC + MA). The primary controlled parameters were as follows:

1. the level of Portland cement hydration ( $\alpha$ ) evaluated by the decrease in the intensity of one of the primary reflexes  $C_3S$  for  $d = 1.76\text{--}1.77 \text{ \AA}$  ( $2\theta = 51.6\text{--}51.9^\circ$ ) in the hydrated powder samples of cement stone at the studied moment of time relative to the samples of the initial binder (Portland cement + mineral additive) until hydration;

2. the relative amount of Portlandite ( $Ca(OH)_2$ ) evaluated by comparing the intensity of primary reflexes for  $d = 4.94\text{--}4.96 \text{ \AA}$  ( $2\theta = 17.87\text{--}17.94^\circ$ ) and  $d = 1.93\text{--}1.94 \text{ \AA}$  ( $2\theta = 46.8\text{--}47.0^\circ$ ) for powder samples of cement stone of modified and control compositions;

3. the relative content of ettringite ( $Ca_6Al_2(SO_4)_3(OH)_{12} \cdot 26H_2O$ ) evaluated by the ratio of the intensity of one of the primary reflexes for  $d = 9.80\text{--}9.84 \text{ \AA}$  ( $2\theta = 8.98\text{--}9.02^\circ$ ) for powder samples of cement stone of modified and control compositions;

4. the relative content of low basic (C–S–H(I)) and high basic (C–S–H(II)) calcium hydrosilicates evaluated by comparing the intensities of one of the primary reflexes  $\alpha\text{-CS}$  ( $d = 3.23\text{--}3.25 \text{ \AA}$  and  $2\theta = 27.4\text{--}27.6^\circ$ ) and  $\beta\text{-CS}$  ( $d = 2.97\text{--}2.99 \text{ \AA}$  and  $2\theta = 29.9\text{--}30.1^\circ$ ) for C–S–H(I) and  $\beta\text{-C}_2\text{S}$  ( $d = 2.79\text{--}2.80 \text{ \AA}$  and  $2\theta = 31.9\text{--}32.1^\circ$ ) for C–S–H(II) in powder samples of cement stone of modified and control compositions calcined at 980–1000 °C.

### 3. Results and Discussion

#### 3.1. Phase composition of the initial components of mineral additives

The results of qualitative and quantitative X-ray phase analysis to determine the primary crystalline phases and their relative concentrations for clay of the Nikitsky deposit are given in Table 2. It was found that the phase composition of the studied clay rock was represented predominantly by minerals of the kaolinite and illite (hydromicas) groups, as well as by quartz modifications, feldspars, and gypsum at their relative content in the overall mass of crystalline phases (wt. %): 39.8; 23.1; 19.8; 14.2 and 3.1, respectively, i.e. the represented clay was polymineral.

**Table 2. Phase composition of Nikitsky deposit clay (before calcination).**

Crystalline phase	Kaolinite	Illite group (hydromicas)	Quartz modifications	Feldspars	Gypsum
Phase content, wt. %	39.8	23.1	19.8	14.2	3.1

The mineralogical composition of the Yelnikovskiy deposit dolomite was represented by phases of the dolomite  $\text{CaMg}(\text{CO}_3)_2$  and calcite  $\text{CaCO}_3$  with the relative phase contents of 52 wt. % and 48 wt. % for dolomite and calcite, respectively. The phase composition of the Atemarskiy deposit limestone was predominantly represented by calcite  $\text{CaCO}_3$  with inclusions of quartz  $\text{SiO}_2$  with the relative phase contents of 96 wt. % and 4 wt. %, respectively (Table 3).

**Table 3. Phase composition of carbonate rocks.**

Type of carbonate rocks	Content of crystalline phases, wt. %		
	Calcite	Dolomite	Quartz modifications
Dolomite of the Yelnikovskiy deposit	48	52	–
Limestone of the Atemarskiy deposit	96	–	4

#### 3.2. Effects of mineral additives dosages on the flowability of plasticized cement paste and physical-mechanical properties of cement stone

The study results confirmed the thickening capability of applied mineral additives increasing in the row of Yelnikovskiy dolomite – thermally activated Nikitskiy clay – thermally activated mixture of Nikitskiy clay and Atemarskiy limestone. Dependencies was found (Fig. 1), according to which the production of modified cement paste of required flowability (spread diameter of at least 250–255 mm) was possible for the contents of DY, TCN and TM(CN+LA) of no more than 18, 11 and 9 % of binder weight, respectively. If these dosages of applied modifiers were increased, this resulted in a significant drop in the flowability of cement systems indicated by a bend with an increased angle of inclination to the X-axis of respective curves expressing dependencies between the content of mineral additives and the mini-cone spread diameter of cement paste.

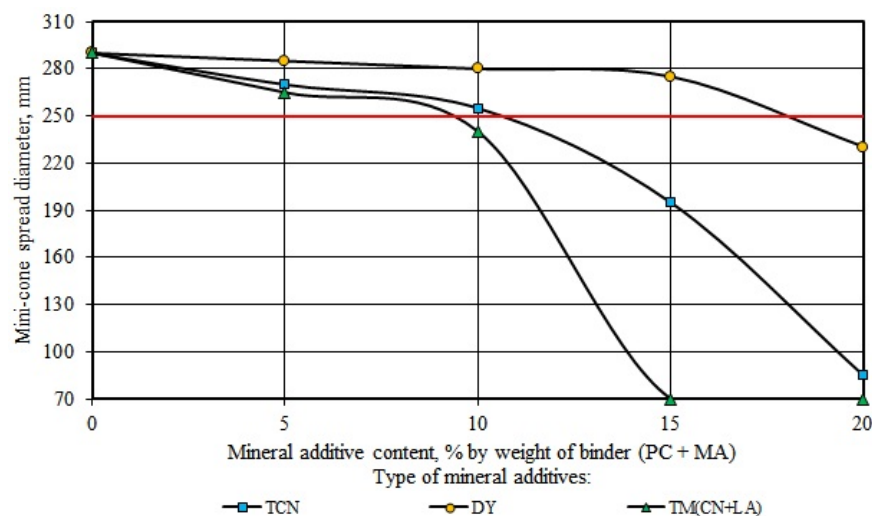


**Figure 1. Influence of the type and dosage of mineral additives on the cement paste flowability.**

Figs. 2 and 3 represent the study results for the effects of the dosages of mineral additives on the primary physical-mechanical properties of cement stone – average density in normal humidity conditions at the age of 28 days, compression strength at the age of 1, 7 and 28 days.

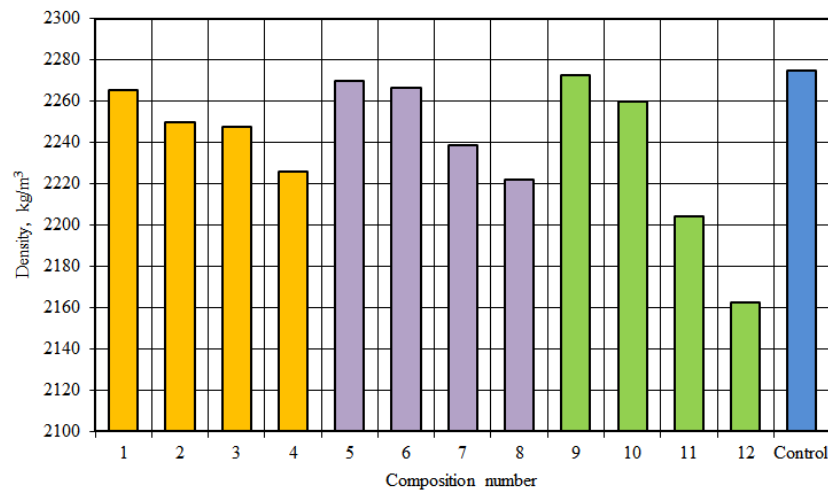


**Figure 2. Average density of the researched cement paste compositions (Table 1).**

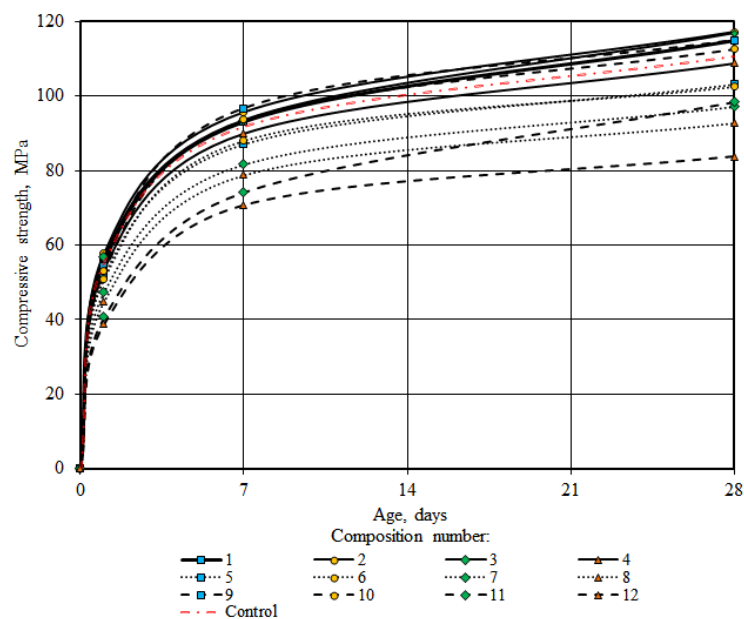


**Figure 3. Compressive strength growth kinetics of the researched cement paste compositions.**

According to the data (Fig. 2), the average density of cement stone for compositions with 5 % of mineral additives of thermally activated Nikitsky clay, Yelnikovskiy dolomite and the thermally activated mixture of Nikitsky clay and Atemarsky limestone was 2265, 2270 and 2272 kg/m<sup>3</sup>, respectively (compositions 1, 5, 9). This was close to a similar indicator for the control additive-free composition (2275 kg/m<sup>3</sup>). It was found that when the dosages of mineral modifiers were increased, the average density of cement stone was reduced insignificantly. It was reaching the minimal values in compositions 4, 8 and 12 with the content of TCN, DY and TM(CN+LA) of 20 % of binder weight (PC + MA) – 2226, 2222 and 2163 kg/m<sup>3</sup>, which is 2.2, 2.3 and 4.9 % less than the control composition. The recorded decrease in the average density of cement stone can be caused by the reduced flowability and compaction efficiency of cement paste when the content of TCN, DY, and TM(CN+LA) additives in the compositions is increased, which have a thickening effect on cement systems.

The results of experimental studies (Fig. 3) showed that the compositions with TCN, DY and TM(CN+LA) mineral additives under study differed in high rates of increasing cement stone compression strength at the age of 1 and 7 days: 41–50 and 75–86 % of the strength at the age of 28 days, respectively.

Data analysis in Fig. 3 showed that when using the additives of calcined polymineral Nikitsky clay and thermally activated mixture of Nikitsky clay and Atemarsky limestone, the highest compression strength of cement stone at the age of 28 days was reached in compositions 2 and 9 (Table 1) with these modifiers having the content of 10 and 5 % of binder weight (PC + MA) – 117.2 and 114.9 MPa, respectively. The analysis results in Fig. 4 showed the optimal content of TCN and TM(CN+LA) mineral additives promoting increased strength of cement systems – max. 19 and 12 % of binder weight, respectively. With the indicated levels of dosages, mineral additives based on calcined Nikitsky clay and thermally active mixture of Nikitsky clay and Atemarsky limestone were active and had increased physical-chemical efficiency. Exceeding

these content levels of mineral additives led to decreased compressive strength of cement stone below the level typical of the control composition. The results obtained are confirmed by data of a number of publications [33, 36], which showed that individual additives of calcined polymineral clays to Portland cement, depending on the activation temperature and grinding fineness, contributed to more significant increase in the strength of cement stone than similar additives of high-quality metakaolin.

The study results (Figs. 3 and 4) showed that Yelnikovskiy dolomite was an inert mineral additive. The increased content of this filler from 5 to 20 % of binder weight (PC + MA) in the formulation of cement systems resulted in consistent reduction of cement stone compression strength from 103.1 to 92.8 MPa, respectively. The achieved compressive strength level of the researched cement stone compositions under study by 7–16 % was less than that of the control composition (110.6 MPa).

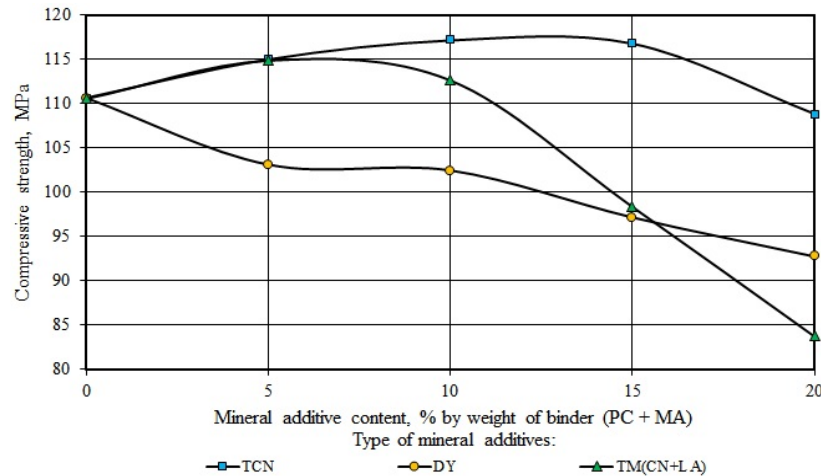


**Figure 4. Influence of the type and dosage of mineral additives on the compressive strength of cement paste at the age of 28 days.**

### 3.3. Influence of mineral additives on the cement paste phase composition

Fig. 5 represents the X-ray diffraction patterns of cement stone powders aged 28 days for compositions 4, 8, 12 containing 20 % of mineral additives and for the control additive-free composition (Table 1).

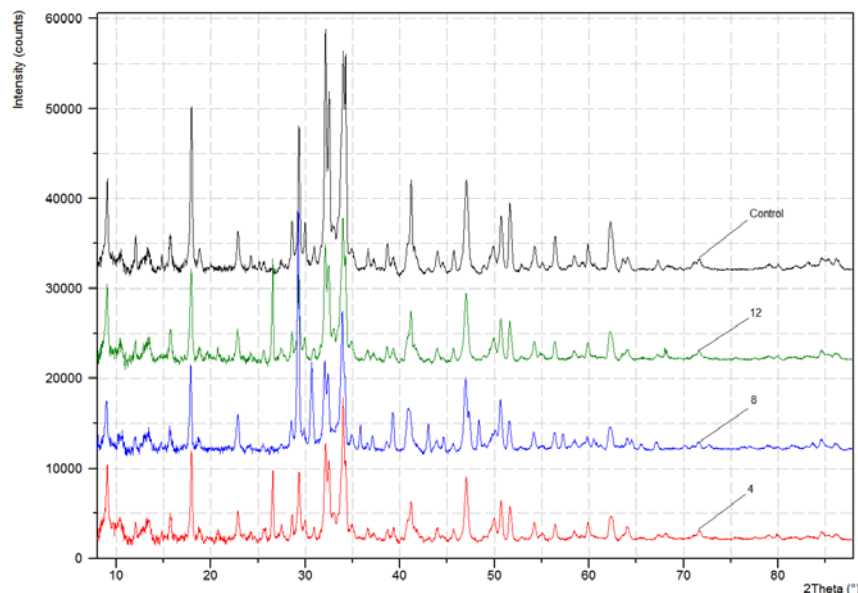


**Figure 5. X-ray powder diffractograms of the researched cement paste compositions at the age of 28 days (Nos. 4, 8, 12 and control additive-free composition).**

The qualitative analysis of the diffraction patterns (Fig. 5) showed that the crystalline part of the cement stone structure of both control additive-free composition and the compositions modified by mineral additives Nos. 4, 8, 12 was represented by the following minerals:

1. the phases of Portland cement clinker not subject to the hydration reaction: alite ( $\text{Ca}_3\text{SiO}_5$ ) with number of inter-plane distances  $d = [\dots; 3.04; \dots; 2.78; 2.75; \dots; 2.62; \dots; 2.19; \dots; 1.77 \text{ \AA}; \dots]$ ; belite ( $\beta\text{-Ca}_2\text{SiO}_4$ ) with  $d = [\dots; 2.89; \dots; 2.79; 2.75; 2.72; \dots; 2.62; \dots; 2.19 \text{ \AA}; \dots]$ ;

2. the hydrate phases: Portlandite ( $\text{Ca}(\text{OH})_2$ ) with  $d = [4.95; 3.12; 2.64; \dots; 1.93; 1.80; 1.69; \dots; 1.49 \text{ \AA}; \dots]$ ; ettringite ( $\text{Ca}_6\text{Al}_2(\text{SO}_4)_3(\text{OH})_{12}\cdot 26\text{H}_2\text{O}$ ) with  $d = [9.82; \dots; 5.65; \dots; 4.72; \dots; 3.89; \dots; 3.48; \dots; 2.78; \dots; 2.57; \dots; 2.21 \text{ \AA}; \dots]$ .

Semi-qualitative X-ray phase analysis of cement stone powders aged 28 days (Table 4) showed that the introduction of mineral additives of thermally activated polymineral Nikitsky clay, Yelnikovsky dolomite and the thermally activated mixture of Nikitsky clay and Atemarsky limestone in cement systems increased hydration levels of Portland cement as compared to the control additive-free composition from 65 to 79, 82 and 77 %, respectively, i.e., by 18–26 %. In this manner, the data showed an intensified processes of Portland cement hydration in the presence of TCN, DY and TM(CN+LA) mineral additives in the cement systems, which was caused by the presence of reactive minerals (kaolinite and illite) in the phase composition of Nikitsky clay, and by the capability of Yelnikovsky dolomite minerals to act as the centers of crystallization of new formations. The established regularities are consistent with the data of other authors, in particular [34].

**Table 4. XRD results of the researched cement paste compositions at the age of 28 days.**

Composition number	Binder composition (Portland cement + mineral additive)	Hydration degree of Portland cement, %	Relative ettringite content $\text{Ca}_6\text{Al}_2(\text{SO}_4)_3(\text{OH})_{12}\cdot 26\text{H}_2\text{O}$	Relative portlandite content $\text{Ca}(\text{OH})_2$	Relative content of low basic calcium hydrosilicates C-S-H(I)	Relative content of high basic calcium hydrosilicates C-S-H(II)
Control	100 % PC	65	100	100	100	100
4	80 % PC + 20 % TCN	79	80	73	255	59
8	80 % PC + 20 % DY	82	62	91	108	130
12	80 % PC + 20 % TM(CN+LA)	77	94	75	238	94

The analysis of experimental data represented in Table 4 showed the content of ettringite ( $\text{Ca}_6\text{Al}_2(\text{SO}_4)_3(\text{OH})_{12}\cdot 26\text{H}_2\text{O}$ ) reduced by 6–38 % in the cement stone samples with additives of calcined polymineral Nikitsky clay, Yelnikovsky dolomite and the thermally activated mixture of Nikitsky clay and Atemarsky limestone relative to the control composition. Decreasing the concentration of the tri-sulfate form of calcium hydrosulfoaluminate could be related to the changes occurring in the composition of the liquid phase (pH, the concentration of  $\text{Ca}^{2+}$ ,  $\text{Al}^{3+}$ ,  $\text{SO}_4^{2-}$  ions, etc.) when hardening cement stone in the presence of these modifiers. This promoted the shift of the balance to the formation of compounds of another chemical and mineralogical nature (calcium hydrosilicates,  $\text{AF}_m$ -phases, etc.).

Silicate phases of Portland cement 500-D0-N amounted to 78 % ( $\text{C}_3\text{S} = 60.4$  % and  $\beta\text{-C}_2\text{S} = 17.5$  %), which caused the predominance of calcium silicate hydrate phases (C–S–H) in the hardening cement stone. Calcium hydrosilicates formed in normal conditions were characterized by widely varying compositions and degrees of crystallization, so they were conditionally divided into two groups [48, 49]: those who had high strength, low basic C–S–H(I) with  $\text{CaO}/\text{SiO}_2 \leq 1.5$  and less durable high basic C–S–H(II) with  $\text{CaO}/\text{SiO}_2 > 1.5$ .

The results of experimental studies given in Table 4 showed that introducing mineral additives of Nikitsky clay, Yelnikovsky dolomite and the thermally activated mixture of Nikitsky clay and Atemarsky limestone into the formulation of cement systems promoted substantial quantitative change in the ratio between the primary hydrate phases in the cement stone – Portlandite and calcium hydrosilicates of various basicity. In particular, as compared to the control composition, in the powder samples of cement stone with TCN and TM(CN+LA) additives aged 28 days, the content of high basic C–S–H(II) and large low-strength crystals of Portlandite  $\text{Ca}(\text{OH})_2$  was reduced by 6–41 % and 25–27 %, respectively. At the same time, the content of fine and high strength low basic C–S–H(I) was increased 2.4–2.6 times.

The discovered change of balance between hydrate phases in the cement stone with additives of Nikitsky clay, Yelnikovsky dolomite and the thermally activated mixture of Nikitsky clay and Atemarsky limestone towards a rise in the volume of the most durable and most stable low-basic C–S–H(I) with  $\text{CaO/SiO}_2 \leq 1.5$  instead of primary crystalline hydrates such as the Portlandite and high-basic C–S–H(II) indicated chemical effect [50] in the action mechanism of these mineral modifiers. This chemical effect was related to the pozzolanic activity of TCN and TM(CN+LA) mineral additives in cement systems and caused by the presence of active silica-containing components in their chemical and mineralogical composition (reactive minerals with amorphized structure).

## 4. Conclusions

The following results were obtained upon the completed experimental studies:

1. Phase composition was established for the initial components of mineral additives – polymineral clay, dolomite and limestone of the Nikitsky, Yelnikovsky, and Atemarsky deposits, the Republic of Mordovia, the Russian Federation, respectively.

2. Effects were found for dosages of mineral additives based on the thermally activated clay and carbonate rocks on the mobility of plasticized cement paste and physical-mechanical properties of cement stone (average density in normal humidity conditions at the age of 28 days, compression strength at the age of 1, 7 and 28 days).

3. We found that mineral additives based on thermally activated clay and carbonate rocks have influence on the phase composition of cement stone aged 28 days.

4. Interrelations and regularities were revealed in the “composition – structure – property” system, which allow optimizing the formulations of modified cement compositions to achieve the required levels of technological and physical-mechanical characteristics. Optimal dosages of mineral additives of calcined clay and thermally activated mixture of clay and limestone were identified, the sizes of which did not exceed 19 and 12 % by binder weight, respectively, which contributed to an increase in strength characteristics of cement systems relative to the control composition without additives. At the same time, the highest compressive strength values of cement stone aged 28 days were recorded for the modifiers contents equal to 10 and 5 % by binder weight.

By generalizing the results of experimental studies, it could be noted that the use of mineral additives of thermally activated polymineral Nikitsky clay and the thermally activated mixture of Nikitsky clay and Atemarsky limestone allowed increasing the rate (level) of Portland cement hydration and consistently changing the phase composition of cement stone:

- optimizing the ettringite concentration,
- decreasing the number of the weakest and corrosion-exposed Portlandite crystals,
- increasing the density and strength of the primary mass of newly formed calcium hydrosilicates by shifting the balance towards an increased content of highly dispersive low basic C–S–H(I) phases instead of high basic C–S–H(II) compounds.

At the same time, the data given in Table 4 proved relative chemical inertness of the Yelnikovsky dolomite additive: concentrations of Portlandite and low basic C–S–H(I) phases in the cement stone sample of composition No. 8 with carbonate filler are close to those of the control composition without mineral additives.

## References

1. Okamura, H., Ouchi, M. Self-compacting concrete. *Journal of Advanced Concrete Technology*. 2003. Vol. 1. No. 1. Pp. 5–15. DOI: 10.3151/jact.1.5
2. Yazici, H., Deniz, E., Baradan, B. The effect of autoclave pressure, temperature and duration time on mechanical properties of reactive powder concrete. *Construction and Building Materials*. 2013. Vol. 42. Pp. 53–63. DOI: 10.1016/j.conbuildmat.2013.01.003
3. Zhou, M., Lu, W., Song, J., Lee, G.C. Application of Ultra-High Performance Concrete in bridge engineering. *Construction and Building Materials*. 2018. Vol. 186. Pp. 1256–1267. DOI: 10.1016/j.conbuildmat.2018.08.036
4. Kubissa, W., Simon, T., Jaskulski, R., Reiterman, P., Supera, M. Ecological High Performance Concrete. *Procedia Engineering*. 2017. Vol. 172. Pp. 595–603. DOI: 10.1016/j.proeng.2017.02.186
5. Dong, S., Zhou, D., Ashour, A., Han, B., Ou, J. Flexural toughness and calculation model of super-fine stainless wire reinforced reactive powder concrete. *Cement and Concrete Composites*. 2019. Vol. 104. Art. no. 103367. DOI: 10.1016/j.cemconcomp.2019.103367
6. Kefelegn, A., Gebre, A. Performance of self-compacting concrete used in congested reinforcement structural element. *Engineering Structures*. 2020. Vol. 214. Art. no. 110665. DOI: 10.1016/j.engstruct.2020.110665
7. Dvorkin, L., Zhitkovsky, V., Stepasyuk, Y., Ribakov, Y. A method for design of high strength concrete composition considering curing temperature and duration. *Construction and Building Materials*. 2018. Vol. 186. Pp. 731–739. DOI: 10.1016/j.conbuildmat.2018.08.014

8. Tolchkov, Yu.N., Mikhaleva, Z.A., Tkachev, A.G., Artamonova, O.V., Kashirin, M.A., Auad, M.S. The Effect of a Carbon Nanotubes-Based Modifier on the Formation of the Cement Stone Structure. *Advanced Materials and Technologies*. 2018. No. 3. Pp. 49–56. DOI: 10.17277/amt.2018.03.pp.049-056
9. Spiesz, Yu.R.P., Brouwers, H.J.H. Development of an eco-friendly Ultra-High Performance Concrete (UHPC) with efficient cement and mineral admixtures uses. *Cement and Concrete Composites*. 2015. Vol. 55. Pp. 383–394. DOI: 10.1016/j.cemconcomp.2014.09.024
10. Ghafari, E., Costa, H., Júlio, E., Portugal, A., Durães, L. The effect of nanosilica addition on flowability, strength and transport properties of ultra high performance concrete. *Materials and Design*. 2014. Vol. 59. Pp. 1–9. DOI: 10.1016/j.matdes.2014.02.051
11. Tran, N.T., Kim, D.J. Synergistic response of blending fibers in ultra-high-performance concrete under high rate tensile loads. *Cement and Concrete Composites*. 2017. Vol. 78. Pp. 132–145. DOI: 10.1016/j.cemconcomp.2017.01.008
12. Chernishov, E.M., Artamonova, O.V., Slavcheva, G.S. Nanomodification of cement-based composites in the technological life cycle. *Nanotechnologies in Construction*. 2020. Vol. 12. No. 3. Pp. 130–139. DOI: 10.15828/2075-8545-2020-12-3-130-139
13. Barabanshchikov, Yu.G., Belyaeva, S.V., Arkhipov, I.E., Antonova, M.V., Shkol'nikova, A.A., Lebedeva, K.S. Influence of superplasticizers on the concrete mix properties. *Magazine of Civil Engineering*. 2017. No. 6. Pp. 140–146. DOI: 10.18720/MCE.74.11
14. Muthalvan, R.S., Ravikumar, S., Avudaiappan, S., Amran, M., Aepuru, R., Vatin, N., Fediuk, R. The Effect of Superabsorbent Polymer and Nano-Silica on the Properties of Blended Cement. *Crystals*. 2021. Vol. 11. No. 11. Art. no. 1394. DOI: 10.3390/cryst11111394
15. Polonina, E.N., Lahayne, O., Eberhardsteiner, J., Potapov, V.V., Zhdanok, S.A., Leonovich, S.N. Nanoindentation Method for Studying the Structure of Modified Cement Stone. *Journal of Engineering Physics and Thermophysics*. 2021. Vol. 94. No. 5. Pp. 1194–1207. DOI: 10.1007/s10891-021-02400-y
16. Xiaoying, L., Jun, L., Zhongyuan, L., Li, H., Jiakun, C. Preparation and properties of reactive powder concrete by using titanium slag aggregates. *Construction and Building Materials*. 2020. Vol. 234. Art. no. 117342. DOI: 10.1016/j.conbuildmat.2019.117342
17. Kosach, A.F., Kuznetsova, I.N., Rashupkina, M.A., Pedun, G.A. Cement stone on quartz-ash-cement binder. *Nanotechnologies in Construction*. 2022. Vol. 14. No. 2. Pp. 83–88. DOI: 10.15828/2075-8545-2022-14-2-83-88
18. Rassokhin, A.S., Ponomarev, A.N., Figovsky, O.L. Silica fumes of different types for high-performance fine-grained concrete. *Magazine of Civil Engineering*. 2018. 78(2). Pp. 151–160. DOI: 10.18720/MCE.78.12
19. Amran, M., Fediuk, R., Murali, G., Avudaiappan, S., Ozbakkaloglu, T., Vatin, N., Karelina, M., Klyuev, S., Gholampour, A. Fly Ash-Based Eco-Efficient Concretes: A Comprehensive Review of the Short-Term Properties. *Materials*. 2021. Vol. 14. No. 15. Art no. 4264. DOI: 10.3390/ma14154264
20. Bily, P., Fladr, J., Chylik, R., Vrablik, L., Hrbek, V. The effect of cement replacement and homogenization procedure on concrete mechanical properties. *Magazine of Civil Engineering*. 2019. No. 2. Pp. 46–60. DOI: 10.18720/MCE.86.5
21. Nizina, T.A., Ponomarev, A.N., Balykov, A.S., Korovkin, D.I. Multicriteria optimisation of the formulation of modified fine-grained fibre concretes containing carbon nanostructures. *International Journal of Nanotechnology*. 2018. Vol. 15. No. 4–5. Pp. 333–346. DOI: 10.1504/IJNT.2018.094790
22. Balykov, A.S., Nizina, T.A., Kyashkin, V.M., Volodin, S.V. Prescription and technological efficiency of sedimentary rocks of various composition and genesis in cement systems. *Nanotechnologies in Construction*. 2022. Vol. 14. No. 1. Pp. 53–61. DOI: 10.15828/2075-8545-2022-14-1-53-61
23. Nizina, T.A., Balykov, A.S., Korovkin, D.I., Volodin, V.V. Modified fine-grained concretes based on highly filled self-compacting mixtures. *IOP Conference Series: Materials Science and Engineering*. 2019. Vol. 481. No. 1. Art. no. 012048. DOI: 10.1088/1757-899X/481/1/012048
24. Balykov, A.S., Nizina, T.A., Volodin, S.V. Optimization of technological parameters for obtaining mineral additives based on calcined clays and carbonate rocks for cement systems. *Nanotechnologies in Construction*. 2022. Vol. 14. No. 2. Pp. 145–155. DOI: 10.15828/2075-8545-2022-14-2-145-155
25. Murat, M. Hydration reaction and hardening of calcined clays and related minerals: II. Influence of mineralogical properties of the raw-kaolinite on the reactivity of metakaolinite. *Cement and Concrete Research*. 1983. Vol. 13. No. 4. Pp. 511–518. DOI: 10.1016/0008-8846(83)90010-8
26. Chakchouk, A., Samet, B., Mnif, T. Study on the potential use of Tunisian clays as pozzolanic material. *Applied Clay Science*. 2006. Vol. 33. No. 2. Pp. 79–88. DOI: 10.1016/j.clay.2006.03.009
27. Tironi, A., Trezza, M.A., Scian, A.N., Irassar, E.F. Kaolinitic calcined clays: Factors affecting its performance as pozzolans. *Construction and Building Materials*. 2012. Vol. 28. No. 1. Pp. 276–281. DOI: 10.1016/j.conbuildmat.2011.08.064.
28. Schulze, S.E., Rickert, J. Suitability of natural calcined clays as supplementary cementitious material. *Cement and Concrete Composites*. 2019. Vol. 95. Pp. 92–97. DOI: 10.1016/j.cemconcomp.2018.07.006
29. Kocak, Y. Effects of metakaolin on the hydration development of Portland–composite cement. *Journal of Building Engineering*. 2020. Vol. 31. Art. no. 101419. DOI: 10.1016/j.jobe.2020.101419
30. Usanova, K., Barabanshchikov, Yu.G., Krasova, A.V., Akimov, S.V., Belyaeva, S.V. Plastic shrinkage of concrete modified by metakaolin. *Magazine of Civil Engineering*. 2021. No. 3. Article no. 10314. DOI: 10.34910/MCE.103.14
31. Wang, Y.Y., Zhao, L., Zhao, J. Effects of Submicron Metakaolin on Hydration and Compressive Strength of Portland Cement Slurry. *KSCE Journal of Civil Engineering*. 2021. Vol. 25. Pp. 2631–2639. DOI: 10.1007/s12205-021-1399-5
32. Li, R., Lei, L., Sui, T., Plank, J. Effectiveness of PCE superplasticizers in calcined clay blended cements. *Cement and Concrete Research*. 2021. Vol. 141. Art. no. 106334. DOI: 10.1016/j.cemconres.2020.106334
33. Rakhimova, N., Rakhimov, R. Advances in development of calcined clays as supplementary cementitious materials. *IOP Conference Series: Materials Science and Engineering*. 2020. Vol. 890. No. 1. Art. no. 012085. DOI: 10.1088/1757-899X/890/1/012085
34. Fernandez, R., Martirena, F., Scrivener, K.L. The origin of the pozzolanic activity of calcined clay minerals: A comparison between kaolinite, illite and montmorillonite. *Cement and Concrete Research*. 2011. Vol. 41. No. 1. Pp. 113–122. DOI: 10.1016/j.cemconres.2010.09.013
35. Volodchenko, A.A., Lesovik, V.S., Cherepanova, I.A., Volodchenko, A.N., Zagorodnjuk, L.H., Elistratkin, M.Y. Peculiarities of non-autoclaved lime wall materials production using clays. *IOP Conference Series Materials Science and Engineering*. 2018. Vol. 327. No. 2. Art. no. 022021. DOI: 10.1088/1757-899X/327/2/022021

36. Rakhimov, R.Z., Rakhimova, N.R., Gayfullin, A.R., Morozov, V.P. Effect of the Addition of Thermally Activated Heavy Loam to Portland Cement on the Properties of Cement Stone. *Inorganic Materials: Applied Research*. 2018. Vol. 9. No. 4. Pp. 679–686. DOI: 10.1134/S2075113318040330
37. Sabir, B.B., Wild, S., Bai, J. Metakaolin and calcined clays as pozzolans for concrete: a review. *Cement and Concrete Composites*. 2001. Vol. 23. No. 6. Pp. 441–454. DOI: 10.1016/S0958-9465(00)00092-5
38. Tironi, A., Castellano, C.C., Bonavetti, V.L., Trezza, M.A., Scian, A.N., Irassar, E.F. Kaolinitic calcined clays – Portland cement system: Hydration and properties. *Construction and Building Materials*. 2014. Vol. 64. Pp. 215–221. DOI: 10.1016/j.conbuildmat.2014.04.065
39. Niu, X., Li, Q., Hu, Y., Tan, Y., Liu, C. Properties of cement-based materials incorporating nano-clay and calcined nano-clay: A review. *Construction and Building Materials*. 2021. Vol. 284. Art. no. 122820. DOI: 10.1016/j.conbuildmat.2021.122820
40. Balykov, A.S., Nizina, T.A., Volodin, V.V., Kyashkin, V.M. Effects of Calcination Temperature and Time on the Physical-Chemical Efficiency of Thermally Activated Clays in Cement Systems. *Materials Science Forum*. 2021. Vol. 1017. Pp. 61–70. DOI: 10.4028/www.scientific.net/MSF.1017.61
41. Demirhan, S., Turk, K., Uluggerger, K. Fresh and hardened properties of self consolidating Portland limestone cement mortars: Effect of high volume limestone powder replaced by cement. *Construction and Building Materials*. 2019. Vol. 196. Pp. 115–125. DOI: 10.1016/j.conbuildmat.2018.11.111
42. Ramezaniapour, A.M., Hooton, R.D. A study on hydration, compressive strength, and porosity of Portland-limestone cement mixes containing SCMs. *Cement and Concrete Composites*. 2014. Vol. 51. Pp. 1–13. DOI: 10.1016/j.cemconcomp.2014.03.006
43. Antoni, M., Rossen, J., Martirena, F., Scrivener K. Cement substitution by a combination of metakaolin and limestone. *Cement and Concrete Research*. 2012. Vol. 42. No. 12. Pp. 1579–1589. DOI: 10.1016/j.cemconres.2012.09.006
44. Tang, J., Wei, S., Li, W., Ma, S., Ji, P., Shen, X. Synergistic effect of metakaolin and limestone on the hydration properties of Portland cement. *Construction and Building Materials*. 2019. Vol. 223. Pp. 177–184. DOI: 10.1016/j.conbuildmat.2019.06.059
45. Hagemann, S.E., Gastaldini, A.L.G., Cocco, M., Jahn, S.L., Terra, L.M. Synergic effects of the substitution of Portland cement for water treatment plant sludge ash and ground limestone: Technical and economic evaluation. *Journal of Cleaner Production*. 2019. Vol. 214. Pp. 916–926. DOI: 10.1016/j.jclepro.2018.12.324
46. Cancio Díaz, Y., Sánchez Berriel, S., Heierli, U., Favier, A.R., Sánchez Machado, I.R., Scrivener, K.L., Martirena Hernández, J.F., Habert, G. Limestone calcined clay cement as a low-carbon solution to meet expanding cement demand in emerging economies. *Development Engineering*. 2017. Vol. 2. Pp. 82–91. DOI: 10.1016/j.deveng.2017.06.001
47. Avet, F., Snellings, R., Alujas Diaz, A., Ben Haha, M., Scrivener, K. Development of a new rapid, relevant and reliable (R3) test method to evaluate the pozzolanic reactivity of calcined kaolinitic clays. *Cement and Concrete Research*. 2016. Vol. 85. Pp. 1–11. DOI: 10.1016/j.cemconres.2016.02.015
48. Taylor, H.F.W. *Cement Chemistry*, 2<sup>nd</sup> edition. London: Thomas Telford Publishing, 1997. 459 p. DOI: 10.1680/cc.25929
49. Chen, J.J., Thomas, J.J., Taylor, H.F.W., Jennings, H.M. Solubility and structure of calcium silicate hydrate. *Cement and Concrete Research*. 2004. Vol. 34. No. 9. Pp. 1499–1519. DOI: 10.1016/j.cemconres.2004.04.034
50. Detwiler, R.J., Mehta, P.K. Chemical and physical effects of silica fume on the mechanical behavior of concrete. *ACI Materials Journal*. 1989. Vol. 86. No. 6. Pp. 609–614.

#### **Information about authors:**

**Tatyana Nizina**, Doctor of Technical Science

ORCID: <https://orcid.org/0000-0002-2328-6238>

E-mail: [nizinata@yandex.ru](mailto:nizinata@yandex.ru)

**Artemy Balykov**, PhD in Technical Science

ORCID: <https://orcid.org/0000-0001-9087-1608>

E-mail: [artbalrun@yandex.ru](mailto:artbalrun@yandex.ru)

**Vladimir Volodin**,

ORCID: <https://orcid.org/0000-0002-3008-6242>

E-mail: [volodinvv1994@gmail.com](mailto:volodinvv1994@gmail.com)

**Vladimir Kyashkin**, PhD in Physical and Mathematical Science

ORCID: <https://orcid.org/0000-0002-3413-247X>

E-mail: [kyashkin@mail.ru](mailto:kyashkin@mail.ru)

*Received 18.05.2020. Approved after reviewing 22.06.2022. Accepted 30.06.2022.*



Research article

UDC 691.32

DOI: 10.34910/MCE.116.3



## Feasibility of concrete mixtures containing coarse and/or fine recycled brick aggregates

A. El-Mir<sup>1</sup> , S. Nehme<sup>2</sup> , J. Assaad<sup>1</sup> 

<sup>1</sup> University of Balamand, Kurah, Lebanon

<sup>2</sup> Budapest University of Technology and Economics, Budapest, Hungary

✉ [joseph.assaad@balamand.edu.lb](mailto:joseph.assaad@balamand.edu.lb)

**Keywords:** brick, concrete aggregates, durability, mechanical properties, recycling

**Abstract.** This paper assesses the feasibility of concrete mixtures containing high replacement rates of fine and/or coarse waste brick aggregates. Three mixture series prepared with different water-to-cement ratios are tested for workability, compressive strength, split tensile strength, modulus of elasticity, water permeability (by capillary or under pressure), and drying shrinkage. Test results showed that the concrete properties remarkably degrade when the coarse natural aggregate fraction (i.e., retained on sieve No. 4) is fully replaced by recycled waste bricks, given their increased porosity that reduces the concrete density and weakens its skeleton. In contrast, the strength and durability remained almost unaltered when the fine natural aggregate fraction was replaced by 50 % recycled waste bricks, and considerably better than equivalent mixtures made using the same amount of recycled fine aggregates derived from hardened waste concrete.

**Citation:** El-Mir, A., Nehme, S., Assaad, J. Feasibility of concrete mixtures containing coarse and/or fine recycled brick aggregates. Magazine of Civil Engineering. 2022. 116(8). Article no. 11603. DOI: 10.34910/MCE.116.3

### 1. Introduction

The recycling of construction and demolition wastes (CDW) in infrastructure engineering works considerably increased in the past few years. Such practice proved efficient to preserve natural resources, almost proportionally to the replacement rate, while reducing the landfill debris and mitigating the carbon dioxide (CO<sub>2</sub>) emissions [1–3]. Also, this is in line with many regulation guidelines (such as Directive 2008/98/EC) and sustainable strategies established to valorize the CDW including their life cycle management and environmental impacts.

The waste concrete constitutes by far the biggest component of CDW which, after crushing, leads to the production of recycled concrete coarse aggregate (rCCA) typically larger than 5 mm size (i.e., retained on sieve No. 4) and recycled concrete fine aggregate (rCFA). The rCCA is composed of natural coarse aggregates with about 30–40 % adhered cement paste that alters the material's texture and increases water absorption [1, 2, 4]. The valorization of rCCA by partial or complete replacement of coarse aggregates in concrete works is well documented in previous studies [1–4]. The curtail in the concrete mechanical properties encountered due to rCCA additions can be mitigated by different methods such as reducing the free mixing water or incorporating supplementary cementitious materials, fibers, and polymers [5–8]. Unlike rCCA, the rCFA is generally considered as unwanted by-product generated from the CDW crushing process. This aggregate fraction is rich with hydrated cement compounds, albeit their re-hydration remains weaker than ordinary cement because of reduced compacity and crystallization degree of the new hydrates [9, 10]. The difficulty to control the poor physical properties (mostly the water absorption and contaminants) are among the main reasons that limited the use of rCFA in new construction and building materials. Several

countries and standard regulations restricted the use of rCFA to mortars intended for masonry and rendering works, applications located in non-aggressive environments, and within limited replacement rates in low-strength concrete grades [11–13].

Bricks are the second most abundant CDW component [14, 15]. Depending on the vitrification process, these are broadly divided into two categories including (1) the semipermeable ones used for ceramic stoneware and tiles having high hardness and low water absorption (i.e., 5 to 8 %) and (2) those used as building stones and roof tiles with relatively higher water absorption (i.e., 12 to 18 %) [16]. Huge amounts of waste bricks are generated each year, which represented in 2018 about 33 % of all CDW produced in Brazil and 54 % in Spain [17]. The manufacture of ceramics also generates large amounts of wastes estimated to be about 19 kg/m<sup>2</sup> of tiling product, which is equivalent to about 30 % of daily production [18]. In 2018, India produced 650 million m<sup>2</sup> of sanitary and tiling products, which generated about 12 billion tons of waste bricks [19].

Just like the waste concrete, waste bricks are generally crushed and sieved to produce recycled brick coarse aggregate (rBCA) larger than 5 mm size and recycled brick fine aggregate (rBFA). Current literature converges that the concrete strength and durability degrade with rBCA, mostly depending on the addition rates and inherent aggregate characteristics such as the hardness and porosity levels [14, 16, 20]. Cachim [21] reported that the concrete compressive strength ( $f'_c$ ) remains practically invariable when the natural coarse aggregate replacement rate by rBCA is less than 15 %. At higher rates, the drop in  $f'_c$  could reach 20 % depending on the brick types. Zhang and Zong [22] suggested that 30 % was an appropriate replacement rate, while Zhu and Zhu [16] found that  $f'_c$  could drop by 45 % when the coarse aggregate fraction is fully replaced by rBCA. Many scholars reported that the mixed use of rBCA and rBFA could improve the concrete strength, given the creation of a denser interfacial transition zone (ITZ) between the mortar and aggregate rough surface [23, 24]. Additionally, the strength gain could be attributed to pozzolanic reactions owing to the rich brick silicon dioxide (SiO<sub>2</sub>) content that promotes the calcium silicate hydrate (C-S-H) development and refines the microstructure. Toledo et al. [25] showed that the  $f'_c$  and modulus of elasticity remain almost unaffected as long as the natural sand replacement by rBFA is less than 20 %. Naceri and Hamina [26] found that finely ground waste bricks having a mean particle diameter smaller than 30 µm can be used up to 30 % cement replacement without detrimental effects on mechanical properties.

The durability of concrete mixtures containing waste bricks is of prime importance, especially knowing the inherent porous nature of such additions. Earlier studies showed that the transfer properties such as the resistance to water permeability and ingress of chloride/sulphate ions could substantially decrease when the natural coarse aggregates are replaced by rBCA [14, 16, 17]. Such phenomenon becomes however less pronounced with the use of rBFA at low replacement rates (i.e., less than 20 %), which may be attributed to the refined porous structure and pozzolanic reactions [16, 23]. Nevertheless, some scholars reported that the brick porosity might be beneficial to promote internal curing with direct consequences on hydration reactions and strength development. For instance, Khatib [27] observed that drying shrinkage could increase by only 10 % when natural sand is fully replaced by rBFA. Other studies showed that shrinkage may be twice to six times higher, due to lower restraining effect and reduced brick modulus of elasticity compared to natural aggregate [21–23]. Bravo et al. [28] noticed that durability properties such as shrinkage, sorptivity, and carbonation could be improved when reducing the mixing water added to compensate the water absorption resulting from the bricks. The resistance against freeze-thaw cycles and thermal conductivity improved due to the increased global porosity of concrete containing waste bricks [28–30].

Limited comparative investigations were carried out to evaluate the effect of waste concrete or brick aggregates on concrete properties and durability. Such studies can be relevant to ascertain the extent of natural aggregate replacement rates that can be incorporated for a specific application, including the benefits and limitations of each kind of recycled aggregate on concrete performance. Zheng et al. [31] are among the few researchers who compared the effect rCCA and rBCA on  $f'_c$  of concrete having 25 and 50 MPa strength grades (i.e., C25 and C50). At 100 % aggregate replacement rate, the  $f'_c$  dropped by 7.2 % and 9.6 % for C25 and C50 mixtures containing rCCA, while this reached 11 % and 13 % for C25 and C50 mixtures prepared with rBCA. However, no information was given regarding the origin and source of parent concrete and brick demolished structures. Khatib [27] observed that the strength decreased by 10 % when the natural sand is replaced by rBFA, while this reached 30% for rCFA. Similar losses were also found by Mobili et al. [32], albeit a slight improvement in mechanical properties was observed in the case of fine waste bricks.

This paper is part of a comprehensive research program undertaken to evaluate the effect of recycled waste bricks on concrete properties including the structural behavior of reinforced concrete members. The waste bricks were crushed and sieved to secure rBFA and rBCA fractions meeting ASTM C33 gradations, which were incorporated at the highest feasible replacement rates of 50 % to 100 %, as will be discussed

later. Three mixture series prepared with different water-to-cement ratio (w/c) are tested, while the evaluated properties included workability,  $f'_c$ , split tensile strength, modulus of elasticity, water permeability (by capillary or under pressure), and drying shrinkage. Special emphasis was placed to compare the hardened properties of concrete mixtures prepared with recycled aggregates derived from waste bricks to those derived from waste concrete. The structural properties determined using 2.2 m long reinforced concrete beams are presented in a follow-up paper. Such data can be useful to contractors, municipalities, and environmental activists to valorize the brick component in CDW during civil and engineering construction works.

## 2. Methods

### 2.1. Materials

CEM III 32,5 N Portland cement complying with BS EN 197-1 [33] was used; its chemical composition (along with the brick wastes) is given in Table 1. Continuously graded siliceous natural coarse aggregate (NCA) and siliceous natural fine aggregate (NFA) were employed; their particle gradations varied respectively from 4.75 to 16 mm and from 0 to 4.75 mm, in accordance with ASTM C33 requirements [34]. A polycarboxylate-based high-range water reducer (HRWR) complying with EN 934-2 [35] was employed; its solid content, specific gravity, and maximum recommended dosage rate are 32 %, 1.07, and 4 % of cement mass, respectively.

**Table 1. Chemical composition for the cement and waste brick.**

	Cement	Brick
SiO <sub>2</sub> , %	25.53	58.67
Al <sub>2</sub> O <sub>3</sub> , %	6.3	13.08
Fe <sub>2</sub> O <sub>3</sub> , %	2.29	0.84
CaO, %	55.59	4.51
MgO, %	4.05	1.32
SO <sub>3</sub> , %	2.34	0.89
K <sub>2</sub> O, %	0.78	2.55
TiO <sub>2</sub> , %	0.28	–
LOI, %	2.15	2.81

Two types of fine and coarse recycled aggregates sourced from waste concrete or brick structures are investigated. A laboratory jaw crusher was used to crush the wastes, which then were carefully sieved to produce similar gradations as the natural fine and coarse aggregate fractions. Typical grading curves are presented in Fig. 1, while the aggregate physical properties are summarized in Table 2. The parent concrete from which the rCCA and rCFA were derived had a compressive strength varying from 35 to 42 MPa [11]. The adhered mortar content determined using a sodium sulphate solution by the freeze-thaw test method was 39%  $\pm$  2.5 % [11, 18].

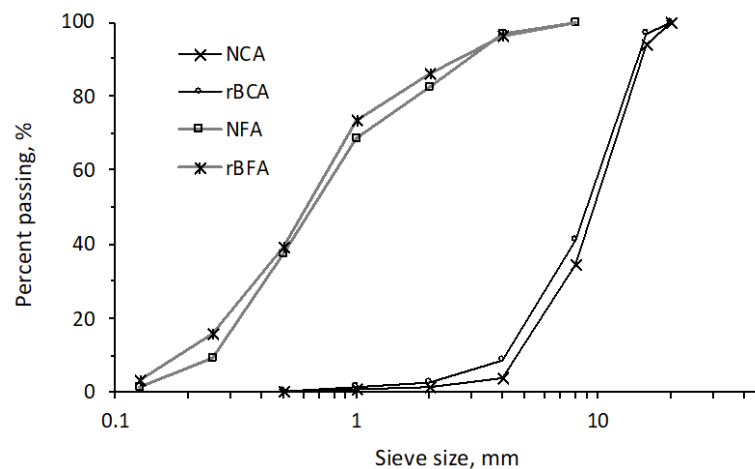


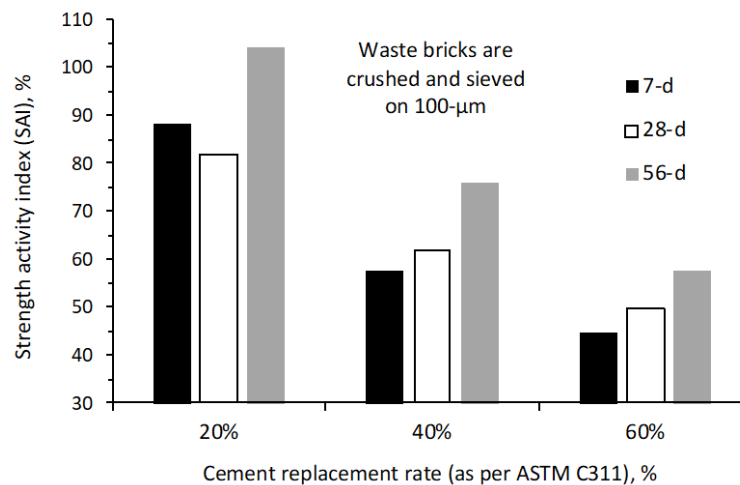
**Figure 1. Particle size distribution curves for NCA, NFA, rBCA, and rBFA.**

**Table 2. Physical properties for the coarse and fine aggregate fractions.**

	Coarse aggregate fraction			Fine aggregate fraction		
	NCA	rBCA	rCCA	NFA	rBFA	rCFA
Specific gravity	2.65	2.13	2.43	2.61	2.1	2.37
Fineness modulus	7.45	6.79	6.77	3.05	2.85	3.1
Water absorption, %	2.1	9.96	7.04	1.31	12.94	9.25
Los Angeles abrasion, %	26.5	31.4	32.6	–	–	–
Material finer than 75- $\mu\text{m}$ , %	–	–	–	0.44	6.4	5.8

Stones of fired clay brick wastes having 215×102.5×65 mm size were collected from demolition sites and crushed to produce the rBCA and rBFA. The compressive strength of the brick blocks was 38 ±3 MPa. It is to be noted that several brick samples were ground finer than 100- $\mu\text{m}$  sieve, and incorporated at 20 %, 40 %, and 60 % replacement rates by cement mass in order to determine the strength activity index (SAI), as per ASTM C311 [36]. The cement-sand-water ratio used for mortar batching was set at 1:2.75:0.5. As shown in Fig. 2, the SAI at 20 % replacement rate was higher than 80 % (reaching 104 % at 56 days), reflecting moderate pozzolanic reactivity equivalent to ASTM C989 Grade 100 pozzolan [37]. The SAI reached 76 % and 58 % at 56 days, despite the relatively high cement replacement rates of 40 % and 60 %, respectively.

The NCA specific gravity was 2.65, while remarkably decreased to 2.13 for rBCA because of increased porosity (Table 2), making this kind of waste brick suitable for semi-lightweight concrete mixtures [14, 38]. The NCA abrasion loss determined as per ASTM C131 [39] was 26.5 %, while increased to 31.4 % and 32.6 % for the rBCA and rCCA, respectively (Table 2). The materials finer than 75- $\mu\text{m}$  remarkably increased from 0.44 % for NFA to 6.4 % and 5.8 % for rBFA and rCFA, respectively, as per ASTM C117 [40]. The corresponding water absorption varied from 1.31 % for NFA to 12.94 % and 9.25 % for rBFA and rCFA, respectively.

**Figure 2. Strength activity index determined using crushed fine bricks.**

## 2.2. Mixture proportions

Three control concrete series proportioned to exhibit lean to high strength grades suitable for residential applications are used in this experimental program (Table 3). The lean mix contained 320 kg/m<sup>3</sup> cement and 180 kg/m<sup>3</sup> water (i.e., w/c of 0.56); its 28-days  $f'_c$  is 38.2 MPa. The higher strength concrete mixtures contained either 360 or 400 kg/m<sup>3</sup> cement together with the same amount of water (i.e., 180 kg/m<sup>3</sup>), which resulted in 0.5 and 0.45 w/c, respectively; the corresponding 28-days  $f'_c$  was 45.7 and 52.3 MPa, respectively. The HRWR was adjusted in all mixtures to secure a similar slump flow of 620 ±10 mm. The fine-to-coarse aggregate ratio remained fixed at 0.45.

**Table 3. Effect of recycled waste bricks on fresh concrete properties.**

	Cement, kg/m <sup>3</sup>	w/c	HRWR, % of cement	Slump* after 30 min, mm	Fresh density, kg/m <sup>3</sup>
0.56-Control	320	0.56	1.76	630	2380
0.5-Control	360	0.5	1.98	610	2365
0.45-Control	400	0.45	2.2	625	2390
0.56-100%rBCA	320	0.56	2.13	590	2195
0.5-100%rBCA	360	0.5	2.39	570	2155
0.45-100%rBCA	400	0.45	2.66	590	2130
0.56-50%rBFA	320	0.56	2.53	590	2310
0.5-50%rBFA	360	0.5	2.84	570	2325
0.45-50%rBFA	400	0.45	3.16	550	2350
0.56-100%rBCA-50%rBFA	320	0.56	2.91	560	2170
0.5-100%rBCA-50%rBFA	360	0.5	3.28	550	2120
0.45-100%rBCA-50%rBFA	400	0.45	3.64	540	2150

\*Initial slump of tested mixtures = 620 ±10 mm.

Each of the control concrete was tested using three different combinations of coarse and/or fine recycled brick aggregates (Table 3). Hence, a 100 % replacement rate was selected to substitute the NCA by rBCA. The cement content, w/c, and fine-to-coarse aggregate ratio remained fixed as described earlier for the control mixtures, while the HRWR adjusted to secure the targeted workability. The second mixture combination consists of replacing the NFA by 50 % rBFA; in fact, preliminary tests showed that higher replacement rates would excessively increase the HRWR demand, which would lengthen setting times beyond 24 hours and detrimentally alter the concrete strength development [5, 28]. Also, a third combination that involves replacing 100 % NCA and 50 % NFA with recycled bricks was considered.

To compensate for the effect of aggregate water absorption during concrete batching, all coarse aggregates (i.e., NCA, rBCA, and rCCA) were pre-soaked overnight in water, and then drained for about 4 hours prior to batching to ensure saturation at or above the saturated surface dry (SSD) condition [4, 27, 7]. Regarding the fine aggregates, the procedure adopted consisted of homogenizing such materials in the mixer with approximately 50 % of mixing water for about 10 minutes, then introducing the remaining ingredients (i.e., coarse aggregate and cement) for concrete batching. Many researchers preconized this mixing approach, as more than 85% of the recycled fine aggregate water absorption takes place within the first 10 min of exposure to water [13, 27, 41]. The batch proportions were adjusted for aggregate surface moisture to maintain constant w/c. After one minute of concrete mixing, the other 50% of water was added followed by the adjusted amount of HRWR to secure the targeted slump flow. Concrete mixing was resumed for two additional minutes. The ambient temperature during mixing and sampling hovered around 21 ± 3 °C.

### 2.3. Test methods

Following the end of concrete mixing, the workability and fresh density were determined as per BS EN 12350-5 [42] and BS EN 12350-6 [43]. The workability test method consists of dropping fifteen times the flow table, and measuring the average concrete spread. The initial slump flow of 620 ±10 mm selected in this study represents a flowable type of concrete requiring light mechanical vibration during in-situ casting. The flow was also determined 30 minutes after the end of mixing, during which the fresh concrete was kept in a bowl covered with a wet burlap. Table 3 summarizes the HRWR demand, slump flow after 30 min, and fresh concrete density.

The fresh concrete was then placed into cubic (150 mm<sup>3</sup>), cylindrical (100×200 mm and 150×300 mm), and prismatic steel molds (75×75×250 mm) for strength and durability assessment (Table 4). All specimens were lightly compacted using a vibrating table for 5 seconds. The specimens were demolded after 24 hours, moist cured in lime saturated water for 7 days (except for drying shrinkage), and then placed in standard conditions of 22 ±3 °C and 55 ±5 % relative humidity until 28 or 56 days. Averages of three measurements were considered for each strength property.

The hardened concrete density and  $f'_c$  were determined using the cubic specimens as per BS EN 12390-7 [44] and BS EN 12390-3 [45], respectively. The splitting tensile strength ( $f_t$ ) was carried out using the 150-mm cubic specimens as per BS EN 12390-6 [46]; the load was gradually applied (i.e., rate of 0.95 kN/s) until the specimen split into two halves. The 150×300 mm cylindrical specimens were used to determine the modulus of elasticity (E), as per BS EN 12390-13 [47]. Three loading cycles were applied;

the displacement values were recorded using a strain-gauge possessing a 0.2 % sensitivity rate. The upper-stress limit for each cylinder was defined as the one-third value of ultimate  $f'_c$ , while the stabilized secant  $E$  value is determined from the third cycle of the stress-strain curves.

**Table 4. Effect of recycled waste bricks on hardened concrete properties.**

	Hard density, kg/m <sup>3</sup>	7-d $f'_c$ , MPa	28-d $f'_c$ , MPa	$f_t$ , MPa	$E$ , GPa	$W_{abs}$ , %	$W_{pen}$ , mm	Max. shrink, $\mu$ m
0.56-Control	2325	17.5	38.2	3.84	28.45	10	25.7	630.3
0.5-Control	2310	24.3	45.7	4.05	–	6.5	18.4	474.2
0.45-Control	2345	26.1	52.3	4.25	31.59	5.2	20.5	422.2
0.56-100%rBCA	2125	17.1	32.2	3.51	27.46	15.4	50.8	711.4
0.5-100%rBCA	2010	22	40.6	4.15	–	11.5	31.8	587.5
0.45-100%rBCA	2090	21.1	44.9	4.9	26.46	8.5	41.5	510.3
0.56-50%rBFA	2235	17.5	38.9	3.22	–	11.5	29.6	691.6
0.5-50%rBFA	2235	18.6	41.5	–	–	10.1	24.5	566.4
0.45-50%rBFA	2245	20.5	49	–	28.44	7.7	21.6	447.5
0.56-100%rBCA-50%rBFA	2095	15.9	33.5	3.45	–	14.5	49.8	802.8
0.5-100%rBCA-50%rBFA	2065	19.2	40.6	–	–	13.4	36.6	634.5
0.45-100%rBCA-50%rBFA	2110	21.5	45.5	–	26.15	11.5	36.4	539.3

The concrete permeability was assessed at 56 days by two methods including the water absorption ( $W_{abs}$ ) and water penetration ( $W_{pen}$ ) tests. The former test was carried out using 100×200 mm cylinders, as per BS 1881-122 [48]. The specimens were initially oven-dried at 110 ±10 °C for 48 hours, which after cooling down to ambient temperature, were fully immersed in a water tank for 72 hours at 22 ±2 °C. The relative masses were measured using a digital balance for oven-dry and SSD conditions, and the water absorption by mass (%) is determined as the change in mass divided by the oven-dried value. The water penetration ( $W_{pen}$ ) depth under pressure was performed on 150 mm cubes, as per BS EN 12390-8 [49]. The surfaces of the cubes were adjusted to a water pressure of 500 ± 50 kPa for 72 ± 2 hours. The specimens were then removed from the apparatus and split in two halves, perpendicularly to the face on which the water pressure was applied. The maximum water penetration depth is recorded using a digital caliper with 0.01-mm precision.

The drying shrinkage was performed using 75×75×250 mm prisms, as per ASTM C157 [50]. Right after the demolding, studs were glued on the longitudinal side of the specimens by applying a special adhesive. The changes in length were measured by means of a demountable mechanical strain gauge with 0.001-mm precision in one day offset during the first week, then three days offset until the month is completed. The temperature and relative humidity in the drying room were maintained at 22 ± 2 °C and 55 % ± 5 %, respectively.

### 3. Results and Discussion

#### 3.1. HRWR demand and slump flow variations

Typical HRWR demand and slump flow loss for 0.56 and 0.45-w/c mixture series are plotted in Fig. 3. The loss in flow was determined as the difference between the initial value of 620 ±10 mm from the one measured 30 minutes after mixing. Regardless of w/c, the use of recycled bricks necessitated higher HRWR to secure the targeted initial slump flow. For example, the HRWR increased from 1.76 % for the control 0.56-w/c mix to 2.13 % when 100 % rBCA is used, while this varied from 2.2 % to 2.66 % for mixtures prepared with 0.45 w/c. Such results are in line with other scholars [11, 24, 51] who attributed this phenomenon to aggregate frictional texture and surface roughness that hinders the ease of flow. The HRWR demand reached respectively 2.53 % and 3.16 % for 0.56 and 0.45-w/c mixtures containing the fine recycled aggregate fraction (i.e., 50 % rBFA), given the porous nature and increased specific surface that could absorb part of the superplasticizer molecules [26–28]. As normally expected, the HRWR demand further increased when both rBCA and rBFA are used, which can be related to the conjuncture detrimental effect of both phenomenon on workability.

As shown in Fig. 3, mixtures incorporating the fine fraction of recycled bricks exhibited remarkable slump flow loss over time. For instance, at 0.45 w/c, a loss of 75 mm was recorded for the concrete containing 50 % rBFA, and reached 85 mm when both rBCA and rBFA are used. While the initial concrete workability is mostly affected by an internal friction phenomenon, the slump flow variation can be associated to the coupled effect of internal friction and water absorption [19, 52]. In fact, as earlier mentioned, the fine recycled aggregate fraction was not in SSD condition prior to batching, thereby increasing the potential of higher water absorption that could reduce concrete workability over time. Actually, the difficulty to control the SSD state of fine recycled aggregates was raised by many researchers, especially since any moisture excess could increase w/c and consequently degrade concrete strength and durability [1, 7, 13].

Generally speaking, the fresh density of control concrete mixtures hovered around  $2375 \pm 15 \text{ kg/m}^3$ , while slightly decreased to about  $2330 \pm 20 \text{ kg/m}^3$  when the fine aggregate fraction was replaced by 50 % rBFA (Table 3). Due to reduced aggregate specific gravity, the fresh density remarkably decreased to  $2160 \pm 30 \text{ kg/m}^3$  when the NCA was fully replaced by rBCA, which will have direct consequences on the concrete strength, as will be discussed later.

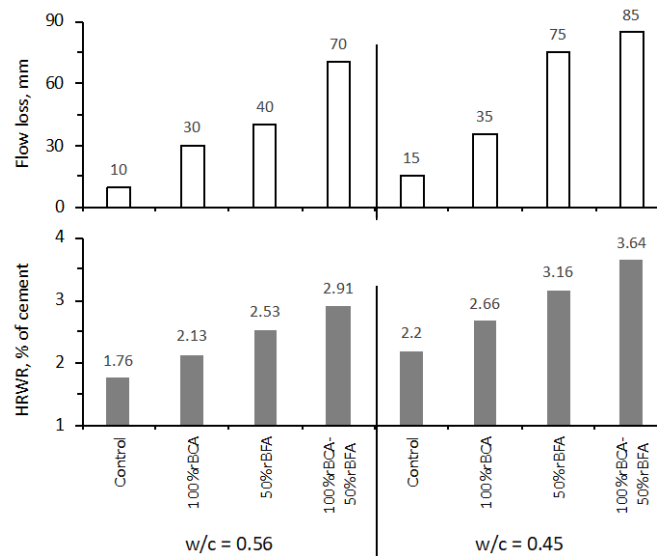


**Figure 3. Effect of rBCA and rBFA additions on HRWR demand and slump flow loss.**

### 3.2. Hardened properties of concrete containing recycled brick aggregates

Fig. 4 plots the absolute values of the hardened properties determined for concrete prepared with 0.56 and 0.45-w/c. For better clarity and analysis of results, Fig. 5 illustrates the corresponding change in properties (i.e.,  $\Delta(\text{Property})$ ) due to recycled brick additions for all tested w/c series. The  $\Delta(\text{Property})$  is normalized with respect to each control mix prepared at given w/c as follows:

$$\Delta(\text{Property}), \% = \frac{(\text{Property of control Mix} - \text{Property of mix with recycled aggregates}) \times 100}{\text{Property of control mix}}$$

#### 3.2.1. Effect on $f'_c$ , $f_t$ , and $E$

Regardless of w/c, the strength reduced when the NCA is fully replaced by rBCA, just like what happens when recycled concrete aggregates are used [7,9]. For example,  $f'_c$  decreased from 38.2 to 32.2 MPa (i.e.,  $\Delta(f'_c)$  of -15.8%) for the 0.56-Control and 0.56-100 % rBCA mixtures, respectively (Figs. 4 and 5). The corresponding  $f_t$  decreased from 3.84 to 3.51 MPa (i.e.,  $\Delta(f_t)$  of -8.6 %), while  $E$  decreased from 28.45 to 27.46 GPa (i.e.,  $\Delta(E)$  of -3.5 %). This can be primarily attributed to the reduced hardness of rBCA fraction (compared to NCA), leading to a weaker concrete skeleton. As summarized in Table 2, the abrasion loss increased from 26.5 % to 31.4 % for NCA and rBCA, respectively. Concurrently, the decrease in strength can be associated with higher aggregate porosity that reduced concrete density including its stiffness for a given applied load [20, 29].

The strength of concrete mixtures containing 50 % rBFA additions did not significantly curtail (compared to control NFA concrete), which maintained the  $f'_c$ ,  $f_t$ , and  $E$  responses within the repeatability of testing (Fig. 4). Hence, a positive  $\Delta(f'_c)$  of +2% was obtained for the 0.56-50 % rBFA mix, while this was -6.4 % for the 0.45-50%rBFA mixture (Fig. 5). The improvement in concrete strength can be attributed to enhanced filler effect (especially the fraction finer than 75  $\mu\text{m}$ ) coupled with some pozzolanic reactions

owing to the brick mineralogical composition that is rich in  $\text{SiO}_2$  content (Tables 1 and 2). This later phenomenon promotes C-S-H development and densifies the ITZ between the mortar and aggregate particles [16, 23, 26]. Additionally, it is important to note that the hardened concrete density was slightly altered with 50 % rBFA additions (i.e.,  $2240 \pm 20 \text{ kg/m}^3$ ), which helped control the drop in strength.

The  $\Delta(f'_c)$  hovered about -12% for the various w/c concrete series prepared using 100 % rBCA and 50 % rBFA (Fig. 5), while the corresponding hardened density was  $2090 \pm 25 \text{ kg/m}^3$  (Table 4). Such strength loss remains lower than the values registered using concrete containing only rBCA, given the filler and pozzolanic effects associated with the fine brick fraction. This practically reveals the benefits of combining both coarse and fine brick fractions to control strength loss, despite the reduction in concrete hardened density. Such sustainable concrete mixtures can drastically reduce the consumption of natural aggregates, yet being suitable for semi-lightweight concrete applications having relatively high compressive strengths [14, 30]. As shown in Table 4, the 28-days  $f'_c$  for mixtures prepared using 100 % rBCA and 50 % rBFA varied from 33.5 to 45.5 MPa, depending on w/c. The E measurement decreased from 31.59 to 26.15 GPa for concrete mixtures having 0.45 w/c.

### 3.2.2. Effect on water permeability

As expected, the resistance against water permeability improved for mixtures made with reduced w/c, given the decreased matrix porosity that hinders the ease of water percolation [7, 10]. For instance,  $W_{abs}$  decreased from 10 % to 6.5 % when w/c was reduced from 0.56 to 0.5, respectively; the corresponding  $W_{pen}$  decreased from 25.7 to 18.4 mm, respectively (Fig. 4). Regardless of w/c, the resistance against permeability remarkably degraded when the NCA is fully replaced by rBCA. The resulting  $W_{abs}$  and  $W_{pen}$  reached 15.4 % and 50.8 mm for the 0.56–100 % rBCA mixture (i.e.,  $\Delta(W_{abs})$  and  $\Delta(W_{pen})$  of 55.2 % and 97.8 %, respectively). Such results are in agreement with  $f'_c$ , albeit each property is affected by a different phenomenon. While the reduced brick hardness mostly influences the strength [21, 23], the higher permeability can be inherently related to the porous rBCA nature (compared to NCA) that increases the overall concrete porosity and easiness towards water permeation.

The resistance against water permeability considerably improved when 50 % of the fine aggregate fraction is replaced by rBFA (Figs. 4 and 5). Hence,  $W_{abs}$  and  $W_{pen}$  slightly increased to 11.5 % and 29.6 mm for the 0.56–50 % rBFA mixture (i.e.,  $\Delta(W_{abs})$  and  $\Delta(W_{pen})$  became 15.7 % and 15.3 %, respectively). As earlier explained, this can be related to a combined filler and pozzolanic effects associated with the fine brick fraction, leading to refined pore size that enhances the concrete resistance towards water permeation [52, 53]. In this context, it is worth noting that the preliminary tests made with 30 % recycled fine brick materials yielded pretty similar or slightly better permeability resistance, as compared to mixtures prepared with only NFA. Hence, unlike the rBCA fraction that increased the overall concrete porosity, recycled bricks are better used in fine fractions.

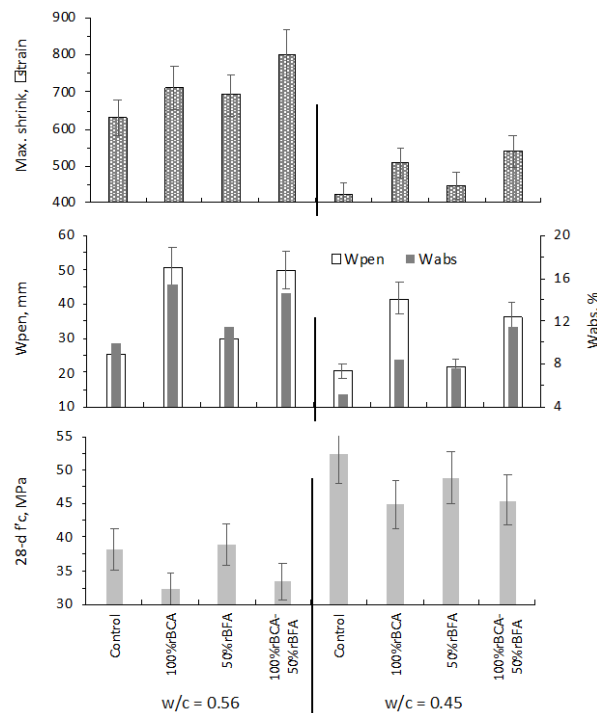


Figure 4. Effect of rBCA and rBFA additions on hardened concrete properties.

As shown in Fig. 5, water permeability degraded when both the recycled fine and coarse brick fractions are incorporated in the same concrete; the resulting  $\Delta(W_{abs})$  and  $\Delta(W_{pen})$  values were similar to those obtained when only the rBCA fraction is used. This physically implies that the porous rBCA nature overshadows the benefits associated with the fine recycled brick fraction, leading to increased concrete porosity that reduces the resistance against water permeability. Fig. 6 plots the relationships between the 28-days  $f'_c$  with respect to  $W_{abs}$  and  $W_{pen}$  for all tested concrete. As expected, mixtures possessing increased  $f'_c$  are characterized by denser microstructure, leading to better resistance against water permeability.

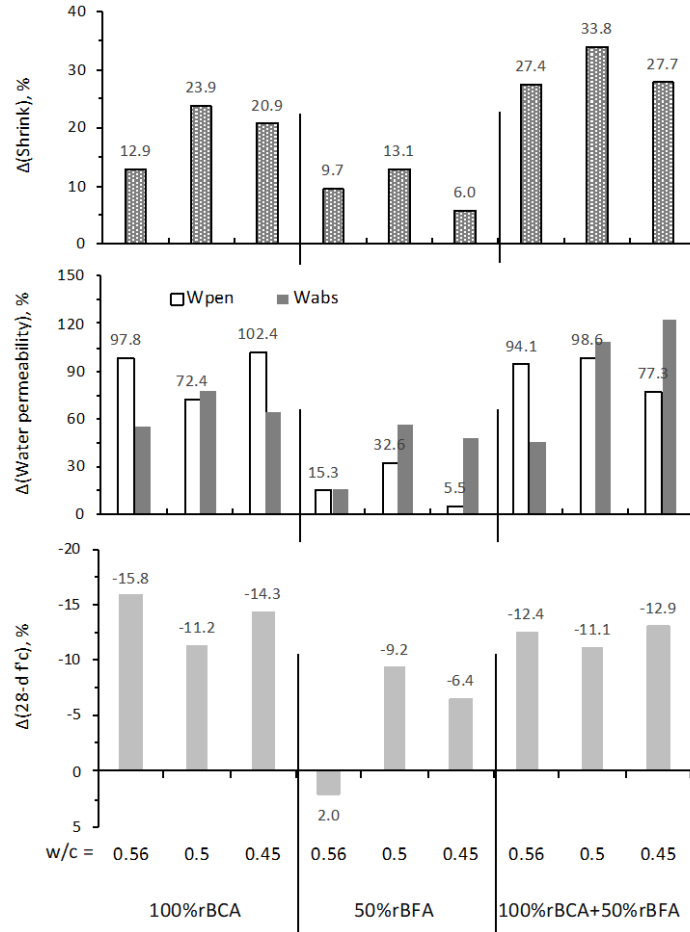


Figure 5. Effect of rBCA and rBFA additions on variations of hardened properties.

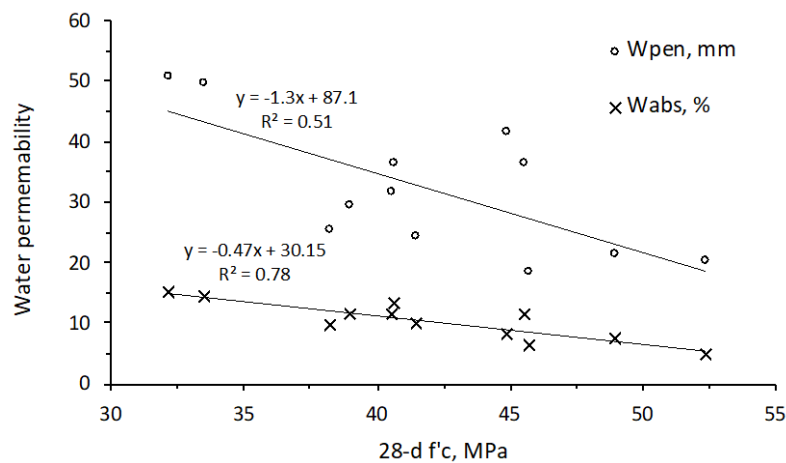


Figure 6. Relationships between 28-days  $f'_c$  with respect to  $W_{abs}$  and  $W_{pen}$  for all tested concrete.

### 3.2.3. Drying shrinkage

Typical variations of drying shrinkage over time for the 0.56 and 0.45-w/c mixtures are plotted in Fig. 7. Clearly, the shrinkage gradually increased during the first 10 days after demolding, and then tends

to stabilize over time depending on w/c and aggregate properties [28, 53, 54]. Hence, the maximum shrinkage reached 630  $\mu\text{m}$  for the 0.56-Control concrete, while decreased to 474 and 422  $\mu\text{m}$  for the control mixtures prepared with 0.5 and 0.45 w/c, respectively. Such behavior is mostly attributed to the loss of capillary water due to evaporation and cement hydration reactions, causing increased proneness of hardened concrete to contraction and volume change. Also, mixtures prepared with less w/c contained relatively higher fine and coarse aggregate contents, which help restraining the concrete volume changes [54].

Although the general shrinkage trends remained similar (Fig. 7), it is clear that rBCA additions accentuated the tendency towards concrete contraction, which increased the maximum shrinkage values recorded after 35 days. For example, this reached 711  $\mu\text{m}$  (i.e.,  $\Delta(\text{Shrink})$  of 13 %) and 510  $\mu\text{m}$  (i.e.,  $\Delta(\text{Shrink})$  of 21 %) for the 0.56–100% rBCA and 0.45-100%rBCA mixtures, respectively (Figs. 4 and 5). Earlier studies showed concrete shrinkage is strongly affected by the aggregate porosity since water may easier diffuse and migrate out of porous aggregates (such as bricks) due to higher gradients [20, 28]. Also, the reduced stiffness (i.e., higher abrasion loss) of rBCA compared to NCA materials could directly degrade the restraining effect, leading to increased shrinkage. This highlights the importance of proper curing to mitigate shrinkage phenomena of concrete containing recycled coarse aggregate bricks.

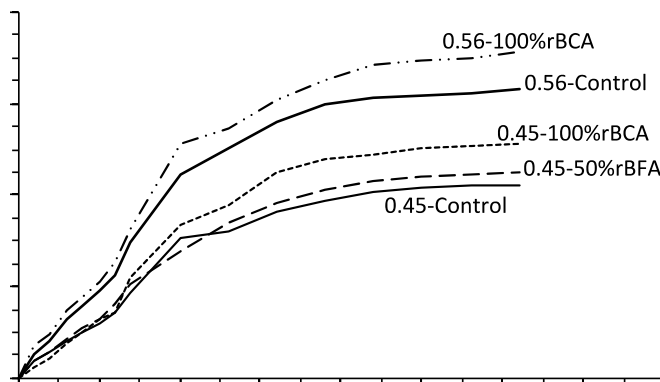


**Figure 7. Effect of rBCA and rBFA additions on drying shrinkage over time.**

The drying shrinkage considerably decreased when the natural sand is partially replaced by 50 % rBFA, as compared to mixtures prepared with 100 % rBCA replacement. Hence, the maximum recorded shrinkage reached 692  $\mu\text{m}$  (i.e.,  $\Delta(\text{Shrink})$  of 9.7 %) and 448  $\mu\text{m}$  (i.e.,  $\Delta(\text{Shrink})$  of 6 %) for the 0.56–50 % rBFA and 0.45–50 % rBFA mixtures, respectively. This can be attributed to a combination of phenomena including the reduced porosity of the fine aggregate fraction together with enhanced filler and pozzolanic effects that strengthen the ITZ between the coarse aggregate and cement matrix [55–57]. Nevertheless, just like what happened with strength development and resistance against water permeability, the conjuncture usage of 100 % rBCA and 50 % rBFA led to increased drying shrinkage, given the inferior coarse aggregate brick properties. A good relationship exists between the 28-days  $f'_c$  and 35-days maximum shrinkage measurements, as shown in Fig. 8. As a general rule, the higher the concrete  $f'_c$ , the lower becomes the shrinkage strains.

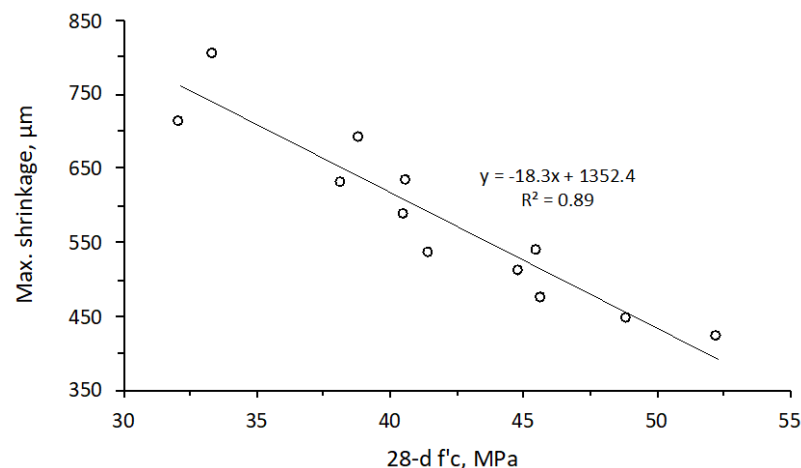


**Figure 8. Relationship between 28-days  $f'_c$  and maximum shrinkage for all tested concrete.**

### 3.3. Comparison between recycled brick vs. concrete aggregates

The comparative effects of recycled aggregates on  $\Delta(f'_c, f_t, E, W_{abs}, \text{ and Shrink})$  for concrete mixtures prepared with 0.56 and 0.45 w/c are plotted in Fig. 9. As noted in the experimental program, the natural coarse aggregate (NCA) fraction was fully replaced by either rBCA or rCCA, while the natural fine aggregate (NFA) fraction was replaced by 50 % rBFA or rCFA.

Although  $f'_c, f_t,$  and  $E$  responses degraded when the NCA is replaced by either type of recycled aggregates, however, it seems quite hard to determine whether such drop was more affected by rBCA or rCCA additions (Fig. 9). Hence, on average, the  $\Delta(f'_c, f_t,$  and  $E)$  hovered within  $-10 \% \pm 5 \%$ , revealing that the drop in concrete properties is practically similar whether rBCA or rCCA materials are used. In contrast, water permeability and drying shrinkage remarkably degraded for concrete containing recycled bricks. Hence,  $\Delta(W_{abs})$  and  $\Delta(\text{Shrink})$  reached respectively about 60 % and 17 % for rBCA concrete, while these were as low as 20 % and 8 % for rCCA concrete. As earlier explained, this can be inherently related to porous rBCA nature that increases the overall concrete porosity and proneness towards water permeation and contraction. In other words, it can be stated that the overall concrete porosity is comparatively less affected by the rCCA fraction since it is composed of NCA particles (having reduced porosity) covered with the adhered porous cement paste [1–3].

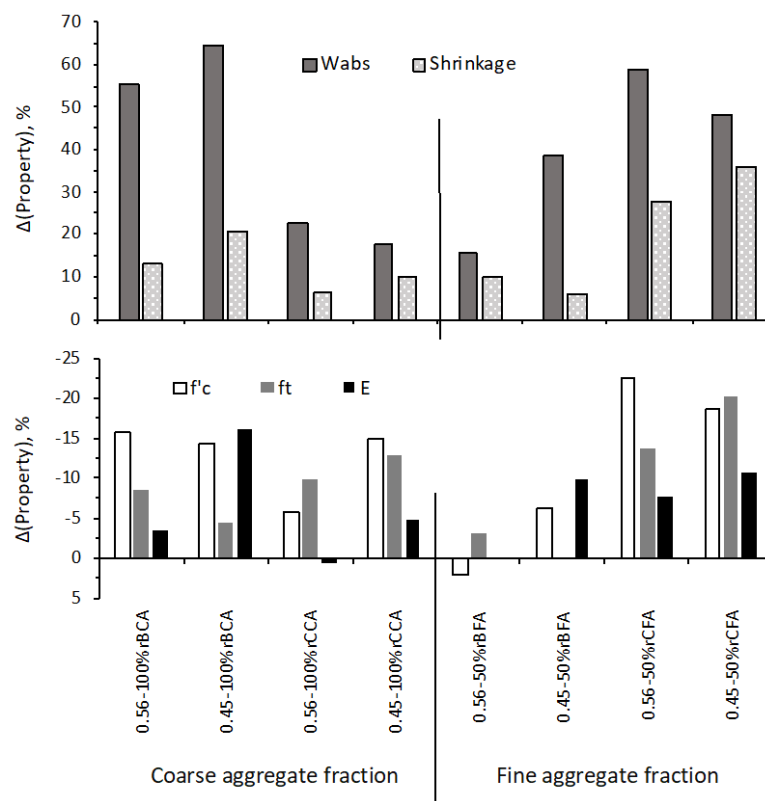


**Figure 9. Comparison between recycled fine and coarse brick and concrete aggregates.**

Unlike the recycled coarse aggregate fraction, the concrete properties appear to be less altered when the recycled brick fine fraction is considered (Fig. 9). Hence, the average  $\Delta(f'_c, f_t,$  and  $E)$  values hovered within  $-5 \% \pm 3 \%$  for rBFA concrete, while these varied within  $-15 \% \pm 5 \%$  for rCFA concrete. Considering that the filler effect remains similar in both types of recycled materials, the comparative improvements recorded in  $f'_c, f_t,$  and  $E$  responses for rBFA concrete can be attributed to the pozzolanic reactions that promoted C-S-H development and densified the ITZ between the mortar and aggregate particles [29, 30]. Also, this phenomenon helped improving the resistance against water permeability and drying shrinkage; the resulting  $\Delta(W_{abs})$  and  $\Delta(\text{Shrink})$  hovered respectively about 27 % and 15 % for rBFA concrete, while these were 53 % and 32 % for rCFA concrete. Thus, unlike the rCFA fraction that is often regarded as an unwanted component in new construction and building materials, the recycled fine brick fraction can better be employed during concrete production.

## 4. Conclusion

This paper is part of a comprehensive research program undertaken to determine the benefits and limitations of recycled bricks in concrete production. Based on the foregoing, the following conclusions can be warranted:

1. Regardless of w/c, the use of recycled bricks necessitated higher HRWR demand to secure the targeted concrete workability. This was attributed to the frictional texture of the coarse aggregate fraction (i.e., rBCA) that hinders the ease of flow, while the porous nature of the rBFA could absorb part of the HRWR molecules.

2. Mixtures incorporating the recycled fine brick fraction exhibited remarkable slump flow loss over time, which was mainly related to the coupled effect of internal friction and water absorption. In fact, this fraction was not in SSD condition prior to batching, which increased water absorption and reduced concrete workability retention.

3. The concrete strength (i.e.,  $f'_c$ ,  $f_t$ , and  $E$ ) including its resistance to water permeability and drying shrinkage degraded when the NCA is fully replaced by rBCA, given the reduced hardness of this aggregate fraction that weakened the concrete skeleton. The curtail in concrete properties was concurrently associated with higher brick porosity that lowered the concrete density and reduced its stiffness for a given load.

4. Unlike the rBCA effect, the concrete properties did not dramatically curtail when the NFA is replaced by 50 % rBFA. The filler effect and pozzolanic brick nature have promoted higher packing density and refined the concrete microstructure.

5. The concrete strength and resistance to permeability and drying shrinkage improved when both recycled fine and coarse brick fractions are incorporated in the same mixture. This practically reveals the benefits of combining both fractions to maintain proper concrete strength properties, despite the decrease in density.

6. The  $f'_c$ ,  $f_t$ , and  $E$  responses degraded almost similarly when the NCA is replaced by either rBCA or rCCA. In contrast, the curtail in water permeability and drying shrinkage was particularly clear for concrete containing recycled bricks, given the porous rBCA nature that increases the overall concrete porosity and proneness towards water permeation and contraction.

7. The concrete properties ( $f'_c$ ,  $f_t$ , and  $E$ ) including the resistance to permeability and drying shrinkage were less altered with the use of the recycled fine brick fraction, as compared to concrete containing the rCFA fraction. This was mostly attributed to the pozzolanic reactions that promoted strength development over time.

## References

- Meng, Y., Ling, T.C., Mo, K.H. Recycling of wastes for value-added applications in concrete blocks: An overview. *Resources, Conservation and Recycling*. 2018. 138. Pp. 298–312. DOI: 10.1016/j.resconrec.2018.07.029
- Galishnikova, V.V., Abdo, S., Fawzy, A.M. Influence of silica fume on the pervious concrete with different levels of recycled aggregates. *Magazine of Civil Engineering*. 2020. 93(1). Pp. 71–82. DOI: 10.18720/MCE.93.7
- Hajmohammadian Baghba, M., Hashemi, S.A.H., Kalbasi Anaraki, K., Hashemi, E.S. Influence of polypropylene-fiber on the mechanical properties of self-compacting-concrete with recycled aggregates. *Magazine of Civil Engineering*. 2020. 99(7). DOI: 10.18720/MCE.99.5
- Ghanbari, M., Abbasi, A.M., Ravanshadnia, M. Production of natural and recycled aggregates: the environmental impacts of energy consumption and CO<sub>2</sub> emissions. *Journal of Materials Cycles Waste Management*. 2018. 20 (2). Pp. 810–822. DOI: 10.1007/s10163-017-0640-2
- Assaad, J.J., Issa, C.A. Effect of Recycled Acrylic-Based Polymers on Bond Stress-Slip Behavior in Reinforced Concrete Structures. *Journal of Materials in Civil Engineering*. 2017. 29(1). Pp. 04016173. DOI: 10.1061/(asce)mt.1943-5533.0001700
- Abdelgader, H.S., Fediuk, R.S., Kurpinska, M., Khatib, J., Murali, G., Baranov, A.V., Timokhin, R.A. Mechanical properties of two-stage concrete modified by silica fume. *Magazine of Civil Engineering*. 2019. 89(5). Pp. 26–38. DOI: 10.18720/MCE.89.3
- Eckert, M., Oliveira, M. Mitigation of the negative effects of recycled aggregate water absorption in concrete technology. *Construction and Building Materials*. 2017. 133. Pp. 416–424. DOI: 10.1016/j.conbuildmat.2016.12.132
- Wang, J., Xie, J., He, J., Sun, M., Yang, J., Li, L. Combined use of silica fume and steel fibre to improve fracture properties of recycled aggregate concrete exposed to elevated temperature. *Journal of Materials Cycles Waste Management*. 2020. 22(3). Pp. 862–877. DOI: 10.1007/s10163-020-00990-y
- Puthussery, J.V., Kumar, R., Garg, A. Evaluation of recycled concrete aggregates for their suitability in construction activities: An experimental study. 2017. *Waste Management*. 60. Pp. 270–276.
- Behera, M., Minocha, A.K., Bhattacharyya, S.K. Flow behavior, microstructure, strength and shrinkage properties of self-compacting concrete incorporating recycled fine aggregate. *Construction and Building Materials*. 2019. 228. Pp. 116819. DOI: 10.1016/j.conbuildmat.2019.116819
- Assaad, J.J., Matar, P., Gergess, A. Effect of quality of recycled aggregates on bond strength between concrete and embedded steel reinforcement. *Journal of Sustainable Cement-Based Materials* 2020. 9(2). Pp. 94–111. DOI: 10.1080/21650373.2019.1692315

12. Deng, Z., Liu, B., Ye, B., Xiang, P. Mechanical behavior and constitutive relationship of the three types of recycled coarse aggregate concrete based on standard classification. *Journal of Material Cycles and Waste Management*. 2020. 22 (1). Pp. 30–45. DOI: 10.1007/s10163-019-00922-5
13. Saba, M., Assaad, J.J. Effect of recycled fine aggregates on performance of geopolymer masonry mortars. *Construction and Building Materials*. 2021. 279. Pp. 122461. DOI: 10.1016/j.conbuildmat.2021.122461
14. Wong, C.L., Mo, K.H., Yap, S.P., Alengaram, U.J., Ling, T.C. Potential use of brick waste as alternate concrete-making materials: A review. *Journal of Cleaner Production*. 2018. 195. Pp. 226–239. DOI: 10.1016/j.jclepro.2018.05.193
15. Islam, S. Aggregate concrete factor ( $\lambda$ ) for burnt clay brick aggregate concrete. *Magazine of Civil Engineering*. 2019. 87 (3). Pp. 46–58. DOI: 10.18720/MCE.87.4.
16. Zhu, L., Zhu, Z. Reuse of Clay Brick Waste in Mortar and Concrete. *Advances in Material Science and Engineering*. 2020. 20. Pp. 1–11. DOI: 10.1155/2020/6326178
17. El-Dieb, AS., Taha, MR., Abu-Eishah, SI. The use of ceramic waste powder (CWP) in making eco-friendly concretes. *IntechOpen*. 2018. Pp. 1–35. DOI: 10.5772/intechopen.81842
18. Singh, A. Ceramic waste in concrete - A Review. *Recent Advances on Engineering, Technology and Computational Sciences (RAETCS) Ceramic*. 2018. Pp. 1–6.
19. Ferreira, S.B., Domingues, P.C., Soares, S.M., Camarini, G. Recycled Plaster and Red Ceramic Waste Based Mortars. *International Journal of Engineering and Technology*. 2015. 7(3). Pp. 209–214. DOI: 10.7763/ijet.2015.v7.793
20. Miličević, I., Štirmer, N., Bjegović, D. Relation between the compressive strength and modulus of elasticity of concrete with crushed brick and roof tile aggregates. *Structural Concrete*. 2017. 18(2). Pp. 366–375. DOI: 10.1002/suco.201500207
21. Cachim, P.B. Mechanical properties of brick aggregate concrete. *Construction and Building Materials*. 2009. 23 (3). Pp. 1292–1297. DOI: 10.1016/j.conbuildmat.2008.07.023
22. Zhang, S., Zong, L. Properties of concrete made with recycled coarse aggregate from waste brick. *Environmental Progress & Sustainable Energy*. 2013. 4. Pp.1283–1289. DOI: 10.1002/ep.11880
23. Dang, J., Zhao, J., Pang, S.D., Zhao, S. Durability and microstructural properties of concrete with recycled brick as fine aggregates. *Construction and Building Materials*. 2020. 262. Pp. 120032. DOI: 10.1016/j.conbuildmat.2020.120032
24. Ge, Z., Feng, Y., Zhang, H., Xiao, J., Sun, R., Liu, X. Use of recycled fine clay brick aggregate as internal curing agent for low water to cement ratio mortar. *Construction and Building Materials*. 2020. 264. Pp. 120280. DOI: 10.1016/j.conbuildmat.2020.120280
25. Toledo Filho, R.D., Gonçalves, J.P., Americano, B.B., Fairbairn, E.M.R. Potential for use of crushed waste calcined-clay brick as a supplementary cementitious material in Brazil. *Cement and Concrete Research*. 2007. 37(9). Pp. 1357–1365. DOI: 10.1016/j.cemconres.2007.06.005
26. Naceri, A., Hamina, M.C. Use of waste brick as a partial replacement of cement in mortar. *Waste Management*. 2009. 29(8). Pp. 2378–2384. DOI: 10.1016/j.wasman.2009.03.026
27. Khatib, J.M. Properties of concrete incorporating fine recycled aggregate. *Cement and Concrete Research*. 2005. 35 (4). Pp. 763–769. DOI: 10.1016/j.cemconres.2004.06.017
28. Bravo, M., de Brito, J., Evangelista, L., Pacheco, J. Durability and shrinkage of concrete with CDW as recycled aggregates: Benefits from superplasticizer's incorporation and influence of CDW composition. *Construction and Building Materials*. 2018. 168. Pp. 818–830. DOI: 10.1016/j.conbuildmat.2018.02.176
29. Zhang, S., He, P., Niu, L. Mechanical properties and permeability of fiber-reinforced concrete with recycled aggregate made from waste clay brick. *Journal of Cleaner Production*. 2020. 268. Pp. 121690. DOI: 10.1016/j.jclepro.2020.121690
30. AlArab, A., Hamad, B., Chehab, G., Assaad, J.J. Use of Ceramic-Waste Powder as Value-Added Pozzolanic Material with Improved Thermal Properties. *Journal of Materials in Civil Engineering*. 2020. 32 (9). Pp. 04020243. DOI: 10.1061/(asce)mt.1943-5533.0003326
31. Zheng, C., Lou, C., Du, G., Li, X., Liu, Z., Li, L. Mechanical properties of recycled concrete with demolished waste concrete aggregate and clay brick aggregate. *Results in Physics*. 2018. Pp. 1317–1322. DOI: 10.1016/j.rinp.2018.04.061
32. Mobili, A., Giosuè, C., Corinaldesi, V., Tittarelli, F. Bricks and concrete wastes as coarse and fine aggregates in sustainable mortars. *Advances in Materials Science and Engineering*. 2018. DOI: 10.1155/2018/8676708
33. BS EN 197-1. Cement-Part 1: Composition, specifications and conformity criteria for common cements. European Committee for Standardization. 2011.
34. ASTM C33. Standard Specification for Aggregates. ASTM International. 2009.
35. BS EN 934-2. Admixtures for concrete, mortar and grout-Part 2: Concrete admixtures Definitions, requirements, conformity, marking and labelling. European Committee for Standardization. 2009.
36. ASTM C311 / C311M-18. Standard test methods for sampling and testing fly ash or natural pozzolans for use in Portland-cement concrete. ASTM International. 2018.
37. ASTM C989 / C989M-18a. Standard specification for slag cement for use in concrete and mortars. ASTM International. 2018.
38. Karaburç, S.N., Yıldız, S.A., Calis, G.C. Evaluation of the basalt fiber reinforced pumice lightweight concrete. *Magazine of Civil Engineering*. 2020. 94 (2). Pp. 81–92. DOI: 10.18720/MCE.94.7
39. ASTM C131. Standard test method for resistance to degradation of small-size coarse aggregate by abrasion and impact in the Los Angeles machine. ASTM International. 2009.
40. ASTM C117-17. Standard test method for materials finer than 75-micron (No. 200) sieve in mineral aggregates by washing. ASTM International. 2017.
41. Erofeev, V.T., Rodin, A.I., Bochkin, V.S., Ermakov, A.A. The formation mechanism of the porous structure of glass ceramics from siliceous rock. *Magazine of Civil Engineering*. 2020. 100 (8). Article No. 10006. DOI: 10.18720/MCE.100.6
42. BS EN 12350-5. Testing Fresh Concrete-Part 5: Flow table test. European Committee for Standardization. 2009.
43. BS EN 12350-6. Testing Fresh Concrete-Part 6: Density. European Committee for Standardization. 2009.
44. BS EN 12390-7. Testing Hardened Concrete-Part 7: Density of Hardened Concrete. European Committee for Standardization. 2009.

45. BS EN 12390-3. Testing Hardened Concrete-Part 3: Compressive strength of test specimens. European Committee for Standardization. 2009.
46. BS EN 12390-6. Testing Hardened Concrete-Part 6: Tensile splitting strength of test specimens. European Committee for Standardization. 2009.
47. BS EN 12390-13. Testing Hardened Concrete-Part 13: Determination of secant modulus of elasticity in compression. European Committee for Standardization. 2013.
48. BS EN 1881-122. Testing Concrete-Part 122 Method for determination of water absorption. European Committee for Standardization. 2011.
49. BS EN 12390-8. Testing Hardened Concrete-Part 8 Depth of penetration of water under pressure. European Committee for Standardization. 2009.
50. ASTM C157-15. Standard Test Method for Length Change of Hardened Hydraulic-Cement Mortar and Concrete. ASTM International. 2015.
51. Begich, Y.E., Klyuev, S.V., Jos, V.A., Cherkashin, A.V. Fine-grained concrete with various types of fibers. Magazine of Civil Engineering. 2020. 97(5). Article No. 9702. DOI: 10.18720/MCE.97.2
52. Poon, C.S., Shui, Z.H., Lam, L., Fok, H., Kou, S.C. Influence of moisture states of natural and recycled aggregates on the slump and compressive strength of concrete. Cement and Concrete Research. 2004. 34 (1). Pp. 31–36. DOI: 10.1016/S0008-8846(03)00186-8
53. Güneş, E., Gesoğlu, M., Mermerdaş, K. Improving strength, drying shrinkage, and pore structure of concrete using metakaolin. Materials and Structures. 2008. 41 (5). Pp. 937–949. DOI: 10.1617/s11527-007-9296-z
54. Zéhil, G.P., Assaad, J.J. Feasibility of concrete mixtures containing cross-linked polyethylene waste materials. Construction and Building Materials. 2019. 226. Pp. 1–10. DOI: 10.1016/j.conbuildmat.2019.07.285
55. El Mir, A., Nehme, S.G., Assaad, J.J. Durability of self-consolidating concrete containing natural waste perlite powders. Heliyon. 2020. 6(1). DOI: 10.1016/j.heliyon.2020.e03165
56. O'Farrell, M., Wild, S., Sabir, B.B. Pore size distribution and compressive strength of waste clay brick mortar. Cement and Concrete Composites. 2001. 23 (1). Pp. 81–91. DOI: 10.1016/S0958-9465(00)00070-6
57. AlArab, A., Hamad, B., Assaad, J.J. Strength and durability of concrete containing ceramic waste powder and blast furnace slag. Journal of Materials in Civil Engineering. 2022. 34 (1). [https://doi.org/10.1061/\(ASCE\)MT.1943-5533.0004031](https://doi.org/10.1061/(ASCE)MT.1943-5533.0004031)

**Information about authors:**

**Abdulkader El-Mir, PhD**

ORCID: <https://orcid.org/0000-0003-4905-7561>

E-mail: [abdulkader.elmir@fty.balamand.edu.lb](mailto:abdulkader.elmir@fty.balamand.edu.lb)

**Salem Nehme, PhD**

ORCID: <https://orcid.org/0000-0003-4729-5048>

E-mail: [salem.nehme@epito.bme.hu](mailto:salem.nehme@epito.bme.hu)

**Joseph Assaad, PhD**

ORCID: <https://orcid.org/0000-0002-2423-451X>

E-mail: [joseph.assaad@balamand.edu.lb](mailto:joseph.assaad@balamand.edu.lb)

*Received 05.06.2021. Approved after reviewing 26.04.2022. Accepted 26.04.2022.*



Research article

UDC 691.545

DOI: 10.34910/MCE.116.4



## Iraqi bentonite as natural pozzolan

A.A. Al-Hammood , Q.J. Frayyeh , W.A. Abbas 

University of Technology, Baghdad, Iraq

✉ 42402@student.uotechnology.edu.iq

**Keywords:** concrete, bentonite, montmorillonite, thermal activation, calcined clay, cementitious materials, pozzolan, compressive strength, strength activity index, tensile strength, fresh properties, water absorption, X-ray diffraction, quantitative XRD

**Abstract.** In this study, Iraqi high-calcium bentonite was used for the first time to prepare natural pozzolan for concrete by the thermal activation method (calcination). Raw bentonite was calcined at 700, 750, 800, 850, 900, and 950°C for 30, 60, 90, and 120 minutes at each temperature. X-ray diffraction and quantitative X-ray diffraction techniques identified the optimal calcination program at 800°C for 90 minutes. In this program, calcination destroyed the crystal structure of bentonite-forming clay minerals, thus converting silicon, aluminium, and iron oxides into chemically reactive amorphous phases. The prepared natural pozzolan achieves a strength activity index of 108.3% at 28 days; additionally, it meets the requirements of the Iraqi specification of pozzolanic materials. The effects of Portland cement replacement with calcined bentonite at 5, 10, 15, 20, 25, and 30% were studied on selected properties of the cementitious binder and concrete. The results indicate that replacement percentage is positively associated with initial and final setting times and negatively correlated with the concrete slump. At seven days, calcined bentonite causes the decline of the compressive strength of concrete, while at 28 days, concretes containing 5, 10, and 15% develop higher compressive strength than the control mix. However, the compressive strength of concretes containing calcined bentonite differs from the control mix by not more than  $\pm 9\%$  at 90 days. Calcined bentonite reduces the concrete splitting strength and density properties, and the absorption at 25% substitution or less.

**Citation:** Al-Hammood, A.A., Frayyeh, Q.J., Abbas, W.A. Iraqi bentonite as natural pozzolan. Magazine of Civil Engineering. 2022. 116(8). Article no. 11604. DOI: 10.34910/MCE.116.4

### 1. Introduction

The sustainability of concrete can improve by utilizing pozzolanic materials as a partial replacement for Portland cement [1]. Natural pozzolan is one of the types of pozzolanic materials; when used as a part of the cementitious binder, it develops some of the fresh properties, mechanical properties, and/or durability of concrete [2, 3]. This research aims to prepare natural pozzolan from Iraqi high-calcium bentonite by the thermal activation method.

Bentonite is clay that consists dominantly of smectite minerals [4]. In addition to smectite minerals, bentonite may contain multiple species of clay minerals such as palygorskite, kaolinite, illite, or others. It may contain non-clay minerals such as quartz, gypsum, feldspar, or others [4, 5]. The unique property of smectite minerals is the potential to swell due to water absorption [6]. In most cases, bentonite contains a high percentage of montmorillonite mineral, a member of the smectite group. Therefore, bentonite may define as clay consisting mainly of montmorillonite mineral [7].

There are numerous allegations about the pozzolanicity of raw bentonite [8–14]. However, these allegations are not supported by conclusive evidence of the occurrence of the pozzolanic reaction between bentonite components and calcium hydroxide resulting from Portland cement hydration [15]. On the

contrary, precise examinations have shown that only minor changes in montmorillonite structure occur in highly alkaline environments [16], and a small fraction of montmorillonite may contribute to pozzolanic reaction [17]. On the other hand, the pozzolanicity of both calcined montmorillonite (CM) and calcined bentonite (CB) has been confirmed in several studies [17–23].

CB modifies the concrete properties in plastic and hardened states due to both pozzolanic and physical actions. In the plastic state, CB incorporation causes a linearly increase in water demand to achieve standard consistency of the paste [23, 24], extends both initial and final setting time [23–25], reduces the workability of concrete [26], and increases the dosage of superplasticizer required for self-compacted mortar [27] and self-compacted concrete [28]. In the hardened state, CB reduces the rate of strength gain due to the low pozzolanic reactivity of CM [21, 29–31]. Therefore, CB incorporation leads to a reduction in compressive strength of concrete at early ages, i.e., 21 days or less [8, 9, 25, 26], but the reductions in concrete strength tend to disappear at later ages, i.e., 28-90 days [25, 26, 28]. The most important effect of CB is enhancing the durability of concrete against alkalis-silica reaction [25], sulfates attack [32], acids attack [26], and chlorides penetration [25, 28]. No previous studies were related to Iraqi bentonite, which differs in chemical and mineralogical compositions.

Given the absence of naturally formed pozzolans in Iraq and the rarity in industries producing pozzolanic materials as waste, the available alternative is to utilize mineral resources in obtaining natural pozzolan. Iraqi bentonite represents a promising source for natural pozzolan production; its validity for this purpose has not previously been investigated.

In Iraq, the petroleum industries are the largest consumer of bentonite. These industries require high swelling bentonite, i.e., sodium bentonite, while the bentonite deposits in Iraq contain only low swelling bentonite, i.e., calcium bentonite [33, 34]. Therefore, Iraqi calcium bentonite shall be processed to convert it to high swelling bentonite before using it to extract the crude oil. Calcium content is the criterion in determining the validity of calcium bentonite to process and thus convert to high swelling bentonite [35]. On this basis, Iraqi bentonite is classified into two classes [33–37]: high grade or low-calcium bentonite in which  $\text{CaO} \leq 5\%$ , and low grade or high-calcium bentonite in which  $\text{CaO} > 5\%$ . High-calcium bentonite requires complex processes to be converted into high swelling bentonite [33, 36, 37]. Because of this, the production of the high swelling bentonite from the high-calcium bentonite is not economically feasible, and the utilization of Iraqi bentonite is limited to the low-calcium bentonite only. In contrast, high-calcium bentonite is considered a useless material. The main objective of this research is to determine the optimum calcination program for producing natural pozzolan from high-calcium Iraqi bentonite, and then study some properties of the cementitious binder and concrete when Portland cement is partially substituted with the prepared pozzolan.

## 2. Materials and Methods

### 2.1. Materials

Bentonite stones were obtained from the Wadi Bashira region in the Western Desert of Iraq. The coordinates of this region are  $32^{\circ}59'48.2''\text{N}$ , and  $39^{\circ}44'53.3''\text{E}$ . Wadi Bashira deposit represents the most important montmorillonitic smectites deposits in Iraq as it contains reverse of more than  $300 \times 10^6$  tons [38]. This deposit contains both high-calcium and low-calcium bentonite. The chemical composition of RB is recorded in Table 1. Fig. 1 shows the status of RB as received.

Ordinary Portland cement (OPC) conforms to IQS 5/2019 type IQS 5-CEMI 32.5R. The chemical composition of OPC is listed in Table 1, and its physical and mechanical properties are listed in Table 2.

Standard sand meets the requirements of the Iraqi code of practice No. 1/198/2012 was used for making mortar for the strength activity index test. For concrete production, round graded gravel 14–5 mm, and natural sand in zone IV according to IQS. 45/1984 were used.



Figure 1. Bentonite stones as received.

**Table 1. Chemical composition of materials.**

	Oxide percentage		
	OPC	RB	CB (80090)
CaO	63.4	7.4	8.3
SiO <sub>2</sub>	21.0	57.6	60.3
Al <sub>2</sub> O <sub>3</sub>	5.0	13.6	14.9
Fe <sub>2</sub> O <sub>3</sub>	3.8	6.3	7.2
MgO	2.3	3.2	3.6
Na <sub>2</sub> O	0.2	1.1	1.1
SO <sub>3</sub>	2.5	1.3	1.5
K <sub>2</sub> O	0.5	0.5	0.6
P <sub>2</sub> O <sub>5</sub>	-	0.9	0.9
TiO <sub>2</sub>	-	1.1	1.3
Cl	-	0.33	0.13
LOI	1.6	-	-
IR	0.3	-	-

**Table 2. Physical and mechanical properties of OPC.**

Property	Result	IQS 5/2019 limit
Compressive strength @ 2 days	19 MPa	10 MPa lower limit.
Compressive strength @ 28 days	34.1 MPa	32.5 MPa lower limit.
Initial setting time	70 min.	45 min. lower limit.
Final setting time	235 min.	600 min. upper limit.
Soundness	0.04%	0.8% upper limit.
Fineness	317 m <sup>2</sup> /kg	250 m <sup>2</sup> /kg lower limit.

## 2.2. Methods

The experimental program included the following sequential steps:

1. The bentonite stones were soaked in water for 24 hours as they absorbed water and turned into a soft paste, then spreading outdoors in direct sunlight for 5 to 10 days to dry. This process aims to facilitate the grinding process and increase its efficiency, as it has been observed that the process of grinding bentonite stones takes longer than the process of grinding dry bentonite paste to achieve the desired result fineness. Fig. 2 shows the drying process of bentonite paste. After drying, the bentonite was ground using a 300 g laboratory grinder for 90 seconds, then sieving the ground bentonite on a 300  $\mu$ m sieve to exclude coarse grinding products. The ground raw bentonite was kept in airtight plastic containers.

**Figure 2. Drying bentonite paste.**

2. Identify the mineral composition of the RB by the XRD technique.

3. Calcination of RB at 700, 750, 800, 850, 900, and 950 °C for 30, 60, 90, and 120 minutes for each calcination temperature. The nomenclature of each experiment shows in Table 3. Each sample was heated at the rate of 30–40 °C/min. until it reached the calcination temperature; it was kept at this temperature  $\pm$  10 °C for the calcination period; then, it was removed from the furnace immediately after the calcination was completing. After that, it was left to cool down at ambient temperature. The purpose of fast cooling is to prevent phase transformations that may occur during slow cooling [39].

**Table 3. Calcination programs.**

		Calcination temperature					
		700°C	750°C	800°C	850°C	900°C	950°C
Calcination period	30 min.	70030	75030	80030	85030	90030	95030
	60 min.	70060	75060	80060	85060	90060	95060
	90 min.	70090	75090	80090	85090	90090	95090
	120 min.	700120	750120	800120	850120	900120	950120

4. Recognize the modifications on crystal phases due to each calcination experiment by XRD technique.

5. Select the probable experiments that disappear the peaks of clay minerals without the formation of new crystal phases.

6. Analyze the results of XRD of the probable examinations by quantitative XRD (QXRD) to determine the residuals of clay minerals.

7. Decide the optimum calcination program that confirms the maximum strength activity index at 28 days.

8. Verification of conformity of CB prepared by the optimum calcination program to the mandatory requirements of IQS 1748/1992 (Pozzolanic materials for use as a mineral admixture in Portland cement concrete).

9. Examine the effects of partial replacement of OPC by CB at 5, 10, 15, 20, 25, and 30 % replacement levels on the properties of the cementitious binder: water requirement, initial and final setting times, and combined water.

10. Study the effects of partial replacement of OPC by CB at 5, 10, 15, 20, 25, and 30 % replacement levels on the properties of concrete: slump, density, absorption, compressive strengths, and splitting tensile strength. The details of concrete mixtures are shown in Table 4.

**Table 4. Details of concrete mixtures.**

Mixture	Material content kg/m <sup>3</sup>				
	OPC	CB	Sand	Gravel	Water
C100B0	450.0	0	650	1000	210
C95B5	427.5	22.5	650	1000	210
C90B10	405.0	45	650	1000	210
C85B15	382.5	67.5	650	1000	210
C80B20	360.0	90	650	1000	210
C75B25	337.5	112.5	650	1000	210
C70B30	315.0	135	650	1000	210

XRD patterns for RB and CB were performed using ADX-2700 diffractometer (manufactured by Angstrom Advanced Inc., Boston, USA), the range of  $2\theta$  is 3–80°, the rate of scanning is 0.05°/sec., the type of radiation is  $\text{CuK}\alpha_1$ , i.e.,  $\lambda = 1.54056\text{\AA}$ , the voltage is 40kV, and the current is 30 mA.

The QXRD of probable experiments were carried out using DIFFRAC.DQUANT software from Bruker UK Limited.

Particle size analyses for CB and OPC were implemented with the NanoBrook 90Plus particle size analyzer (Brookhaven Instruments Corporation, NY, USA). The size range of the device is 0.3 nm – 6  $\mu\text{m}$ , the scattering angle is 90°, the laser type is a temperature-controlled red semiconductor laser, the laser wavelength is 660 nm, the liquid of the test solution is ethanol, and the test precision is  $\pm 1\%$ . This device determines the equivalent diameter of the specimen's particles suspended in ethanol and subjected to the laws of Brownian motion using the dynamic scattered light technique.

Tests of water required to achieve standard consistency, initial setting time, and final setting time were carried out according to the Iraqi code of practice 1/198/2012.

Specimens of cementitious paste were prepared by mixing 200 g of the cementitious binder with 80 g of water (0.4 w/cm); the hardened pastes were cured in saturated lime water for 90 days. Five grams were taken from each specimen, dried at 40 °C for a constant mass, and weighted. A dried paste was ignited for 30 minutes at 1000 °C and then weighted. The combined water is determined as the following:

$$\% W_c = \left[ \frac{(m_{40} - m_{1000})}{m_{40}} \right] \times 100,$$

where  $W_c$ ,  $m_{40}$  and  $m_{1000}$  are the combined water, the mass of dried specimens, and the mass of the ignited specimen, respectively.

The tests and requirements of the CB as a pozzolanic material were carried out according to IQS 1748/1992.

Concrete mixtures were prepared according to the Iraqi code of practice 248/1991. Slump test was carried out according to Iraqi code of practice 354/1992, density test according to BS EN 12390-7:2009 (water saturated mass and actual measurements volume), absorption test according to BS 1881-122:2011, compressive strength test according to Iraqi code of practice 348/1992, and splitting tensile strength according to BS EN 12390-6:2009. All concrete specimens are 100mm cubes.

### 3. Results and Discussions

#### 3.1. Physical effects of calcination

The calcination process turns the powder of RB from yellow colour to red colour. The colour of CB gets darker with the increase in the calcination temperature. Fig. 3 illustrates the changes in bentonite colour due to different calcination programs. The red colour is attributed to the formation of hematite  $Fe_2O_3$ , and the dark colour is attributed to the formation of magnetite  $Fe_3O_4$  [40]. The formation of hematite and/or magnetite indicates a partial or complete dissociation of the crystal structure of clay minerals that make up bentonite, as the iron cation represents the central part of some tetrahedrons in the tetrahedral sheet and the central part of some octahedrons in the octahedral sheet. The calcination process causes the iron cation to be released from the crystal structure and forms iron oxides  $Fe_2O_3$  and  $Fe_3O_4$ .

The bentonite powder tends to agglomerate with an increase in calcination temperature, and the formed lumps harden at higher temperatures. Table 5 elucidates the status of CB after calcination, and Figure 4 shows the statuses of some experiments. The formation of lumps is an indication to start the sintering process and formation of new crystalline phases. The formation of lumps makes it necessary to re-grind CB before using it as pozzolanic material.

**Table 5. Status of CB after calcination.**

experiment	status
70030, 70060, 70090, 700120, 75030, 75060, 75090, 750120, and 80030. 80060, 80090, and 85030.	Powder A mixture of friable lumps and powder
800120, 85060, 85090, 850120, 90030, 90060, 90090, 900120, 95030, 95060, 95090, and 950120.	Hard lumps

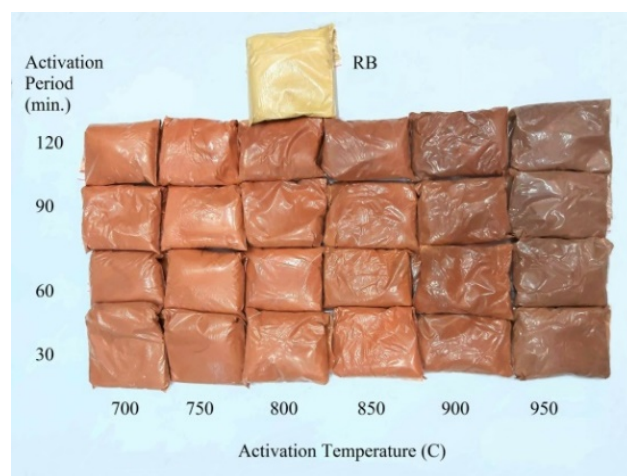


**Figure 3. Colour of bentonite at different activation temperatures.**



**Figure 4. Status of some experiments.**

The calcination process leads to a weight loss of RB by about 18–22 %. The major weight loss is ascribed to the free water release, the adsorbed water molecules from the surfaces of clay minerals, and the hydroxyl groups from the structure of clay minerals. The minor weight loss is attributed to the decarbonisation of dolomite and removing water molecules from the gypsum.

### 3.2. XRD and QXRD

The result of the XRD test of RB is shown in Fig. 5; Fig. 6–11 show the XRD pattern of each experiment compared to the XRD pattern of RB.

RB consists of Ca-montmorillonite as a major clay mineral, kaolinite, and palygorskite as minor clay minerals, and quartz, dolomite, and gypsum as minor non-clay minerals; Table 6 shows the crystal properties of clay minerals in RB.

**Table 6. Clay minerals in RB.**

Mineral	hkl	d (Å)	2 $\theta$
Ca-montmorillonite	001	15	5.8
	005	3	29.3
	100	4.5	19.8
	300	1.5	62.1
Palygorskite	040	4.5	19.8
	101	4.3	20.8
	231	3.3	26.5
Kaolinite	020	4.5	19.8
	111	3.4	26.5
	-223	1.8	50.1
	203	1.5	60.1
	-3-31	1.5	62.1

The calcination process causes structural changes in the montmorillonite mineral. The peak of 001 plane (at 5.8° 2 $\theta$ ) has shifted to the right by (4–5° 2 $\theta$ ) in all experiments at 700 °C and 750 °C, and in 80030 and 85030 experiments which mean the reduction in basal spacing from 15 Å to 9–10 Å due to removing water molecules layers. The maximum shifting to 14.8° 2 $\theta$  occurred in the 80060 experiment in which the basal spacing has shrunk to 6 Å; the shifting of 001 peak associates with reductions in the intensity, indicating that the strains in the montmorillonite crystal are non-uniform [41], i.e., degrade the crystallinity. For the same experiments, the peak of 100 plane (at 19.8° 2 $\theta$ ) preserves its location and intensity, which elucidates that the structural changes in the c-axis do not mean the destruction of the montmorillonite crystal [19]. In experiments 80090, 800120, and 85060, the peaks of the montmorillonite and other clay minerals disappear. That is strong evidence of transforming the crystalline phases of the clay minerals into amorphous and/or cryptocrystalline phases. This conclusion is confirmed by QXRD, which shows the absence of clay minerals in experiments 80090, 800120, and 85060, as shown in Fig. 12–14.

Despite the absence of the peaks of the clay minerals in the 85090 and 850120 experiments and all experiments at 900 °C and 950 °C but this absence is associated with the appearance of new peaks. The new peaks indicate the formation of highly crystalline inert phases such as cristobalite, spinel, and/or magnesium aluminium silicate (MgAl<sub>2</sub>Si<sub>4</sub>O<sub>12</sub>) [19]. The results obtained are compatible with previous studies, which showed that the amorphization temperature of montmorillonite mineral lies in the range of 800–900 °C [42].

Based on XRD and QXRD results, experiments 80090, 800120, and 85060 are the probable experiment for adoption as an optimum calcination program.

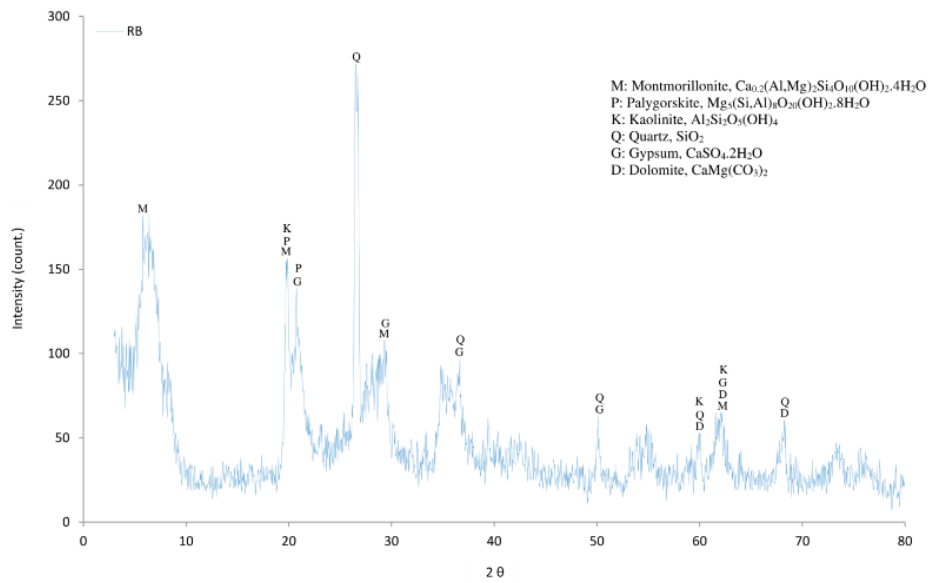


Figure 5. XRD pattern of raw bentonite.

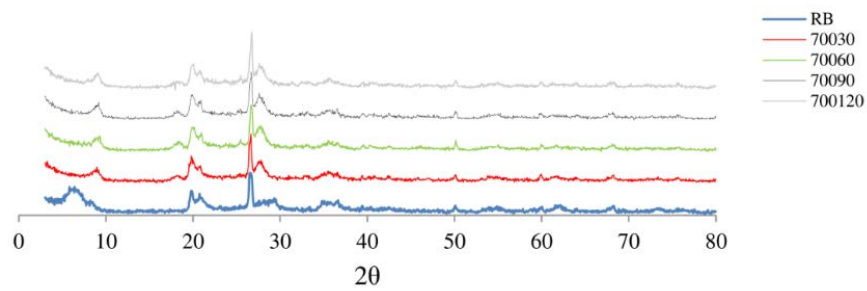


Figure 6. XRD pattern of RB and CB at 700 °C.

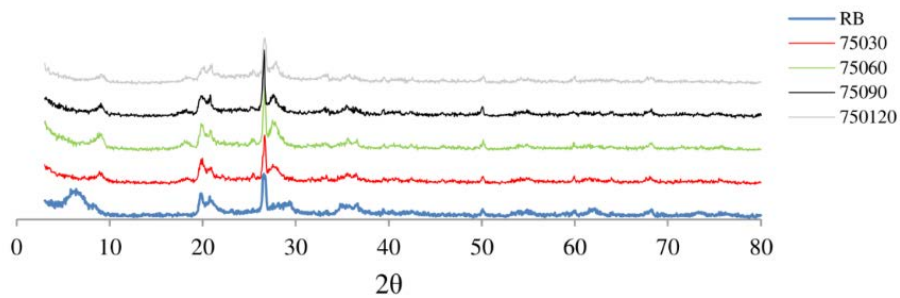


Figure 7. XRD pattern of RB and CB at 750 °C.

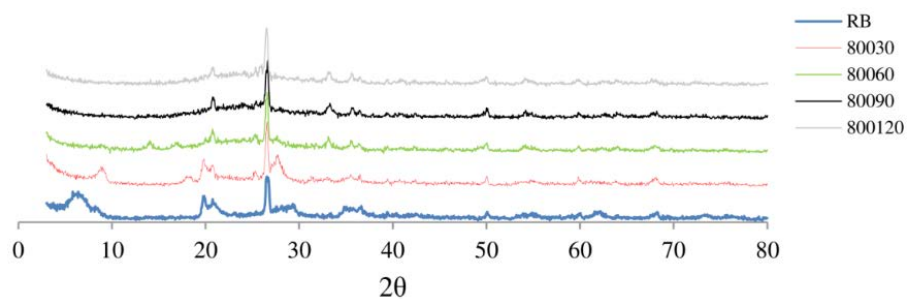


Figure 8. XRD pattern of RB and CB at 800 °C.

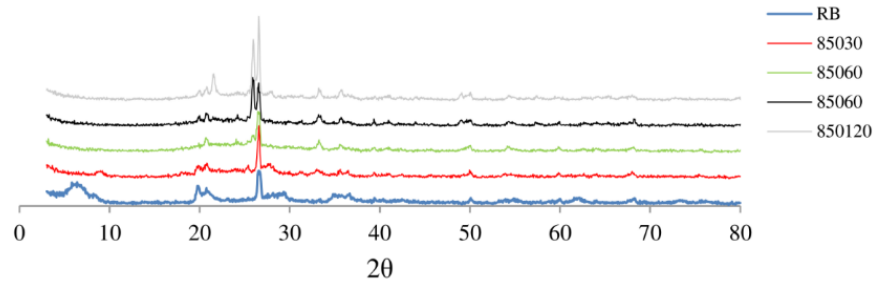


Figure 9. XRD pattern of RB and CB at 850°C.

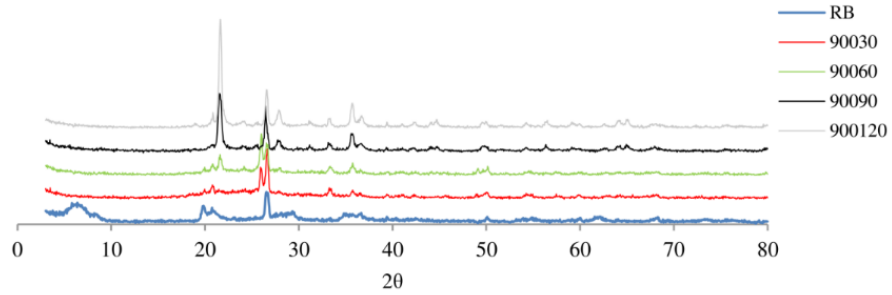


Figure 10. XRD pattern of RB and CB at 900°C.

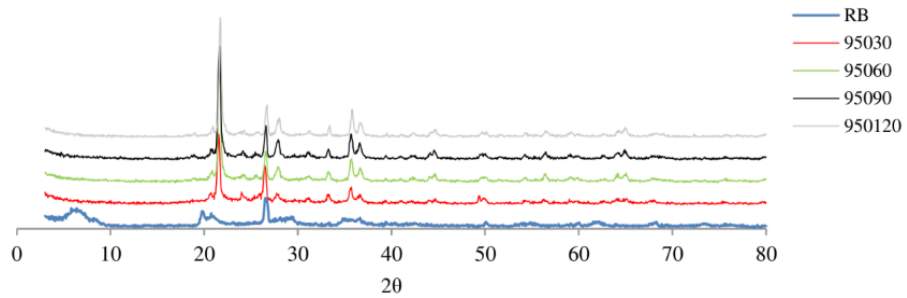


Figure 11. XRD pattern of RB and CB at 950°C.

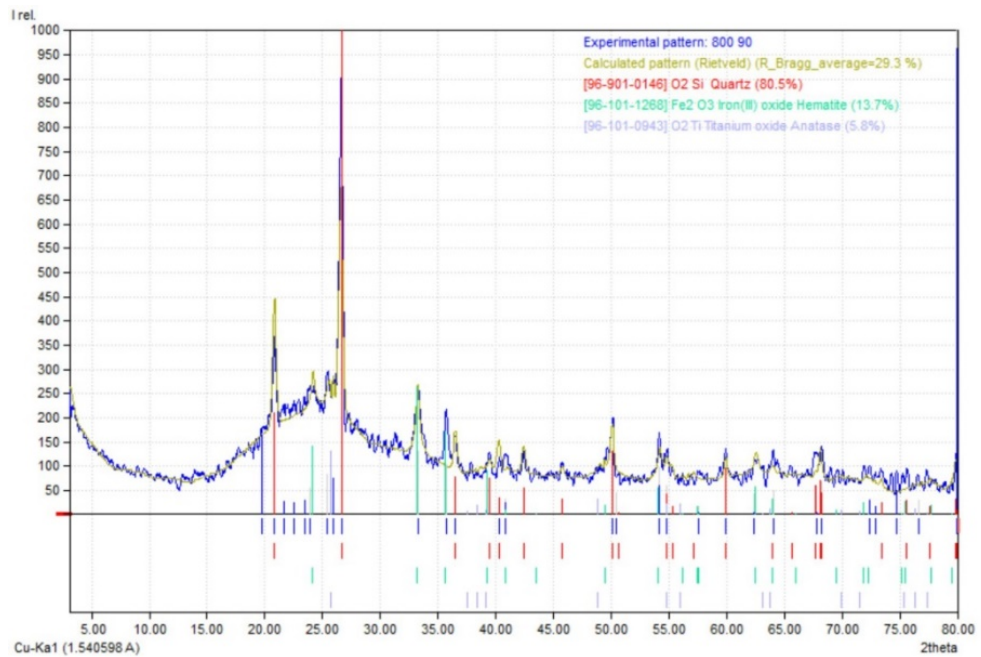


Figure 12. QXRD for 80090 experiment.

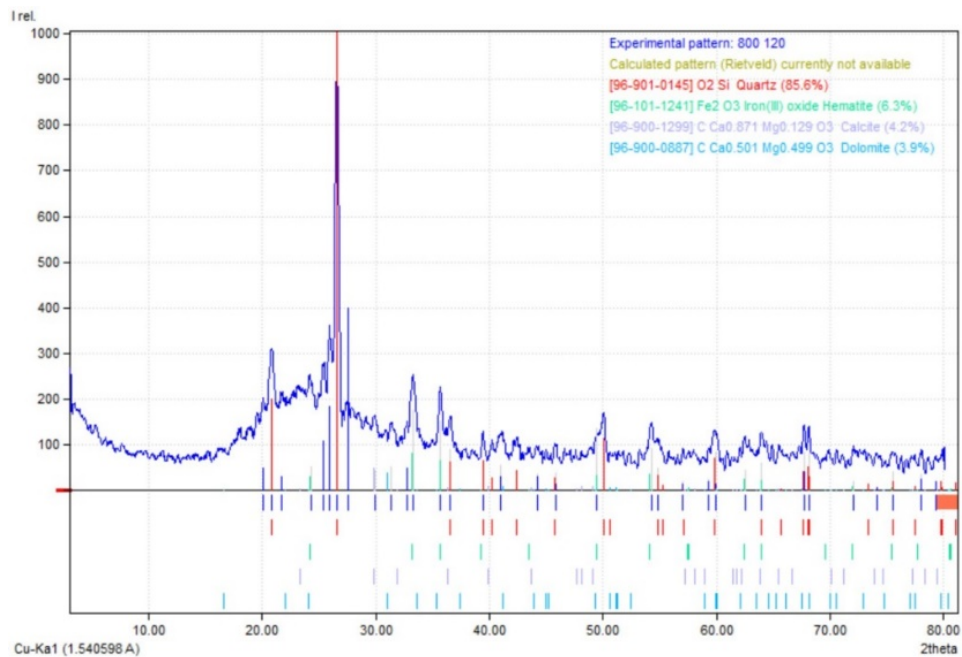


Figure 13. QXRD for 800120 experiment.

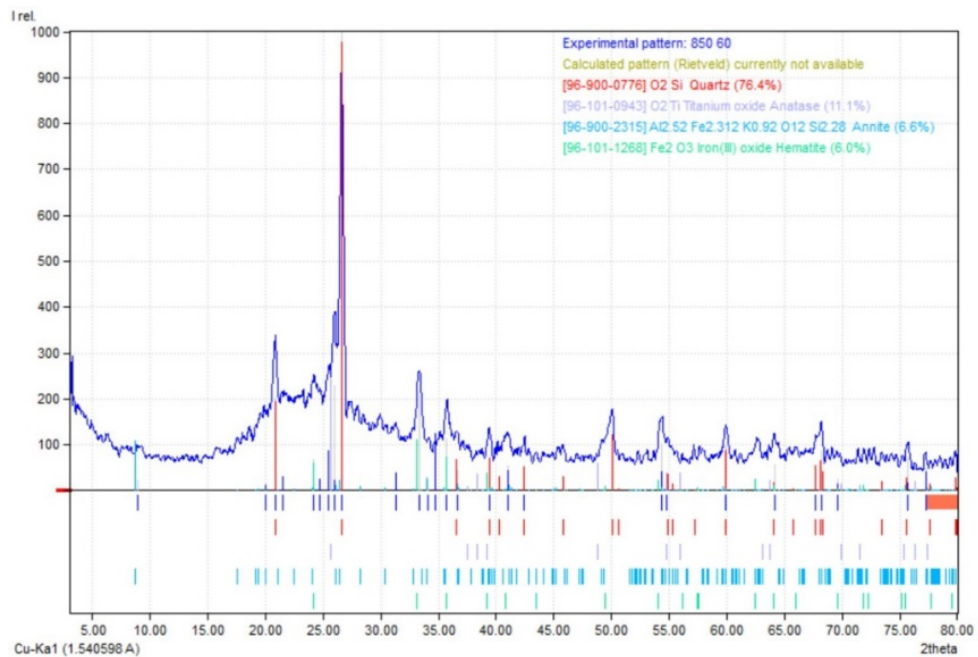


Figure 14. QXRD for 8560 experiment.

### 3.3. Strength activity index

The SAIs of probable experiments at both 7 and 28 days are listed in Table 7. At the age of 7 days, all SAIs were less than 100%, indicating the low reactivity of CB. At 28 days, all probable experiments developed SAI equal to or more than 100%. The highest 28 days SAI (108.3%) is that of the 80090 experiment. Therefore, the 80090 experiment was adopted as the optimum calcination program.

**Table 7. SAI for probable experiments.**

	$f_{7d}$	$SAI_{7d}$	$f_{28d}$	$SAI_{28d}$
Control	34.3	100%	36	100%
80090	26.6	77.6%	39	108.3%
800120	31.3	91.3%	35.8	99.4%
85060	26	75.8%	38.3	106.4%

### 3.4. Properties of pozzolanic materials

CB prepared according to the optimum calcination program (80090) meets the mandatory requirements of IQS 1748/1992. The results of the tests are reported in Table 8.

The particles size distribution of both CB and OPC are shown in Figure 15. The equivalent diameters of OPC and CB are listed in Table 9.

**Table 8. Properties of CB.**

Chemical properties		
Property	Result	IQS 1748/1992 limits
$\Sigma$ (SiO <sub>2</sub> +Al <sub>2</sub> O <sub>3</sub> +Fe <sub>2</sub> O <sub>3</sub> )	82.4%	70.0% min.
SO <sub>3</sub>	1.5%	4.0% max.
Moisture content	0.4%	3.0% max.
Loss on ignition	0.4%	10.0% max
Physical properties		
Property	Result	IQS 1748/1992 limits
Amount retained on 45 $\mu$ m	0%	34% max.
Strength activity index @ 28 days	108.3%	75% min.
Water requirement	99%	115% max.
Soundness	0.05%	0.8% max.
Specific gravity	2.57	–

**Table 9. Equivalent diameters (in nanometers) of CB and OPC particles.**

	D <sub>5</sub>	D <sub>25</sub>	D <sub>50</sub>	D <sub>75</sub>	D <sub>95</sub>
CB	340.6	588.7	860.6	1258.2	2174.6
OPC	601.8	855.8	1092.8	1395.4	1984.4

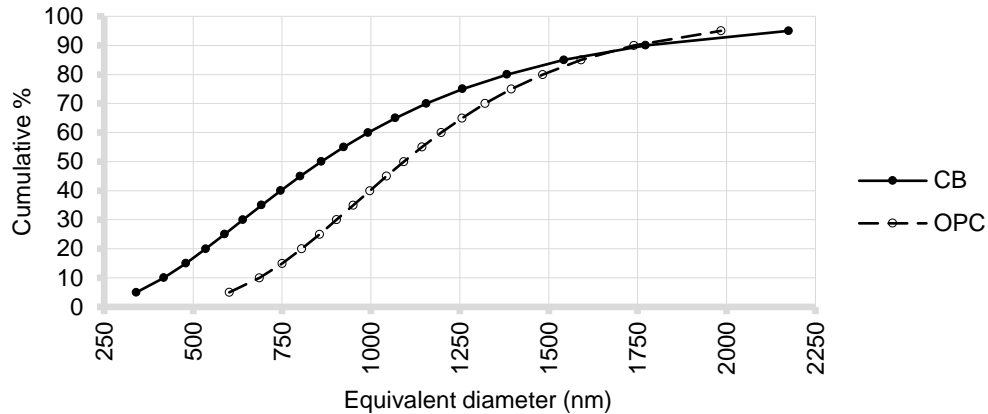


**Figure 15. Particle size distribution of CB and OPC.**

### 3.5. Properties of cementitious binder

OPC replacement by CB causes increases in water required to achieve the standard consistency of cementitious binder. Fig. 16 shows the linear relation between w/cm and the percentage of OPC replacement.

According to Feng et al. [43], the ultrafine powder, which has average particles diameter smaller than the average of cement particles diameter, influence the fluidity of the cementitious binder by two opposed effects: filling effect, which leads to reduce fluidity due to increase water demand, and dispersing effect which leads to increase fluidity due to release trapped water between cement flocks. The amorphous nature of CB, the platy shape of CB particles, and the relatively low specific CB gravity are the reasons why the filling effect dominates the dispersing effect.

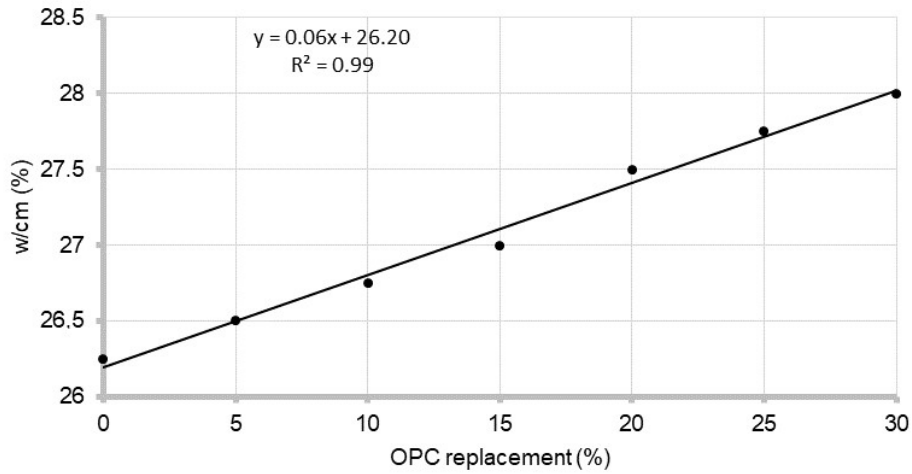


**Figure 16. Effect of OPC replacement by CB on water required to achieve standard consistency.**

Both initial and final setting times extend linearly with the percentage of cement substitution, as shown in Figure 17. The reductions in C<sub>3</sub>A and C<sub>3</sub>S contents due to OPC substitution, the low reactivity of CB components, phosphates in CB, and higher water content are the reasons for the delay in both initial and final setting time.

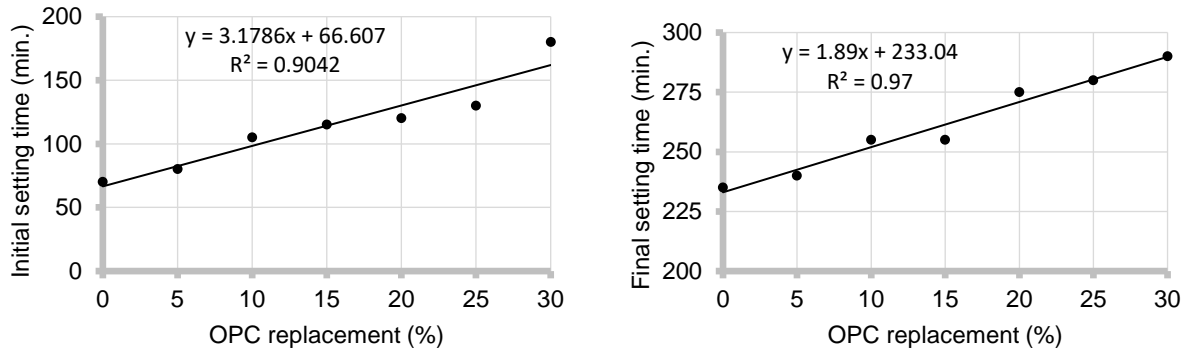


**Figure 17. Effect of OPC replacement by CB on the setting time of cementitious binder.**

CB incorporation causes a slight increase in combined water at 5 % replacement, while at 10 % replacement, a significant increase in combined water was observed. Accordingly, the cementitious binder containing CB at levels of 5 and 10 % produces more hydration products than products resulting from OPC’s hydration alone, as all the hydration products contain chemically combined water. The increase in the hydration products is attributed to the pozzolanic reaction. At 15–30 % replacement, the percentage of combined water reduces gradually as the OPC substitution increase due to the increase of unreacted CB. The combined water percentage is higher than the percentage calculated based on replacing OPC with an inert material, which indicates the contribution of the pozzolanic reaction to the structure of the hardening paste at any replacement level within the range of 5–30 %, as shown in Fig. 18.

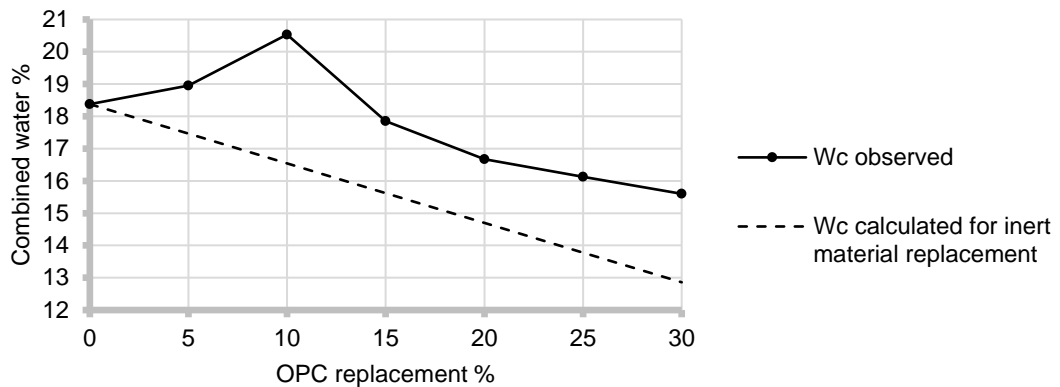


**Figure 18. Effect of OPC replacement by CB on the combined water.**

Similar observations of the effects of calcined bentonite on the properties of the cementitious binder were reported by Darweesh and Nagieb [23].

### 3.6. Workability

Its lower specific gravity characterizes CB than OPC, so the volume of CB required to replace a specific weight of OPC is greater than the volume of the substituted OPC. This increase in the volume of cementitious binder, and its relatively higher surface area due to CB finesse, require an increase in the mixing water to maintain the same workability. In the case of fixation the amount of mixing water, an increase in the volume and surface area of the cementitious binder leads to a decrease in concrete workability. Fig. 19 shows the effect of CB on the slump of concrete. It is noticeable that the slump value decreases as the CB content increases. The effect of CB in reducing the slump has previously been reported by Ahmad et al. [9].

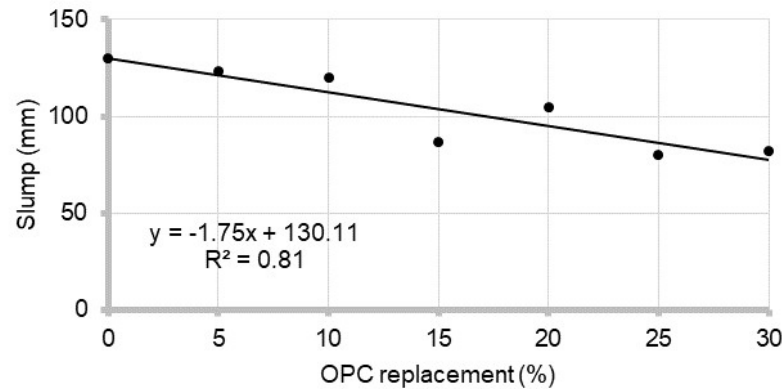


Figure 19. Effect of OPC replacement by CB on the slump of concrete.

### 3.7. Concrete density

Concrete density decreases slightly due to the replacement of OPC by CB. The amount of decrease in density is proportional to the replacement percentage, as shown in Fig. 20. The density reduction is attributed to the lower specific gravity of CB compared to the specific gravity of OPC. It is also observed that the density increases with age due to the progression of the hydration process and thus reducing the total porosity.

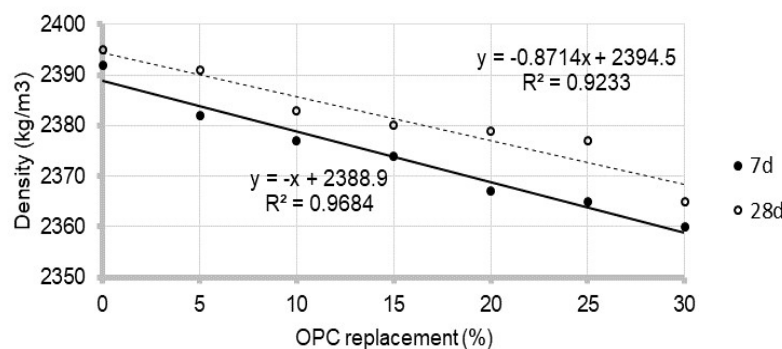


Figure 20. Effect of OPC replacement by CB on concrete density.

### 3.8. Concrete absorption

The partial replacement of OPC with CB results in two opposing effects on concrete absorption, one of which is positive and reduces absorption because of a modification of the pore structure caused by pozzolanic reaction and the physical effect of unreacted bentonite fine particles filling the pores. The second is negative, resulting in higher absorption resulting from the reduction of cement content and, therefore, a reduction in hydration products. At substitution levels of 5 and 10 %, the interaction between these two opposing effects causes a slight decline in absorption due to their comparative equivalence. In contrast, at substitution levels 15–25 %, the positive effect prevails due to the pozzolanic reaction and the physical effect overriding the adverse consequences of reducing cement. However, at the high replacement level, 30 %, the negative effect prevails because the lack of cement is irreplaceable. The influence of CB in reducing concrete absorption was also reported by Ur Rehman et al. [44]. Fig. 21 elucidates the effect of CB on concrete absorption.

### 3.9. Compressive strength

The results of the compressive strength test are illustrated in Fig. 22. At seven days age, OPC replacement by CB causes a decline in compressive strength at any replacement level and the reduction magnitude proportion to substitution percentage. The reduction in strength is attributed to the slow hydration of the cementitious mixture of OPC and CB compared with OPC. There are many reasons for the relatively slow hydration due to the incorporation of CB as part of the cementitious binder. First, CB contains a fraction of inert minerals such as quartz; second, the slow dissolution of CM in the alkaline environment [17, 21, 30, 31], and third, the reduction in  $C_3A$  and  $C_3S$  due to OPC substitution. At 28 days of age, the mixtures containing 5, 10, and 15 % CB develop compressive strength more than the control mixture. At 90 days of age, compressive strength differences tend to decrease by no more than  $\pm 9$  % from the control mixture.

Partial replacement of OPC by CB leads to numerous factors that have opposite effects on the compressive strength of concrete. The intensity of the impact of each factor varies according to the percentage of replacement and the age of the concrete. The factors divide into two categories: positive factors, which increase compressive strength, and negative factors, which decrease compressive strength.

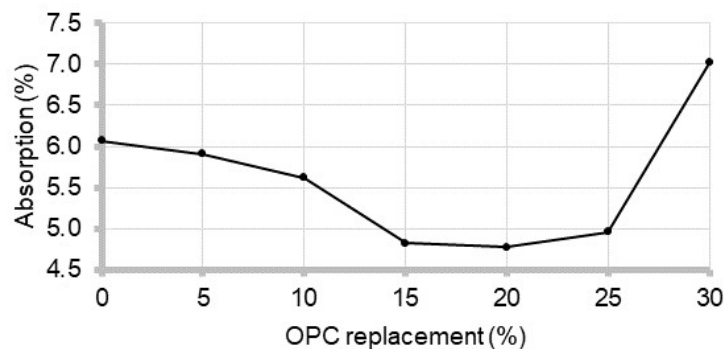


**Figure 21. Effect of OPC replacement by CB on concrete absorption.**

The positive factors are the pozzolanic reaction which leads to replacing  $Ca(OH)_2$  with C-S-(A)-H in both matrix and interfacial transition zone, the modification of pore structure by reducing the fraction of large pores, which have an adverse effect on the concrete strength, the decrement in free water content which leads to reduce disjoining pressure subsequently increase the compressive strength, the addition of new nucleation sites by ultrafine particles of CB, the increment of the cementitious paste fraction due to variance between the specific gravity of CB and OPC, and the retardation effect due to low reactivity of CB which leads to reduce the early age deformations and more uniformity in the distribution of the hydration products.

The negative factors are the reduction in OPC content which causes the reduction in hydration products, the decrease in the rate of strength gain due to CB's low reactivity, and the increment in an unreacted fraction of cementitious binder due to the consumption of  $Ca(OH)_2$  by the pozzolanic reaction.

The negative factors are dominant at early ages for any replacement level, while at 28 days, the positive factors are major at 5, 10, and 15 % replacement, and minor at 20, 25, and 30 %. At later ages, the factors are comparable approximately. The optimum replacement level is 5 %, which causes a strength gain of 12 and 9 % from the control mixture strength at 28 and 90 days, respectively.

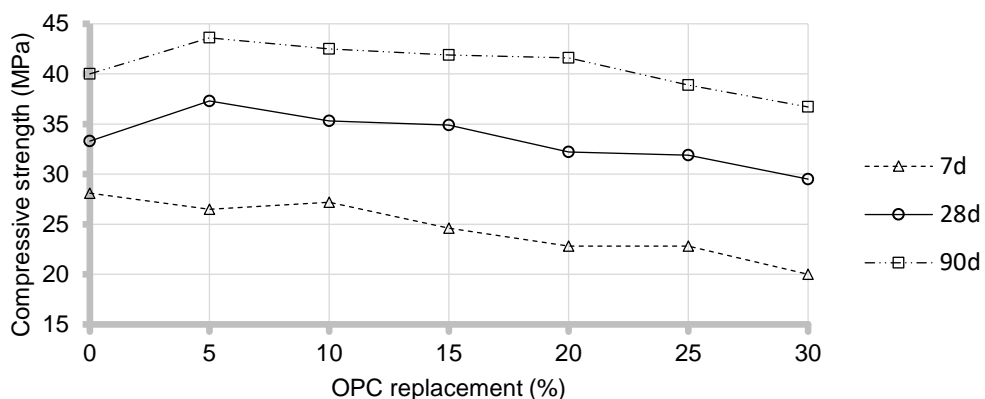


**Figure 22. Effect of OPC replacement by CB on compressive strength.**

The compressive strength results are consistent with those reported in the previous literature [9, 25, 44].

### 3.10. Splitting tensile strength

OPC replacement by CB causes decreases in the splitting tensile strength at all replacement levels at 28 and 90 days age, as shown in Fig. 23.

Despite the strong positive correlation between tensile and compressive strengths to the degree of expression of tensile strength as a function of compressive strength, inverse relations were recorded in some experiments when adding pozzolanic materials. In some cases, an increase in the compressive strength was observed as a result of replacing a percentage of Portland cement with pozzolan, at the same time, a decrease in the splitting strength was observed [45–49]; In other cases, a decrease in the compressive strength was recorded with an increase in tensile strength [50, 51].

Martin [52] observed rising in splitting tensile strength associated with the decline in compressive strength due to absorption increase in some types of rocks. The similar observation was recorded by Chen et al. [53] in concrete specimens due to increased moisture content from 80 to 100 %; in addition, it is well known that the flexural strength of saturated concrete is more than the flexural strength of dry concrete [54]. Therefore, free water may positively influence tensile strength due to Stefan's adhesion force (SAF) instead of disjointing pressure in compression. SAF proposed to explain the increase in concrete tensile strength with increasing relative humidity [55] and strain rate [56].

According to the absorption test results, CB incorporation causes reductions in free water content, consequently reducing SAF and thus reducing splitting tensile strength.

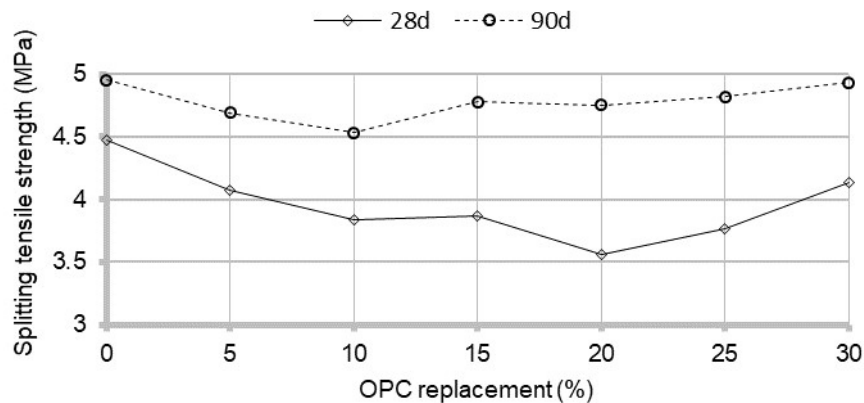


Figure 23. Effect of OPC replacement by CB on splitting tensile strength.

## 4. Conclusions

According to the results acquired in this study, the following conclusions can be drawn:

1. Iraqi high-calcium bentonite is suitable for preparing natural pozzolan by the method of calcination (thermal activation).
2. The optimum calcination program is 800 °C for 90 min.
3. Its slow reactivity characterizes pozzolan prepared from Iraqi bentonite; that is, it has a retarder effect on the initial and final setting time, reducing the strength gain rate.
4. CB has a reducing effect on concrete workability, and the amount of reduction is proportional to the replacement level.
5. Significant reductions in concrete absorption were observed at 15–25 % replacement levels.
6. CB reduces the compressive strength at 7 days in proportion to CB content. At 28 days, a low replacement level (5 %) leads to optimum strength gain of 12 %, moderate levels (10–20 %) does not cause a significant change in strength, and high levels (20–30 %) reduces strength by about 10 %. At 90 days, the maximum strength gain is 9 % at 5 % replacement, the maximum strength loss is 9 % at 30 % replacement, and no significant change in strength at 10–25 % replacement levels.
7. CB reduces the splitting tensile strength at any replacement level at all ages.

## References

1. ACI Committee E-701. ACI Education Bulletin E3-13 – Cementitious materials for concrete. Farmington Hills, MI 48331, U.S.A., 2013. E3-2 p.
2. Dedeloudis, C., Zervaki, M., Sideris, K., Juenger, M., Alderete, N., Kamali-Bernard, S., Villagrán, Y., Snellings, R. Properties of Fresh and Hardened Concrete Containing Supplementary Cementitious Materials. 25. Cham, Springer International Publishing, 2018. 181–231 p. ISBN: 978-3-319-70605-4.
3. ACI Committee 232. ACI 232.1R-12 – Report on the use of raw or processed natural pozzolans in concrete. Farmington Hills, MI 48331, U.S.A., 2012.
4. Grim, R.E., Güven, N. Bentonites: geology, mineralogy, properties and uses. Amsterdam, The Netherlands, Elsevier Scientific Publishing Company, 1978.
5. Pusch, R. Bentonite clay: environmental properties and applications. CRC Press, 2015.
6. Velde, B. Introduction to clay minerals – chemistry, origins, uses and environmental significance. London, United Kingdom, Chapman and Hall, 1992.
7. Bergaya, F., Lagaly, G. General introduction: clays, clay minerals, and clay science. Handbook of Clay Science. Amsterdam, The Netherlands, Elsevier Ltd., 2006. Pp. 1–18.
8. Mirza, J., Riaz, M., Naseer, A., Rehman, F., Khan, A.N., Ali, Q. Pakistani bentonite in mortars and concrete as low cost construction material. Applied Clay Science. 2009. 45 (4). Pp. 220–226. DOI: 10.1016/j.clay.2009.06.011.
9. Ahmad, S., Barbhuiya, S.A., Elahi, A., Iqbal, J. Effect of Pakistani bentonite on properties of mortar and concrete. Clay Minerals. 2011. 46 (1). Pp. 85–92. DOI: 10.1180/claymin.2011.046.1.85.
10. Targan, Ş., Olgun, A., Erdogan, Y., Sevinc, V. Effects of supplementary cementing materials on the properties of cement and concrete. Cement and Concrete Research. 2002. 32 (10). Pp. 1551–1558. DOI: 10.1016/S0008-8846(02)00831-1.
11. Mesboua, N., Benyounes, K., Benmounah, A. Study of the impact of bentonite on the physico-mechanical and flow properties of cement grout. Cogent Engineering. 2018. 5 (1). Pp. 1446252. DOI: 10.1080/23311916.2018.1446252.
12. Shabab, M.E., Shahzada, K., Gencturk, B., Ashraf, M., Fahad, M. Synergistic effect of fly ash and bentonite as partial replacement of cement in mass concrete. KSCE Journal of Civil Engineering. 2016. 20(5). Pp. 1987–1995. DOI: 10.1007/s12205-015-0166-x.
13. Karthikeyan, M., Raja Ramachandran, P., Nandhini, A., Vinodha, R. Application on partial substitute of cement by bentonite in concrete. International Journal of ChemTech Research. 2015. 8 (11). Pp. 384–388.
14. Akbar, J., Alam, B., Ashraf, M., Afzal, S. Evaluating the effect of bentonite on strength and durability of high performance concrete. IJASGE. 2013. 2 (1). Pp. 1–5.
15. Al-Hammood, A.A., Frayyeh, Q.J., Abbas, W.A. Raw bentonite as supplementary cementitious material – a review. Journal of Physics: Conference Series. 2021. 1795 (1). Pp. 012018. DOI: 10.1088/1742-6596/1795/1/012018.
16. Takahashi, T., Ohkubo, T., Suzuki, K., Ikeda, Y. High resolution solid-state NMR studies on dissolution and alteration of Na-montmorillonite under highly alkaline conditions. Microporous and Mesoporous Materials. 2007. 106 (1–3). Pp. 284–297. DOI: 10.1016/j.micromeso.2007.03.008
17. Garg, N., Skibsted, J. Thermal Activation of a Pure Montmorillonite Clay and Its Reactivity in Cementitious Systems. The Journal of Physical Chemistry C. 2014. 118 (21). Pp. 11464–11477. DOI: 10.1021/jp502529d
18. Alani, S., Hassan, M.S., Jaber, A.A., Ali, I.M. Effects of elevated temperatures on strength and microstructure of mortar containing nano-calcined montmorillonite clay. Construction and Building Materials. 2020. 263(120895). Pp. 120895. DOI: 10.1016/j.conbuildmat.2020.120895.
19. He, C., Makovicky, E., Osbaeck, B. Thermal treatment and pozzolanic activity of Na- and Ca-montmorillonite. Applied Clay Science. 1996. 10 (5). Pp. 351–368. DOI: 10.1016/0169-1317(95)00037-2.
20. Taher, A. Effect of heat treatment on the behaviour of montmorillonite clay in the presence of lime. Role of Cement Science in Sustainable Development. Scotland, UK, Thomas Telford Publishing, 2003. Pp. 311–318.
21. Fernandez, R., Martirena, F., Scrivener, K.L. The origin of the pozzolanic activity of calcined clay minerals: A comparison between kaolinite, illite and montmorillonite. Cement and Concrete Research. 2011. 41 (1). Pp. 113–122. DOI: 10.1016/j.cemconres.2010.09.013.
22. He, C., Osbaeck, B., Makovicky, E. Pozzolanic reactions of six principal clay minerals: Activation, reactivity assessments and technological effects. Cement and Concrete Research. 1995. 25 (8). Pp. 1691–1702. DOI: 10.1016/0008-8846(95)00165-4.
23. Darweesh, H.H.M., Nagieb, Z.A. Hydration of calcined bentonite Portland blended cement pastes. IJCT. 2007. 14 (3). Pp. 301–307.
24. Penson, C.R. Calcined calcium bentonite clay as a partial replacement of Portland cement in mortar. University of British Columbia, Okanagan, Canada, 2019.
25. Trümer, A., Ludwig, H.-M., Schellhorn, M., Diedel, R. Effect of a calcined Westerwald bentonite as supplementary cementitious material on the long-term performance of concrete. Applied Clay Science. 2019. 168. Pp. 36–42. DOI: 10.1016/j.clay.2018.10.015.
26. Memon, S.A., Arsalan, R., Khan, S., Lo, T.Y. Utilization of Pakistani bentonite as partial replacement of cement in concrete. Construction and Building Materials. 2012. 30. Pp. 237–242. DOI: 10.1016/j.conbuildmat.2011.11.021.
27. Laidani, Z.E.-A., Benabed, B., Abousnina, R., Gueddouda, M.K., Khatib, M.J. Potential pozzolanicity of Algerian calcined bentonite used as cement replacement: optimisation of calcination temperature and effect on strength of self-compacting mortars. European Journal of Environmental and Civil Engineering. 2020. Pp. 1–23. DOI:10.1080/19648189.2020.1713898.
28. Laidani, Z.E.-A., Benabed, B., Abousnina, R., Gueddouda, M.K., Kadri, E.-H. Experimental investigation on effects of calcined bentonite on fresh, strength and durability properties of sustainable self-compacting concrete. Construction and Building Materials. 2020. 230 (10). Pp. 117062. DOI: 10.1016/j.conbuildmat.2019.117062.
29. Tironi, A., Trezza, M.A., Scian, A.N., Irassar, E.F. Assessment of pozzolanic activity of different calcined clays. Cement and Concrete Composites. 2013. 37. Pp. 319–327. DOI: 10.1016/j.cemconcomp.2013.01.002.
30. Hollanders, S., Adriaens, R., Skibsted, J., Cizer, Ö., Eisen, J. Pozzolanic reactivity of pure calcined clays. Applied Clay Science. 2016. 132–133. Pp. 552–560. DOI: 10.1016/j.clay.2016.08.003.
31. Garg, N., Skibsted, J. Dissolution kinetics of calcined kaolinite and montmorillonite in alkaline conditions: Evidence for reactive Al(V) sites. Journal of the American Ceramic Society. 2019. 102 (12). Pp. 7720–7734. DOI: 10.1111/jace.16663.

32. Rehman, S.U., Yaqub, M., Ali, T., Shahzada, K., Khan, S.W., Noman, M. Durability of mortars modified with calcined montmorillonite clay. *Civil Engineering Journal*. 2019. 5 (7). Pp. 1490–1505. DOI: 10.28991/cej-2019-03091347.
33. Al-Ajeel, A.W.A., Abdullah, S.N., Al-Dahan, D.K. Upgrading of montmorillonite claystone from Wadi Bashira, West Iraq, by carrier flotation. *Iraqi Bulletin of Geology and Mining*. 2014. 10 (1). Pp. 107–115.
34. Al-Ajeel, A.W.A., Kshash, J.M., Mahdi, S.N. Sodium activation of Iraqi high grade montmorillonite claystone by dry method. *Iraqi Bulletin of Geology and Mining*. 2013. 9 (1). Pp. 65–73.
35. Al-Bassam, K.S., Abdul Rahman, S.M., Rashid, S.C. Cation exchange capacity in Iraqi industrial montmorillonitic claystones and their use in the estimation of montmorillonite content in the reduced clay. *Iraqi Bulletin of Geology and Mining*. 2011. 7(3). Pp. 1–17.
36. Toama, H.Z., Al-Ajeel, A.W.A., Abdullah, S.N. Beneficiation of low grade calcium bentonite claystone. *Engineering and Technology Journal*. 2018. 36 (5A). Pp. 546–554. DOI: 10.30684/etj.36.5A.10.
37. Al-Ajeel, A.W.A., Abdullah, S.N. Upgrading of montmorillonite claystone (Digma Formation) from Wadi Bashira, Western Desert, Iraq. *Iraqi Bulletin of Geology and Mining*. 2010. 6 (2). Pp. 149–157.
38. Mohammed, I.Q. Bentonite and smectite-rich shale deposits of Iraq. *Iraqi Bulletin of Geology and Mining*. 2019. Special Is (8). Pp. 175–202.
39. Khalifa, A.Z., Pontikes, Y., Elsen, J., Cizer, Ö. Comparing the reactivity of different natural clays under thermal and alkali activation. *RILEM Technical Letters*. 2019. 4. Pp. 74–80. DOI: 10.21809/rilemtechlett.2019.85.
40. Martirena Hernández, J.F., Almenares-Reyes, R., Zunino, F., Alujas-Diaz, A., Scrivener, K.L. Color control in industrial clay calcination. *RILEM Technical Letters*. 2020. 5. Pp. 1–7. DOI: 10.21809/rilemtechlett.2020.107.
41. Cullity, B.D., Stock, S.R. Elements of X-ray diffraction. 3<sup>rd</sup> ed. Harlow, Essex, England, Pearson Education Limited, 2014.
42. Al-Hammood, A.A., Frayyeh, Q.J., Abbas, W.A. Thermally activated bentonite as a supplementary cementitious material – a review. *Engineering and Technology Journal*. 2021. 39 (2A). Pp. 206–213. DOI: 10.30684/etj.v39i2A.1733.
43. Feng, N.-Q., Shi, Y.-X., Hao, T.-Y. Influence of ultrafine powder on the fluidity and strength of cement paste. *Advances in Cement Research*. 2000. 12 (3). Pp. 89–95. DOI:10.1680/adcr.2000.12.3.89.
44. Ur Rehman, S., Yaqub, M., Noman, M., Ali, B., Khan, M.N.A., Fahad, M., Abid, M.M., Gul, A. The influence of thermo- mechanical activation of bentonite on the mechanical and durability performance of concrete. *Applied Sciences*. 2019. 9 (24). Pp. 5549. DOI: 10.3390/app9245549.
45. Varshney, H. Utilization of rice husk ash in concrete as cement replacement. *IOSR Journal of Mechanical and Civil Engineering*. 2016. 1 (1). Pp. 28–33.
46. Rodríguez de Sensale, G. Strength development of concrete with rice-husk ash. *Cement and Concrete Composites*. 2006. 28 (2). Pp. 158–160. DOI: 10.1016/j.cemconcomp.2005.09.005.
47. Shukla, A., Singh, C.K., Sharma, A.K. Study of the properties of concrete by partial replacement of ordinary Portland cement by rice husk ash. *International Journal of Earth Sciences and Engineering*. 2011. 4 (6). Pp. 965–968.
48. Jhatial, A.A., Mohamad, N., Goh, W.I., Mo, K.H., Sohu, S.H. Incorporation of palm oil fuel ash and egg shell powder as Supplementary Cementitious Materials in Sustainable Foamed Concrete. *Tehnicky vjesnik – Technical Gazette*. 2020. 27 (5). Pp. 1394–1402. DOI: 10.17559/TV-20190326112511.
49. Nair, D.G., Sivaraman, K., Thomas, J. Mechanical properties of rice husk ash (RHA) – high strength concrete. *American Journal of Engineering Research (AJER)*. 2013. 3(Xx). Pp. 14–19.
50. Krishna, N.K., Sandeep, S., Mini, K.M. Study on concrete with partial replacement of cement by rice husk ash. *IOP Conference Series: Materials Science and Engineering*. 2016. 149. Pp. 012109. DOI: 10.1088/1757-899X/149/1/012109.
51. Sooraj, V.M. Effect of palm oil fuel ash (POFA) on strength properties of concrete. *International Journal of Scientific and Research Publications*. 2013. 3 (6). Pp. 1–7.
52. Martin, R.A. The effect of moisture on the compressive and tensile strength on a variety of rock materials. University of Missouri at Rolla, 1966. 134 p.
53. Chen, X., Wanshan, H., Jikai, Z. Effect of moisture content on compressive and split tensile strength of concrete. *Indian Journal of Engineering and Materials Sciences*. 2012. 19. Pp. 427–435.
54. Neville, A.M. Properties of concrete. 4<sup>th</sup> ed. Harlow, Essex, England, Pearson Education Limited, 2004.
55. Cadoni, E., Labibes, K., Albertini, C., Berra, M., Giangrasso, M. Strain-rate effect on the tensile behaviour of concrete at different relative humidity levels. *Materials and Structures*. 2001. 34 (1). Pp. 21–26. DOI: 10.1007/BF02482196.
56. Min, F., Yao, Z., Jiang, T. Experimental and numerical study on tensile strength of concrete under different strain rates. *The Scientific World Journal*. 2014. 2014. Pp. 1–11. DOI: 10.1155/2014/173531.

#### **Information about authors:**

##### **Amer Al-Hammood,**

ORCID: <https://orcid.org/0000-0001-6361-7153>

E-mail: [42402@student.uotechnology.edu.iq](mailto:42402@student.uotechnology.edu.iq)

##### **Qais Frayyeh, PhD**

ORCID: <https://orcid.org/0000-0002-3667-0191>

E-mail: [40012@uotechnology.edu.iq](mailto:40012@uotechnology.edu.iq)

##### **Waleed Abbas, PhD**

ORCID: <https://orcid.org/0000-0001-8287-2782>

E-mail: [waleed.a.abbas@uotechnology.edu.iq](mailto:waleed.a.abbas@uotechnology.edu.iq)

Received 24.07.2021. Approved after reviewing 31.05.2022. Accepted 02.06.2022.



Research article

UDC 624.074.3:539.3

DOI: 10.34910/MCE.116.5



## Stress condition of orthotropic vault structure with cylindrical anisotropy

A-Kh.B. Kaldar-ool<sup>1</sup> , E.K. Opbul<sup>2</sup> 

<sup>1</sup> Tuvan State University, Kyzyl. Republic of Tuva, Russia, [oorzhaka-h@mail.ru](mailto:oorzhaka-h@mail.ru), 0000-0002-5304-3747

<sup>2</sup> St. Petersburg State University of Architecture and Civil Engineering, St. Petersburg, Russia

✉ [oorzhaka-h@mail.ru](mailto:oorzhaka-h@mail.ru)

**Keywords:** barrel vaults, brickwork, anisotropy, elasticity modulus, elasticity constants, stress condition

**Abstract.** This work considers analytical calculation of brickwork barrel vault, material structure of which has a pronounced variability of elastic constants. In normative documents, brickwork is considered as a complex two-component building material with elastoplastic properties. However, there are no clear recommendations that consider the variability of the elastic properties of brickwork. This article considers influence of anisotropic properties of a brickwork three-centered flat-arched vault on its stress condition on the basis of the elasticity theory. The calculation of a flat-arched vault is based on the classic theory of bending a curved curvilinearly-anisotropic beam in view of the properties of brickwork materials with cylindrical anisotropy. We cite a mathematical solution of a differential equation of fourth order in partial derivative with two variables for an anisotropic orthotropic body in polar coordinates for creation of mathematical models describing changes in the vault material elasticity modulus. Based on the solution to the curved orthotropic body anisotropy problem, we obtained correlations between elastic constants in the main anisotropy directions.

**Citation:** Kaldar-ool, A-Kh.B., Opbul, E.K. Stress condition of orthotropic vault structure with cylindrical anisotropy. Magazine of Civil Engineering. 2022. 116(8). Article no. 11605. DOI: 10.34910/MCE.116.5

### 1. Introduction

Study object is brickwork barrel vault of complex curvilinear outline. Brickwork is an orthotropic two-component material with elastoplastic properties. In vaulted structures, depending on the direction, in a three-dimensional coordinate system, brickwork has different elastic properties. In the case of two-dimensional problem, variability manifests itself in tangential (circumferential) and radial directions.

It is well known that elastic constants include the values of the modulus of elasticity and Poisson's ratio of the masonry. Ignoring the elastic properties variability factor in calculations, for example, at the design stage, can lead to serious errors or accidents during operation. Moreover, in brickwork vaulted ceilings, anisotropy is observed not only in the material itself, but also in structural layout. In view of more frequent progressive collapses, theoretical studies based on calculation of the strength and stress state of stone vaulted structures, taking into account the properties of anisotropy, are extremely critical.

According to Professor S.G. Lekhnitsky's theory [1], brickwork barrel vaults [2] can be viewed as an orthotropic body with cylindrical anisotropy [3] for which laws of mechanics of anisotropic bodies are valid.

In the classical practice of constructing buildings and structures, including brickwork ceilings, load-bearing vaults of different geometric shapes and layouts were used. Methods of their calculation were mainly based on the laws of elasticity theory, considering the vault as a hinged-supported elastic body. Approximate methods of limiting equilibrium, proposed by Maurice Levy, and a graphical method for determining the pressure curve, based on experiments on the destruction of vaults, are used.

A particularly noteworthy study [4] examines the technical condition of historical buildings, where strength characteristics of brickwork vaulted structures is assessed on the basis of numerical modeling. The study [5] considers flat circular double-hinged vaults, statically loaded with a uniformly distributed load in the form of pressure. The authors managed to analytically solve the geometrically nonlinear deformability and stability of the vaults. Behavior of Prussian brick-concrete vaults based on numerical model built in the Abaqus software package is shown in a scientific paper [6]. Finite element analysis of the behavior of a stonework single-span arched bridge is presented in a scientific study [7]. Laboratory and numerical analysis of the destruction of stone arches on models with and without reinforcement can be found in a scientific study [8]. In the original paper [9], the behavior of an arch from a dry joint of masonry subjected to a lateral load was investigated using the finite element method and rigid blocks based on a micromodeling strategy, a nonlinear analysis was also presented taking into account various combinations of displacement of the supports (vertical, horizontal and oblique). The article [10] presents the original results of experimental studies to reduce the seismic vulnerability of stone vaults using a composite reinforced mortar. The authors of work [11] argue that displacements, observed in many historical masonry structures are concentrated at the joints of stonework and can be significant before collapse becomes a global problem. Therefore the stability modeling using discrete element modeling is particularly relevant. In order to reuse the building complex of Monte Pio port and the upper warehouses of the Palazzo Monte di Pietà, in work [12], numerical studies of two-level stone vaults were carried out and the technical condition was checked for the stability of building structures in accordance with the current Italian building codes. In scientific work [13], based on analytical formulation of the problem, the angle of friction is investigated as a geometric constraint of brickwork sample in order to find a possible range of minimum values of the thickness of round and elliptical vaults from masonry under static loads based on the limit state analysis theorem. Numerical studies of the stability of masonry vaults are presented in works [14, 15] including a unified formulation of historical stone structures modeled as 2D assemblies of rigid blocks interacting on frictional contact surfaces without stress. Experimental evaluation and development of numerical and analytical modeling of ancient masonry vaults and vaults, reinforced with composite systems, are given in work [16]. The study [17] examines the effect of stereotomy on the value of the minimum thickness of a semicircular brickwork vault: a material with low tensile strength. In the scientific work [18], on the basis of historical, experimental and numerical analysis and the results of field studies using our own software LiABlock\_3D, a spatial rigid block model of the entire structural unit was built. The work [19] proposes combined precast and cast-in-situ construction of metro station in Shanghai in the form of a large-span underground vault of 56 elements of ribbed arched segments to be assembled as triple-hinged arches. In the construction of large diameter tunnels, a new mechanized technology for the construction of precast arches has been proposed [20]. For a preliminary assessment of damage in the form of cracks, for example, in the process of mechanized construction, numerical and laboratory experiments were carried out on an arch made of volcanic rock, i.e. tuff; the research results are given in work [21]. Work [22] represents experimental studies of stonework cylindrical vaults made of thin brick tiles; the vaulted structure is considered as a permanent formwork with subsequent reinforcement based on reinforced concrete.

**The purpose of the study** is to create a calculation system based on the well-known theory of bending of a curved anisotropic beams, given in work [1].

To achieve this goal, the following **problems** are solved:

1. Determining the elasticity moduli of bricks and mortar.
2. Determining the elasticity modulus of brickwork and the anisotropic index depending on the main anisotropy directions.
3. Determining the elasticity parameters of brickwork that allow to obtain elastic constants of the vault material.
4. Analytical calculation for evaluating the stress condition of a barrel vault in the form of a curved orthotropic beam with a cylindrical anisotropy.

## 2. Methods

According to regulatory document [23], the elastic modulus of soft-mud bricks  $E_0^{brick}$  is determined on the basis of deformation of cubes or prisms cut from bricks using the formula:

$$E_0^{brick} = 200 \div 1200 \cdot R_{brick}, \quad (1)$$

where  $R_{brick}$  is brick compressive strength [2, 3].

In a residential buildings design manual [25], the elastic modulus of mortar  $E_0^{mortar}$  in a compressed bed joint is determined using the formula:

$$E_0^{mortar} = \frac{t_{mortar}}{\lambda_{mortar}}, \quad (2)$$

where  $t_{mortar}$  is the joint thickness;  $\lambda_{mortar}$  is compression compliance of a manually laid horizontal mortar joint under short-term loads determined according to the formula:

$$\lambda_{mortar} = 1.5 \cdot 10^{-3} \cdot R_{mortar}^{\frac{2}{3}} \cdot t_{mortar},$$

$R_{mortar}$  is the mortar strength limit [2, 3].

Then within the framework of the task at hand, we use the phenomenological method of rheology in order to find out the brickwork elasticity modulus on the main axes of anisotropy.

According to, we can reconstruct the real pattern of material behavior under load using more complicated schemes combining elastic and viscous elements. If we take elastic (bricks) and viscous (mortar) materials and connect them in parallel (at the vault head) and in series (at the vault abutments), we obtain rheological models: Kelvin and Maxwell bodies in the following form [3].

For parallel connection of elements:

$$E_r = E_0^{brick} + E_0^{mortar}. \quad (3)$$

For series connection of elements:

$$E_t = \frac{E_0^{brick} \cdot E_0^{mortar}}{E_0^{brick} + E_0^{mortar}}, \quad (4)$$

where  $E_r$ ,  $E_t$  are constant elasticity modulus of the brickwork anisotropy, respectively, in the radial and tangential (circular) directions.

A partial fourth-order differential equation in polar coordinates for anisotropic body has the following form[1]:

$$\begin{aligned} & \frac{1}{E_t} \cdot \frac{\partial^4 F}{\partial r^4} + \left( \frac{1}{G_{rt}} - 2 \frac{\mu_{rt}}{E_r} \right) \cdot \frac{1}{r^2} \frac{\partial^4 F}{\partial r^2 \partial \theta^2} + \frac{1}{E_r} \cdot \frac{1}{r^4} \frac{\partial^4 F}{\partial \theta^4} + \\ & + \frac{2}{E_t} \cdot \frac{1}{r} \frac{\partial^3 F}{\partial r^3} - \left( \frac{1}{G_{rt}} - 2 \frac{\mu_{rt}}{E_r} \right) \frac{1}{r^3} \frac{\partial^2 F}{\partial r \partial \theta^2} - \frac{1}{E_r} \cdot \frac{1}{r^2} \frac{\partial^2 F}{\partial r^2} + \\ & + \left( 2 \frac{1 - \mu_{rt}}{E_r} + \frac{1}{G_{rt}} \right) \frac{1}{r^4} \frac{\partial^2 F}{\partial \theta^2} + \frac{1}{E_r} \cdot \frac{1}{r^3} \frac{\partial F}{\partial r} = 0, \end{aligned} \quad (5)$$

where  $\mu_{rt}$ ,  $G_{rt}$  are Poisson's ratio and elastic modulus, respectively.

When solving equation (5) in plane elastic problem for a circular plate with cylindrical anisotropy, the stress function was taken as a sum of polynomials proposed by E.K. Ashkenazi:

$$F = \sum_{i=1}^n x^k \cdot f_k(y), \quad (6)$$

where  $f_k(y)$  is an unknown function satisfying differential equation (5).

Solving equation (5) with the substitution of the corresponding derivatives of the stress function (6) and rearrangement result in second-order algebraic equation (7), the roots of which are respectively equal [26]:

$$B^2 - \frac{2}{3}(5 + k^2)B - \frac{5}{3}k^4 + \frac{14}{3}k^2 + 1 = 0. \quad (7)$$

Professor V.N. Glukhikh states in his studies [26] that cylindrically anisotropic materials differ by elasticity parameters  $(B_{(1)}, B_{(2)})$  and can be divided into 2 groups:

- for the first group, elasticity parameter is characterized by three extremes as axes turn from the radial direction to the tangential one, i.e. from  $0^\circ$  to  $90^\circ$ :

$$B_{(1)} = 3 - k^2; \quad (8)$$

- the second group with two extremes:

$$B_{(2)} = \frac{1 + 5k^2}{3}. \quad (9)$$

The studying the plane stress condition of an anisotropic material often encounters the following problem: the elastic constants are known for a certain coordinate system  $x, y$  and it is required to find the elastic constants for a new coordinate system  $x', y'$ . For an orthotropic body, it is inconvenient to use the main coordinate system and recalculate the elastic constants [1].

The known formulas as per [26] in view of elasticity parameter  $B_{(1)}$  of anisotropic bodies for elasticity modulus  $E_{x'}$ , shear modulus  $G_{x'y'}$ , Poisson's ratio  $\mu_{x'y'}$ , will have a simpler form, which is of prime importance for engineering calculations:

$$\frac{1}{E_{x'}} = \frac{\cos^4 \theta}{E_r} + \frac{\sin^4 \theta}{E_t} + \frac{B_{(1)}}{E_t} \cdot \cos^2 \theta \cdot \sin^2 \theta; \quad (10)$$

$$\frac{1}{G_{x'y'}} = \frac{8(k^2 - 1)}{E_t} \cdot \sin^2 \theta \cdot \cos^2 \theta + \frac{1}{G_{rt}}; \quad (11)$$

$$\mu_{x'y'} = -E_{x'} \left[ \frac{2(k^2 - 1)}{E_r} \cdot \sin^2 \theta \cdot \cos^2 \theta + \frac{\mu_{rt}}{E_t} \right], \quad (12)$$

where  $G_{rt} = \frac{E_t}{3 - k^2 + 2 \cdot \mu_{rt}}$  is shear modulus;  $G_{x'y'}$  and  $\mu_{x'y'}$  respectively, the shear modulus and Poisson's ratio in a new coordinate system.

Similarly, studies [26] recommend calculation formulas for anisotropic materials belonging to the 2<sup>nd</sup> group  $B_{(2)}$ :

$$\frac{1}{E_{x'}} = \frac{\cos^4 \theta}{E_r} + \frac{\sin^4 \theta}{E_t} + B_{(2)} \cdot \frac{1}{E_t} \cdot \sin^2 \theta \cdot \cos^2 \theta; \quad (13)$$

$$\frac{1}{G_{x'y'}} = \frac{8 \cdot (1 - k^2)}{3 \cdot E_t} \cdot \sin^2 \theta \cdot \cos^2 \theta + \frac{1}{G_{rt}}; \quad (14)$$

$$\mu_{x'y'} = -E_{x'} \left[ \frac{2 \cdot (1 - k^2)}{3 \cdot E_t} \cdot \sin^2 \theta \cdot \cos^2 \theta - \frac{\mu_{rt}}{E_t} \right], \quad (15)$$



$$f_1(r) \cdot \cos(\theta) = \left( A \cdot r^{1+\beta_1} + B \cdot r^{1-\beta_1} + C \cdot r + D \cdot r \cdot \ln r \right) \cdot \cos \theta + \\ + \left( A' \cdot r^{1+\beta_1} + B' \cdot r^{1-\beta_1} + C' \cdot r + D' \cdot r \cdot \ln r \right) \cdot \sin \theta, \quad (19)$$

where  $A, B, C, D$  are arbitrary complex constant determined from boundary conditions and free-end conditions;  $A', B', C', D'$  are conjugate values.

Stresses  $\sigma_r, \sigma_\theta, \tau_{r\theta}$  are expressed through the stress function:

$$\left\{ \begin{array}{l} \sigma_r = \frac{1}{r} \cdot \frac{\partial F(r)}{\partial r} + \frac{1}{r^2} \cdot \frac{\partial^2 F(r)}{\partial \theta^2} \\ \sigma_\theta = \frac{\partial^2 F(r)}{\partial r^2} \\ \tau_{r\theta} = -\frac{\partial}{\partial r} \left( \frac{1}{r} \cdot \frac{\partial F(r)}{\partial \theta} \right) \end{array} \right. \quad (20)$$

Boundary conditions:

$$\left\{ \begin{array}{l} \text{when } r = r_d \sigma_r = 0, \tau_{r\theta} = 0; \\ \text{when } r = r_t \sigma_r = -(q + F) \cos \varphi, \tau_{r\theta} = 0. \end{array} \right. \quad (19)$$

Then the condition is true:

$$\left. \begin{array}{l} \int_{r_d}^{r_t} \sigma_\theta \partial r = -\frac{R_\theta}{h} \\ \int_{r_d}^{r_t} \sigma_\theta r \partial r = 0 \\ \int_{r_d}^{r_t} \tau_{r\theta} \partial r = \pm \frac{R_r}{h} \end{array} \right\}. \quad (21)$$

Arbitrary constants included in expression (19) are determined on the basis of boundary conditions (21) and (22).

Normal stresses in the main directions are determined according to [1] by formulas (23), (24) using the Mathcad software system:

$$\left. \begin{array}{l} \sigma_r = \frac{q}{b} \cdot \left[ P + Q \cdot \left( \frac{r}{r_t} \right)^{k-1} + R \cdot \left( \frac{r_t}{r} \right)^{k+1} \right] + \\ \quad + \frac{q}{r_t \cdot b \cdot g_1} \cdot \frac{r_t}{r} \cdot \left[ \left( \frac{r}{r_t} \right)^{\beta_1} + c^{\beta_1} \cdot \left( \frac{r_t}{r} \right)^{\beta_1} - (1 + c^{\beta_1}) \right] \cdot \frac{\cos(\phi - \psi)}{\cos \psi} \cdot \cos \theta \\ \sigma_\theta = \frac{q}{b} \cdot \left[ P + Q \cdot k \cdot \left( \frac{r}{r_t} \right)^{k-1} + R \cdot k \cdot \left( \frac{r_t}{r} \right)^{k+1} \right] + \\ \quad + \frac{q}{r_t \cdot b \cdot g_1} \cdot \frac{r_t}{r} \cdot \left[ (1 + \beta_1) \cdot \left( \frac{r}{r_t} \right)^{\beta_1} + (1 + \beta_1) \cdot c^{\beta_1} \cdot \left( \frac{r_t}{r} \right)^{\beta_1} - (1 + c^{\beta_1}) \right] \cdot \frac{\cos(\phi - \psi)}{\cos \psi} \cdot \cos \theta \\ \tau_{r\theta} = \frac{q}{r_t \cdot b \cdot g_1} \cdot \frac{r_t}{r} \cdot \left[ \left( \frac{r}{r_t} \right)^{\beta_1} + c^{\beta_1} \cdot \left( \frac{r_t}{r} \right)^{\beta_1} - (1 + c^{\beta_1}) \right] \cdot \frac{\cos(\phi - \psi)}{\cos \psi} \cdot \cos \theta \end{array} \right\} \quad (23)$$

where

$$\left. \begin{aligned}
 P &= \frac{1}{2 \cdot (k^2 - 1) \cdot (1 - c^{2k}) \cdot g} \cdot [2 \cdot k \cdot (k - 1) \cdot (1 - c^{k+1}) + 2 \cdot k \cdot (k + 1) \cdot c^{k+1} \cdot (1 - c^{k-1}) - \\
 &\quad - (k^2 - 1) \cdot (1 + c) \cdot (1 - c^{2k}) \cdot m], \\
 Q &= \frac{1}{2 \cdot (k - 1) \cdot (1 - c^{2k}) \cdot g} \cdot [-(k - 1) \cdot (1 - c^2) - 2 \cdot k \cdot c^2 \cdot (1 - c^{k-1}) + (k - 1) \cdot (1 + c) \cdot \\
 &\quad \cdot (1 - c^{k+1}) \cdot m], \\
 R &= \frac{1}{2 \cdot (k + 1) \cdot (1 - c^{2k}) \cdot g} \cdot [(k + 1) \cdot c^{2k} \cdot (1 - c^2) - 2 \cdot k \cdot c^{k+1} \cdot (1 - c^{k+1}) - (k + 1) \cdot \\
 &\quad \cdot (1 + c) \cdot c^{2k} \cdot (1 - c^{1-k}) \cdot m]
 \end{aligned} \right\} \quad (24)$$

$$c = \frac{r_d}{r_t}; \quad m = \frac{\sin \varphi \cdot \sin(\varphi - \psi)}{\cos \psi}; \quad g = \frac{(1 - c^2)}{2} - \frac{k}{k+1} \cdot \frac{(1 - c^{k+1})^2}{1 - c^2} + \frac{k \cdot c^2}{k-1} \cdot \frac{(1 - c^{k-1})^2}{1 - c^{2k}};$$

$$g_1 = \frac{2}{\beta_1} \cdot (1 - c^{\beta_1}) + (1 + c^{\beta_1}) \cdot \ln c; \quad b = 1 - \text{a single element width.}$$

It is stated in study [1] that coefficient  $\beta_1$  included in formula (23):

$$\beta_1 = \sqrt{1 + \frac{E_t}{E_r} \cdot (1 - 2 \cdot \mu_{rt}) + \frac{E_t}{G_{rt}}} \quad (25)$$

### 3. Results and Discussion

Initial data for practical calculation:

Elastic modulus of a brick of grade Mbrick = 102 and  $R_{\text{brick}} = 10.03$  MPa according to [2], obtained by the formula (1) is  $E_0^{\text{brick}} = 12036$  MPa.

Elastic modulus of the solution of grade Mmortar = 22 and  $R_{\text{mortar}} = 2.14$  MPa, according to the formula (2) is  $E_0^{\text{mortar}} = 2140$  MPa.

Radial and tangential moduli of elasticity of brickwork according to formulas (3, 4), respectively  $E_r = 14176$  MPa and  $E_t = 1816$  MPa.

Poisson's ratio according to K.P. Yakovlev [27] –  $\mu_{rt} = 0.15$

For a practical calculation example, Table 1 shows the collection of loads.

**Table 1. Collection of loads per 1 running meter barrel vault in section at the crest part.**

No	Name	Regulatory load, kN/m	Coefficient reliability $\gamma_f$	Estimated load, kN/m
1	Curb self weight $q_{c.s.w.}$ ( $\gamma = 18$ kN/m <sup>3</sup> ) 18·h in the crest part	15.3	1.1	16.83
2	Backfill weight $q_{b.w.}$ ( $\gamma = 18$ kN/m <sup>3</sup> )	Variable	1.3	–
3	Ground floor weight $q_{g.f.}$ $t=55$ m: cement-sand mortar $t=28.4$ mm ( $\gamma=18$ kN/m <sup>3</sup> ) marble chips $t=15$ mm ( $\gamma = 16$ kN/m <sup>3</sup> )	0.511 0.24	1.3	0.976
4	live load [8.2, table.8.3, p. 3]	2	1.2	2.4
5	Experimental live load	–	–	10.0
	Total:			30.206

The values of the vault loads in the crest part per running meter at an angle  $\varphi = 0^\circ$  (see Fig. 3) and according to Table 1 are  $q = 30.206 \text{ kN/m}$ .

If the supporting surfaces are assumed to be horizontal (Fig. 3), then we have  $\varphi = 0, \psi = 0, \theta = \pi/2, \cos(\varphi - \psi) = 0$ .

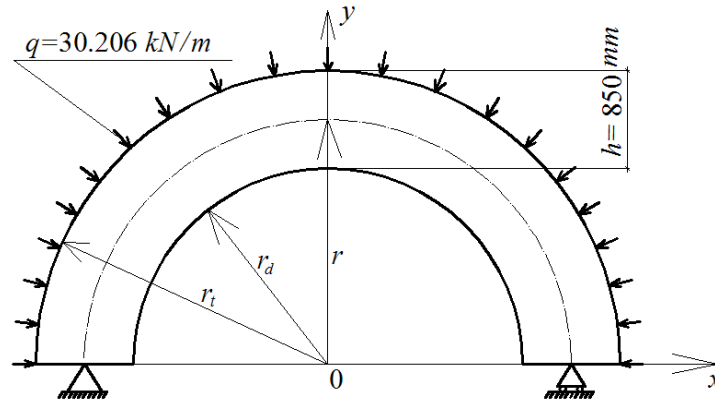


Figure 3. Calculation scheme of the vault.

Bending of curvilinearly anisotropic beam: the radius axis of slope part of vault  $r = 12.16 \text{ m}$ ; vault inner radius  $r_d = 11.73 \text{ m}$ , outer radius  $r_t = 12.58 \text{ m}$ .

1. Using known formulas (10, 13), we find out the elastic constants of brick and mortar, including for brickwork.

The values of theoretical elastic moduli of brick and mortar are presented in Tables 2–5.

**Table 2. Theoretical elastic modulus of brick at  $B_{(1)} = 3 - k^2$  according to the formula (1), (MPa).**

$\theta^\circ$	$0^\circ$	$15^\circ$	$30^\circ$	$45^\circ$	$60^\circ$	$75^\circ$	$90^\circ$
$k^2=0.5$	24072	20190	14810	12036	11330	11700	12036

**Table 3. Theoretical elastic modulus of brick at  $B_{(2)} = \frac{1+5k^2}{3}$  according to the formula (1), (MPa).**

$\theta^\circ$	$0^\circ$	$15^\circ$	$30^\circ$	$45^\circ$	$60^\circ$	$75^\circ$	$90^\circ$
$k^2=0.5$	24072	23480	21400	18050	14810	12730	12036

**Table 4. Theoretical elastic modulus of mortar at  $B_{(1)} = 3 - k^2$  according to formula (2), (MPa).**

$\theta^\circ$	$0^\circ$	$15^\circ$	$30^\circ$	$45^\circ$	$60^\circ$	$75^\circ$	$90^\circ$
$k^2=0.5$	4280	3591	2634	2140	2014	2080	2140

**Table 5. Theoretical elastic modulus of mortar at  $B_{(2)} = \frac{1+5k^2}{3}$  according to formula (2), (MPa).**

$\theta^\circ$	$0^\circ$	$15^\circ$	$30^\circ$	$45^\circ$	$60^\circ$	$75^\circ$	$90^\circ$
$k^2=0.5$	4280	4174	3804	3210	2634	2263	2140

The values of theoretical brickwork elasticity moduli are presented in Tables 6, 7.

**Table 6. Theoretical brickwork elasticity modulus at  $B_{(1)} = 3 - k^2$  ( $E_0=12036$  MPa).**

$\theta^\circ$	$0^\circ$	$15^\circ$	$30^\circ$	$45^\circ$	$60^\circ$	$75^\circ$	$90^\circ$
According to formulas (10, 13) $k^2=0.128$	14176	6146	2698	1816	1638	1729	1816

**Table 7. Theoretical brickwork elasticity modulus at  $B_{(2)} = \frac{1+5k^2}{3}$  (MPa).**

$\theta^\circ$	$0^\circ$	$15^\circ$	$30^\circ$	$45^\circ$	$60^\circ$	$75^\circ$	$90^\circ$
According to formulas (10, 13) $k^2=0.128$	14176	12092	7660	4337	2698	2006	1816

2. The coefficient is determined  $\beta_1$ .

According to [1], for parameter  $B_{(1)}$  we have:

$$\frac{E_t}{G_{rt}} - 2 \cdot \mu_{rt} \frac{E_t}{E_r} = B_{(1)}. \quad (26)$$

With regard for expression (18), (26) and (8) obtained in study [26], from formula (25) we get a parameter equal to:

$$\beta_1 = \sqrt{1 + k^2 + 3 - k^2} = 2.$$

At  $\beta_1 = 2$  stress distribution is analogous to that in an isotropic beam. Studies [26] confirmed relationship (8) mathematically.

If elastic constants meet the condition:

$$\frac{E_t}{E_r} (1 - 2 \cdot \mu_{rt}) + \frac{E_t}{G_{rt}} = 3, \quad (27)$$

then  $\beta_1 = 2$  and stress distribution will be exactly the same as in an isotropic beam.

If we transform the radical expression (23) for  $\beta_1$ , we obtain from solution [1] the same root from formula (8), i.e.  $\frac{E_t}{E_r} - 2 \cdot \mu_{rt} \cdot \frac{E_t}{E_r} + \frac{E_t}{G_{rt}} = 3$  or if  $\frac{E_t}{E_r} = k^2$  we shall obtain:  $k^2 - 2 \cdot \mu_{rt} \cdot k^2 = 3 - k^2$ , what we have obtained  $B_{(1)} = 3 - k^2$  (8) earlier as a result of theoretical studies [1].

$$\text{Or we may use this formula } \beta_1 = \sqrt{1 + k^2 + \frac{1 + 5 \cdot k^2}{3}} = \frac{2\sqrt{1 + 2 \cdot k^2}}{\sqrt{3}},,$$

$$\text{If } k^2 = 1 \text{ we get the same result } \beta_1 = \frac{2\sqrt{1 + 2 \cdot k^2}}{\sqrt{3}}.$$

Due to substitution of known ratio so felastic moduli in equation (27), we obtain the same expression (8), which was similarly obtained by S.G. Lekhnitskiy in equation [1] for a curvi linear cylindrically anisotropic orthotropic beam. As to the second elastic parameter  $B_{(2)}$ , there are no corresponding studies.

It should be noted that to find the ratio  $\beta_1$ , which is necessary for the theoretical study of the stress condition of the brickwork of vaults in the form of cylindrically anisotropic orthotropic bodies, the authors first used the second elastic parameter  $B_{(2)}$ .

In particular, the elasticity parameter  $B_{(2)}$  is recommended to be used to improve the methods for calculating the stress condition and slope part of flat-arched vault. At the same time, orthotropic materials with cylindrical anisotropy can be conventionally divided into two groups.

For the first group of materials that satisfy condition (8), the change in elastic modulus from  $0^\circ$  to  $90^\circ$  (from the radial to the tangential direction) occurs through an intermediate extreme point when the layers are tilted at an angle of  $30^\circ$  to the force line.

For the second group, there is no intermediate bending point and elastic modulus changes from  $0^\circ$  to  $90^\circ$  smoothly.

Fig. 4 shows the obtained numerical values of the distribution of radial  $\sigma_r$  and tangential  $\sigma_\theta$  stresses depending on the radius  $r$ , considering calculated elastic moduli and ratio  $\beta_1$ .

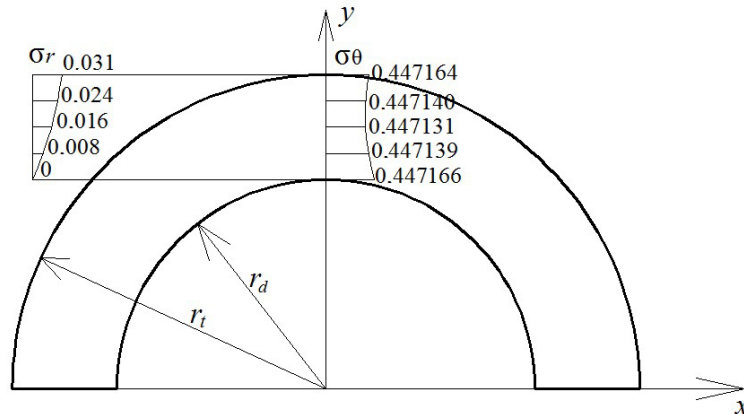


**Figure 4. Stress distribution  $\sigma_r$  and  $\sigma_\theta$  (MPa) in the crest part of the vault depending on radius  $r$  at the vault head at angle  $\varphi = 0$ .**

#### 4. Conclusion

Using the example of solving the problem of bending a curved beam with cylindrical anisotropy, an approximate method for calculating the stress state of masonry duct vaults is proposed, taking into account the properties of anisotropy.

Findings:

Based on the phenomenological method of rheology and elastic moduli ( $E_0^{brick}$ ,  $E_0^{mortar}$ ), obtained through the experimental strength limits of brick and mortar ( $R_{brick} = 10.03$  MPa,  $R_{mortar} = 2.14$  MPa), the elastic moduli of brickwork in the radial and tangential directions are determined, equal to  $E_r = 14176$  MPa and  $E_t = 1816$  MPa, respectively.

As a result of taking into account the properties of anisotropy at an angle of  $90^\circ$  using the MathCad software package, we obtained:

- elasticity parameters:  $B_{(1)} = 2.872$  with coefficient  $\beta_1 = 2$  and  $B_{(2)} = 0.547$  with coefficient  $\beta_1 = 1.392$ ;
- modules for parameters  $B_{(1)}$  and  $B_{(2)}$ , equal: for brick  $E_0^{brick} = 12036$  MPa, mortar  $E_0^{mortar} = 2140$  MPa and brickwork  $E_x = 1816$  MPa;
- maximum stress in the locking part, equal to:  $\sigma_r = 0.031$  MPa and  $\sigma_t = 0.447164$  MPa.

## References

1. Lekhnitskiy, S.G. Anisotropic plates. Moscow, 1957. 463 p. (rus)
2. Kaldar-ool, A-Kh.B., Babanov, V.V., Allahverdiv, B.M., Saaya, S.S. Additional load on barrel vaults of architectural monuments. *Magazine of Civil Engineering*. 2018. 08 (84). Pp. 15–28. DOI: 10.18720/MCE.84.2
3. Kaldar-ool, A-Kh.B., Glukhikh, V.N., Opbul, E.K., Saaya, S.S. Stress condition of brick barrel vaults in view of anisotropic properties. *Magazine of Civil Engineering*. 2021. 105(5). Article No. 10509. DOI: 10.34910/MCE.105.9Skripchenko, I.V., Bespalov, V.V., Lukichev, S.Y., Zimin, S.S. Unconventional cases of the stone vaults. *Construction of Unique Buildings and Structures*. 2017. 2 (53). Pp. 87–95.
4. Lalin, V.V., Dmitriev, A.N., Diakov, S.F. Nonlinear deformation and stability of geometrically exact elastic arches. *Magazine of Civil Engineering*. 2019. 5 (89). S. 39–51. DOI: 10.18720/MCE.89.4
5. Orlovich, R.B., Nowak, R., Vatin, N.I., Bespalov V.V. Natural oscillations of a rectangular plates with two adjacent edges clamped. *Magazine of Civil Engineering*. 2018. 82 (6). Pp. 95–102. DOI: 10.18720/MCE.82.9
6. Aydin, A.C., Ozkaya, S.G. The finite element analysis of collapse loads of single-spanned historic masonry arch bridges (Ordu, Sarpdere Bridge). *Engineering Failure Analysis*. 2018. 84. Pp. 131–138. DOI: <https://doi.org/10.1016/j.engfailanal.2017.11.002>.
7. Varró, R., Bögöly, G., Görög, P. Laboratory and numerical analysis of failure of stone masonry arches with and without reinforcement. *Engineering Failure Analysis*. 2021. DOI: <https://doi.org/10.1016/j.engfailanal.2021.105272>
8. Ferrero C., Calderini C., Portioli F., Roca P. Large displacement analysis of dry-joint masonry arches subject to inclined support movements. *Engineering Structures*. 2021. 238 (112244). DOI: <https://doi.org/10.1016/j.engstruct.2021.112244>
9. Boem, I., Gattesco, N. Cyclic behavior of masonry barrel vaults strengthened through Composite Reinforced Mortar, considering the role of the connection with the abutments. *Engineering Structures*. 2021. 228 (111518). DOI: <https://doi.org/10.1016/j.engstruct.2020.111518>
10. Dell'Endice, A., Iannuzzo, A., DeJong, M.J., Mele, T.V., Block, P. Modelling imperfections in unreinforced masonry structures: Discrete element simulations and scale model experiments of a pavilion vault. *Engineering Structures* 2021. 228 (111499). DOI: <https://doi.org/10.1016/j.engstruct.2020.111499>
11. Lucchesi, M., Pintucchi, B., Zani, N. The masonry vaults of the cellars in the canal system of Livorno. *Procedia Structural Integrity*. 2018. 11. Pp. 177–184. DOI: <https://doi.org/10.1016/j.prostr.2018.11.024>
12. Gaspar, O., Sajtos, I., Sipos, A.A. Friction as a geometric constraint on stereotomy in the minimum thickness analysis of circular and elliptical masonry arches. *International Journal of Solids and Structures*. 2021. 225 (111056). DOI: <https://doi.org/10.1016/j.ijsolstr.2021.111056>
13. Ricci, E., Fraddosio, A., Piccioni, M.D., Sacco, E., A new numerical approach for determining optimal thrust curves of masonry arches. *European Journal of Mechanics – A/Solids*. 2019. 75. Pp. 426–442. DOI: <https://doi.org/10.1016/j.euromechsol.2019.02.003>
14. Portioli, F.P. Rigid block modelling of historic masonry structures using mathematical programming: a unified formulation for non-linear time history, static pushover and limit equilibrium analysis. *Bulletin of Earthquake Engineering*. 2020. 18 (1). Pp. 211–239. DOI: <https://doi.org/10.1007/s10518-019-00722-0>
15. Bertolesi, E., Milani, G., Carozzi, F.G., Poggi, C. Ancient masonry arches and vaults strengthened with TRM, SRG and FRP composites: Numerical analyses. *Composite Structures*. 2018. 187. Pp. 385–402. DOI: <https://doi.org/10.1016/j.compstruct.2017.12.021>
16. Orsolya, G., András, A. Sipos & István Sajtos Effect of stereotomy on the lower bound value of minimum thickness of semi-circular masonry arches. *International Journal of Architectural Heritage*. 2018. 12. DOI: <https://doi.org/10.1080/155830-58.2017.1422572>
17. Cascini, L., Brando, G., Portioli, F.P., Forgione, R.M., Mazzanti, C., Vasta, M. Force-Based Seismic Evaluation of Retrofitting Interventions of Historic Masonry Castles by 3D Rigid Block Limit Analysis: Experimental and Numerical Analysis in Building Rehabilitation and Strengthening. 2020. 10 (15), 5035. DOI: <https://doi.org/10.3390/app10155035>
18. Zhang, J.-L., Liu, X., Zhao, J.-B., Yuan, Y., Mang, H. Application of a combined precast and in-situ-cast construction method for large-span underground vaults. *Tunnelling and Underground Space Technology*. 2021. Vol. 111. 103795. DOI: <https://doi.org/10.1016/j.tust.2020.103795>
19. Wang, Q., Qin, Q., Jiang, B., Xu, S., Zeng, Z., Luan, Y., Liu, B., Zhang, H. Mechanized construction of fabricated arches for large-diameter tunnels. *Automation in Construction*, 2021, Vol. 124. 103583. DOI: <https://doi.org/10.1016/j.autcon.2021.103583>.
20. Castellano, A., Camassa, D., Fraddosio, A., Scacco, J., Piccioni, M.D., Milani, G. Dynamic damage identification for a full-scale parabolic tuff barrel vault under differential settlements of the supports. *Construction and Building Materials*. Vol. 291. 2021. 123271. DOI: <https://doi.org/10.1016/j.conbuildmat.2021.123271>
21. López López, D., Bernat-Maso, E., Gil, L., Roca, P. Experimental testing of a composite structural system using tile vaults as integrated formwork for reinforced concrete. *Construction and Building Materials*. Vol. 300. 2021. 123974. DOI: <https://doi.org/10.1016/j.conbuildmat.2021.123974>
22. Russian Set of Rules SP 15.13330.2012. Masonry and reinforced masonry structures. The actual formulation of Construction Norms and Regulations II-22-81\*. Moscow: FAU "FCS". 2012. 86 p. (rus)
23. Guidance book for designers of industrial, residential and public buildings. Calculation and theoretical reference book. 2-nd ed., revised. Edited by A.A. Umanskiy. Moscow. 1972. 599 p. (rus)
24. Residential Building Design Guide. No. 3. The design of residential buildings (to SNiP 2.08.01-85) 2.08.01-85). Moscow. 1989. 305 p. (rus)
25. Glukhikh, V.N., Khrabrova, O.Yu. Bending of Sawn Wood Products Obtained from Conventional Sawing and Parallel to Generatrix Sawing. *Architecture and Engineering*. 2016. 1 (1). Pp. 4–9. DOI: <https://doi.org/10.23968/2500-0055-2016-1-1-4-9>
26. Yakovlev, K.P. Brief physical and technical reference book, Moscow, 1960. 411 p. (rus)

**Information about authors:**

**Anay-Khaak Kaldar-ool**, PhD in Technical Science

ORCID: <https://orcid.org/0000-0002-5304-3747>

E-mail: [oorzhaka-h@mail.ru](mailto:oorzhaka-h@mail.ru)

**Eres Opbul**, PhD in Technical Science

ORCID: <https://orcid.org/0000-0002-7796-2350>

E-mail: [fduecnufce@mail.ru](mailto:fduecnufce@mail.ru)

*Received 22.08.2021. Approved after reviewing 31.05.2022. Accepted 31.05.2022.*



Research article

UDC 624.154

DOI: 10.34910/MCE.116.6



## Temperature effects on the design parameters of a geothermal pile

W. Arai<sup>1</sup> , F. Masroui<sup>2</sup> , A. Abdallah<sup>2</sup> , S. Rosin-Paumier<sup>2</sup> , O. Sraj<sup>3</sup> , M. Khatib<sup>4</sup> 

<sup>1</sup> University of Balamand, Kurah, Lebanon

<sup>2</sup> University of Lorraine, Vandoeuvre-lès-Nancy, France

<sup>3</sup> Advanced Construction Technology Services, Jeddah, Saudi Arabia

<sup>4</sup> ISSEA-Cnam Lebanon, Beirut, Lebanon

✉ [wahib.arairo@balamand.edu.lb](mailto:wahib.arairo@balamand.edu.lb)

**Keywords:** geostructures, pressuremeter, heat transfer, temperature, conductivity, finite element method

**Abstract.** In geotechnical engineering, geostructures with thermo-active functions establish direct thermal exchange between the ground and buildings. They can transfer energy from or into the ground to heat or cool a building. However, adapting foundation piles, completely or in part, to produce energy piles results in heat exchange with the soil, which changes the temperature of the soil and could thereby and affects the geotechnical properties and load bearing capacity of the geostructure. Most calculations of the bearing capacities of deep foundations conducted in France are currently based on in-situ testing results using a pressuremeter. Using finite element method to model the pressuremetric behaviour of a compacted soil subjected to thermo-mechanical variations is the main motivation for this work. In this study, several pressuremeter tests were conducted on a compacted illitic soil in a laboratory tank at temperatures between 1° and 40°C. The impact of temperature variation on the limit pressure (Pl), the creep pressure (Pf) and the Ménard pressuremeter modulus (EM) were determined. The results showed a significant decrease for both limit pressure (Pl) and creep pressure (Pf) with the increase of temperature. Numerical simulations of these tests were used to calibrate a bilinear constitutive model, taking into account temperature effects on soil compressibility within a coupled thermo-mechanical framework. Thereafter, a case study of a heat exchanger pile was simulated using the proposed approach.

**Acknowledge:** This study was part of the GECKO research program funded by ANR.

**Citation:** Arai, W., Masroui, F., Abdallah, A., Rosin-Paumier, S., Sraj, O., Khatib, M. Temperature effects on the design parameters of a geothermal pile. Magazine of Civil Engineering. 2022. 116(8). Article no. 11606. DOI: 10.34910/MCE.116.6

### 1. Introduction

Geothermal energy is considered as an energy source, which has many advantages over than the conventional energy sources (concerning cost, reliability and environmental). Thermally active structures such as diaphragm walls, piles, tunnel linings, and basement walls present a promising and sustainable way for buildings heating and cooling as cited by Fromentin et al. [1], Laloui et al. [2] and Brandl [3]. The functioning of thermo-active geostructures are based on variations of the surrounding soil temperature (about 12 °C) over a range from 4 to 30 °C as discussed by Peron et al. [4]. To design heat exchanger systems, the coupled behavior between temperature variations and induced stress/strain must be taken into consideration as recommended by McCartney et al. [5], which may affect long-term performance of geostructures.

The objective of this work is to expand the understanding and measuring the impact of temperature variation on pressuremeter parameters, the pressuremetric response of soil under coupled thermal and mechanical loads to help in establishing a more effective geotechnical design criteria.

In this study, the foundation piles were considered as deep ones, and transferred the loads to depth. These foundations piles work through a combination of two phenomena's: tip resistance and lateral skin friction along the length of the pile. Several experimental investigations on the effect of temperature on soil behaviour have shown that a variation in temperature affects soil mechanical parameters (cohesion, elastic modulus, friction angle, etc.).

Modaressi and Laloui [6] summarised two major effects of heating on clays: the first one consider a thermal reversible dilation in the case of over-consolidated soils, while the second discuss an irreversible contraction in the case of a small over-consolidation ratio.

Similar results have been obtained by Burghignoli et al. [7] and later by Cekerevac and Laloui [8] for different clayey soils containing different ratios of kaolinite, illite, smectite and chlorite. For instance, these experimental results show that soil can undertake irreversible deformation when subjected to a temperature increase under a constant mechanical load equivalent to or slightly less than the preconsolidation stress.

In recent years, efforts have been made to optimise the energy performance of thermo-active geostructures. For example, in-situ tests were performed by Brandl [9], Bourne-Webb et al. [10] and Amatya et al. [11].

Several methods have been developed for determining the stress-strain response of vertically loaded piles. Two different approaches have been widely used, the finite difference model, and the finite element approach with two-dimensional elements defining the soil-pile interface.

In the finite difference approach, the pile is divided into rigid block connected by springs simulating the stiffness of the pile. Each element is subjected to an elastoplastic interaction with the soil interface. The load-transfer curves describe the relation between the shaft friction and the pile displacements, along with the relation between the pressure at the tip of the pile and the pile displacement. To introduce the effect of cyclic temperature variation, several authors like Knellwolf et al. [12], Bourne-Webb et al. [13] have added an unloading term to the load-transfer curve to characterise the reversible behaviour of the soil-pile interaction due to thermal cyclic loading. However, the soil and soil-pile interface properties remain constant with temperature.

In another approach, different constitutive soil models have been developed to introduce the effect of the temperature on the yield surface by Graham et al. [14], Cekervac and Laloui [8]. The soil-pile interface can be defined by zero thickness elements as discussed by several authors such as Goodman et al. [15], De Gennaro and Frank [16], Said [17] or thin layer elements as cited by Desai and Faruque [18].

Currently, the use of finite element methods in engineering to assess thermo-hydro-mechanical behaviour remains limited because the method is time consuming and constitutive models (for soil and soil-pile interface) frequently require numerous parameters that are difficult to access. Therefore, there is a need to develop efficient soil models that involve a few accessible parameters and are still able to reproduce correctly the soil behaviour. The simplest methods of simulating the soil-pile behaviour remain the ones based on the use of load-transfer curves.

Several load-transfer curves are available in the literature of Randolph and Wroth [19], Frank and Zhao [20] also Armaleh and Desai [21]. Load-transfer curves are defined using the pressuremeter modulus, the limit pressure, the pile diameter and the piling method. The pressuremeter is a standard in-situ test for soils and rocks providing information on strength and stiffness parameters and were mentioned by AFNOR [22] and ASTM D 4719 [23]. It provides a means of designing piles that meet both failure and deformation criteria.

The design method based on pressuremeter parameters proposed by Knellwolf et al. [12] is based on the following considerations: (1) the main component of the displacement is the axial displacement of the pile. The radial displacements of the pile are neglected, (2) the Young's modulus and coefficient of thermal expansion of the pile remain constant and independent of the temperature change, (3) the soil and soil-pile interface properties are not affected by the temperature.

In this paper, the conformity of Knellwolf hypotheses is interpreted based on the experimental results described later and the current state of knowledge of the thermo-mechanical coupled behavior of soils. The first hypothesis, which considering only the axial strain of the pile induced by temperature, matches with the results of a study by Olgun et al. [24]. Despite the fact that several experimental studies have shown that thermal cycles induces volume changes as described by Abuel-Naga et al. [25, 26] the axial displacement remains the major component.

The experimental results of Shoukry et al. [27] do not match with the second hypotheses of Knellwolf et al. [12], Amatya et al. [11], and Bourne-Webb et al. [13], as they show that the concrete elastic modulus is affected by the temperature change.

With respect to assumption no. 3, the experimental results of the pressuremetric tests conducted under controlled temperatures developed here and several researches were achieved by numerous authors like Graham et al. [14], Cekerevac and Laloui [8], Abuel-Naga et al. [28–30], show that soil-engineering properties are temperature-dependent. Therefore, it is highly probable that the temperature influences the soil-structure interface behavior. The lateral confining effective stress on the soil-pile interface could be misestimated leading to a miscalculation of the pile shaft resistance under thermal cyclic load of heating/cooling. Further investigation is required to confirm this point.

In this study, the soil used, the experimental device and the mini-pressuremeter method are described. Then, the thermal transfer associated with the heating and cooling phases before the pressuremeter tests is numerically simulated. A finite element model based on a bilinear constitutive law is used to simulate the mini-pressuremeter tests. In this model, the soil compressibility is temperature-dependent in a coupled thermo-mechanical framework. Afterwards, the experimental and numerical results are presented and discussed, focusing mainly on the thermal induced effect on the geotechnical design parameters of energy piles. A model problem of geothermal pile is developed using the proposed model with finite element method, in axisymmetric stationary conditions. Unlike other proposed models based on pressuremeter parameters proposed by Knellwolf et al. [12], Amatya et al. [11], and Bourne-Webb et al. [13], the soil-pile interaction properties depend on the temperature variation. Finally, the effect of cyclic temperature variation on the mechanical behaviour of the pile is concluded.

## 2. Methods

To investigate the effect of thermal loading on the pressuremeter parameters of a compacted soil, a small-scale tank was developed in the laboratory, and mini-pressuremeter tests were performed on the compacted soil.

Ever since the finite element was described early by Turner et al. [32] and applied to the analysis of elasticity problems, a huge number of methodologies for modeling the variation formulation of certain other field problems such as seepage, heat conduction, or consolidation that are of interest in soil mechanics have been established.

The obtained experimental results were compared with the same model using a finite element software. The objective of this comparison is to validate the experimental results and highlight the effectiveness of the proposed model.

### 2.1. Material and experimental device

Arginotech©, an illitic soil from eastern Germany was studied. It contains 76 % illite, 10 % kaolinite, 12 % calcite and traces of quartz and feldspar. Illite shows temperature-dependent behaviour as discussed by Tanaka et al. [33]. It is a non-swelling clay present in variable proportions in soils due to mineral illitisation as expressed by Lynch [34].

The grain size distribution of the soil was determined using a laser granulometer device (Figure 1b). Almost 85 % of the particles of the considered material were clay particles, and 15 % were silt particles. The Atterberg limits were determined according to AFNOR [35] and the results are as follows: liquid limit ( $LL = 65\%$ ), plastic limit ( $PL = 34\%$ ), and plasticity index ( $PI = 31\%$ ). The standard Proctor curve obtained for the illitic soil mentioned in AFNOR [22] defines an optimum water content ( $w/c$ ) equal to 31.26 % and a maximum dry density of 1.42 mg/m<sup>3</sup> (Figure 1a). The soil is considered as class A3 according to the French soil classification standard [36] and as a fat clay, MH, according to the Unified Soil Classification System ASTM [37].

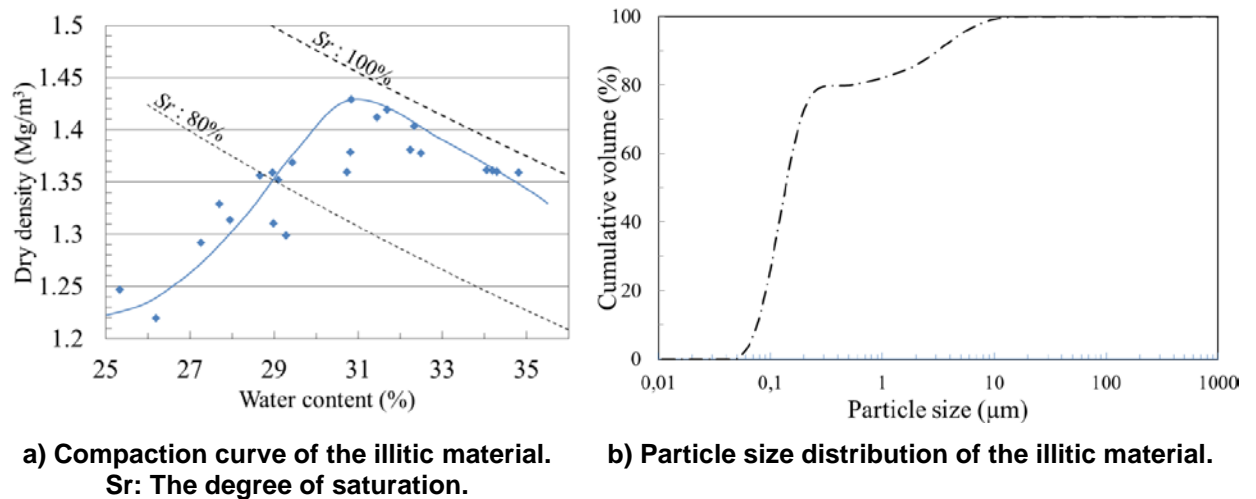


**Figure 1. Characteristic of the studied illitic soil.**

The thermal conductivity of the material studied was measured with the KD2Pro© thermal properties analyser equipped with an SH1 sensor. The suction of the studied material was measured with a WP4C water potential meter. The samples were prepared at the same dry density and the same water content as the compacted soil in the tank. In such conditions, the thermal conductivity  $\lambda$  reached 0.81; 0.83; and 0.88 W.m/K at 1°, 20° and 40 °C, respectively. The measured suction reached 220 and 380 kPa at 20° and 40 °C, respectively.

## 2.2. Sample preparation and compaction in the small-scale model

The small-scale model consisted of a stainless steel cylindrical container with a height of 800 mm and a diameter of 600 mm. The soil was compacted using a dynamic compactor and a metallic plate to distribute uniformly the compaction energy over the whole surface of the soil layers, each 70 mm thick.

Thermal sensors (7 sensors) were introduced within the container to monitor temperature inside the compacted soil during the imposed temperature variations.

A Vulcatherm® thermoregulator was connected to stainless steel tubes welded to the outer contour of the soil cylinder. A solution of ethylene glycol and water was circulated in the tubes to impose the thermal variations (1, 20 or 40 °C). Insulating sleeves were placed on the steel tubes to reduce heat transfer with the surrounding atmosphere (Figure 2). Finally, a box made of 40 mm thick extruded polystyrene plates, was used to insulate the whole assembly.

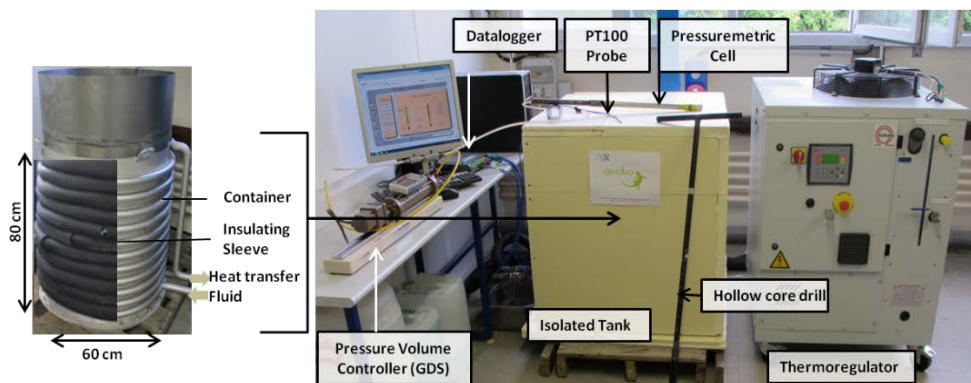


**Figure 2. Experimental device designed to carry out temperature controlled mini-pressuremetric tests.**

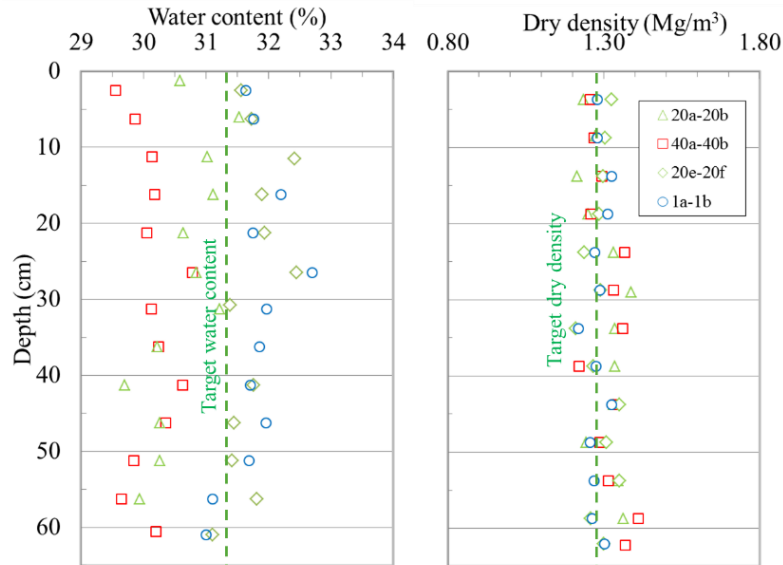
In this study, two tanks were prepared with the illitic material, compacted at the Proctor optimum water content of 31.3 % and a dry density of 1.29 mg/m<sup>3</sup>, corresponding to 90 % of the Proctor maximum dry density. An initial temperature of  $T_{i1} = T_{i2} = 20$  °C was applied to the soil for 75 hours before the thermal loading. Then, tank 1 was heated to  $T_{f1} = 40$  °C for 75 h, and tank 2 was cooled to  $T_{f2} = 1$  °C for 75 h.

## 2.3. Mini-pressuremeter tests

The test consists of introducing a cylindrical probe with a flexible membrane, which can expand radially into a drilled core to the desired testing depth. Pressure is applied to the walls of the borehole by

the probe, and the soil deformation volume is measured. Three parameters are used to mention the pressuremeter  $E_M$ ,  $p_L$  and  $p_f$ .

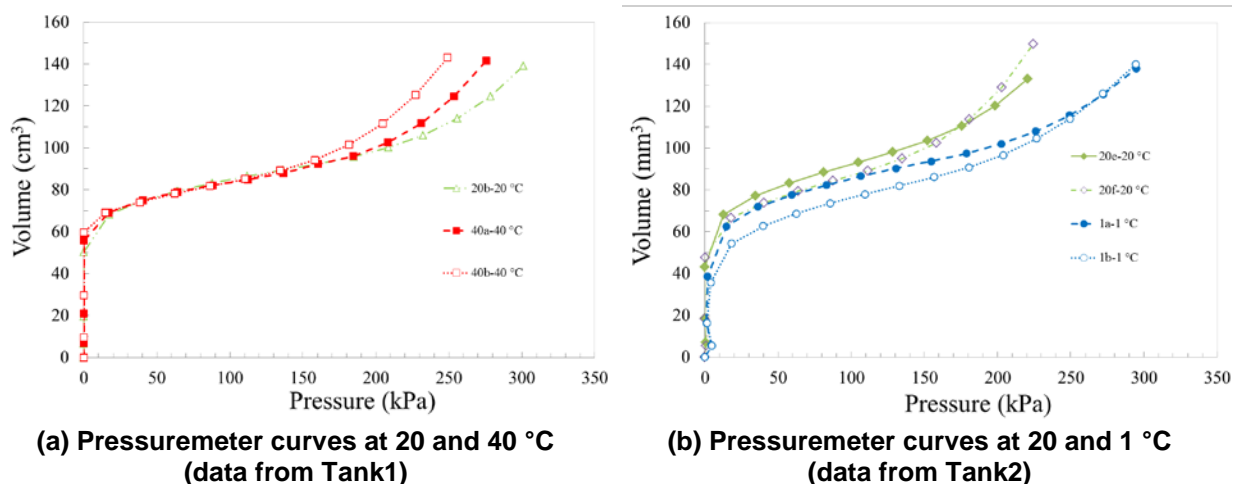
Before each mini-pressuremeter test, a 630 mm core was drilled with a diameter equal to the mini-pressuremeter probe. The cored material characteristics (i.e. the water content and the dry density) were measured each 25 mm in height. All water contents range between 29.7 % and 32.6 %, while the dry densities ranged from 1.23 to 1.40  $\text{Mg/m}^3$  (Fig. 3). These distributions as a function of depth showed acceptable deviations ( $\pm 3\%$ ) in comparison with the target values and validated the suitable overall homogeneity of the sample. The mini-pressuremeter tests were carried out with an APAGEO® mini-pressuremeter probe. The pressuremeter test consisted of applying increasing incremental pressure rate of 25 kPa per minute as recommended by AFNOR [22], and ASTM D4719 [23]. The equilibrium volume of the probe was measured for each pressure increment and the volume as function of the applied pressure were plotted with a maximum reached volume of the probe of 140.000  $\text{mm}^3$ .



(a) Water content distribution over depth (b) dry density distribution over depth

Figure 3. Water content and dry density distribution in both tanks.

In the tank 1, two mini-pressuremeter tests (Fig. 4) were carried out at an initial temperature of  $T_{i1} = 20^\circ\text{C}$  (20a, 20b) and two others at  $T_{f1} = 40^\circ\text{C}$  (40a, 40b). In the second tank, two mini-pressuremeter tests were performed at  $T_{i2} = 20^\circ\text{C}$  (20e, 20f) and two others at  $T_{f2} = 1^\circ\text{C}$  (1a, 1b).



(a) Pressuremeter curves at 20 and 40 °C (data from Tank1)

(b) Pressuremeter curves at 20 and 1 °C (data from Tank2)

Figure 4. Pressuremeter curves.

To control the thermal diffusion in the studied illitic soil, seven thermal sensors were introduced at different positions in the tank: D1 = 50 mm, D2 = 150 mm, D3 = 300 mm from the lateral boundary (Fig. 5). The temperature variation was recorded throughout the test.

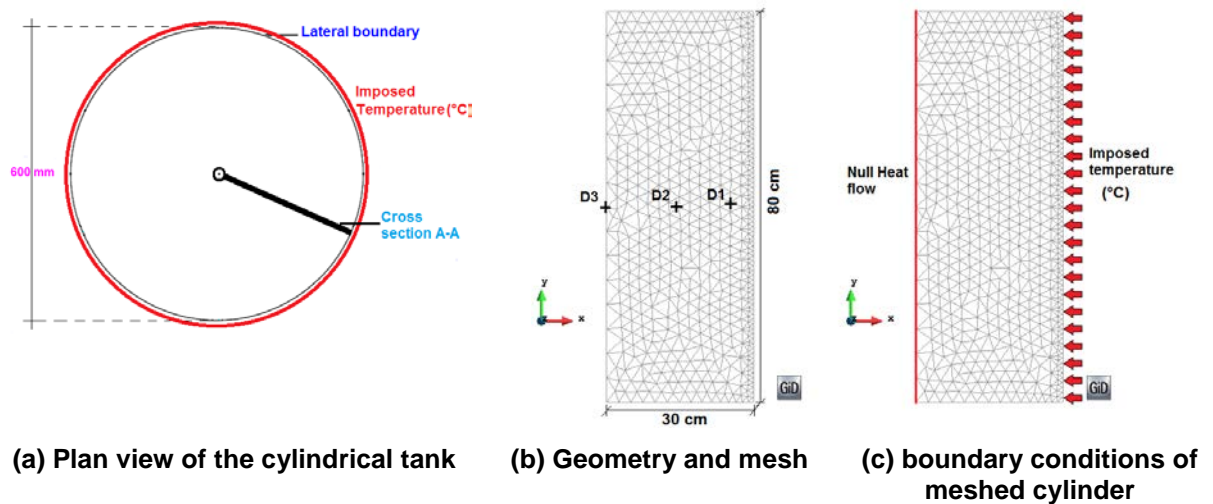


**Figure 5. Simulation the heat propagated in the cylindrical tank.**

During the heating phase, a temperature of 41 °C was applied; the referred 40 °C temperature was reached after approximately 22 hours, 40 hours, and 47 hours of heating at 50 mm, 150 mm and 300 mm from the heat source respectively. For the cooling phase, a temperature of 1 °C was applied. At steady state, the temperature was approximately 2 °C. This temperature was reached after 39 hours, 67 hours and 75 hours for points 50 mm, 150 mm and 300 mm from the lateral boundary respectively.

#### 2.4. Pressuremeter parameters of the soil submitted to thermal variations

The first test at 20 °C has failed due to membrane leakage. The results of the other tests carried out at different constant temperatures are presented in Fig. 4(a). The pressuremeter curve consists of three parts. First, the probe volume increases to reach contact with the wall of the borehole. Then a linear increase of the volume with increasing pressure is observed, in this part, the pressuremeter modulus  $E_M$  (deduced from the slope of the pressuremeter curve) is calculated, and finally, large displacements take place and the soil reaches its plastic domain. The creep pressure,  $p_f$ , the boundary between the second and third steps of the test, is determined on the creep pressuremeter curve (standard NF P94-110-1, AFNOR [22]). The limit pressure is the extrapolated pressure at which the injected volume reaches twice the initial volume of the hole. The pressuremeter parameters  $E_M$ ,  $p_L$  and  $p_f$  for each test are summarized in Table 1

The results showed a negligible effect of temperature variation on  $E_M$  parameter, while the  $p_f$  and  $p_L$  pressures increased with cooling (decrease of temperature). The material undergoes plasticity earlier when heated since the plastic deformations started earlier for the tests at 40 °C, than at 20 °C and 1 °C, approving a reduction of the elastic zone.

**Table 1. Experimental results of different pressuremeter tests carried out at different constant temperatures tank1 (20 -40-20 °C) and Tank 2 (20-1-20 °C).**

Test	Test number	Temperature (°C)	$E_M$ (MPa)	$p_f$ (MPa)	$P_L$ (MPa)	$E_M / p_L$
Tank1	20b	20	3.54	0.198	0.357	9.916
	40a	40	3.52	0.163	0.317	11.104
	40b	40	2.94	0.162	0.283	10.389
Tank2	20e	20	2.28	0.14	0.316	7.215
	20f	20	2.29	0.143	0.258	8.876
	1a	1	2.85	0.207	0.365	7.808
	1b	1	2.49	0.19	0.357	6.974

The drop of the studied parameters could be justified by the thermal softening due to increasing temperature. Similar results concerning the decrease of the yield limit with heating were also detected in triaxial tests for other types of materials achieved by Lingnau et al. [38], Marques et al. [39], Uchaipichat and Khalili [40].

## 2.5. Numerical simulation

Two different numerical simulations are presented in this section. The first simulation concerns thermal transfer during the heating and cooling phases. The second simulation focuses on the mini-pressuremeter test parameters under controlled temperatures. The numerical calculations were carried out using the Code\_Bright finite element code Olivella et al. [41]. For each simulation, the numerical strategy is detailed first, describing the different steps of the modelling. Then the numerical setup is presented, with the considered mesh, also initial and boundary conditions. Finally, the results are interpreted.

### 2.5.1. Thermal transfer approach

Thermal transfer between the lateral boundary and the soil generated a variation in the tank temperature profile.

For soils, the conduction is considered as the primary heat transfer mode especially in clayey soils where the hydraulic conductivity is very small. The main thermos-physical properties that control the heat flow by conduction are  $D$ ,  $\lambda$ ,  $C_v$ . The relation between the three properties is given as follows:

$$D = \frac{\lambda}{C_v}. \quad (1)$$

Many studies have considered that the total heat capacity of a given soil is the resultant of the heat capacities of the soil components to estimate  $C_v$  De Vries and Afgan [42]. These thermal properties depends on the mineral composition of soil and on its porosity  $n$  as follows:

$$C_v = (1-n)\rho_{cs}c_{T_s} + n\rho_{cw}c_{T_w}. \quad (2)$$

The conductive heat flow  $i_c$  is governed by Fourier's law:

$$i_c = -\lambda \nabla T. \quad (3)$$

Different formulations for the thermal conductivity  $\lambda$  have been proposed in the literature. This parameter has been related to soil properties such as mineralogical composition, dry density, pore fluid, degree of saturation, water content, temperature, and geometrical arrangement of soil particles following the recommendations of Brandon and Mitchell [43, 44].

It is reasonable to assume that the thermal conductivity of the soil remains constant, since the experimental test conditions requiring complete isolation of the tank and the small variation of thermal conductivity of the soil within the studied ranges of temperature.

To validate the main assumptions concerning the heat transfer including (1) consideration of conductive heat transfer only, (2) the use of a constant thermal conductivity, and (3) consideration of the medium as homogeneous with respect to apparent properties without taking into account the contribution of each phase, a basic numerical study was performed.

Owing to the symmetry of the problem (i.e., load and geometry axial symmetry of the tank), the problem can be reduced to a two-dimensional axisymmetric condition with respect to the vertical axis (oy). The soil mass was discretised into an unstructured mesh of triangular finite elements. A null flux was imposed on the symmetry axis. Only the temperature was fixed on the outer border; no mechanical load was taken into account. Initially, the temperature of the soil was homogeneous and constant ( $T_i = 20$  °C). The thermal loads were applied continuously by imposing a constant temperature on the outer lateral boundary. The parameters used in the simulation are summarised in Table 2. It should be noted that in the studied case, only the apparent conductivity and apparent specific heat were considered (Table 2). Other heat transfer processes (i.e., convection and radiation) have been neglected.

**Table 2. Parameters used in the numerical simulation of heat transfer.**

$C_v$ , (J/kg.K)	$\lambda$ (W.m/K)
1796	0.924

In this section, the main results of heat propagation simulation are presented. The calculation was performed using the finite element code Code\_Bright. Initially, the temperature was uniform ( $T_i = 20\text{ }^\circ\text{C}$ ). Two simulations were performed. Following the experimental conditions, for the first simulation, the imposed temperature at the lateral outside boundary was  $41\text{ }^\circ\text{C}$  for 75 h. For the second simulation, the lateral outside imposed temperature was  $1\text{ }^\circ\text{C}$  for 75 h.

The time variation of the temperature, plotted in Figure 6, shows the heat transfer phenomenon at different positions from the heat source:  $D1 = 50\text{ mm}$ ;  $D2 = 150\text{ mm}$ ;  $D3 = 300\text{ mm}$  (see Fig. 5 for more details of the geometry and the position of heat sensors). According to Fig. 6, the numerical model, with the parameters given in Table 2, is able to reproduce the heat propagation correctly at different distances from the heat source. A slightly higher value for heat conductivity than the experimentally measured value was used to superimpose the experimental and numerical results. However, the difference remains in the range of accuracy of the KD2Pro© thermal properties analyzer used ( $\pm 10\%$ ), and both curves (the numerical and the experimental one) converge to the same steady state limit.

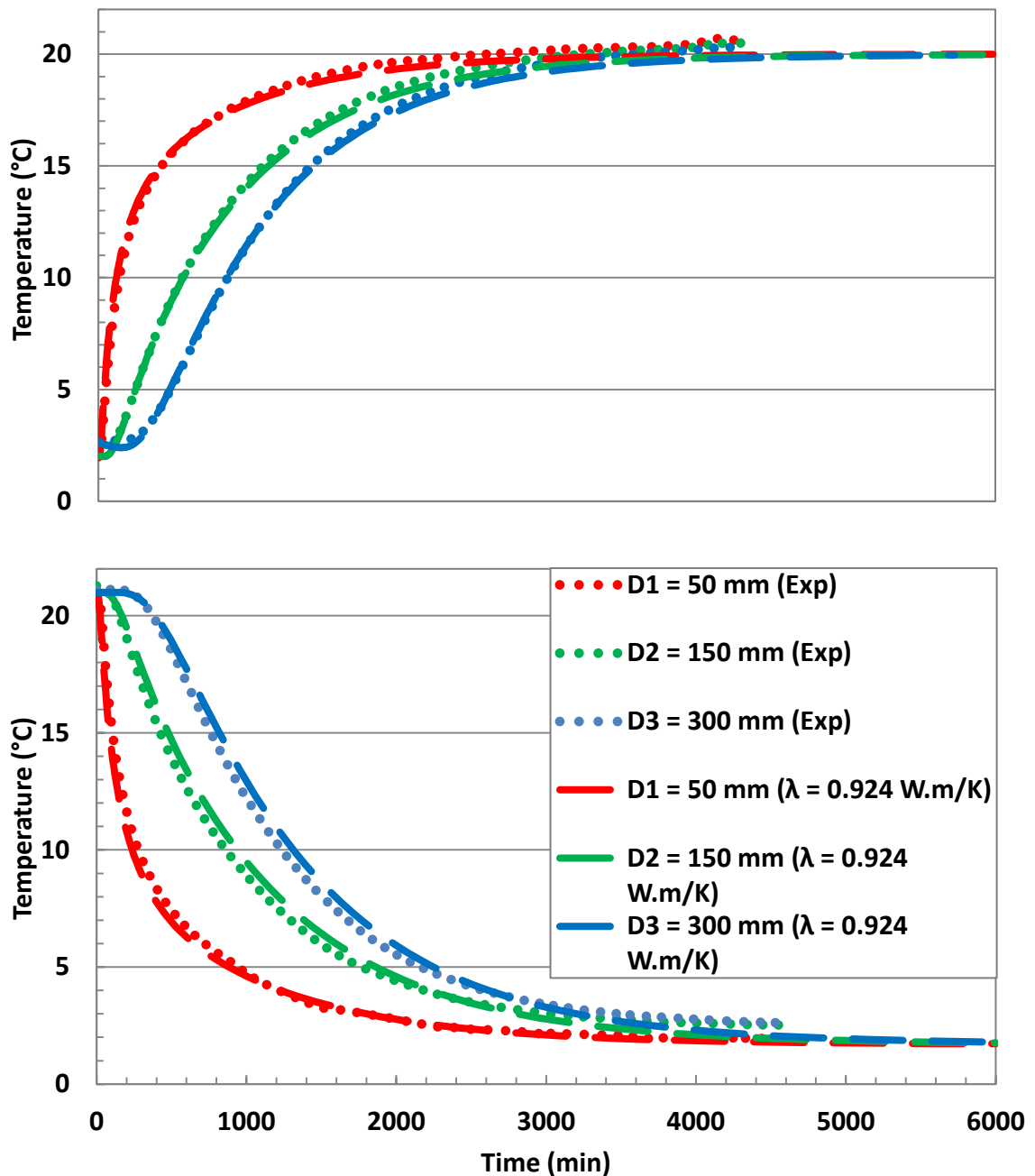


Figure 6. Time evolution of the temperature at different distances from the imposed heat temperature ((a):  $T = 40\text{ }^\circ\text{C}$  (b):  $T = 1\text{ }^\circ\text{C}$ ) on the outer lateral boundary starting from initial temperature ( $T = 20\text{ }^\circ\text{C}$ ).

2.5.2. Simulation of mini-pressurometer tests at different imposed temperatures

The mini-pressurometer tests performed in the compacted soil at various temperatures were modelled using a bilinear elastoplastic model. In this section, the model parameters are presented, and the effect of temperature on the pressurometer parameters ( $E_M, p_L, p_f$ ) is discussed.

Bilinear model simulating the pressurometer results

Soils are mainly frictional granular media, with mechanical behaviour that is well described within the framework of elasto-plasticity theory. The model used here to characterise the mechanical behaviour of the soil is a basic bilinear model. The main equations and parameters used are presented in the following text.

The bilinear model involves four parameters:  $E_0, E_c, \nu,$  and  $\epsilon_{v\text{limit}}$ .

The limit between the initial ( $E_0$ ) and final ( $E_c$ ) slope is given by the definition of the limit strain  $\epsilon_{v\text{limit}}$ . The stress-strain relation describing the mechanical behaviour is given by the following equations:

$$\begin{aligned} \text{If } \epsilon < \epsilon_{v\text{limit}} &\rightarrow \sigma = E_0\epsilon \\ \text{If } \epsilon > \epsilon_{v\text{limit}} &\rightarrow \sigma = E_0\epsilon_{v\text{limit}} + E_c(\epsilon - \epsilon_{v\text{limit}}). \end{aligned} \tag{4}$$

Fig. 7 shows the stress-strain relation with the different parameters involved to characterise the mechanical behaviour.

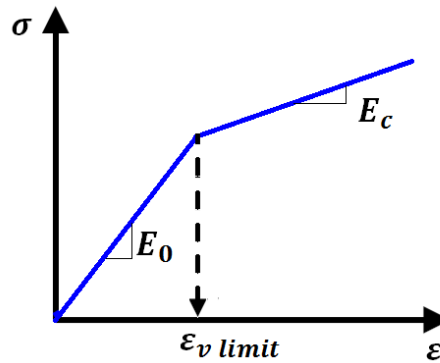
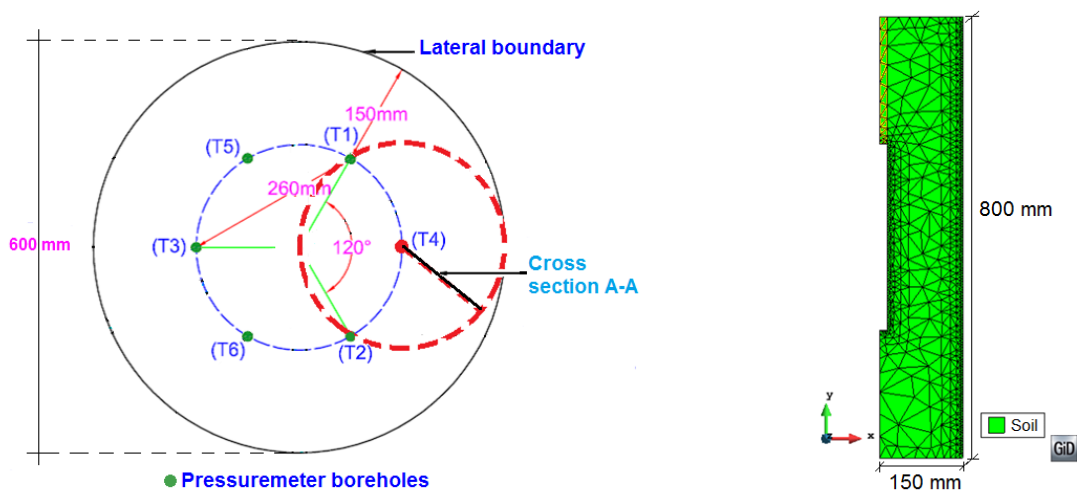


Figure 7. Bilinear model defining the stress-strain relation.

Geometry, mesh and boundary conditions for the mini-pressurometer thermally controlled test

The geometry of the tank, with its adopted mesh was presented in Fig. 8. The calculation was performed in two steps: the thermal loading phase, involving the application of a constant temperature throughout the soil and; the execution of the mini-pressurometer test at 150 mm from the boundary.



(a) geometry of the tank in plan view

(b) meshed axisymmetric vertical view

Figure 8. Numerical simulation view.

The boundary conditions for the two calculation steps are given in Fig. 9. Zero horizontal displacement conditions were applied to the outer lateral border, and a total fixity condition was imposed on the lower limit. The first part of the mini-pressuremeter test, which corresponds to the probe inflation to contact the wall of the hole, was not simulated because it is not necessary for determining the pressuremeter parameters (i.e., the pressuremeter modulus and the creep and limit pressures). Only the pseudo-elastic and plastic parts of the pressuremeter curves are considered (zones 2 and 3 in Fig. 10).

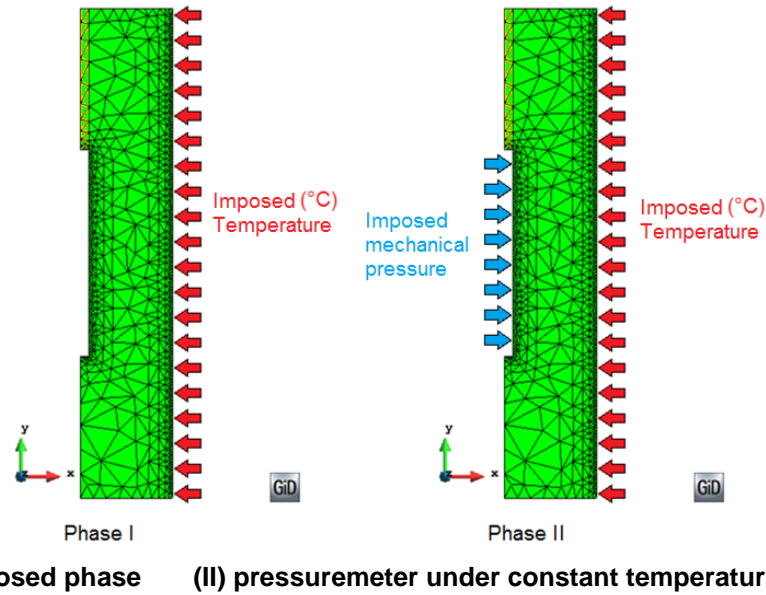


Figure 9. Boundary conditions for the two calculation steps.

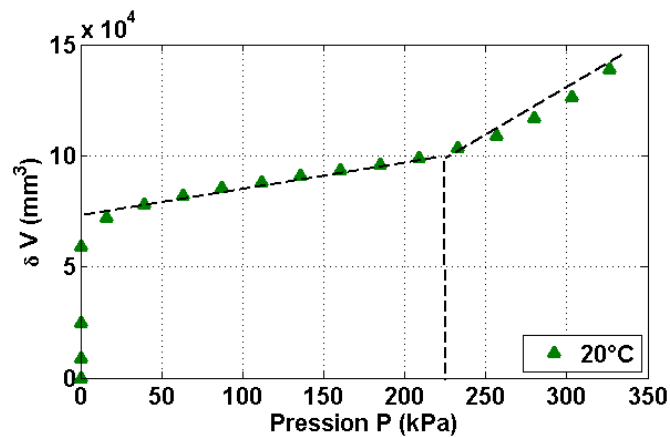


Figure 10. Determination of model parameters ( $E_0$ ,  $E_c$ ,  $\varepsilon_{vlimit}$ ) according to temperature variation with initial and final slopes and strain limit value.

According to the French design standard for deep foundations, Young's modulus can be related to the pressuremeter modulus by using  $\alpha$ . The relation between  $E_0$  and  $E_M$  is given by the following equation:

$$E_0 = \frac{(1+\nu)(1-2\nu)}{\alpha(1-\nu)} E_M. \quad (5)$$

Ménard [45] was estimated  $\alpha$  for clayey soils from the  $E_M/p_L$  ratio and was found that  $\alpha = 0.5$ . To include the effect of temperature variation on the mechanical behaviour, the model parameters were determined, as functions of temperature, as follows:

$E_0$  was calculated, based on the pressuremeter modulus  $E_M$  (equation 5),  $E_c$  was fitted to the corresponding experimental test results, and  $\varepsilon_{vlimit}$  was calibrated according to the experimental results.

$\nu = 0.3$  was considered constant.

For each simulation, the values of the mechanical parameters are summarised in Table 3. These parameters were defined according to the average value of the pressuremeter modulus for the two tests at the same temperature. It should be noted that thermal parameters were kept unchanged and identical to those given in Table 2.

**Table 3. Mechanical parameters used for the simulation of pressuremeter tests for different temperatures.**

Tanks	Temp (°C)	$E_M$ (MPa)	$E_0$ (MPa)	$\varepsilon_{vlimit}$	$\nu$	$E_c$ (MPa)
Tank1	20	3.54	5.27	0.00335	0.3	0.3
	40	3.231	4.8	0.00218		
Tank2	20	2.285	3.39	0.003	0.3	0.3
	1	2.666	3.96	0.0035		

The parameter's calibration shows that  $E_0$  and  $\varepsilon_{vlimit}$  are temperature dependent, while  $E_c$  remains constant (Fig. 10).

### 3. Results and Discussions

#### 3.1. Pressuremeter parameters of the soil submitted to thermal variations

The main experimentally results of mini-pressuremeter test simulations under controlled temperature are presented in this section. The volume variations versus the applied pressure are shown for the two tanks in Fig. 11. The proposed bilinear model was calibrated by comparing experimental data to analytical simulations. The model is able to reproduce the volumetric variations against the applied pressure at a constant temperature correctly. Moreover, these curves show that the pseudo-elastic behaviour can be considered slightly sensitive to temperature. The pressuremeter modulus decreases slightly when the temperature increases. However, the effect of temperature is more significant on the two other parameters; creep pressure  $p_f$  and the limit pressure  $p_L$ .

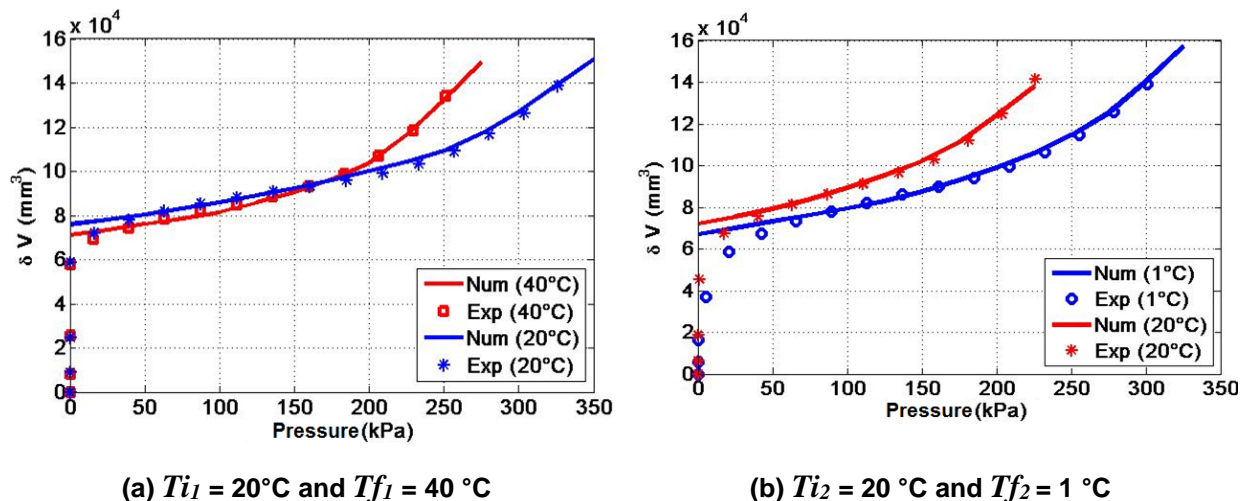


**Figure 11. Numerical and experimental variation of volumetric deformation against applied pressure under variable  $T_i$  and  $T_f$ .**

The creep pressure decreased significantly with the increase in temperature. In the numerical model, this resulted in a decrease of the limit deformation  $\varepsilon_{vlimit}$ . This means that the soil exhibited a thermal softening. Qualitatively, this result represents a transition to a more ductile behavior. These results match those obtained by Hueckel et al. [46], Laloui [47], who found that the yield surface decreased with increasing temperature.

As a first approach, a linear relation between the temperature  $T$  and the  $\varepsilon_{vlimit}$  is considered. According to the experimental results, the following relation can be proposed for the material studied (Fig. 12):

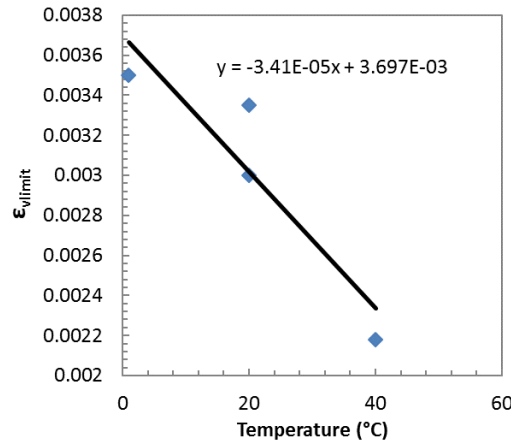


Figure 12. Proposed linear variation of  $\varepsilon_{vlimit}$  against temperature.

$$\varepsilon_{vlimit} = -3.41e^{-5}T + 3.697e^{-3} \quad (6)$$

This relationship has been introduced into the finite element code to take into account the effect of temperature on mechanical behavior for a better simulation of the interaction between the energy pile and the soil. Other formulations involving cyclic thermal variation are to be investigated.

### 3.2. Simulation of the energy pile behaviour using simplified model

A concrete pile of 1 m diameter and 20 m length was studied. A parametric study has been performed to ensure adiabatic boundary conditions in order to select the soil mass boundary dimension. The horizontal radius was set to 50 m from the pile lateral surface and the height of the soil mass to 60 m. The complete domain was simulated using a 2D axisymmetric model. Stationary analyses were executed to determine the magnitude of soil strength in response to thermal pile loading.

Fig. 13 shows the dimensions of the simulated domain and the pile. The temperature was assumed to be constant throughout the pile length, based on the results reported by Suryatriyastuti et al. [48]. An analysis of this uncoupled thermo-mechanical model was carried out using finite element code (Code\_Bright). First, the mechanical load due to the weight of the building was considered; then, the thermal load was applied. The pile was maintained in rigid contact with the surrounding soil. The surrounding soil was modelled with bilinear conditions and the parameters were temperature-dependent.

The thermal loading is applied as stationary condition in the pile; a fixed condition is assigned on the bottom boundary; a null head flow condition is imposed on the lateral boundary. The thermal loads were applied continuously over a one-year period and homogeneously over the whole pile section with the values summarised in Table 4. Table 5 summarises the thermo-mechanical properties of the materials used in this case study.

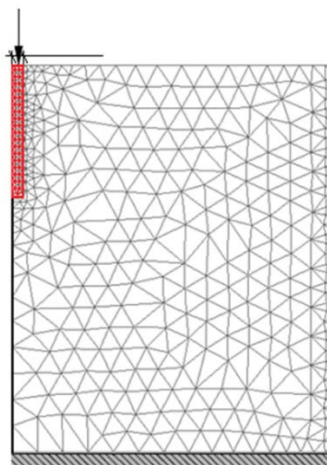


Figure 13. Mesh and geometry of the studied heat exchanger pile.

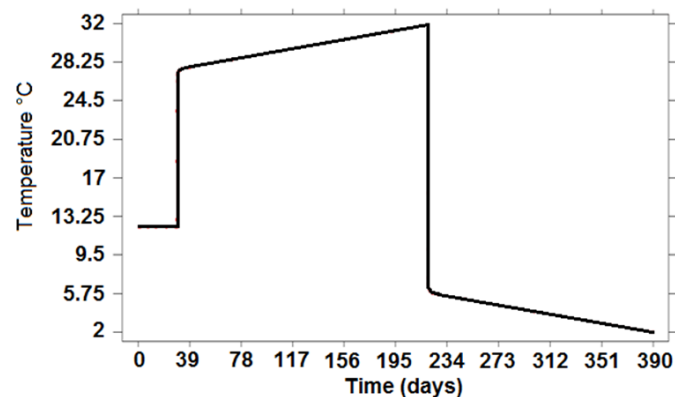
**Table 4. Applied temperature in the heat-exchanger pile.**

Calculation step	Pile Temperature (°C)	Period (days)
1	16	30
2	32	180
3	2	180

The variation of the applied temperature is shown in Figure . The ground temperature was initially generated taking into consideration its variation with depth between 12° and 17 °C. This temperature was kept constant throughout the test, since the study is limited to stationary analysis. After that, the top of the pile was loaded with up to 270 kPa corresponding to the mechanical load applied by the upper structure. The system was then subjected to two different seasonal thermo-active pile temperatures (2 °C during winter and 32 °C during summer).

**Table 5. Thermo-mechanical properties of the materials.**

Soil			
Mechanical Parameters		Thermal Parameters	
$E_0$ (MPa)	5.27	$\alpha_T$ (°C <sup>-1</sup> )	25. 10 <sup>-6</sup>
$\nu$	0.3	$\lambda$ (W.m/K)	1.25
$E_c$ (MPa)	0.3	$c_{Ts}$ (J/kg.K)	1700
$\varepsilon_{vlimit}$	Equ.(6)	$c_{Tw}$ (J/kg.K)	4180 J/kg.K
		Initial porosity $\phi$	0.52
		$\rho_{cs}$ (kg/m <sup>3</sup> )	2680
		$\rho_{cw}$ (kg/m <sup>3</sup> )	1000
Concrete Pile			
Mechanical Parameters		Thermal Parameters	
$E$ (MPa)	20.10 <sup>3</sup>	$\alpha_T$ (°C <sup>-1</sup> )	1.2 10 <sup>-5</sup>
$\nu$	0.26	$\lambda$ (W.m/K)	0.8
		$c_{Ts}$ (J/kg.K)	800

**Figure 14. Thermal loading path.**

The evolution of the ground temperature profile after the activation of the thermo-active pile was shown in Fig. 15. It can be observed that the ground temperature equilibrium is notably disturbed due to seasonal thermal variations in the pile. Furthermore, the ground temperature at a distance of approximately one pile diameter from the pile center changes completely over the entire depth of the pile length.

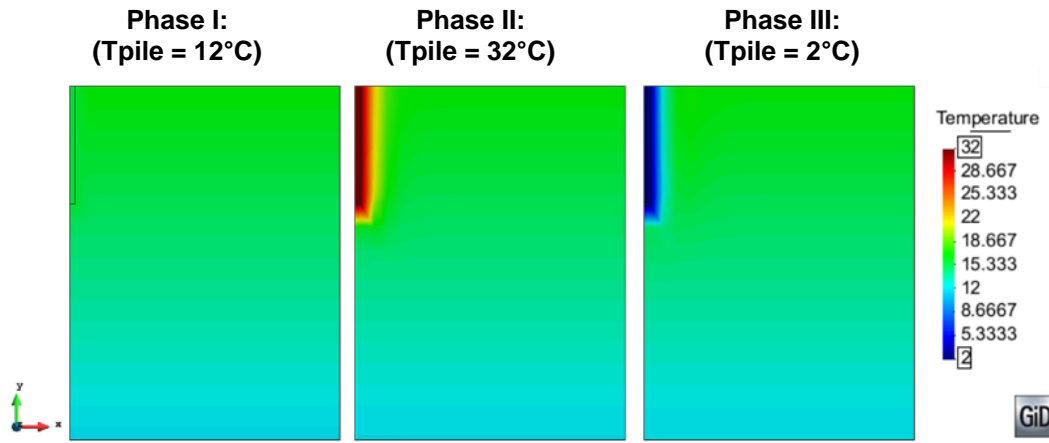


**Figure 15. Temperature diffusion profiles at the end of each thermal loading.**

The contour plot of temperature-induced axial displacement according to the diffusion within the system was shown in Fig. 16. The radial thermal displacements are insignificant compared to the axial thermal displacements due to the very small ratio between the diameter and the length of the pile. As expected, the extreme displacement values are concentrated within the concrete pile and at the soil surface. The negative values represent downward settlement, and the positive values represent upward heave.

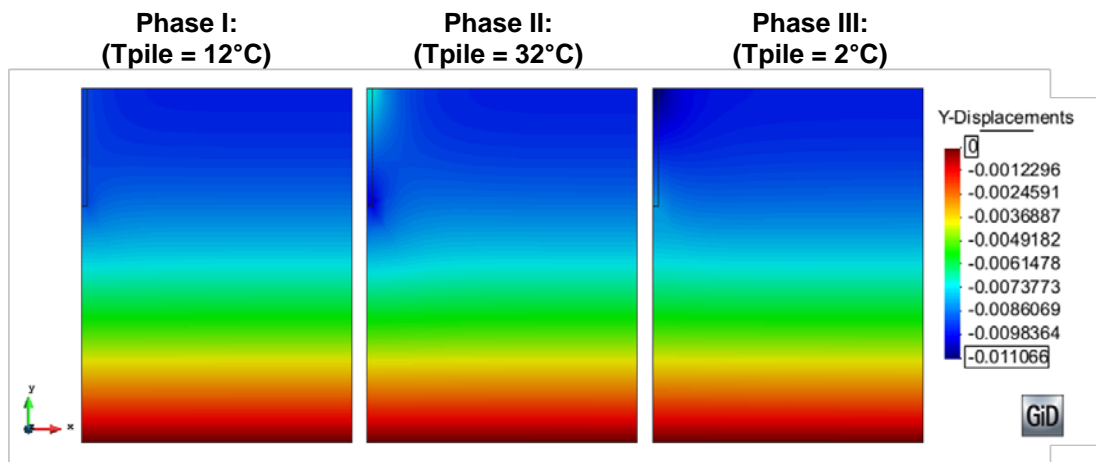


**Figure 16. Contour of vertical displacement (in m) at the end of each thermal loading.**

The effect of temperature variation on axial displacement at the soil surface was clearly visible in Fig. 17. During the first phase of loading, the settlement at the top of the pile corresponded to the response of the soil due to the applied mechanical load. In the progressive heating phase, the pile expanded with a relative head displacement of 2.1 mm. Then, the pile exhibited contractive behavior, and the final relative head displacement was -11 mm. However, over the entire length of the pile, there was a point that underwent no change in axial displacement over the entire period of thermal loading, called a null point as named by Knellwolf et al. [12], Bourne-Webb et al. [13].

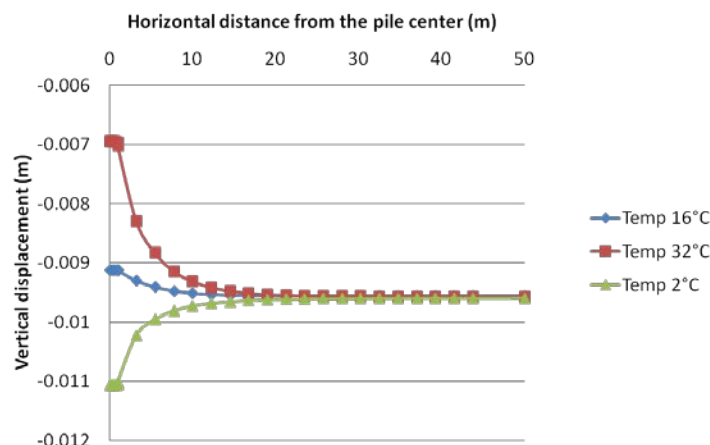


**Figure 17. Vertical displacement at the soil surface at the end of each thermal loading step.**

This point can be found in line with opposite responses to the movement of the head and of the base of the pile (Fig. 18). The latter is due to the lack of restraint at the pile head, which allows the pile to move freely. Thus, all the free thermal strain is observed. In Fig. 18 it can be observed that the null point moves with the imposed temperature. Therefore, the position of the null point depends not only on the pile confinement and the amount of freedom but also on the cyclic temperature variation.

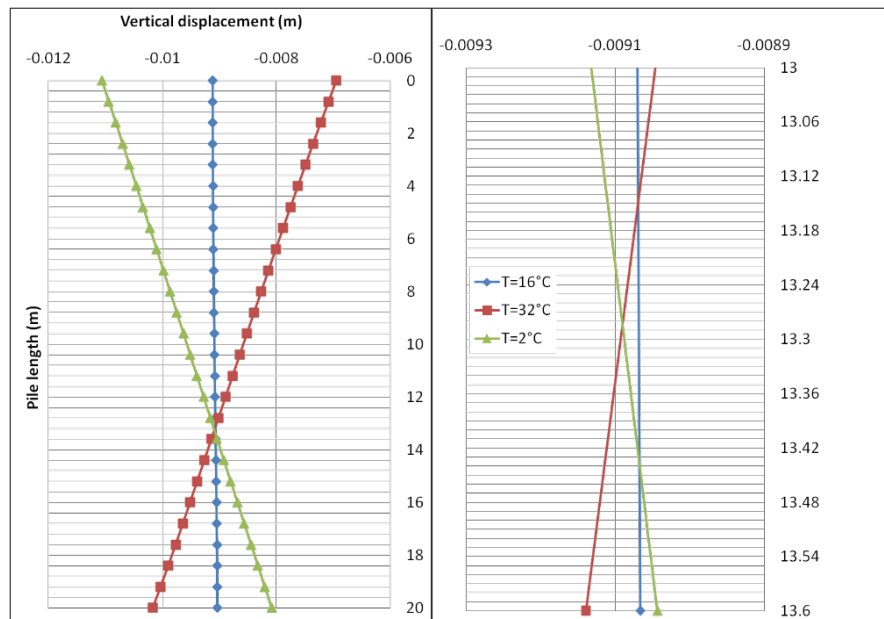


**Figure 18. Mechanical response of the pile induced by temperature variation.**

This model was used to investigate an alternative design method for a heat exchanger pile and the surrounding ground. The method developed depends on the pressuremeter parameters and their variation as functions of temperature. The case study was chosen to include the most representative characteristics of a heat exchanger pile, including seasonal temperature variations.

## 4. Conclusions

Experimental and numerical analysis of the effect of temperature on pressuremetric parameters have been conducted in this study. The main contributions of this paper include the followings:

1. The development and exploitation of an experimental device to study the effect of temperature on pressuremetric parameters;
2. The establishment of a simplified bilinear model with temperature-dependent parameters;
3. The development of a model problem of heat exchanger piles using this temperature-dependent bilinear model.

The results obtained with the mini-pressuremeter tests showed that the limit pressure and the creep pressure decrease with temperature while the pressuremeter modulus remains almost constant. These results reflect a softening behaviour with increasing temperature.

Next, a bilinear elastoplastic model was proposed to simulate the effect of temperature changes on mechanical parameters. To verify the proposed simplified model of the temperature-induced variations, a series of finite element simulations was developed that assumed controlled temperatures. Good agreement was reached between the experimental results and the model in which a relation between the parameters and temperature was proposed.

The proposed design method was finally used to study the coupled response of a heat exchanger pile. A case study was simulated using the newly developed approach. The results showed that the temperature variation inside the pile induced additional thermal stresses in the concrete pile and at the soil-pile contact zone. One novel aspect of the proposed thermo-mechanical model is that it takes into account the thermal dependency of the pressuremeter parameters.

## References

1. Formentin, A., Pahud, D., Laloui, L., Moreni, M. Pieux échangeurs: conception et règles de prédimensionnement. *Revue française de Génie Civil*. 1999. 3 (6). Pp. 387–421. DOI: 10.1080/12795119.1999.9692263
2. Laloui, L., Moreni, M., Vulliet, L. Comportement d'un pieu bi-fonction. *Canadian Geotechnical Journal*. 2003. 40 (2). Pp. 388–402. DOI: 10.1139/t02-117

3. Brandl, H. Energy Foundations and other thermo-active ground structures: *Géotechnique*. 2006. 56 (2). Pp. 81–122. DOI: 10.1680/geot.2006.56.2.81
4. Péron, H., Knellwolf, C., Laloui, L. A Method for the Geotechnical Design of Heat Exchanger Piles. *Geotechnical Special Publication*. 2011. Pp. 470–479. DOI: 10.1061/41165(397)49
5. McCartney, J.S., LaHaise, D., LaHaise, T., Rosenberg, J.E. Application of Geoexchange Experience to Geothermal Foundations. *Art of Foundation Engineering Practice*. 2010. Pp. 411–422. DOI: 10.1061/41093(372)19
6. Modaressi, H., Laloui, L. A thermo-viscoplastic constitutive model for clays. *International Journal for Numerical and Analytical Methods in Geomechanics*. 1997. 21 (5). Pp. 313–335. DOI: 10.1002/(SICI)1096-9853(199705)21:5<313::AID-NAG872>3.0.CO;2-5
7. Burghignoli, A., Desideri, A., Milizaino, S. A laboratory study on the thermomechanical behavior of clayey soils. *Canadian geotechnical journal*. 2000. 37 (4). Pp. 764–780. DOI: 10.1139/cgj-37-4-764
8. Cekerevac, C., Laloui, L. Experimental study of thermal effects on the mechanical behaviour of a clay. *International journal for numerical and analytical methods in geomechanics*. 2004. 28 (3). Pp. 209–228. DOI: 10.1002/nag.332
9. Brandl, H. Energy piles and diaphragm walls for heat transfer from and into the ground. *Proceedings of 3. International Seminar Deep Foundations on Bored and Auger Piles (BAP III)*, Ghent. 1998. Pp. 37–60. ISBN 90-5809-022-1
10. Bourne-Webb, P.J., Amatya, B., Soga, K., Amis, T., Davidson, C., Payne, P. Energy pile test at Lambeth College, London: geotechnical and thermodynamic aspects of pile response to heat cycles. *Géotechnique*. 2009. 59 (3). Pp. 237–248. DOI: 10.1680/geot.2009.59.3.237
11. Amatya, B.L., Soga, K., Bourne-Webb, P.J., Amis, T. and Laloui, L. Thermo-mechanical Behaviour of Energy Piles. *Géotechnique*. 2012. 62 (6). Pp. 503–519. DOI: 10.1680/geot.10.P.116
12. Knellwolf, C., Péron, H., Laloui, L. Geotechnical Analysis of Heat Exchanger Piles. *Journal of Geotechnical and Geoenvironmental Engineering*. 2011. 137(10). Pp. 890–902. DOI: 10.1061/(ASCE)GT.1943-5606.0000513
13. Bourne-Webb, P.J., Amatya, B.L., Soga, K. A framework for understanding energy pile behaviour. *Proceedings of the Institution of Civil Engineers – Geotechnical Engineering*. 2013. 166 (2). Pp. 170–177. DOI: 10.1680/geng.10.00098
14. Graham, J., Tanaka, N., Crilly, T., Alfaro, M. Modified Cam-Clay modeling of temperature effects in clays. *Canadian Geotechnical Journal*. 2001. 38 (3). Pp. 608–621. DOI: 10.1139/cgj-38-3-608
15. Goodman, R.E., Taylor, R.L. Brekke, T.L. A model for the mechanics of jointed rock. *Journal of the Soil Mechanics and Foundations Divisions*. 1968. 94 (3). Pp. 637–659.
16. De Gennaro, V., Frank, R. Modélisation de l'interaction sol-pieu par la méthode des éléments finis. In *Bulletin des Laboratoires des Ponts et Chaussées*: 256–257. Paris, 2005. Pp. 107–133.
17. Said, I. Comportement des interfaces et modélisation des pieux sous charge axiale. *Sciences of the Universe. Ecole des Ponts Paris Tech*, 2006. 274 p.
18. Desai, C., Faruque, M. Constitutive model for (geological) materials. *Journal of Engineering Mechanics*. 1984. 110(9). Pp. 1391–1408.
19. Randolph, M.F. Worth, C.P. Analysis of deformation of vertically loaded piles. *Journal of Geotechnical Engineering Division*. 1978. 104 (12). Pp. 1465–1488.
20. Frank, R., Zhao, S.R. Estimation par les paramètres pressiométriques de l'enfoncement sous charge axiale des pieux forés dans les sols fins. *Bull. liaison Labo P. et Ch.*, 119 Paris. 1982. Pp. 17–24.
21. Armaleh, S., Desai, C.S. Load-deformation response of axially loaded piles. *Journal of Geotechnical Engineering*. 1987. 113 (12). Pp. 1483–1500.
22. AFNOR, NF P94-110-1. Sols: reconnaissance et essais; Essai pressiométrique Ménard – Partie 1: essai sans cycle. Paris: Association Française de Normalisation. 2000.
23. ASTM, D 4719-07. Standard Test Methods for Prebored Pressuremeter Testing in Soils. West Conshohocken: ASTM International (Unified Soil Classification System). 2007.
24. Olgun, C.G., Ozudogru, T.Y., Arson, C.F. Thermo-mechanical radial expansion of heat exchanger piles and possible effects on contact pressures at pile-soil interface. *Géotechnique Letters*. 4 (3). 2014. Pp. 170–178. DOI: 10.1680/geolett.14.00018
25. Abuel-Naga, H.M., Bergado, D.T. Chaiprakaikeow, S. Innovative thermal technique for enhancing the performance of prefabricated vertical drain during the preloading process. *Geotextiles and Geomembranes*. 2006. 24 (6). Pp. 359–370. DOI: 10.1016/j.geotexmem.2006.04.003
26. Abuel-Naga, H.M., Bergado, D.T., Bouazza, A. Ramana, G.V. Volume change behavior of saturated clays under drained heating conditions: experimental results and constitutive modeling. *Canadian Geotechnical Journal*. 2007. 44 (8). Pp. 942–956. DOI: 10.1139/t07-031
27. Shoukry, S.N., William, G.W., Downie, B., Riad, M.Y. Effect of moisture and temperature on the mechanical properties of concrete. *Construction and Building Materials*. 2011. 25 (2). Pp. 688–696. DOI: 10.1016/j.conbuildmat.2010.07.020
28. Abuel-Naga, H.M., Bergado, D.T., Grino, L., Rujivipat, P. Thet, Y. Experimental evaluation of engineering behavior of soft bangkok clay under elevated temperature. *Journal of Geotechnical and Geoenvironmental Engineering*. 2006. 132 (7). Pp. 902–910. DOI: 10.1061/(ASCE)1090-0241(2006)132:7(902)
29. Abuel-Naga, H.M., Bergado, D.T., Lim, B.F. Effect of temperature on shear strength and yielding behavior of soft Bangkok clay. *Soils and Foundations*. 2007. 47 (3). Pp. 423–436. DOI: 10.3208/sandf.47.423
30. Abuel-Naga, H.M., Bergado, D.T., Bouazza, A. Pender, M.J. Thermomechanical model for saturated clays. *Geotechnique*. 2009. 59(3). Pp. 273–278. DOI: 10.1680/geot.2009.59.3.273
31. GSHPA. Thermal Pile Design, Installation and Materials Standards, Ground Source Heat Pump Association, [Online]. System requirements: Adobe Acrobat Reader. URL: [http://www.gshpa.org.uk/GSHPA\\_Thermal\\_Pile\\_Standard.html](http://www.gshpa.org.uk/GSHPA_Thermal_Pile_Standard.html). (date of application: 07.10.2021).
32. Turner, M.J., Clough, R.W., Martin, H., Topp, J. Stiffness and deflection analysis of complex structures. *Journal of the Aerospace Sciences*. 1956. 23 (9).
33. Tanaka, N., Graham, J. Crilly, T. Stress-strain behaviour of reconstituted illitic clay at different temperatures. *Engineering Geology*. 1997. 47 (4). Pp. 339–350. DOI: 10.1016/S0013-7952(96)00113-5

34. Lynch, F.L. Frio shale mineralogy and the stoichiometry of the smectite-to-illite reaction: the most important reaction in clastic sedimentary diagenesis. *Clays and Clay Minerals*. 1997. 45 (5). Pp. 618–631.
35. AFNOR, NF P94-051. Sols: reconnaissance et essais - Détermination des limites d'Atter-berg – Limite de liquidité à la coupelle – Limite de plasticité au rouleau. Paris: Association Française de Normalisation. 1993.
36. GTR. Guide technique: Réalisation des remblais et des couches de forme. Paris: LCPC. 2000.
37. ASTM, D 2487-06. Standard Practice for Classification of Soils for Engineering Purposes. West Conshohocken: ASTM International (Unified Soil Classification System). 2006.
38. Lingnau, B.E., Graham, J., Yarechewski, D., Tanaka, N., Gray, M.N. Effects of temperature on strength and compressibility of sand-bentonite buffer. *Engineering Geology*. 1996. 41(1-4). Pp. 103–115. DOI: 10.1016/0013-7952(95)00028-3
39. Leroueil, S., Marques, M.E.S., Almeida, M.S.S. Viscous behaviour of St-Roch-de-l'Achigan clay, Quebec. *Canadian Geotechnical Journal*. 2004. 41 (1). Pp. 25–38. DOI: 10.1139/t03-068
40. Uchaipichat, A., Khalili, N. Experimental investigation of thermo-hydro-mechanical behaviour of an unsaturated silt. *Géotechnique*. 2009. 59 (4). Pp. 339–353. DOI: 10.1680/geot.2009.59.4.339
41. Olivella, S., Gens, A., Ramirez, J. C., Alonso, E.E. Numerical formulation for a simulator (Code\_Bright) for the coupled analysis of saline media. *Engineering Computations*. 1996. 13 (7). Pp. 87–112. DOI: 10.1108/02644409610151575
42. DeVries, D.A. Afgan, N.H. Heat and Mass Transfer in the Biosphere. Scripta book Co. Washington. 1975.
43. Brandon, T.L., Mitchell, J.K. Factors influencing the thermal resistivity of sands. *Journal of the Geotechnical Engineering*. 1989. 115 (12). Pp. 1683–1698.
44. Mitchell, J.K. Fundamental of soil behavior. John Wiley & Sons, Inc. New York. 1993.
45. Ménard, L. The Ménard Pressuremeter: Interpretation and Application of Pressuremeter Test Results to Foundation Design, Sols-Soils. 1975. 26 p.
46. Hueckel, T., Borsetto, M. Thermoplasticity of saturated soils and shales: constitutive equations. *Journal of Geotechnical Engineering*. 1990. 116 (12). Pp. 1765–1777. DOI: 10.1061/(ASCE)0733-9410(1990)116:12(1765)
47. Laloui, L. Thermo-mechanical behavior of soils. *Revue Française de Génie Civil*. 2001. 5 (6). Pp. 809–843. DOI: 10.1080/12795119.2001.9692328
48. Suryatriyastuti, M.E., Mroueh, H., Burlon, S. Understanding the temperature-induced mechanical behaviour of energy pile foundations. *Renewable and Sustainable Energy Reviews*. 2012. 16 (5). Pp. 3344–3354. DOI: 10.1016/j.rser.2012.02.062

#### **Information about authors:**

**Wahib Arai**, PhD

ORCID: <https://orcid.org/0000-0002-1708-0233>

E-mail: [wahib.arairo@balamand.edu.lb](mailto:wahib.arairo@balamand.edu.lb)

**Farimah Masrouri**, PhD

ORCID: <https://orcid.org/0000-0001-6680-494X>

E-mail: [Farimah.Masrouri@ensg.inpl-nancy.fr](mailto:Farimah.Masrouri@ensg.inpl-nancy.fr)

**Adel Abdallah**, PhD

ORCID: <https://orcid.org/0000-0001-9784-2818>

E-mail: [adel.abdallah@univ-lorraine.fr](mailto:adel.abdallah@univ-lorraine.fr)

**Sandrine Rosin-Paumier**, PhD

ORCID: <https://orcid.org/0000-0001-9271-7153>

E-mail: [sandrine.rosin@univ-lorraine.fr](mailto:sandrine.rosin@univ-lorraine.fr)

**Omar Sraj**,

ORCID: <https://orcid.org/0000-0002-7163-9915>

E-mail: [omar.sraj@hotmail.com](mailto:omar.sraj@hotmail.com)

**Milad Khatib**, PhD

ORCID: <https://orcid.org/0000-0002-0140-0941>

E-mail: [milad.khatib@isae.edu.lb](mailto:milad.khatib@isae.edu.lb)

Received 22.09.2021. Approved after reviewing 23.06.2022. Accepted 27.06.2022.



Research article

UDC 699.812+691.175

DOI: 10.34910/MCE.116.7



## Intumescent compounds for fireproofing of polymer pipelines

V.V. Bogdanova<sup>1</sup> , O.I. Kobets<sup>1</sup> , O.N. Buraya<sup>1</sup> , A.A. Ustinov<sup>2</sup> , O.A. Zybina<sup>2</sup> 

<sup>1</sup> Research Institute for Physical Chemical Problems of the Belarusian State University, Minsk, Republic of Belarus

<sup>2</sup> Peter the Great St. Petersburg Polytechnic University, St. Petersburg, Russia

✉ [au.spbpu@gmail.com](mailto:au.spbpu@gmail.com)

**Keywords:** fire clutch, thermoformable composite, polymer binder, intumescent system, foaming ability, heat-insulating efficiency, thermal analysis

**Abstract.** Reducing the rate of fire spread in buildings through the intersections of enclosing building structures with polymer pipelines is achieved by using fire clutches equipped with liners made of expandable materials. In case of a fire, it is ensured that the spread of flame through polymer pipelines is hindered due to formation of a heat-insulating foamed layer. This layer does not allow the polymer low-melting pipelines to heat up to 120°C. Comparative assessment of heat-insulating and mechanical properties of two intumescent composites and their charred products were carried out to clarify the reasons for their heat-insulating efficiency. Composites included the same intumescent system (ammonium polyphosphate / pentaerythritol / dolomite / thermally expanded graphite) and different polymer binders. The research was conducted using the following methods: complex thermal and X-ray analyses, scanning electron microscopy, a number of standard and original techniques. It was established that heat-insulating ability of a charred layer is determined by temperature intervals in which interactions of initial components occur. The best mechanical, heat-insulating and morphological properties of investigated intumescent composites and their charred layers are achieved when temperature ranges referred to formation of organo-mineral framework and volatile thermolysis products are coinciding. For the composites studied in this paper, this temperature range was 350–400 °C. Thanks to this knowledge, it becomes possible to develop new fire-retardant composites with improved properties instead of selecting the components in empirical way. As a result, the general quality of fire-retardant materials may grow and their properties will be sufficient not only to meet the construction requirements, but to properly operate in case of fire as well, practically justifying the predicted effect.

**Acknowledge:** The research is partially funded by the Ministry of Science and Higher Education of the Russian Federation as part of World-class Research Center program: Advanced Digital Technologies (contract No. 075-15-2020-934 dated 17.11.2020)

**Citation:** Bogdanova, V.V., Kobets, O.I., Buraya, O.N., Ustinov, A.A., Zybina, O.A. Intumescent compounds for fireproofing of polymer pipelines. Magazine of Civil Engineering. 2022. 116(8). Article no. 11607. DOI: 10.34910/MCE.116.7

### 1. Introduction

Fire retardant coatings (or thermoformable coatings, TFC) have proven themselves effective as means of preventing the fire spread along building communications. They are also finding the niche as a part of constructive elements themselves, for example, in fire clutches (Fig. 1, a-d). These composites include such ingredients as polymer binders, pore-forming agents, dehydrating agents, combustion retardants, mineral fillers [1–9], and carbon materials (e.g., thermally expanded graphite, TEG, that has

recently found a lot of applications [10–18]). Combined together and exposed to heating, such composites tend to expand and provide thermal insulation to protected surface.

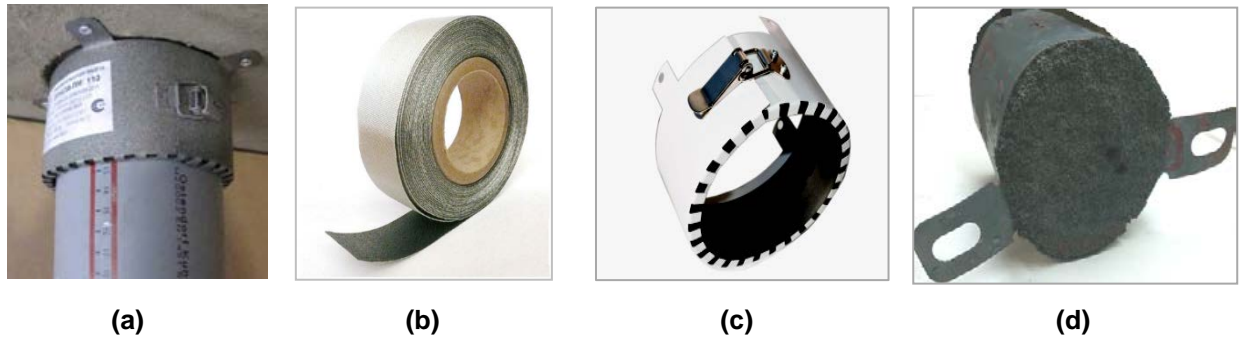


**Figure 1. Fire sleeve – preventive fire protection of polymer pipelines crossing floors in a multi-storey building: (a) fireproofing sleeve fixed on a protected polymer pipeline; (b) a tape-insert made of a polymer expandable composite - the main working element of a fire clutch; (c), (d) fire clutch with liner before and after fire tests.**

There are requirements for fire retardant composites used as filler in fire couplings: the integrity of polymer pipeline exposed to heating for 15-180 minutes must be ensured; and the temperature on unheated side of a pipeline, when thermal degradation already begins, must not exceed 120 °C. In addition, TFCs themselves must be durable and elastic, as well as the foamed layer must not only provide thermal insulation, but also be able to withstand the convective air currents in case of fire.

Applying fire retardant composites in order to protect the pipelines is not a new technique; in [19] authors suggest a fire retardant material with thixotropic properties and high viscosity, which at high temperatures becomes a foam-silicate with low conductivity and low mechanical strength; such properties ensure both the heat insulation of a pipeline or a cable connection, and an easy removal of foamed substance from the cavity between pipeline's surface and clutch.

Intumescent coatings may also be applied to surfaces of polymer cables directly; however, the dry coating must possess high values of flexural strength, which is a problem. It's being solved by using an intumescent compound as a filler in roll materials; such material, for example, was developed in [20], and it passed certification tests showing R15, R45 and R60 fire resistance limits when applied to steel beam. In [21] authors propose a set of fire retardant bendable roll materials describing their advantages over intumescent paints: adoption of the form of constructive element (waste minimization), the speed of installation, installation at any time of the year and under different climatic conditions; such materials are also finding good application in oil and gas complex where hydrocarbon fires may take place. So, there is no doubt that intumescent compounds in different forms are finding a good niche in different areas of construction.

However, development of new TFCs is mostly based on empirical ideas and hindered because of many requirements applied to them. The lack of theoretical knowledge about the processes occurring in these materials under heating conditions doesn't allow to affect their properties directly at the development stage. The abovementioned factors mostly refer to TFCs containing TEG as a foaming agent. Thermally expanded graphite, after decomposition of its layered structure at the initial stages of heating, forms bulk folded heat insulating structures [22]. In general, the heat insulating effect of TEG is based on chemical (interaction of graphite with an acid in its interlayer space resulting in formation of water vapor, CO<sub>2</sub>, SO<sub>2</sub>) and physical mechanisms [22, 23]. However, TEG being an ingredient of fire retardant compositions deteriorates physical and mechanical properties of initial coatings and products of their thermolysis [14, 23, 24].

The studies were carried out to optimize the formulation of a fire retardant composition based on melamine-formaldehyde resin [25]; the main goals were to reduce the time and cost of new TFCs development, and to obtain information about the factors that make a decisive contribution to their fireproofing ability. At the same time, a correlation was found between the heat insulating ability and the quantitative content of carbon-containing (pentaerythritol) and foaming (TiO<sub>2</sub>) agents in the TFC. Also, the contribution of a polymer binder to heat insulating ability of TFC must also be taken into account and studied properly.

Such studies focused on assessing the correlation between the nature of polymer binder and the properties of TFCs were carried out in [4, 26, 27]; TFCs contained ammonium polyphosphate, pentaerythritol, melamine and / or titanium dioxide. The authors of [4, 26] used water-dispersed copolymers of vinyl acetate, acryl, styrene and vinyl toluene acrylate as polymer binders. In [27], organosilicon polymer and acrylic copolymer were used as binders. However, there is a lack of information about the reasons for

the different efficiency of TFCs containing various polymer binders, thus direct development of expandable materials with required heat insulating properties is hindered.

Comparative studies of TFCs containing identical char-forming system and various polymer binders were carried out in order to obtain information on the reasons for the different heat insulating efficiency. The abovementioned is the main goal of the current study.

## 2. Materials and Methods

Two waterborne compositions (TFC1 and TFC2) were selected for the study, made on the basis of the following polymer dispersions: a vinyl acetate-ethylene emulsion of Mowilith LDM 1865 WP and a styrene-acrylic emulsion of Osacril OSA H with the same content (40 %) in the investigated compositions. A mixture of ammonium polyphosphate (APP,  $\text{NH}_4\text{PO}_3$ ), pentaerythritol (PET,  $\text{C}_5\text{H}_{12}\text{O}_4$ ), and dolomite (DI,  $\text{CaMg}(\text{CO}_3)_2$ ) was used as a char-forming system (CFS) in both TFCs. Each of the compositions additionally contained the same amount of TEG. The fractional mass ratio of the CFS components in both compositions was: AFP: PET: DI: TEG = 1.7: 0.8: 1: 1.

The foaming capacity of TFC was estimated by the coefficient of foaming, calculated from the relative change in the thickness of the samples during heating in the dynamic mode in the temperature range from 20 to 200–800 °C every 100 °C:  $K = \delta_l / \delta_0$ , where  $K$  is a coefficient of foaming;  $\delta_l$  is the thickness of foamed layer mm;  $\delta_0$  is the initial thickness of the TFC sample, mm [28].

The value of heating rate was 10 °C / min. The coating was considered satisfactorily foamed if the value of  $K$  was at least 10.

The mechanical strength (relative compression deformation) of the foamed products formed as a result of TFCs heating was determined according to the laboratory method: the products of heat treatment of a TFC sample at 500 °C for 10 min were subjected to tests. The relative compression deformation ( $\varepsilon$ , %) was determined by the formula:  $\varepsilon = \frac{h_0 - h_{res}}{h_0} \cdot 100\%$ , where  $h_0$  and  $h_{res}$  are the height (mm) of the heated foamed sample before and after applying the load ( $\sim 8 \text{ kg} / \text{m}^2$ ) [29].

X-ray phase analysis (XPA) of initial and charred composites was carried out on a DRON-2 diffractometer (Cu  $K\alpha$  – radiation). Crystalline phases were identified using the ICDD software [30].

The microstructure of the surface of sections of foamed char residues after testing TFC samples was investigated using a LEO1420 scanning electron microscope (K. Zeiss, Germany).

The data of complex thermal analysis (differential scanning calorimetry – DSC, thermogravimetric analysis – TG, differential thermogravimetric analysis - DTG) was obtained in temperature range 20–600 °C (heating rate 10 °C / min in an oxygen / nitrogen atmosphere) using Netzsch STA 449 C setup.

Fire tests on heat insulating ability of a TFC sample (50×350 mm) embedded in two turns inside the body of a standard fire sleeve fixed to a fragment of a polypropylene (PP) pipe were carried out according to the laboratory method described in [31]. The method of conducting the fire tests, simulating the conditions stated in GOST R 53306–2009, was somewhat different from the standard method: in the laboratory furnace, the temperature regime was set with a lower final temperature inside the furnace (850 °C instead of 1000 °C), while taking into account the smaller size of the test chamber (17×22×32 cm) respectively scaled the amount of combustible load (the length of the PP pipe with a diameter of 40 mm with a wall thickness of 4 mm was 250 mm). During the tests, the time was measured in minutes until the limit state was reached: temperature of 120 °C on the unheated surface of a polymer pipe fragment and/or deformation, destruction of a polymer pipe fragment behind the enclosing structure from the unheated side. The tests were considered completed when one of the limit states was reached. The layout of the sample, the arrangement of thermocouples and the graph of the temperature regime in the laboratory test setup are shown in Fig. 2 a, b.

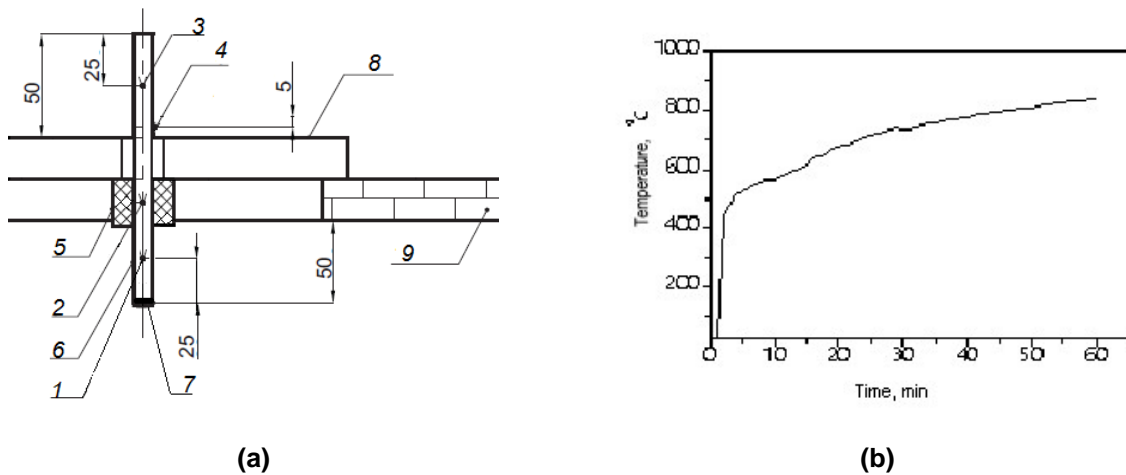


**Figure 2. Schematic layout of the sample and thermocouples in the laboratory setup (a), graph of the rate of temperature rise in the chamber of the laboratory test furnace (b).**

1–3 – thermocouples located in the internal cavity of the pipeline fragment;  
 4 – thermocouples located on the unheated surface of the pipelines fragment;  
 5 – fire coupling (cut-off protective device); 6 – a fragment of a polymer pipeline;  
 7 – plug; 8 – furnace cover; 9 – furnace; all dimensions in fig. (a) are in mm

### 3. Results and discussion

To obtain more complete information on heat insulating ability of TFC1 and TFC2, not only the limiting factor was measured - the time of reaching 120 °C on the unheated side of the pipeline, but also the change in temperature inside the cavity of the pipeline from heated (thermocouple 1) and unheated (thermocouple 3) sides, as well as in the middle of the sleeve (thermocouple 2) with a sample of the thermoformable composition (Fig. 3, a).

It follows from the results of fire tests that the fire resistance limit of TFC2 is 1.8 times higher compared to TFC1. At the same time, thermocouples 1 – 3 (Fig. 3, a, b) located in the fire clutch (2), inside the polymer pipe from the heated side (1) and from the unheated side above the foamed test sample (3), show that the rate of temperatures rising during 10- and 40-minute heating are higher for TFC1 compared to TFC2 by 1.3; 1.8; 3.1 and 1.1; 1.4; 1.8 times respectively.

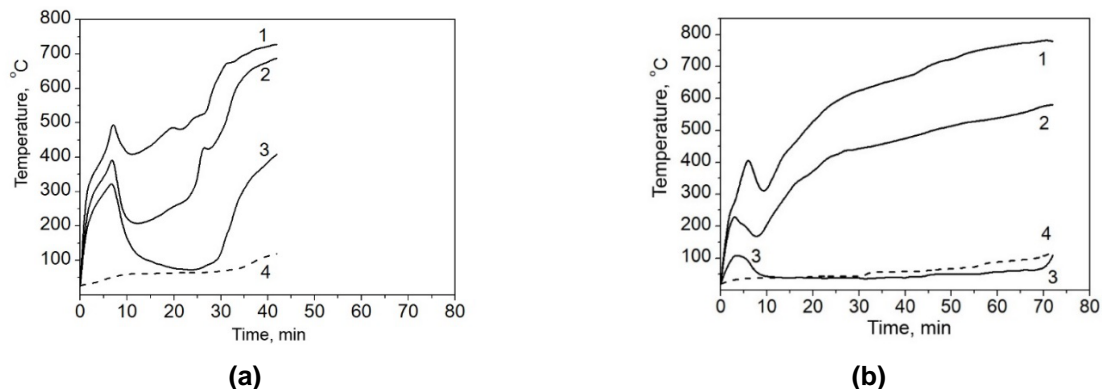


**Figure 3. Graphs of temperature change depending on time while heating a fragment of a polymer pipeline with a fire sleeve containing: (a) TFC1; (b) TFC2.**

For composition TFC1, as compared to TFC2, on all thermocouples (1–3) located inside the polymer pipe, at the initial stage of testing (the first 10 min), higher maxima of temperature rise were recorded. This fact indicates a lower thermal insulating ability of the solid products of TFC1 thermolysis. It should be noted that during the first 10 minutes from the start of the tests, when in both cases a rapid short-term rise in temperature was observed inside the polymer pipe, no change in its external state was observed. Fire tests were stopped when one of the limiting states was reached: for TFC1 after registering the beginning of deformation of the polymer pipe (Fig. 4, a), and for TFC2 – upon reaching a temperature of 120 °C on the unheated side of the polymer pipe while maintaining its original integrity (Fig. 4, b).

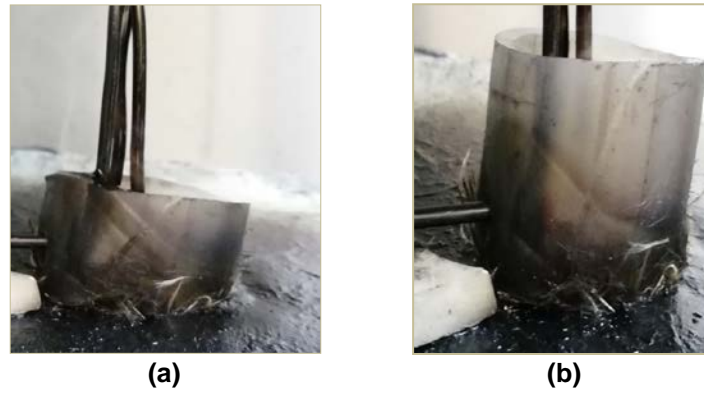


**Figure 4. Photo fixation of the state of polymer pipe from the unheated side at the end of fire tests of TFC1 (a) and TFC2 (b).**

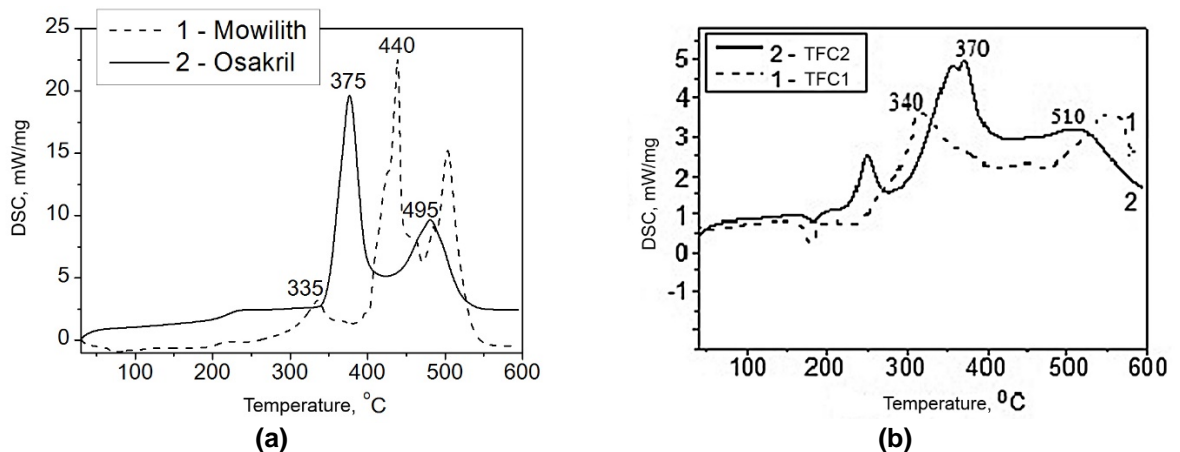
To determine the reasons for the different thermal insulating properties of the investigated compositions, comparative studies of the foaming ability and physico-mechanical properties of solid products of TFC1 and TFC2 at temperatures of 20–800 °C with an interval of 100 °C were carried out (Table 1) [32]. When comparing mechanical characteristics of the investigated compositions with their thermal protective efficiency, it should be noted that the rate of foaming is higher in the entire investigated temperature range for sample TFC2 with best fire resistance. The relative compression strain ( $\varepsilon$ , %) for the thermolysis products of TFC1 (20 %) is 5.7 times bigger than that of TFC2 (3.5 %), which is an additional factor that determines the low thermal insulating ability of TFC1.

**Table 1. Physical and mechanical properties of TFCs charred products.**

Sample	Parameter	Temperatures range, °C					
		20–300	20–400	20–500	20–600	20–700	20–800
TFC1	$K$	5.3	7.8	8.1	7.2	5.3	7.3
	$\rho$ , g/cm <sup>3</sup>	0.139	0.062	0.067	0.047	0.057	0.034
	$\Delta m$ , %	12.5	36.4	46.2	57.1	64.7	70.6
TFC2	$K$	8.9	19	14.9	10.5	9.2	9.2
	$\rho$ , g/cm <sup>3</sup>	0.136	0.034	0.037	0.038	0.041	0.039
	$\Delta m$ , %	9.4	44.8	52.4	64.3	70	72.9

Making a conclusion on the factors that determine effectiveness of TFCs is incorrect if only the values of mechanical parameters of charred layers are assessed. Comparative studies on behavior of both TFCs themselves and their components under heating conditions were carried out at the next stage.

Fig. 5 (a-c) shows the differential scanning calorimetry data for individual polymer binders, TFCs based on them, and a charring system. Thermal transformations of individual polymer binders occur in different temperature ranges (Fig. 5, a): temperatures of the onset of weight loss and exo-effects accompanied by almost complete weight loss are 216 °C, 335, 440, 503 °C for Mowilith; and 231, 375, 495 °C for Osakril.



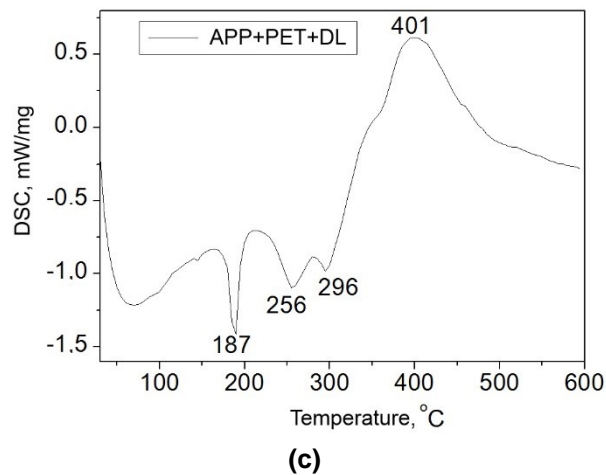


**Figure 5. DSC data for: a – binders; b – TFCs; c – charring system; curve numbers correspond to: 1 – Mowilith binder or TFC1 based on Mowilith; 2 – Osakril binder or TFC2 based on Osakril.**

According to DSC data (Fig. 5, b), changes in the maxima of thermal effects are observed when comparing data for polymer binders and TFCs. This is explicitly for TFC1, where the exo-effects of individual Mowilith in the range of 440 and 503 °C (Fig. 5, a) were transformed into exo-peaks with maxima at 340 and 540 °C (Fig. 5, b). A slightly different effects occur in TFC2, where the shift of the main exo-effect of the individual Osakril (375 °C) is practically not observed, while the temperature of the second exo-effect (495 °C) shifts to higher point (510 °C).

Endo-effects in charring system are recorded in the range of 200–320 °C which can be observed in DSC curves (Fig. 5, c); such effects are typical for components of intumescent compound. With a further increase in temperature, a broad exo-effect is recorded with a maxima of 401 °C. Proceeding from the fact that this effect is accompanied by insignificant weight loss, it is assumed to be due to structural transformations of thermolysis products of CFS components.

To verify this assumption, an X-ray study of the charred products and their physical state in the temperature range of 200–600 °C was conducted (Table 2). No visible changes in the state of the initial intumescent compound are observed in the range from 200 °C to 250 °C. The onset of sintering without changing the color of the original compound becomes noticeable at about 300 °C. The processes of melting and formation of a foamed layer occur in the temperature range of 300–400 °C, and complete foaming of the heated compound occurs at 400–500 °C [33].

**Table 2. X-ray phase analysis (XRD) data and the physical state of charred products obtained by heating the intumescent compound.**

T, °C	Physical state	XRD data
200	P	CaMg(CO <sub>3</sub> ) <sub>2</sub> , NH <sub>4</sub> PO <sub>3</sub> , C <sub>5</sub> H <sub>12</sub> O <sub>4</sub>
250	P	CaMg(CO <sub>3</sub> ) <sub>2</sub> , NH <sub>4</sub> PO <sub>3</sub> , C <sub>5</sub> H <sub>12</sub> O <sub>4</sub>
300	S	CaMg(CO <sub>3</sub> ) <sub>2</sub> , NH <sub>4</sub> PO <sub>3</sub> , C <sub>5</sub> H <sub>12</sub> O <sub>4</sub> , UP
400	F	CaMg(CO <sub>3</sub> ) <sub>2</sub> , CaCO <sub>3</sub> , UP
500	F	CaMg(CO <sub>3</sub> ) <sub>2</sub> , CaCO <sub>3</sub> , UP
600	F	CaMg(CO <sub>3</sub> ) <sub>2</sub> , CaCO <sub>3</sub> , UP

Note 1 – Indication of physical state: P – powder; S – sintering; F – foaming.

Note 2 – UP – unidentified phase.

According to X-ray phase analysis, the change in intensity of reflections of individual components of the CFS on the X-ray diffraction patterns appears at about ~ 300 °C. At this temperature, in addition to the initial components (APP, PET, DL), an unidentified phase was detected by X-ray diffraction, the appearance of which can be explained by APP thermolysis resulting in formation of a mixture of polyphosphoric acids that initiate PET esterification reactions [34], as well as formation of products of interaction with carbonate component. At the same time, in temperature range from 300 °C to 400 °C, according to XRD, the main crystalline phases are CaMg(CO<sub>3</sub>)<sub>2</sub> and CaCO<sub>3</sub> with a decrease in intensity of their reflections followed by an increase in heating temperature. Presumably, as the temperature rises, the carbonate Ca-Mg-containing salt dissociates into its constituent CaCO<sub>3</sub> and MgCO<sub>3</sub> with their simultaneous interaction with condensed phosphoric acids formed during APP thermolysis [35]. At 400 °C, the peaks referred to crystalline phases of PET and APP disappear from X-ray diffraction patterns of CFS, which indicates the intensification of

interaction between products of thermal decomposition of CFS components. Thus, as a result of X-ray examination of solid products of TFC thermolysis, it was found that the exothermic effect on DSC curve in range of 300–400 °C (Fig. 5, c) is due to formation of an unidentified organo-mineral product.

An important aspect affecting the qualitative and quantitative characteristics of thermoformable composites is the formation of gaseous products while TFCs heating; those products take part in formation of heat insulating porous structures [35, 36]. In accordance with this, it is of interest to consider the data of DTG study of TFCs and their components. According to DTG data for film-forming agents (Mowilith, Osakril) and polymer compositions based on them (TFC1, TFC2), it can be seen (Fig. 6 a, b) that weight loss occurs at a maximum rate in the temperature range of 300–400 °C. At the same time, for Osakril and TFC2, the maximum temperatures are 30–40 °C higher than those for Mowilith and TFC1. Intensive thermolysis of the charring system is recorded in the temperature range 220–350 °C with a maximum at 244 °C (Fig. 6, c).

Comparison of thermal transformations of individual binders, TFCs and CFSs with the fire resistance limit of the composites suggests the existence of a dependence of heat insulating efficiency of TFCs both on the nature of polymer binder and on the coincidence of temperature ranges of thermal transformations of all components of charring composites.

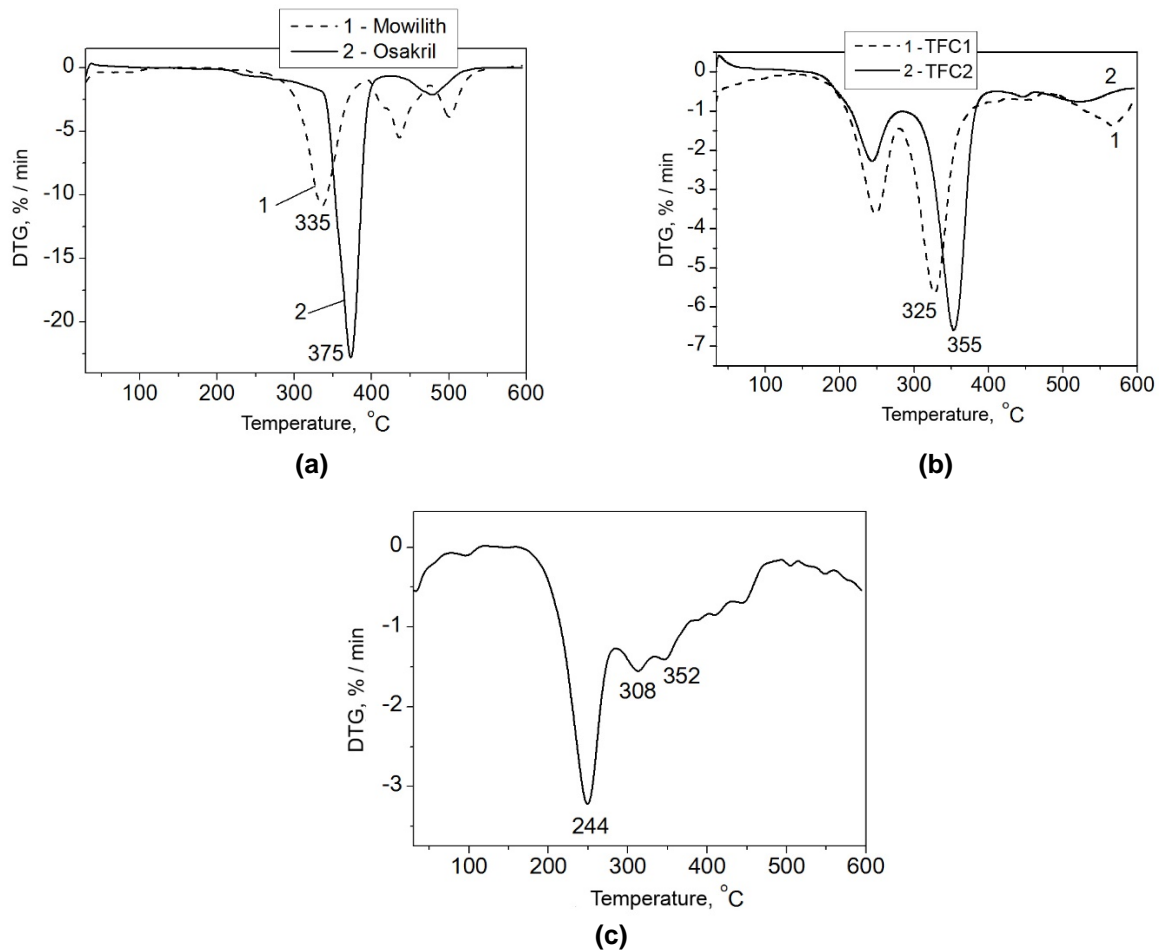


**Figure 6. DTG study data for: a – binders; b – TFCs; c – gas-char-forming system; curve numbers correspond to: 1 – Mowilith binder or TFC1 based on Mowilith; 2 – Osakril binder or TFC2 based on Osakril.**

To understand the reasons for the different heat-insulating performances of TFC1 and TFC2 containing the same charring compositions and different polymer binders, it is of interest to compare the temperature ranges of thermal transformations of CFS, Mowilith and Osakril. Thus, individual binders differ significantly in temperature maxima of the rate of weight loss caused by the formation of gaseous products (Fig. 6, a): for Mowilith – 335 °C, for Osakril – 375 °C. The same trend persists for compositions based on these binders (Fig. 4, b): TFC1 – 325 °C, TFC2 – 355 °C. DTG curves show a peak in the rate of weight loss with a maxima of 244 °C, due to gasification of CFS (Fig. 6, c). X-ray studies show that an intense interaction between products of CFSs decomposition occur in the temperature range of 300–400 °C leading to formation of amorphous organo-mineral products. Due to this, we assumed that high heat-insulating efficiency of TFC2 may be explained by coincidence of temperature intervals in which the formation of organo-mineral framework and its foaming occurs. Coincidence of the temperature ranges (350–400 °C)

referred to intense formation of gaseous products and, at the same time, formation of an organo-mineral framework was established for TFCs based on Osakril binder; this composite has the highest heat-insulating ability.

This assumption is confirmed by the data of thermogravimetric analysis: the total mass loss at 500 °C for TFC1 is 68 %, and for TFC2 – 50 %.

An additional fact in favor of the formation of a frame structure are values of physical and mechanical properties of charred products: the foaming coefficient of TFC1 and TFC2 in temperature range of 20–400 °C is 19.0 and 7.8 (Table 1). In addition, charred layers formed as a result of fire tests were investigated by scanning electron microscopy (SEM). It was found that in case of TFC2 a more uniform porous charred structure was formed in comparison to TFC1 (Fig. 7, a, b). The morphological structure of charred layer is known to affect its mechanical strength and heat insulating properties [3, 36].

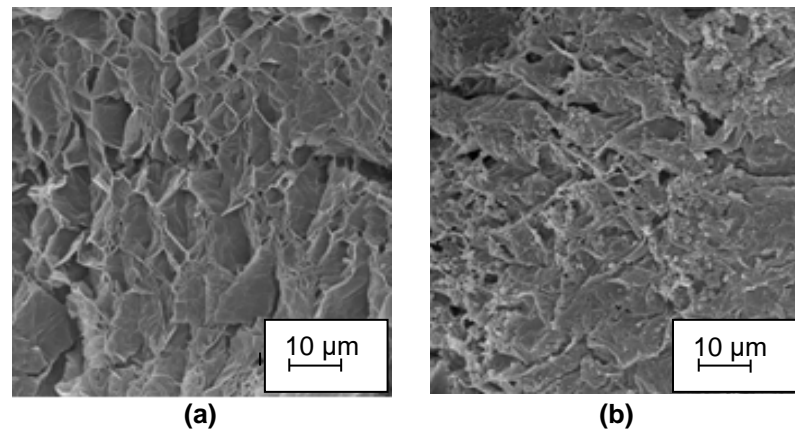


**Figure 7. Microstructure of charred layers according to scanning electron microscopy: a – TFC1; b – TFC2.**

The assessment of data on thermal and phase transformations of TFCs and their components was conducted. It shows the importance of knowing the temperature ranges in which transformation of components occur. This knowledge allows to consciously choose the components of TFC on development stage, thus creating new composites with better properties. Such composites may find wider niche in modern construction because of their better compliance to building requirements.

## 4. Conclusions

1. A study of two intumescent composites based on two different polymer binders (vinyl-acetate ethylene (Mowilith) and styrene-acrylic (Osakril) emulsions) and the same char-forming system (APP: PET: DL: TEG = 1.7: 0.8: 1: 1) was conducted in order to clarify their possible application as a part of fire clutches. Such properties of intumescent composites and charred layers as foaming ability, mechanical strength, structural morphology and heat-insulating ability were investigated. Test methods included thermal analysis (DSC, TG, DTG), X-ray phase analysis and scanning electron microscopy.

2. It was established that heat-insulating ability of a charred layer is determined by temperature intervals in which interactions of TFC components occur. The best mechanical, heat-insulating and morphological properties of investigated intumescent composition with higher heat-insulating ability and its charred layer are achieved when temperature ranges referred to formation of organo-mineral framework and volatile thermolysis products are coinciding. Such temperature range for this composition that was established in the current work is 350–400 °C.

3. Results of this research are opening the way to more conscious approaches to developing of fire retardant composites based on intumescent systems. As many components of such composites are chosen empirically, the properties of final materials may not be sufficient; and if polymer binder and intumescent system are selected according to their thermolysis ranges, a more effective composite may be developed. Such statement may result in a wider use of fire retardant composites in civil engineering.

## References

1. Garashchenko, A.N., Berlin, A.A., Kulkov, A.A. Methods and means for providing required fire-safety indices of polymer composite structures. *Pozharovzryvobezopasnost/Fire and Explosion Safety*. 2019. Vol. 28. No. 2. Pp. 9–30 (rus). DOI: 10.18322/PVB.2019.28.02.9-30
2. Weil, E.D. Fire-Protective and Flame-Retardant Coatings – A State-of-the-Art Review. *J. of Fire Sciences*. 2011. Vol. 29 (3). Pp. 259–286. DOI: 10.1177/0734904110395469

3. Alongi, J., Han, Z., Bourbigot, S. Intumescence: Tradition versus novelty. A comprehensive review. *Progress in Polymer Science*. 2015. Vol. 51. Pp. 28–73. DOI: 10.1016/J.PROGPOLYMSCI.2015.04.010 Corpus ID: 135569093
4. Kalafat, K., Taran, N., Plavan, V., Bessarabov, V., Zagoriy, G., Vakhitova, L. Comparison of fire resistance of polymers in intumescent coatings for steel structures. *Eastern-European Journal of Enterprise Technologies*. 2020. 4 (10 (106)). Pp. 45–54. DOI: 10.15587/1729-4061.2020.209841
5. Osipov, I.A., Zybina, O.A. Increase in fire resistance of building expansion joints via intumescent sealant composition. *Magazine of Civil Engineering*. 2014. No. 8. Pp. 20–24 (rus). DOI: 10.5862/MCE.52.3
6. Bourbigot, S., Sarazin, J., Samyn, F., Jimenez, M. Intumescent ethylene-vinyl acetate copolymer: reaction to fire and mechanistic aspects. *Polymer Degradation and Stability*. 2019. Vol. 161. P. 235–244. DOI: 10.1016/j.polyimde-gradstab.2019.01.029
7. Puri, R.G., Khanna, A.S. Intumescent coatings: A review on recent progress. *Journal of Coatings Technology and Research*. 2017. V. 14. Pp. 1–20. DOI: 10.1007/s11998-016-9815-3
8. Oliveira, R.B.R.S., Moreno Junior, A.L., Vieira, L.C.M. Intumescent paint as fire protection coating. *Ibracon structures and materials journal*. 2017. Vol. 10. No. 1. Pp. 220–243. <http://dx.doi.org/10.1590/S1983-41952017000100010>
9. Myronyuk, O., Baklan, D., Barrat, S., Yezhov, S., Svidersky, V. Influence of plasticizers on fire retarding properties of carbon foams of intumescent coatings. *Eastern-European Journal of Enterprise Technologies*. 2019. 2/6 (98). Pp. 22–28. DOI: 10.15587/1729-4061.2019.162554
10. Duquesne, S., Bachelet, P., Bellayer, S., Mertens, W. Influence of inorganic fillers on the fire protection of intumescent coatings. *Journal of Fire Sciences*. 2013. 31 (3). Pp. 258–275. DOI 10.1177/0734904112467291
11. Zheng, Z., Yan, J., Sun, H., et al. Preparation and characterization of microencapsulated ammonium polyphosphate and its synergistic flame-retarded polyurethane rigid foams with expandable graphite. *Polym Int*. 2014. 63. Pp. 84–92.
12. Gillani, Q.F., Ahmad, F., Mutalib, M.I.A., Melor, P.S., Ullah, S., Arogundade, A. Effect of dolomite clay on thermal performance and char morphology of expandable graphite based intumescent fire retardant coatings. *Procedia Engineering*. 2016. Vol. 148. Pp. 146–150. DOI: 10.1016/j.proeng.2016.06.505
13. Bourbigot S., Sarazin J., Bensabath T., Samyn F., Jimenez M. Intumescent polypropylene: Reaction to fire and mechanistic aspects. *Fire Safety Journal*. 2019. Vol. 105. Pp. 261–269. DOI: 10.1016/j.firesaf.2019.03.007
14. Zav'yalov D.E., Zybina O.A., Chernova N.S., Varlamov A.V., Mnatsakanov S.S. Fire intumescent compositions based on the intercalated graphite. *Russian Journal of Applied Chemistry*. 2010. Vol. 83. No. 9. Pp. 1679–1682. DOI: 10.1134/S1070427-210090351
15. Yasir M., Ahmad F., Yusoff P., Ullah S., Jimenez M. Latest trends for structural steel protection by using intumescent fire protective coatings: a review. *Surface Engineering*. 2020. Vol. 36. No. 4. Pp. 334–363. DOI: 10.1080/02670844.2019.1636536
16. Chian Y.M., Kun Y.M., Huat S.L., Han B.J., Durairaj R., Ching N.T., Yuen T.J. Optimization of Flame-Retardant Additives on Fire Protection Performance and Thermal Properties of Water-Based Intumescent Coating. *Journal of Advanced Research in Applied Mechanics*. 2018. Vol. 49. No. 1. Pp. 12–23. Journal homepage: [www.akademiabaru.com/aram.html](http://www.akademiabaru.com/aram.html) Corpus ID: 92995804
17. Ji W., Yao Y., Guo J., Zhang S. Toward an understanding of how red phosphorus and expandable graphite enhance the fire resistance of expandable polystyrene foams. *Journal of Applied Polymer Science*. 2020. DOI: 10.1002/app.49045
18. Ullah S., Ahmad F., Shariff A., Bustam M. The effect of 150 µm expandable graphite on char expansion of intumescent fire retardant coating. In: *AIP Conference Proceedings*. 2014. 1621 (1). Pp. 355–362. DOI:10.1063/1.4898492
19. Gravit, M., Denisenko, V., Borisova, A. Fire retardant device for pipeline and cable duct. *MATEC Web of Conferences*. 2018. Vol. 193. 02020. DOI: 10.1051/mateconf/201819302020
20. Gravit, M.V., Prusakov, V.A., Korotin, I.G., Timofeev, N.S., Simonenko, Y.B. Intumescent structural curve-following fire protection of civil structures and cable lines. *Pozharovzryvobezopasnost/Fire and Explosion Safety*. 2020. 29(3). Pp. 18–32. (rus) DOI: 10.22227/PVB.2020.29.03.18-32
21. Gravit, M., Simonenko, Y., Yablonskii, L. 3D-flexible intumescent fire protection mesh for building structures. *E3S Web of Conferences*. 2019. Vol. 91. Art. no. 02004. DOI: 10.1051/e3sconf/20199102004
22. Salvatore, M., Carotenuto, G., De Nicola, S., Camerlingo, C., Ambrogi, V., Carfagna, C. Synthesis and Characterization of Highly Intercalated Graphite Bisulfate. *Nanoscale Research Letters*. 2017. 12:167. Pp. 1–8. DOI 10.1186/s11671-017-1930-2
23. Dasari, A., Yu, Z.-Z., Cai, G.-P., Mai, Y.-W. Recent Developments in the fire retardancy of polymeric materials. *Progress in polymer science*. 2013. Vol. 38. Pp. 1357–1387. <http://dx.doi.org/10.1016/j.progpolymsci.2013.06.006>
24. Zoleta, J.B. Improved pyrolysis behavior of ammonium polyphosphate-melamine-expandable (APP-MEL-EG) intumescent fire retardant coating system using ceria and dolomite as additives for I-beam steel application. *Heliyon*. 2020. Vol. 6. Pp. 1–8. DOI: 10.1016/j.heliyon.2019.e03119
25. Bogdanova, V.V., Arestovich, D.N., Kirlica, V.P. Research of main recipe factors providing a dominant impact on the thermal insulating capacity and atmospheric resistance of fire protective coatings. *Vestsi Natsyonal'nai akademii navuk Belarusi. Seryya fizika-technichnykh navuk = Proceedings of the National Academy of Sciences of Belarus. Physicaltechnical series*. 2017. No. 4. Pp. 24–31 (in Russian). <https://vestift.belnauka.by/jour/article/view/344/323>
26. Pimenta, J.T., Goncalves, C., Hiliou, L., Coelho, J.F.J., Magalhaes, F.D. Effect of binder on performance of intumescent coatings. *Journal of Coatings Technology Research*. 2016. 13 (2). Pp. 227–238. <http://dx.doi.org/10.1007/s11998-015-9737-5>
27. Bardina, O.I., Korshak, Yu.V., Vasilenko, O.A. The study of fire-resistant polymer coatings of intumescent type. *Chemistry and technology of organic Substances*. 2019. 4 (12). Pp. 25–32. (In Russian) [https://www.elibrary.ru/download/elibrary\\_415686-92\\_20700356.pdf](https://www.elibrary.ru/download/elibrary_415686-92_20700356.pdf)
28. Svod Pravil SP 433.1325800.2019. *Ognezashchita stalnykh konstruksiy. Pravila proizvodstva rabot [Code of Rules SP 433.1325800.2019. Fire protection of steel structures. Rules for the production of works.] (rus)*
29. Mezhgosudarstvennyy standart GOST EN 826-2011. *Izdeliya teploizolyatsionnyye, primenyayemyye v stroitelstve. Metody opredeleniya kharakteristik szhatiya [Interstate standard GOST EN 826-2011. Thermal insulation products used in construction. Methods for determining the characteristics of compression] (rus)*
30. Powder diffraction file ICPDS / Int. Centre for diffraction data. Swarthmore. 1989. <http://padabum.com/d.php?id=111170>
31. Bogdanova, V.V., Kobets, O.I. Fire-thermo-insulating properties of intumescent composites based on polyolefins depending on nature and content of fillers. *Polymer Materials and technologies*. 2018. Vol. 4. No. 4. Pp. 64–71 (rus). DOI: 10.32864/polymmattech-2018-4-4-64-71

32. Schaumann, P., Kirsch, T. Protected steel and composite connections: Simulation of the mechanical behaviour of steel and composite connections protected by intumescent coating in fire. *Journal of Structural Fire Engineering*. 2015. No. 6(1). Pp. 41–48.
33. Korotkov, A.S., Gravit, M. 3D-map modelling for the melting points prediction of intumescent flame-retardant coatings. *SARand QSAR in Environmental Research*. 2017. Vol. 28. No. 8, 3. Pp. 677–689. DOI: 10.1080/1062936X.2017.1370725
34. Rudakova, T.A., Yevtushenko, Yu.M., Grigoryev, Yu.A., Batrakov, A.A. Ways of reducing the temperature of foaming in the system ammonium polyphosphate – pentaerythritol in intumescent systems. *Pozharovzryvobezopasnost / Fire and Explosion Safety*. 2015. 24 (3). Pp. 24–31 (rus). DOI: 10.18322/PVB.2015.24.3.24-31 Corpus ID: 105576739
35. Zybina, O., Gravit, M. *Intumescent Coatings for Fire Protection of Building Structures and Materials*. Springer Series on Polymer and Composite Materials. 2020. Publisher Springer International Publishing. XI, r.210. ISBN 978-3-030-59422-0. DOI: 10.1007/978-3-030-59422-0
36. Kang, J., Takahashi, F., T'ien, J.S. In situ thermal-conductivity measurements and morphological characterization of intumescent coatings for fire protection. *Journal of Fire Sciences*. 2018. Pp. 1–19. DOI: 10.1177/0734904118794955

**Information about authors:**

**Valentina Bogdanova**, Doctor of Chemical Sciences

ORCID: <https://orcid.org/0000-0002-8557-9925>

E-mail: [bogdanova@bsu.by](mailto:bogdanova@bsu.by)

**Olga Kobets**, PhD of Chemical Sciences

ORCID: <https://orcid.org/0000-0002-6702-7430>

E-mail: [kobets@bsu.by](mailto:kobets@bsu.by)

**Oksana Buraya**,

ORCID: <https://orcid.org/0000-0002-6241-1281>

E-mail: [fhp@bsu.by](mailto:fhp@bsu.by)

**Andrei Ustinov**,

ORCID: <https://orcid.org/0000-0001-6350-5338>

E-mail: [au.spbpu@gmail.com](mailto:au.spbpu@gmail.com)

**Olga Zybina**, Doctor of Technical Sciences

ORCID: <https://orcid.org/0000-0001-9401-7206>

E-mail: [zybina.oa@spbstu.ru](mailto:zybina.oa@spbstu.ru)

Received 27.09.2021. Approved after reviewing 08.07.2022. Accepted 19.07.2022.



Research article

UDC 697.94

DOI: 10.34910/MCE.116.8



## Sorption materials for indoor environment cleaning from microorganisms

I.A. Golubev<sup>1</sup> , D.Y. Vlasov<sup>2</sup> , I.M. Tsarovtseva<sup>3</sup> , M.A. Mayorova<sup>3</sup> , V.V. Chipizubov<sup>4</sup> ,  
N.O. Shaposhnikov<sup>1</sup> 

<sup>1</sup> Peter the Great St. Petersburg Polytechnic University, St. Petersburg, Russia

<sup>2</sup> St. Petersburg State University, St. Petersburg, Russia

<sup>3</sup> "B.E. Vedeneev VNIIG", JSC, St. Petersburg, Russia

<sup>4</sup> LLC "Cribrol", St. Petersburg, Russia

✉ [golubev2m@gmail.com](mailto:golubev2m@gmail.com)

**Keywords:** air cleaning technology, indoor environment, environmentally friendly technologies, pathogenic microorganisms, human habitat, thermally expanded graphite, activated graphite, polymer sorbent, composite materials, air filter, air pollution, air quality

**Abstract.** The article touches upon the problem of working area air pollution by pathogenic microorganisms. The problem's solution requires increased efficiency of filtration materials. Using thermally expanded graphite and Cribrol® polymer composite material, we analyzed air purification quality of multifunctional rooms in comparison with traditional activated carbon. The filtration materials properties were studied using a set of analytical methods. The air was pumped through tested materials in a volume of 500–2000 liters with the use of PU-1B sampling device depositing microorganisms on the nutrient medium. We showed that activated graphite and Cribrol® are effective in cleaning the air from bacteria (cell sizes do not exceed 1 micron), as well as larger microorganisms (from 3 microns or more). Activated graphite completely trapped microorganisms in all test variants. The filtration capacity of the new materials turned out to be higher than that of traditional activated carbon, which indicates the prospects for their further research and practical application.

**Acknowledge:** The research is partially funded by the Ministry of Science and Higher Education of the Russian Federation as part of World-class Research Center program: Advanced Digital Technologies (contract No. 075-15-2020-934 dated 17.11.2020).

**Citation:** Golubev, I.A., Vlasov, D.Y., Tsarovtseva, I.M., Mayorova, M.A., Chipizubov, V.V., Shaposhnikov, N.O. Sorption materials for indoor environment cleaning from microorganisms. Magazine of Civil Engineering. 2022. 116(8). Article no. 11608. DOI: 10.34910/MCE.116.8

### 1. Introduction

The spread of microorganisms through microbial-dust aerosols can have a noticeable effect on the human environment. The particular attention in this regard is paid to the occurrence of the pathogenic or conditionally pathogenic microorganisms (macroscopic fungi – micromycetes and bacteria) in the indoor environment. This problem has been attracting the attention of specialists all over the world for the past decades [1–8]. Being in the premises with a high content of spores in the air for a long time, a person may experience deterioration of well-being, allergic reactions, etc. The contact with human respiratory organs is explained by the small size of the spores of many mold fungi, which allows them to reach even the alveoli of the lungs. Typically, the size of the fungal spores ranges from 2 to 10 microns, while the size of the

bacterial cells transported by air is less than 1 micron. Most often, the accumulation of the fungi in the air of premises for various purposes is associated with the open growth and sporulation of colonies of micromycetes on building materials in areas of increased moisture [9]. The studies of air microbiota in Russia took place in residential and working buildings, museums, libraries, the subway, at polar stations [7, 10–13]. According to WHO recommendations [14], the content of indoor spores should not exceed 500 spores per 1 cubic meter. In many cases, these values are significantly higher, which requires special measures to reduce the number of the micromycetes in the indoor air. The first thing that is required in this regard is the regular monitoring of the indoor air environment. Such control is needed not only in residential and working premises, but also in engineering structures, such as the subway, where there are favorable conditions for accumulation and spread of microorganisms. For sampling and analysis of air samples sampling devices of various configurations are used. The typical samplers (aspirators) suck air containing various particles onto the collecting surface (nutrient medium or filters). The collection efficiency of such devices depends on a combination of factors, including the intake air speed, the shape and diameter of the suction nozzle, the distance between the nozzle and the collection surface, the diameter of the surface pores and the collection time, as well as the inertial properties of the microorganisms associated with their size and density. The filter samplers pump air through filters with different pore sizes. These samplers are most commonly used for collecting aerosols. In Russia, the certified device for sampling the air environment is the sampling device PU-1B (Manufacturer – "Khimko", Moscow). This device has been vastly tested, including in conditions of high latitudes (Arctic and Antarctic), where it has shown its sufficiently high efficiency.

The second important aspect is air purification. The improvement of indoor air quality is most often achieved through the use of air purifiers. The use of filters in such installations is the most commonly used approach to solving this problem. The filtration efficiency depends on the material used for this purpose. These studies are currently focused on finding effective, environmentally friendly and technologically accessible filters.

The purpose of the work is to evaluate the effectiveness of the new filtration materials for multipurpose cleaning of the air environment from microorganisms living indoors.

## 2. Methods

**Analysis of the effectiveness of the known filtration materials.** The main requirement for the sorbents for air and water purification is their high sorption capacity. The most important characteristic of the sorbents is porosity, which characterizes the degree of the surface development, as well as specific surface area (SD,  $\text{m}^2/\text{g}$ ). The greater the specific surface value of the sorption material, the greater the number of active pores, presented in the volume of its structure, as a result of which the sorption capacity of the material increases proportionally [15–18].

All the methods (technologies) of increasing the surface area of materials are directed primarily to the development of the existing micropores and the formation of new ones by removing individual microstructural elements.

The various types of activated carbon have become the most widely used in the world practice as materials for indoor air sorption purification. The best samples of activated carbon are obtained by the activation method. The essence of the activation process consists in the opening of the pores in the carbon material in a closed state. This is achieved thermally: the material is pre-impregnated with a solution of zinc chloride, potassium carbonate and either heated to 400–600 °C without air access, or with superheated steam at a temperature of 700–900 °C under strictly controlled conditions. And, if conventional activated carbons have a specific surface area of 20–70  $\text{m}^2/\text{g}$ , then modified ones already have 200–850  $\text{m}^2/\text{g}$ .

The indirect and non-obvious analogues of carbon materials (UM) are sorbents based on dispersed natural flake graphite. This type of materials has a low specific surface area (up to 5  $\text{m}^2/\text{g}$ ), but is well regenerated, technologically advanced, inert to all media and numerous aggressive compounds [19].

In principle, it is possible to significantly increase the specific surface area of the UM by intercalating graphite-like blocks, followed by their stratification. Thermally expanded graphite (TEG) is obtained specifically by this method: by introducing acid anions into dispersed natural graphite, followed by heating. The natural UM processed in this way have a specific surface area already up to 80–200  $\text{m}^2/\text{g}$  (according to some literature sources up to 600– $\text{m}^2/\text{g}$ ). Thus, TEG is a very promising adsorbent for purification of polluted water and gas media.

Thermally expanded graphite (TEG) is widely used for the manufacture of graphite seals, and technology for its production has been known since the 1960s. Some scientists and a number of enterprises [20] were trying to use the TEG properties for water purification, but for a number of reasons their attempts

were unsuccessful. The resulting "technical" TEG cannot be used in filters, due to low quality and a large amount of impurities, as well as unstable results in the quality of purification.

To obtain their own carbon material (Fig. 1) based on thermally expanded graphite, as well as to identify its applicability as a sorption material for air and water purification, the authors conducted appropriate laboratory tests with varying synthesis parameters and parallel analysis of the properties and quality of the obtained products. The obtained material properties were controlled by the differential scanning calorimetry and X-ray phase analysis methods. Bulk density was measured according to the VNIEM technique standard (OST 16-0689.031-74).



**Figure 1. Carbonic sorbent based on TEG.**

The developed technology for producing TEG [21], based on the short-term heat treatment of a graphite composition in the presence of the developed inhibitor, makes it possible to obtain a carbonic sorbent (activated graphite) based on TEG with high sorption characteristics (specific surface area  $Sud = 2000 \text{ m}^2/\text{g}$ ) many times higher than all known filter materials (Fig. 2). Thus, the specific surface area of absorbent carbon is  $Sud = 450\text{--}750 \text{ m}^2/\text{g}$ . The chemical purity and environmental safety of the product allow it to be used for water treatment needs.

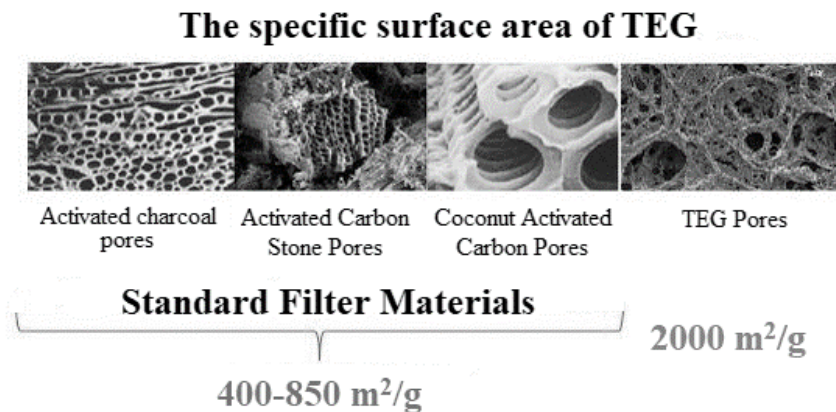


**Figure 2. Comparison of the TEG specific surface area with Absorbent carbon.**

When the thermally expanded graphite is compacted in the filter, a strong, porous structure is created, similar in its properties to a membrane. By adjusting the compaction degree, it is possible to achieve different porosity values of the filter load and set the required material throughput for certain polluting components, depending on the required purification degree.

The Cribrol® polymer composite is also a competitive material for the cleaning of gas-air mixtures. Its structure is formed according to the ratio of through and non-through pores of different diameters, uniformly distributed throughout the volume of the filtering partition, set in the polymerization process (Fig. 3) [22]. The technological process makes it possible to obtain the porous percolating material with a given pore system: micropores, mesopores and macropores. This ensures versatility in the production of materials with different performance characteristics for solving various tasks.

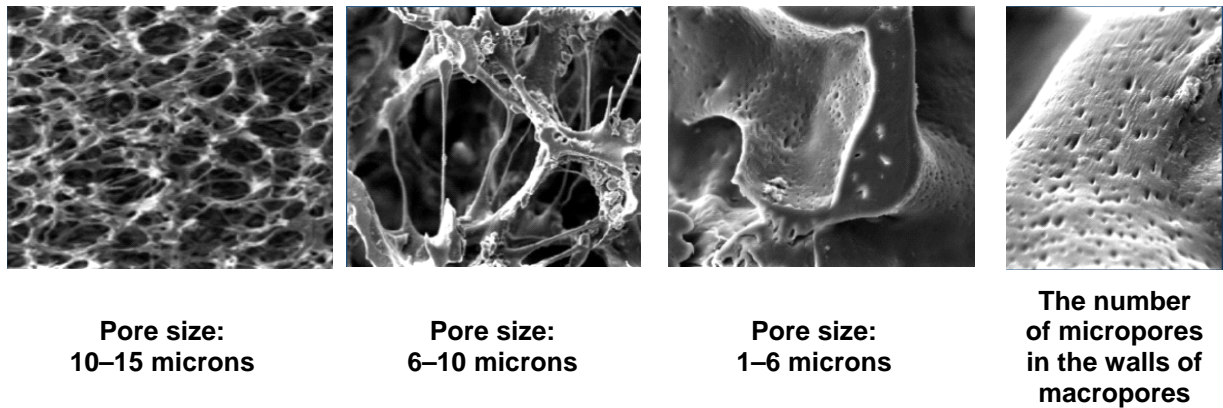


**Figure 3. Pore combination in Cribrol® materials.**

For these materials, there is no concept of surface area, since they are bulk, porous materials. One filter cartridge Cribrol® combines three technological functions – sorption, coalescence and inertial separation, which proceed sequentially in a stream of liquids and gases passing through a porous partition (Fig. 4).

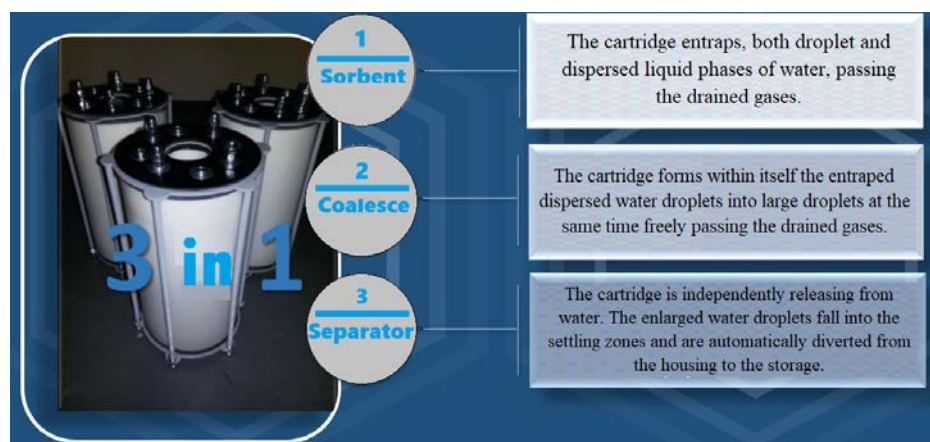


**Figure 4. The principle of Cribrol® cartridges operation.**

These unique properties of Cribrol® materials determine their effective use for solving various technological problems associated with the separation of dispersed phases of liquids contained in gaseous media, which, in particular, can transport infectious agents – bacteria, fungi and viruses [23].

Two rooms, differing in their purpose and conditions, were selected as objects for evaluating the effectiveness of the new sorption materials:

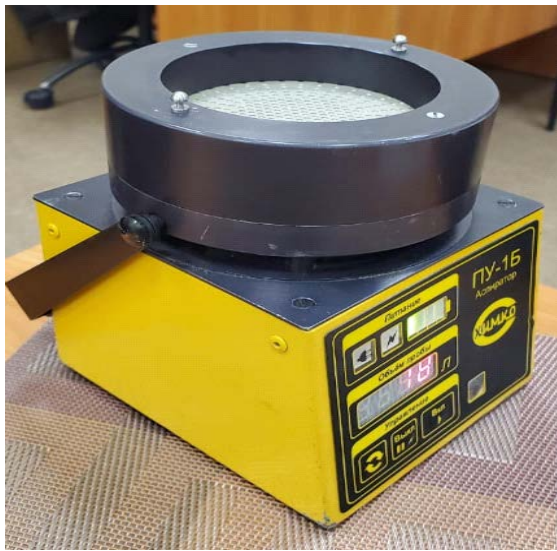
1) an office space, where people stay daily during working hours (without external signs of biological damage to materials and sufficient ventilation);

2) a library space, where books and archival documents are stored for a long time with weak ventilation.

The microbiological sampling of the air environment in the office and in the library spaces was carried out using a PU-1B aspirator (a Russian-certified sampling device for taking air samples), through which air was pumped in a volume of 500–2000 liters, depositing microorganisms in Petri dishes on the nutrient medium. When air was pumping, filtration materials were placed in its path. The control was conducted with the air samples without the use of filtration materials. When taking a sample, the device was positioned at a level of about 1 m from the surface. Each sample was taken three times for Czapek medium (to determine the number of fungi) and FMH (fermented meat hydrolysate) – to determine the total microbial number of organotrophic bacteria).

As tested substances, new filtration materials were used: Cribrol®, thermally expanded graphite (EG) and activated carbon (AC).

For the testing, the material was placed in the over-frame space of the sampling device PU-1B in such a way that the material covered the hopper above the nozzles of the device and air could be pumped through it (Fig. 5).



a



b



c



d

**Figure 5. The experimental installation for the testing of new filtration compositions: a) control (sampling device with an unfilled hopper), b) thermally expanded graphite (filled hopper), c) Cribrol®, d) activated carbon**

After pumping air in rooms for various purposes through the tested materials, Petri dishes were removed from the PU-1B device, maintaining sterility, and incubated in laboratory conditions at a temperature of +25 °C. After 10 days, the number of grown colonies was calculated (Fig. 6) and colony-forming units (CFU) were recalculated per 1 m<sup>3</sup> of the air (in accordance with the PU-1B device operating manual).



a

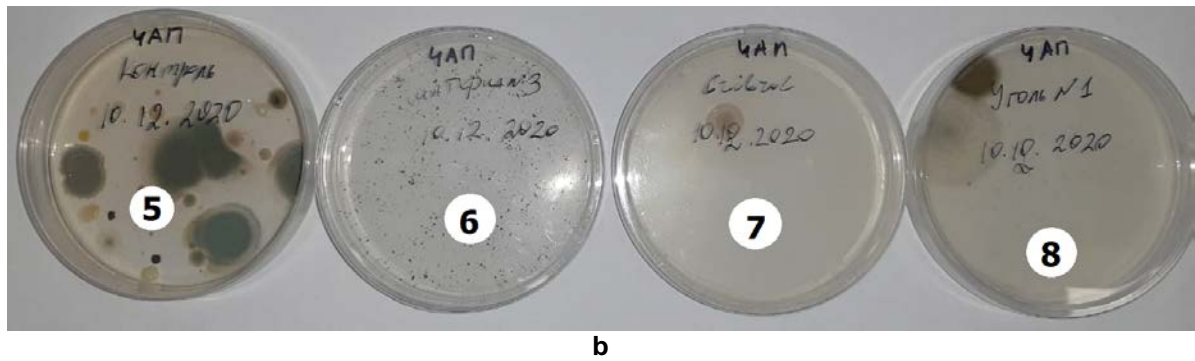


**Figure 6.** An example of counting colonies of bacteria and microscopic fungi after the sampling in different figure versions of the experiment: a) cleaning from bacteria, b) cleaning from fungi  
 1 – Control (120 CFU); 2 – Thermally expanded graphite (0 CFU); 3 – Cribrol® (2 CFU);  
 4 – Activated carbon (50 CFU); 5 – Control (17 CFU); 6 – Thermally expanded graphite (0 CFU);  
 7 – Cribrol® (1 CFU); 8 – Activated carbon (2 CFU).

### 3. Results and Discussion

The results of the experiments (Table 1) showed high efficiency of the used materials for the air purification in rooms for various purposes. The highest efficiency was demonstrated by the EG composition, which completely detained microorganisms (fungi and bacteria) in all test variants. The Cribrol® composition in various modifications also showed significant effectiveness (a decrease in the number of cells by an order of magnitude and higher in comparison with the control). The AC composition showed high efficiency against fungi (micromycetes), while the effect of air purification from bacteria was lower. It must be noted, that the number of bacteria in the air of the office and library was several times higher than of micromycetes in control samples.

**Table 1. Determination of the number of bacteria and fungi in rooms for various purposes with different test variants of sorption materials**

Sample No.	The filter material	The filter material mass	Nutrient medium	Air volume	The number of the grown colonies	CFU per 1 cubic meter of air
<b>The office space</b>						
1	Activated carbon		Czapek	500	2	4
2	Activated carbon		FMH	500	50	110
3	Cribrol®		Czapek	500	1	2
4	Cribrol®		FMH	500	2	4
5	EG		Czapek	500	0	0
6	EG		FMH	500	0	0
7	Control		Czapek	500	17	34
8	Control		FMH	500	120	290
9	Cribrol	10,570	Czapek	500	0	0
10	Cribrol	9,910	FMH	500	3	6
11	Cribrol	9,010	Czapek	1000	1	1
12	Cribrol	10,670	FMH	1000	0	0
13	Cribrol	9,210	Czapek	2000	0	0
14	Cribrol	9,310	FMH	2000	10	5
15	Cribrol®+H2O	16,300	Czapek	1000	2	2
16	Cribrol®+H2O	22,870	FMH	1000	0	0
17	Control		Czapek	1000	31	35
18	Control		FMH	1000	54	58
19	Control		Czapek	2000	26	14
20	Control		FMH	2000	128	79
21	EG	2,280	Czapek	1000	0	0
22	EG	2,650	FMH	1000	0	0
23	EG	2,570	Czapek	2000	0	0
24	EG	2,290	FMH	2000	0	0

Sample No.	The filter material	The filter material mass	Nutrient medium	Air volume	The number of the grown colonies	CFU per 1 cubic meter of air
<b>The library space</b>						
25	Control		FMH	1000	42	45
26	Control		FMH	2000	52	28
27	Control		Czapek	1000	6	6
28	Control		Czapek	2000	10	5
29	EG	3,030	FMH	1000	0	0
30	EG	2,810	FMH	2000	0	0
31	EG	2,400	Czapek	1000	0	0
32	EG	2,390	Czapek	2000	0	0
33	EG	37,640	FMH	1000	100	100
34	EG	37,870	Czapek	1000	2	2

Thus, all the compounds included in the tests demonstrated different effectiveness in cleaning the air from microorganisms. The tested materials purified the air from small bacterial cells (not exceeding 1 micron in size), as well as larger micromycete spores (from 3 microns or more). Whereas in all control variants, dozens of colonies of micromycetes (from the genera *Cladosporium*, *Penicillium*, *Aspergillus*) and organotrophic bacteria colonies germinated on nutrient media. Some of the identified microorganisms were typical for the indoor environment of buildings with different microclimates [24–27]. They are also commonly found on various building materials and can spread through the air [28, 29]. In variants with sorption materials, either single colonies were noted, or they were absent altogether. If, as a comparison of the air purification quality indicators of the working space, we could draw an analogy between the efficiency of activated carbon and activated graphite, then the result directly depends on the value of the specific surface area: the higher it is, the more microorganisms can be sorbed from the air. There is no doubt that EG has an advantage here.

Since the studied Cribrol® material has a mechanism fundamentally different from the sorption processes occurring in activated graphite and carbon, a direct comparison with its analogues is not entirely correct. However, the obtained efficiency in air purification makes it possible to consider it, as well as EG, as materials analogous to traditional activated carbons. It is also worth considering that according to the manufacturer's statements, the greatest efficiency of this material is observed during the separation of aerosols, since Cribrol® works better in the "wetted" state.

In addition, despite the fact that during the tests the difference in cleaning efficiency was observed after 2000 liters of filtered air, the question of the compared materials resource remains open.

These experiments, as well as the Cribrol® material effectiveness studies in the "wetted" state, are planned to become a part of the subsequent studies.

#### 4. Conclusion

1. Activated carbon (AC) widely used in world practice has low efficiency as a sorption material for air purification from microorganisms.
2. The best effect is shown by filtration materials Cribrol® and thermally expanded graphite (EG). They clean the air in rooms for various purposes from small bacterial cells, as well as large micromycetes.
3. The air purification efficiency obtained during the tests allows considering Cribrol®, as well as EG, as analogues to traditional activated carbons.

#### References

1. Takahashi, T. Airborne fungal colony-forming units in outdoor and indoor environments in Yokohama, Japan. *Mycopathologia*. 1997. 139 (1). Pp. 23–33. DOI: 10.1023/a:1006831111595
2. Garrett, M.H., Rayment, P.R., Hooper, M.A., Abramson, M.J., Hooper, B.M. Indoor airborne fungal spores, house dampness and associations with environmental factors and respiratory health in children. *Clinical and experimental allergy: journal of the British Society for Allergy and Clinical Immunology*/ 1998. 28 (4). Pp. 459–467. DOI: 10.1046/j.1365-2222.1998.00255.x
3. Gorny, R.L., Dutkiewicz, J., Krysinska-Traczyk, E. Size distribution of bacterial and fungal bioaerosols in indoor air. *Ann Agric Environ Med*. 1999. No. 6. Pp. 105–113.
4. Koch, A., Heilemann, K.J., Bischof, W., Heinrich, J., & Wichmann, H. E. Indoor viable mold spores – a comparison between two cities, Erfurt (eastern Germany) and Hamburg (western Germany). *Allergy*. 2000. 55 (2). Pp. 176–180. DOI: 10.1034/j.1398-9995.2000.00233.x

5. Stranger, M., Potgieter-Vermaak, S.S., Van Grieken, R. Comparative overview of indoor air quality in Antwerp, Belgium. *Environment International*. 2007. 33 (6). Pp. 789–797. DOI: 10.1016/j.envint.2007.02.014
6. Grinn-Gofron, A., Mika, A. Selected airborne allergenic fungal spores and meteorological factors in Szczecin, Poland, 2004–2006. *Aerobiologia*. 2008. 24 (2). Pp. 89. DOI: 10.1007/s10453-008-9088-0
7. Bogomolova, Ye.V., Velikova, T.D., Goryayeva, A.G., Ivanova, A.M., Kirtsideli, I.Yu., Lebedeva, Ye.V., Mamayeva, N.Yu., Panina, L.K., Popikhina, Ye.A., Smolyanitskaya, O.L., Trepova, Ye.S. Mikroskopicheskiye griby v vozdukh Sankt-Peterburga [Microfungi in the air of Saint-Petersburg]. Sankt-Peterburg: Khimizdat, 2011. 215 p.
8. Thrasher, J.D. Fungi, bacteria, nano-particulates, mycotoxins and human health in water-damaged indoor environments. *J Comm Pub Health Nurs*. 2016. 2 (115). Pp. 2. DOI: 10.4172/jcphn.1000115
9. Torvinen, E., Meklin, T., Torkko, P., Suomalainen, S., Reiman, M., Katila, M.L., Nevalainen, A. Mycobacteria and fungi in moisture-damaged building materials. *Applied and environmental microbiology*. 2006. 72 (10). Pp. 6822–6824. DOI: 10.1128/AEM.00588-06
10. Velikova, T.D., Popikhina, E.A., Goryaeva, A.G., Trepova, E.S. Air microflora of libraries in Russia. *Abstr. XV Congress of European Mycologists*. St-Petersburg, 2007. TREEART LLC. P. 106–107.
11. Kirtsideli, I.Yu., Vlasov, D.Yu., Krylenkov, V.A., Rolle, N.N., Barantsevich, Ye.P., Sokolov, V.T. Sravnitelnoye issledovaniye aeromikoty arkticheskikh stantsiy po severnomu morskomu puti [Comparative study of airborne fungi at arctic stations near water area of the northern sea route]. *Ekologiya cheloveka*. 2018. No. 4. Pp. 16–21. DOI: 10.33396/1728-0869-2018-4-16-21
12. Kirtsideli I.Yu., Bogomolova E.V. Development of microfungi communities in the indoor air of St. Petersburg museums. *Mikologiya i Fitopatologiya*. 2008. 42 (2), Pp. 128–136.
13. Vlasov, D.Yu., Teshebayev, Sh.B., Zelenskaya, M.S., Kirtsideli, I.Yu., Ryabusheva, Yu.V. Mikologicheskoye porazheniye materialov v pomescheniyakh kak faktor riska dlya zdorovya polyarnikov [Mycological damage of materials in the indoor environment as a risk factor for the health of polar explorers]. *Gigiyena i sanitariya*. 2019. 98 (1). Pp. 17-21. DOI: 10.47470/0016-9900-2019-98-1-17-21
14. WHO. Indoor air quality: biological contaminants. Report on a WHO meeting. WHO regional publications. European series. 1990. No. 31. P. 67.
15. Fenelonov, V.B. Poristyy uglerod [Porous carbon]. Novosibirsk: Institut kataliza SO RAN, 1995. 518 p.
16. Klimenko, N.A., Koganovskiy, A.M. Razvitiye issledovaniy v oblasti adsorbtsii i adsorbtsionnoy tekhnologii [Development of researchers in the field of adsorption and adsorption technology]. *Khimiya i tekhnologiya vody*. 1998. 20 (1). Pp. 32–41.
17. Tarasevich, Yu.I. Fiziko-khimicheskiye osnovy i tekhnologii primeneniya prirodnykh i modifitsirovannykh sorbentov v protsessakh ochistki vody [Physico-chemical bases and technologies of application of natural and modified sorbents in water purification processes]. *Khimiya i tekhnologiya vody*. 1998. 20 (1). Pp. 42–51.
18. Panasevich, A.A., Klimova, G.M., Tarasevich, Yu.I. Sorbenty na osnove prirodnykh dispersnykh mineralov dlya izvlecheniya NPAV iz stochnykh vod [Sorbents based on natural dispersed minerals for the extraction of waste water from wastewater]. *Khimiya i tekhnologiya vody*. 1991. 13 (5). Pp. 412–418.
19. Fialkov, A.S. Uglerod. Mezhsloyevyye soyedineniya i kompozity na yego osnove [Carbon. Interlayer compounds and composites based on it]. M.: Aspekt Press, 1997. 718 p.
20. Kalabekov, G.O., Kalabekov, O.A., Kudryashov, A.F., Kudryashova, N.V., Moskalev, Ye.V. Sposob polucheniya vspennogo grafita [Process for Producing Expanded Graphite]. Patent Russia no. 2377177, 2009.
21. Golubev, I.A., Golubev, A.V., Novikov, M.G. Sposob polucheniya termorasshirenogo grafita [Method of producing thermally expanded graphite]. Patent Russia no. 2690449, 2018.
22. Chipizubov, V.V., Ashkinazi, L.A. Sostav i sposob polucheniya fil'tra na osnove poristogo polivinilformalya [Composition and method for obtaining a filter based on porous polyvinyl formal]. Patent Russia no. 2445147, 2012 (rus)
23. Chipizubov, V.V., Sukhonin, P.N., Petrash, V.V. Perspektivnost primeneniya poristykh kompozitnykh materialov v izdeliyakh dlya zashchity organov dykhaniya ot virusnykh i bakterialnykh infektsiy [Prospects for the use of porous composite materials in products for respiratory protection from viral and bacterial infections]. *Vestnik meditsinskogo instituta «REAVIZ». Reabilitatsiya, Vrach i Zdorovye*. 2021. No. 1. Pp. 11–16. DOI: 10.20340/vmi-rvz.2021.1.COVID.2
24. Haddrell, A.E., Thomas, R.J. Aerobiology: experimental considerations, observations, and future tools. *Applied and environmental microbiology*. 2017. 83 (17). e00809-17. DOI: 10.1128/AEM.00809-17
25. Armstrong-James, D. Future directions for clinical respiratory fungal research. *Mycopathologia*. 2021. Pp. 1–12. DOI: 10.1007/s11046-021-00579-5
26. Tomomatsu, K., Oguma, T., Baba, T., Toyoshima, M., Komase, Y., Taniguchi, M., Asano, K. Effectiveness and safety of omalizumab in patients with allergic bronchopulmonary aspergillosis complicated by chronic bacterial infection in the airways. *International archives of allergy and immunology*. 2020. 181 (7). Pp. 499–506. DOI: 10.1159/000507216
27. Tiew, P.Y., Dicker, A.J., Keir, H.R., Poh, M.E., Pang, S L., Mac Aogáin, M., Chotirmall, S.H. A high-risk airway mycobiome is associated with frequent exacerbation and mortality in COPD. *European Respiratory Journal*. 2021. 57 (3). DOI: 10.1183/13993003.02050-2020
28. Ponizovskaya, V.B., Rebrikova, N.L., Kachalkin, A.V., Antropova, A.B., Bilanenko, E.N., Mokeeva, V.L. Micromycetes as colonizers of mineral building materials in historic monuments and museums. *Fungal biology*. 2019. 123 (4). Pp. 290–306. DOI: 10.1016/j.funbio.2019.01.002
29. Kirtsideli, I.Yu., Vlasov, D.Yu., Abakumov, E.V., Barantsevich, E.P., Novozhilov, Yu.K., Krylenkov, V.A., Sokolov, V.T. Airborne fungi in arctic settlement Tiksi (Russian Arctic, coast of the Laptev Sea) // Czech polar reports. 2017. 7 (2). Pp. 300–310. DOI: 10.5817/CPR2017-2-29

### **Information about authors:**

**Ivan Golubev**, PhD in Technical Science

ORCID: <https://orcid.org/0000-0001-7516-3566>

E-mail: [golubev2m@gmail.com](mailto:golubev2m@gmail.com)

**Dmitriy Vlasov,**

ORCID: <https://orcid.org/0000-0002-0455-1462>

E-mail: [Dmitry.Vlasov@mail.ru](mailto:Dmitry.Vlasov@mail.ru)

**Inga Tsarovtseva,**

ORCID: <https://orcid.org/0000-0002-9840-0701>

E-mail: [in\\_pilgrim@mail.ru](mailto:in_pilgrim@mail.ru)

**Margarita Mayorova,**

ORCID: <https://orcid.org/0000-0002-4291-2695>

E-mail: [mayorovama@vniiq.ru](mailto:mayorovama@vniiq.ru)

**Vitalii Chipizubov,**

ORCID: <https://orcid.org/0000-0003-0654-8651>

E-mail: [cribrol@mail.ru](mailto:cribrol@mail.ru)

**Nikita Shaposhnikov,**

ORCID: <https://orcid.org/0000-0003-3542-2492>

E-mail: [shaposhnikovno@gmail.com](mailto:shaposhnikovno@gmail.com)

*Received 07.10.2021. Approved after reviewing 01.06.2022. Accepted 14.06.2022.*



Research article

UDC 624

DOI: 10.34910/MCE.116.9



## An improved lateral restrained local fuse used in concentric braces

A. Kachooee 

Amin University, Tehran, Iran

✉ [ali.kachooee@semnan.ac.ir](mailto:ali.kachooee@semnan.ac.ir)

**Keywords:** local fuse, concentric bracing, ductility capacity, energy absorption capacity, load bearing capacity, steel structures

**Abstract.** The present paper continues a series of the authors' studies on improving conventional concentrically braced frames (CBFs). In previous works, the authors equipped a CBF with a restrained local fuse to improve its behavior, thus introducing local fuse–auxiliary element concentric braces (LF-AECBs). The mechanism of LF-AECBs with a restricted fuse in the length increased the ductility and energy dissipation capacity of the bracing system by limiting the overall buckling locally to the compressive zone. However, further numerical studies suggested that due to early buckling, now local, the restrained local fuse could not be exploited until the failure. Therefore, this study introduces an improved local fuse–auxiliary element concentric brace (ILF-AECB) to fix the issue. Numerical studies are also done to determine the optimal shape of ILF-AECBs in order to obtain maximum energy dissipation capacity and ductility under cyclic loading. In this article, the results of experimental and numerical studies show that ILF-AECBs with a new formulation delaying the fuse buckling completely succeed in using the full capacity of the local fuse for energy dissipation and ductility. Moreover, the analytical study shows that the frame equipped with ILF-AECB offered much better performance in terms of energy dissipation and reduction of the input demand to the structural elements compared to the similar CBFs.

**Citation:** Kachooee, A. An improved lateral restrained local fuse used in concentric braces. Magazine of Civil Engineering. 2022. 116(8). Article no. 11609. DOI: 10.34910/MCE.116.9

### 1. Introduction

An off-center bracing system was introduced by Moghaddam and Estekanchi [1]. This structural system was invented for improving concentrically braced frame (CBF) behavior [2]. As shown in Fig. 1, it basically consists of the non-straight tension strut AOC with an eccentricity designated as  $e$ . The midpoint is connected to the corner by the third member. Once the load is applied, all these three members are stretched, therefore, act in tension. In the recent decade, some research has been conducted on this structural system [3–6]. In [6], some numerical studies have been performed using the ANSYS software on a frame with off-center bracing system with optimum eccentricity and circular element created, called the OBS\_C\_O model. The obtained results revealed that it would be useful to use a circular dissipater for increasing the ductility of off-center bracing system.

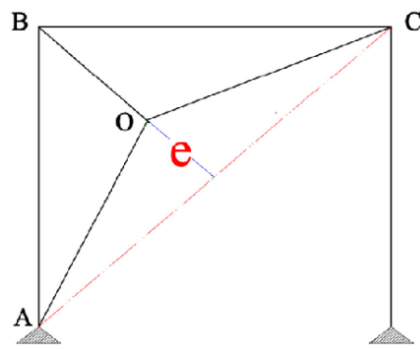


**Figure 1. Off-center bracing system.**

A cast modular ductile bracing system (CMDB) was introduced as an alternative for the special CBF structures [7, 8]. As shown in Fig. 2, these structural systems are made of a cast component in the middle and ends of the braces. A cruciform cross-section is utilized for CMDB because this section increases energy dissipation capacity and low cycle fatigue life; in turn, they cause reduced brace failure probability. A system similar to the above one was proposed by Seker et al. to replace the conventional concentric braces [9]. The system uses a three-part steel brace and the idea behind it is to develop an elastic buckling extension of a multi-part column, which includes post-buckling deformations. Their results indicate consistent and symmetric hysteresis responses of this new concentric brace under cyclic loading. These studies have also proven far more energy dissipation capacity than the conventional concentric bracing system.

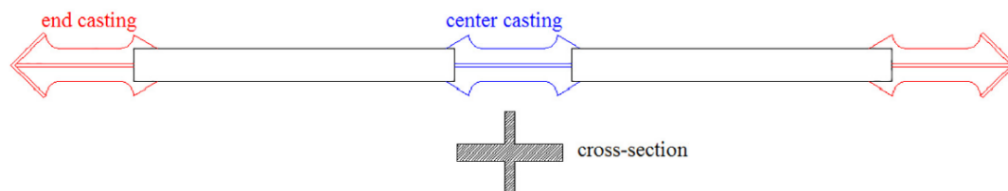
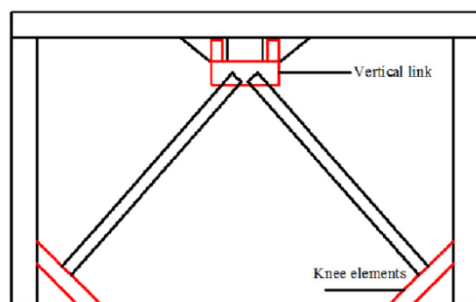
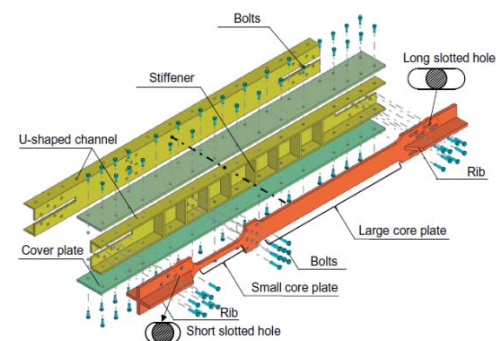


**Figure 2. Schematic of the CMDB system.**

The use of two-level or multi-level control systems is another method for improving the seismic behavior of structures, which has recently been under the focus of researchers. The main idea in these structural systems [10–14] is to combine different control systems with various stiffness and strength values, which results in desirable energy absorption in the structure for various earthquake intensities. Zahrai and Vosooq [11] introduced a dual system in which a combination of a vertical link beam and knee elements was used to maintain energy absorption. To improve the seismic performance in this structural system (Fig. 3a), the vertical link beam is used as an energy absorption element in the small loads area and knee elements are used for energy absorption under intense earthquakes. In another study, researchers introduced full steel double-stage yield buckling-restrained braces (DYB) (Fig. 3b) [13, 14]. The core plate of DYB consists of two small and big plates joined together serially. The deformation capacity of the small core is restricted by a stopper mechanism. At first, the deformation of DYB is focused on the small core and, when the stopper mechanism stops the deformation of this core, the displacement of DYB is transferred to the big core, hence DYBs have two stages of yielding. An experimental study conducted by Sun et al. showed that the DYB possesses higher energy dissipation capacity and seismic resistance than the traditional concentric bracing [13].



**(a) Zahrai and Vosooq model**



**(b) DYB model**

**Figure 3. Some kinds of two-level control systems.**

Another invented structural system for improving seismic performance of structures with concentric bracings is the application of the buckling restrained brace (BRB) [15–19]. As shown in Fig. 4, this structural system uses bracings, including a casing and core, which removes the main shortcoming of the concentrically braced structural systems, i.e. buckling in compression [15, 16, 18]. Naghavi et al. [20] compared the response of BRB frames with the traditional concentrically braced ones. They found that the BRB system remarkably increased the ductility capacity and energy dissipation compared to the traditional concentrically braced frame. Qiu et al. [21] provided a method to correct the defect of the BRB system, that is, inability in reducing the residual drift story of the concentrically braced frames after an earthquake. In this study, the use of smart materials was suggested to remove the entire drift of residual story or make it negligible.

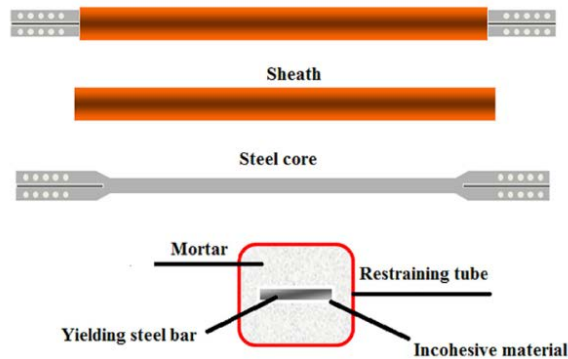


**Figure 4. Buckling restrained brace (BRB) component.**

Another method that has been developed as a substitute for conventional concentric braces is all-steel tube-in-tube buckling controlled brace, called (TinT-BCB) (Fig. 5) [22–24]. Seker and Shen [23] reported that the hysteresis response of this brace was consistent and symmetrical under cyclic loading. Factors affecting the response of these braces include the friction between tubes, the distance between the internal and external tubes, and the thickness ratio of the inner and outer tubes. In this brace, optimal performance generally results from a system with smallest possible gap, low friction, and a heavier outer tube.

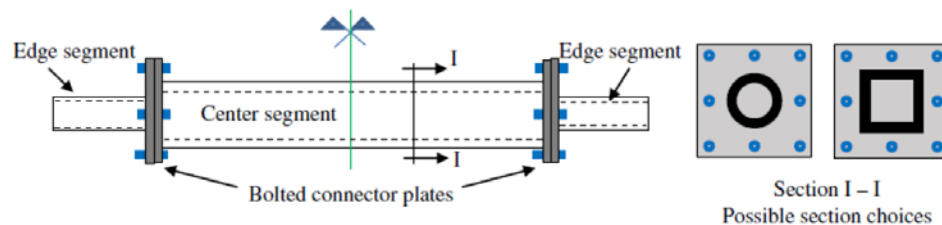


**Figure 5. Seker et al. model [23].**

Kachooee et al. [25] sought to reduce the input demand to the bracing joints by recommending a cross-section reduction fuse. According to Fig. 6, the fuse was placed within a particular length at the end of the brace. The results of this numerical study showed that the fuse not only reduced the input demand to the brace joints, but also the energy dissipation capacity of the bracing system. The reason was that reducing the cross-sectional area of the brace decreased the buckling capacity of the system, preventing the brace under cyclic loading from creating complete hysteresis loops and leading to a reduction in the energy dissipation capacity of the bracing system. In another study, Kafi and Kachooee tried to correct this defect using auxiliary elements placed around the fuse, resulting in the innovation of local fuse – auxiliary element concentric braces (LF-AECBs) (Fig. 7) [26].

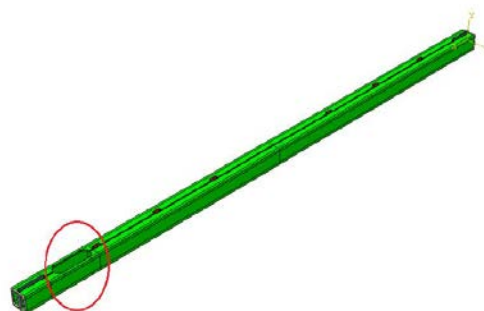


**Figure 6. Kachooee et al. model.**

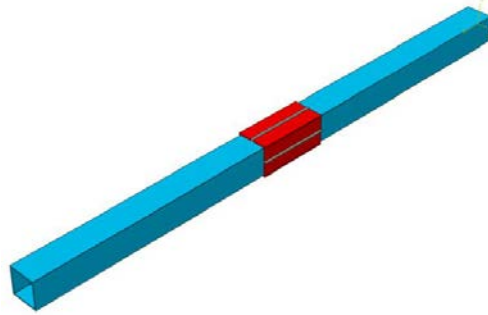


**Figure 7. The LF-AECB model.**

The results of this numerical study showed better performance of the new system in terms of energy dissipation and ductility capacity than that provided in [25]. However, the earlier buckling prevented the fuse capacity from being used thoroughly.

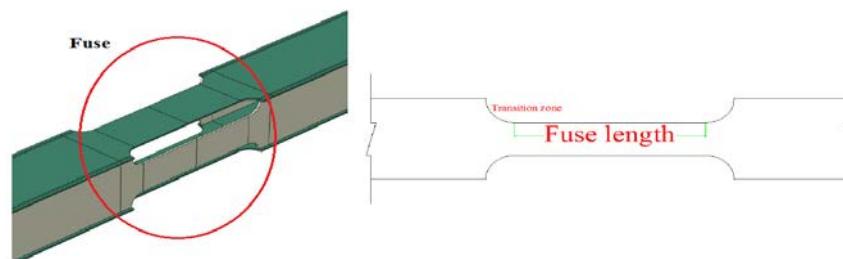
A new method is offered in this study to solve the problem of the fuse provided by Kafi and Kachooee [26] and improve the behavior of the concentric braces using numerical and experimental studies. In fact, the proposed formulation of LF-AECB bracing allows the coaxial bracing to exploit the fuse capacity until the failure. This increases the ductility and energy absorption of the proposed model. In this method, a local fuse is used along the brace with a newer formulation than that of Ref. [26]. The design of this local fuse is in such a way that the brace buckles locally and in the fuse length. In order to prevent fuse local buckling, auxiliary elements are used in the fuse region. This causes a symmetrical and stable behavior of the brace under cyclic loading, which results in optimal ductility and a considerable amount of energy dissipation capacity. A complete introduction of the mentioned brace, called improved LF-AECB (ILF-AECB), is provided in the following. Numerical studies were also done to determine its optimal shape in order to obtain maximum energy dissipation capacity and ductility in an ILF-AECB under cyclic loading. In the end, the responses of ductility, loadbearing capacity, and energy dissipation capacity of the concentrically braced frame equipped with the system suggested in this study are compared with a traditional similar concentrically braced frame using a numerical study conducted in ABAQUS 6.12 [27].

## 2. Methods

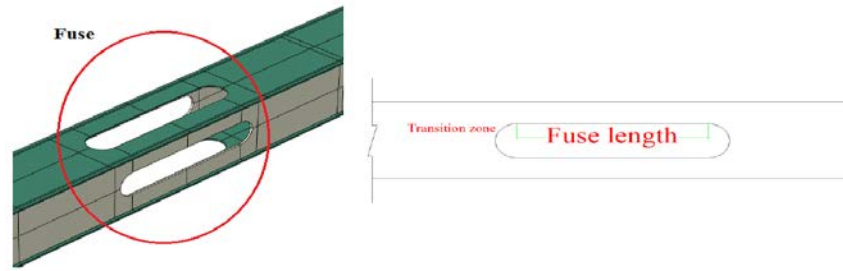
### 2.1. ILF-AECB bracing components

#### 2.1.1. Formulation for calculating fuse area and length

The general pattern of the fuse (Fig. 8 and 9) for two different section-shapes of the brace indicates that the local fuse is generated by reducing the cross-section of the brace. Also, a transition zone has been considered to prevent stress concentration. Fig. 8 has shown two methods for creating the fuse in the box sections. In Fig. 8a, the sides of the fuse have been cut in the outer part to create the fuse. Also, in Fig. 8b, the method of creating the fuse has been presented through the internal cutting of box sides. It is worth mentioning that in Fig. 9, the method of creating the fuse for the braces with I section has shown, which have been reinforced with the vertical plates parallel to the web section. In this brace, the reinforcement plates have been removed in that area to create the fuse, and the cross-section of the brace has been decreased through this method.



**(a) creating the fuse through trimming external faces of the brace section**



(b) creating the fuse through trimming internal faces of the brace section

Figure 8. Local fuse in the box-shape ILF-AECBs.

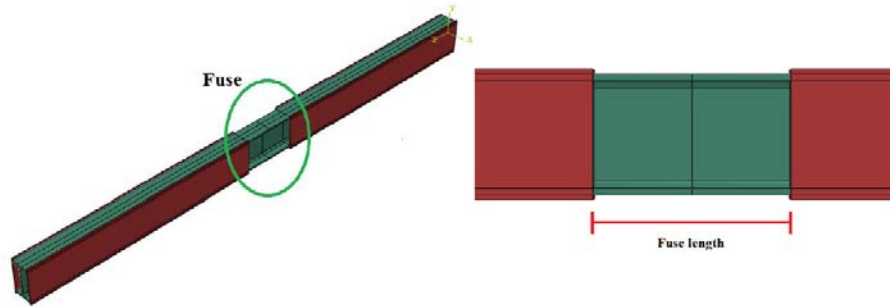


Figure 9. Local fuse in the I-shape ILF-AECBs.

In order to calculate the cross-sectional area of the fuse, the demand load exerted to the brace ( $P_{demand}$ ) should first be obtained from the analyses. After calculating  $P_{demand}$ , Eq. (1) must be satisfied based on the Iranian steel structure code [28]:

$$P_{demand} \leq 0.9P_{y,brace}, \quad (1)$$

where  $P_{y,brace}$  is the yield load-bearing capacity of the brace and a coefficient of 0.9 is the strength reduction factor according to the Iranian steel structure code [28].  $P_{y,brace}$  can be calculated using Eq. (2):

$$P_{y,brace} = A_{brace} \cdot F_y, \quad (2)$$

where  $A_{brace}$  and  $F_y$  are the cross-sectional area and the yield stress of the brace materials, respectively. The cross-sectional area of the brace can be obtained using Eqs. (1) and (2):

$$A_{brace} \geq \frac{P_{demand}}{0.9F_y}. \quad (3)$$

After calculating the cross-sectional area of the brace, the slenderness coefficient of it should be checked to select the brace profile. The following expression should be controlled to make sure that the buckling of the brace does not take place before its yielding:

$$\left( \lambda_{brace} = \frac{k \cdot l_{brace}}{r_{min,brace}} \right) \leq 80, \quad (4)$$

(4Ошибка! Закладка не

определена.)

where  $\lambda_{brace}$ ,  $k$ ,  $l_{brace}$ , and  $r_{min,brace}$  are the slenderness factor, effective length coefficient, and the length of the brace and radius of gyration around the weak axis of the brace section, respectively. This must be examined to make sure that the buckling of the brace occurs after its yielding. In other words, this equation makes the designer choose a profile that satisfies it. The coefficient 80 is selected in accordance with ST37 steel materials according to DIN 17100, and if the material is changed, the desired value should be calculated according to the new material. The cross-sectional area of the fuse can be obtained after the verification of Eq. (4). For this purpose, the ultimate loadbearing capacity of the fuse,  $P_{u,fuse}$  (Eq. (5)) can

be obtained from multiplying the steel material yield stress  $F_y$  by  $C_{pr}$  (the coefficient of material hardening) and  $R_y$  (the coefficient for the specifications of the brace profile) coefficients based on the Iranian steel structures code [28], which must be less than or equal to the minimum yield capacity of the brace,  $P_{y,brace}$  :

$$P_{u,fuse} = A_{fuse} \cdot R_y \cdot C_{pr} \cdot F_y \leq (P_{y,brace} = A_{brace} \cdot F_y), \quad (5)$$

where  $A_{fuse}$  is the cross-sectional area of the fuse and  $R_y$  and  $C_{pr}$  can be obtained from Table 1 and Eq. (6) based on the Iranian steel structures code [28]:

**Table 1.  $R_y$  coefficients for different shape sections of braces.**

Section Shapes	$R_y$
Rolled tabular and box shape sections	1.25
Others rolled shape sections	1.2
Brace sections made of plates and belts	1.15

$$1.1 \leq C_{pr} = \frac{F_y + F_u}{2F_u} \leq 1.2. \quad (6)$$

In Eq. (6),  $F_u$  is final stress of the brace materials. According to Eq. (5), the cross-sectional area of the fuse can be calculated by Eq. (7):

$$A_{fuse} \leq \frac{A_{brace}}{C_{pr} \cdot R_y}. \quad (7)$$

After calculating the cross-sectional area of the fuse, it must be verified whether or not the profile chosen for the fuse can tolerate the demand load. In other words, the fuse section is the critical unit of the brace that should tolerate the demand load exerted to the brace. Therefore, Eq. (8) should be modified as:

$$P_{demand} \leq A_{fuse} \cdot F_y. \quad (8)$$

If Eq. (8) is satisfied, the selected profile is proper for both the fuse and the brace; otherwise, a new and bigger profile should be chosen and the calculations should be restarted. Based on the formulation obtained from Eq. (7) for calculating the cross-sectional area of the fuse, a numerical study is conducted using ABAQUS 6.12. The aim of this study is to examine the presented formulation and performance of the suggested method designed based on the mentioned formulation. In this study, a local fuse is calculated by Eq. (7) and placed in a distance of 25 cm from the end of a double-UNP120 brace. The length of the brace and fuse are respectively 414 cm and 5 cm. In order to prevent the local buckling of the fuse, the boxes have been installed as the auxiliary element and around the fuse with a 1-millimeter distance according to Fig. 10. Also, a stopper has been used in order to the concurrent horizontal movement of the internal and external auxiliary elements. This stopper has been tied to the external auxiliary element. The more detailed explanations about applying the auxiliary elements in ILF-AECB braces have been proposed in the 2.1.2 section of the paper. The mechanical specifications of the steel materials and the geometric specifications of the model are provided in Table 2. Also, the fixed end supports have been used in the study. In addition, the numerical model designed in ABAQUS 6.12 is illustrated in Fig. 10.

**Table 2. Material mechanical properties and geometric properties of the studied model.**

Yield stress	Ultimate stress	Yield strain	Ultimate strain	Area brace section	Area fuse section
2400 kg/cm <sup>2</sup>	3700 kg/cm <sup>2</sup>	0.0012	0.20	34 cm <sup>2</sup>	22.60 cm <sup>2</sup>

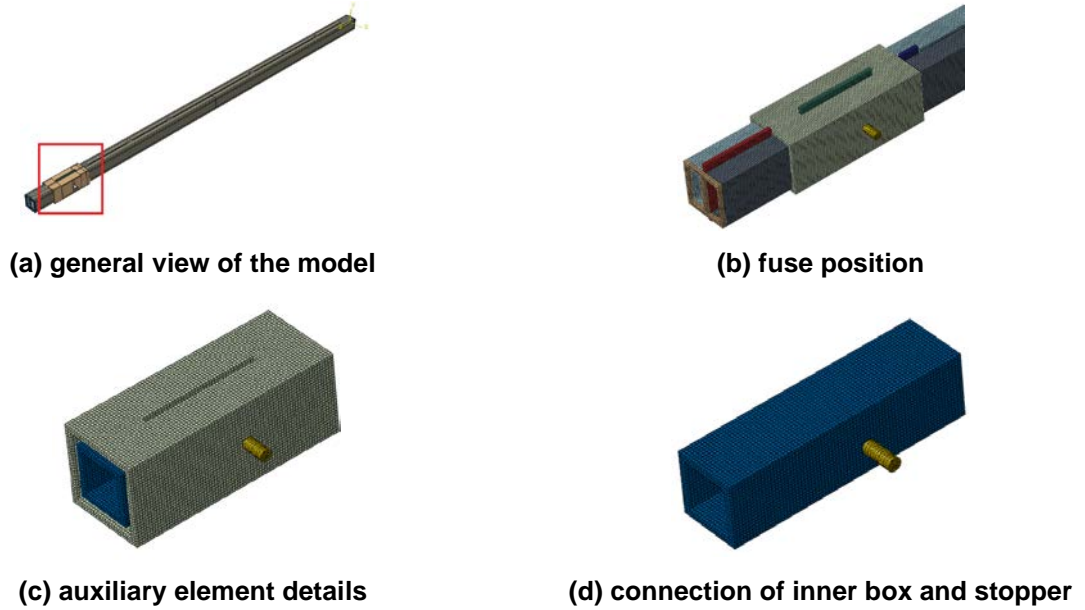


Figure 10. The numerical model in this study.

As shown in Fig. 11, the overall buckling takes place before the fuse reaches its ultimate loadbearing capacity. In other words, the hardening of steel material has caused the brace to reach its yield load before the fuse reaches the ultimate loadbearing capacity. According to Eq. (9), global buckling takes place in the model during the compressive cycle corresponding to the tensile cycle of the brace yielding due to a significant reduction in the stiffness compared to its elastic stiffness after yielding the materials.

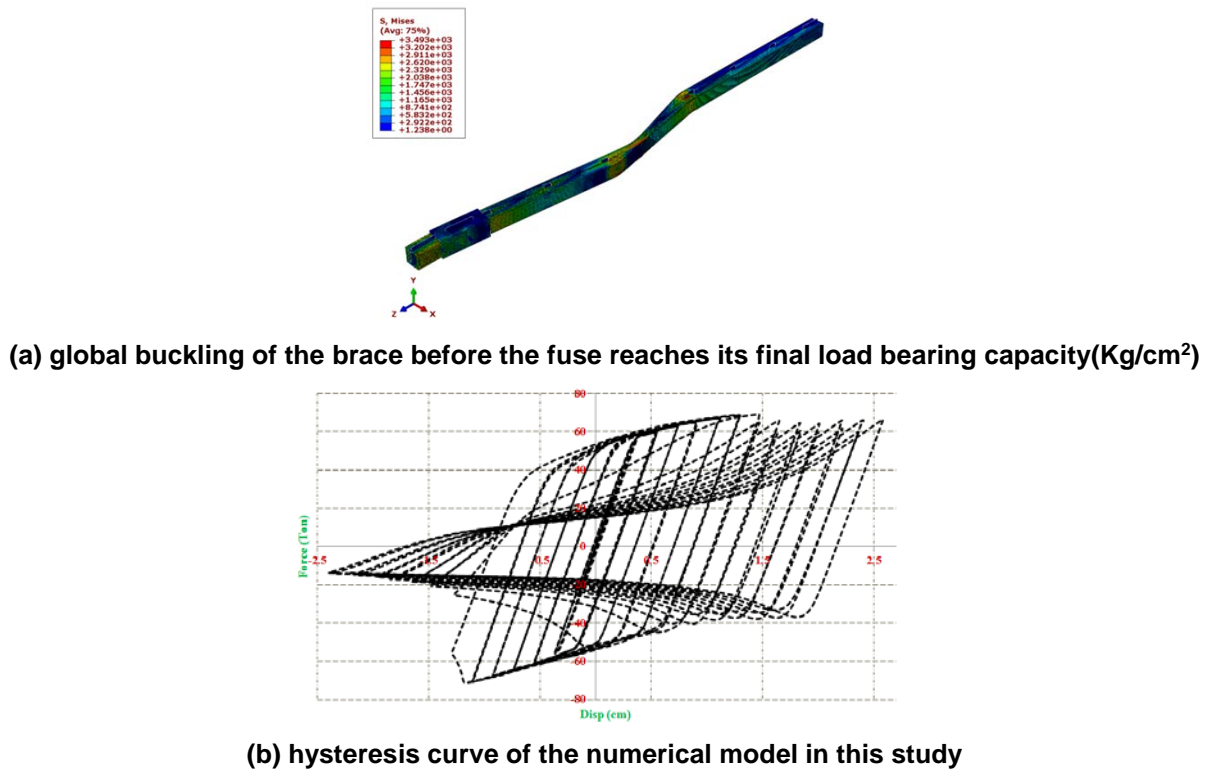


Figure 11. Results of the numerical study.

$$\sigma_{Cr} = \frac{\pi^2 \cdot E}{\lambda^2} \tag{9}$$

In the above equation,  $\sigma_{Cr}$  is the critical stress,  $E$  is the elastic modulus, and  $\lambda$  is the slenderness factor of the element under compression.

According to the results obtained in this numerical study and using experimental results in real situations provided in a previous study by Bazzaz et al. [3–6], the steel yields a load less than the theoretical yield load. Therefore, a reduction coefficient of 0.8 is used in calculating yield capacity of the brace to make sure that the fuse reaches its ultimate loadbearing capacity and fails before the overall buckling of the brace. The studies provided in the following sections have confirmed that this value is suitable for the reduction coefficient. In addition, according to the experimental studies provided in this article, the ultimate stress of the steel materials,  $F_u$ , can be used directly instead of using  $R_y \cdot C_{pr} \cdot F_y$  equation in the calculations of ultimate loadbearing capacity of the brace, which is provided by the Iranian steel structures code [28]. According to Table 3, the two experimental studies carried out here on braces with a box profile made of plate and the braces with the I-beam profile have shown slight differences between the equation provided in the Iranian steel structures code [28] and the ultimate stress of the steel materials.

**Table 3. Final stress values in comparison with those of  $C_{pr} \cdot R_y \cdot F_y$  in the models.**

Model name	$C_{pr} \cdot R_y \cdot F_y$ (MPa)	$F_u$ (MPa)
Box shape brace	$1.15 \cdot 1.15 \cdot 294 = 388.8$	385
I shape brace	$1.2 \cdot 1.2 \cdot 322 = 463.6$	462.1

According to the above descriptions, Eqs. 5 and 7 are finally defined as the following, respectively:

$$P_{u,fuse} \leq 0.8(P_{y,brace} = A_{brace} \cdot F_y); \quad (10)$$

$$A_{fuse} \leq \frac{0.8 \cdot A_{brace} \cdot F_y}{F_u}. \quad (11)$$

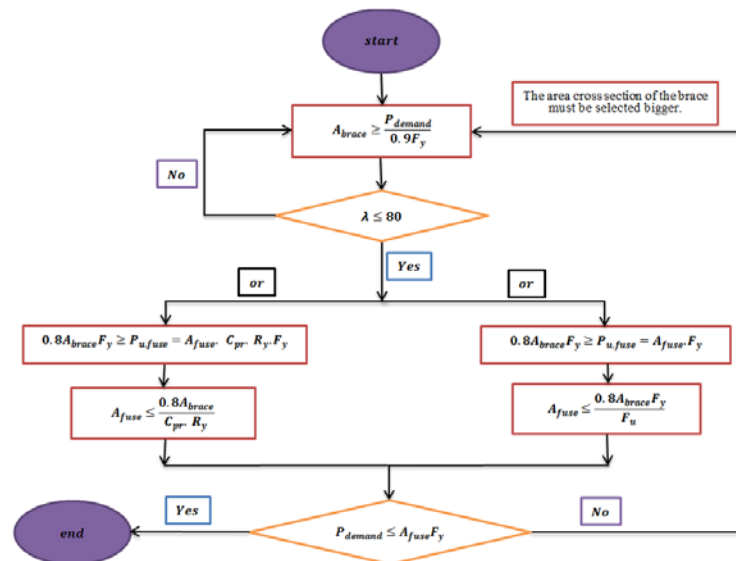


**Figure 12. Flowchart of the brace and the fuse area calculation.**

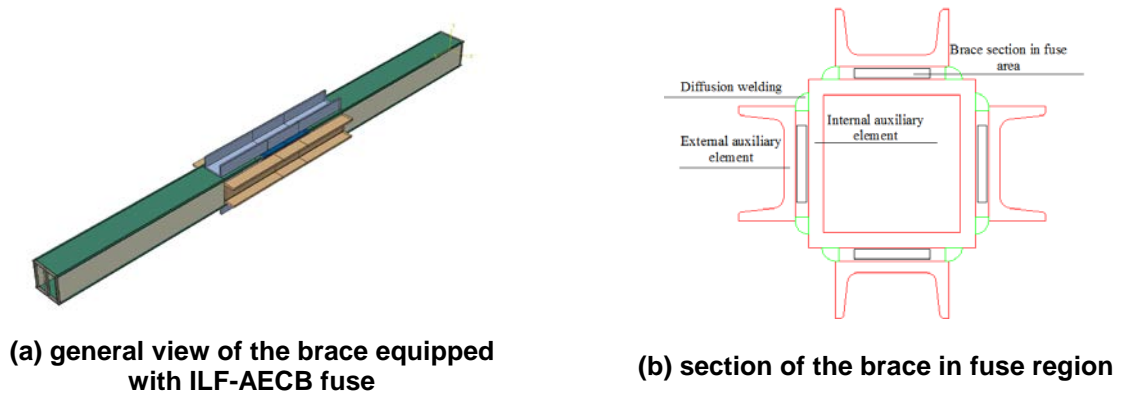
It should be noted that the capacity of the designed brace is equal to the fuse capacity based on Eq. (11), and the loadbearing capacity of the total cross-sectional area of the brace does not affect its loadbearing capacity. Moreover, the fuse length for ILF-AECBs is calculated in such a way that the fuse slenderness should be larger than the slenderness of the brace so that the overall buckling does not take place in the brace during the performance of the ILF-AECB against the exerted load. Due to this matter, Eq. (12) must be satisfied for ILF-AECBs:

$$l_{fuse} \geq \frac{k \cdot l_{brace}}{r_{min,brace}} \cdot r_{min,fuse}, \quad (12)$$

where  $r_{min,brace}$  is the radius of gyration of the weakest piece of the fuse. Also,  $k$  is the compressive effective length coefficient of the element, which is chosen according to the end conditions of the brace.

### 2.1.2. Auxiliary elements in the ILF-AECB bracing

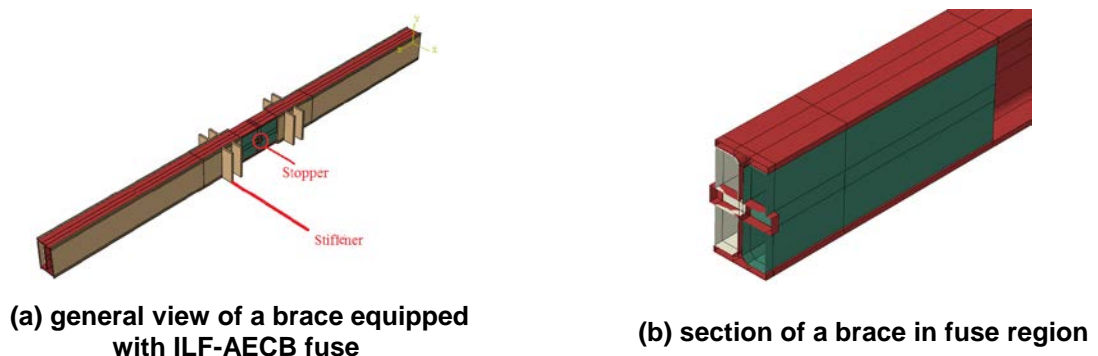
The second component in ILF-AECBs is the auxiliary element. Depend on the braces shape, auxiliary element can have several parts. For braces with a box-shape profile section, the auxiliary elements generally include the external and internal parts of the fuse with 1 mm distance from the fuse walls so that they cannot affect the fuse loadbearing capacity. The rationale behind the existence of the auxiliary element in the ILF-AECB is to prevent local buckling of the brace in the fuse area. As it is evident from Fig. 13, auxiliary element is made up of an inner rectangular tube and four outer channels for bracings with a box section.



**Figure 13. A box-shaped brace equipped with the ILF-AECB fuse.**

The length of these internal and external elements should be at least 150 mm more than the fuse length plus the transition zones. The thickness of these elements must also be selected in such a way to be able to neutralize the lateral displacement of the fuse. To fix the position of the four external channels, one end of them must also be welded to the brace and to the inner tube throughout both sides of the channels in the fuse region using the diffusion welding (Fig. 13b), which also fixes the position of the inner tube.

In the I-shaped cross-section ILF-AECBs (Fig. 14), the auxiliary elements are composed of two steel elements placed within the web of the beam and reinforcing plates connected thereto. These elements are designed and placed in a manner to have a 1-mm gap between the web and reinforcing plates. As in the previous model, the length of the auxiliary elements must be at least 150 mm larger than all fuse ends, so that it has the necessary performance to prevent the fuse from local buckling. As shown in Fig. 14a, a stopper is used in the middle of the fuse length to fix the position of the auxiliary elements. According to this figure, stiffeners with a minimum thickness of 8 mm and a minimum width of 50 mm with a height equal to that of the reinforcing plate are also used to increase the strength of the reinforcing plates and prevent their local buckling in the fuse zone. These stiffeners must be placed on reinforcing plates approximately 50 mm apart from the edge of the plate and each other.



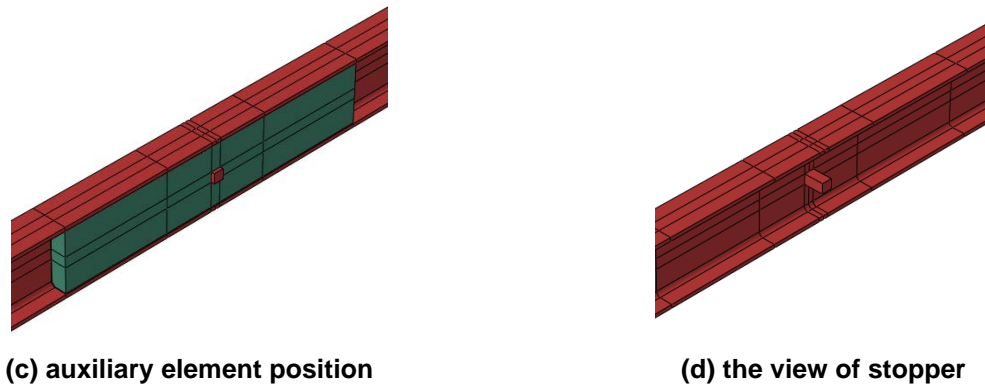


**Figure 14. An I-shaped brace equipped with the ILF-AECB fuse.**

It is noteworthy that in all the studies carried out for this paper, the used auxiliary elements surrounding fuse were so rigid and solid, thus the behavior of the studied braces was completely dependent on fuse behavior and no unusual behavior was seen in models due to auxiliary element weakness. However, it should be mentioned that inappropriate selection of surrounding auxiliary elements of the fuse in terms of rigidity and strength can surely affect the performance and proper behavior of ILF-AECBs. Thus, it seems necessary to carry out an accurate study on the determination of rigidity and strength parameters for surrounding auxiliary elements of the fuse in the future.

### 3. Result and Discussion

#### 3.1. Experimental study

##### 3.1.1. Test setup, material properties, and loading pattern

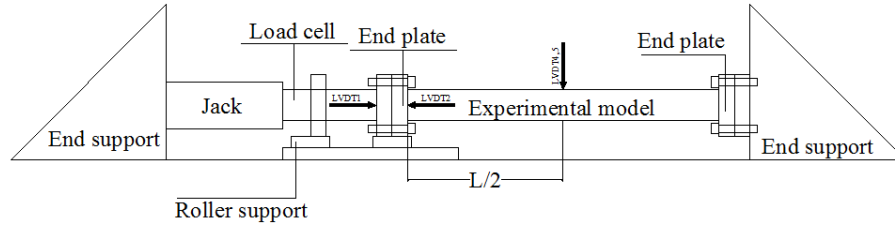
In this study, an experimental research was conducted to investigate the behavior of the ILF-AECB bracing system. The studied brace models and their test setup are shown in Fig. 15. The brace sections are box-shaped and I-shaped in the first (Fig. 15a) and the second (Fig. 15b) models, respectively. The fully detailed of these shape sections has been presented in Fig. 16. According to Fig. 15, both ends of the models are welded to the end plates as fixed. The end plates are also connected to a rigid frame on one side using high resistance 10.9 bolts and a 100-ton load cell on the other side. A 200-ton jack was used to apply load to the models. According to Fig. 15, two strain gauges were also inserted in the middle distance between the end load plate and the center brace for both the models. Six and five LVDTs were also used in different parts of the models according to Fig. 15 (a and b).



**(a) ILF-AECB brace with box-shaped section**



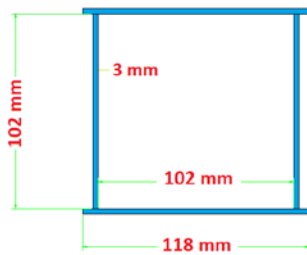
(b) ILF-AECB brace with I-shaped section and reinforcement plates



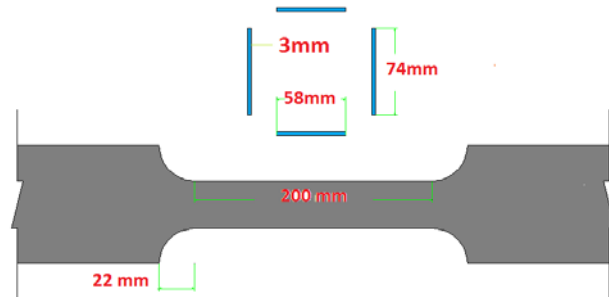
(c) Schematic diagram of the experimental specimens

Figure 15. Experimental setup.

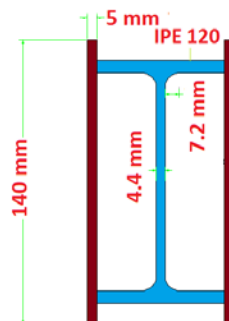
The brace profile and the details of the fuse used for both the models are presented in Fig. 16. The length of all specimens is equal to 200 cm. The cross-sectional area and length of the fuse in the box-shape brace are considered equal to 792 mm<sup>2</sup> and 200 mm, respectively, based on Eqs. (2) and (3). These parameters in the I-shaped brace are 1320 mm<sup>2</sup> and 200 mm, respectively. For box-shape model (Fig. 13b), a 100.100.6 mm box is the inner auxiliary element and four standard 60 mm channels are the external auxiliary elements. A length of 600 mm was selected for all auxiliary elements in both models.



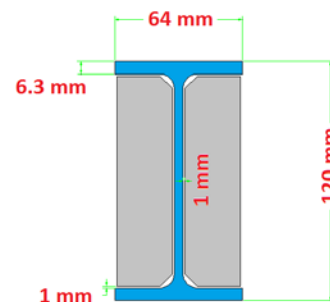
(a) cross-section of the box-shaped brace (mm)



(b) fuse detail in the box-shaped brace (mm)



(c) cross-section of the I-shaped brace (mm)



(d) fuse detail in the I-shaped brace (mm)

Figure 16. Details of the brace section and fuse in specimen models.

The steel materials (that were be ST37) used in the specimen models have specific mechanical characteristics (Table 4) that are obtained using the standard tensile test shown in Fig. 17. In this paper,

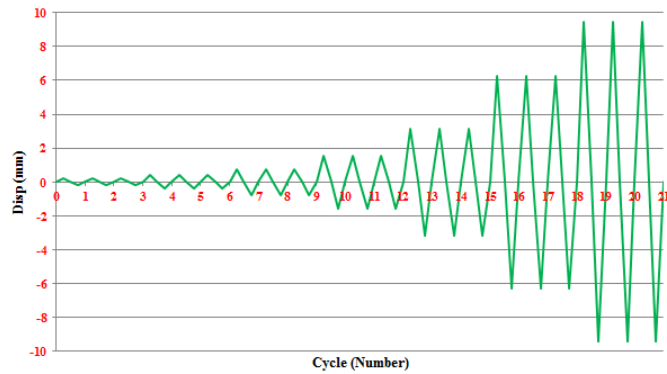
the ATC-24 loading pattern [29] is used to obtain hysteresis responses of the experimental (section 3.1) and numerical (section 3.2) models, as shown in Fig. 18.

**Table 4. Material properties.**

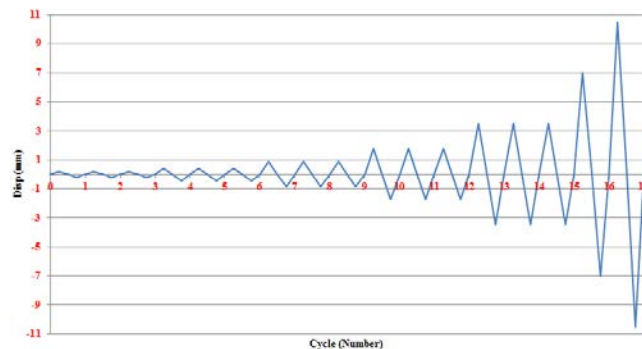
Model	Yielding stress [MPa]	Yielding strain	Ultimate stress	Ultimate strain	
Box-shape model	294	0.0025	385 MPa	0.1571	
I-shape model	IPE12 Plate	308 265	0.0019 0.0017	475 MPa 416 MPa	0.19 0.31



**Figure 17. Standard tension test of steel material (based on the ASTM E8 standard).**



**(a) Load pattern for the box-shaped model**



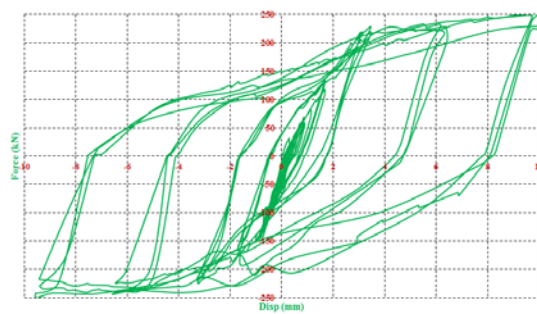
**(b) Load pattern for the I-shaped model**

**Figure 18. The ATC24 load pattern.**

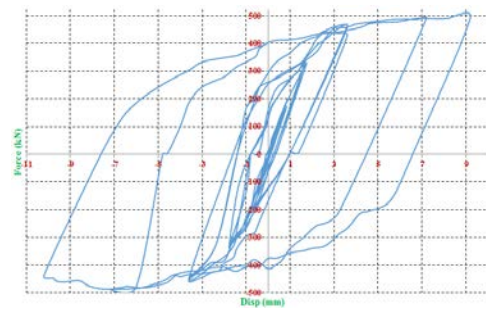
**3.1.2. Interpretation of experimental results**

Fig. 19 represents the hysteresis curves obtained from the specimen models. As shown in this figure, the ILF-AECB has been able to provide a consistent and symmetric behavior under cyclic loading in these

models. The tubby- and spindle-shaped curves obtained for the studied specimen models indicate that the mechanism defined in the ILF-AECB bracing system has been able to function correctly and prevent brace buckling. As shown in Fig. 19, the specimen models show no losses of the tensile and compressive strengths under cyclic loading. Besides, the corresponding load bearing capacity has also increased in the models with increasing the amount of displacement applied to the brace. The behavior of the box-shaped specimen model under cyclic loading is illustrated in Fig. 20. As shown in Fig. 20a, the internal and external auxiliary elements have succeeded in preventing the fuse from local buckling, so that the brace can continue to operate without the loss of strength in compressive load. According to Fig. 20b, the brace stops functioning and rupture occurs in the end zone of the fuse in the tensile loading cycle. The behavior of the I-shaped cross-section ILF-AECB bracing system is presented in Fig. 21. In this model, the auxiliary elements have also been able to prevent the fuse from the local buckling and eventually the brace is torn in the middle of the fuse in the tensile loading cycle (Fig. 21b). However, it is important to mention that the friction between the fuse components and auxiliary elements definitely resulted in the earlier failure of the fuse. This subject has decreased the fuse capacity in bearing of more deformation and energy absorption. The study of this topic, in detail, is necessary in the future.



(a) Box-shaped ILF-AECB brace



(b) I-shaped ILF-AECB brace

Figure 19. Hysteresis curve of specimen models.



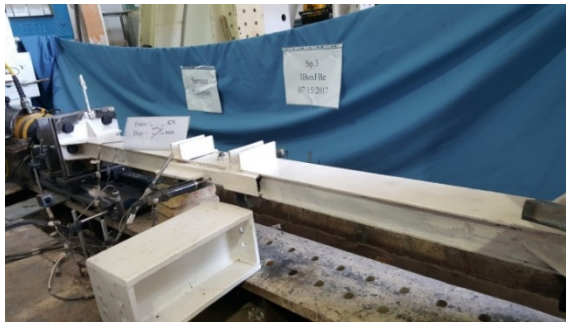
(a) prevention of fuse local buckling by auxiliary elements



(b) tearing of brace at the end of the fuse

Figure 20. Failure of the box-shaped model.

The envelope curves of specimen models are presented in Fig. 22. According to these curves, the box-shaped model in the tensile region has undergone an initial yielding in the fuse region at a displacement of 0.3 mm and a corresponding load of 32.6 kN. In addition, the maximum load bearing capacity of the model (251.2 kN) occurred at a corresponding displacement of 10.2 mm; after this displacement, the model was ruptured and broken in the fuse end zone. The brace offers a good performance in both the compressive and the tensile zones. In this zone, the braces have undergone an initial yielding at a displacement of 0.33 mm and a corresponding compressive load of 99.6 kN. Then, the brace was able to reach a maximum compressive load of 250.1 kN, which corresponds to a displacement of 9.54 mm. In the other model (Fig. 22b) the I-shaped cross-section ILF-AECB was able to provide a good performance in tensile and compressive loads. In the tensile region of this model, it has undergone an initial yield at a load of 97.5 kN and a displacement of 0.865 mm, and has experienced a maximum tensile strength of 493 kN at a corresponding displacement of 9.2 mm. In the compression zone, the mentioned specimen model withstands the compressive load without any buckling. In this region, an I-sectional specimen model has undergone an initial yield in a load of 209 kN and a corresponding displacement of 0.845 mm. Then, it was able to reach a maximum load bearing capacity of 487 kN at 7.2 mm displacement. The model has experienced a 438 kN load at a displacement of 10.2 mm in the compression zone during the last loading cycle. Finally, the model is torn in the center of the fuse after the last loading cycle and during the tensile loading cycle (Fig. 21b).

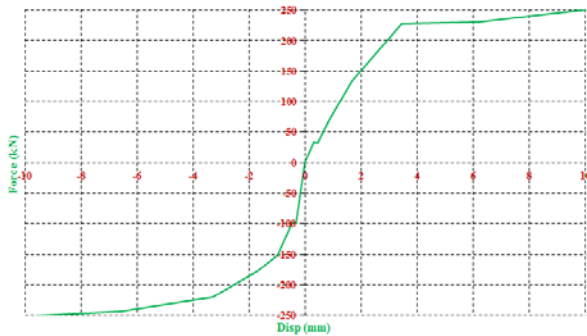


(a) prevention of the fuse local buckling by auxiliary elements

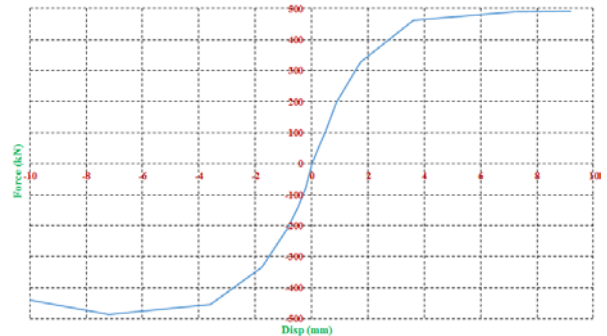


(b) tearing of the brace in the middle of the fuse

Figure 21. Failure of the I-shaped model.



(a) Box-shaped ILF-AECB



(b) I-shaped ILF-AECB

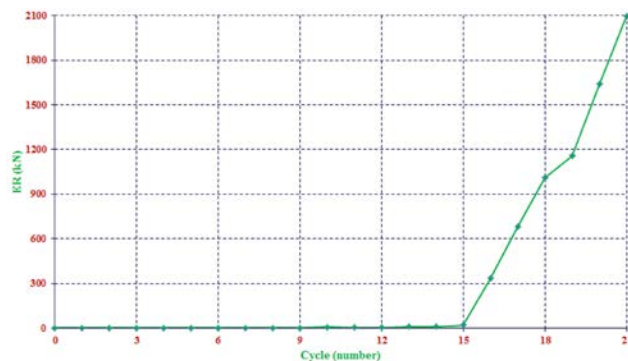
Figure 22. Envelope curves of specimen models.

With respect to the abovementioned issues and according to Eq. (13), the tensile ductility,  $\mu_t$ , and the compressive ductility,  $\mu_c$ , are 34 and 29 for the box-shaped specimen model, and 10.6 and 12 for the I-shaped specimen model, respectively. This amount of ductility, especially in the compression zone, is far greater than that of conventional concentric bracing systems, which indicates a more ductile behavior of the ILF-AECBs than that of conventional concentric braces.

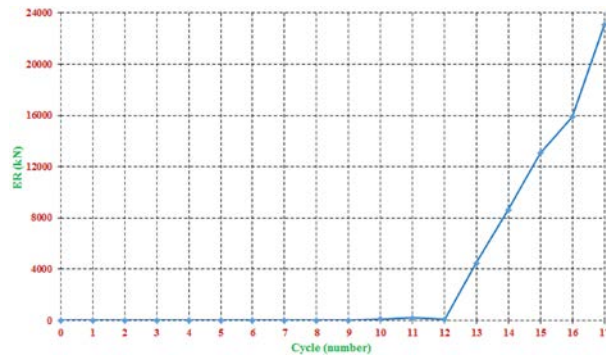
$$\mu = \frac{\delta_u}{\delta_y} \tag{13}$$

In Eq. (13),  $\mu$ ,  $\delta_y$ , and  $\delta_u$ , are the ductility, the yield displacement, and the ultimate displacement of the element, respectively.

The amounts of energy dissipated by the box-shaped and I-shaped specimen models were equal to 19728 kN.mm and 22283 kN.mm, respectively. Fig. 23 depicts the relative energy curves, ER, of the mentioned models. Each point in this curve represents the amount of energy dissipated by the brace in each loading cycle to the mean of the maximum compressive and tensile displacements corresponding to that cycle.



(a) Box-shaped ILF-AECB



(b) I-shaped ILF-AECB

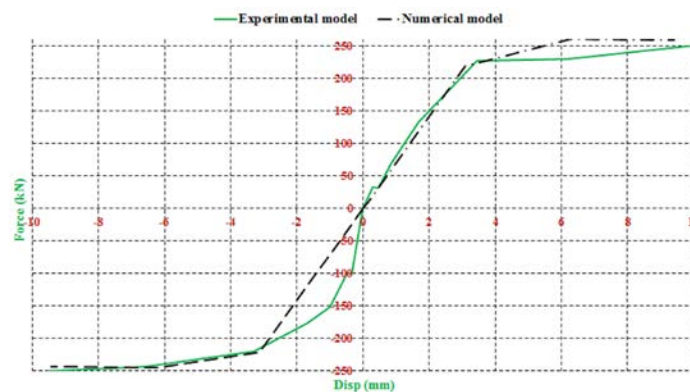
**Figure 23. ER curves of specimen models.**

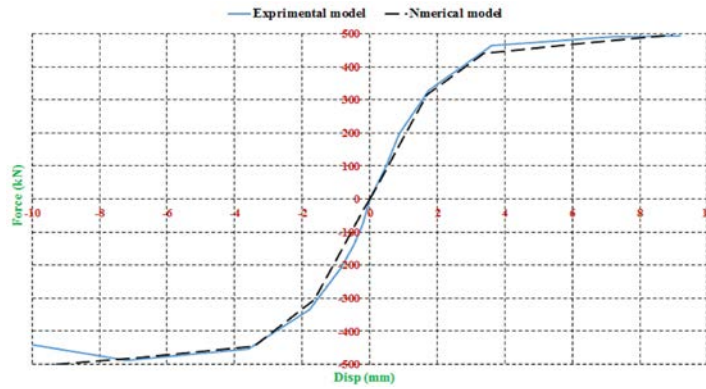
Generally, when the amount of a brace energy dissipation increases with increasing the imposed displacement thereto, then it can be concluded that the brace has a desirable energy dissipation capacity, which is clearly shown in Fig. 23. With respect to this figure, it can be concluded that the ILF-AECBs are able to increase their relative energy dissipation capacity up to their ultimate performance due to the fact that buckling is not going to occur therein. In the case of common concentric bracing systems, however, the amount of ER decreases significantly after the overall buckling [26].

### 3.2. Numerical study

#### 3.1.3. Verification of numerical study

First of all, the results of numerical studies need to be validated using the results of experimental studies. For this purpose, the Fuse-expr-box and Fuse-expr-I numerical models were generated corresponding to their specimen models in Abaqus 6.12 (2012) software using SOLID elements in three-dimensional form and then subjected to uniform loading (Fig. 13 and 14). The mechanical properties of the numerical models are provided in Table 4. These materials were defined in ABAQUS by a bi-linear curve with a moderate hardening slope in the plastic region (nearly 0.001 of elastic slope). This curve is symmetric in tension and compression. In addition, the element contacts of the numerical models were defined by the Interaction Module and surface-to-surface contact. The tangential behavior of the contact areas in the numerical models was frictionless. To create buckling conditions for the entire numerical models, an initial displacement 0.01 times as large as the bracing length was applied to the middle of the bracing. The mesh size of 1 cm was applied. To more critical areas and the joints of two parts, a mesh size of 0.5 cm was applied. Also, C3D8l elements were applied to the meshing of all parts. The envelope curves of the specimen models and the capacity curves of numerical models are compared in Fig. 24. As shown in this figure, the numerical models have been able to provide a good estimate of the capacity of the specimen models.

**a) The box-shaped ILF-AECB**

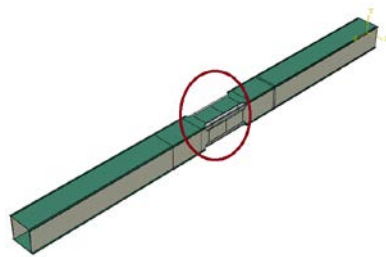


b) The I-shaped ILF-AECB

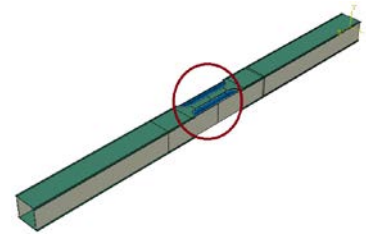
**Figure 24. A comparison between envelope curves of specimen models and their corresponding numerical models.**

#### 3.1.4. The effect of the local fuse shape

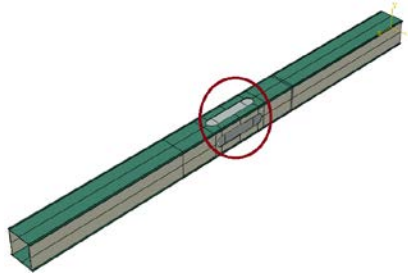
This section examines the effect of the fuse shape on the box-shaped ILF-AECB hysteresis response. For this purpose, four models were made in the Abaqus 6.12 software (Fig. 25,). The Fuse-expr-box model corresponds to the specimen model, where the fuse is created by equally reducing the cross-sectional area on four sides of the brace section. In this model, the fuse is also created by trimming the outer region of the brace sides. In the Fuse-expr-2face model, the fuse is only created on two sides of the brace by trimming the outer zone of them. In the Fuse-cutside and Fuse-cutside-2face models, the fuses are also created by cutting the inner zone of the bracing sides, with the difference that the fuse is distributed equally on four sides of the brace in the former, but it is only created on two sides of the brace in the latter.



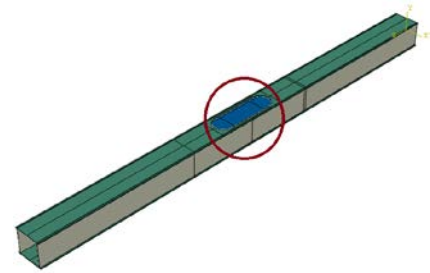
a) Fuse-expr-box model



b) Fuse-expr-2face model



c) Fuse-cutside model



d) Fuse-cutside-2face model

**Figure 25. Numerical models for examining the influence of the fuse shape.**

Fig. 26 compares the hysteresis responses of numerical models. As shown in this figure, the Fuse-cutside and Fuse-expr-box models, with fuses evenly distributed over their sides, have the most stable and tubby hysteresis curves. The Fuse-cutside model also offers better performance within the two models.

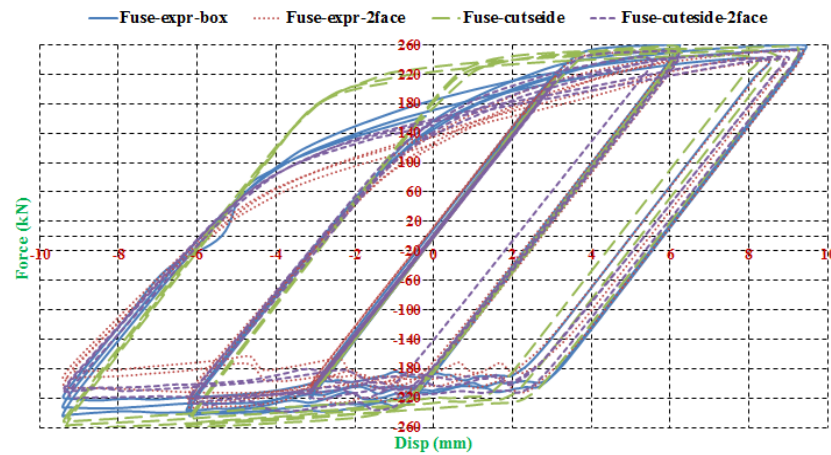


**Figure 26. A comparison between hysteresis curves of box-shaped numerical models.**

The overall behavior of numerical models is the same under cyclic loading, but minor differences in load bearing and energy absorption capacities have caused a distinction between them. The Fuse-expr-box model has the greatest maximum tensile load bearing capacity (260 kN). The maximum load bearing capacities are 258 and 252 kN in the Fuse-cutside model and in the other two models, respectively. The greatest maximum bearing capacity value among the studied numerical models is only about 3 % higher than the smallest values of these parameters. The Fuse-cutside model has maximum compressive load bearing capacity (262.5 kN), with values of 243, 232, and 238 kN in the Fuse-expr-box, Fuse-expr-2face, and Fuse-cutside-2face models, respectively. The maximum load bearing capacity of the Fuse-cutside model was 8 %, 13 %, and 10 % higher than the Fuse-expr-box, Fuse-expr-2face, and Fuse-cutside-2face models, respectively. Also, the energy dissipated by the Fuse-cutside model (21411 kNmm) is higher than those of 19728, 17474, and 18492 kNmm for Fuse-expr-box, Fuse-expr-2face, and Fuse-cutside-2face models, respectively. In other words, the Fuse-cutside model has been able to dissipate about 8.5 %, 22.5 %, and 16 % more energy than Fuse-expr-box, Fuse-expr-2face, and Fuse-cutside-2face models, respectively, under the cyclic loading. According to the content presented in this section, it can be concluded that the ILF-AECB provides its best performance against cyclic loading, when the localized fuse is evenly distributed between the bracing faces and is created by trimming its internal zone of those faces.

In the case of I-shaped cross-section ILF-AECB, the most optimal and economical form of the brace cross section is the same as what presented for the Fuse-expr-I model. As seen in the box cross-section ILF-AECB, the maximum difference in the energy dissipation capacity was 22.5 % between the compared models. However, if it is required to form a new shape of the fuse in I-shaped cross-section braces, it will require a local cut in I section part of the brace and the reinforcing plates connected thereto. This fact will greatly increase the cost of constructing I-shaped cross-section ILF-AECBs, making them uneconomical. However, in the ILF-AECBs with I cross-section, which is similar to the Fuse-expr-I model, the fuse can easily be implemented at no cost in the construction site. Therefore, it can be concluded that even an improvement of 22.5 % in the energy dissipation capacity, which is the maximum improvement of this parameter, is not considered a significant improvement in comparison to the increase in the implementation cost of the I-shaped cross-section ILF-AECB in fuse shapes, except for the fuse shape in the Fuse-expr-I model. For this reason, the study on the various fuse shapes in I-shaped section braces is ignored herein.

### 3.3. Comparative analysis study

In this section of the study, the behavior of ILF-AECB frames is compared with that of the conventional concentrically braced frame. For this purpose, a 5-story building with a chevron braced lateral resistant system was first designed with the assumption of symmetry and regularity in the plan and height based on the Iranian steel structures code [28] using the ETABS 9.7.4 software [30]. The plan of the building is illustrated in Fig. 27. The height of all stories and the width of all spans are 3 m 4 m, respectively. According to these dimensions, the frame diagonal, which is equal to the length of the brace, is 3.61 m. The building frame was designed with the assumption that the frame to the ground, the beam to the column, and the brace to the frame are all connected in a pinned manner. Furthermore, the building location was assumed to be in Tehran city and the type of the soil was assumed to be D in the analysis. The dead and live loads of the stories were respectively assumed to be 540 and 200 kg/m<sup>2</sup>, while those of the roof were assumed to be 570 and 150 kg/m<sup>2</sup>, respectively. In addition, the load of the walls was distributed uniformly and was considered to be 195 kg/m<sup>2</sup>.

After the completion of the analysis, the maximum force in the braces of each story was extracted from the ETABS software. Then, the brace was designed based on the formulation of the ILF-AECB. The profiles of the fuse and the brace, as well as the fuse length were obtained based on Eqs. 11 and 12, respectively. In order to classify the profiles of the building, the design forces for the braces of the first and second floors were considered the same as the maximum force (41 ton) of the first floor. For other floors, the maximum force of the brace was the same as that (25 ton) in the third floor. Interestingly, the smallest choice profile of the brace should be Box120\*120\*8 in designing the braces to satisfy Eq. (4), with assumptions of yield stress and ultimate stress being equal to 2400 and 3700 kg/cm<sup>2</sup>, respectively (the slenderness of the brace is less than 80).

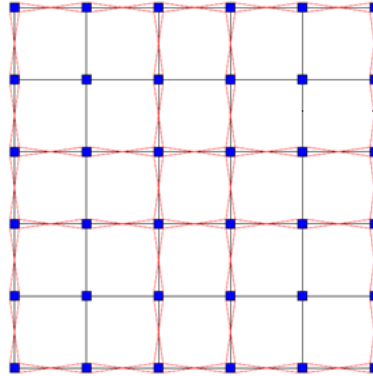


**Figure 27. The plan of the studied analytical model.**

The cross-sectional area of this profile is 35.84 cm<sup>2</sup> and that of the fuse is 20.8 cm<sup>2</sup> for the mentioned profile based on Eq. (11). Hence, the designed fuse in this profile has a yield load of 51 ton. In other words, the smallest selected profile of the brace, which is obtained based on the slenderness equation, automatically satisfies both demand loads. Due to the points mentioned above, therefore, the bracing profile in all spans and floors was considered to be Box120\*120\*8. Also, the fuse length is 25 cm for the profile mentioned above based on Eq. (12). After obtaining the profile for the brace, the beams and columns for the building mentioned above with the chevron bracing resistant system were designed using ETABS. The final structural elements obtained from the design are provided in Table 5.

**Table 5. Structural elements of the studied models.**

Story	Brace	Beam	Column	Fuse Area (cm <sup>2</sup> )	Fuse Length (cm)
1	BOX120*120*8	IPE160	BOX160*160*12.5	20.80	25
2	BOX120*120*8	IPE160	BOX160*160*10	20.80	25
3	BOX120*120*8	IPE160	BOX120*120*10	20.80	25
4	BOX120*120*8	IPE160	BOX120*120*10	20.80	25
5	BOX120*120*8	IPE160	BOX120*120*10	20.80	25

After the above steps and designing the building, a frame of the building was extracted (all braced frames of the building were the same) to compare the behavior of the ILF-AECB frame with that of the conventional concentrically braced frame. Then, this frame was modeled in ABAQUS with two different modes as a 2D model. In the first mode, the frame was modeled as a concentrically braced frame, named CBF, in ABAQUS software (Fig. 28). In the second mode, a model was created named the ILF-AECB, where the beams and columns are the same as the previous model (CBF), but the brace is modeled as ILF-AECB. In this model, the brace is divided into three parts. At the two ends, the profile of Box120\*120\*8, which was obtained from the design and used for the CBF model, is used for this case. In the middle, which is 30 cm away from the end of the brace with a length equal to the fuse length (25 cm), an element is embedded with the same cross-sectional area of the fuse (20.8 cm<sup>2</sup>). For modeling the auxiliary elements to prevent the fuse from local buckling, this section of the brace was restricted locally with defining a specific boundary condition, which avoids the displacement of the fuse in the direction perpendicular to the length of the brace. Fig. 29 shows the ILF-AECB model. A 2D beam element with shear flexible linear meshing was used in all the modeling processes.

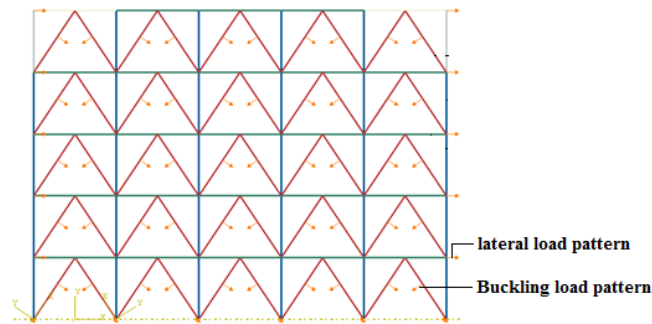


**Figure 28. The CBF model.**

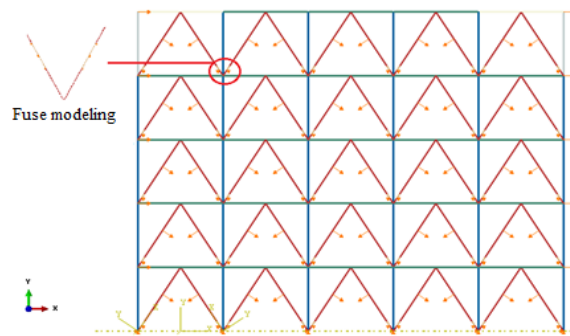


**Figure 29. The ILF-AECB model.**

After the completion of modeling, a nonlinear static analysis was done for each model to compare the response of the ILF-AECB with that of the CBF. An inverted triangle displacement loading plan with a displacement pitch of 2 mm was used in both analyses. After analyzing the models, the curves of their capacities were obtained as shown in Fig. 30, showing that the base shear of the ILF-AECB model is less than that of the CBF model for all displacement pitches. The maximum difference of the base shear between both models is 15 % in the elastic area, which varies from 15 % to 20 % in the non-elastic area with increasing the displacement. This shows that the use of ILF-AECBs in the structure reduces the base shear, which is the base of designing the main structural elements in comparison to the conventional concentrically braced frame, resulting in the use of lighter structural elements in the structure and thus reducing the construction costs of the structure. Moreover, the lower base shear in the ILF-AECB than that of the CBF model demonstrates that the fuse elements in the former have desirably lessened the input energy to the structure, which is also proved previously in the numerical and experimental studies.

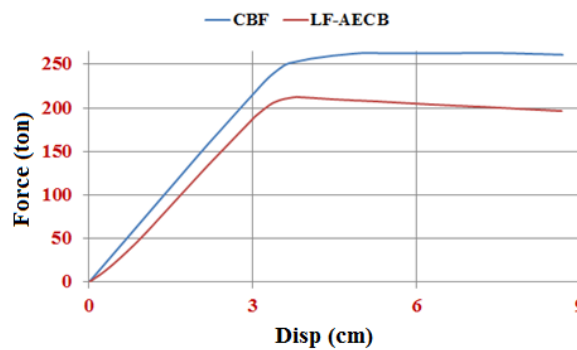


**Figure 30. Comparing the capacity curves of analytical models.**

In order to compare the lost energy by the ILF-AECB frame with that of the concentrically braced frame, two one-story single-span frames of the first story of the above mentioned frames were chosen (Fig. 31) and underwent a displacement nonlinear static cyclic loading. After modeling the frames, a displacement loading pattern with a displacement step of 2 mm was applied to the columns of the frames in a cyclic form (Fig. 31). Then, the hysteresis curves of the frames were obtained as in Fig. 32.

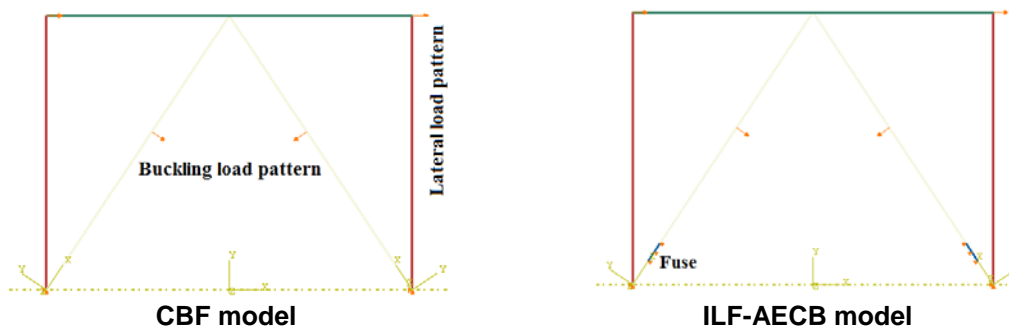


Figure 31. One-story one-opening studied frames.

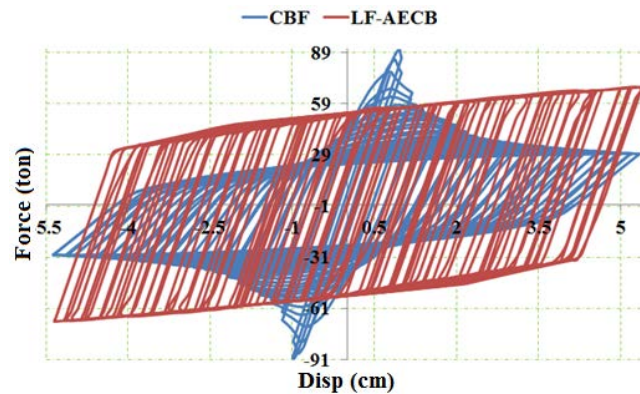


Figure 32. Hysteresis curves of studied frames.

As shown in Fig. 32, the conventional concentrically braced frame had a significant initial elastic stiffness as expected, and it could withstand a base shear of 91 ton elastically without any energy absorption. After this load and due to the buckling of the braces, the frame lost its loadbearing capacity, and its load decreased from 91 ton to about 29 ton (almost 69 % reduction). The energy absorption of this frame was around 121.5 ton-m. However, the scenario is different in the ILF-AECB frame, which entered the non-linear area from a base shear of 50 ton and began to absorb the energy due to the existence of the locally restricted fuses in this frame. Afterward, the frame could tolerate loads up to 68.5 ton of the base shear in larger loading cycles due to the hardening of the steel materials of the fuse without any sudden drop in the loadbearing capacity. The dissipated energy in this frame was about 243.5 ton-m. According to the above points, it is finally concluded that the ILF-AECB could provide more stable behavior, more energy absorption (about two times), and lower maximum base shear (about 15%) than the CBF frame. This would be expected from the ILF-AECB frame before performing the nonlinear static analysis. The final deformation of the frame is illustrated in Fig. 33.

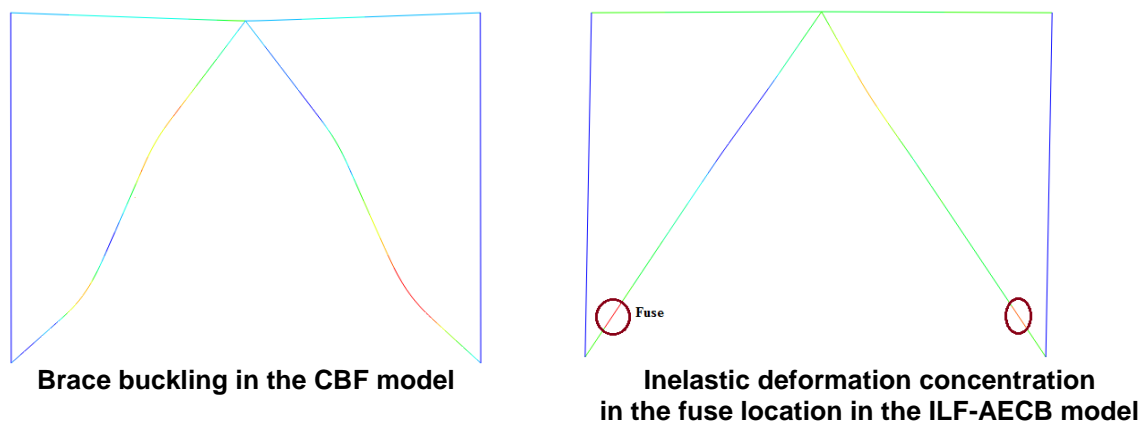


Figure 33. Final deformations(cm) in the studied frames.

#### 4. Conclusion

In this study, a new ILF-AECB has been introduced as an alternative to conventional concentric bracings using numerical and experimental studies. The rationale behind the creation of the ILF-AECB is

to improve the behavior of this element in the compressive zone by preventing the concentric brace from buckling. For this reason, a local fuse was created in the brace to prevent the overall buckling in the brace and the bracing buckling was limited locally to this zone. Then, the local buckling was prevented through the use of auxiliary elements in the fuse region, which resulted in a stable and symmetric cyclic response, and thus, tubby and spindle shaped hysteresis curves were created for this element under cyclic loading. Therefore, the following results are presented in this study:

- The ILF-AECB provides a stable and symmetric response to cyclic loading because it uses a restricted lateral fuse mounted on the ILF-AECB, which prevents it from buckling and causes the brace to have a desirable performance in a compressive zone as the tensile zone.
- Due to the absence of brace buckling, the ILF-AECB has a very high ductility in the compressive zone, as the tensile zone, while conventional concentric braces have an undesirable ductility due to the brace buckling in the compressive zone, and in many cases, the bracing behavior is considered only in the tensile region.
- The ER curve is ascending for the ILF-AECB, meaning that the energy dissipated in each cycle of displacement loading increases significantly with displacement increment in the brace. In conventional concentric braces, however, the amount of ER reduces significantly after brace buckling and, as a result, full brace capacity will not be used for energy dissipation.
- The shape of the local fuse applied to the brace is an effective factor in the box-shaped ILF-AECB system cyclic response. According to the results of this article, it can be concluded that the optimal fuse shape for getting the best performance of the box-shaped ILF-AECB system will be achieved when the fuse is evenly distributed between the brace sides and is obtained by trimming the internal regions of these faces, as in the Fuse-outside model. In the case of I-shaped cross-section ILF-AECBs, the energy absorption improvement is not very significant as to become superior to economical aspect of its construction because the optimal economical form of the fuse type is the same as that used in the Fuse-expr-I model and in the other modes of the fuse shape. Therefore, the other fuse shapes were ignored in these bracings.
- In this article, a comparison of the analytical studies between the single-span one-story frame of the LF-AECB and the conventional single-span one-story concentrically braced frame showed more stable performance, lower base shear (about 15 %), and more energy dissipation (about two times) for the LF-AECB frame.

## References

1. Moghaddam, H., Estekanchi, H. On the characteristics of off-centre bracing system. *Journal of Constructional Steel Research*. 1995. 35 (3). Pp. 361–376. DOI: 10.1016/0143-974X(94)00050-R
2. Moghaddam, H., Estekanchi, H. Seismic behavior of off-centre bracing systems. *Journal of Constructional Steel Research*. 1999. 51 (2). Pp. 177–196. DOI: 10.1016/S0143-974X(99)00007-3
3. Bazzaz, M., Kheyroddin, A., Kafi, M.A., Andalib, Z. Evaluation of the seismic performance of off-centre bracing system with ductile element in steel frames. *Steel and Composite Structures*. 2012. 12(5). Pp. 445–464. DOI: 10.12989/scs.2012.12.5.445
4. Bazzaz, M., Kheyroddin, A., Kafi, M.A., Andalib, Z., Esmaili, H. Evaluating the seismic performance of off-centre bracing system with circular element in optimum place. *International Journal of Steel Structures*. 2014. 14 (2). Pp. 293–304. DOI: 10.1007/s13296-014-2009-x
5. Bazzaz, M., Andalib, Z., Kafi, M.A., Kheyroddin, A. Evaluating the performance of OBS-C-O in steel frames under monotonic load. *Earthquakes and Structures*. 2015. 8 (3). Pp. 697–710. DOI: 10.12989/eas.2015.8.3.699
6. Bazzaz, M., Andalib, Z., Kheyroddin, A., Kafi, M.A. Numerical comparison of the seismic performance of steel rings in off-centre bracing system steel rings in off-centre bracing system. *Steel and Composite Structures*. 2015. 19 (4). Pp. 917–937. DOI: 10.12989/scs.2015.19.4.917
7. Federico, G., Fleischman, R., Ward, K. Buckling control of cast modular ductile bracing system for seismic-resistant steel frames. *Journal of Constructional Steel Research*. 2012. 71. Pp. 74–82. DOI: 10.1016/j.jcsr.2011.11.010
8. Ward, K.M., Fleischman, R.B., Federico, G. A cast modular bracing system for steel special concentrically braced frames. *Engineering Structures*. 2012. 45. Pp. 104–116. DOI: 10.1016/j.engstruct.2012.05.025
9. Seker, O., Akbas, B., Seker, P.T., Faytarouni, M., Shen, J. Three-segment steel brace for seismic design of concentrically braced frames. *Journal of Constructional Steel Research*. 2017. 137. Pp. 211–227. DOI: 10.1016/j.jcsr.2017.06.035
10. Balendra, T., Yu, C.H., Lee, F.L. An economical structural system for wind and earthquake loads. *Engineering Structures*. 2001. 23. Pp. 491–501. DOI: 10.1016/S0141-0296(00)00061-4
11. Zahrai, S.M., Vosooq, A.K. Study of an innovative two-stage control system: Chevron knee bracing & shear panel in series connection. *Structural Engineering and Mechanics*. 2013. 47 (6). Pp. 881–898. DOI: 10.12989/sem.2013.47.6.881
12. Cheraghi, A., Zahrai, S.M. Innovative multi-level control with concentric pipes along brace to reduce seismic response of steel frames. *Journal of Constructional Steel Research*. 2016. 127. Pp. 120–135. DOI: 10.1016/j.jcsr.2016.07.024
13. Jiangbo, S., Peng, P., Haishen, W. Development and experimental validation of an assembled steel double-stage yield buckling restrained brace. *Journal of Constructional Steel Research*. 2018. 145. Pp. 330–340. DOI: 10.1016/j.jcsr.2018.03.003
14. Barbagallo, F., Bosco, M., Marino, E.M., Rossi, P.P. Achieving a more effective concentric braced frame by the double-stage yield BRB. *Engineering Structures*. 2019. 186. Pp. 484–497. DOI: 10.1016/j.engstruct.2019.02.028
15. Iwata, M., Kato, T., Wada, A. Buckling-restrained braces as hysteretic dampers. 3<sup>rd</sup> International Conference STESSA. 2000. Montreal. Canada.

16. Sabelli, R., Mahin, S., Chang, C. Seismic demands on steel braced frame buildings with buckling-restrained braces. *Engineering Structures*. 2003. 25 (5). Pp. 655–66. DOI: 10.1016/S0141-0296(02)00175-X
17. Kiggins, S., Uang, C.M. Reducing residual drift of buckling-restrained braced frames as a dual system. *Engineering Structures*. 2006. 28 (11). Pp. 1525–1532. DOI: 10.1016/j.engstruct.2005.10.023.
18. Hoveidae, N., Tremblay, R., Rafezy, B., Davaran, A. Numerical investigation of seismic behavior of short-core all-steel buckling restrained braces. *Journal of Constructional Steel Research*. 2015. 114. Pp. 89–99. DOI: 10.1016/j.jcsr.2015.06.005
19. Maurya, A., Eatheron, M.R., Matsui, R., Florig, S.H. Experimental investigation of miniature buckling restrained braces for use as structural fuses. *Journal of Constructional Steel Research*. 2016. 127. Pp. 54–65. DOI: 10.1016/j.jcsr.2016.07.019
20. Naghavi, M., Rahnavard, R., Thomas, R.J., Malekinejad, M. Numerical evaluation of the hysteretic behavior of concentrically braced frames and buckling restrained brace frame systems. *Journal of Building Engineering*. 2019. 22. Pp. 415–428. DOI: 10.1016/j.jobe.2018.12.023
21. Qiu, C., Zhang, Y., Li, H., Qu, B., Hou, H., Tian, L. Seismic performance of Concentrically Braced Frames with non-buckling braces: A comparative study. *Engineering Structures*. 2018. 154. Pp. 93–102. DOI: 10.1016/j.engstruct.2017.10.075
22. Shen, J., Seker, O., Sutchiewcharn, N., Akbas, B. Cyclic behavior of buckling-controlled braces. *Journal of Constructional Steel Research*. 2016. 121. Pp. 110–125. DOI: 10.1016/j.jcsr.2016.01.018
23. Seker, O., Shen, J. Developing an all-steel buckling controlled brace. *Journal of Constructional Steel Research*. 2017. 131. Pp. 94–109. 2017. DOI: 10.1016/j.jcsr.2017.01.006
24. Momenzadeh, S., Seker, O., Faytarouni, M., Shen, J. Seismic performance of all-steel buckling-controlled braces with various cross-sections. *Journal of Constructional Steel Research*. 2017. 139. Pp. 44–61. DOI: 10.1016/j.jcsr.2017.09.003
25. Kachooee, A., Kafi, M.A., Gerami, M. The Effect of Local Fuse on Behavior of Concentrically Brace Frame by a Numerical Study. *Civil Engineering Journal*. 2018. 4 (3). Pp. 655–667. DOI: 10.28991/cej-0309123
26. Kafi, M.A., Kachooee, A. The behavior of concentric brace with bounded fuse. *Magazine of Civil Engineering*. 2018. 78. Pp. 16–29. DOI: 10.18720/MCE.78.2
27. ABAQUS Ver .6.12. User's Manual. RI. USA. 2012.
28. Guidelines for design of steel structures .The tenth chapter of the National Building Regulations. Iran. 2013.
29. Zhou, F., Fang Ch., Chen, Y. Experimental and numerical studies on stainless steel tubular members under axial cyclic loading. *Engineering Structures*. 2018. 171. Pp. 72–85. DOI:10.1016/j.engstruct.2018.05.093
30. ETABS Ver 9.7.4. User's Manual. CSI. USA. 2005.

**Information about author:**

**Ali Kachooee, PhD**

ORCID: <https://orcid.org/0000-0003-3648-2905>

E-mail: [ali.kachooee@semnan.ac.ir](mailto:ali.kachooee@semnan.ac.ir)

*Received 10.10.2021. Approved after reviewing 21.06.2022. Accepted 22.06.2022.*



Research article

UDC 697.1:699.86

DOI: 10.34910/MCE.116.10



## Thermal mode of a room with integrated regulation of microclimate systems

O.D. Samarin 

National Research Moscow State University of Civil Engineering, Moscow, Russia

 [samarin-oleg@mail.ru](mailto:samarin-oleg@mail.ru)

**Keywords:** microclimate, temperature, heat balance, heat gain, regulation, integral algorithm, transmission coefficient, civil engineering, building, construction industry

**Abstract.** An air-conditioned room with automatic regulation of its microclimate systems using complex control algorithms is one of the most complex objects for calculating non-stationary thermal regime, so this mode is still insufficiently studied. At the same time, such facilities are typical for providing internal weather parameters in civil buildings. In this paper, we consider a simplified mathematical formulation and solution to the problem of changing the temperature of internal air in a room equipped with a back-ground supply ventilation system and automated local cooling systems under variable thermal effects. The main equations connecting the most important components of the heat flow in the room are analyzed, given we neglect the heat accumulation of the array of fences in the first approximation. The dependence on time for the deviation of the room air temperature from the setpoint and the expression for the moment of time at which the maximum temperature deviation is observed, when the heat flow changes abruptly and the equipment of local cooling systems is regulated according to the integral law are presented. Calculations were made to confirm the obtained analytical solution using a finite-difference approximation of the differential equations of heat balance and heat transfer, as well as by comparing the solution obtained by the author earlier, taking into account the spread of the temperature wave in fences, on the example of one of the currently existing residential buildings in the climatic conditions of Moscow. It is noted that the estimated value of the largest temperature deviation from the setpoint (dynamic control error) and the time for this deviation in the considered problem statement do not depend on the transmission coefficient of the regulator. The obtained relations are proposed to be used for an approximate assessment of the non-stationary thermal regime of an air-conditioned room served by local cooling systems controlled by the integral law, as well as for determining the required parameters of the regulator, including using multivariate calculations with changes in the parameters of the problem.

**Citation:** Samarin, O.D. Thermal mode of a room with integrated regulation of microclimate systems. Magazine of Civil Engineering. 2022. 116(8). Article no. 11610. DOI: 10.34910/MCE.116.10

### 1. Introduction

In the present paper, as an object of a study it is considered the behavior under the conditions of variable thermal effects of the internal air temperature in premises equipped with automated local cooling systems and background supply ventilation system.

The set of internal meteorological parameters in premises must be maintained within the limits determined first of all by the conditions of human comfort or the maintenance of technological process, which, in turn, are mainly associated with life safety requirements. In fact, the hygrothermal regime is stabilized mainly with the help of automatic regulation and control of engineering systems for microclimate maintenance allowing for building's own thermal capacity. At the same time, since the thermal effects on premises and their heat losses are almost always variable, this task turns out to be significantly non-steady.

The issues of calculating the temperature change in air-conditioned premises in the course of appearance of thermal disturbances have been studied for quite a long time. So, some simplified analytical solutions to this problem are even given in reference and educational literature. Of course, they mainly relate only to the thermal regime of insulated enclosures when cooling a building under the conditions of emergency shutdown of heat supply systems or on periodic changes in heat fluxes without taking into account the overall heat balance of premises. However, it can be noted that in recent years more complex papers have been published, in particular, [1, 2], but their results in many cases turn out to be complicated enough, at which point it is difficult to use them for engineering calculations. At the same time, numerical methods are more used for study non-steady regimes and their modeling. Therefore, publications [3, 4], for example, may be interesting in this respect, and especially approaches of this type are currently characteristic of foreign papers, among which there are quite typical studies [5–7]. However, a number of options for these solutions relate to objects of a specific type, operating in limited areas and under special conditions, for example, underground pipelines [8], or for ventilated facades combined with natural ventilation systems [9]. The work [10] is devoted to the non-stationary gas regime of a room with the release of harmful substances contained in building materials in it and the management of this regime, but the theoretical basis of the processes considered there and the results obtained can in many ways be extended to the thermal regime. Moreover, the authors of some studies in this area, on the contrary, solve the inverse problem – on determination of thermophysical characteristics of a material by studying temperature fluctuations [11–13] or using thermography methods [14]. Papers [15–19] are devoted to the modeling of processes in premises as a whole. Thus, in [15] it is presented a very detailed multiparameter numerical model of a simulation type, but it applies only to the cold season in the presence of heating. The publications [16–19] are also quite holistic, for example, in [16, 17] they talk about the use of the principles of fuzzy logic in organization of microclimate control, and [18, 19] are mostly based on the methods of automatic control theory, but their results are still quite difficult for use in engineering practice. Finally, there are studies concerning the general principles of the management of engineering systems of a building and the energy saving under these conditions, for example, [20–22], but due to their general nature, they also do not have specific dependencies of interest to us.

On the basis of differential equation of the balance of convective heat for premises as a whole, the author in article [23] managed to find an analytical solution to the problem of the temperature drop in the event of emergency shutdown of heat supply. However, more complicated cases require additional consideration when such an equation is nevertheless amenable to integration. First of all, we are talking about regimes when the premises are serviced by standard systems for maintenance of internal microclimate, equipped with the appropriate equipment for their automatic regulation, which makes it possible to provide the required set of internal meteorological parameters under variable thermal effects. Therewith, in many cases, control algorithms with an integral component are preferable, when the control action is proportional to the sum of the accumulated deviation from the moment the thermal disturbance appears, and, therefore, the control process will be carried out until this deviation is completely eliminated. Thus, in contrast to simpler proportional controllers, this circuit is devoid of their main disadvantage, namely, a non-zero static control error.

However, it should be noted that in the engineering practice of recent years, the more typical situation is when the temperature of the air in premises and the temperature of surfaces of their enclosing structures is actually maintained at the required level, mainly due to local cooling systems, for example, of the “chiller-fancoil” type or split systems. They use complete recirculation of the air cooled and, therefore, do not take part in the overall air balance of premises. Another fairly common option is the installation of radiant panel cooling systems, the most common of which in recent times are chilled ceilings. In all these cases, the provision of the sanitary-hygiene requirements is accounted for a part of mechanical supply air system, namely, the maintenance of the necessary cleanliness of the internal air, and if at the same time it is provided the cooling of the inflow, then this process serves mainly to reduce, as far as possible, the heat load on the local cooling systems so that hot air does not enter the premises.

In publication [24], the author obtained a very general analytical solution to the problem of change of the temperature in the premises under these conditions using the integral law of climate system regulation. The corresponding dependence is written in the form of a fairly rapidly convergent series in powers of the independent variable, which is the square root of the time period elapsed since the appearance of the thermal disturbance. However, it is advisable to consider the possibility of some simplification of this solution on retention of its physical validity, which will expand the possibilities of its analysis and comparison with existing analogues, with the simultaneous identification of limits when such a simplification is permissible, and, thereby, with an evaluation of the degree of influence of various parameters of the problem on the behavior of internal temperature.

Therefore, the relevance of the proposed work consists in the need to search for simpler analytical dependences of the time variation of the internal air temperature in premises cooled by local automated

systems, taking into account the amount of heat input, the thermal stability of premises and the characteristics of the controller, as well as the relationship of these characteristics with the maximum temperature deviation from a given value. These dependencies should be written in the form of final formulas acceptable for engineering use, but, at the same time, physically based, having satisfactory accuracy and allowing for evaluative multivariate calculations to analyze the behavior of the temperature in premises and synthesize the corresponding automatic control system. The application of the results achieved in this case will be possible for a very wide range of objects of a similar type.

The objective of the paper is to develop simplified analytical methods for calculating the non-steady thermal regime of premises served by local automated cooling systems in the presence of a background unregulated inflow. The tasks of the study are the following:

- setting up of a basic system of differential equations describing the heat balance and heat exchange in air-conditioned premises, taking into account the presence of automated systems for microclimate maintenance;
- obtention of an analytical solution of this system in the form of final formulas upon a jump-like thermal effect and regulation of cooling systems according to the integral law;
- construction of analytical dependencies for the maximum deviation of the air temperature in premises from the setpoint and for the moment in time when this deviation is observed, and their confirmation by comparison with the data of program generation;
- identification of limits when the introduced simplifications are acceptable, and evaluation of the degree of influence of the problem parameters on the thermal conditions of premises based on comparing the results with the general analytical solution obtained by the author in paper [24].

## 2. Methods

Let's write the equation of the balance of convective heat for the air in premises within the framework of its one-zone model in the following form:

$$Q_{in} + G_s c_a (t_s - t_{in}) / 3600 - Q_c - \Lambda (t_{in,0} - t_{in}) = V_r c_a \rho_a \frac{dt_{in}}{d\tau}, \quad (1)$$

where  $Q_{in}$  is the delivery of sensible heat to the air of premises from sources, W;  $Q_c$  is the amount of regulated heat flow, W, from local cooling systems, which is designed to compensate for heat gain;  $V_r$  is the volume of premises, m<sup>3</sup>;  $\tau$  is the time interval, s, from the moment of the variable thermal effect;  $G_s$  is the mass flow rate, kg/h, which is usually considered equal to the value of the exhaust flow rate  $G_{ex}$  due to the almost instantaneous stationarity of the air balance of premises in comparison with the thermal;  $c_a = 1005$  J/(kg·K) is the air specific heat;  $\rho_a = 1.2$  kg/m<sup>3</sup> is its density;  $t_{in}$  is the temperature of internal air in the premises, °C;  $t_s$  is the inflow temperature, °C;  $t_{in,0}$  represents the controlled level  $t_{in}$ , or the so-called setpoint;  $\Lambda$  is the total index of convective heat transfer on surfaces in the premises, W/K. It is calculated as  $\alpha_m \sum A_i$ , where  $\alpha_m$  is the average coefficient of convective heat transfer, which in the first approximation can be taken in the amount of 3.7 W/(m<sup>2</sup>·K), and  $\sum A_i$  is the sum of the areas of surfaces of the enclosing structures facing the room, m<sup>2</sup>. It is assumed that the initial temperature of these surfaces is averagely equal to  $t_{in,0}$ . Thus, the equation (1), in comparison with the one presented in [24] in the last term of the left side, takes into account only the flow of convective heat due to heat transfer on the surfaces of enclosures, and does not consider the temperature change of the structure material itself. But on the right side there is a complex representing the amount of heat that goes for change in the temperature of the volume of air contained in premises. Further, it will be shown that in this case, neglecting it in the considered formulation of the problem can lead to incorrect results. At the same time, as in [24], it is assumed here that  $t_s = \text{const}$ , since regulation is still carried out due to local cooling systems.

If the level  $t_{in}$  is automatically maintained by a controller in which a continuous integral law is realized by means of the necessary change in  $Q_c$  value, it is easiest to write the additional coupling equation in the following form:

$$\frac{dQ_c}{d\tau} = K_c (t_{in,0} - t_{in}). \quad (2)$$

Here  $K_c$  is the equivalent transfer coefficient of an automated system,  $W/(K \cdot s)$ , via the channel “ $t_{in} \rightarrow$  derivative of  $Q_c$ ”. Using the concept of excess temperature  $\theta_{in} = t_{in} - t_{in,0}$ , and term-by-term differentiating (1) with respect to  $\tau$  for the possibility to plug there the expression (2), we write (1) in the canonical form:

$$\frac{d^2\theta_{in}}{d\tau^2} + A \frac{d\theta_{in}}{d\tau} + B\theta_{in} = 0. \quad (3)$$

Parameters  $A$ ,  $s^{-1}$ , and  $B$ ,  $s^{-2}$ , can be determined here by the following formulas:

$$A = \frac{G_s c_a / 3600 + \Lambda}{V_r c_a \rho_a}, \quad B = \frac{K_c}{V_r c_a \rho_a}. \quad (4)$$

It is easy to see that the differential equation (3) refers to linear homogeneous equations of the 2<sup>nd</sup> order with constant coefficients, as a result of which the simplest operational solution method can be applied to it. The characteristic equation for (3) will have the following form:

$$p^2 + Ap + B = 0, \quad (5)$$

where  $p$  is the Heaviside operator. In fact, in this case, the premises are treated as a second-order linear inertial link. From (5) we get:

$$p_{1,2} = \left( -A \pm \sqrt{A^2 - 4B} \right) / 2, \quad (6)$$

and finally write down the general solution in the following form:

$$\theta_{in} = C_1 \exp(p_1\tau) + C_2 \exp(p_2\tau), \quad (7)$$

where  $C_1$  and  $C_2$  are constants that can be obtained from the initial conditions. Obviously, that at  $\tau = 0$  and  $\theta_{in} = 0$ , whence  $C_1 = -C_2$ . From (1) it can be found that in this case there is a relation

$$V_r c_a \rho_a \frac{dt_{in}}{d\tau} = -Q_{in}, \quad \text{whence we have:}$$

$$\theta_{in} = -\frac{Q_{in}}{V_r c_a \rho_a \sqrt{A^2 - 4B}} \left[ \exp(p_1\tau) - \exp(p_2\tau) \right]. \quad (8)$$

It should be noted that, by virtue of relations (4) the equation (3) does not admit asymptotics at  $V_r \rightarrow 0$ , and in the case of eliminating the corresponding term from the right side of (1), it is easy to show that then the variables become separable, and the resulting solution will have an absolutely exponential form. This does not correspond to the physical meaning of the problem under consideration, since when using the integral control law, the controlled value, as it is known, passes through a maximum and then tends to zero – either monotonically or in an oscillatory manner, depending on the parameters of the object and the controller (oscillations will obviously be observed at  $A^2 < 4B$ ). That is why, in this case, taking into account the  $V_r$  is mandatory, even given that this complicates the solution to a certain extent, although due to the constancy of the coefficients in (3), this is not critical at all.

### 3. Results and Discussion

For the sake of clarity, it is advisable to give an example of calculating the  $t_{in}$  value according to expression (8) in the premises with parameters  $A = 0.0059 \text{ s}^{-1}$  (which corresponds to  $V_r = 42 \text{ m}^3$ ,

$\sum A_i = 49 \text{ m}^2$ ,  $G_s = 430 \text{ kg/h}$  and  $K_c = 0.25 \text{ W/(K}\cdot\text{s)}$ , whence  $B = 4.9 \cdot 10^{-6} \text{ s}^{-2}$ . In the course of calculations, the initial  $t_{in,0}$  value was taken equal to  $+20 \text{ }^\circ\text{C}$ , and the value of heat gain jump  $Q_{in} = 500 \text{ W}$ . The corresponding graph is shown in Fig. 1 as a solid curve. For comparison, the dotted line shows the results of numerical modeling upon the same initial data using the computer software developed by the author, which is based on the direct solution of the system of differential equations of non-steady heat transfer in enclosures and heat transfer on their surfaces [23]. The dash-dot line shows the dependence of the internal temperature on time, obtained using an analytical solution that takes into account the heat capacity of the near-surface layer of the enclosing structures facing the premises [24].

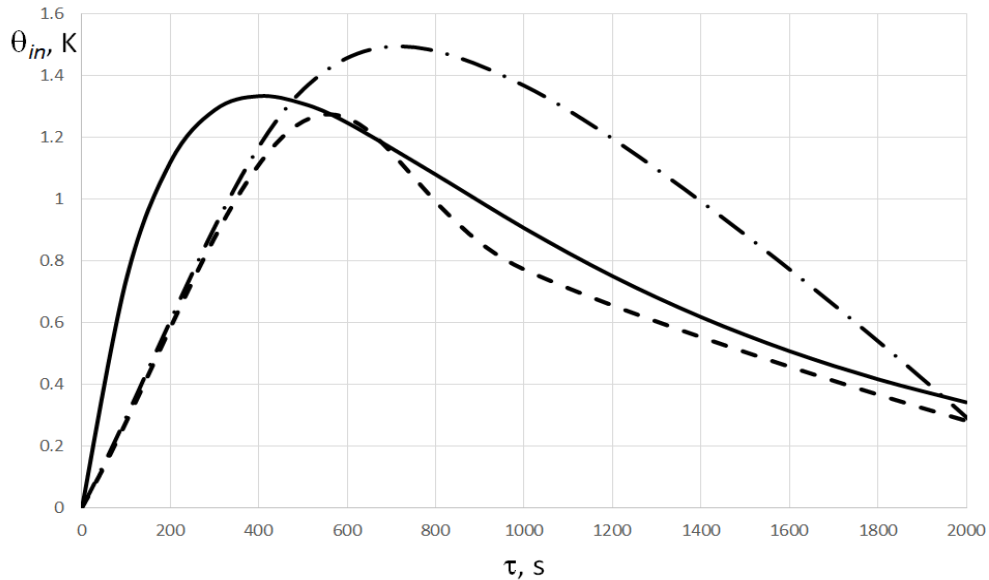


**Figure 1. Dependence of  $\theta_{in}$  on time for the premises under study (solid line – according to formula (8), dotted line – numerical calculation, dash-dotted line – analytical solution [24]).**

It can be pointed out that the numerical calculation data show a fairly satisfactory coincidence with an expression (8), especially for large  $\tau$  values, in any case, from the point of view of the value of the maximum deviation  $t_{in}$  and the time when it occurs. Moreover, this coincidence turns out to be even closer than with the results of analytical calculations, with which the maximum proximity manifests itself, on the contrary, in the initial period, at the stage of temperature deviation increase. Apparently, this is related to the fact that the analytical solution [24] still gives a better asymptotic behavior at  $\tau \rightarrow 0$ , while at higher  $\tau$  prevails the fact that, up to a certain limit, when the penetration of the temperature wave into the thickness of the material of enclosures already becomes significant, the simplified equation (3) describes quite well the real process of regulation of the temperature in premises. In any case, the solution (8), on the one hand, shows its physical validity and suitability for rough estimates, taking into account its relative simplicity and the possibility of carrying out necessary operations to find the maximum and solving other problems of analysis, and on the other hand, it also confirms the sufficient reliability of more exact analytical solution [24].

The expression for the moment in time  $\tau_{max}$ , s, at which it is observed the maximum temperature deviation from the setpoint, can be obtained from the condition  $d\theta_{in}/d\tau = 0$ , whence, bearing in mind that in real conditions for stable automatic control systems, the ratio of the parameters  $A^2/B$  is much greater than 1 (in particular, for the example under consideration, it is equal to 7.16), and neglecting the small terms, we can write down the approximate formula:

$$\tau_{max} = \frac{\ln(A^2/B)}{A}. \quad (9)$$

In our case, the  $\tau_{max}$  value turns out to be equal to 332 s, while the graph in Fig. 1 gives a value of about 380 s, i.e., the error is about 13 percent, but taking into account the simplicity of dependence (9) and its deliberately estimated character, this can be deemed quite satisfactory. However, both the numerical

calculation and the analytical solution [24] lead to higher  $\tau_{\max}$  (about twice). This is physically more justified, since these options already take into account the influence of heat inertia of the array of enclosing structures, which leads to a shift in the moment of a maximum temperature deviation to a later term. Nevertheless, within the framework of the problem under consideration, the expression for  $\tau_{\max}$  is auxiliary, necessary for estimation of the maximum level  $\theta_{in}$ , i.e.  $\theta_{\max}$  that interests us the most. Plugging (9) to (8) and, neglecting once again small terms, we obtain:

$$\theta_{\max} = \frac{Q_{in}}{G_s c a / 3600 + \Lambda}. \quad (10)$$

It is easily seen that this expression has a very simple physical meaning, namely, it turns out that within the model used, and the maximum temperature deviation from the setpoint is determined by the heat-assimilating ability of the air in the background ventilation system and the resulting heat flux due to heat transfer on the surfaces of enclosures. In our example, the  $\theta_{\max}$  value according to formula (10) will be equal to 1.66 °C, which is 25–30 percent higher than directly according to the dependence graph (8) and according to the calculation data for the rest of the options in accordance with Fig. 1, so the relation (10) gives the result with a certain margin due to neglect of the influence of the thermal inertia of enclosures. It should also be said that for the general nature of the dependence (8) depicted in Fig. 1, one can find a significant similarity with the relations that lead, for example, to the authors [15] and [16] under similar initial conditions, and the observed temperature deviations from the initial values generally correspond to the level that is noted in [25] under close regimes. In addition, Fig. 2 shows a comparison of the calculation results according to expression (8), shown earlier in Fig. 1, with the data of full-scale measurements of the non-stationary thermal regime of a room serviced by an automated air heating system under similar control conditions given in [26] (dotted line), after normalization by the magnitude of the maximum temperature deviation. It can be seen that, up to the moment of maximum and even somewhat further, experimental measurements give a similar nature of dependence, which further confirms the theoretical provisions of the proposed work. The dash-dotted line represents the change in the relative concentration of harmful impurities in the room air  $C_r$ , according to [10] also under similar control conditions after bringing to the appropriate deviation scale and time. Although the equations describing the gas regime differ somewhat from those considered here, the simplifications adopted in the derivation (8), namely the neglect of heat accumulation of the structural material, bring (8) closer to the result that can be obtained for changing the concentration, which is confirmed by Fig. 2.

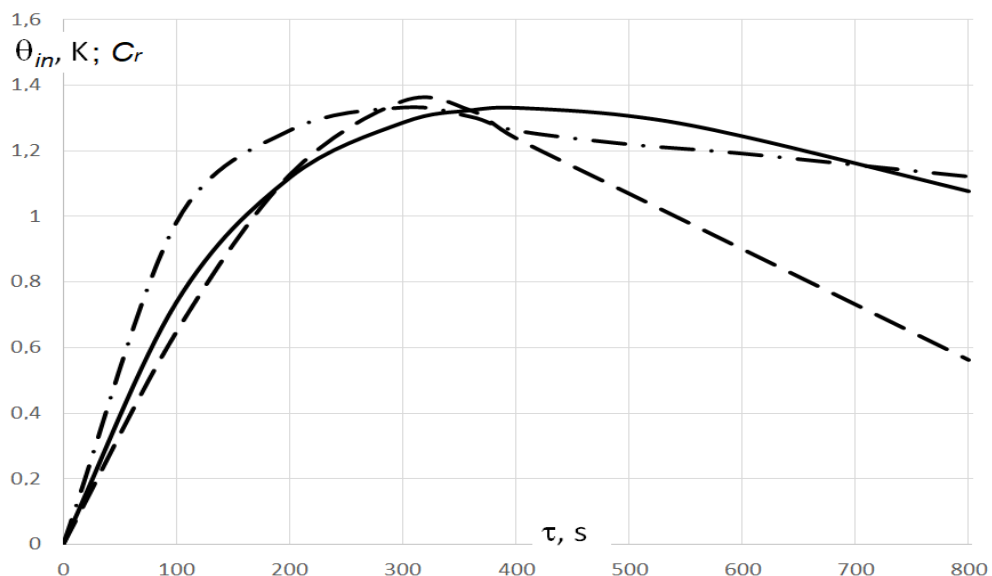


**Figure 2. Dependence of  $\theta_{in}$  on time for the premises under study (solid line – according to formula (8), dotted line – full-scale measurements [26], the dash-dotted line is the same according to [10] for the relative concentration of the harmful substance  $C_r$ ).**

## 4. Conclusion

1. It is shown that the simplified analytical solution obtained in the paper, which describes the change in  $t_{in}$  value in premises served by a background uncontrolled inflow and automated local cooling systems, subject to their control according to the integral law, for an abrupt change in heat input, it satisfactorily describes the real process of heating or cooling, at least at not too small  $\tau$  values.

2. It is noted that the discovered dependence for  $t_{in}$  is expressed explicitly through exponential functions of  $\tau$  and allows to easily analyze the problem and the subsequent synthesis of the automatic control system by varying the numerical coefficients in the solution.

3. It was confirmed that, as in other versions of the problem statement, the maximum deviation of  $t_{in}$  from the setpoint (dynamic control error) is proportional to the value of thermal disturbance, however, in the considered embodiment, the estimated level of this deviation and the moment in time, for which it is observed, are not directly related to the value of the controller gain.

4. It is proved that, all other things being equal, the simplified solution gives the maximum coincidence with the data of numerical calculations for the moments in time, starting with the maximum deviation  $t_{in}$ , since the analytical solution [24] still gives better asymptotics at  $\tau \rightarrow 0$ .

5. It is shown that the results obtained additionally confirm the reliability and practical applicability of the previously found analytical solution [24], which takes into account the thermal stability of the enclosures of premises in the course of propagation of a temperature wave in the material of the enclosing structures.

6. It is noted that the obtained simplified solution is quite successfully confirmed by the nature of the dependencies discovered by a number of authors by experimental measurements under appropriate conditions, including for changing the concentration of harmful impurities, which in physical sense should be described by equations similar to (8).

7. It is proposed to apply the relations obtained in the paper for an approximate analytical assessment of the non-steady thermal regime of air-conditioned premises served by local cooling systems equipped with an automation system with an integral control mode, to check the conditions for human comfort and safety of his life, as well as to determine the required parameters of the regulator, in particular using multivariate calculations with change in task parameters.

## References

- Rafalskaya, T.A. Reliability and controllability of systems of centralized heat supply. Eastern European Scientific Journal. 2016. 2. P. 228–235. DOI: 10.12851/EESJ201604C06ART10
- Rafalskaya, T.A. Simulation of thermal characteristics of heat supply systems in variable operating. Journal of Physics: Conference Series. XXXV Siberian Thermophysical Seminar, STS 2019. 2019. P. 012140. DOI: 10.1088/1742-6596/1382/1/012140. URL: <https://iopscience.iop.org/article/10.1088/1742-6596/1382/1/012140/pdf> (data obrashcheniya: 07.01.2022)
- Malyavina, E.G. Rashchet tempa ostyvaniya pomescheniya posle otklyucheniya teplosnabzheniya [Calculation of the rate of cooling of a room after turning off the heat supply]. Promyshlennoe i grazhdanskoe stroitel'stvo [Industrial and Civil Engineering]. 2015. 2. Pp. 55–58. URL: <http://pgs1923.ru/ru/index.php?m=4&y=2015&v=02&p=00&r=14> (date of treatment: 07.05.2020 (rus))
- Doroshenko, A.V. Imitacionnaya termodinamicheskaya model' zdaniya [Simulation thermodynamic model of the building]. BST: Byulleten' stroitel'noy tekhniki [Bulletin of construction equipment]. 2017. 12. Pp. 42–43. URL: <https://elibrary.ru/item.asp?id=30598682> (date of treatment: 07.05.2020 (rus))
- De Rosa, M., Bianco, V., Scarpa, F., Tagliafico, L.A. Modelling of energy consumption in buildings: an assessment of static and dynamic models. Russian Journal of Construction Science and Technology. 2016. V. 2. 1. Pp. 12–24. DOI: 10.15826/rjcost.2016.1.002
- Liu, C.-S. An integral equation method to recover non-additive and non-separable heat source without initial temperature. International Journal of Heat and Mass Transfer. 2016. Vol. 97. Pp. 943–953. DOI: 10.1016/j.ijheatmasstransfer.2016.03.003
- Horikiri, K., Yao, Y., Yao, J. Modelling conjugate flow and heat transfer in a ventilated room for indoor thermal comfort assessment. Building and Environment. 2014. 77. Pp. 135–147. DOI: 10.1016/j.buildenv.2014.03.027
- Bouhacina, B., Saim, R., Oztop, H.F. Numerical investigation of a novel tube design for the geothermal borehole heat exchanger, Applied Thermal Engineering. 2015. 79. Pp. 153–162. DOI: 10.1016/j.applthermaleng.2015.01.027
- Mansurov, R.Sh., Rafalskaya, T.A., Efimov, D.I. Mathematical modeling of thermal technical characteristics of external protections with air layers. E3S Web of Conferences. 22nd International Scientific Conference on Construction the Formation of Living Environment, FORM 2019. 2019. P. 06007. DOI: 10.1051/e3sconf/20199706007. URL: [https://www.e3s-conferences.org/articles/e3sconf/pdf/2019/23/e3sconf\\_form2018\\_06007.pdf](https://www.e3s-conferences.org/articles/e3sconf/pdf/2019/23/e3sconf_form2018_06007.pdf) (data obrashcheniya: 07.01.2022)
- Zemitis, J., Borodinecs, A., Lauberts, A. Ventilation impact on VOC concentration caused by building materials. Magazine of Civil Engineering. 2018. 8 (84). Pp. 130–139. DOI:10.18720/MCE.84.13
- Sáez Blázquez, C., Farfán Martín, A., Martín Nieto, I., González-Aguilera, D. Measuring of thermal conductivities of soils and rocks to be used in the calculation of a geothermal installation. Energies. 2017. 10 (6). Pp. 795. DOI: 10.3390/en10060795
- Ozturk, A. Overall heat transfer coefficient of functionally graded hollow cylinder. Solid State Phenomena. 2017. 267 SSP. Pp. 177–181. DOI: 10.4028/www.scientific.net/SSP.267.177

13. Li, N., Chen, Q. Experimental study on heat transfer characteristics of interior walls under partial-space heating mode in hot summer and cold winter zone in China. *Applied Thermal Engineering*. 2019. Vol. 162. Pp. 114264. DOI: 10.1016/j.applthermaleng.2019.114264
14. Marino, B.M., Muñoz, N., Thomas, L.P. Estimation of the surface thermal resistances and heat loss by conduction using thermography. *Applied Thermal Engineering*. 2017. Vol. 114. Pp. 1213–1221. DOI: 10.1016/j.applthermaleng.2016.12.033
15. Bilous, I.Yu., Deshko, V.I., Sukhodub, I.O. Building energy modeling using hourly infiltration rate. *Magazine of Civil Engineering*. 2020. 4 (96). Pp. 27–41. DOI: 10.18720/MCE.96.3
16. Faouzi, D., Bibi-Triki, N., Draoui, B., Abène, A. Modeling a fuzzy logic controller to simulate and optimize the greenhouse microclimate management using Matlab Simulink. *International Journal of Mathematical Sciences and Computing*. 2017. Vol. 3. 3. Pp. 12–27. DOI: 10.5815/ijmsc.2017.03.02
17. Latif, M., Nasir, A. Decentralized stochastic control for building energy and comfort management. *Journal of Building Engineering*. 2019. Vol. 24. Pp. 100739. DOI: 10.1016/j.jobe.2019.100739
18. Ryzhov, A., Ouerdane, H., Gryazina, E., Bisch, A., Turitsyn, K. Model predictive control of indoor microclimate: existing building stock comfort improvement. *Energy Conversion and Management*. 2019. Vol. 179. Pp. 219–228. DOI: 10.1016/j.enconman.2018.10.046
19. Serale, G., Capozzoli, A., Fiorentini, M., Bernardini, D., Bemporad, A. Model predictive control (MPC) for enhancing building and HVAC system energy efficiency: problem formulation, applications and opportunities. *Energies*. 2018. Vol. 11. 3. Pp. 631. DOI: 10.3390/en11030631
20. Belussi, L., Barozzi, B., Bellazzi, A., Danza, L., Devitofrancesco, A., Ghellere, M., Guazzi, G., Meroni, I., Salamone, F., Scamoni, F., Scrosati, C., Fanciulli, C. A review of performance of zero energy buildings and energy efficiency solutions. *Journal of Building Engineering*. 2019. Vol. 25. Pp. 100772. DOI: 10.1016/j.jobe.2019.100772
21. Sha, H., Xu, P., Yang, Z., Chen, Y., Tang J. Overview of computational intelligence for building energy system design. *Renewable and Sustainable Energy Reviews*. 2019. Vol. 108. Pp. 76–90. DOI: 10.1016/j.rser.2019.03.018
22. Kharchenko, V., Boyarchuk, A., Brezhnev, E., Andrashov, A., Ponochovnyi, Y. Monte-Carlo simulation and availability assessment of the smart building automation systems considering component failures and attacks on vulnerabilities. *Advances in Intelligent Systems and Computing*. 2019. Vol. 761. Pp. 270–280. DOI: 10.1007/978-3-319-91446-6\_26
23. Samarin, O.D. Raschet ostyvaniya pomescheniy zdaniya v avariynykh rezhimakh dlya obespecheniya nadezhnosti ikh teplosnabzheniya [The calculation of cooling of building in emergency conditions to ensure reliability of their heating]. *Vestnik MGSU [Papers of MSUCE]*. 2019. Vol. 14. 4 (127). Pp. 496–501. DOI: 10.22227/1997-0935.2019.4.496-501. URL: <http://vestnikmgsu.ru/r/> (date of treatment: 07.05.2020) (rus)
24. Samarin, O.D. Thermal mode of a room with integrated regulation of cooling systems. *Magazine of Civil Engineering*. 2021. 103 (3). Article No. 10312. DOI: 10.34910/MCE.103.12
25. Odineca, T., Borodinecs, A., Korjakins, A., Zajecs, D. The impacts of the exterior glazed structures and orientation on the energy consumption of the building. *IOP Conference Series: Earth and Environmental Science*. 2019. Vol. 290 (1). P. 012105. DOI:10.1088/1755-1315/290/1/012105. URL: <https://iopscience.iop.org/issue/1755-1315/290/1> (data obrashcheniya: 07.01.2022)
26. Lysak, O. Analysis of the temperature distribution in a space heated by a dynamic (fan) storage heater. *Eastern-European Journal of Enterprise Technologies*. 2017. Vol. 3. 8 (87). Pp. 17–25. DOI: 10.15587/1729-4061.2017.103778

#### **Information about author:**

**Oleg Samarin**, PhD of Technical Science

ORCID: <https://orcid.org/0000-0003-2533-9732>

E-mail: [samarin-oleg@mail.ru](mailto:samarin-oleg@mail.ru)

*Received 19.11.2021. Approved after reviewing 28.06.2022. Accepted 28.06.2022.*



Research article

UDC 691.335

DOI: 10.34910/MCE.116.11



## Processing, characterization and hardening mechanism of one-part geopolymer cement

H.M. Khater , A.M. El Nagar , M. Ezzat 

Housing and Building National Research Center, Cairo, Egypt

✉ [topaz75@gmail.com](mailto:topaz75@gmail.com)

**Keywords:** mechanical properties, smart materials, multifunctional composites, engineering properties, microstructure imaging

**Abstract.** Sustainable development of technologies for the industrial waste utilization for building construction areas are given considerable worldwide attention due to their advantages in reduction of greenhouse gases compared to Portland cement as well as conservation of raw materials resources used in cement production. Therefore, geopolymer materials are introduced, not only for the environmental issue, but also because they can reduce carbon dioxide emission caused by Ordinary Portland Cement (OPC) by 80% to 90% in building construction. In this paper, we aim to produce an eco-friendly one-part geopolymer cement with low carbon dioxide emission as an alternative for traditional cements, as well as to conserve the natural resources. The current work focuses on the utilization of industrial wastes rather than natural raw materials with the just-add-water technique for pre-prepared one-part geopolymer cement, which can be applied in various building industries. In the current paper, different types of activators with various ratios and varying firing temperatures from 500 up to 1000°C are studied. The analysis showed that firing of nix at 800°C using 10 and 20% potassium carbonate results in better mechanical strength reaching 550 and 650 Kg/cm<sup>2</sup> after 28 days of hardening.

**Funding:** Housing and Building National Research Center

**Citation:** Khater, H.M., El Nagar, A.M., Ezzat, M. Processing, characterization and hardening mechanism of one-part geopolymer cement. Magazine of Civil Engineering. 2022.116(8). Article no. 11611. DOI: 10.34910/MCE.116.11

### 1. Introduction

The ecological consequences of human activities have come to worldwide attention and are causing environmental concerns all over the globe. In the early and mid-1980s, the concept of sustainable development began spreading [1], while scientists have been striving to make sustainable industrial processes more popular. Industrial ecology is the most efficient way to achieve sustainability [2] by using, in particular, industry-generated by-products. The construction industry contributes to about one-third of the energy-related global CO<sub>2</sub> emissions, which makes it a significant sector often targeted as part of the mitigation strategies to reduce carbon footprint [3]. Since Portland cement is the most common binder used for building materials, its production share amounts to 5–8% of global anthropogenic emissions [4].

With the demand for local cement on the rise, its estimated production may continue to increase in the upcoming years [5]. Clinker production leads to an increase in carbon dioxide emissions through calcination process and fuel combustion. Many studies were conducted to decrease clinker consumption by blending in pozzolanic and cementitious materials, by using an alternative agricultural waste fuel as well. Reduction of CO<sub>2</sub>, particularly in this industry, remains a challenge; therefore, many approaches have been proposed to reduce the cement consumption. The use of alternating binders of aluminosilicate minerals can be considered another possible way to reduce the environmental impact of cement [6], which becomes

reactive on activation of suitable materials using alkaline solutions. Through poly-condensation, they turn into a hardened 3D molecule network called geopolymer.

Geopolymer, also referred to as an alkali-activated material, is used as a binder system similar to Portland cement that hardens at room temperature [7]. In addition to that, they have lower carbon footprint compared with Portland cement, exhibit good mechanical properties such as high early strength, excellent resistance to acid, and exceptional resistance to immersion [8]. Curing at an elevated temperature also helps to accelerate the early strength development of geopolymers [9]. However, the traditional synthesis known as the two-part geopolymer, which is typically cured at an elevated temperature system, is difficult to implement in field scale applications [10, 11]. Meanwhile, one-part geopolymer-based binder system uses dry solid aluminosilicate precursors and solid alkali, which form a binder just by adding water, similar to the OPC binder system. In terms of the environmental impacts, an average reduction of 24% for one-part geopolymers and 60% for two-part geopolymers in comparison to OPC were reported in [12].

Researches for developing one-part binders based on the chemistry of alkali aluminosilicate have been largely focused on the mechanical properties produced upon hydration. Other properties related to hydration products of those cements, such as chemical and dimensional stability, moisture and weathering resistance, as well as other hydration properties of these cements have not been investigated.

Additional studies are required to understand more and improve the chemical composition of produced cements, as well as the effectiveness and efficiency of converting raw material blends into hydraulic cements. The produced binder needs to be systematically characterized to qualify for the developed hydraulic cements standards used in concrete production. For the creation of new hydraulic cements, ASTM C1157 [13] and ATSM C559 [14] were the primary performance-based standards employed in this development work. ASTM C1157 criteria are mostly based on ASTM C150 [15] (Standard Specification) performance limitations.

Muthukrishnan et al. [16] looked into the development of early age strength due to alkali reactions in order to formulate a suitable 3D printable one-part geopolymer concrete. On the rheological properties of concrete, the effect of activator content, additives such as magnesium aluminosilicate, and retarder (sucrose) dose were explored. The results showed that the formulated one-part geopolymer with magnesium aluminosilicate, activator, and sucrose content of 0.75 wt%, 10 wt%, and 1.5 wt% of the binder, respectively, performed well.

The main purpose of this research is the production of one-part geopolymer cement that can be produced by just-add-water sequence and applied in building industries by incorporation in mortar and concrete instead of Portland cement with a comparison of its effect on the behavior of the produced materials. The produced materials were expected to be of higher qualification that encourages their use in infrastructure buildings and coastal buildings exposed to severe aggressive medium. The sequence of producing one-part alkali activated cement using various factors was characterized using FTIR, XRD, and SEM; in addition, compressive strength was measured.

## 2. Material and Methods

### 2.1. Materials

The material used in this investigation was Egyptian local clay collected from El-Sheik Fadl-Minia, Egypt. The geological setting of the sampling area was studied by Abd El-Wahed [17]. It is composed of clay beds measuring about 25.9 m, as shown in Fig. 1. The clay sections mainly contain dark-colored, gypsiferous clay, highly laminated and fissile in parts. On the other hand, there are two ferruginous red bands in the upper part, glauconitic shale, and glauconitic sand capped by a nummulitic limestone ledge. In addition, Abd El-Wahed reported that based on the change in color and/or lithology, the clay section is differentiated into 11 beds different in their thickness, the smallest being 0.10 m and the largest – 9 m.

Albite, feldspar, blast furnace slag and cement dust were used as materials enriched in alkalis in addition to sodium and potassium carbonate for production of one-part cement. The chemical compositions of all raw materials are given in Table 1, whereas their mineralogical characterization is presented in Fig. 2. The Egyptian local clay material is formed from montmorillonite, kaolinite, gypsum and quartz. However, albite and feldspar used are composed of muscovite, microcline and albite, just like the main components. Blast furnace slag is mostly amorphous, while cement kiln dust is composed mainly of portlandite, anorthite, sylvite and larnite.

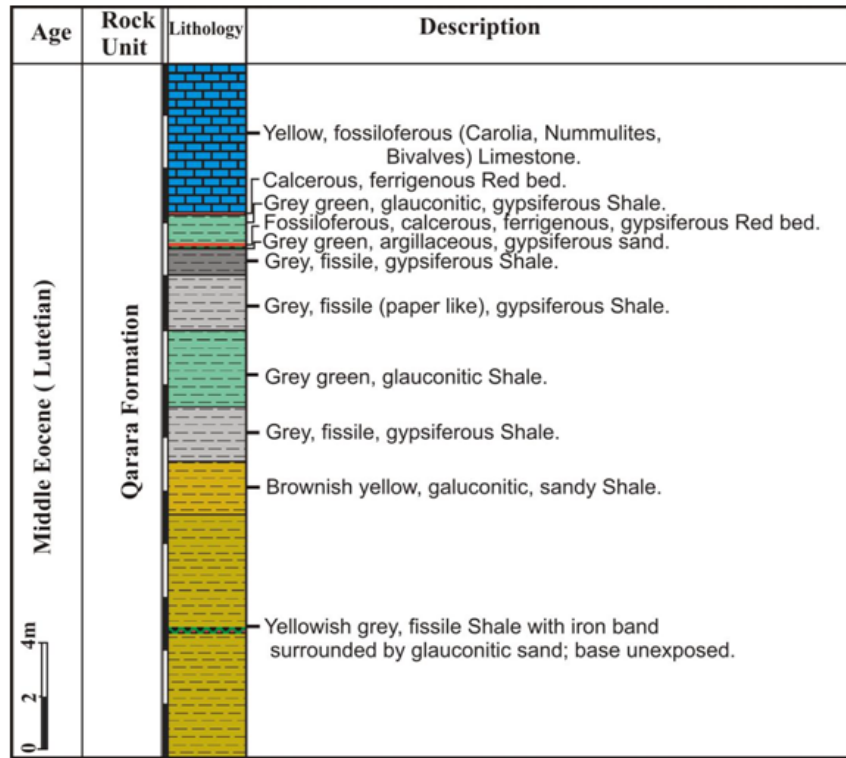


Figure 1. Stratigraphic section of El-Sheikh Fadl sampling area.

Table 1. Chemical composition of starting materials (Mass, %).

Oxide content (%)	SiO <sub>2</sub>	Al <sub>2</sub> O <sub>3</sub>	Fe <sub>2</sub> O <sub>3</sub>	CaO	MgO	SO <sub>3</sub>	K <sub>2</sub> O	Na <sub>2</sub> O	TiO <sub>2</sub>	MnO	P <sub>2</sub> O <sub>5</sub>	Cl-	L.O.I	BaO	SrO	Total	Notes
BFS	36.67	10.31	0.50	38.82	1.70	2.17	1.03	0.48	0.57	4.04	0.04	0.050	0.12	3.28	0.18	99.96	--
Local Clay	46.80	18.90	8.23	4.02	3.35	1.39	0.70	0.55	1.16	--	0.27	0.66	13.80	--	--	99.82	--
Albite	69.54	14.46	0.13	0.33	0.04	0.03	11.54	3.14	0.01	--	0.03	--	0.66	--	--	99.76	--
Feldspar	65.10	17.80	0.42	0.34	0.10	0.03	13.60	2.01	--	--	0.01	0.03	0.49	--	0.02	99.92	--
CKD	4.91	2.12	2.40	49.30	0.61	18.50	5.73	0.32	0.18	0.01	0.08	8.58	6.50	--	--	99.73	Free Lime= 15.50

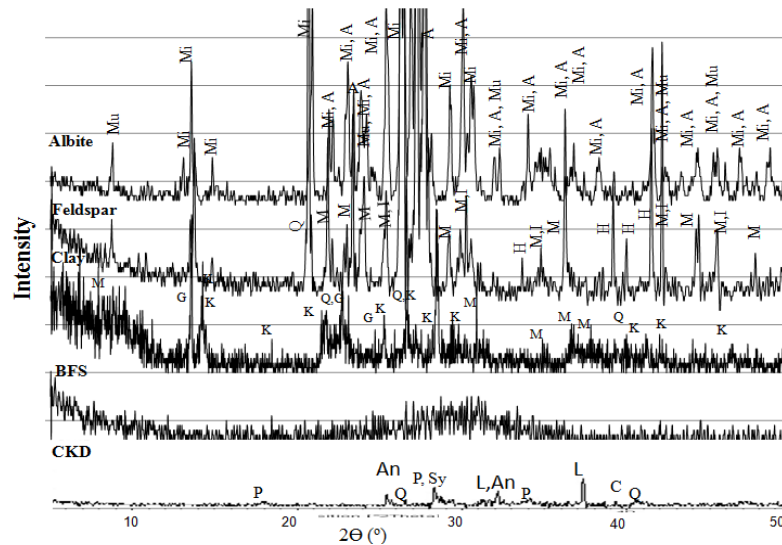


Figure 2. X-Ray diffraction pattern of the starting raw materials. [M: Montmorillonite, I: Illite, G: Gypsum, Q: Quartz, K: Kaolin, Mi: Microcline, Mu: Muscovite, A: Albite, C: Calcite, P: Portlandite, An: Anorthite, L: Larnite, Sy: Sylvite, H: Hematite].

## 2.2. Geopolymer preparation and curing

One-part geopolymer is prepared by firing the aluminosilicate precursor along with an activator or alkali-rich materials ( $K_2CO_3$ ,  $Na_2CO_3$ , albite, feldspar and CKD) as shown in Table 2 at the requested temperature followed by rapid quenching in order to produce amorphous constituents that can be used for binder production by just-add-water sequence. The fired materials were then sieved in to obtain a fine powder with an average grain size of 90  $\mu m$  in order to simulate the ordinary cement grain size. The samples were then mixed with tap water, molded and left undisturbed under ambient temperature for 24 hrs in a cube-shaped steel mold, then subjected to curing temperature of 40°C with 100% relative humidity (R.H.) to be able to activate reaction with moderate temperature and simulate the upmost temperature worldwide. At testing time, specimens were removed from their curing conditions, dried well at 80°C for 24 hrs, then tested for their compressive strength. Finally, the resulted crushed specimens were immersed in a stopping solution of methyl alcohol/acetone [18, 19] in order to prevent further hydration, and then preserved in a well tight container until the time of examination.

**Table 2. Composition of the geopolymer mixes (Mass, %).**

Mix	BFS, %	Clay, %	$Na_2CO_3$ , %	$K_2CO_3$ , %	CKD, %	Albite, %	Feldspar, %	Water/binder	Total $M_2O/Al_2O_3$	$SiO_2/Al_2O_3$	Total $M_2O/SiO_2$
g0	0	100	20	--	--	--	--	0.16	1.11	2.48	0.26
g1	20	80	20	--	--	--	--	0.16	1.22	2.61	0.28
g2	40	60	20	--	--	--	--	0.16	1.36	2.76	0.29
g3	60	40	20	--	--	--	--	0.16	1.53	2.96	0.30
g4	80	20	20	--	--	--	--	0.16	1.76	3.22	0.32
A1	40	60	--	20	--	--	--	0.26	1.09	2.76	0.23
A2	40	60	--	--	20	--	--	0.26	0.21	2.77	0.05
A3	40	60	--	--	--	20	--	0.26	0.29	3.09	0.06
A4	40	60	--	--	--	--	20	0.26	0.29	2.93	0.06
A1-500	40	60	--	20	--	--	--	0.26	1.09	2.76	0.23
A1-600	40	60	--	20	--	--	--	0.26	1.09	2.76	0.23
A1-700	40	60	--	20	--	--	--	0.26	1.09	2.76	0.23
A1-900	40	60	--	20	--	--	--	0.26	1.09	2.76	0.23
A1-1000	40	60	--	20	--	--	--	0.26	1.09	2.76	0.23
A1-T-5	40	60	--	5	--	--	--	0.26	0.36	2.76	0.08
A1-T-10	40	60	--	10	--	--	--	0.26	0.60	2.76	0.13
A1-T-25	40	60	--	25	--	--	--	0.26	1.36	2.76	0.28
A1-T-30	40	60	--	30	--	--	--	0.26	1.58	2.76	0.34

## 2.3. Methods of investigation

Chemical investigation for starting materials was performed using XRF-Axios (PW4400) WD-XRF Sequential Spectrometer, while mineralogical characterization was performed by using Philips PW 3050/60 Diffractometer with a Cu-K $\alpha$  source. Mechanical testing was carried out using five tones German Brüf digital compression testing machine with a loading rate of 100 Kg/min. FT-IR was used for elucidation of the amorphous constituents of geopolymer composites using Jasco-6100 with the aid of KBr binder in the range

from 400 to 4000  $\text{cm}^{-1}$  [20,21]. Microstructure imaging was done using Scanning Electron Microscopy – SEM Inspect S (FEI Company, Netherland) equipped with an energy dispersive X-ray analyzer (EDX).

### 3. Results and Discussion

XRD pattern of fired one-part geopolymer cement at 800°C for 2 hrs, having various ratio of blast furnace slag as a partial replacement of local clay mineral and activated by 20% sodium carbonate is presented in Fig. 3. The pattern illustrates an increased intensity of nephline phase [22, 23] as an alkali-rich crystalline phase [(K, Na)  $\text{AlSiO}_4$ ].

Moreover, the incorporation of alkali during the thermal pre-activation process resulted in the formation of a new Na-rich phase (a partially disordered per-alkaline aluminosilicate,  $[\text{Na}_2\text{O}]_x [\text{NaAlO}_2]_y [\text{NaAlSiO}_4]$ , represented by phase P in Fig. 2, PDF# 01-076-2385 when  $x > 0$ ,  $y = 0$ ; represented by phase  $\text{P}\alpha$ , PDF# 00-049-0004, both described below as Na-aluminosilicate for brevity). The last two phases increased up to 40% slag replacement reflecting the disorder of the produced one-part constituent. On increasing slag content to 60%, new phases are formed (sodalites and gehlenite) reflecting increase in crystalline phases with increasing slag ratio [21]. Gehlenite is most likely derived from the chemical interaction between thermally decomposed silicate and alumina derived from the other compounds present in the unreacted clay/slag mix, such as microcline, which are no longer observed in the thermally treated mix.

Larnite was also detected for 60% slag content, reflecting the alteration of the alumina/silica ratio due to participation in the formation of amorphous aluminosilicate constituents. Further increasing of slag ratio up to 80% resulted in the increase of larnite, gehlenite and sodalite phases in addition to the formation of sharp and intense peak of hematite; all the previous phases resulted in diminishing the efficiency of the formed binder.

FTIR spectra of one-part geopolymer cement having various slag ratios and activated by 20% sodium carbonate and fired at 800°C for 2 hrs are shown in Fig. 4. The pattern shows a gradual increase in the main asymmetric band of T-O-Si at about 975  $\text{cm}^{-1}$  with minor shifting to lower wave number, where T=Si or Al with increasing slag ratio up to 40%. This is accompanied by diminishing of the shoulder at about 1085  $\text{cm}^{-1}$  for un-solubilized silica.

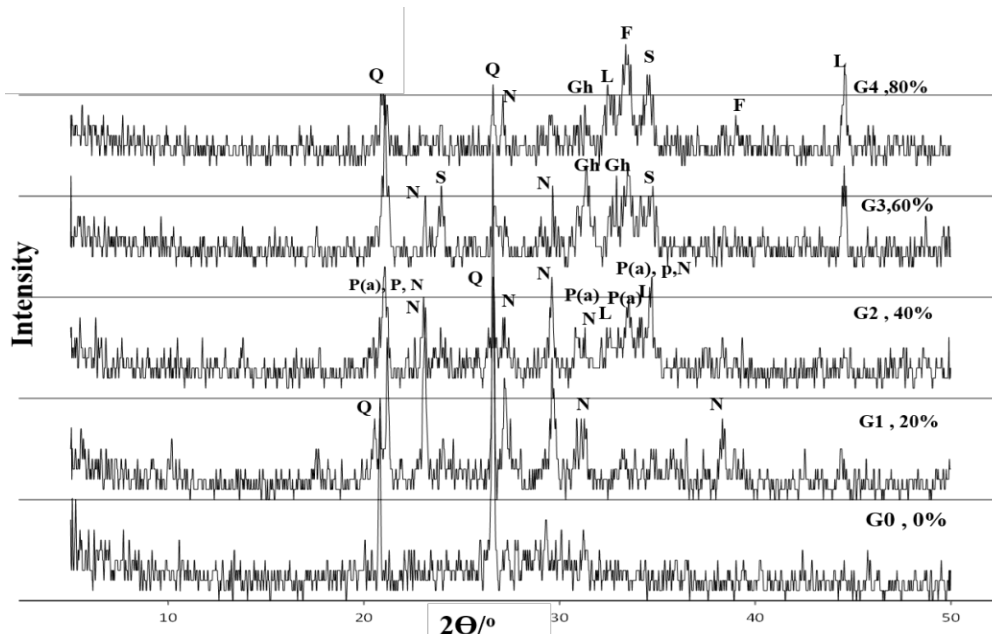
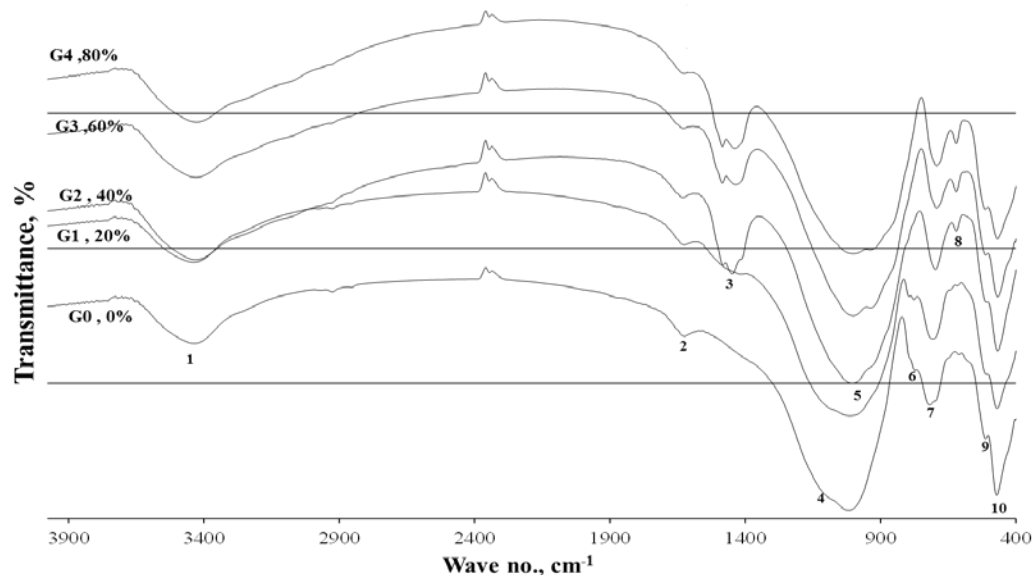


Figure 3. XRD pattern of one-part geopolymer cement having various slag ratios, fired at 800°C for 2 hrs. [Q: Quartz, N: Nephline, L: Larnite, P: Peralkaline, P(a): Peralkalinealfa, S: Sodalite, Gh: Gehlenite, F: Hematite].



**Figure 4. FTIR spectra of one part geopolymer cement having various slag ratios, fired at 800°C for 2 hrs. [1: Stretching vibration of O-H bond, 2: Bending vibrations of (HOH), 3: Stretching vibration of CO<sub>2</sub>, 4: Asymmetric stretching vibration (Si-O-Si), 5: Asymmetric stretching vibration (T-O-Si), 6: Symmetric stretching vibration (Si-O-Al), 7, 8: Symmetric stretching vibration (Si-O-Si), 9, 10: Bending vibration (Si-O-Si and O-Si-O)].**

The increase of the main asymmetric band on the expense of the un-solubilized silica reflects the increased formation of amorphous N-A-S in accordance with XRD pattern Fig. 3, which depicts the growth of per-alkaline and per-alkaline alfa with slag ratio increasing to 40%. The broad vibration mode appearing between 630 and 690  $\text{cm}^{-1}$  is associated with the existence of a range of deformed 4-membered silicate ring structures indicating a disordered state within these solid powders [24, 25]. However, the bands appearing between 750–550  $\text{cm}^{-1}$  are related to vibration of silicate ring structures, and a reduction in the wave number within this region associated with a reduced number of bridging oxygen in the corresponding ring structure [25].

On further increasing of slag ratio to 60% and 80%, decrease in intensity of asymmetric band is observed with the splitting of symmetric band at 688  $\text{cm}^{-1}$  into two bands at about 613 and 688  $\text{cm}^{-1}$  for symmetric stretching of Si-O-Si, as well as its bending vibration. The decreased symmetric stretching vibration of Si-O-Si at about 760  $\text{cm}^{-1}$  reflects the increased deformation of the formed binder.

XRD pattern of fired one-part geopolymer cement prepared at 800°C for 2 hrs of 40:60% slag to local Egyptian clay activated by 20% of various activators is presented in Fig. 5. From the pattern, it can be noticed that using of potassium carbonate as an activator results in the formation of an amorphous structure with an increased intensity of Sylvie (KCl), as well as an increased intensity of nephline phase [22, 23] as an alkali-rich crystalline phase [(K, Na) AlSiO<sub>4</sub>]. Moreover, there is an intense akermanite peak at  $2\theta$  of 31.13°, with the formation of Na-rich phase (a partially disordered per-alkaline aluminosilicate,  $[\text{Na}_2\text{O}]_x [\text{NaAlO}_2]_y [\text{NaAlSiO}_4]$ , represented by phase P in Fig. 2, PDF# 01-076-2385 when  $x > 0$ ,  $y = 0$ ; represented by phase P $\alpha$ , PDF# 00-049-0004, both described below as Na-aluminosilicate for brevity).

Using alkali-rich cement kiln dust results in the formation of crystalline Lucite feldspars, akermanite, as well as larnite phase, which is dicalcium silicate phases susceptible for formation of CSH upon hydration. The increased crystalline phases decrease or diminish disordered aluminosilicate phases. Using sodium carbonate results in the formation of intense peaks of disordered Na-rich phases (per-alkaline and per-alkaline alfa, as well as nephline) as the main phases that favor to be of high reactivity as potassium carbonate. Using feldspar and albite on the other hand, leads to an intense increase in the crystalline phases (albite, muscovite, microcline and mullite), with the formation of small peaks of disordered Na-rich phases. It is clear that the use of the last two activators results in an increase in crystallinity of the formed powder, and thus may negatively affect their hydration performance.

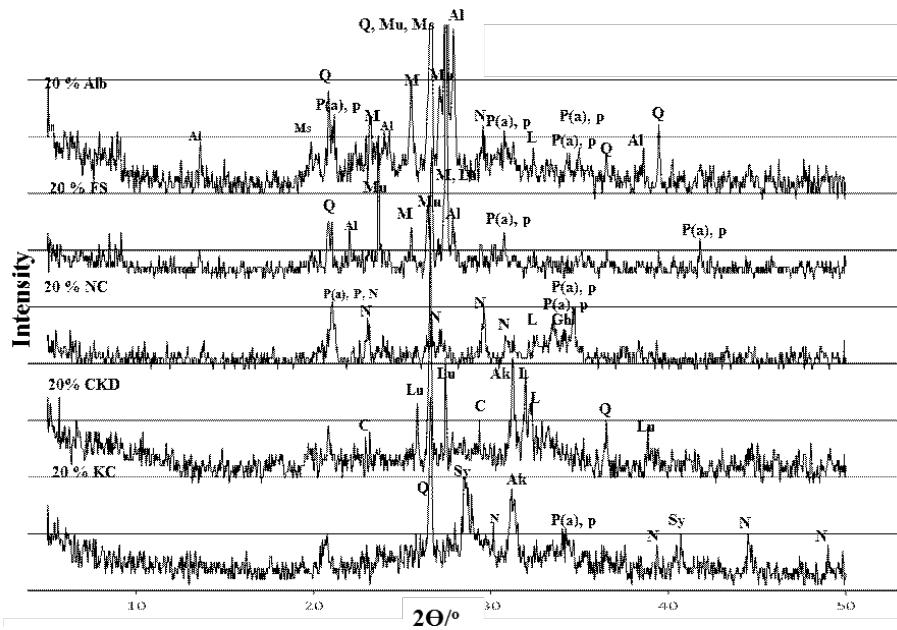


**Figure 5.** XRD pattern of one part geopolymer cement having various types of activators, fired at 800° C for 2 hrs. [Q:Quartz, Mu: Mullite, M: Microcline, Ms: Muscovite, C: Calcite, Gh: Gehlenite, N: Nepheline, Sy: Sylvite, Lu: Lucite, L: Larnite, Ak: Akermanite, Al: Albite, P: Peralkaline, P(a): Peralkaline].

FTIR spectra of one-part geopolymer powder having 40:60% slag to local clay activated with various activators and fired at 800°C for 2 hrs are shown in Fig.(6). The pattern illustrates the increased intensity of the main asymmetric band of T-O-Si at about 975  $\text{cm}^{-1}$  upon using potassium carbonate activator followed by sodium carbonate one, whereas using cement kiln dust, feldspar and albite results in an increase in intensity of the shoulder at about 1085  $\text{cm}^{-1}$  for un-solubilized silica, in the same sequence, which reflects the increase in crystalline phases matching XRD elucidations. The broad vibration mode appearing between 630 and 690  $\text{cm}^{-1}$  is associated with the existence of a range of deformed 4-membered silicate ring structures indicating a disordered state within these solid powders activated by K and Na-carbonate, which have intense peaks at this region [24, 25]. The decreased symmetric stretching vibration of Si-O-Al at about 760  $\text{cm}^{-1}$  reflects an increase in deformation of the formed binder.

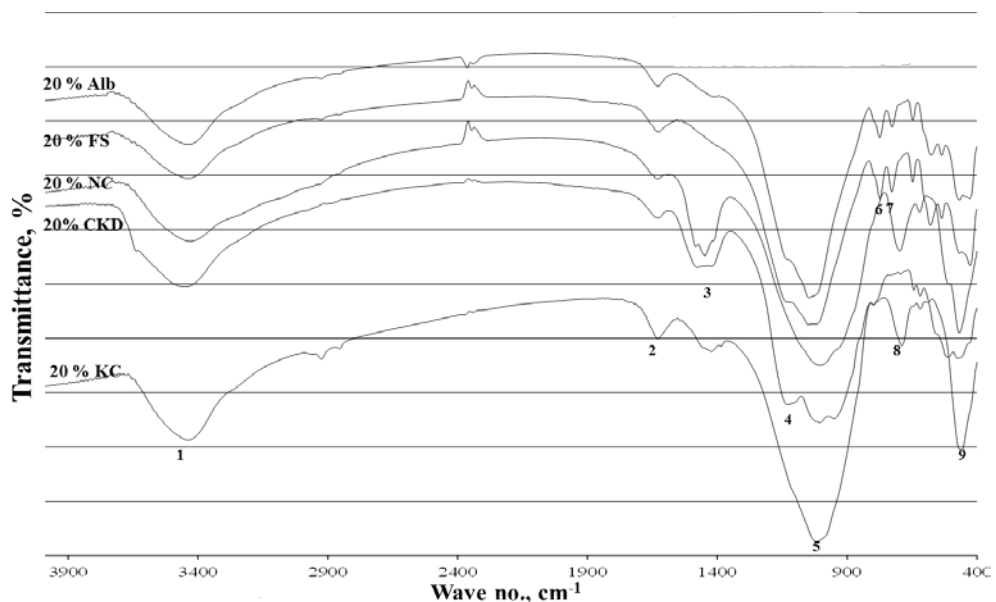


**Figure 6.** FTIR spectra of one part geopolymer cement having various types of activators, fired at 800° C for 2 hrs. [1: Stretching vibration of O-H bond, 2: Bending vibrations of (HOH), 3: Stretching vibration of  $\text{CO}_2$ , 4: Asymmetric stretching vibration (Si-O-Si), 5: Asymmetric stretching vibration (T-O-Si), 6,7: Symmetric stretching vibration (Si-O-Al), 8: Symmetric stretching vibration (Si-O-Si), 9: Bending vibration (Si-O-Si and O-Si-O)].

However, elaboration of the transformations was encountered on using various temperatures from 500 to 1000°C for potassium carbonate activated samples; and these variations is noticed using XRD analysis presented in Fig. 7. From the previous pattern, a clear and intense change from amorphous structure which is represented by nepheline phase [22, 23] as an alkali-rich crystalline phase  $[(K, Na) AlSiO_4]$  and Na-rich phase (a partially disordered per-alkaline aluminosilicate phase P and phase P $\alpha$  with increasing temperature up to 800°C. In addition, there is a gradual transformation from calcium aluminate phases to larnite phases as temperature increased from 500 to 700°C, which both diminishes with the formation of the disordered phases as well as potassium rich sylvite phases at 800°C. Further temperature increase to 1000°C results in the formation of intense peaks for crystalline phases (albite, muscovite, microcline, mullite, gehlenite and hematite), with the formation of small peaks of disordered Na-rich phases. Where, the increase of temperature up 1000°C results in sintering and an increase in crystallinity of the formed powder and so may negatively affect the hydration performance of formed geopolymer.

The FTIR spectra of one-part geopolymer cement activated by potassium carbonate at temperatures ranging from 500 to 1000°C for 2 hrs are shown in Fig.(8). The pattern illustrates an increase in intensity of the main asymmetric band of T-O-Si at about 975  $cm^{-1}$  with temperature increase up to 800°C and with a clear decrease in intensity of the shoulder at about 1085  $cm^{-1}$  for un-solubilized silica, in the same sequence, which reflects increase of amorphous structure at the expense of crystalline one coinciding with XRD elucidations. However, further increase in temperature results in sharp decrease in asymmetric band with a shift to left, which implies an increase in crystallinity. A sharp decrease in the carbonate bands as well as O-H bands with temperature up to complete vanishing at 1000°C is noticed.

The broad vibration mode appearing between 630 and 690  $cm^{-1}$  is associated with the existence of a range of deformed 4-membered silicate ring structures indicating a disordered state of these solid powders activated by K and Na-carbonate which have intense peaks at this region increasing up to 800°C, with a decrease in intensity of the symmetric stretching vibration of Si-O-Si at about 760  $cm^{-1}$ , which reflects the increased deformation of the formed binder.

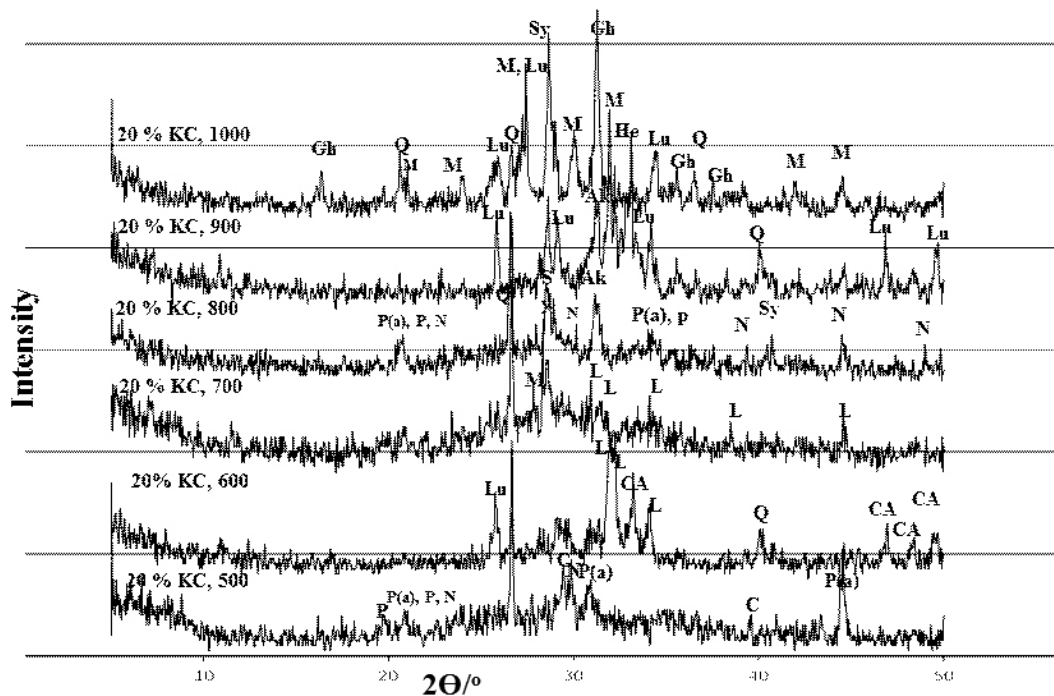
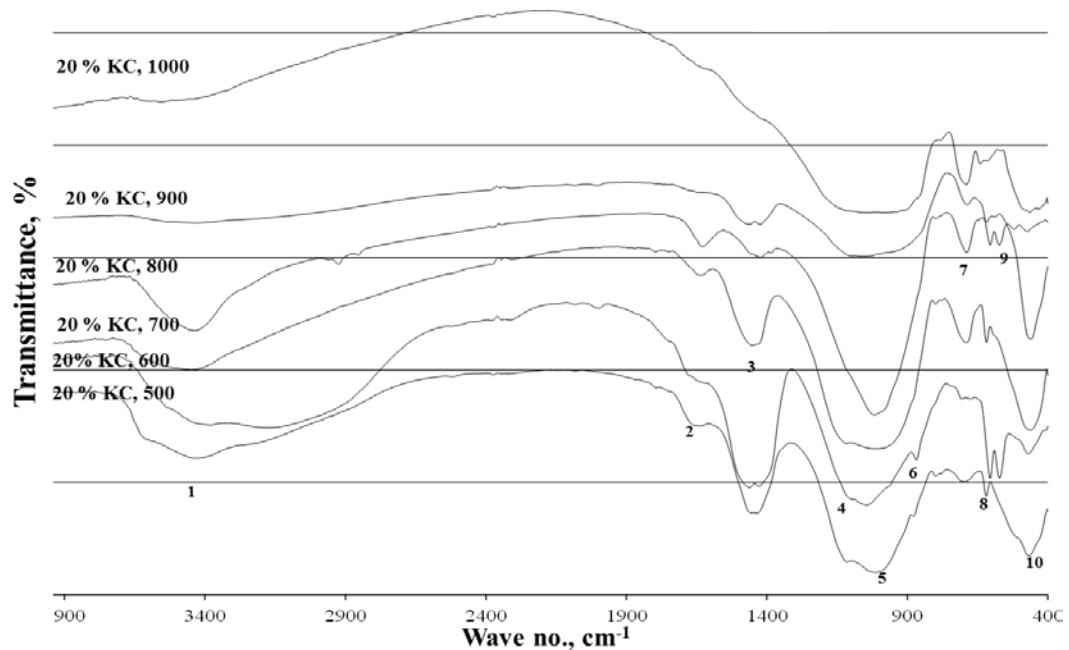


Figure 7. XRD pattern of one part geopolymer cement having various types of activators, fired at 800° C for 2 hrs. [Q: Quartz, Mu: Mullite, M: Microcline, N: Nepheline, Sy: Sylvite,, Lu: Lucite, L: Larnite, Ak: Akermanite, Gh: Gehlenite, CA: Tricalcium aluminate].



**Figure 8. FTIR spectra of one part geopolymers having various types of activators, fired at 800°C for 2 hrs. [1: Stretching vibration of O-H bond, 2: Bending vibrations of (HOH), 3: Stretching vibration of CO<sub>2</sub>, 4: Asymmetric stretching vibration (Si-O-Si), 5: Asymmetric stretching vibration (T-O-Si), 6: Out of plane bending vibration of CO<sub>2</sub>, 7,8,9: Symmetric stretching vibration (Si-O-Si), 10: Bending vibration (Si-O-Si and O-Si-O)].**

On the other hand, using various ratios of potassium carbonate activator from 5 to 30% (Fig. 9) results in a gradual increase in intensity of the main asymmetric band of T-O-Si at about 975 cm<sup>-1</sup> up to 20% followed by a decrease with further increase in potassium carbonate activator. The shoulder of un-solubilized silica at about 1085 cm<sup>-1</sup> decreased up to 20%, then was exposed to a gradual increase in intensity up to 30%. The vibration mode appearing between 630 and 690 cm<sup>-1</sup> for deformed 4-membered silicate ring structures and disordered state, increased sharply up to 30% within these solid powders activated, with nearly diminishing of the symmetric stretching vibration of Si-O-Al at about 760 cm<sup>-1</sup>, which in turn reflects an increase in deformation of the formed binder.

The results of compressive strength of 28 days of the four groups of hardened one-part geopolymers cement are shown in Fig. 10. In the previous Figure, the strength for one-part mixes activated by 20% Na<sub>2</sub>CO<sub>3</sub> having various slag ratios gradually increase with slag ratio up to 40%, giving about 84 Kg/cm<sup>2</sup>, while further increase of slag percent results in a decrease in strength, giving about 72 and 66 Kg/cm<sup>2</sup> for 60 and 80% of slag. The strength behavior of this pattern was confirmed by XRD and FTIR, which reflected the increased amorphous content with slag up to 40%. On the other hand, using various activators in the ratio of 20% (Fig. 10B) results in an extra increase in the compressive strength, 650 g/cm<sup>2</sup>, for mixes activated by potassium carbonate, while the rest of the used activators acquired strength values of less than 100 Kg/cm<sup>2</sup>. As confirmed by XRD and FTIR pattern, there was a sharp increase in disordered phases with a decrease in the crystalline phases on using the potassium carbonate activator, while the crystalline phases were predominant for other mixes incorporating different types of activators leading to strength decline.

However, on using various temperatures for preparation of one-part cement with 20% potassium carbonate and forming of hardened paste (Fig.10C), the strength pattern confirmed that 800°C was the optimal temperature for formation of high strength pastes giving about 650 Kg/cm<sup>2</sup>. On varying the ratio of potassium carbonate activator in the mix from 5 to 30%, there was a gradual strength increase up to 650 Kg/cm<sup>2</sup> on using 20% of activator ratio as depicted from (Fig. 10D), while it was clear that on further increase of activator, strength declined down to 375 and 273 Kg/cm<sup>2</sup> for 25 and 30% of activator, respectively.

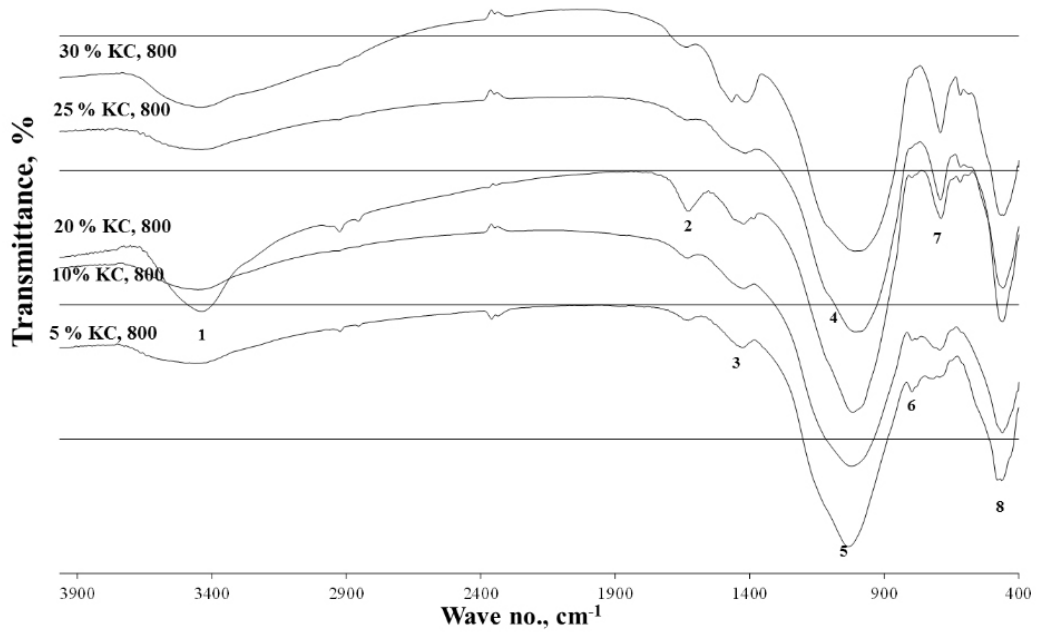


**Figure 9.** FTIR spectra of one-part geopolymer cement having various ratios of potassium carbonate activator, fired at 800°C for 2 hrs. [1: Stretching vibration of O-H bond, 2: Bending vibrations of (HOH), 3: Stretching vibration of CO<sub>2</sub>, 4: Asymmetric stretching vibration (Si–O–Si), 5: Asymmetric stretching vibration (T–O–Si), 6: Symmetric stretching vibration (Si–O–Al), 7: Symmetric stretching vibration (Si–O–Si), 8: Bending vibration (Si–O–Si and O–Si–O)].

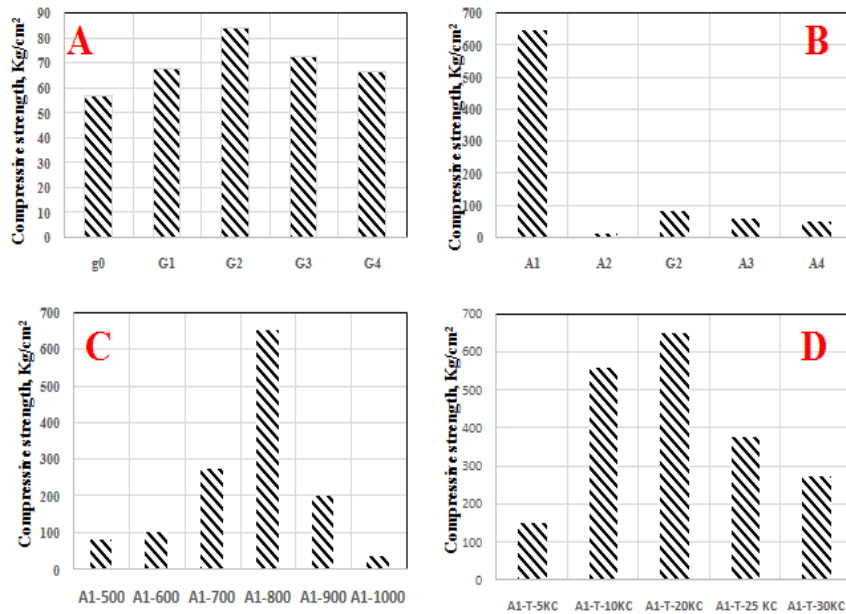


**Figure 10.** Compressive strength of 28 days of one-part geopolymer cement incorporating; A) various slag ratios, B) various types of activators, C) various firing temperatures for the optimum activators, D) various ratios of optimum activators.

Scanning electron micrographs of 28 days hardened one-part geopolymer pastes prepared by using 20% of different activators fired at 800°C are presented in Fig. 11. It can be observed from the micrograph (A), that the mix activated by NC, leads to formation of small geopolymer plates with small micropores spreading within the structure. However, the use of KC (B) activator results in the formation of massive geopolymer plates spreading within the matrix. The increased geopolymer structure by using potassium carbonate activator could be attributed to the increased amorphous constituents leading to the formation and growth of the amorphous geopolymer N-A-S-H gel as well as binding gels (C–(A)–S–H) resulting in a dense and compact structure [26, 27]. The previous observation is confirmed by the increased compressive

strength of KC sample and by the increased intensity of the asymmetric Si-O-Al in FTIR as well as disordered peralaktine phases in XRD. As the use of alkali-rich feldspars (C) results in the formation of heterogeneous structures with little interaction between the formed geopolymer and an increase in porosity within the matrix as well as a spread of carbonates on the matrix, this reflects the low degree of polymerization as a results of low reactivity of the used binder.

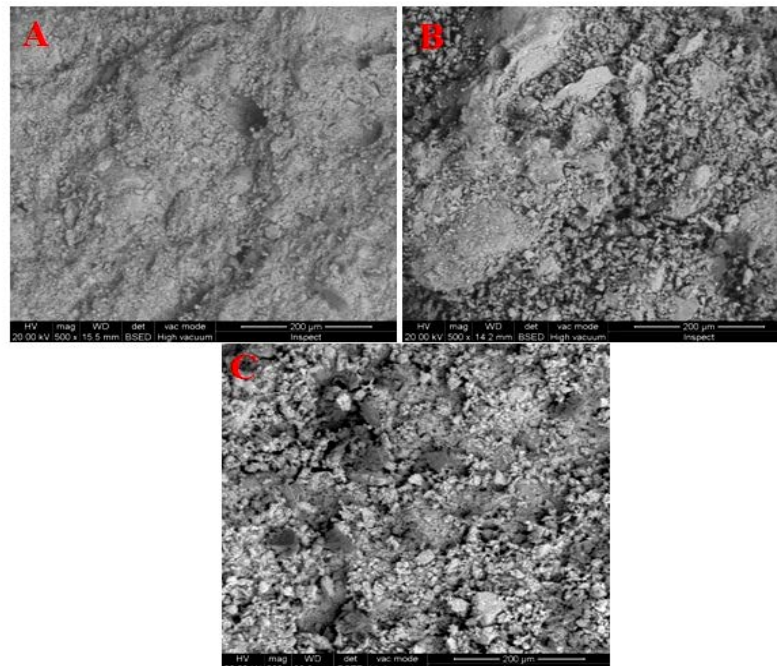


**Figure 11. SEM of 28 days of hardened one-part geopolymer cement paste prepared by using different activators; A) 20% NC, B) 20% KC, C) 20% FD.**

Scanning electron micrographs of 28 days hardened one-part geopolymer pastes prepared by using 20%  $K_2CO_3$  activator and fired at different temperatures are presented in Fig. 12. The micrographs show the growth of the geopolymer structure with increasing of firing temperature up to  $800^\circ C$  with the formation of massive geopolymer plates (N-A-S-H); while at a lower temperature, small plates are formed in addition to CSH within the matrix. Further increase in temperature to  $900^\circ C$  leads to sintering of the used binder and formation of weakly interacting crystalline structure resulting in formation of low reactivity and affecting the mechanical performance negatively as confirmed by XRD and FTIR.

On the other hand, using various ratios of potassium carbonate activator as presented in Fig. 13 results in the growth of three-dimensional geopolymer network with an increase in activator ratio up to 20%. A higher ratio of activator forms a matrix rich in wide pores, which results in termination of the formed geopolymer chains leading to formation of short chains rather than three dimensional networks [21]. Moreover, the micrograph Fig. 12C illustrates the increase in porosity leading to low cohesion between the reacting particles. Although, the increase in contents of Si and Al in the aqueous phase results in increase in formation of oligomeric precursors by increasing of dissolution rates, extremely high NaOH concentrations inhibit this reaction. As it is seen in Fig. 12, the oligomeric silicate species such as  $Si_4O_8(OH)_6^{2-}$  and  $Si_4O_8(OH)_4^{4-}$  lose their stability in favor of mononuclear silicate species like  $SiO(OH)_3^-$  and  $SiO_2(OH)_2^{2-}$  at extremely high alkaline conditions [28]. This means the equilibrium reaction shifted towards monomeric species due to exposure to extremely high alkaline conditions with minimization of the oligomeric silicate species concentration in the aqueous phase and thus led to lower polycondensation rate, which is then measured with the compressive strength of the geopolymeric materials.

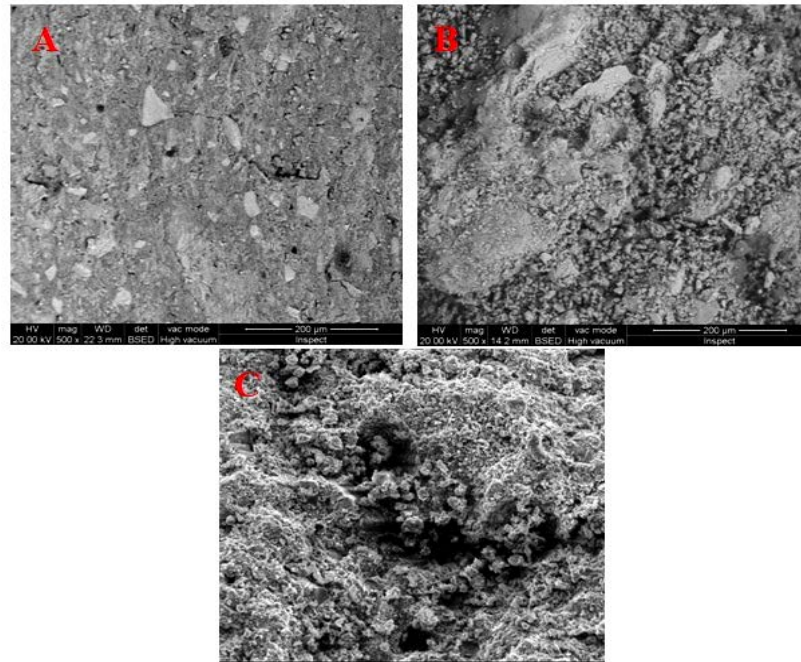


**Figure 12.** SEM of 28 days of hardened one-part geopolymer cement paste prepared using 20% potassium carbonate, fired at various temperatures; A) 700°C, B) 800°C, C) 900°C.

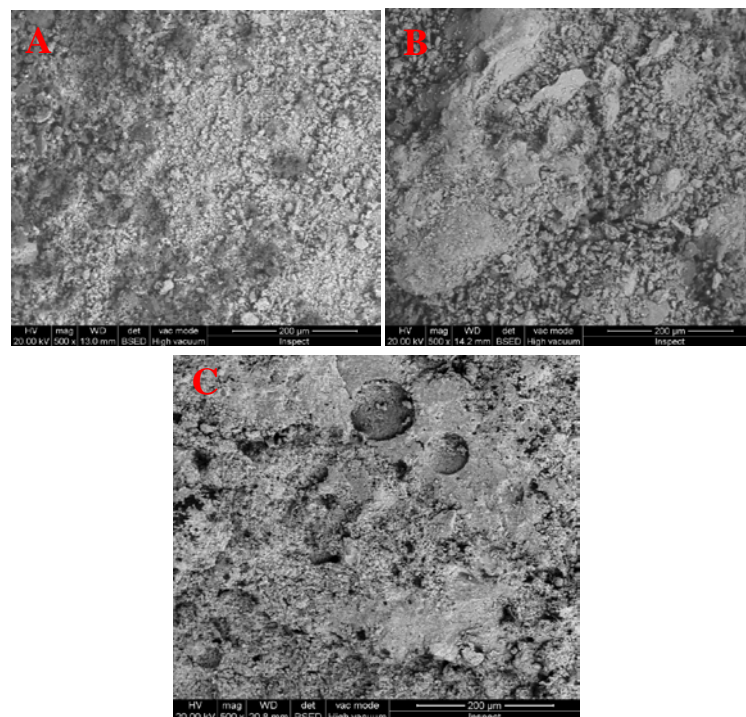


**Figure (13):** SEM of 28 days of hardened one part geopolymer cement paste formed by various potassium carbonate activator ratios, A) 10 %, B) 20 %, C) 25%.

The elucidations depicted from SEM micrographs can be also confirmed by molar oxide ratios (Table 2). The molar oxide ratios were varied depending on the matrix composition, where the binder formed by activation using potassium carbonate gave  $\text{SiO}_2/\text{Al}_2\text{O}_3 = 2.48$ , total alkalis/ $\text{Al}_2\text{O}_3 = 1.11$ , total alkalis/ $\text{SiO}_2 = 0.26$ . Since the other mixes have high alkalis/ $\text{Al}_2\text{O}_3$  more than 1.1 up to 1.76, this increase leads to the consumption of the geopolymer resulting in the formation of short geopolymer chains as confirmed by previously discussed mechanical properties. At the same time, matrix activated by cement kiln dust as well as albite has low alkalis/ $\text{Al}_2\text{O}_3$  lower than 0.30. This also coincides with previous data and as stated by [29] for  $\text{Si}/\text{Al} \geq 1.65$ , the specimens showed a homogenous microstructure as shown in the previous SEM figures, where there is an increased compaction as revealed from interaction between geopolymer constituents, leading to an extra enhancement in matrix performance, which is positively reflected on their mechanical properties as in  $\text{K}_2\text{CO}_3$  mix; on the other hand, the use of other activators

leads to formation of crystalline matrix with low mechanical strength. It was suggested that the optimum range of oxide molar ratios  $[30-32] 0.2 < M_2O/SiO_2 < 0.48$ ,  $3.3 < SiO_2/Al_2O_3 < 4.5$ ,  $M_2O/Al_2O_3$ , is 0.8 to 1.6 resulting in three-dimensional networks with a more branched structure, thus forming a homogeneous and compact structure.

## 4. Conclusions

The main concluded remarks are listed below:

1. Partial replacement of Egyptian local clay by water-cooled slag up to 40% by using sodium carbonate activator and firing at 800°C for 2hrs results in formation of an amorphous powder.
2. Using potassium carbonate activator in the mix results in the formation of predominant disordered aluminosilicate phases.
3. Varying the activation temperature for 20% potassium carbonate samples results in an increased disordered structure up to 800°C, while varying the ratio of  $K_2CO_3$  from 5 to 30% results also in the formation of amorphous phases up to 20%.
4. FTIR and XRD confirm the above-mentioned elucidations.
5. The highest compressive strength of hardened samples for binder activated by 20%  $K_2CO_3$  at 800°C was about 650 Kg/cm<sup>2</sup> after 28 days, and was about 375 Kg/cm<sup>2</sup> and 273 Kg/cm<sup>2</sup> for binder activated by 25% and 30% potassium activator respectively. The performance of the hardened samples is confirmed by SEM micrographs represent a homogenous microstructure for the sample activated by 20%  $K_2CO_3$ .
6. The overall results can suggest a low cost simple tool for preparation of one-part geopolymer binder, which can be easily prepared without deleterious effects from activators upon mixing.

## References

1. Robinson, J. Squaring the Circle. Some Thoughts on The Idea of Sustainable Development. *Ecol. Econom.* 2004. 48(4). Pp. 369–384.
2. Blissett, R.S., Rowson, N.A. A Review of the multi-Component utilization of coal fly ash. *Fuel.* 2012. 44. Pp. 1–23.
3. Towards a Zero-Emission, Efficient, and Resilient Buildings and Construction Sector: Global Status reports, 2017.[Online].URL: [www.worldgbc.org/sites/default/files/UNEP%20188\\_GABC\\_en%20%28web%29.pdf](http://www.worldgbc.org/sites/default/files/UNEP%20188_GABC_en%20%28web%29.pdf) (accessed on 15 May 2018).
4. Worrell, E., Price, L., Martin, N., Hendriks, C., Ozawa, M.L. Carbon Dioxide Emissions from the Global Cement Industry. *Annu. Rev. Energ. Environ.* 2001. 26. Pp. 303–329.
5. Cement Manufacturers Association of the Philippines Inc (CeMAP). Annual cement Industry Report. Technical Report, Pasig City, Philippines, 2015.
6. Zhang, Z., Zhu, Y., Yang, T., Li, L., Zhu, H., Wang, H. Conversion of local industrial wastes into greener cement through geopolymer technology: A case study of high-magnesium nickel slag. *J. Clean. Prod.* 2017. 141. Pp. 463–471.
7. Xie, J., Kayali, O. Effect of initial water content and curing moisture conditions on the development of fly ash-based geopolymers in heat and ambient temperature. *Constr. Build. Mater.* 2014. 67 (Pt A). Pp. 20–28.
8. Djobo, J.N.Y., Elimbi, A., Tchakouté, H. K., Kumar, S. Mechanical properties and durability of volcanic ash based geopolymer mortars. *Constr. Build. Mater.* 2016. 124. Pp. 606–614.
9. Peng, M.X., Wang, Z.H., Xiao, Q.G.; Song, F., Xie, W., Yu, L.C., Huang, H.W., Yi, S.J. Effects of alkali on one-part alkali-activated cement synthesized by calcining bentonite with dolomite and  $Na_2CO_3$ . *Appl. Clay Sci.* 2017. 139. Pp. 64–71.
10. Provis, J.L. Activating solution chemistry for geopolymers. *Geopolymers: Structures, Processing, Properties, and Industrial Applications.* Woodhead Publishing. Cambridge, UK. 2009. Pp. 50–71.
11. Nematollahi, B., Sanjayan, J., Shaikh, F.U.A. Synthesis of heat and ambient cured one-part geopolymer mixes with different grades of sodium silicate. *Ceram. Int.* 2015. 41. Pp. 5696–5704.
12. Luukkonen, T., Abdollahnejad, Z., Yliniemi, J., Kinnunen, P., Illikainen, M. One-part alkali-activated materials: A review. *Cem. Concr. Res.* 2018. 103. Pp. 21–34.
13. Malenab, R.A.J., Ngo, J.P.S., Promentilla, M.A.B. Chemical Treatment of Waste Abaca for Natural Fiber-Reinforced Geopolymer Composite. *Materials.* 2017. 10. Pp. 579–589.
14. ASTM C1157. Standard Performance Specification for Hydraulic Cement, ASTM International. West Conshohocken PA, USA, 2011.
15. ASTM C595, Standard Specification for Blended Hydraulic Cements. ASTM International. 15 - West Conshohocken, PA, USA, 2005.
16. ASTM C150, Standard Specification for Portland Cement. ASTM International. West Conshohocken, PA, USA, 2019.
17. Muthukrishnan, S., Ramakrishnan, S., Sanjayan, J. Effect of alkali reactions on the rheology of one-part 3D printable geopolymer concrete. *Cement and Concrete Composites.* 2021. 116. 10389.
18. Abd El-Wahed, G. Sedimentology and Assessment of the Middle Eocene El Minya Clay Deposits for Ceramic Industries on the Light of their Chemical, Mineral and Microstructure Characteristics. M.Sc. Department of Geology, Mansoura University. 2013.
19. Saikia, N., Usami, A., Kato, S., Kojima, T. Hydration behavior of ecocement in presence of metakaolin. *Resource Progressing Journal.* 2004. 51 (1). Pp.35–41.
20. Khater, H.M., Influence of metakaolin on resistivity of cement mortar to magnesium chloride solution. *Ceramics – Silikáty J.* 2010. 54 (4). Pp. 325–333.

21. Vargas, A.S., Denise, C.C. Dal Molin, Ângela, B. Masuero, Antônio.C.F. ; Joao Castro-Gomes; Ruby M. Strength development of alkali-activated fly ash produced with combined NaOH and Ca(OH)<sub>2</sub> activators. Cement and concrete composites. 2014. 53. Pp. 341–349.
22. Panyas, D., Giannopoulou, I.P., Perraki, T. Effect of synthesis parameters on the mechanical properties of fly ash-based geopolymers. Colloids and Surfaces A: Physicochem. Eng. Aspects. 2007. 301. Pp. 246–254.
23. Buhl, J. C. Synthesis and Characterization of the Basic and Non-Basic Members of the Cancrinite-NatrodavynneFamily. Thermo- chim. Acta. 1991. 178. Pp. 19–31.
24. Lambert, P., Page, C.L., Short, N.R. Pore Solution Chemistry of the Hydrated System Tricalcium Silicate/Sodium Chloride/Water. Cem. Concr. Res. 1985. 15(4). Pp. 675–680.
25. Ke, X., Bernal, S.A.; Ye, N., Provis, J.L., Yang, J. One-Part Geopolymers Based on Thermally Treated Red Mud/NaOH Blends. J. Am. Ceram. Soc. 2015. 98(1). Pp. 5–11.
26. Sitarz, M., Handke, M., Mozgawa, W. Identification of Silicoxygen Rings in SiO<sub>2</sub> Based on IR Spectra. Spectrochim. Acta A. 2000. 56(9). Pp.1819–1823.
27. Khater, H.M. Influence of electric arc furnace slag on characterisation of the produced geopolymer composites. építőanyag J. Silicate Based Compos. Mater. 2015. 67(3). Pp. 82–88.
28. Khater, H.M, El Nagar, A.M. Sustainable production of eco-friendly MWCNT-geopolymer composites with superior sulfate resistance. Advanced composites and hybrid materials,. Springer. 2020. 3. Pp. 375–389.
29. Baes, C. F., Mesmer, R. E. The Hydrolysis of Cations. John Willey & Sons. New York, 1976.
30. Duxson, P., Provis, J. L., Lukey, G. C., Mallicoat, S. W., Kriven, W. M., van Deventer, J. S. J Understanding the relationship between geopolymer composition, microstructure and mechanical properties. Colloids and Surfaces. Colloids and Surfaces A, Physicochemical and Engineering Aspects. 2005. 269 (1-3). Pp. 47–58.
31. Davidovits, J. Mineral Polymers and Methods of Making Them. US Patent 4,349,386, 1982.
32. Davitovits, J., Davitovits, M., Davitovits, N. Process for obtaining a geopolymericalumino-silicate and products thus obtained. US Patent 5,342,595, 1994.
33. Davidovits, J. Chemistry of geopolymeric systems terminology. Proceeding of Second International Conference Geopolymer. 1999. Pp. 9–40.

**Information about authors:**

**Hesham Moustafa Khater, PhD**

ORCID: <https://orcid.org/0000-0002-9832-5895>

E-mail: [hkhater4@gmail.com](mailto:hkhater4@gmail.com)

**Abdeen El Nagar, PhD**

ORCID: <https://orcid.org/0000-0002-8272-4349>

E-mail: [abdeenelnagar@yahoo.com](mailto:abdeenelnagar@yahoo.com)

**Mohamed Ezzat, PhD**

ORCID: <https://orcid.org/0000-0003-4186-9135>

E-mail: [topaz75@gmail.com](mailto:topaz75@gmail.com)

Received 22.11.2021. Approved after reviewing 31.05.2022. Accepted 01.06.2022.



Research article

UDC 691.328.43

DOI: 10.34910/MCE.116.12



## Size effect of cube specimen on strength of expanded clay fiber-reinforced concrete

**Yu.G. Maskalkova** , **V.A. Rzhevutskaya** 

*Belarusian-Russian University, Mogilev, Belarus*

✉ [julia43@tut.by](mailto:julia43@tut.by)

**Keywords:** lightweight concrete, expanded clay concrete, fiber reinforced concrete, fibers, polypropylene fibers, compressive strength, reference specimens, cube size, size effect

**Abstract.** The object of research is expanded clay concrete reinforced with polymer fiber made of polypropylene. Dispersed reinforcement with polymer fibers is one of the priority directions for modifying lightweight concrete, in particular, expanded clay concrete. The article presents the influence of the binary variability of the key factor (edge size of 100 and 150 mm of cube-shaped specimens) on the values of the compressive cube strength of expanded clay fiber-reinforced concrete. **Methods.** The article presents the experimental studies of the influence of the reinforcing polypropylene fibers content (1.5 % by cement weight) and edge size of cubes (100 mm or 150 mm) on the compressive cube strength of expanded clay fiber-reinforced concrete. **Results.** Even distribution of fiber throughout the volume provides the effect of crack stopping, regardless of the fiber and concrete type. However, this effect does not appear at small volumes of concrete (in cubes with dimensions of 100×100×100 mm). The empirical data allowed us to state that tests on 100 mm edge cube specimens may produce incorrect values of compressive cube strength. Therefore, it is recommended to test cubes with an edge of 150 mm or more. **Conclusions.** The results of testing cubes with an edge of 150 mm and 100 mm of lightweight fiber-reinforced concrete demonstrate fundamentally different effects, and testing cubes with an edge size of 100 mm does not guarantee obtaining correct results.

**Acknowledgements:** The authors would like to thank S. V. Danilov, PhD. in Engineering, Associate Professor, and the Head of the Department of Industrial and Civil Construction of the Belarusian-Russian University, for his support in manufacturing and testing of experimental specimens.

**Citation:** Maskalkova, Yu.G., Rzhevutskaya, V.A. Size effect of cube specimen on strength of expanded clay fiber-reinforced concrete. Magazine of Civil Engineering. 2022. 116(8). Article no. 11612. DOI: 10.34910/MCE.116.12

### 1. Introduction

The object of the study is expanded clay concrete reinforced with polymer fiber made from polypropylene C<sub>3</sub>H<sub>6</sub>.

Expanded clay concrete is a promising building material for the manufacture of load-bearing structures since this type of concrete allows reducing thermal conductivity, material consumption, and significantly increasing fire resistance of these structures [1, 2]. Many studies of researchers are devoted to lightweight concrete (including expanded clay concrete) modified with polypropylene fiber (PPf). There is no consensus on the optimal percentage of dispersed reinforcement of lightweight concrete with polypropylene fiber; however, based on the results of studies of various researchers [3–5], it was established that the content of polymer fiber in concrete should not be more than 2 % by concrete volume. The synthetic fiber content in concrete should be in the range of 0.5–1.5 %, as stated in [4]. For instance, according to [5], the percentage value of fiber reinforcement of 2 % is the upper limit. If this reinforcement percentage is higher, it is problematic to achieve the concrete mixture homogeneity. If this value is

exceeded, the strength of fiber-reinforced concrete is always lower than the strength of unreinforced concrete, and it can lead to an attenuation of the structure due to oversaturation with polymer fiber [6] and cause of defects [7, 8].

The results are often contradictory despite numerous studies. According to an analysis of the PPF effect on the strength characteristics of lightweight concrete, the obtained results can be conditionally divided into four groups:

1. strength does not change;
2. strength changes unevenly;
3. strength decreases;
4. strength increases.

The results of the analytical review are shown in Table 1.

**Table 1. Analytical review devoted to the effect of dispersed reinforcement with polymer fiber on the strength of lightweight concrete.**

Strength change	Authors	Year of publication	The main features of the study	Research results
1. Strength does not change	Kroviakov, S.O., Mishutin, A.V., Pishev, O.V., Kryzhanovskij, V.O. [9]	2018	Modified expanded clay concrete with the addition of polypropylene fiber in an amount of 0–1.2 kg/m <sup>3</sup> was investigated.	The compressive strength of specimens practically did not change; an increase of flexural tensile strength was noted.
	Kastornykh, L.I., Detochenko, I.A., Arinina, E.S. [10]	2017	Self-compacting lightweight concrete (5–10 mm grain size of expanded clay aggregate, 12 mm PPF length) was investigated.	The compressive strength of self-compacting expanded clay fiber-reinforced concrete practically did not change. The strength changes were insignificant (strength values of 21.51 MPa, 23.36 MPa, and 22.91 MPa with a fiber contents of 0 %, 1.4 %, and 2.0 %, respectively).
	Fantilli, A.P., Chiaia, B., Gorino, A. [11]	2016	Expanded clay concrete (3–8 mm grain size of coarse aggregate) with the addition of PP-fiber in amounts of 0 %, 1.4 %, and 2.0 % (by cement weight) was investigated.	The insignificant effect of polymer fiber on the compressive strength was noted.
	Bogutskii, V.L. [7]	2013	Modified shipbuilding expanded clay concrete was investigated with the addition of polypropylene fiber in an amount of 0–1.2 kg/m <sup>3</sup> .	
2. Strength changes unevenly	Karamloo, M., Afzali-Naniz, O., Doostmohamad, A. [12]	2020	Self-compacting lightweight concrete with polyolefin macro fibers in an amount of 0.1 %–0.5 % by concrete volume (0.48 %–2.43 % by cement weight) was studied.	The fiber content of 0.1 % by concrete volume had a positive effect on the strength; in other cases, the strength decreased.
	Altalabani, D., Bzeni, D.K.H., Linsel, S. [13]	2020	Self-compacting lightweight concrete (2–10 mm grain size of coarse aggregate) with micropolypropylene fiber 12 mm length and a dose of 0.91 kg/m <sup>3</sup> was investigated.	The uneven change of the strength characteristics of self-compacting lightweight concrete was noted.
	Qiu, J., Xing, M., Zhang, C., Guan, X. [14]	2020	Coal gangue ceramsite concrete with the addition of polypropylene fiber in the amount of 0.07–0.13 % by concrete volume (0.17–0.34 % by cement weight) was investigated.	The fiber content of 0.07 % by concrete volume had a positive effect on the compressive strength of concrete; in other cases, the strength decreased with the increase of the reinforcement percentage.
	Ghasemzadeh Mousavinejad, S.H., Shemshad Sara, Y.G. [15]	2019	Scoria lightweight aggregate concrete with polypropylene fiber addition in the amount of 0.2 % by concrete volume (0.1 % by cement weight) was investigated. Cement content of 500 kg/m <sup>3</sup> and 425 kg/m <sup>3</sup> were considered.	The uneven change of strength with different cement content was noted according to the results.

Strength change	Authors	Year of publication	The main features of the study	Research results
3. Strength decreases	Yahaghi, J., Muda, Z.C., Beddu, S.B. [16]	2016	Oil palm shells concrete reinforced with polypropylene fiber in an amount of 0.1–0.3 % by concrete volume (0.38–1.15 % by cement weight) was studied.	The decrease of concrete strength with the increase of the fiber amount was noted in all cases.
	Loh, L.T., Yew, M.K., Yew, M.C., Beh, J.H., Lee, F.W., Lim, S.K., Kwong, K.Z. [17]	2021	Lightweight concrete modified with polypropylene, basalt, and a mixture of these types of fiber in the amounts of 0.1 %, 0.3 %, and 0.1 + 0.3 % by concrete volume, respectively, was investigated.	The strength increase of lightweight fiber-reinforced concrete was found in all cases.
	Divyah, N., Thenmozhi, R., Neelamegam, M., Prakash, R. [18]	2021	Lightweight concrete modified with basalt fiber 18 mm length was studied.	Dispersed reinforcement made it possible to increase the compressive strength of lightweight concrete.
	Kuryatnikov, Iu.Iu., Kochetkov, R.S. [6]	2019	Lightweight concrete modified with basalt fiber 1 cm length was studied.	Dispersed reinforcement made it possible to increase the compressive strength of lightweight concrete from 45.7 to 62.6 MPa (by more than 30 %).
4. Strength increases	Li, J.J., Niu, J.J., Wan, C.J., Liu, X., Jin, Z. [19]	2017	High performance lightweight aggregate concrete reinforced by polypropylene fiber in an amount of 0.53–1.37 % by concrete volume (0.26–0.67 % by cement weight) was investigated.	The increase of the strength of high performance lightweight aggregate fiber-reinforced concrete was established in all cases.
	Li, J.J., Niu, J.G., Wan, C.J., Jin, B., Yin, Y.L. [20]	2016	High performance lightweight aggregate concrete with the addition of polypropylene fiber in the amount of 0.53–1.37 % by volume of concrete was studied.	The strength increase of high performance lightweight aggregate concrete was established in all cases, except for reinforcement ratio of 1.37 % by concrete volume.
	Corinaldesi, V., Moriconi, G. [21]	2015	Self-compacting lightweight aggregate concrete with micro polypropylene fiber (dose of 5 kg/m <sup>3</sup> ) was investigated.	The strength increase of self-compacting fiber-reinforced lightweight concrete by 10% was established.
	Yew, M.K., Mahmud, H.B., Ang, B.C., Yew, M.C. [22]	2015	High-strength oil palm shell lightweight concrete with polypropylene fiber in an amount of 0.25–0.5 % by concrete volume.	The concrete strength of high-strength oil palm shell lightweight concrete increased (from 40.9 to 46.6 MPa) with an increase of the reinforcement ratio.

The improvement of the strength characteristics of expanded clay fiber-reinforced concrete is justified in [6, 23] by the formation of a cement-mineral structure. The uneven change in the strength characteristics of self-compacting expanded clay concrete modified with polypropylene fiber is explained in [13] by the uneven distribution of fiber in the concrete mixture.

The fiber length should preferably be commensurate with the grain size of the coarse aggregate, so expanded clay aggregate is in the center of the cell formed by the fibers [8]. The use of polypropylene fiber of different length has a more pronounced positive effect on the strength characteristics of concrete than the addition of polypropylene fiber of the same length; it was concluded in [24].

According to the studies presented in this article, such an ambiguous assessment of the change in strength characteristic resulting from the addition of polymer fiber to the concrete mixture may be associated with the size of the specimens.

Previously, when conducting our own investigations, we also took the indicated dimensions as standard; however, the cube specimens of both standard sizes (with the edge of 100 mm and with the edge of 150 mm) were made in an amount of at least 9 for each size in each Series. When processing the data, we noticed that for each experimental Series the coefficient of variation turned out to be more than the allowable value of 13.5 %. Then there was an assumption that for lightweight fiber-reinforced concrete the traditional approach should be corrected [25].

In order to test this assumption, we carried out the analysis of the experimental data of various researchers published in open access peer-reviewed sources [3–5, 12, 14–16, 19, 20, 22, 26–28] (Table 2, Fig. 1).

**Table 2. Compressive cube strength of fiber-reinforced concrete.**

Authors, country	Concrete type, fiber type	Fiber content, %		Mean value of compressive strength with an edge of cube, mm		Remark
		by cement weight	by concrete volume	100	150	
Ramujee, K [3], India	Concrete, polypropylene fiber	0	0	–	33.7	
		2.96	0.5	–	40.9	
		5.92	1.0	–	44.12	
		8.88	1.5	–	45.25	
Nkem Ede, A., Oluwabambi Ige, A. [4], Nigeria	Concrete, polypropylene fiber	11.84	2.0	–	40.5	
		0	0	–	20.8	
		0.5	0.25	–	22.87	
		1	0.5	–	21.76	
Pothisiri, T., Soklin, C. [5], Thailand	Concrete, polypropylene fiber	1.5	0.75	–	20.29	
		2	1	–	20.05	
		0	0	–	25.5	Fiber was added: to the finished mix
		1.3	0.2	–	26.6	with coarse aggregate
Sun, Z., Xu, Q. [26], China, U.S.A.	Concrete, polypropylene fiber	1.3	0.2	–	25.1	with fine aggregate
		1.3	0.2	–	25.5	
		0	0	50.1	–	
		–	0.45	52.1	–	
Mazaheripour, H., Ghanbarpour, S., Mirmoradi, S.H., Hosseinpour, I. [27], Iran	Self-compacting concrete, polypropylene fiber	–	0.9	53.6	–	
		–	1.35	46.8	–	
		0	0	25.3	–	
		0.18	0.1	24.6	–	
Qiu, J., Xing, M., Zhang, C., Guan, X. [14], China	Coal gangue ceramsite concrete, polypropylene fiber	0.36	0.2	26.3	–	
		0.54	0.3	24.6	–	
		0	0	50.8	–	
		0.17	0.07	55.8	–	
Ghasemzadeh Mousavinejad, S.H., Shemshad Sara, Y.G. [15], Iran	Lightweight concrete (scoria as coarse aggregate), polypropylene fiber	0.25	0.1	48.5	–	
		0.34	0.13	43.8	–	
		0	0	22.0	–	Cement 500 kg/m <sup>3</sup>
		0.1	0.2	29.0	–	Cement 450 kg/m <sup>3</sup>
Yahaghi, J., Muda, Z.C., Beddu, S.B. [16], Malaysia	Oil palm shells concrete, polypropylene fiber	0	0	26.5	–	Cement 425 kg/m <sup>3</sup>
		0.38	0.1	25.8	–	Cement 425 kg/m <sup>3</sup>
		0.77	0.2	47.38	–	
		1.15	0.3	46.29	–	
Karamloo, M., Afzali-Naniz, O., Doostmohamadi, A. [12], Iran	Self-compacting lightweight concrete (expanded clay as coarse aggregate), polyolefin macro fibers	0	0	40.77	–	
		0.48	0.1	42.03	–	
		1.45	0.3	40.53	–	
		2.43	0.5	38.9	–	

Authors, country	Concrete type, fiber type	Fiber content, %		Mean value of compressive strength with an edge of cube, mm		Remark
		by cement weight	by concrete volume	100	150	
Yew, M.K., Mahmud, H.B., Ang, B.C., Yew, M.C. [22], Malaysia	Oil palm shell lightweight concrete, monofilament-polypropylene fiber	–	0	–	40.9	
		–	0.25	–	42.4	
		–	0.375	–	44.9	
		–	0.5	–	46.6	
		0	0	–	39.7	
Li, J.J., Niu, J.J., Wan, C.J., Liu, X., Jin, Z. [20], China	Lightweight concrete (lytag as coarse aggregate), high performance polypropylene fiber	0.26	0.53	–	40.7	
		0.36	0.74	–	41.6	
		0.46	0.95	–	43	
		0.57	1.16	–	42.2	
		0.67	1.37	–	40.8	
Li, J.J., Niu, J.G., Wan, C.J., Jin, B., Yin, Y.L. [19], China	Lightweight concrete (lytag as coarse aggregate), high performance polypropylene fiber	0	0	–	37.6	
		0.26	0.53	–	38.3	
		0.36	0.74	–	39.5	
		0.57	1.16	–	38.7	
		0.67	1.37	–	37.2	

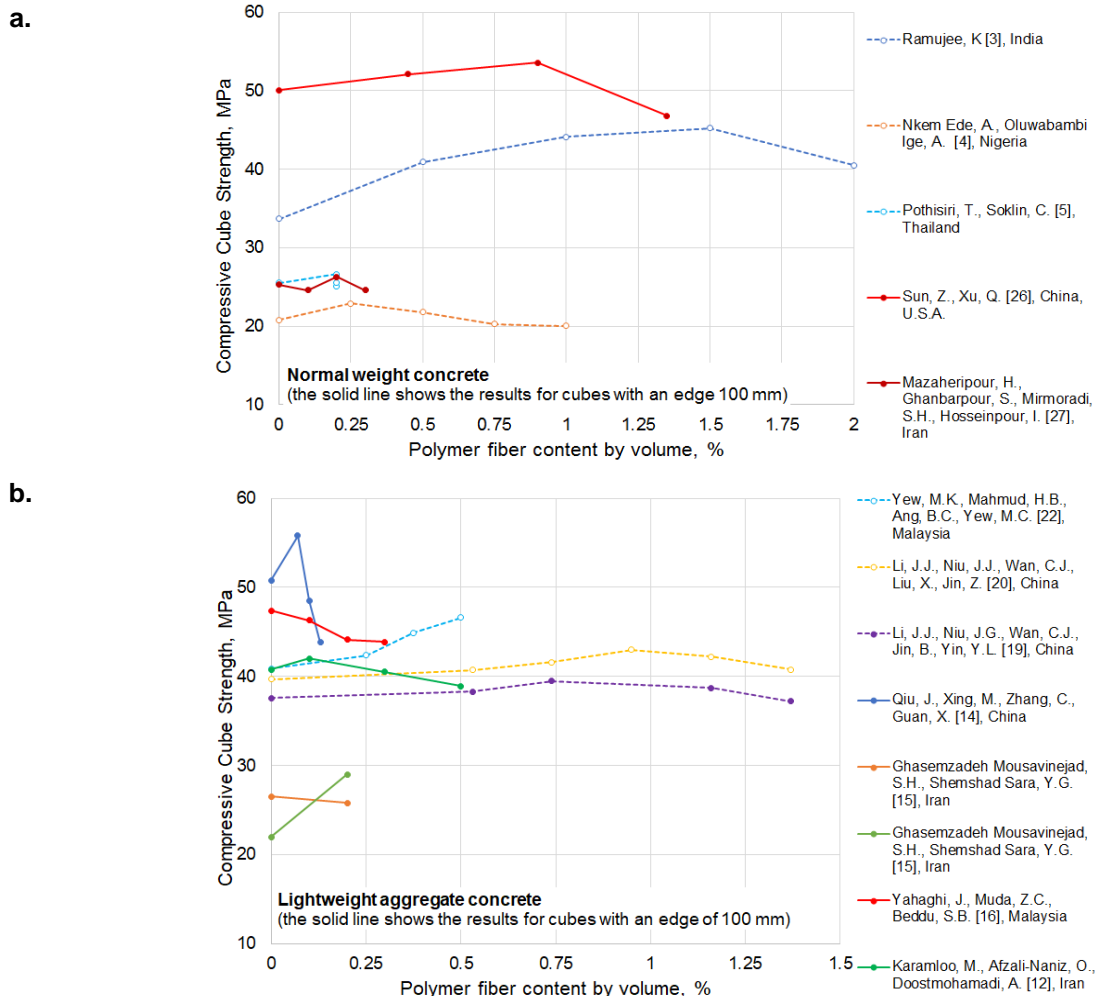


**Figure 1. Results of determining the compressive cube strength of lightweight fiber-reinforced concrete (the solid line shows the results for cubes with an edge of 100 mm): (a) curves for normal weight concrete; (b) curves for lightweight aggregate concrete.**

Despite the fact that cubes with different sizes were not tested in any considered studies [3–5, 12, 14–16, 19, 20, 22, 26–28] (Table 2, Fig. 1), and the types and classes of concrete differed, the following regularity can be noticed. When testing specimens (cubes) were made of dense aggregate concrete, regardless of specimen size (Fig. 1, (a)), similar (comparable) dependencies of compressive cube strength depending on the fiber content were obtained. When testing specimens (cubes) were made of lightweight concrete (Fig. 1, (b)), no such dependency was found. Thus, the role of the specimen size on the results of the compressive strength test for lightweight fiber-reinforced concrete is more significant than for lightweight concrete without dispersed fibers or dense aggregate concrete compositions.

In addition, in [29] for lightweight fiber-reinforced concrete with fiberglass, the discrepancy between the obtained values of strength was stated when testing specimens of different sizes in the shape of cubes and cylinders. According to [30], when testing cylinders with different heights and diameters (made of lightweight concrete without dispersed reinforcement), dimensions had no significant effect on the obtained strength values.

The determination coefficient was rather low ( $R^2 = 0.61$ ) in [31] when testing lightweight concrete cubes while the size and shape of the specimens did not affect the results for normal weight concrete.

An analytical review of the studies (Table 2, Fig. 1) also shows that researchers typically produce cubes of only one size for testing (usually 100 mm or 150 mm). It is well known that the size of the specimens depends on the particle size of the aggregate and must be at least seven diameters. This condition is based on the regularities of the mechanics of destruction of heterogeneous building materials. In this regard, the cube edge dimensions of 100 mm and 150 mm are accepted as standard. However, fiber-reinforced concrete is a composite material in which the fiber is not a structural element, but is a reinforcing fiber. The review of studies on lightweight fiber-reinforced concrete [12, 14–16, 19, 20, 22] indirectly confirms that the size can affect the obtained values of compressive cube strength.

At the same time, in studies devoted to the effect of specimen sizes on the obtained strength values [29–32], cylinder sizes (height and diameter) mainly vary, since the design value is determined based on the characteristic compressive strength of concrete. However, control and assessment of concrete strength in laboratory conditions are traditionally carried out on specimens in the shape of cubes; therefore, it is important to evaluate the accuracy of the obtained results when determining not only cylinder strength but also cube strength of concrete.

The investigation of this issue is also relevant because many researchers studying the features of the work of building structures (beams, slabs, columns, etc.) made of fiber-reinforced concrete, often produce specimens of only one type (usually cubes or cylinders) and size.

Thus, for setting the purpose of the study, the key factor is the variability in the size of the specimens of lightweight concrete with fiber. At the same time, the influence of other factors (concrete density and fiber content) on the object of the study should be excluded, which is achieved by using a constant concrete composition.

In accordance with the above, the purpose of the study is to determine the role of the size of the specimen in the shape of the cube (100 and 150 mm) of lightweight fiber-reinforced concrete (based on expanded clay aggregate) on the results of testing strength for short-term uniaxial loading.

The subject of the study is the experimental justification of the use of cubes with an edge size of at least 150 mm to obtain the correct values of the compressive cube strength of expanded clay fiber-reinforced concrete with the addition of micro-reinforcing constructional fiber.

In accordance with the purpose, the task of the study is to establish the effect of the specimen size (cube with an edge of 100 mm and 150 mm) on the mean value of compressive cube strength of expanded clay fiber-reinforced concrete with PPf content of 1.5 % by cement weight (0.36 % by concrete volume). When setting research tasks, the factor of fiber concentration is taken into account. The concrete composition is constant. The variation of the specimen size is binary: 100 and 150 mm.

According to earlier studies, for expanded clay fiber-reinforced concrete with PPf, the percentage of fiber reinforcement of 0.36 % by concrete volume is the most effective among the studied percentages (the PPf contents of 0.12 %, 0.24 % and 0.36 % by volume were studied) [33]. In this regard, to establish the binary variability of the experimental cube dimensions (the edge size of 100 and 150 mm) and the strength of expanded clay fiber-reinforced concrete, the reinforcement percentage  $\rho_{PPf} = 1.5$  % by cement weight (0.36 % by concrete volume) was chosen.

## 2. Methods

Specimens for investigation of mean values of compressive cube strength of expanded clay concrete and expanded clay fiber-reinforced concrete with PPF were made in the shape of cubes in metal molds with an edge size of 150 mm and 100 mm (according to GOST 10180: Concretes. Methods for strength determination using reference specimens).

The following proportion of the expanded clay concrete mixture for the manufacture of specimens (cubes) was:

$$C : S : G = 1 : 1.84 : 0.79, W/C = 0.52.$$

The following materials were used for preparation of the concrete mix.

1. The coarse aggregate – expanded clay gravel produced by OJSC Plant of expanded clay gravel in Novolukoml (Belarus) with particle size of 4–10 mm (Table 3).

**Table 3. Characteristics of expanded clay gravel.**

Particle size	Bulk density	Specific density	Mean value of expanded clay grain	Compressive cylinder strength	Porosity	Water absorption by mass (by volume)
4–10 mm	390 kg/m <sup>3</sup>	2.35 g/cm <sup>3</sup>	0.8 g/cm <sup>3</sup>	1.03 MPa	83.23 %	16.7 % (13.4 %)

2. The fine aggregate – medium-sized river sand (according to particle size distribution, the content of particles with a size of more than 0.25 mm by weight is over 50 %) (Table 4). The river sand deposit is Pavlovskoye in the Mogilev region (the floodplain of the Dnieper River, Belarus). The river sand was homogeneous in terms of maximum fine aggregate heterogeneity ( $U_{\max} = 3.55 < 4$ ).

**Table 4. Characteristics of river sand.**

Bulk density	Specific density	Average density	Fineness modulus	Porosity
1670 kg/m <sup>3</sup>	2.46 g/cm <sup>3</sup>	1670 kg/m <sup>3</sup>	2.13	32.32 %

3. The Binder – Portland cement (CEM I 42.5N) produced by OJSC Belarusian Cement Plant (Belarus) (Table 5). The chemical and mineralogical composition of the cement clinker is presented in Table 6.

**Table 5. Characteristics of Portland cement.**

Bulk density	Specific density	Average density	Water requirement of normal consistency	Compressive strength at 28 days	Spread of cement paste
1140 kg/m <sup>3</sup>	3.05 g/cm <sup>3</sup>	1140 kg/m <sup>3</sup>	25–28 %	48.08 MPa	105 mm

**Table 6. The chemical and mineralogical composition of the cement clinker.**

The chemical composition of the cement clinker	SiO <sub>2</sub> , %	21.71
	Al <sub>2</sub> O <sub>3</sub> , %	5.27
	Fe <sub>2</sub> O <sub>3</sub> , %	3.74
	CaO, %	66.20
	MgO, %	1.30
the ratio by mass (CaO)/(SiO <sub>2</sub> )		3
The mineralogical composition of the cement clinker	C <sub>3</sub> S, %	60.55
	C <sub>2</sub> S, %	16.59
	C <sub>3</sub> A, %	7.63
	C <sub>4</sub> AF, %	11.38

4. The reinforcing polypropylene fiber – constructional micro-fiber (CMF) made of granules of a high-modulus thermoplastic polymer (C<sub>3</sub>H<sub>6</sub> polypropylene) by structural modification (Table 7). Polypropylene fiber produced by LLC RUSSEAL (Russia).

**Table 7. Characteristics of polypropylene fiber**

Property	Value
Length	12 mm
Diameter	50 $\mu\text{m}$
Shape	round
Density	0.91 g/cm <sup>3</sup> at 20 °C
Elongation before break	21 %
Melting point	more than 160 °C
Electrical conduction	low
Chemical resistance	high
Alkali resistance	high

The following percentages of PPf reinforcement were studied:

- $\rho_{PPf} = 0$  % (control specimens without reinforcement);
- $\rho_{PPf} = 1.5$  % by cement weight (0.36 % by concrete volume).

According to [5], comparable strength values of the fiber-reinforced concrete specimens were obtained with the same content of polypropylene fiber (0.2 % by concrete volume) although the polymer fiber was introduced into the concrete mixture at different preparation stages (simultaneously with the coarse aggregate; simultaneously with the fine aggregate; into the finished concrete mix) (Table 2). It was also proved in [34] that provided the mix is thoroughly mixed, the moment the polymer fiber is introduced does not significantly affect the strength characteristics.

In this study for the manufacture of specimens, water initially was poured into the concrete mixer drum; next, the required amount of PPf was added to the water in portions; then cement, sand, and expanded clay gravel were added in a sequence. The time of mixing was increased by 15 % compared to the mixing time of expanded clay concrete mixture without fiber reinforcement.

The main technological equipment and measuring instruments were used in this study:

- electronic balance VK-3000 and VE-15T produced by JSC MASSA-K, Russia;
- concrete mixer B-160 produced by Denzel, Germany;
- portable concrete vibrator MVE 1501 produced by LTD Masalta engineering Co., China;
- universal testing machine RGM-1000-M-1 produced by LLC Metrotest, Russia;
- microscreeener MS LaboMed-1 produced by LLC Labor-Microscopes, Russia;
- metal measuring rules produced by LTD Tukzar, China.

### 3. Results and Discussion

All specimens (cubes with dimensions of 100×100×100 mm and 150×150×150 mm) were tested for short-term uniaxial loading on universal testing machine in the laboratory of the Belarusian-Russian University according to GOST 10180. The rate of loading application was 0.4–0.6 MPa/s.

Table 8 shows the test results of experimental expanded clay concrete and expanded clay fiber-reinforced concrete cubes with dimensions of 100×100×100 mm and 150×150×150 mm. The results of testing specimens are without taking into account the data rejected during the processing. The content of polypropylene fiber is given in % by cement weight.

**Table 8. Experimental data processing results.**

PPf reinforcement, %	Nominal edge size of cube, mm	Number of specimens in Group	Mean density, kg/m <sup>3</sup>	Mean value of compressive cube strength $f_{1cm,cube}$ , MPa	Standard deviation, $s$ , MPa	The coefficient of variation ( $Var$ ), %	Relative range of variation	Mean value of specific compressive cube strength, $\varphi_{1cm,cube}$ , kN·m/kg
0	100	31	1462	13.07	1.33	10.21	0.39	8.94
	150	10	1484	13.13	0.55	4.18	0.11	8.85
1.5	100	42	1445	10.98	1.83	15.50	0.66	7.59

	150	41	1457	13.87	1.56	11.26	0.43	9.49
0	100, 150	41	1467	13.08	1.18	9.06	0.39	8.92
1.5	100, 150	83	1460	12.41	2.18	17.56	0.78	8.25

Table 8 shows the statistics for the mean compressive cube strength. However, due to the heterogeneity of the porous coarse aggregate (expanded clay gravel), even with the same concrete mixture for experimental cubes, the density varies within 1355–1655 kg/m<sup>3</sup> (Fig. 2).

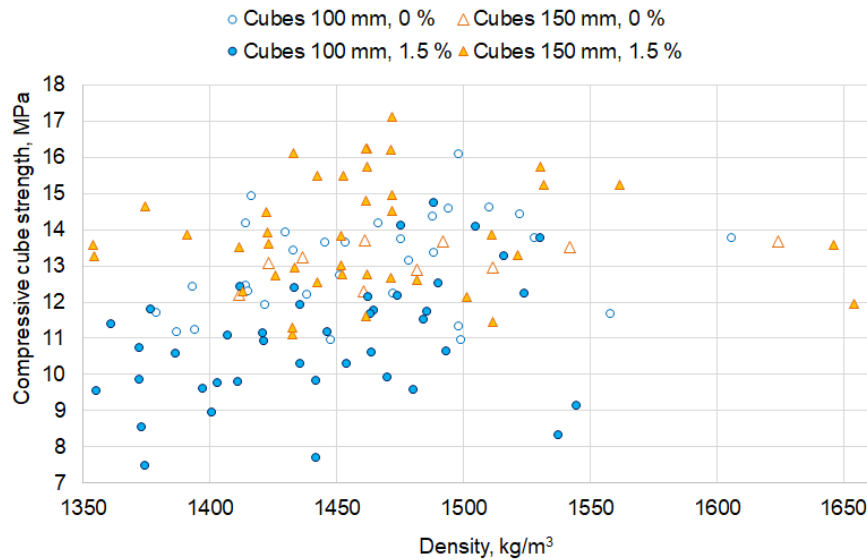


**Figure 2. Actual values of the main physical and mechanical characteristics of experimental cubes: density (kg/m<sup>3</sup>) and compressive cube strength,  $f_{lc,cube,i}$  (MPa).**

However, it is important that the non-variability of the specimens, which is generally controlled by constant consumption of lightweight aggregate, should be taken into account when analyzing the strength, i.e., use a criterion that would take into account the spread in strength values caused by a change in the density of the specimens due to the heterogeneity of the aggregate. Such criterion can be, for example, specific strength (Table 8).

Specific strength is usually used to reflect the ratio of strength characteristics and density of lightweight concrete: the higher this value, the lower the density and higher the strength of lightweight concrete. The trend of specific compressive strength corresponds to the trend of compressive strength, which was established by other researchers [19] and is shown in Fig. 3.

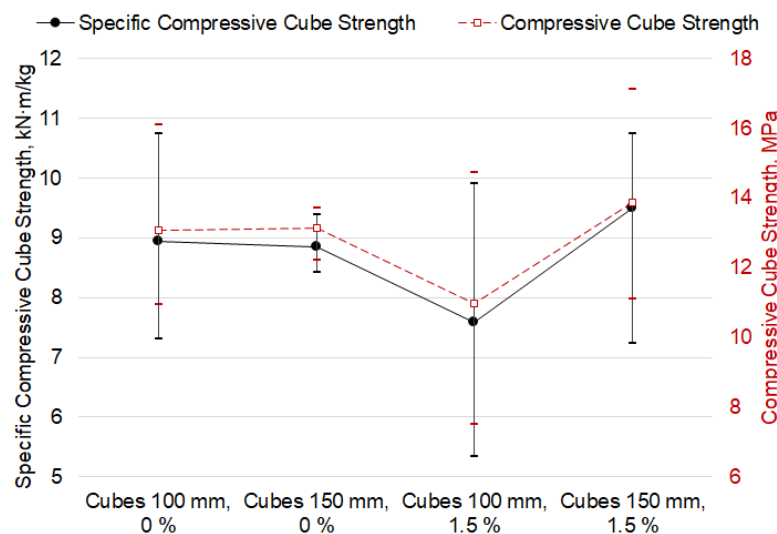


**Figure 3. The values of the specific compressive cube strength and compressive cube strength for the studied Groups of experimental cubes.**

Further in the article, the statistical analysis of the data is based on the values of the specific compressive cube strength. The use of values of specific compressive cube strength instead of the mean

for statistical processing makes it possible to exclude the effect of scatter in the density values of the specimens and establish only the influence of the key parameter (the edge size of the experimental cubes).

Basic statistics for cube-shaped specimens are presented in Table 9.

**Table 9. Basic statistics for Groups of specimens**

Group of specimens	Group 1	Group 2	Group 3	Group 4
Characteristics of Group	Edge size of 100 mm, $\rho_{PPf} = 0 \%$	Edge size of 150 mm, $\rho_{PPf} = 0 \%$	Edge size of 100 mm, $\rho_{PPf} = 1.5 \%$	Edge size of 150 mm, $\rho_{PPf} = 1.5 \%$
Sample size, $n$	31	10	42	41
Expectation (Sample Mean), $m$ , kN·m/kg	8.94	8.85	7.59	9.49
Standard Error of the Mean (SEM), $\delta_m$	0.16	0.11	0.17	0.17
Median, kN·m/kg	8.92	8.74	7.74	9.57
Standard Deviation, $s$ , kN·m/kg	0.87	0.36	1.09	1.12
Sample Variance, $s^2$ , kN·m/kg <sup>2</sup>	0.75	0.13	1.19	1.25
Minimum, $f_{lcm,cube,min}$ , kN·m/kg	7.30	8.41	5.34	7.23
Maximum, $f_{lcm,cube,max}$ , kN·m/kg	10,74	9,38	9,90	11,63
Range, kN·m/kg	3.44	0.97	4.56	4.40
Skewness	-0.04	0.25	-0.17	-0.08
The coefficient of variation ( $Var$ )	10 %	4 %	14 %	12 %
Relative range of variation	0.38	0.11	0.60	0.46
95 % Confidence Interval of the Mean ( $\alpha = 0.05$ ), kN·m/kg	$\pm 0.32$	$\pm 0.26$	$\pm 0.34$	$\pm 0.35$
Upper Confidence Limit, kN·m/kg	9.26	9.11	7.93	9.85
Lower Confidence Limit, kN·m/kg	8.62	8.59	7.25	9.14

According to Table 9, it is obvious that for expanded clay concrete (without fiber reinforcement) the size of the cube does not affect the obtained values of the mean specific compressive cube strength (on condition the edge size is at least 7 times greater than the maximum aggregate grain size). This way,  $\varphi_{lcm,cube,100} = 8.94$  kN m/kg and  $\varphi_{lcm,cube,150} = 8.85$  kN·m/kg.

However, for expanded clay fiber-reinforced concrete with a polypropylene fiber content of 1.5 % by cement weight, the discrepancy between the mean values is obvious:  $\varphi_{lcm,PPf,cube,m,100} = 7.59$  kN·m/kg,  $\varphi_{lcm,PPf,cube,m,150} = 9.49$  kN·m/kg. At the same time, judging by cubes with an edge size of 100 mm, as a result of the addition of PPf, the mean value of specific compressive cube strength of expanded clay concrete decreased by 15 %. According to tests of cubes with an edge size of 150 mm, the specific compressive strength increased slightly by 7 %.

In addition, for all groups of specimens (cubes), except for Group 3 (edge size of 100 mm,  $\rho_{PPf} = 1.5 \%$ ), the coefficient of variation does not exceed 13.5 %, and only for Group 3 the coefficient of variation is more than 13.5 %. Group 3 also demonstrates the largest value of relative range of variation.

Thus, as a result of the investigation, a difference was revealed in the mean values of the specific strength of expanded clay fiber-reinforced concrete, obtained according to experimental data for cubes with an edge size of 100 mm and 150 mm. It is necessary to establish how significant this difference is. In addition, the difference in the strength of specimens of the same composition but of different sizes can be associated with the objective error of mechanical tests of concrete strength or such difference indicates a correlation between the strength of the concrete and the dimensions of the specimens.

Visually, the differences in the test results of cubes are presented on box-and-whisker chart (Fig. 4).

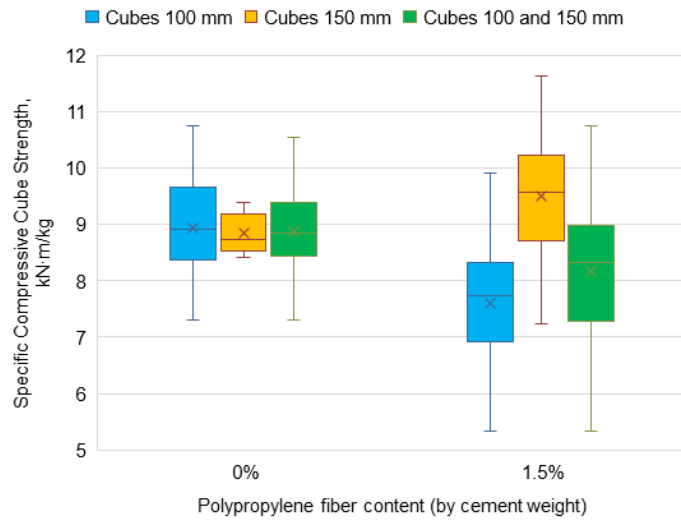


**Figure 4. Box-and-whisker chart for testing cubes.**

The chart in Fig. 4 clearly demonstrates the significant effect of the size of the cubes on the obtained specific strength when PPF is added, i.e., the size effect is observed. Such dependence was not established for expanded clay concrete without fiber reinforcement.

When testing the hypothesis by the method of the confidence interval (data based on one-sample *t*-test), the following was established. Based on the data obtained in Table 9, for the sample of Group 1, the mathematical expectation of 8.94 kN·m/kg falls into the confidence interval of Group 2; thus, the null hypothesis of equality of means is not rejected. For the sample of Group 3, the mathematical expectation of 7.59 kN·m/kg does not fall into the confidence interval of Group 4, therefore the null hypothesis is rejected (Fig. 5).

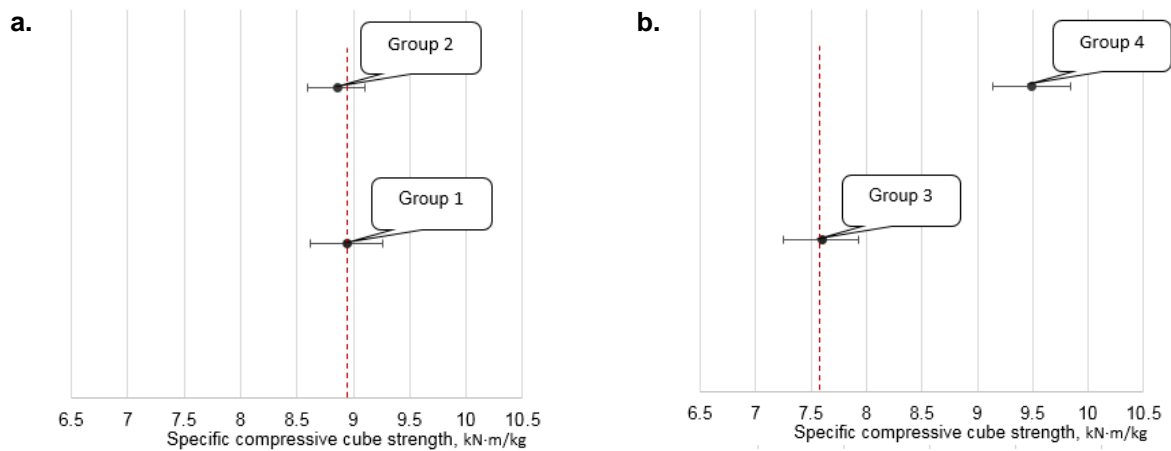


**Figure 5. Upper and lower confidence limit for: (a) Group 1 and Group 2; (b) Group 3 and Group 4.**

To clarify the obtained results, first, it is necessary to test the statistical hypothesis of the correspondence of the empirical distribution (frequency histogram) of the controlled parameter (specific compressive cube strength) to the normal distribution.

The number of class-intervals for plotting a frequency histogram was assigned based on the sample size according to the Sturges rule:

$$k = 1 + 3.322 \lg n. \tag{1}$$

The largest number of results (sample size) was  $n = 42$ , then  $k = 6$ . The maximum range was  $(11.63 - 5.34) = 6.30$  kN·m/kg, then 'height' of class-interval was  $h = 6.30 / 6 = 1.05$  kN·m/kg. For the convenience of plotting  $h = 1.1$  kN·m/kg was taken.

Observed frequencies were determined according to the initial data (Table 9). Expected frequencies were determined according to the traditional method based on the sample mean and sample variance using the Gaussian function.

The null hypothesis that observed frequency distribution in a sample is consistent with theoretical frequency distribution; it was tested by Pearson's chi-squared test. The level of significance was accepted as  $\alpha = 0.05$ .

The calculation results are summarized in Table 10.

**Table 10. Results of Pearson's chi-squared test ( $\chi^2$ ).**

Number of class-interval	Class interval, kN·m/kg	Observed frequency $O_i$	Relative observed frequency $O_i / N$	Expected frequency $E_i$	$\chi^2$	Results of chi-squared test
Cubes with edge size of 100 mm, $\rho_{PPf} = 0\%$						
1	6...7.09	0	0.000	0.01	0.01	$\chi^2 = 1.1$ ;
2	7.1...8.19	0	0.000	0.39	0.39	$\chi^2_{0.05;30} = 43.8$ ;
3	8.2...9.29	6	0.194	4.60	0.43	$\chi^2 \ll \chi^2_{0.05;30}$ ;
4	9.3...10.39	12	0.387	13.73	0.22	$p\text{-value} = 0.95452$ ;
5	10.4...11.49	11	0.355	10.27	0.05	$p\text{-value} \gg \alpha = 0.05$ .
6	11.5...12.59	2	0.065	1.92	0.00	
	$\Sigma$	31	1.000	30.91	1.1	
Cubes with edge size of 150 mm, $\rho_{PPf} = 0\%$						
1	8.3...8.59	0	0.000	0.41	0.41	$\chi^2 = 2.3$ ;
2	8.6...8.89	3	0.300	1.80	0.79	$\chi^2_{0.05;9} = 16.9$ ;
3	8.9...9.19	3	0.300	3.49	0.07	$\chi^2 < \chi^2_{0.05;9}$ ;
4	9.2...9.49	2	0.200	2.96	0.31	$p\text{-value} = 0.67672$ ;
5	9.5...9.79	2	0.200	1.10	0.74	$p\text{-value} > \alpha = 0.05$ .
	$\Sigma$	10	1.000	9.77	2.3	
Cubes with edge size of 100 mm, $\rho_{PPf} = 1.5\%$						
1	6...7.09	4	0.095	2.95	0.37	$\chi^2 = 0.8$ ;
2	7.1...8.19	10	0.238	10.54	0.03	$\chi^2_{0.05;41} = 56.9$ ;
3	8.2...9.29	15	0.357	15.67	0.03	$\chi^2 \ll \chi^2_{0.05;41}$ ;
4	9.3...10.39	10	0.238	9.70	0.01	$p\text{-value} = 0.97649$ ;
5	10.4...11.49	3	0.071	2.50	0.10	$p\text{-value} \gg \alpha = 0.05$ .
6	11.5...12.59	0	0.000	0.27	0.27	
	$\Sigma$	42	1.000	41.63	0.8	
Cubes with edge size of 150 mm, $\rho_{PPf} = 1.5\%$						
1	7.1...8.19	0	0.000	0.56	0.56	$\chi^2 = 1.6$ ;
2	8.2...9.29	6	0.146	4.32	0.65	$\chi^2_{0.05;40} = 55.8$ ;
3	9.3...10.39	12	0.293	12.97	0.07	$\chi^2 \ll \chi^2_{0.05;40}$ ;
4	10.4...11.49	14	0.341	15.07	0.08	$p\text{-value} = 0.90070$ ;
5	11.5...12.59	8	0.195	6.79	0.22	$p\text{-value} \gg \alpha = 0.05$ .
6	12.6...13.69	1	0.024	1.18	0.03	
	$\Sigma$	41	1.000	40.89	1.6	

Since in all cases the value of  $\chi^2$  (Table 10) is significantly less than its critical value ( $\chi^2 \ll \chi^2_{crit}$ ) and the  $p\text{-value}$  for the chi-square distribution ( $\chi^2$ ) significantly exceeds the established level of significance

( $p\text{-value} \gg \alpha = 0.05$ ); therefore, there is no reason to reject the hypothesis that the random variable is normally distributed.

Experimental data were used to plot relative frequency histograms and polygons (Fig. 6) for expanded clay fiber-reinforced concrete (with PPF). For clarity, histograms and polygons for cubes with an edge size of 150 mm and 100 mm are shown in one figure. The histograms and polygons show that although both values are normally distributed, their mathematical expectations are different.

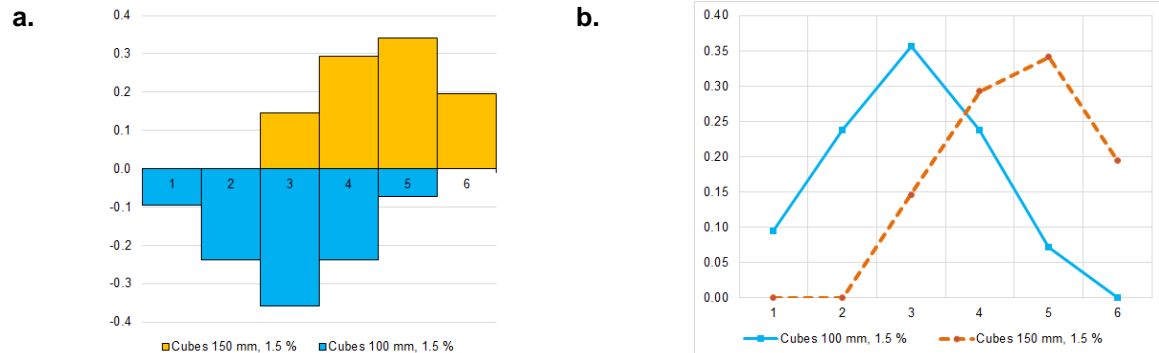


**Figure 6. Relative frequency: (a) histogram; (b) polygons for the test results for short term uniaxial loading of expanded clay fiber-reinforced concrete cubes with edge size of 150 mm and 100 mm ( $\rho_{PPf} = 1.5\%$  by cement weight).**

Two-sample  $F$ -test for variances was chosen to determine the statistical significance of the difference in the variances of the samples. The analysis results are shown in Table 11.

**Table 11. Results of  $F$ -test for hypothesis test for equality of variances**

Group of specimens	Results of $F$ -test
Group 1 (edge size of 100 mm, $\rho_{PPf} = 0\%$ ) and Group 2 (edge size of 150 mm, $\rho_{PPf} = 0\%$ )	$F = 5.814$ ; $F_{0.05;30;9} = 2.864$ ( $\alpha = 0.05$ ); $F > F_{0.05;30;9}$ ; $p\text{-value} = 0.004 < \alpha = 0.05$ . Sample variances are significantly different.
Group 3 (edge size of 100 mm, $\rho_{PPf} = 1.5\%$ ) and Group 4 (edge size of 150 mm, $\rho_{PPf} = 1.5\%$ )	$F = 1.058$ ; $F_{0.05;40;41} = 1.686$ ( $\alpha = 0.05$ ); $F < F_{0.05;40;41}$ ; $p\text{-value} = 0.429 > \alpha = 0.05$ . Sample variances are not significantly different.

According to the performed analysis, there is no reason to reject the null hypothesis of the equality of the variances of Group 3 and Group 4 since  $F < F_{crit}$  and the  $p\text{-value}$  significantly exceeded the established level of significance ( $\alpha = 0.05$ ).

$T$ -test for two-sample assuming unequal variances was used to assess the significance of the difference in the mean values of Group 1 and Group 2 obtained from the presented samples. This test was chosen due to assessing the differences in the mean values of two unrelated samples, which are normally distributed, and the samples may be unequal in size and with different variances.

In the case of assessing the significance of the difference between the mean values of Group 3 and Group 4, a  $t$ -test for two-sample assuming equal variances was selected according to the minimum difference in variances (Table 11). The results are shown in Table 12 (basic statistics for samples are presented in Table 9).

**Table 12. Results of  $t$ -test for hypothesis test for difference of sample means.**

Characteristics of specimens	Results of $t$ -test
Expanded clay concrete (without reinforcement), cubes with the edge size of 100 mm	Two-tailed test at $\alpha = 0.05$ ;
Expanded clay concrete (without reinforcement), cubes with the edge size of 150 mm	$t = 0.477$ ; $t_{0.05;36} = 2.028$ ;
Expanded clay fiber-reinforced concrete (with PPF);	$t < t_{0.05;36}$ ; $p\text{-value} = 0.636$ . Sample means are not significantly different.

$\rho_{PPf} = 1.5\%$ ), cubes with the edge size of 100 mm	Two-tailed test at $\alpha = 0.05$ ;
Expanded clay fiber-reinforced concrete (with PPf;	$t = 7.832$ ; $t_{0.05;81} = 1.99$ ;
$\rho_{PPf} = 1.5\%$ ), cubes with the edge size of 150 mm	$t > t_{0.05;81}$ ; $p\text{-value} = 1.606 \cdot 10^{-11} \approx 0$ .
Sample means are significantly different.	

According to the data analysis, for expanded clay fiber-reinforced concrete, the differences in mean values of the specific compressive cube strength of specimens with the same composition but different sizes (100 mm and 150 mm) are statistically significant.

A single factor analysis of variance (ANOVA) was chosen to confirm the significance of the difference in mean values obtained from the results of testing cubes with an edge of 100 mm and an edge of 150 mm. This analysis was selected based on the normal distribution of data from two unrelated samples with minimal differences in the variances. The analysis results are shown in Table 13.

**Table 13. Data results of ANOVA: Single Factor (MS Excel)**

ANOVA: Single Factor						
SUMMARY						
Groups	Count	Sum	Mean	Variance		
Cubes, edge size of 100 mm	42	318.9357	7.593708	1.18597		
Cubes, edge size of 150 mm	41	389.2111	9.492953	1.254728		
Analysis of Variance						
Source of Variation	SS	df	MS	F	p-value	F <sub>crit</sub>
Between Groups	74.83714	1	74.83714	61.34573	1.6057E-11	3.95885
Within Groups	98.81386	81	1.219924			
Total	173.651	82				

According to the performed analysis (Table 13) at the level of significance  $\alpha = 0.05$ , the F-test significantly exceeds its critical value ( $F = 61.35 \gg F_{0.05;1;81} = 3.96$ ); therefore, the null hypothesis is rejected

Thus, it is possible to state a significant influence of the factor on the study results (size of cubes), i.e., the sizes of the samples have a significant effect on the obtained values of the specific compressive cube strength of expanded clay fiber-reinforced concrete, and this fact should be taken into account when planning experimental studies.

It should be noted that when calculating the mean values of compressive cube strength of expanded clay fiber-reinforced concrete using cubes with dimensions of  $100 \times 100 \times 100$  mm, as well as cubes with dimensions of  $100 \times 100 \times 100$  mm and  $150 \times 150 \times 150$  mm at the same time, the cube strength in both cases turned out to be lower in comparison with the control specimens (without fiber). According to the data test only of cubes with dimensions of  $150 \times 150 \times 150$  mm, the strength increased due to the addition of fiber.

Getting lower mean value of cube strength is not critical. A downward deviation in the subsequent design of structures will provide an additional margin of safety. However, when assessing the effectiveness of fiber reinforcement, this deviation is significant. According to the chart in Fig. 3, based on the results of testing cubes with an edge of 100 mm, the strength of expanded clay concrete decreases with the addition of polypropylene fiber ( $\rho_{PPf} = 1.5\%$ ), i.e., fiber reinforcement negatively affects the strength characteristics. At the same time, according to the results of testing cubes with an edge of 150 mm, the strength of expanded clay concrete does not decrease as a result of the fiber addition, i.e., the negative effect of fiber reinforcement on strength is not noted.

In connection with the above, it is advisable to evaluate the correctness of the obtained data and to establish the recommended size of cubes for determining the cube strength of expanded clay fiber-reinforced concrete. This can be done by testing the strength of specimens in shape of cylinders.

Cylinders (with a diameter of 150 mm and a height of 300 mm) made in the same series with cubes were tested. The results of determining the mean value of cylinder compressive strength and comparison with the mean value of compressive cube strength are shown in Table 14.

**Table 14. Mean values of compressive strength for cube and cylinder of expanded clay fiber-**

**reinforced specimens.**

PPf reinforcement by cement weight, %	Mean value of compressive cube strength $f_{cm,PPf,cube}$ , MPa, with edge size of, mm		Mean value of compressive cylinder strength $f_{cm,PPf,cyl}$ , MPa (cylinder diameter of 150 mm, height of 300 mm)	Ratio $\frac{f_{cm,PPf,cyl}}{f_{cm,PPf,cube}}$ with edge size of, mm	
	100	150		100	150
1.5	10.98	13.87	12.6	1.15	0.91

Table 14 shows that the mean value of cube strength  $f_{cm,cube}$  is lower than the mean value of cylinder strength  $f_{cm,cyl}$  (when testing cubes with dimensions of 100 × 100 × 100 mm). This is unlikely due to the significant influence of friction forces between the press plates and surfaces of the specimen, which, as is known, prevent the free development of transverse deformations and causes the so-called 'jacketing effect'.

In accordance with Saint-Venant's principle, the stresses caused by the forces of friction on the support surface are significant only in the area, dimensions of which are commensurate with the dimensions of the loaded surface area. Thus, the middle part in prisms and cylinders (with a height exceeding double cross-sectional size) is free from the influence of friction forces, and longitudinal cracks appear in the middle part of the prisms before failure, propagating up and down to the support surface area. For this reason, with a correctly performed investigation, the cube strength cannot be lower than the cylinder strength. When testing cubes with dimensions of 150 × 150 × 150 mm, the cube strength is greater than the cylinder strength.

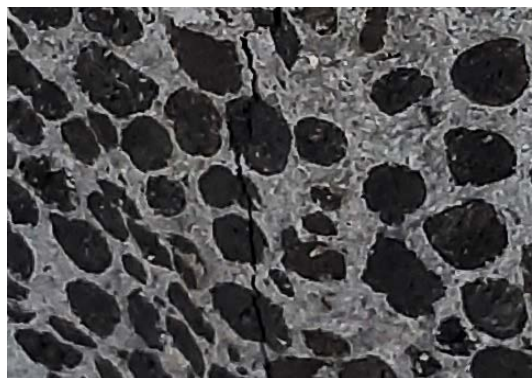
On this basis, it can be concluded that in order to assess the strength of expanded clay fiber-reinforced concrete, cubes with an edge size of at least 150 mm should be tested. Tests on cubes with an edge of 100 mm may demonstrate underestimated strength values.

Lower values of the cube strength compared to the cylinder strength of expanded clay concrete (without fiber) were also noted in [30]. The authors connected this fact to a much less expressed size effect for lightweight concrete in comparison with normal weight concrete. Authors of [30] tested cubes with an edge of 150 mm, the diameter of the cylinders was varied from 80 to 150 mm (diameters of 80, 100, 125, and 150 mm), and the number of twin specimens was taken as 6 or 7. At the same time, for control specimens (cube with dimensions of 150 × 150 × 150 mm, cylinder with the diameter of 150 mm and the height of 300 mm), the cube strength turned out to be greater than the cylinder strength.

It is also indicated in [15] that due to an increase of polymer fiber content, the air is entrained and an empty space is formed, leading to a decrease in strength. The reason for the decrease in the compressive cube strength of expanded clay concrete containing polypropylene fiber may be the uneven distribution of PP-fibers in the hardened concrete leading to an increase in porosity. The noted effects have a significant influence on the test results of specimens with small sizes (cubes with an edge of 100 mm).

In this study expanded clay gravel with a maximum grain size of  $d_g = 10$  mm was used, the average layer of the cement matrix width was approximately  $a_m \approx 10$  mm (Fig. 7 (a)). Polypropylene fibers are 'included' in the hardened cement (Fig. 7 (b, c)); it is clearly visible when examining the slices of the specimen using the microscreener.

a.



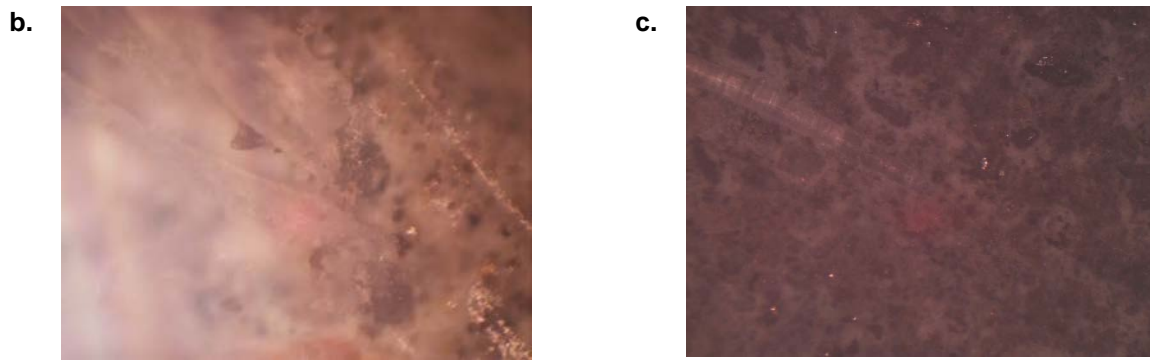


**Figure 7. Slices of expanded clay concrete specimen: (a) without magnification; (b) magnification 10x; (c) magnification 4x.**

The value of a characteristic element of the expanded clay concrete structure (the minimum element during the material properties test will appear but not of particular elements of the macrostructure) is:

$$l_0 = 5 \cdot (d_g + a_m) = 5 \cdot (10 + 10) = 100 \text{ mm.}$$

Since grains of coarse aggregate (expanded clay) with a properly selected fiber length are in the center of the cell formed by reinforcing fibers [8, 24], the dimensions of the characteristic element obviously increase. Then in all cases  $l_0 > 100 \text{ mm}$ .

It is necessary to take the minimum specimen size  $h_{\min}$  not less than the size of the characteristic element  $l_0$ , to obtain correct data, i.e.,  $h_{\min} \geq l_0$ . In this way,  $h_{\min} > 100 \text{ mm}$ .

The main crack initiation with an intragranular mechanism of expanded clay concrete failure can lead to momentary failure since tensile stresses at the crack tip quickly reach critical values. Momentary failure is associated with a high upper limit of microcracks formation for lightweight concrete [35].

The dangerous cracks are less likely to develop for small specimens than large ones due to the use of scale factors. However, Kholmyanskiy M. M. [36] proposed to assign a scale factor depending not only on the specimen size, but also taking into account the effects of dangerous crack stopping.

Evenly distributed fibers throughout the concrete volume provide the effect of crack stopping, regardless of the fiber type and the concrete type. Experimental verification of this can be found in many studies, for example, in [3–5, 37, 38]. Moreover, this effect becomes more evident as the specimen volume increases. At the same time in [36], the author noted that the stopping effect does not appear if the volume of concrete is too small.

Since the volume of the testing cubes ( $100 \times 100 \times 100 \text{ mm}$ ) is small (comparable to  $l_0$ ), the introduction of fiber does not provide the effect of crack stopping. This statement is in good agreement with the classical theory of Kholmyanskiy M. M. [36].

Summarizing the above, in order to determine the cube strength of lightweight concrete with polymer fiber content, it is recommended to test specimens (cubes) with an edge of at least 150 mm for short-term uniaxial loading test.

Obviously, the effect of fiber reinforcement on the strength characteristics of lightweight aggregate concrete depends on the type of aggregate and reinforcing fiber. Results may also differ with other fiber content. This justifies additional research.

## 4. Conclusions

1. In the study, based on the tests carried out on standard cube-shaped specimens with an edge size of 100 mm and 150 mm, the size effect of cubes on the obtained values of the mean compressive cube strength of expanded clay fiber-reinforced concrete was established. This statement contradicts the established world practice since the cube dimensions of  $100 \times 100 \times 100 \text{ mm}$  are considered generally accepted. Nevertheless, these sizes of cube specimens were originally used to assess the cube strength of dense aggregate concrete, and lightweight fiber-reinforced concrete cubes with dimensions of  $100 \times 100 \times 100 \text{ mm}$  were taken as standard for testing without sufficient justification for the possibility of their correct application. Statistical analysis of experimental data allows us to conclude that for specimens of the same composition but different sizes, the differences in the mean values of specific compressive cube strength of expanded clay fiber-reinforced concrete are statistically significant. Thus, the binary variability of the key factor (cube edge size: 100 and 150 mm) and mean values of compressive cube

strength of expanded clay fiber-reinforced concrete (polypropylene fiber with content of 1.5 % by cement weight) were established.

2. The use of cubes with an edge size of 100 mm is incorrect to determine the strength of expanded clay fiber-reinforced concrete since, in this case, the mean value of compressive cube strength is less than the mean value of cylinder compressive strength, and it contradicts the mechanics of concrete failure. In addition, polypropylene fibers do not provide effect of crack stopping if specimen sizes are comparable to the dimensions of a characteristic element of the expanded clay concrete structure. Consequently, the use of cubes with an edge size of 100 mm for testing does not guarantee correct results for lightweight concrete reinforced by polypropylene fiber. In connection with the above, it is recommended to use standard cube specimens with an edge size of 150 mm or more to obtain the mean value of compressive cube strength for expanded clay fiber-reinforced concrete with polypropylene fiber.

3. It is necessary to change the size of the cube by at least three values to establish the relationship between the size of the specimen and the compressive cube strength of lightweight fiber-reinforced concrete. For further analysis, the choice of cubes with the edge size of 70, 100, 150, and 200 mm seems sufficient. In addition, it is possible to change the fiber content (polypropylene and others) for justification of this study results. If the results of further studies with varying sizes of cube specimens and fiber content are statistically significant, it seems appropriate to amend the standard documents regulating the method for determining the compressive cube strength for lightweight fiber-reinforced concrete.

## References

1. Efremenko, A.S. High-strength lightweight concretes based on finely ground composite binders using the ash of waste heaps: monograph, St. Petersburg. 2019. 128 p. (rus)
2. Fallah, S., Nematzadeh, M. Mechanical properties and durability of high-strength concrete containing macro-polymeric and polypropylene fibers with nano-silica and silica fume. *Construction and Building Materials*. 2017. 132. Pp. 170–187. DOI: 10.1016/j.conbuildmat.2016.11.100
3. Ramujee, K. Strength properties of polypropylene fiber reinforced concrete. *International Journal of Innovative Research in Science, Engineering and Technology*. 2013. 8 (2). Pp. 3409–3413. URL: <https://www.rioi.com/open-access/strength-properties-of-polypropylene-fiber-reinforced-concrete-.php?aid=46458>
4. Nkem Ede, A., Oluwabambi Ige, A. Optimal polypropylene fiber content for improved compressive and flexural strength of concrete. *IOSR Journal of Mechanical and Civil Engineering*. 2014. 11 (3). Pp. 129–135. DOI: 10.9790/1684-1134129135
5. Pothisiri, T., Soklin, C. Effects of mixing sequence of polypropylene fibers on spalling resistance of normal strength concrete. *Engineering Journal*. 2014. 18 (3). Pp. 55–63. DOI: 10.4186/ej.2014.18.3.55
6. Kuryatnikov, Iu.Iu., Kochetkov, R.S. Development of mathematical models of physical and mechanical properties of modified ceramzytone concrete. *Materials of the IV International Scientific and Technical Conference*. 2019. Pp. 64–69. (rus)
7. Bogutskii, V.L. Strength properties of modified shipbuilding expanded clay concrete. *Bulletin of the ODABA*. 2013. 51. Pp. 35–40. (rus)
8. Belousov, I.V., Shilov, A.V., Meretukov, Z.A., Mailian, L.D. The use of fiber-reinforced concrete in reinforced concrete structures. *Engineering journal of Don*. 2017. 4. Pp. 1–16. (rus)
9. Kroviakov, S.O., Mishutin, A.V., Pishev, O.V., Kryzhanovskij, V.O. Composition effect on the strength of modified expanded clay lightweight concrete. *Bulletin of the ODABA*. 2018. 71. Pp. 107–112.
10. Kastornykh, L.I., Detochenko, I.A., Arinina, E.S. Effect of water-retaining additives on some properties of self-compacting concretes. Part 2. Rheological characteristics of concrete mixes and strength of self-compacting concretes. *Construction Materials*. 2017. 11. Pp. 22–27. (rus)
11. Fantilli, A.P., Chiaia, B., Gorino, A. Ecological and mechanical assessment of lightweight fiber-reinforced concrete made with rubber or expanded clay aggregates. *Construction and Building Materials*. 2016. 127. Pp. 692–701. DOI: 10.1016/j.conbuildmat.2016.10.020
12. Karamloo, M., Afzali-Naniz, O., Doostmohamadi, A. Impact of using different amounts of polyolefin macro fibers on fracture behavior, size effect, and mechanical properties of self-compacting lightweight concrete. *Construction and Building Materials*. 2020. 250. DOI: 10.1016/j.conbuildmat.2020.118856
13. Altalabani, D., Bzeni, D.K.H., Linsel, S. Mechanical properties and load deflection relationship of polypropylene fiber reinforced self-compacting lightweight concrete. *Construction and Building Materials*. 2020. 252. Pp. 119084. DOI: 10.1016/j.conbuildmat.2020.119084
14. Qiu, J., Xing, M., Zhang, C., Guan, X. Micro-pore structure characteristics and macro-mechanical properties of PP fibre reinforced coal gangue ceramsite concrete. *Journal of engineering (Stevenage, England)*. 2020. 2020 (12). Pp. 1192–1197. DOI: 10.1049/joe.2019.1296
15. Ghasemzadeh Mousavinejad, S.H., Shemshad Sara, Y.G. Experimental study effect of silica fume and hybrid fiber on mechanical properties lightweight concrete. *Iranian Journal of Science and Technology – Transactions of Civil Engineering*. 2019. 43 (2). Pp. 263–271. DOI: 10.1007/s40996-018-0137-9
16. Yahaghi, J., Muda, Z.C., Beddu, S.B. Impact resistance of oil palm shells concrete reinforced with polypropylene fibre. *Construction and Building Materials*. 2016. 123. Pp. 394–403. DOI: 10.1016/j.conbuildmat.2016.07.026
17. Loh, L.T., Yew, M.K., Yew, M.C., Beh, J.H., Lee, F.W., Lim, S.K., Kwong, K.Z. Mechanical and thermal properties of synthetic polypropylene fiber-reinforced renewable oil palm shell lightweight concrete. *Materials*. 2021. 14. Pp. 2337. DOI: 10.3390/ma14092337
18. Divyah, N., Thenmozhi, R., Neelamegam, M., Prakash, R. Characterization and behavior of basalt fiber-reinforced lightweight concrete. *Structural Concrete*. 2021. 22 (1). Pp. 422–430. DOI: 10.1002/suco.201900390

19. Li, J.J., Niu, J.J., Wan, C.J., Liu, X., Jin, Z. Comparison of flexural property between high performance polypropylene fiber reinforced lightweight aggregate concrete and steel fiber reinforced lightweight aggregate concrete. *Construction and Building Materials*. 2017. 157. Pp. 729–736. DOI: 10.1016/j.conbuildmat.2017.09.149.19
20. Li, J.J., Niu, J.G., Wan, C.J., Jin, B., Yin, Y.L. Investigation on mechanical properties and microstructure of high performance polypropylene fiber reinforced lightweight aggregate concrete. *Construction and Building Materials*. 2016. 118. Pp. 27–35. DOI: 10.1016/j.conbuildmat.2016.04.116
21. Corinaldesi, V., Moriconi, G. Use of synthetic fibers in self-compacting lightweight aggregate concretes. *Journal of Building Engineering*. 2015. 4. Pp. 247–254. DOI: 10.1016/j.jobbe.2015.10.006
22. Yew, M.K., Mahmud, H.B., Ang, B.C., Yew, M.C. Influence of different types of polypropylene fibre on the mechanical properties of high-strength oil palm shell lightweight concrete. *Construction and Building Materials*. 2015. 90. Pp. 36–43. DOI: 10.1016/j.conbuildmat.2015.04.024
23. Iarmakovskii, V.N. Physicochemical structural and technological foundations for the production of high-strength and highly durable structural lightweight concrete. *Construction Materials*. 2016. 6. Pp. 6–10. (rus)
24. Yang, X., Liang, N., Liu, X.R., Zhong, Z. An improved constitutive statistical damage model of a multisize polypropylene-fiber reinforced concrete under compression. *Mechanics of Composite Materials*. 2019. 55 (3). Pp. 385–392. DOI: 10.1007/s11029-019-09819-8
25. Maskalkova, Yu., Rzhnevskaya, V. Compressive strength of expanded clay fiber-reinforced concrete. *AlfaBuild*. 2021. 19. DOI: 10.34910/ALF.19.4
26. Sun, Z., Xu, Q. Microscopic, physical and mechanical analysis of polypropylene fiber reinforced concrete. *Materials Science and Engineering A: Structural Materials: Properties, Microstructure and Processing*. 2009. 527 (1). Pp. 198–204. DOI: 10.1016/j.msea.2009.07.056
27. Mazaheripour, H., Ghanbarpour, S., Mirmoradi, S.H., Hosseinpour, I. The effect of polypropylene fibers on the properties of fresh and hardened lightweight self-compacting concrete. *Construction and Building Materials*. 2011. 25 (1). DOI: 10.1016/j.conbuildmat.2010.06.018
28. Blazy, Ju., Blazy R. Polypropylene fiber reinforced concrete and its application in creating architectural forms of public spaces. *Case Studies in Construction Materials*. 2021. 14. Pp. e00549. DOI: 10.1016/j.cscm.2021.e00549
29. Hamad, A.J. Size and shape effect of specimen on the compressive strength of HPLWFC reinforced with glass fibres. *Journal of King Saud University – Engineering Sciences*. 2017. 29. Pp. 373–380. DOI: 10.1016/j.jksues.2015.09.003
30. Domagała, L. Size effect in compressive strength tests of cored specimens of lightweight aggregate concrete. *Materials*. 2020. 13 (5). DOI: 10.3390/ma13051187
31. Yehia, S., Abdelfatah, A., Mansour D. Effect of aggregate type and specimen configuration on concrete compressive strength. *Crystals*. 2020. 10 (7). DOI: 10.3390/cryst10070625
32. Sim, J., Yang, K., Kim, H., Choi, B. Size and shape effects on compressive strength of lightweight concrete. *Construction and Building Materials*. 2013. 38. Pp. 854–864. DOI: 10.1016/j.conbuildmat.2012.09.073
33. Maskalkova, Yu.G., Rzhnevskaya, V.A. The effective reinforcement ratio of expanded clay concrete by polypropylene fiber. *Construction of Unique Buildings and Structures*. 2020. 93. DOI: 10.18720/CUBS.93.3
34. Dong, H. Preparation and performance analysis of polypropylene fiber-reinforced concrete composite. *Asia-Pacific journal of chemical engineering*. 2020. 15 (S1). DOI: 10.1002/apj.2445
35. Semenyuk, S.D., Moskal'kova, Yu.G. Calculation method for the formation of microcracks taking into account the density of claydite concrete. *Russian Journal of Building Construction and Architecture*. 2019. 41 (1). Pp. 59–67. DOI: 10.25987/VSTU.2018.41.1.006
36. Kholmyanskiy, M.M. Concrete load-bearing capacity and its forecast by linear damage mechanics. *Concrete and reinforced concrete*. 1984. 7. Pp. 38–40. (rus)
37. Sunak, P.O., Synii, S.V., Krantovska, O.M., Ksonshkevych, L.M., Parasiyk, B.O. Investigation properties of resistance fiber reinforced concrete. *Modern technologies and methods of calculations in construction*. 2019. 12. Pp. 199–206. DOI: 10.36910/6775-2410-6208-2019-2(12)-24. (ukr.)
38. Babych, Ye.M., Andriichuk, O.V., Kysliuk, D.Ya., Savitskiy, V.V., Ninichuk, M.V. Results of experimental research of deformability and crack-resistance of two span continuous reinforced concrete beams with combined reinforcement. *IOP Conference Series: Materials Science and Engineering*. 2019. 708 (1). Pp. 1–8. DOI: 10.1088/1757-899X/708/1/012043

#### **Information about authors:**

**Yuliya Maskalkova**, PhD in Technical Science

ORCID: <https://orcid.org/0000-0002-4107-2452>

E-mail: [julia43@tut.by](mailto:julia43@tut.by)

**Valeryia Rzhnevskaya**,

ORCID: <https://orcid.org/0000-0001-8854-5408>

E-mail: [valeriarzhnevskaya@gmail.com](mailto:valeriarzhnevskaya@gmail.com)

*Received 18.01.2022. Approved after reviewing 11.02.2022. Accepted 14.02.2022.*



Research article

UDC 624.044

DOI: 10.34910/MCE.116.13



## Elastic-plastic deformation of a round plate reinforced with stiffeners

R.I. Khalmuradov, K. Khudoynazarov , U.A. Nishanov

Samarkand State University, Samarkand, Uzbekistan

✉ [khayrullakhudoynazarov@gmail.com](mailto:khayrullakhudoynazarov@gmail.com)

**Keywords:** elastoplasticity, tensor, deformation, nonlinear vibrations, finite deformation, nonlinear equation, reinforce plate

**Abstract.** The present paper studies the stress-strain state of a round reinforced with stiffeners plate of elastic-plastic material carried out of a refined theory of the type by S.P. Timoshenko. It is believed that plate vibrations are excited by a pulsed load. The relationship between displacement and deformation is assumed to be geometrically non-linear. The plate consists of sheathing and rib reinforcement of a quadrangular cross section. The lining materials of the reinforcing ribs are considered identical and obeying Hooke's law. The cross sections of the ribs are constant and are independent of the radial coordinate. The height of the ribs and their locations are set using a single column function. The number of methods of finite differences the solution to the problem. In this case, deformations, forces, moments, and transverse forces are determined at the centers of the grid elements, and displacement and rotation angles are determined at the grid nodes. Given the location of the ribs, the deflection of the central point and the force calculated, depend on the radial co-ordinate and time. Particularly, it was found that the smallest deflection of the central point is achieved when the rib is located in the middle of the radius of the plate; the location of the ribs near the edge of the plate can lead to a decrease in the load-bearing capacity of the structure compared to an un-reinforced plate.

**Citation:** Khalmuradov, R.I., Khudoynazarov, K., Nishanov, U.A. Elastic-plastic deformation of a round plate reinforced with stiffeners. Magazine of Civil Engineering. 2022. 116(8). Article no. 11613. DOI: 10.34910/MCE.116.13

### 1. Introduction

Thin elastic structures and their elements are widely used in modern technology and construction. In most cases, these elements operate under the influence of various dynamic loads of a wide range and are in difficult operating conditions [1, 2]. For achieving the desired structural rigidity and increase in strength, its thin-walled part is reinforced with ribs. The ribs increase rigidity, increase the strength of the structure and do not significantly increase the weight of the structure. In addition, the ribs very well transmit forces close to concentrated loads. At the same time, a reduction in the material consumption of structures, beneficial in design. Therefore, in studies of the dynamic nature of plates reinforced by stiffeners, special attention is paid to determining the strength characteristics of plates of increased stiffness under the influence of compressive loads.

The solution to the problems pertaining to the deformation of ribbed plates has been carried out through both analytical and numerical methods. Using analytical methods for calculating plates and shells, supported by stiffeners as other elements of engineering structures, it is possible to calculate their deformed and stressed states with a given or acceptable accuracy.

In mathematical terms, the analytical methods for solving dynamic problems of ribbed plates and shells are complex [3]. Therefore, researchers have tried to overcome these difficulties by limiting the configurations of the ribbed plates and to be content with relatively simple configurations. Due to these difficulties in the scientific literature, till recently, little work has been done using analytical methods of calculation. In article [4] considers a ribbed plate with its structural orthotropy and analyzes its stressed state by analytical, numerical (finite element method) and experimental methods. It has been proved that the reinforcement of the plates with ribs of constant cross-section allows significant reduction of stress in its sections in comparison to an un-supported plate. It has also been noted that the literature on the analytical calculation of the stress-strain state of ribbed plates is quite scanty.

The work [5] is devoted consider shells of a stepped variable thickness when a thickness variation is set by means of unit bar graph functions equal to a difference of two unit functions. It enables for considering ribs, reinforcement plates and cutouts in one structure; a rib and shell contact is arranged along a strip.

In the process of performing dynamic calculations of the elements of structural engineering, the study of their natural vibrations along with the determination of natural frequencies and their natural forms, plays a large role [6, 7]. The same is true for ribbed plates and shells, since the reinforcements change both the spectrum of natural frequencies and the shape of the vibrations [8]. In this direction, one can note articles [9, 10], where the free vibrations of circular and annular plates reinforced on external contours were studied.

Some questions of the dynamic stability of reinforced orthotropic gentle shells of double curvature and viscoelastic flexible plates of variable stiffness under compression were studied in [11, 12]. In the work [11] explored orthotropic shallow shells of double curvature, as well as cylindrical panels that are reinforced from the concave side by an orthogonal grid of stiffeners. The external transverse load acting on the structure is uniformly distributed and has a linear dependency on time. A geometrically nonlinear variant of the model which also takes into account orthotropy of the material and transverse shears are considered. The model is presented as a functional of total deformation energy of the shell. In the paper [12] the dynamic stability of viscoelastic plates of variable stiffness is analyzed. The deflections are described by partial integro-differential equations of motion. The Bubnov–Galerkin method based on monomial and polynomial approximation of deflections is used to reduce the problem to ordinary integro-differential equations with time as an independent variable.

The complexity of analytical calculations forced the authors to limit themselves to a relatively small amount by taking into account the physical and mechanical properties of materials. Therefore, in many studies, numerical methods have been used to solve such problems [13, 14]. For specific ribbed plates, some questions of the numerical calculation of the dispersion curve and the ways to solve them using the finite element method were presented in the scientific work of Finnveden, S. [15]. Based on the obtained analytical, numerical and experimental results, a comparative analysis has been made. The features of wave propagation in directions parallel to the ribs were investigated numerically.

Some problems in solving applied problems using numerical methods, in particular, the finite difference method, for solving the dynamics problems of ribbed rectangular and round plates, plates and shells under the action of pulsed loads were considered in [16–18]. The dynamic behavior of ribbed plates and shells under pulsed loading was also studied by [18]. The effectiveness of the various methods for modeling the influence of reinforcing elements using the generalized Dirac function was analyzed.

A review and some analysis of scientific papers devoted to the method of numerical calculations of various aspects of ribbed structures are available were made in [19] The ideas underlying some numerical developments are related to the spectral finite element or wave methods of finite elements can be viewed in [20]. Numerical calculations of the required parameters are a relatively new and promising area of research into the behavior of ribbed structural elements and, in particular, the plates [21, 22].

The dynamic behavior of a ribbed plate over a surface that moves a linear distributed load studied by [23]. The paper [24], based on the geometrically nonlinear theory of deformation of Mindlin–Reissner shells, analyzes the stress-strain state of shallow shell structures of double curvature, reinforced by the concavity side with a different number of edges.

There have been numerous publications and a continuous expansion of the field of applicability of ribbed plates and shells. However, the problem of formulating more refined models which describe the dynamic processes in them and search for effective analytical methods for solving the corresponding initial-boundary value problems of mathematical physics with allowance for nonlinear properties, such as boarding and ribs, still persists.

Thus, it can be noted that in the study of dynamic processes occurring in ribbed structural elements under the action of pulsed and other fleeting loads, plastic properties are rarely taken into account due to mathematical difficulties. Therefore, to date, a small number of works in the scientific literature have

concerned themselves with the analytical calculation of ribbed plates and shells which take into account the plastic properties of their material.

The present article is devoted to the numerical calculation of a round plate reinforced by a finite number of annular ring stiffeners and also taking into account for the elastoplastic properties of the plate and ribs materials.

## 2. Methods

### 2.1. Mathematical model of the problem

In a cylindrical coordinate system  $(r, \varphi, z)$ , a round elastoplastic plate is considered, pinched at the edge and reinforced by the ring stiffeners. In this case, the  $z$ -axis is directly perpendicular to the plane of the plate. It is believed that the structure consists of a skin and rigidly reinforced ribs to it, the materials of which are the same and obey Hooke's law. The ribs have quadrangular cross sections and are attached to the inner surface of the plate.

A pulsed load  $P(t)$  acting on the outer surface of the plate excites oscillations of the plate. The cross sections of the ribs are the same and constant (Fig. 1).

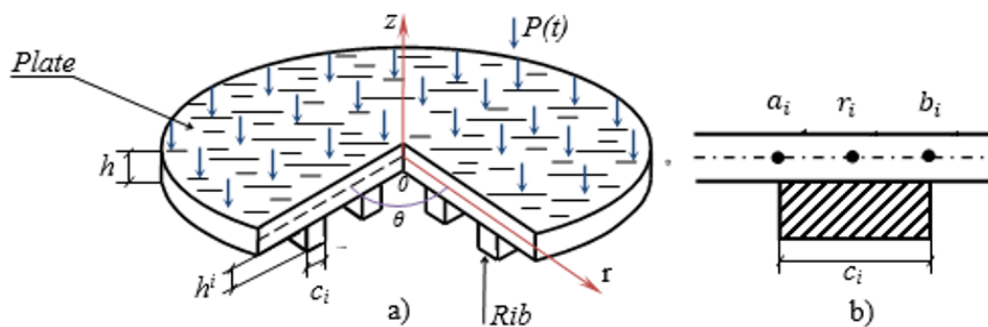


Figure 1. General view of the ribbed plate (a) and cross section of the ribs (b).

The height of the ribs and their location  $H(r_i)$  is determined by using the unit column functions  $\delta(r - r_i)$

$$H(r) = \sum_{i=1}^m h^i \delta(r - r_i), \quad \delta(r - r_i) = \begin{cases} 0, & r < a_i, r > b_i, \\ 1, & a_i < r < b_i, \end{cases}$$

Here  $a_i = r_i - c/2$ ;  $b_i = r_i + c/2$ ;  $r_i$  - is the coordinate of the midpoint of the contact of the  $i$ -th rib and casing;  $h$  and  $c$  are the height and width of the ribs;  $m$  is the number of ribs;

For describing the stress-strain state of the plate, we use the Timoshenko type - nonlinear theory of plate's vibration. Given the asymmetry of the problem, the equations of motion of the plate can be written as follows [1]:

$$\begin{aligned} (N_1 r)' - N_2 &= r \rho \left[ \frac{\partial^2 u}{\partial t^2} (h + F) + \frac{\partial^2 \psi}{\partial t^2} S \right]; \quad (rQ)' + (N_1 r w')' = r \rho \frac{\partial^2 w}{\partial t^2} (h + F) - rP; \\ (rM_1)' - M_2 - rQ &= r \rho \left[ \frac{\partial^2 \psi}{\partial t^2} \left( \frac{h^3}{12} + J \right) + \frac{\partial^2 u}{\partial t^2} S \right], \end{aligned} \quad (1)$$

where  $\rho$  is the density of the plate material;  $h$  is the thickness of the skin;

$$F = \sum_{i=1}^m F^i(r) \delta(r - r_i); \quad S = \sum_{i=1}^m S^i(r) \delta(r - r_i); \quad J = \sum_{i=1}^m J^i(r) \delta(r - r_i);$$

$F^i(r)$ ,  $S^i(r)$ ,  $J^i(r)$  are accordingly, the cross-sectional area, the static moment, and the moment of inertia of the section relative to the coordinate axis of the element of the  $i$ -rib, with a width equal to unity and height  $h^i(r)$  in the section  $r = \text{const}$ ;  $P(t)$  - is the function of the external load.

Boundary conditions for the structure under consideration:

a) conditions of hard pinching at the edge of the plate:  $u = w = \psi = 0$ ;

b) the conditions of symmetry in the center of the plate:  $u = \frac{\partial w}{\partial r} = \psi = 0$  at  $r = 0$ .

The initial conditions characterizing the state of the plate at  $t = 0$  are assumed to be zero, i.e.  $u = w = 0$ .

## 2.2. Accounting for plastic deformations

The displacements of an arbitrary point of the normal to the middle surface of the plate with the  $z$  coordinate are as in [25]

$$u^z = u + z\psi, \quad w^z = w$$

in accordance with taking into account the axisymmetric loading

$$v^z = v = 0,$$

where  $u$ ,  $v$ ,  $w$  are the displacements of the points of the middle surface of the plate along the coordinate axes;  $\psi$  is the angle of rotation of the normal to the median surface of the plate.

Deformation

$$\varepsilon_1 = \varepsilon_1^0 + z\varepsilon_1^1, \quad \varepsilon_2 = \varepsilon_2^0 + z\varepsilon_2^1$$

are expressed through the displacements  $u$ ,  $w$  and the angle of rotation of the normal to the median surface  $\psi$  as follows:

$$\varepsilon_1^0 = \frac{\partial u}{\partial r} + \frac{1}{2} \left( \frac{\partial w}{\partial r} \right)^2, \quad \varepsilon_2^0 = \frac{u}{r}, \quad \varepsilon_1^1 = \frac{\partial \psi}{\partial r}, \quad \varepsilon_2^1 = \frac{\psi}{r}, \quad \varepsilon_{13}^0 = \frac{\partial w}{\partial r} + \psi.$$

To describe the dynamic deformation beyond the elastic limit, we use the theory of plastic flow [26]. Focusing on the step-by-step method of solving problems, we divide the loading time into  $N$  small, numbered in increasing order of steps. The increment of plastic deformation at step  $n$  is denoted by

$$\Delta_n \varepsilon_\alpha^p, \quad (n = 1, 2, \dots, N; \alpha = 1, 2, 13).$$

An algorithm for calculating plastic deformations of a plate is constructed in the light of [26, 27]. First find  $\sigma_1$  and  $\sigma_2$ . In this case, the values of plastic deformation at the  $m$ -th step of loading are used. From the stresses thus found, it is possible to determine the stress intensity:

$$\sigma_i^{(\gamma)} = \sqrt{\sigma_1^2 + \sigma_2^2 - \sigma_1 \sigma_2},$$

$\gamma$  is the order of approximation to the strain diagram  $\gamma = 1, 2, 3, \dots$ .

If  $\sigma_i^{(1)}$  at the considered point of the grid region of the plate for  $t > (n+1)\tau$  is less than the value  $\sigma_i$  calculated at step  $n$ , then the material is elastically unloaded at the point and we proceed to consider the next node or layer of the grid. Otherwise, we look for the increment  $\Delta_{n+1} \varepsilon_i^p$ , which is written in the form

$$\sum_{L=1}^{\gamma} \Delta_{n+1}^L \varepsilon_i^p, \text{ after which we find the following plastic strains}$$

$$\Delta_{n+1}^{\gamma} \varepsilon_1^p = \Delta_{n+1}^{\gamma} \varepsilon_i^p (\sigma_1 - \sigma_2 / 2) / \sigma_i^{(\gamma)}; \Delta_{n+1}^{\gamma} \varepsilon_2^p = \Delta_{n+1}^{\gamma} \varepsilon_i^p (\sigma_2 - \sigma_1 / 2) / \sigma_i^{(\gamma)}. \quad (2)$$

Here the increments of plastic deformation are determined from the following relation

$$\Delta_{N+1}^{\gamma} \varepsilon_i^p = \left(1 - \frac{E_1}{E}\right) \frac{\sigma_i^{(\gamma)}}{E} - \frac{E_1}{E} \left( \sum_{n=1}^N \Delta_n \varepsilon_i^p + \sum_{L=0}^{\gamma-1} \Delta_{N+1}^L \varepsilon_i^p \right) - \varepsilon_i^y,$$

where  $E_1 = \frac{4}{3}(\sigma_P - \sigma_T) \frac{100}{\delta}$  is the hardening modulus,  $\sigma_T$  is the yield strength,  $\sigma_P$  is the tensile strength and  $\delta$  is the residual elongation, which were determined according to the references.

Stresses are found by the stress intensity formula. If in the next iteration,  $\sigma_i^{(\gamma)}$  exceeds the diagrammatic stress values at the found level of plastic deformations, the calculations are repeated. The approach to the deformation diagram continues until the stresses  $\sigma_1, \sigma_2$  differ from those calculated at the previous iteration by less than 0.5 ... 1.0 MPa, after which the transition of consideration to the next node or time layer takes place, i.e. all calculations are performed before the condition  $|\Delta_{N+1}^{\gamma} \varepsilon_{rj}^p - \Delta_{N+1}^{\gamma-1} \varepsilon_{rj}^p| < \delta$ , is satisfied, which provides a sufficient approximation to the deformation diagram.

At the  $N$ -th loading step, the total strain  $\varepsilon_i$  is represented as the sum of the elastic and plastic components

$$\varepsilon_l = \varepsilon_i^y + \sum_{n=1}^N \Delta_n \varepsilon_l^p, \text{ here } l=1,2,3.$$

### 2.3. Physical equations

The relationship between stress and strain acting at the points of the sheathing and ribs are written as

$$\begin{aligned} \sigma_1 &= \frac{E}{1-\mu^2} \left[ \varepsilon_1 + \mu \varepsilon_2 - \sum_{n=1}^N (\Delta_n \varepsilon_1^p + \mu \Delta_n \varepsilon_2^p) \right]; \\ \sigma_2 &= \frac{E}{1-\mu^2} \left[ \varepsilon_2 + \mu \varepsilon_1 - \sum_{n=1}^N (\Delta_n \varepsilon_2^p + \mu \Delta_n \varepsilon_1^p) \right]; \quad \sigma_{13} = \frac{E}{2(1+\mu)} \left[ \varepsilon_{13} - \sum_{n=1}^N \Delta_n \varepsilon_{13}^p \right]; \end{aligned} \quad (3)$$

where  $\varepsilon_{13} = f(z) \left( \frac{\partial w}{\partial r} + \psi \right)$ ;  $E, \mu$  is the elastic modulus and Poisson's ratio of the material of the lining or ribs [26];  $f(z)$  is a function characterizing the law of the distribution of stresses  $\sigma_{13}$  across the plate thickness:  $f(z) = f_0(z)$  for the smooth part;  $f(z) = f_1(z)$  at the points where the edges are located:

$$f_0(z) = 6 \left[ 0.25 - \left( \frac{z}{h} \right)^2 \right], \quad f_1(z) = \frac{3h(h+2H)}{2(h+H)^2} \left( 1 + 2 \frac{z}{h} \right) \left[ 1 - 2 \frac{z}{h+2H} \right],$$

where  $H$  is the height of the rib.

The forces, transverse forces and moments per unit length of the section, acting in the section of the plate, reinforced by ribs, have the following form:

$$N_1 = N_1^0 + N_1^R, \quad N_2 = N_2^0 + N_2^R, \quad M_1 = M_1^0 + M_1^R, \quad M_2 = M_2^0 + M_2^R, \quad Q = Q^0 + Q^R.$$

The forces, transverse forces and moments related to a smooth plate have the following form [1]:

$$\begin{aligned}
N_1^0 &= Eh \left[ \varepsilon_1^0 + \mu \varepsilon_2^0 - \frac{1}{1-\mu^2} \sum_{n=1}^N \left( \Delta_n^1 \varepsilon_1^p + \mu \Delta_n^1 \varepsilon_2^p \right) \right]; \\
N_2^0 &= Eh \left[ \varepsilon_2^0 + \mu \varepsilon_1^0 - \frac{1}{1-\mu^2} \sum_{n=1}^N \left( \Delta_n^1 \varepsilon_2^p + \mu \Delta_n^1 \varepsilon_1^p \right) \right]; \\
M_1^0 &= D \left[ \varepsilon_1^1 + \mu \varepsilon_2^1 - \frac{Eh}{1-\mu^2} \sum_{n=1}^N \left( \Delta_n^2 \varepsilon_1^p + \mu \Delta_n^2 \varepsilon_2^p \right) \right]; \\
M_2^0 &= D \left[ \varepsilon_2^1 + \mu \varepsilon_1^1 - \frac{Eh}{1-\mu^2} \sum_{n=1}^N \left( \Delta_n^2 \varepsilon_2^p + \mu \Delta_n^2 \varepsilon_1^p \right) \right]; \\
Q^0 &= \frac{k^2 Eh}{2(1+\mu)} \varepsilon_{13}^0 - \frac{E}{2(1+\mu)} \int_{-h/2}^{h/2} f(z) \sum_{n=1}^N \Delta_n \varepsilon_{13}^p dz.
\end{aligned} \tag{5}$$

Here  $E, \mu$  are the elastic modulus and Poisson's ratio of the material of a smooth plate

$$D = \frac{Eh^3}{12(1+\mu)};$$

$f(z)$  is a function characterizing the law of stress distribution over the thickness of the structure:

$$\Delta_n^1 \varepsilon_l = \frac{1}{h} \int_{-h/2}^{h/2} \Delta_n \varepsilon_l^p dz; \quad \Delta_n^2 \varepsilon_l = \frac{1}{h} \int_{-h/2}^{h/2} \Delta_n \varepsilon_l^p dz; \quad l = 1, 2. \tag{6}$$

The forces, moments, and shear forces acting in the sections of the ribs have the following form:

$$\begin{aligned}
N_1^R &= \int_{h/2}^{h/2+H} \sigma_1^R dz = A \left( \varepsilon_1^0 + \mu \varepsilon_2^0 \right) + B \left( \frac{\partial \psi}{\partial r} + \mu \frac{\psi}{r} \right) - G \sum_{n=1}^N \left( \Delta_n^3 \varepsilon_1^p + \mu \Delta_n^3 \varepsilon_2^p \right); \\
N_2^R &= \int_{h/2}^{h/2+H} \sigma_2^R dz = A \left( \varepsilon_2^0 + \mu \varepsilon_1^0 \right) + B \left( \frac{\psi}{r} + \mu \frac{\partial \psi}{\partial r} \right) - G \sum_{n=1}^N \left( \Delta_n^3 \varepsilon_2^p + \mu \Delta_n^3 \varepsilon_1^p \right); \\
M_1^R &= \int_{h/2}^{h/2+H} \sigma_1^R z dz = B \left( \varepsilon_1^0 + \mu \varepsilon_2^0 \right) + C \left( \frac{\partial \psi}{\partial r} + \mu \frac{\psi}{r} \right) - G \sum_{n=1}^N \left( \Delta_n^4 \varepsilon_1^p + \mu \Delta_n^4 \varepsilon_2^p \right); \\
M_2^R &= \int_{h/2}^{h/2+H} \sigma_2^R z dz = B \left( \varepsilon_2^0 + \mu \varepsilon_1^0 \right) + C \left( \frac{\psi}{r} + \mu \frac{\partial \psi}{\partial r} \right) - G \sum_{n=1}^N \left( \Delta_n^4 \varepsilon_2^p + \mu \Delta_n^4 \varepsilon_1^p \right); \\
Q^R &= \int_{h/2}^{h/2+H} \sigma_{13}^R dz = D_{13} \left( \frac{\partial w}{\partial r} + \psi \right) - G_{13} \int_{h/2}^{h/2+H} f_1(z) \sum_{n=1}^N \Delta_n \varepsilon_{13}^p dz;
\end{aligned} \tag{7}$$

Here

$$\Delta_n^3 \varepsilon_l = \int_{h/2}^{h/2+H} \Delta_n \varepsilon_l^p dz; \quad \Delta_n^4 \varepsilon_l = \int_{h/2}^{h/2+H} \Delta_n \varepsilon_l^p z dz; \quad l = 1, 2; \quad A = GF; \quad B = GS; \quad D_{13} = G_{13}H(r);$$

$$C = GJ; \quad G = \frac{E}{1-\mu^2}; \quad G_{13} = \frac{k^2 E}{2(1+\mu)}; \quad k^2 = \frac{5}{6}; \quad E, \mu, G \text{ are elastic constants of the material of}$$

the ribs.

#### 2.4. Numerical methods for solving the problem

Below we briefly describe the main points of the finite difference method as applied to the equations of the theory of ribbed plates (1) - (7). The scheme of the numerical solution of the problem by the finite difference method is based on the determination of displacements and rotation angles at the nodes of the grid, and deformations, forces, moments and transverse forces - in the center of the element [27].

The approximation of derivatives in an element has the following form:

$$\left[ \frac{\partial f}{\partial r} \right]_{i+1/2} = \frac{f_{i+1} - f_i}{\Delta r_i}, \quad (8)$$

where  $\Delta r_i = r_i - r_{i-1}$ ;  $f_i$  is function values in points  $r_i$ ,  $1 \leq i \leq N + 1$ .

To approximate the equations of motion (1), which are centered at the nodal points, the central differences are used:

$$\left[ \frac{\partial f}{\partial r} \right]_i = \frac{f_{i+1/2} - f_{i-1/2}}{\Delta r_{i+1/2}} \quad (9)$$

non-differentiable terms in equations (1) are reduced to a node by averaging the corresponding values in the elements:

$$f_i = \frac{f_{i+1/2} + f_{i-1/2}}{2}. \quad (10)$$

The time derivatives were approximated by expressions of the form

$$\left[ \frac{\partial^2 w}{\partial t^2} \right]_i^n = \frac{w_i^{n+1} - 2w_i^n + w_i^{n-1}}{\tau^2}, \quad (11)$$

where  $\tau$  is time step,  $n$  is index defining the time layer.

The right side of the 1st, 3rd equations of system (1) contains two unknown functions. Therefore, before passing to finite-difference analogues, the 1st and 3rd equations must be solved as a system of

algebraic equations for  $\frac{\partial^2 u}{\partial t^2}$  and  $\frac{\partial^2 \psi}{\partial t^2}$ . Then, in differential equations, replace the derivatives with

relations of the type (8) - (11). The resulting finite-difference analogue of system (1) has the form

$$\begin{aligned} u_i^{n+1} &= 2u_i^n - u_i^{n-1} + \tau^2 \left\{ \frac{1}{a} U_i^n - \frac{b}{ac - b^2} \left( \psi_i^n - \frac{b}{a} U_i^n \right) \right\}; \\ w_i^{n+1} &= 2w_i^n - w_i^{n-1} + \frac{\tau^2}{a} W_i^n; \quad \psi_i^{n+1} = 2\psi_i^n - \psi_i^{n-1} + \frac{\tau^2}{ac - b^2} \left( \Psi_i^n - bU_i^n \right), \end{aligned} \quad (12)$$

where  $a = \rho(h + F)$ ,  $b = \rho S$ ,  $c = \rho(h^3 / 12 + J)$ ;

$$\begin{aligned} U_i^n &= \frac{(rN_1)_{i+1/2}^n - (rN_1)_{i-1/2}^n}{\Delta r_{i+1/2} r_{i+1/2}} + \frac{(N_2)_{i+1/2}^n - (N_2)_{i-1/2}^n}{2r_{i+1/2}}; \\ W_i^n &= \frac{(rQ)_{i+1/2}^n - (rQ)_{i-1/2}^n}{\Delta r_{i+1/2} r_{i+1/2}} + \frac{w_i^n - w_{i-1}^n}{\Delta r_i} \frac{1}{\Delta r_{i+1/2}} \frac{(rN_1)_{i+1/2}^n - (rN_1)_{i-1/2}^n}{\Delta r_{i+1/2}} + \\ &\quad + \frac{w_{i+1}^n - 2w_i^n - w_{i-1}^n}{(\Delta r_i)^2} \frac{(N_1)_{i+1/2}^n + (N_1)_{i-1/2}^n}{2} + P_{i+1/2}^n; \\ \Psi_i^n &= \frac{(rM_1)_{i+1/2}^n - (rM_1)_{i-1/2}^n}{\Delta r_{i+1/2} r_{i+1/2}} - \frac{(M_2)_{i+1/2}^n + (M_2)_{i-1/2}^n}{2r_{i+1/2}} - \frac{Q_{i+1/2}^n + Q_{i-1/2}^n}{2}. \end{aligned}$$

From relations (2) and (3) we obtain finite-difference expressions for calculating deformations

$$\begin{aligned} (\varepsilon_1)_{i+1/2}^n &= \frac{u_{i+1}^n - u_i^n}{\Delta r_{i+1/2}} + \frac{1}{2} \left( \frac{w_{i+1}^n - w_i^n}{2\Delta r_{i+1/2}} \right)^2; \quad (\varepsilon_2)_{i+1/2}^n = \frac{u_{i+1}^n + u_i^n}{2r_{i+1/2}}; \\ (\varepsilon_{13})_{i+1/2}^n &= f(z) \left( \frac{w_{i+1}^n - w_i^n}{\Delta r_{i+1/2}} + \frac{\psi_{i+1}^n + \psi_i^n}{2} \right); \quad (\varepsilon_1^z)_{i+1/2}^n = (\varepsilon_1)_{i+1/2}^n + z \frac{\psi_{i+1}^n - \psi_i^n}{\Delta r_{i+1/2}}; \\ (\varepsilon_2^z)_{i+1/2}^n &= (\varepsilon_2)_{i+1/2}^n + z \frac{\psi_{i+1}^n + \psi_i^n}{2r_{i+1/2}}. \end{aligned} \quad (13)$$

The values of stresses, forces, moments and cutting forces are found by formulas (4) - (7), using expressions as in (13).

Formulas of (12) apply only to the internal points of the computational domain. For determining the values of the functions at the boundary points, we use the boundary conditions a) and b) described in the previous section. The hard pinching conditions approximated exactly, and the symmetry conditions are written in finite differences using the following expression:

$$\left[ \frac{\partial w}{\partial r} \right]_1^n = \frac{3w_1^n - 4w_2^n + w_3^n}{2\Delta r_2}. \quad (14)$$

The grid functions on two adjacent time layers, necessary to start the calculations, give the initial conditions, from which we obtain equalities of the form

$$w_i^1 = w_i^2 = 0. \quad (15)$$

Using the above equalities, we can find  $u_i^n$ ,  $w_i^n$ ,  $\psi_i^n$  for any moment of time and any point of the difference grid.

Finite-difference expressions (8) - (12), (14) provide a 2-order approximation. Equalities (15) approximate the initial conditions with the first order of accuracy. The general discrepancy in the approximation of the boundary value problem under consideration by difference relations does not exceed  $O(\Delta r^2 + \tau^2)$ . When the grid steps tend to zero, the residuals also tend to zero. Therefore, difference equations approximate the original differential equations.

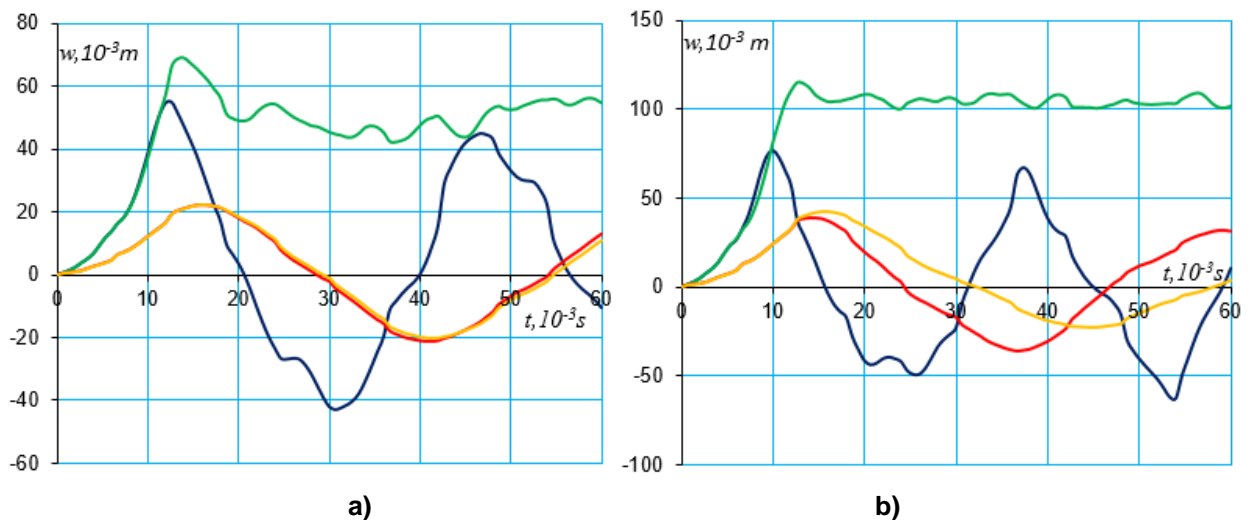
The study of the stability of difference schemes is a difficult task. It is especially difficult to solve for circuits approximating multidimensional nonlinear boundary value problems. The stability of the circuit investigation (12) is studied by numerical experiments. The sighting values of the grid steps ensuring the stability of the calculations found from the Courant condition, are as follows  $\tau_1 \leq \Delta r / c_1$  here

$$c_1 = \sqrt{E / \rho(1 - \mu^2)}.$$

Thus, the solution of differential equations (1) is reduced to calculations using recurrence formulas (12).

### 3. Results and Discussions

The deflections of the central point of an unreinforced and reinforced by four edges of plates for different values of the amplitude  $P_0$  of the external exponential load are calculated. The results are presented in Figs. 2-4 in the form of graphs according to the deflection  $w$  and time  $t$ , and various values of the amplitude of the external exponential load is equal to 2.5; 5; 7.5; 10 MPa.



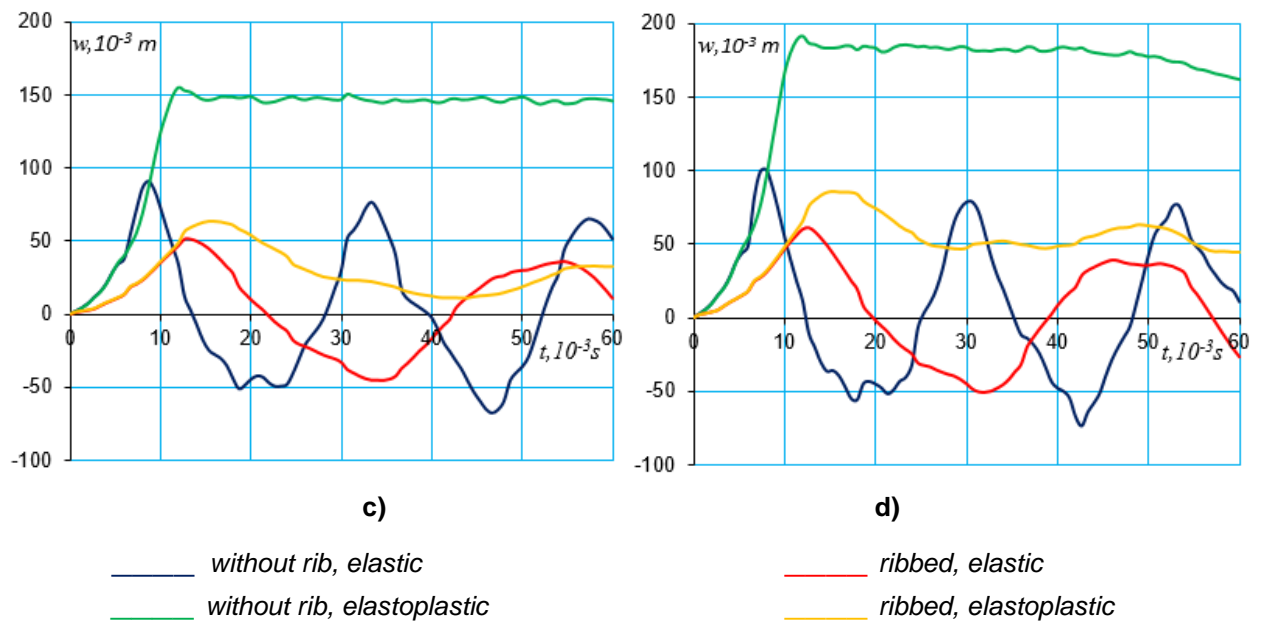


**Figure 2. According to the deflection of the central point reinforced by four ribs and unreinforced plates at a)  $P_0 = 2.5$  MPa; b)  $P_0 = 5$  MPa; c)  $P_0 = 7.5$  MPa; d)  $P_0 = 10$  MPa.**

Fig. 2,a shows graphs of the deflection of central points reinforced by four ribs and unreinforced plates with an external load amplitude of 2.5MPa. From the graphs presented, it follows that for an unreinforced plate, taking into account plastic deformation, leads to an increase in the deflection values for all time instants. For example, the maximum values of the deflection of the central point calculated by the elastic and elastic-plastic models differ by 32%. In the case when the plate is reinforced by 4 ribs, the graphs of the dependences of the deflection on time, in the elastic and elastic-plastic cases, merge. This shows that under external exponential loads, the amplitudes of which do not exceed 2.5MPa, the influence of plastic deformation can be neglected to calculate the plates reinforced by four edge of the plate. In a particular case, for the elastic model of the plate and stiffening ribs, the results obtained coincide with the analogous results of the work [28].

At an external load with an amplitude of 5MPa and higher, Fig. 2 b-d, the effect of plastic deformation on the deflection cannot be neglected. As the results show in Fig. 2 b-d, the larger the amplitude of the external load the higher is the deflection obtained by the elastic-plastic model as compared to the elastic model, for example, the maximum value of the elastic-plastic deformation of a smooth plate at  $P_0 = 2.5$ MPa is  $\approx 0.068$  m; at  $P_0 = 5$ MPa it is equal  $t_0 \approx 0.12$ m; at  $P_0 = 7.5$ MPa it is equal  $t_0 \approx 0.151$ m; and at  $P_0 = 10$ MPa it is equal  $t_0 \approx 0.190$  m.

With an increase in amplitude of the external load, the difference between the values of deflection of the central point calculated by the elastic and elastic-plastic models increases. For example, for a point in time equal to 0.003 s the specified difference reaches: a) at  $P_0 = 5$  MPa -  $t_0 \approx 0,015$  m; b) at  $P_0 = 7.5$  MPa -  $t_0 \approx 0.07$  m; c) at  $P_0 = 10$  MPa -  $t_0 \approx 0.098$  m.

The graphs of the deflection of the central point of both smooth and reinforced plates, obtained on the basis of the elastic model, for all values of the external load, are pronouncedly sinusoidal in nature. At the same time, the graphs obtained on the basis of the elastic-plastic model, having reached a relative maximum under the action of average load (Fig. 2 b, c), have a straightforward character, with a transition to a slowly descending curve with increasing external load (Fig. 2 d).

Fig. 3a) shows graphs of the dependence of the deflection of the central point of the plate on the radial coordinate with an external load amplitude equal to  $P_0 = 2.5$  MPa, calculated by the elastic-plastic model. The cases of non-reinforcement and reinforcement of the plate by one ( $n = 1$ ), two ( $n = 2$ ) and four ( $n = 4$ ) ribs for the time  $t = 0.0012$  s were also considered. The graphs show the effect of reducing deflection by reinforcing the plate with stiffeners, which is 43% for one, 62% for two, and 73% for four reinforcing ribs. From this it follows that the calculation method allows you to achieve the desired value of the deflection by varying the number of ribs.

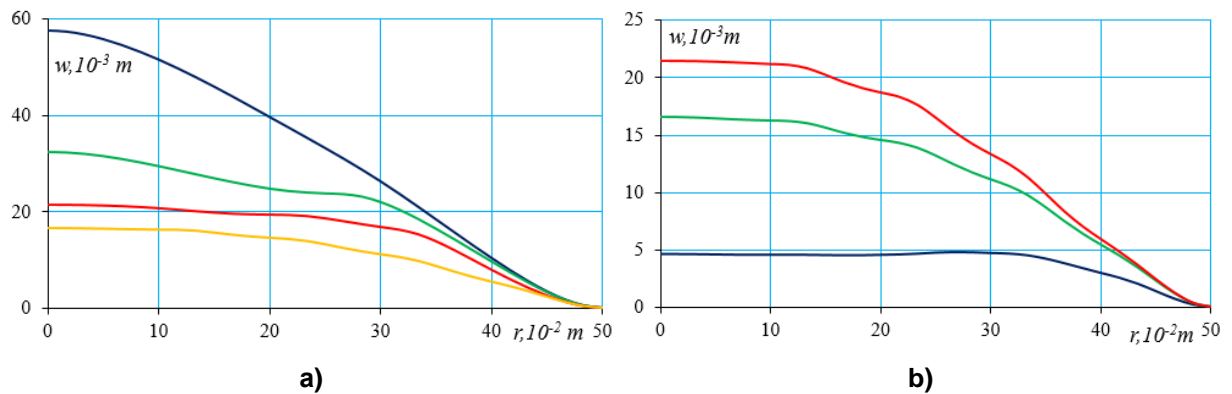


**Figure 3. According to the deflection on the radial coordinate at  $P_0 = 2.5\text{MPa}$**

**a)  $n = 1,2,4; t = 0.0012\text{ s}$  ( \_\_\_ without rib, \_\_\_ 1rib, \_\_\_ 2rib, \_\_\_ 4rib);**

**b)  $n = 4$  ( \_\_\_  $t = 0.0006\text{s}$ , \_\_\_  $t = 0.0012\text{s}$ , \_\_\_  $t = 0.0018\text{s}$ ).**

Fig. 3b) shows the plots of deflection of the central point reinforced by four ( $n = 4$ ) plate edge on the radial coordinate at different points in time:  $t = 0.0006\text{s}$ ;  $0.0012\text{ s}$ ;  $0.0018\text{s}$ . Calculations show that with an increase in the duration of the external load, the deflection values increase, for example, the deflection value at the time  $t = 0.0018\text{ s}$  is four times higher than the value at the time  $t = 0.0006\text{ s}$ , i.e. with an increase in the action of an external force by three times, the deflection value increases by four times.

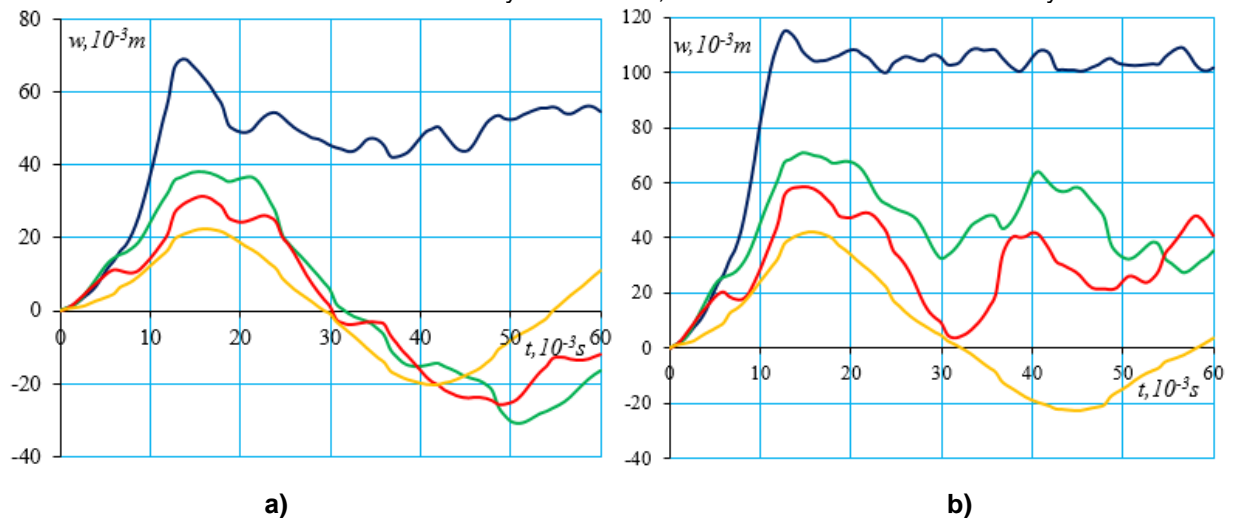


**Figure 4. According to deflection on time at  $n = 1,2,4$ : a)  $P_0 = 2.5\text{ MPa}$ ; b)  $P_0 = 5\text{ MPa}$**

**( \_\_\_ without rib, \_\_\_ 1 rib, \_\_\_ 2rib, \_\_\_ 4 rib).**

Fig. 4 a) and Fig. 4b) show the graphs of deflection of the central point of unreinforced and reinforced by one ( $n=1$ ), two ( $n=2$ ) and four ( $n=4$ ) stiffeners for different external load amplitudes equal to - a) at  $P_0 = 2.5\text{ MPa}$ ; and b) at  $P_0 = 5\text{ MPa}$ . The deflection on time in all cases are oscillatory in nature. For an unreinforced plate in both cases of external load, these oscillations, after reaching the maximum value, have relatively small oscillation amplitudes. In reinforced plates this does not occur. Here, the oscillation amplitude is much higher. The difference between the deflection values at the maximum and minimum points in the case of  $n=1$  and  $P_0 = 2.5\text{ MPa}$  is approximately  $0.068\text{ m}$  at  $P_0 = 5\text{ MPa}$ ; and at  $P_0 = 5\text{ MPa}$  it is equal to  $0.032\text{ m}$  etc. A comparison of the dependences in Fig. 4 a) and Fig. 4 b) shows that with an increase in the amplitude of the external load by a factor of two, in the case of an unsupported plate, the deflection increases by 1.65 times; if there are two reinforcement ribs this indicator decreases by 1.5 times.

The forces and moments in unreinforced and reinforced plates are calculated from the elastic and elastic-plastic models, which confirm the above conclusions. In fact, the proposed elastoplastic model for calculating a reinforced circular plate allows to determine the deflections, forces and moments at arbitrary points of the plate by coordinate and time. Comparative analysis of constitutive relations and the obtained numerical results of calculating the plate deflection by elastic and elastic-plastic models show that the proposed model is a generalization of the elastic model of the work [1] for the case of taking into account the plastic properties of materials of a circular plate and stiffening ribs. In this case, the proposed numerical

method for calculating a reinforced plate based on an elastoplastic model, in the absence of reinforcing stiffening ribs, coincides with the method for calculating elastic-plastic plates proposed in the work [26].

## 4. Conclusions

The conclusions arrived at in the paper are the following:

- an elastoplastic model for calculating a round discretely finned plate is proposed, which allows one to determine the deflection, forces and moments at the points of the plate.
- the deflections of the central point of an unreinforced and reinforced by four edges of plates for different values of the amplitude  $P_0$  of the external exponential load are calculated. The results are presented in the form of graphs of the dependence of the deflection  $w$  and time  $t$  for various values of the amplitude of the external exponential load equal to 2.5; 5; 7.5; and 10 MPa;
- the maximum deflection values of the central point of the plate, calculated by elastic and elastoplastic models, differ by 32 %. In the case when the plate is supported by 4 ribs, the graphs of the dependences of the deflection on time in the elastic and elastoplastic cases merge. This shows that under external exponential loads, the amplitudes of which do not exceed 2.5 MPa, the influence of plastic deformation can be neglected for calculating the plate, backed by a large number of stiffeners;
- numerical calculations of the deflection, forces, and moments at the points of the fin plate show that the proposed model and calculation method allow us to achieve the desired value of deflection by varying the number of ribs.

## References

1. Il'in, V.P., Karpov, V.V. Ustoychivost rebristych obolochek pri bolshich peremesheniyyakh [Stability of ribbed shells for large displacements]. Leningrad: Stroyizdat, 1986. 168 p. (rus)
2. Karpov, V.V. Prochnost i ustoychivost podkreplennykh obolochek vrasheniya: v 2 chastyakh. Chast 1: Modeli i algoritmy issledovaniya prochnosti i ustoychivosti podkreplennykh obolochek vrasheniya [Strength and Stability of Reinforced Shells of Revolution, in 2 parts, Part 1: Models and Algorithms of Studying the Strength and Stability of Reinforced Shells of Revolution]. Moskov: Fizmatlit, 2010. 288 p. (rus)
3. Karpov, V.V., Semenov, A.A. Mathematical model of deformation of orthotropic reinforced shells of revolution. Magazine of Civil Engineering. 2013. No. 5. Pp. 100–106. DOI: 10.5862/MCE.40.11
4. Popa, C.T., Iatan, R.T., Manescu, C.I. Stress states in plane and ribbed circular plates. Journal Proceedings in Manufacturing Systems. 2013. 8(1). Pp. 53–58.
5. Karpov, V.V. Models of the shells having ribs, reinforcement plates and cutouts. International Journal of Solids and Structures. 2018. 146(1). Pp. 117–135. DOI: 10.1016/j.ijsolstr.2018.03.024Get rights and content
6. Khodzhaev, D., Abdikarimov, R., Vatin, N. Nonlinear oscillations of a viscoelastic cylindrical panel with concentrated masses. MATEC Web of Conferences. EECE-2018. 2018. 245. 01001. DOI: 10.1051/mateconf/201824501001
7. Khudoynazarov, K.K., Burkutboyev, Sh.M. Mathematical modeling of the rotating cylindrical shell torsional vibrations factored in the internal viscous fluid. Matematicheskoe Modelirovanie i Chislennyye Metody. 2017. No. 16. Pp. 31–47. DOI: 10.18698/2309-3684-2017-4-3147
8. Ichchou, M.N., Berthaut, J., Collet, M. Accepted for publication. Multi-mode wave propagation in ribbed plates, Part II, Predictions and comparisons. International Journal of Solids and Structures. 2008. 45(5). Pp. 1196–1216. DOI: 10.1016/j.ijsolstr.2007.08.020
9. Stuart, R. J., Carney, J.F. Vibration of edge reinforced annular plates. Journal of Sound and Vibration. 1974. 35(1). Pp. 23–33.
10. Stuart, R.J., Sarney, J.F. Vibration of annular plates with edge-beams. Journal AIAA. 1974. 12(1). Pp. 5–6.
11. Semenov, A.A. Dynamic buckling of stiffened orthotropic shell structures. Magazine of Civil Engineering. 2018. 82(6). Pp. 3–11. DOI: 10.18720/MCE.82.1
12. Abdikarimov, R.A., Khudayarov, B.A. Dynamic stability of viscoelastic flexible plates of variable stiffness under axial compression. International Applied Mechanics, New York. 2014. Vol. 50. No. 4. Pp. 389–398. DOI: 10.1007/s10778-014-0642-x
13. Popa C., Anghelina F.V., Despa V. Finite element and experimental analysis of stresses state for circular plates. IOP Conf. Series: Materials Science and Engineering. 444. 062019. 2018. DOI: 10.1088/1757-899X/444/6/062019.
14. Khudayarov, B.A., Ruzmetov, K., Turaev, F., Vakhobov, V., Khidoyatova, M., Mirzaev S.S., Abdikarimov, R. Numerical modeling of nonlinear vibrations of viscoelastic shallow shells. Engineering Solid Mechanics. 2020. 8(3). Pp. 199–204.
15. Finnveden, S. Spectral finite element analysis of the vibration of straight fluid-filled pipes with flanges. J. of Sound and Vibration. 1996. 199(1). Pp. 125–154. DOI: 10.1006/jsvi.1996.0602
16. Khodzhaev, D.A., Abdikarimov, R.A., Mirsaidov, M.M. Dynamics of a physically nonlinear viscoelastic cylindrical shell with a concentrated mass. Magazine of Civil Engineering. 2019. 91(7). Pp. 39–48. DOI: 10.18720/MCE.91.4
17. Loh, H.C., Carney, J.F. Vibration and Stability of Spinning Annular Plates Reinforced With Edge Beams. Journal of Applied Mechanics. 1997. 44(3). Pp. 499–501.
18. Galiev, Sh.U., Karshiev, A.B. Chislenniy analiz tochnosti modeley rebristogo sfericheskogo kupola, podverjennogo impulsnomu nagrujeniyu [Numerical analysis of the accuracy of models of a ribbed spherical dome subject to pulsed loading]. Problemi prochnosti. 1990. No. 5. Pp. 83–86. (rus)
19. Banerjee, S., Kundu, T. Elastic wave propagation in sinusoidally corrugated waveguides. Journal of Acoustical Society of America. 2006. 119 (4). Pp. 2006–2017. DOI: 10.1121/1.2172170
20. Banerjee, S., Kundu, T. Symmetric and anti-symmetric Rayleigh-Lamb modes in sinusoidally corrugated waveguides // International Journal of Solids and Structures. 2006. 43(21). Pp. 6551–6567. DOI: 10.1016/j.ijsolstr.2006.01.005.

21. Gavric L. Finite element computation of dispersion properties of thin walled waveguides. Journal of Sound and Vibration. 1994. 173 (1). Pp. 113–124
22. Houillon, L., Ichchou, M.N., Jezequel, L. Wave motion in thin walled structures. Journal of Sound and Vibration. 2005. 281(3–5). Pp. 483–507. DOI: 10.1016 / j.jsv.2004.01.020.
23. Antufiev, V.A., Egorova, O.V., Kuznetsova, E.L. Dinamika rebristoy plastini pod deystviem podvijnoy nagruzki [Dynamics of a stiffened plate under moving loads]. Izvestiya TulGU. Technicheskie nauki. 2017. No. 7. Pp. 344–350. (rus)
24. Karpov, V.V., Ignat'ev, O.V., Semenov, A.A. The stress-strain state of ribbed shell structures. Magazine of Civil Engineering. 2017. No.6. Pp. 147–160. DOI: 10.18720/MCE.74.12.
25. Galiyev, Sh.U., Babich, Y.N., Semenov, A.A., Juraxovskiy, S.V., Nechitaylo, N.V., Romashenko, V.A. Chislennoe modelirovanie volnovykh processov v ogranichennykh sredax [Numerical Simulation of wave processes in confined media]. Kyiv: Naukova Dumka, 1989. 199 p. (rus)
26. Galiyev, Sh.U. Dinamika gidrouprugoplasticheskikh system [Dynamics of hydroelastoplastic systems]. Kyiv: Naukova Dumka, 1981. 276 p. (rus)
27. Khudoynazarov, K., Abdirashidov, A. Nestatsionarnoe vzaimodeystviye uprugoplasticheski deformiruyemykh elementov konstruksiy s jidkostyu [Nonstationary interaction of elastoplastic deformable structural elements with a liquid]. Tashkent: FAN, 2005. 220 p. (rus)
28. Khalmuradov, R., Khudoynazarov, K., Nisnonov, U. Nonlinear vibrations ribbed circular plate under influence of pulse loading. International Journal of Advanced Research in Science, Engineering and Technology. 2018. 5(3). Pp. 5289–5296.

**Information about authors:**

**Rustam Khalmuradov**, Doctor of Technical Science

E-mail: [rustami@list.ru](mailto:rustami@list.ru)

**Khayrulla Khudoynazarov**, Doctor of Technical Science

ORCID: <https://orcid.org/0000-0001-8994-9738>

E-mail: [khayrullakhudoynazarov@gmail.com](mailto:khayrullakhudoynazarov@gmail.com)

**Utkir Nishanov**, PhD

E-mail: [utkir1978@mail.ru](mailto:utkir1978@mail.ru)

Received 11.05.2020. Approved after reviewing 26.04.2022. Accepted 12.06.2022.



Research article

UDC 699.8

DOI: 10.34910/MCE.116.14



## Additional measures protecting buildings from climatic influences

T.A. Belash<sup>1</sup> , T.V. Ivanova<sup>2</sup> , D.A. Ivashintsov<sup>2</sup> 

<sup>1</sup> JSC Research Center of Construction, Moscow, Russia

<sup>2</sup> "Vedeneev VNIIG", JSC, St. Petersburg, Russia

✉ [belashta@mail.ru](mailto:belashta@mail.ru)

**Keywords:** climatic influences, negative and positive temperatures, ETFE system, dome, canopy

**Abstract.** The Russian territory is characterised by a great variety of different climatic zones with complex weather conditions. There are a large number of people living in these areas. New towns and cities are being built. Ensuring comfortable conditions for people to live and stay in the buildings of various purposes is of great importance for the implementation of social programmes adopted by the Russian government for the near future. Construction practice has developed a certain approach to the materials and structures that protect buildings from the effects of various climatic factors such as extremely high or low temperatures. However, the dramatic climate change that has been taking place on our planet in recent decades has led to additional research and the search for new structural and architectural solutions. This article presents the results of pre-design and construction solutions for public buildings in hot and harsh climates. Different materials for building envelopes are considered and thermal calculations are carried out. The ETFE membrane system is shown to be a versatile material that can be recommended for different climate zones. Particular attention is paid to additional structural measures such as the introduction of special canopies or enclosed spaces in the form of domed structures, which add a certain architectural expression to both the individual building and the group of buildings as a whole.

**Citation:** Belash, T.A., Ivanova, T.V., Ivashintsov, D.A. Additional measures protecting buildings from climatic influences. Magazine of Civil Engineering. 2022. 116(8). Article no. 11614. DOI: 10.34910/MCE.116.14

### 1. Introduction

Climatic effects are distinguished by rich variety over the vast territory of the Russian Federation: harsh climate with low temperatures, hot climate with high positive temperatures at high and low humidity, abrupt temperature changes, strong winds, cyclones, hurricanes etc. Today, scientists all over the world are noticing significant changes happening with the planet climate that may become the cause of disturbances in functioning of the planet biological and ecological systems and thus have negative impact on human health and living [1]. In this regard, it becomes of primary significance that comfortable, favorable and safe conditions are created for people to stay and work in various purpose buildings. The issue has become especially relevant since the adoption by the Government of the Russian Federation of the social and economical development programs for the nearest future of the country according to which the development of the Arctic coast, Far East, southern regions will be of special significance.

According to construction norms SP 131.13330.2020 "SNiP 23-01-99 Construction Climatology, the territory of Russia is divided into climatic zones, each one of them having different temperature and humidity characteristics".

The territories with hot climate include vast lands in the Lower Volga Region, Caspian Depression, Krasnodar Krai, Stavropol Krai, and Crimea. These regions are characterized both with humid and dry hot climate.

Certain principles and approaches to design, construction, and operation of buildings were formed in the said climatic conditions. They are stated in such documents as SanPiN 2.2.1-2.1.1.1076-01 Hygienic Requirements for Insolation and Solar Protection of Residential and Public Buildings and Territories, SP 50.13330.2012 "SNiP 23-02-2003 Heat Protection of Buildings" (2018 version with changes No. 1,2), SP 25.13330.2012 "SNiP 2.02.04-88 Bases and Foundations on Permafrost Soils, SP 370.1325800.2017 Solar Protection Devices for Buildings", etc.

The developed and tested architectural, structural and planning solutions are widely presented in various literature. Thus, in works [2–4], the issues of adaptation to climate, the peculiarities of the influence of a hot climate on construction sites in various southern countries, for example in Iran, are considered. Evaluation of the effectiveness of various constructive measures to protect buildings from a hot climate is presented in [5–7]. The issues of energy saving in the southern regions are reflected in the works [8–9]. The peculiarities of the influence of low temperatures on the building in the northern regions are presented in [10–13]. At the same time, special attention is currently paid by specialists to the constructive solutions of facade systems [14–15]. The complex of existing structural solutions and climate studies for a building can be conditionally divided into the following groups: urban planning measures, a complex of space-planning solutions and constructive measures that ensure optimal conditions for people to stay in buildings. Implementation of all practices provides for the required level of comfort in buildings and creates the required conditions for emergency-free operation of construction facilities. Here it should be mentioned that specific operational difficulties usually occur in public buildings of significant size inside which large numbers of people can stay and move around simultaneously in order to perform some functions. The examples of such public buildings are shopping malls, transportation buildings, exhibition pavilions, etc. The effects that climatic factors have on such objects becomes quite significant. This especially noticeable nowadays due to global climate change on the planet. Events that took place in 2021 in Texas, USA, may be used as an example of climatic anomalies. A significant snowfall and abrupt temperature drop happened in this state while this territory has always been distinguished by dry and hot climate. In this regard, a need arises to arrange for further studies and to develop additional architectural layout, and structural practices, structures including not only the new construction materials for coverage or guarding structures but also development of special structural solutions protecting the construction facilities from negative climatic effects. Different studies are being made in this sphere, and new structures are being searched for both in Russia and abroad. All of the aforesaid confirms the relevance and necessity of such questions to be asked.

It is known that solar protection devices (SPDs) of various types are used in hot climate regions in order maintain comfortable conditions inside. Stationary SPDs became widely used in Russia and they are used not only for protective purposes but also to form the architectural composition of buildings. Solar protection devices can be installed on the windows: outdoors in the window opening and indoors. Domestic and foreign materials, technologies, solutions allowing for implementation of a rich variety of solar protection devices became widely used on the Russian construction market.

Installation of additional solar protection devices onto cooling structures being protected from overheating became widely spread in Arabic architecture. This solution has influenced the design of architectural facades of buildings where the guarding structures are built as floral elements of Arabic pattern [16–17]. The structures are shaping the facade architectural space and simultaneously protecting it from overheating. The set objective is achieved by means of using a cover on top of the facade made of golden "umbrella modules" which are opened and closed depending on illumination and are automatically controlled from a single center.

Original design of the building facade was developed in Doha, Qatar. The 231 meter tall building has a metallic mesh facade which is used as a sun screen (the temperature in the city rises up to plus 50 °C in hot time of the year) and is also a certain additional decoration to architectural image of the building.

Such additional elements can also be built as wide-span structures that provide additional shading to the construction facility, facilitate air circulation, and protect the building from possible precipitation. An example of such structures is the solution built as a tent covering the Göbekli Tepe temple complex archaeological site in Turkey from climatic effects and not only protecting the artifacts within but also creating favorable and comfortable conditions for visitors of the historical object as well.

Equally complicated conditions are experienced by people in buildings located in northern regions. Living there shall be arranged so that such factors as low temperatures, snowstorms, strong wind currents, and indoor insolation only in particular hours are taken into account. All these have significant impact on people's physical and moral state. As of today, a large number of space-planning, structural solutions have been developed using modern technologies. One of such solutions is the use of dome space where all

conditions are created for living. The enclosed space allows for comfortable staying inside, prevents winds and snow from getting into the internal space. Special unified modules [14] have been developed for rotation camps. They provide protection and also may broaden the architectural layout options when building residential areas in northern regions.

Analysis of modern tendencies in development of architectural forms, special construction solutions for buildings of various purpose in regions with complicated climatic conditions shows that they are quite diverse. Still, not all the tendencies are efficient, low-cost, technologically simple, or could be implemented both in hot and severe northern climate.

Many protective structures are mostly used in foreign construction practice and not adapted on the Russian market. In this regard, the objective of these studies is to further study and look for structural, architectural layout solutions in harsh conditions of the climatic zones specific to the Russian Federation.

The objects of the study are public buildings, as which the buildings of the exhibition complex, shopping center, transport buildings are considered.

The tasks of the study were as follows:

- development of additional structural suggestions and selection of materials which improve protection from low or high temperatures for some public buildings;
- performance of front-end engineering design;
- performance of thermophysical and strength calculation studies for
- justification of the suggested structures;
- evaluation of the feasibility of suggested solutions to be used in construction practice.

## 2. Materials and Methods

Architectural and numerical simulation methods were used to fulfill the set tasks.

At the first stage of the study, the issues of additional protection for various purpose public buildings in regions with hot dry climate under the influence of high positive temperatures were reviewed. At this stage, the study was performed using the architectural simulation methods.

A building for various exhibitions was chosen as the study object. The building is located in the driest region in the European part of Russia, Kalmykia. Absence of significant number of water bodies at the taken territory has severe impact on air dryness in this region.

The architectural layout solution covers all the necessary premises for exhibitions, a set of service and utility premises, etc. A version of the general layout and the building facade are given in Fig. 1. A version of a dome structure providing the guarding and solar protective functions was suggested as the solar protection device during the building engineering. In order to ensure protection of the structure from solar rays, several versions of guarding structures were studied, for example, single glazing, triple-pane windows, and ETFE film applied in 3 rows. Considering the architectural layout solution of the building being designed and the peculiarities of its erection in especially hot weather conditions, the ETFE membrane material was selected as the final solution as the desired curvilinear shape and dramatic architectural facade could be achieved using the film.

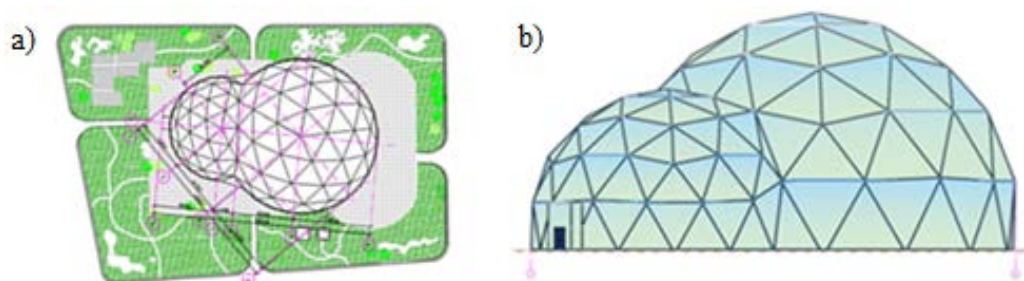


**Figure 1. Exhibition Complex Building Under Design in Hot Climate Region of Kalmykia: a – general layout version; b – facade in within axes 1–4.**

Membrane technology [18–20] is becoming more and more spread in regions not only with hot climate but also in the Far North, Far East, and Siberia due to its high process and operational qualities such as wide operational range of outdoor temperatures, high strength, low weight, fire safety, resistance to UV radiation, high energy-efficiency, and other.

In order to evaluate the feasibility of using the mentioned technology in Kalmykia conditions, the authors performed structural calculations of the dome structure to assess ingress of solar radiation heat through the coverage considering the rated national recommendations.

The structural solution of the coverage was calculated in SCAD software complex. The calculation diagram in shown in Fig. 2.

Numerical simulation methods were used at this stage of the study.

At the next stage of the study, a shopping mall building in hot climate of the city of Astrakhan was reviewed. The building is of rectangular shape, approximately 13 meters tall, three-story with a basement. Service premises as well as some utility and auxiliary premises are located on the floors of the buildings. During the study, main attention was paid to the building coverage as this zone is mostly affected by overheating. Applying the architectural simulation methods, the authors designed the coverage structure as a system of beams made of metal pipes 300 mm in diameter (Fig. 3). The beams are mounted in crosswise pattern forming a diamond shaped space between them. The beam resting joints are made as hinges. Metal elements are interconnected using bolted joints. The space between the beams is filled with ETFE membranes spanned in three layers just like in the previous version of the exhibition pavilion. The shopping mall facades are design fully glazed. Figure 4 shows the calculation diagram of the object being studied. The calculation studies were performed using the numerical simulation methods based on the finite-element method. The calculations were made in SCAD software complex.

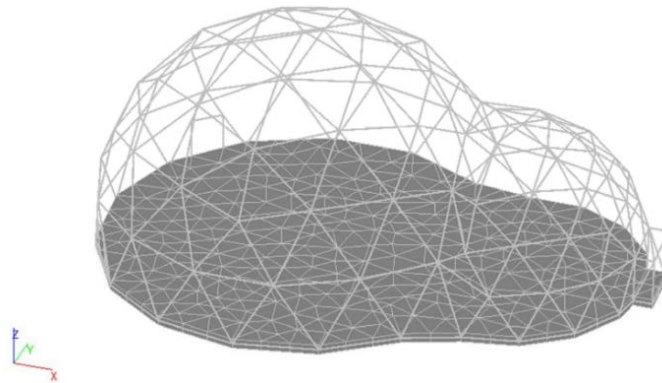


**Figure 2. Calculation Diagram of Exhibition Pavilion Coverage.**

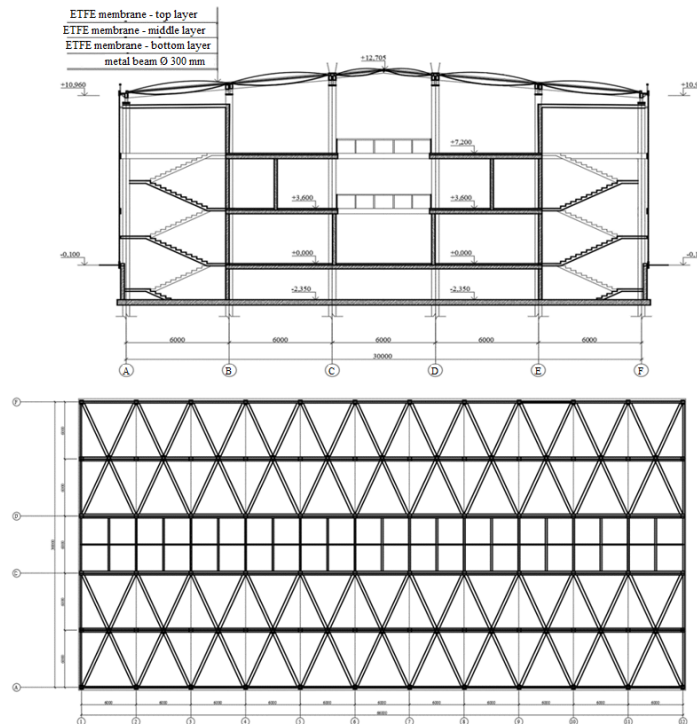


**Figure 3. Shopping Mall Building Under Design in Astrakhan:  
a – lateral section of the building under design;  
b – metal framework of the coverage structure (top view).**

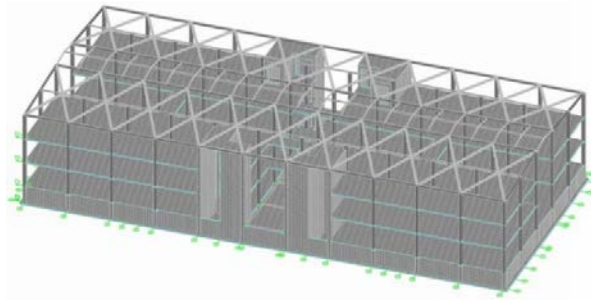


**Figure 4. General View of Calculation Diagram.**

Additionally to public buildings, the study covered railway stations where significant crowding of people moving in different directions occurs. Premises in such buildings are large and long. The description of space-planning and structural solution for the building reviewed is given in the work by the authors [21]. The main idea of additional protection of the building from overheating consisted in creation of a metal shed (or “umbrella”) filled with solar protection glass with soft coverage (Fig. 5). Within the study, heat from solar radiation was evaluated and calculations were made for a shed designed of metal tubular elements. Regions with low temperatures were also reviewed additionally to the hot climate zones in this study.

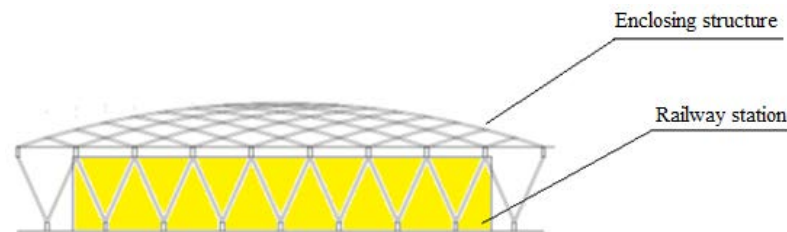


**Figure 5. General View of Metal Shed.**

The authors developed different versions of protection for transportation facilities from harsh climatic conditions in the Northern climatic zone. Thus, a design solution was developed for a railway station in Salekhard using, for example, a geodetic dome. Among its peculiarities in terms of the designed solution, one should note lightness of its structure, coverage of larger area, stream-line form which prevent ingress of wind and snow into the inner space of the station (Fig. 6).

Besides, a city building layout diagram was developed for rotation camps located along the Arctic coast. The specialty of this diagram lies in the centering core with passages running to it from the residential modules which provides for comfortable moving around the settlement. The centering core incorporates shopping, entertainment, sport, office and other premises. The core is also covered with a geodetic dome.

All calculation studies were performed using the numerical simulation methods. The calculations were divided into 2 stages. At the first stage, the entire complex of thermotechnical calculations was performed. At the second stage, structural calculations were made with the aim of checking the strength and resistance of the taken structural elements in terms of protection from climatic effects: either from high positive or from low temperatures.

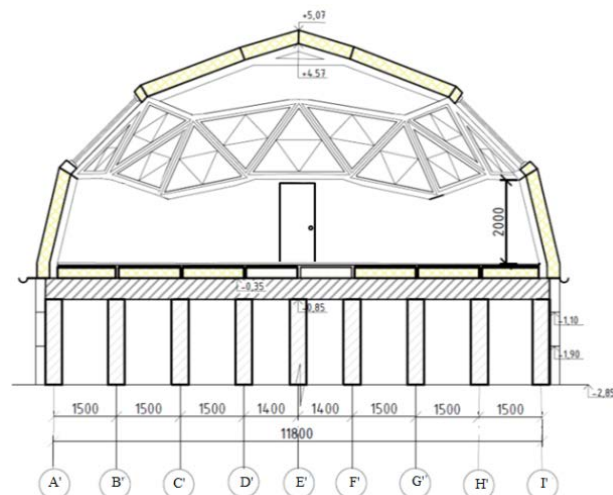


**Figure 6. Example of Railway Station Space Coverage with a Geodetic Dome.**

Well-known methods given, for example, in SP 50.13330.2012 (2018 version with changes No. 1,2), were used for thermotechnical calculations, and according to them, the heat protection coverage of the building shall comply with certain requirements as follows:

a) element-wise requirements (reduced resistance to heat transfer of individual structures shall not be less than nominal values);

b) complex requirements (specific heat protection characteristic of the building shall not exceed the nominal value);

c) sanitary and hygienic requirements (temperature on the inner surfaces of the guarding structures shall be not lower than the minimum allowable values).

Table 1 contains characteristics of materials used, for example, in study involving the exhibition pavilion in Kalmykia.

**Table 1. Characteristics of materials used in study involving the exhibition pavilion in Kalmykia.**

Structural element	Thickness, m	Thermal conductivity, W/m·°C	Thermal resistance to heat transfer m <sup>2</sup> ·°C/W
Dual-pane window SunGuard High Performance Silver 35-16	0.024	–	0.7
Triple-pane window EKA SOFTLINE 70	0.042	–	0.76
ETFE film (3 rows of film)	0.003	0.17	0.0176

Similarly the characteristics of guarding structures were set for other solutions made at the pre-design studies stage. For example, wall structures made of aerated concrete, bricks, sandwich panels, etc. were studied as guarding structures of the railway station. The temperature values were taken in accordance with the climatic norm temperature values. Beside the thermotechnical ones, some calculations were made for air- and vapor-permeability and an evaluation was made of the solar radiation heat coming through the wall structures and the coverage.

As all the suggested structural solutions are spatial structures, strength calculations using numerical simulation methods in SCAD software complex were made for all suggested design solutions additionally to the thermophysical calculations. In this regard, initially calculation diagrams were built for each object in the form of finite-element spatial models. Herewith, the following allowance were made:

- the calculations were made at the elastic stage;
- interaction with the soil base was implemented as per the “rigid platform” hypothesis.

The calculation procedure included the following:

1. Collection of loads;
2. Strength and deformation calculations;
3. Evaluation of internal forces occurring in the additional protection structures of the building under the set loads.

The results of the calculations are deformation diagrams, moment diagrams for longitudinal and transverse forces.

### 3. Results and Discussion

Evaluation of the results of thermophysical calculations showed that the taken versions of guarding structures comply with the thermotechnical requirements and the air- and vapor-permeability requirements. Herewith, a multi-layer structure made of aerated concrete with spun glass insulation was taken for the final version of guarding structures of the railway station because such structure is preferable for hot climate. As for the exhibition building, all the suggested versions also comply with all necessary thermotechnical requirements. Still, considering the possibility of temperature differential and extremely high temperatures, the ETFE membrane systems were selected as they have unique physical and chemical properties with one important advantage additionally to the ones mentioned above – adaptivity to snow and shower rain loads characteristic of climatic zone III.

Aggregated estimation of heat losses for the railway station building in northern regions showed that use of the dome shape caused reduction of heat losses by 1.5 as compared to rectangular shape.

Some of the results of structural calculations made by the authors are shown in Fig. 7–9.

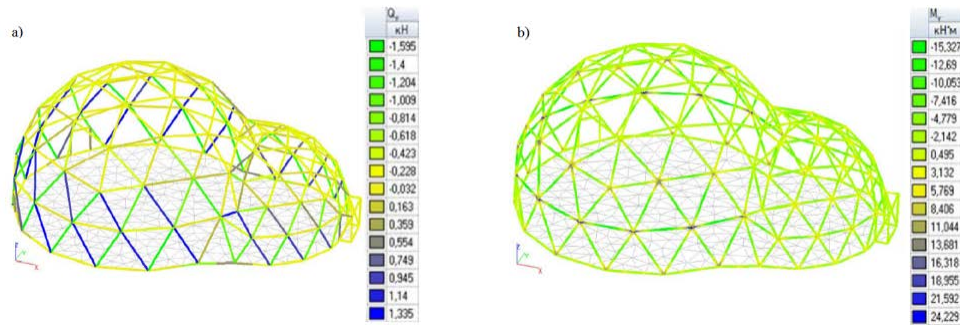


**Figure 7. Structural Calculation Results for Exhibition Complex:**  
**a – isofields in elements created by transverse forces;**  
**b – isofields in elements created by force moments.**

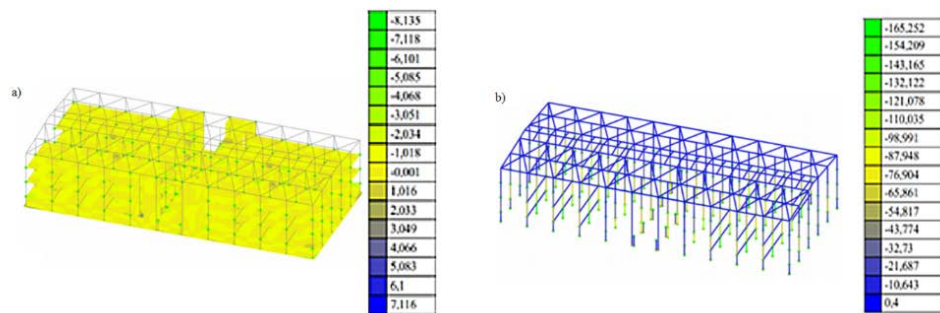


**Figure 8. Structural Calculation Results for Shopping Mall:**  
**a – isofields of stresses  $M_{xy}$ ;**  
**b – values of forces  $N$  in shafts of the diagram.**

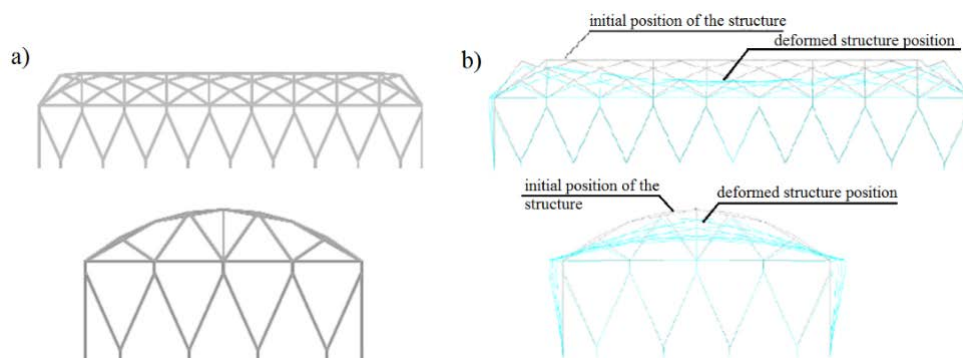


**Figure 9. Calculated Theoretical Study of Guarding Structure for Railway Station:**  
**a – calculation diagrams;**  
**b – structural deformations.**

The figures show changes in the stress-strain state in the structures under consideration. The stress values are represented on the plots of moments, transverse and longitudinal forces. In tabular form, in the form of a color scale, changes in effort from minimum to maximum values are shown. Thus, the analysis of these values for the exhibition complex shows that the maximum values for the longitudinal compressive forces plot are 121 kN, and stretching is 175 kN. For the diagram of transverse forces, the maximum value for compression was 15.3 kN, stretching 24.2 kN. Taking into account the calculations performed, the sections of the elements were selected. For the exhibition complex, the dome structure consists of pipes of circular cross-section 100×3 mm. The calculations performed showed the stability of this structure to the loads acting on it. The received values of forces and displacements are in acceptable values.

The performed structural calculations and design studies for additional devices protecting from temperature impacts are simple and reliable solutions that can be used in construction. Their main advantage is simplicity of erection, low cost, reparability, and high degree of protection from various climatic factors.

The performed complex of pre-design studies of the types of buildings reviewed as well as the estimation of obtained thermophysical parameters of guarding structures indicate that well-known solutions and materials as well as new technologies such as the ETFE membrane systems can be used in the climatic conditions in questions. Moreover, studies have shown that this system can be used both in hot and harsh

climate which makes it quite universal and broadens the area of its use. The study has confirmed that when solving the tasks related to building protection from climatic factors, the task of the highest importance is to select the material for guarding wall structures and for coverage structures as well. Herewith, the protection material shall be not only efficient in terms of thermophysical properties, readily available, repairable, low-cost and so on, but it also shall make the building facade architecturally expressive while blending seamlessly into urban environment.

The idea of making protective spaces as domes or any other additional structural solutions allows creating certain microclimate indoors which is especially important for public buildings. Heat losses are significantly reduced indoors when such solutions are used. It shall be noted, the closed spaces are the most reasonable solution, especially on the Arctic coast.

The performed studies were compared with the results presented in [22–25]. Comparison of the results showed that the considered additional structures provide the necessary level of protection in terms of thermal and physical parameters for the specified climatic areas of construction and meets the requirements of strength and stability, taking into account the loads acting on them.

#### 4. Conclusion

Based on the performed studies, the following conclusions may be made:

1. Significant climate change on the planet that has been happening in recent years indicates that a serious approach shall be applied when designing buildings and structures in different climate regions of the Russian Federation.
2. Versions have been suggested and justified for use of additional structural elements in the form of dome roofs, sheds, membrane coverages, etc. to provide protection from different temperature effects.
3. Based on the performed calculated theoretical studies, it has been determined that the suggested additional architectural structural elements provide protection both from low negative and high positive temperatures.
4. Feasibility of implementation of the architectural structural elements has been shown by the example of some public and industrial buildings such as shopping malls, exhibition and transportation complexes.
5. It has been confirmed that the use of ETFE-type membrane system is the most preferable in different climatic zones for efficient protection from climatic effects.

#### References

1. Pearlmutter, D. Architecture and Climate: The Environmental Continuum. *Geography Compass*. 2007. 1 (4). Pp. 752–778. DOI: 10.1111/j.1749-8198.2007.00045.x
2. Rubio-Bellido, C., Pulido-Arcas, J., Cabeza-Lainez, J. Adaptation Strategies and Resilience to Climate Change of Historic Dwellings. *Sustainability*. 2015. 7(4). Pp. 3695–3713. DOI: 10.3390/su7043695
3. Mahdavinjad, M., Badri, N., Fakhari, M., Haqshenas, M. The role of domed shape roofs in energy loss at night in hot and dry climate (case study: Isfahan Historical Mosques` Domes in Iran). *American Journal of Civil Engineering and Architecture*. 2013. Vol. 1. No. 6. Pp. 117–121. DOI: 10.12691/ajcea-1-6-1
4. Soleymanpour, R., Parsaee, N., Banaei, M. Climate Comfort Comparison of Vernacular and Contemporary Houses of Iran. *Procedia – Social and Behavioral Sciences*. 2015. 201. Pp. 49–61. DOI: 10.1016/j.sbspro.2015.08.118
5. Soleimani, Z., Calautit, J., Hughes, B. Computational Analysis of Natural Ventilation Flows in Geodesic Dome Building in Hot Climates. *Computation*. 2016. 4(3). 31. DOI: 10.3390/computation4030031
6. Karaseva, L.V. Sun Protection of Buildings: Stages and Perspectives of Development. *Materials Science Forum*. 2018. 931. Pp. 759–764. DOI: 10.4028/www.scientific.net/msf.931.759
7. Belash, T.A., Kuznetsov, A.V. Energy efficient wall enclosing structures. *IOP Conference Series: Materials Science and Engineering (MSE)*. 2018. 463. 032052. DOI: 10.1088/1757-899x/463/3/032052
8. Dvoretzky, A., Klevets, K., Spiridonov, A. Low-energy architecture in the south of Russia. *IOP Conf. Series: Materials Science and Engineering*. 2019. 698. 033050. DOI: 10.1088/1757-899x/698/3/033050
9. Klevets, K., Dvoretzky, A., Spiridonov, A. Eco-efficiency of passive solar heating. *E3S Web of Conferences*. 2019. 138. 01018. CATPID-2019. DOI: 10.1051/e3sconf/201913801018
10. Ulitsky, V.M., Gorodnova, E.V. The construction of transport infrastructure on permafrost soils. *Procedia engineering: Elsevier Ltd*. 2017. No. 189. Pp. 421–428. DOI: 10.1016/j.proeng.2017.05.067
11. Podkovyrina, K.A., Podkovyrin, V.S., Nazirov, R.A. Osobennosti proektirovaniya zdaniy i sooruzheniy v severnykh shirotakh s tochki zreniya stroitel'noy fiziki [Features of the design of buildings and structures in northern latitudes from the point of view of construction physics]. *Urbanistika*. 2017. No. 4. Pp. 78–85. DOI: 10.7256/2310–8673.2017.4.24964. (rus)
12. Ovsjannikov, S.I. Formirovanie teploizoljacionnyh ogradhdajushhih konstrukcij kupol'nyh stroenij dlja rajonov Krajnego Severa [Formation of heat-insulating enclosing structures of domed buildings for the regions of the Far North] / S.I. Ovsjannikov, A.A. Suska, S.A. Shevchenko. *Stroitel'nye materialy i izdelija*. 2019. Vol. 2. No. 4. Pp. 21–26. DOI: 10.34031/2618–7183–2019–2–4–21–26. (rus)

13. Zhivotov, D., Latuta, V. Using geodesic domes of wood and thermoplastics for rotational camps in the arctic and northern territories. Pp. 22–28. DOI: 10.23968/2500-0055-2020-5-3-22-28
14. Mohammad, A.K. Technological Interventions in Building Facade System: Energy Efficiency and Environmental Sustainability. Architecture Research. 2020. Vol. 10. No. 2. Pp. 45–53. DOI: 10.5923/j.arch.20201002.01
15. Heidari Matin, N., Eydgahi, A. Factors affecting the design and development of responsive facades: a historical evolution. Intelligent Buildings International. 2019. Pp. 1–14. DOI:10.1080/17508975.2018.1562414
16. Attia, S. Evaluation of adaptive facades: The case study of Al Bahr Towers in the UAE. QScience Proceedings. 2016. 8. DOI: 10.5339/qproc.2016.qgbc.8
17. Karanouh, A., Kerber, E. Innovations in dynamic architecture. Journal of Facade Design and Engineering. 2015. 3(2). Pp. 185–221. DOI: 10.3233/fde-150040
18. ETFE. Technology and Design. Annette LeCuyer. Birkhäuser Basel, 2008. 160 p. DOI: 10.1007/978-3-7643-8624-5
19. Lamnatou, C., Moreno, A., Chemisana, D., Reitsma, F., Clariá, F. Ethylene tetrafluoroethylene (ETFE) material: Critical issues and applications with emphasis on buildings. Renewable and Sustainable Energy Reviews. 2018. 82. Pp. 2186–2201. DOI: 10.1016/j.rser.2017.08.072
20. Hu, J., Chen, W., Zhao, B., Yang, D. Buildings with ETFE foils: A review on material properties, architectural performance and structural behavior. Construction and Building Materials. 2017. 131. Pp. 411–422. DOI: 10.1016/j.conbuildmat.2016.11.062
21. Belash, T.A., Ivanova, Zh.V., Najdenova, V.V. Obespechenie komfortnyh uslovij jekspluatacii transportnyh ob'ektov v uslovijah zharkogo klimata [Ensuring comfortable operating conditions for transport facilities in hot climates] Promyshlennoe i grazhdanskoe stroitel'stvo. 2020. No. 2. Pp. 23–28. DOI: 10.33622/0869-7019.2020.02.23-28. (rus)
22. Hosseini, S.M., Mohammadi, M., Rosemann, A., Schröder, T., Lichtenberg, J. A morphological approach for kinetic façade design process to improve visual and thermal comfort: Review. Building and Environment. 2019. Vol. 153. Pp. 186–204. DOI: 10.1016/j.buildenv.2019.02.040
23. López-Ordóñez, C., Crespo Cabillo, I., Roset Calzada, J., Coch Roura, H. The Role of Thermal Insulation in the Architecture of Hot Desert Climates. In: Littlewood, J., Howlett, R., Capozzoli, A., Jain, L. (eds) Sustainability in Energy and Buildings. Smart Innovation, Systems and Technologies. 2020. Vol. 163. Springer, Singapore. [https://doi.org/10.1007/978-981-32-9868-2\\_37](https://doi.org/10.1007/978-981-32-9868-2_37)
24. Shaviv, E. Climate and building design – tradition, research and design tools. 1984. 7(1). Pp. 55–69. DOI: 10.1016/0378-7788(84)90045-8
25. Lamnatou, Chr., Moreno, A., Chemisana, D., Reitsma, F., Clariá, F. (2017). Ethylene tetrafluoroethylene (ETFE) material: Critical issues and applications with emphasis on buildings. Renewable and Sustainable Energy Reviews. 2018. Vol. 82. P. 3. Pp. 2186-2201. DOI: 10.1016/j.rser.2017.08.072

**Information about authors:**

**Tatiana Belash**, Doctor of Technical Science

ORCID: <https://orcid.org/0000-0002-4577-8794>

E-mail: [belashta@mail.ru](mailto:belashta@mail.ru)

**Tatyana Ivanova**, PhD in Technical Science

ORCID: <https://orcid.org/0000-0001-6662-317X>

E-mail: [ivanovatv@vniig.ru](mailto:ivanovatv@vniig.ru)

**Dmitry Ivashintsov**, Doctor of Technical Science

ORCID: <https://orcid.org/0000-0002-2468-3382>

E-mail: [vniig@vniig.ru](mailto:vniig@vniig.ru)

Received 19.03.2022. Approved after reviewing 02.09.2022. Accepted 09.09.2022.



Research article

UDC 681.7.035:552.55

DOI: 10.34910/MCE.116.15



## Porous glass ceramics from siliceous rocks with high operating temperature

A.I. Rodin , A.A. Ermakov , V.M. Kyashkin , N.G. Rodina , V.T. Erofeev 

National Research Mordovia State University, Saransk, Republic of Mordovia, Russia

✉ [al\\_rodin@mail.ru](mailto:al_rodin@mail.ru)

**Keywords:** glass ceramic, construction material, thermal insulation, siliceous rocks, aluminium oxide, compressive strength, thermal conductivity, thermal analysis

**Abstract.** Porous glass-ceramic materials although light weighted have relatively high strength, low thermal and sound conductivity, high corrosion resistance, and are non-combustible, etc. They can be obtained from siliceous rocks, the reserves of which are huge. The article considers the obtaining of porous glass ceramic materials with an operating temperature exceeding 900 °C. The materials are obtained from siliceous rocks, Na<sub>2</sub>CO<sub>3</sub>, Al<sub>2</sub>O<sub>3</sub> and KCl. Mechanochemical activation of raw materials was carried out in a planetary ball mill. The resulting charge mixture was annealed at a temperature of 850 °C. Experimental results were obtained by using X-ray diffraction (XRD) and thermal (TA) analysis, scanning electron microscopy (SEM), X-ray microtomography (Micro-CT). Physical-mechanical, thermophysical properties and chemical stability of obtained materials were examined. The main crystalline phase of glass ceramics from the calcite-free charge mixture is anorthoclase and quartz. Apart from that samples with calcite charge mixture contain wollastonite and devitrite. The increased content of Al<sub>2</sub>O<sub>3</sub> in the charge mixture displays nepheline in glass ceramics. Calcite in the charge mixture has a significant effect on the microstructure of porous glass ceramics. The number of open pores in the material increases from ≈ 5 % to > 50 %. The compressive strength of porous glass-ceramic materials derived from siliceous rocks reaches 5.1 MPa. In terms of strength, they are significantly superior to foam glass. The minimum thermal conductivity of glass ceramics is 0.065 W/(m·°C) at a sample density of 244 kg/m<sup>3</sup>. Samples withstand temperature drops by 230 °C. The material has a high chemical stability and can be operated at temperatures reaching 920 °C inclusively. The obtained materials can be used as thermal insulation of boiler equipment, melting furnaces, etc.

**Acknowledgement:** The study was funded by a grant Russian Science Foundation No. 21-79-10422, <https://rscf.ru/project/21-79-10422/>

**Citation:** Rodin, A.I., Ermakov, A.A., Kyashkin, V.M., Rodina, N.G., Erofeev, V.T. Porous glass ceramics from siliceous rocks with high operating temperature. Magazine of Civil Engineering. 2022. 116(8). Article no. 11615. DOI: 10.34910/MCE.116.15

### 1. Introduction

Porous glass-ceramic materials although light weighted have relatively high strength, low thermal and sound conductivity, high corrosion resistance, and are non-combustible, etc. [1, 2]. Porous glass ceramic is not inferior in many properties to other modern building materials [3–5]. They are highly sought for various purposes during the construction and repair of facilities. In civil engineering, this material can be used for mounting wall enclosing structures [6], insulation of facades, roofs, floors [7], in the decoration of structures [8], etc. The industry puts them to use in refractory lining of furnaces [2], for heat and sound insulation [9], protection of structures from corrosion [10], etc.

Porous glass-ceramic materials are obtained from slags of various industries [11–13], glass waste [14], fly ash [1, 7, 15, 16] and other components. Many scholarly works consider the production of porous glass-ceramic materials from siliceous rocks [17–20]. The reserves of such rocks in the world are immense [17, 21]. Diatomite, zeolite-containing tripoli, opoka are activated with aqueous solutions of high concentrated NaOH, granulated, and then annealed. We have proposed a method for obtaining porous glass ceramics from zeolite-containing rocks. The method allows to obtain samples in the form of blocks [22]. The rock, together with sodium carbonate or thermonatrite, was exposed to mechanochemical activation in a planetary mill. The resulting charge mixture was put into the molds of the required size and then annealed [23]. When annealed, zeolite minerals in the charge mixture are dehydrated sealing surface hydroxyl groups in micropores. At a temperature of more than 670 °C, the charge mixture begins to melt. Hydroxyl groups condense, water vapor releases foaming the charge mixture [24]. The obtained materials have relatively high strength, low thermal conductivity. However, their limiting operating temperature does not exceed 850 °C [22, 23]. This is not enough for thermal insulation of many industrial facilities [2].

There is a great deal of research into the influence of glass ceramics' chemical and phase composition on its operating temperature. The limiting temperature of glass ceramics decreases following the increase in Fe<sub>2</sub>O<sub>3</sub> and CaO added to its composition [13, 25, 26]. The influence of MgO on its properties is similar to that of CaO [27], but many siliceous rocks compositions have a low MgO content [17, 18, 23]. The resistance of ceramic materials derived from industrial waste or artificially created glass to a lasting exposure to high temperatures raises after the increase of Al<sub>2</sub>O<sub>3</sub> in their composition [28, 29]. The technology of obtaining porous glass ceramics from siliceous rocks differs from those referred above. There are differences in the chemical and phase composition of materials [19, 23]. The increased content of amorphous SiO<sub>2</sub> in the siliceous charge mixture's composition decreases the limiting operating temperature of porous glass ceramics. Na<sub>2</sub>O and Fe<sub>2</sub>O<sub>3</sub> produce negative effect as well [23]. Research findings dealing with the effect of CaO and Al<sub>2</sub>O<sub>3</sub> on the limiting operating temperature of porous glass ceramics from siliceous rocks have not been found.

The objective of research: to obtain porous glass-ceramic materials from siliceous rocks with an operating temperature of more than 900 °C in one stage of charge mixture heating; to study the structure and properties of the obtained materials.

Tasks:

- by utilizing the X-ray diffraction (XRD) and thermal (TA) analysis to determine the effect of calcite and aluminum oxide content in the charge mixture on its phase composition after mechanochemical activation, phase transformations in the charge mixture during heating and the phase composition of annealed porous glass ceramics;
- by employing scanning electron microscopy (SEM) and X-ray microtomography (Micro-CT) to study the microstructure of porous glass ceramics from siliceous rocks;
- to establish the influence of the phase composition of porous glass ceramic samples on their physical and mechanical properties (density, porosity, bending strength and compressive strength);
- to determine the thermophysical properties (thermal conductivity, thermal shock resistance, limiting operating temperature) of porous glass-ceramic material samples;
- to determine the chemical stability of the developed materials to water, aqueous solutions of acids and alkalis.

## 2. Methods

### 2.1. Materials

To fabricate samples of porous glass-ceramic materials the following components were used:

- Siliceous rocks: R1 is zeolite-containing tripoli (calcite content is 0%), R2 is zeolite-containing tripoli (calcite content is 10.5 %), R3 is diatomite. Humidity of raw materials components is less than 1 %. The chemical and mineralogical composition of the rocks is shown in Table 1 and 2, respectively.

**Table 1. Chemical composition.**

Composition No.	Chemical composition (wt.%)							
	SiO <sub>2</sub>	CaO	Al <sub>2</sub> O <sub>3</sub>	Fe <sub>2</sub> O <sub>3</sub>	K <sub>2</sub> O	MgO	TiO <sub>2</sub>	Na <sub>2</sub> O
1	2	3	4	5	6	7	8	9
R1 (Tripoli)	70.94	2.38	12.38	3.52	1.71	1.66	0.50	0.14
R2 (Tripoli)	67.86	7.74	7.61	1.99	1.56	1.07	0.34	0.17
R3 (Diatomite)	81.47	1.51	5.34	2.05	0.97	0.89	0.25	0.20

Continuation of table

Chemical composition, (wt.%)									
SO <sub>3</sub>	P <sub>2</sub> O <sub>5</sub>	ZrO <sub>2</sub>	MnO	Cr <sub>2</sub> O <sub>3</sub>	NiO	SrO	BaO	V <sub>2</sub> O <sub>5</sub>	LOI
10	11	12	13	14	15	16	17	18	19
0.02	0.26	0.02	0.01	0.01	0.01	0.06	0.00	0.01	6.37
0.06	0.15	0.01	0.01	0.01	0.00	0.06	0.02	0.01	11.32
1.77	0.03	0.01	0.01	0.01	0.00	0.01	0.02	0.01	5.45

**Table 2. Mineralogical composition of rocks.**

Composition No.	Mineralogical composition, %					
	Quartz	Calcite	Heulandite	Muscovite	Cristobalite	Amorphous phase
R1	29.1	0.0	18.6	16.1	16.2	20.0
R2	15.5	10.5	20.4	13.1	20.5	20.0
R3	10.9	0.0	0.0	8.1	0.0	80.0

- Sodium carbonate. Chemical formula: Na<sub>2</sub>CO<sub>3</sub>. The purity is ≥ 99 %. The additive was introduced to reduce the melting temperature and foaming of the charge mixture. The required concentration of the additive was determined by us earlier [22].
- Aluminum Oxide. Chemical formula: Al<sub>2</sub>O<sub>3</sub>. The purity is ≥ 97 %. The additive was introduced to increase the limiting operating temperature of porous glass-ceramic materials. Theoretical assumptions on increasing the operating temperature of glass ceramics owing to the introduction of Al<sub>2</sub>O<sub>3</sub> are described in the Introduction.
- Potassium chloride. Chemical formula: KCl. The purity is ≥ 99 %. The addition of KCl is necessary to obtain a uniform pore structure in glass ceramics. The required concentration of the additive was determined by us in earlier works [22].

## 2.2. Compositions and fabrication of samples

The charge mixture for porous glass-ceramic samples was obtained by joint grinding (mechanochemical activation) of siliceous rocks, sodium carbonate, aluminum oxide and potassium chloride. The raw materials were ground in a planetary ball mill Retsch PM 400. Grinding time – 35 min. The overload inside the crushing cylinder is 20G. The resulting charge mixture was annealed in a metal form in a muffle furnace. The internal size of the mold is 120×120×260 mm. Before annealing, the molds were coated with clay. Annealing procedure: heating to 670 °C at a speed of 4.5 °C/min, holding at 670 °C – 1 hour, heating to the temperature of 850 °C at a speed of 4.5 °C/min, holding at 850 °C – 30 minutes. The holding at 670 °C is necessary to complete the decomposition of select minerals of the charge mixture (calcite, muscovite). If this stage is excluded from the technological cycle, samples of porous glass ceramics will have an uneven macrostructure. Holding at 850 °C is necessary for the completion of all phase formation processes [22]. The molds with the resulting material after annealing cooled down together with the furnace to 40 °C. Then the forms were disassembled. The samples were sawed and tested. The diagram of the experiment is shown in Fig. 1.

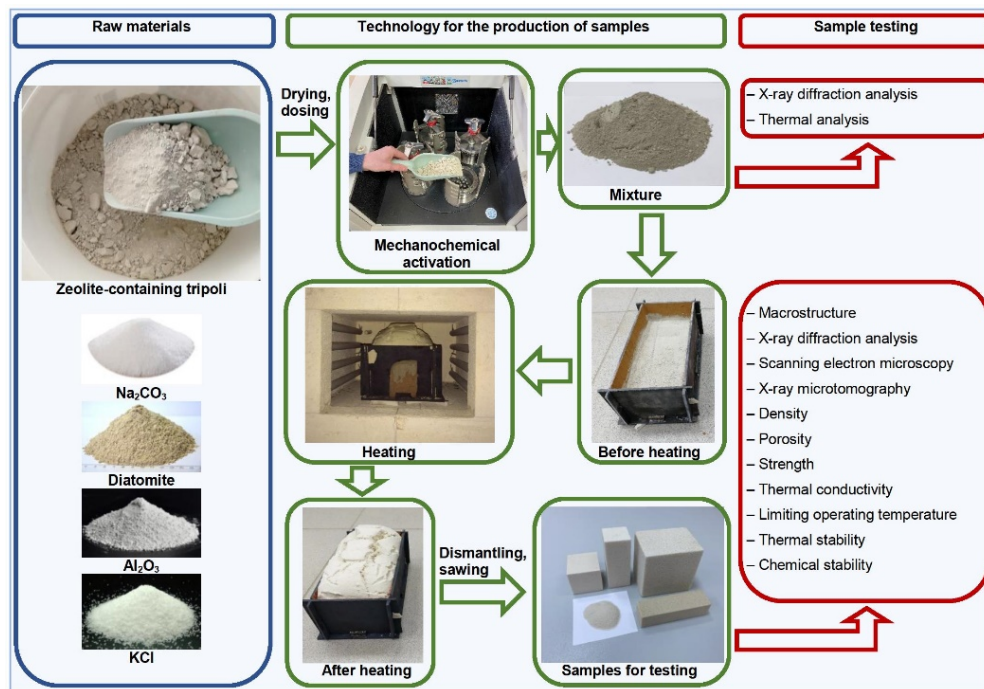


Figure 1. Diagram of the experiment.

In the course of experiment, 16 charge mixture compositions were tested. The compositions are presented in Table 3.

Table 3. Compositions, examined in work.

Composition No.	Charge mixture composition, %					
	Siliceous rock (chemical composition see Table 1)			Al <sub>2</sub> O <sub>3</sub>	Na <sub>2</sub> CO <sub>3</sub>	KCl
	R1	R2	R3			
C1	81.4	0	0	0		
C2	80.38	0	0	1.02		
C3	79.36	0	0	2.04		
C4	78.35	0	0	3.05		
C5	52.73	25.97	2.70	0		
C6	51.36	25.30	2.70	2.04		
C7	50	24.63	2.70	4.07		
C8	48.63	23.96	2.70	6.11		
C9	25.07	50.90	5.43	0	18.4	0.2
C10	24.06	48.86	5.43	3.05		
C11	23.05	46.81	5.43	6.11		
C12	22.05	44.76	5.43	9.16		
C13	0	73.26	8.14	0		
C14	0	69.19	8.14	4.07		
C15	0	65.12	8.14	8.14		
C16	0	61.05	8.14	12.21		

### 2.3. Analytical techniques

Methods for obtaining experimental data:

- X-ray diffraction analysis (XRD) of charge mixture samples and annealed materials was made by using the Epyrean PANalytic diffractometer (Netherlands). The samples were grinded to a fraction of less than 90  $\mu\text{m}$ . Diffraction patterns were identified in CuK $\alpha$  emission in the scan range  $2\theta = 4\text{--}80^\circ$ . The PIXcel3D semiconductor detector operated in linear scanning mode. The step size is 0.0067  $^\circ/\text{min}$ , the counting time is 150 seconds. The qualitative phase composition of the samples was determined by the Hanawalt method using the ICDD PDF-2 database.

- Thermal analysis (TA) of charge mixture samples was made by using the TGA/DSC1 apparatus (Switzerland).  $20 \pm 0.1$  mg of charge mixture was put into an 150-ml. alumina crucible. By tapping the crucible on the table, the sample was compacted. The crucible with the charge mixture was then placed in the apparatus to be heated in the range between 30 and 850 °C at a rate of 10 °C/min.
- Scanning electron microscopy (SEM) of porous glass-ceramic samples was performed using the Quanta 200 3D device (USA). The samples were scanned at a pressure of 60 Pa, with an accelerating voltage of 30 kV and an operating distance of 15 mm.
- X-ray microtomography (Micro-CT) was made using the SkyScan 1172 apparatus (Belgium). Samples with a size of  $15 \pm 1$  mm were X-rayed at 67 kV and 110 mcA. The angle of rotation of the supporting post is 360°, the rotation pace is 0.6°. Images were collected with a resolution of 6.9  $\mu\text{m}$ . Images processed with CTvox software (Skyscan, Belgium).
- The true density of porous glass ceramic samples ( $\rho_0$ ,  $\text{g/cm}^3$ ) was determined using a pycnometer. The tests were effectuated on grinded (fraction < 20  $\mu\text{m}$ ) and dried samples. The arithmetic mean of the test results of two samples of each composition was taken as the result.
- Porosity (open, closed and total) was determined on cubic-form samples with a side plane size of  $50 \pm 5$  mm. First, the volume ( $V$ ,  $\text{cm}^3$ ) and the weight of dry samples ( $m_0$ , g) were determined. Then they were placed in a cylindrical tank with water for vacuuming. The water level in the cylindrical tank was at least 20 mm higher than the samples. The hydrometer was used to determine the water density ( $\rho_w$ ,  $\text{g/cm}^3$ ). The air was pumped out of the cylindrical tank. The residual pressure in the working chamber was 2,000 Pa. The samples were held in the vacuum for at least 2 hours. Testing samples were taken out of the tank after weight stabilisation. After water saturation, the samples weight was measured indoors ( $m_1$ , g).

The apparent density ( $\rho$ ,  $\text{g/cm}^3$ ) was calculated by the formula (1):

$$\rho = \frac{m_0}{V}. \quad (1)$$

Total porosity ( $P_t$ , %) was calculated by the formula (2):

$$P_t = \frac{\rho_0 - \rho}{\rho} \cdot 100. \quad (2)$$

Open porosity ( $P_o$ , %) was calculated by the formula (3):

$$P_o = \frac{m_1 - m_0}{V \cdot \rho_w} \cdot 100. \quad (3)$$

Closed porosity ( $P_c$ , %) was calculated by the formula (4):

$$P_c = P_t - P_o. \quad (4)$$

The arithmetic mean of the test results of three samples of each composition was taken as the final result.

- The compressive strength of porous glass-ceramic materials was determined on dry cubic samples with a side plane of  $90 \pm 5$  mm. The maximum destructive force was identified when the sample was fractured (cracks appeared) or deformed in the surface layers by 10 % of the initial height. The arithmetic mean of the test results of five samples of each composition was taken as the final result.
- The bending strength was determined on dry samples-beams with side plane sizes  $120 \times 30 \times 30$  mm. The sample was placed on two cylindrical supports with a diameter of  $6 \pm 0.1$  mm. The distance between the axes of the supports is  $100 \pm 1$  mm. The load on the sample was applied by a rod with a diameter of  $6 \pm 0.1$  mm. The rod was put along the entire width of the sample at an equal distance from the supports. The rate of application of the load is 5 mm/min. The load was identified at the moment of sample's destruction. The bending strength was determined according to the standard formula. The arithmetic mean of the test results of three samples of each composition was taken as the final result.

- The thermal conductivity of the material was determined by the probe method using the MTCM–1 apparatus (mobile thermal conductivity meter). The experiment was carried out on samples of cubic shape with a side plane of  $90\pm 5$  mm. The samples were previously dried. A hole with a diameter of 6 mm and a depth of 50 to 60 mm was drilled in the center of the side plane. The apparatus (MTCM–1) and the prepared samples were kept for 2 days in the laboratory at a temperature of  $22\pm 1$  °C. A probe with a diameter of 6 mm was immersed into the hole. Kept making readings of the apparatus. The arithmetic mean of the test results of five samples of each composition was taken as the final result.
- The thermal shock resistance ( $\Delta T$ , °C) of the materials was revealed against the appearance of cracks on the samples during abrupt cooling. Dry samples of cubic shape (side plane length  $50\pm 5$  mm) were kept in a thermostat at a temperature of 110 °C for at least 2 hours. Heated samples were quickly (< 10 seconds) removed from the thermostat and immersed in a water container (water temperature –  $20\pm 2$ °C). The samples were kept in water for  $65\pm 5$  seconds. The experiment was repeated increasing the thermostat temperature by 10 °C until cracks appeared on all samples. The thermal shock resistance of each sample was calculated by the formula (5):

$$\Delta T = T_t - T_w - 10, \quad (5)$$

where  $T_t$  is the thermostat temperature at which the sample was kept (°C);  $T_w$  is water temperature in the container (°C); 10 is the thermostat temperature difference between the subsequent and previous tests (°C).

When determining the thermal shock resistance, the arithmetic mean of the test results of four samples of each composition was taken as the final result.

- The limiting operating temperature of porous glass-ceramic materials was estimated by the residual change in the size of the samples ( $90\times 40\times 40$  mm) after heating. The samples were measured with an accuracy of 0.01 mm and put in a vertical position in a muffle furnace. The samples were heated in the furnace at a rate of 10° C/min to a temperature 50 °C less than the set temperature. To the limiting temperature heated at a rate of 2 °C/min. The samples were kept at a given temperature for 2 hours. If after the test the sample sizes changed by < 1 %, the experiment was repeated increasing in the limiting temperature by 10 °C. The arithmetic mean of the test results of three samples of each composition was taken as the final result
- The chemical stability of the materials was estimated by the mass loss of powdered samples after boiling in distilled water, an aqueous solution of 6N HCl, a mixture of equal volumes of 1N solutions of  $\text{Na}_2\text{CO}_3$  and NaOH. Porous glass ceramic materials were grinded to a fraction of 0.315–0.630 mm. A dried sample weighing  $5\pm 0.0005$  g was placed in a test jar and drenched with  $100\pm 0.5$  cm<sup>3</sup> of reagent. The test jar was connected to a backflow condenser and boiled for 3 hours. After boiling, an aggressive liquid was discharged. The sample was washed with distilled water. The washed sample was drained through a funnel with a paper ash-free filter. The filter with the sample was placed in a quartz crucible and annealed (1 hour) in a muffle furnace at a temperature of  $800\pm 10$  °C. The crucible with the sample was cooled down in an oven to 150 °C, then in a desiccator with  $\text{CaCl}_2$  to room temperature and weighed. The arithmetic mean of the test results of two samples of each composition was taken as the final result.

### 3. Results and Discussion

#### 3.1. Charge mixture XRD

The results of the charge mixture XRD after mechanochemical activation are shown in Fig. 2. For clarity, the XRD patterns are presented in the scan range  $2\Theta = 5\text{--}50^\circ$ .

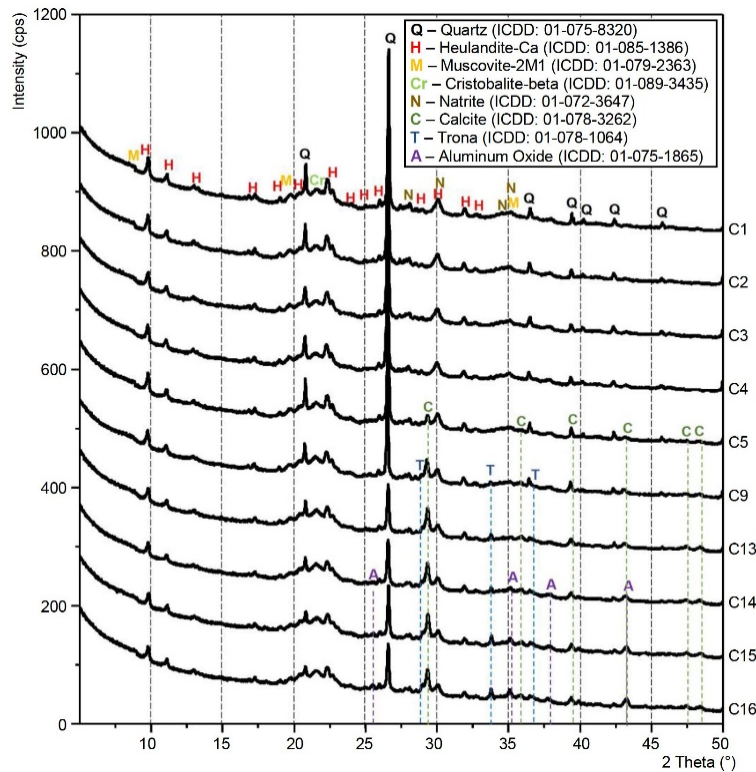


**Figure 2. Charge mixture XRD patterns.**

Based on the results of the XRD of the charge mixture samples (Fig. 2), the following was found out. The crystalline phase of the C1–C4 samples is represented (in addition to the data in Table 2) by the mineral natrite [ $\text{Na}_2\text{CO}_3$ , ICDD: 01-072-3647]. X-ray patterns of samples C5, C9, C13–C16 additionally showed peaks of the calcite's phase [ $\text{CaCO}_3$ , ICDD: 01-078-3262]. This phase is part of the R2 rock. The intensity of the lines increased with the increase in the amount of R2 rock in the charge mixture composition. In samples C9, C13–C16, additionally, there is a new phase of trona [ $\text{Na}_3\text{H}(\text{CO}_3)_2(\text{H}_2\text{O})_2$ , ICDD: 01-078-1064], and in samples C14–C16 – aluminum oxide [ $\text{Al}_2\text{O}_3$ , ICDD: 01-075-1865].

X-ray patterns of samples C1–C4 and C5 show a wide halo in the region of  $33\text{--}39^\circ$  ( $2\theta$ ), which corresponds to the amorphous (nanocrystalline) phase. The effect may be attributed to sodium silicate hydrates. The formation of these compounds in a siliceous charge mixture after mechanochemical activation is described in the scholarly literature [24]. The intensity of the halo decreases with the increase in the amount of calcite and aluminum oxide in the charge mixture (Samples C5, C9, C13–C16). At the same time, the intensity of the natrite peaks decreases and the number of tronas in the samples increases. There is evidence in the scholarly literature for the formation of trona in the siliceous charge mixture after alkaline activation [24].

### 3.2. Charge mixture TA

By employing differential thermal analysis (DTA) and differential thermogravimetry (DTG), phase transformations in the charge mixture during heating were examined. The results are shown in Fig. 3.

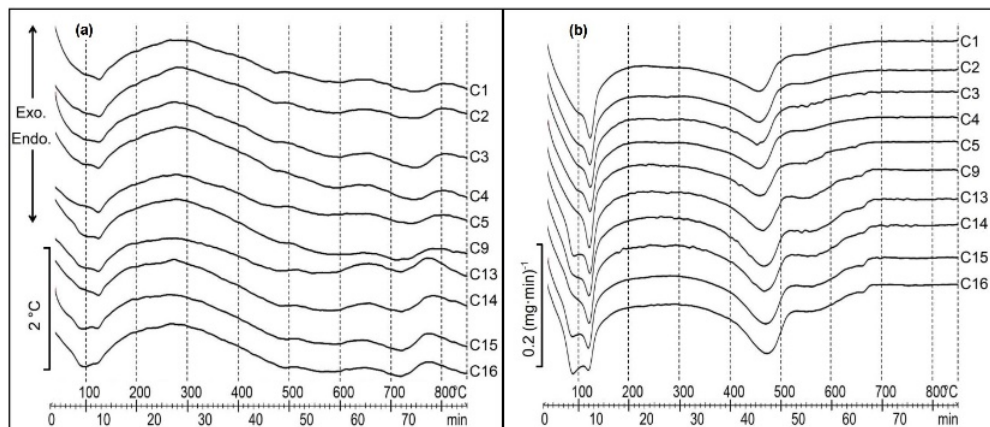


**Figure 3. DTA (a) and DTG (b) curves of charge mixture samples.**

Results of experimental analysis (Fig. 3) allow us to estimate the phase transformations in the charge mixture during heating. The first endothermic effect (Fig. 3a) and mass loss (Fig. 3b) in the temperature range from 80 to 110 °C confirm the XRD findings. The effect reflects the increase in the amount of trona in the charge mixture in response to the increase of calcite and simultaneously  $\text{CaCO}_3$  and  $\text{Al}_2\text{O}_3$  (Samples C9, C13–C16) in its composition.

The endothermic effect (Fig. 3a) with a peak at a temperature of  $\approx 120$  °C is associated with the release of water from sodium silicate hydrates. The effect is accompanied by weight loss (Fig. 3b). The formation of sodium silicate hydrates caused by mechanochemical activation of a siliceous charge mixture is considered in the article [24]. The intensity of the thermal effect and the rate of weight loss at a temperature of  $\approx 120$  °C decreases with the increase of  $\text{CaCO}_3$  and simultaneously  $\text{CaCO}_3$  and  $\text{Al}_2\text{O}_3$  in the charge mixture (Samples C9, C13–C16). It can be assumed that this is due to the decrease in the amount of reaction active  $\text{SiO}_2$  in the charge mixture. The decrease in the amount of trona and increase in sodium silicate hydrates in the charge mixture composition with a high CaO content is described in [30]. The effect occurred after intensive and lasting mechanochemical activation of the charge mixture, which facilitates the formation of reaction active  $\text{SiO}_2$ .

The following endothermic effect is reflected by DTA curves (Fig. 3a) in the temperature range from 300 to 510 °C. The effect is accompanied by a large loss of sample weight reflected by the DTG curves (Fig. 3b). In the siliceous charge mixture, sodium silicates are intensively formed in this temperature range. The findings are confirmed by the results in [24]. A large loss of mass is related with the decarbonization of sodium carbonate. The peak of the effect is slightly shifted to the region of high temperatures because of the increase of  $\text{CaCO}_3$  and  $\text{Al}_2\text{O}_3$  (Samples C1–C16) in the charge mixture composition.

The endoeffect and the insignificant rate of samples weight loss (C1–C4) in the temperature range from 510 to 650 °C are caused by the release of water vapor during condensation of OH groups. Many authors have observed a similar effect when annealing zeolite-containing rocks activated with alkaline solutions [18, 22, 24]. In this temperature range, surface hydroxyl groups (Si–O–H) are sealed in micropores [22, 24]. DTG curves of samples with calcite in the composition (C5–C16) in the temperature range from 510 to 620 °C, show that the rate of mass loss increases (Fig. 3b). The effect is additionally related with calcite decarbonization.

Insignificant endothermic effect and loss of samples weight at temperatures from 650 to 670 °C is related with decarbonization of unreacted  $\text{CaCO}_3$ . The effect has not been reflected by DTG curves on samples without calcite (C1–C4). Based on the results of experimental analysis (Fig. 3), the exposure temperature for obtaining samples of porous glass ceramics with a uniform pore structure (670 °C) was determined. The required exposure time is established experimentally.

The melting of the charge mixture begins at a temperature of  $> 680$  °C. An endothermic effect is observed (Fig. 3a). The effect is that samples retain their mass. DTG curves in this temperature range (Fig. 3b) show straight lines. The effect of  $\text{CaCO}_3$  and  $\text{Al}_2\text{O}_3$  on the initial melting temperature of the charge is insignificant. The maximum of softening effect of the charge mixture shifts to the region of lower temperatures if there is increase in calcite in the rock. The shift of the peak of the endothermic effect from  $\approx 750$  °C for sample C1 (0 % calcite) to  $\approx 720$  °C for sample C13 (10.5 % calcite) was found. When Aluminum Oxide was introduced into the charge mixture composition, no change in the peak of the temperature effect was found. The appearance of a molten in the siliceous charge mixture in this temperature range was mentioned by other authors [17–19]. During the melting of the charge mixture, the free OH groups in the micropores condense and are released as water vapor [22, 24]. The charge mixture foams. The porosity of the glass ceramic material depends on the amount and viscosity of the molten in the charge mixture and the volume of gas released at a particular time. In this work, these properties were regulated by the heating rate of the charge mixture. The heating rate of the charge mixture – 4.5 °C/ min was determined experimentally.

The results of experimental analysis (Fig. 3) allow to estimate the crystallization temperature of the charge mixture. The crystallization of the siliceous charge mixture without calcite is characterized by a wide peak (exothermic effect) reflected by the DTA curve (Fig. 3a). The peak maximum at a temperature of  $\approx 800$  °C. The effect does not change when  $\text{Al}_2\text{O}_3$  is introduced into the charge mixture in the amount of  $\leq 3.05$  %. The exothermic effect of crystallization shifts to the region of lower temperatures in response to the increase of calcite in the charge mixture composition. The peak maximum shifts to a temperature of  $\approx 770$  °C when heating a siliceous charge mixture with a calcite content equal to 10.5 % (Sample C13, Fig. 3a). The peak is obvious and more intensive in comparison with compositions without calcite (C1–C4). The effect of  $\text{Al}_2\text{O}_3$  in the amount of  $\leq 12.21$  % on the crystallization of the siliceous charge mixture with calcite (10.5 %) is insignificant (Samples C13–C16). The intensity and temperature of the peak maximum remain almost unchanged.

### 3.3. Porous glass ceramics' XRD

X-ray pattern of samples of porous glass ceramic materials are shown in Fig. 4. For visual clarity, patterns are presented in the scan range  $2\theta = 10\text{--}45^\circ$ .

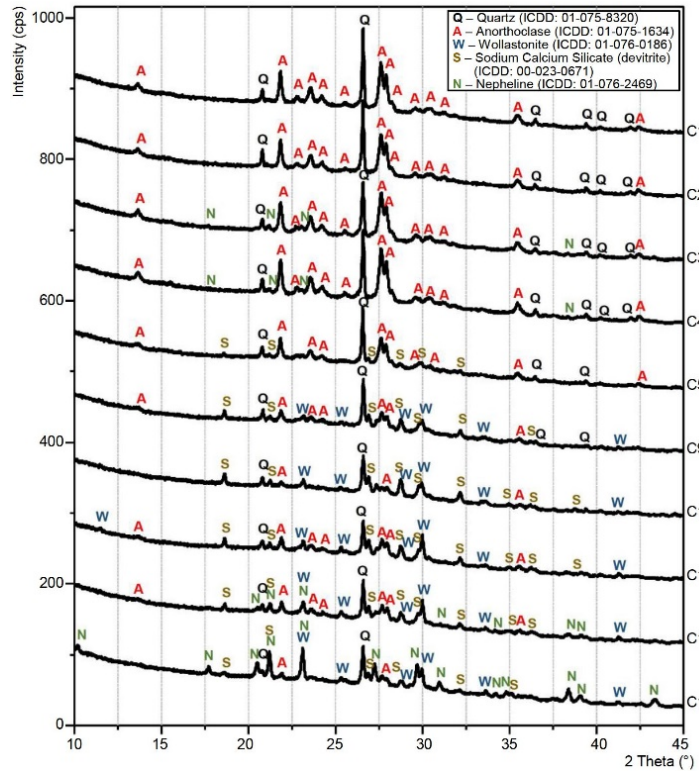


**Figure 4. X-ray patterns of glass ceramic samples.**

Based on the XRD results of glass ceramic samples (Fig. 4), the following has been established. On all X-ray patterns (Fig. 4), in the scan range from  $17$  to  $37^\circ$  ( $2\theta$ ), there is a non-monotonic change in the background (halo), probably caused by the presence of an amorphous phase. The change of the amorphous halo depending on the amount of  $\text{CaO}$  and  $\text{Al}_2\text{O}_3$  in the composition of the material has not been detected. The main crystalline phases of C1–C4 samples are anorthoclase  $[(\text{Na}_{0.85}\text{K}_{0.14})(\text{AlSi}_3\text{O}_8)]$ , ICDD: 01-075-1634 and quartz  $[\text{SiO}_2]$ , ICDD: 01-075-8320]. The samples were obtained from a charge without calcite in the composition. After increasing the amount of  $\text{Al}_2\text{O}_3$  additive in the charge mixture to 2.04 % or 3.05 %, the nepheline's phase additionally appeared in glass ceramics  $[\text{Na}_3\text{K}(\text{Si}_{0.553}\text{Al}_{0.447})_8\text{O}_{16}]$ , ICDD: 01-076-2469]. The amount of new phase is insignificant. It is known from the scholarly literature that in porous glass ceramics made of zeolite tuff plagioclase may be present instead of anorthoclase [18, 24].

With the increase of the calcite in charge mixture, the intensity of the anorthoclase lines decreased. New lines appeared on X-ray patterns. The lines correspond to the crystalline phases of wollastonite  $[\text{CaSiO}_3]$ , CDD: 01-076-0186] and sodium calcium silicate (devitrite)  $[\text{Na}_2\text{Ca}_3\text{Si}_6\text{O}_{16}]$ , ICDD: 00-023-0671]. The intensities of the lines of the new phases increased in response to the increase of  $\text{CaCO}_3$  in the rock composition to 10.5 % (Fig. 4, C5, C9, C13). The results obtained are consistent with the previously obtained research findings [22].

X-ray patterns of C13–C16 were obtained on samples from siliceous rock with calcite amount equal to 10.5 %. When amount of  $\text{Al}_2\text{O}_3$  in the charge mixture was increased to 8.14 %, the intensity of the devitrite lines decreased, and those of wollastonite and anorthoclase increased. The nepheline lines appeared on the X-ray patterns. Further increase in the concentration of  $\text{Al}_2\text{O}_3$  to 12.21 % caused the decrease in the amount of wollastonite in the composition, and the anorthoclase and devitrite lines practically disappeared. Nepheline has become the main crystalline phase of glass ceramics. The formation of the nepheline's phase in glass ceramics caused by the increased amount of  $\text{Al}_2\text{O}_3$  in the composition of the material was also observed by other researchers [31].

### 3.4. Porous glass ceramics macrostructure

A scan of the surface of porous glass ceramic samples is shown in Fig. 5.

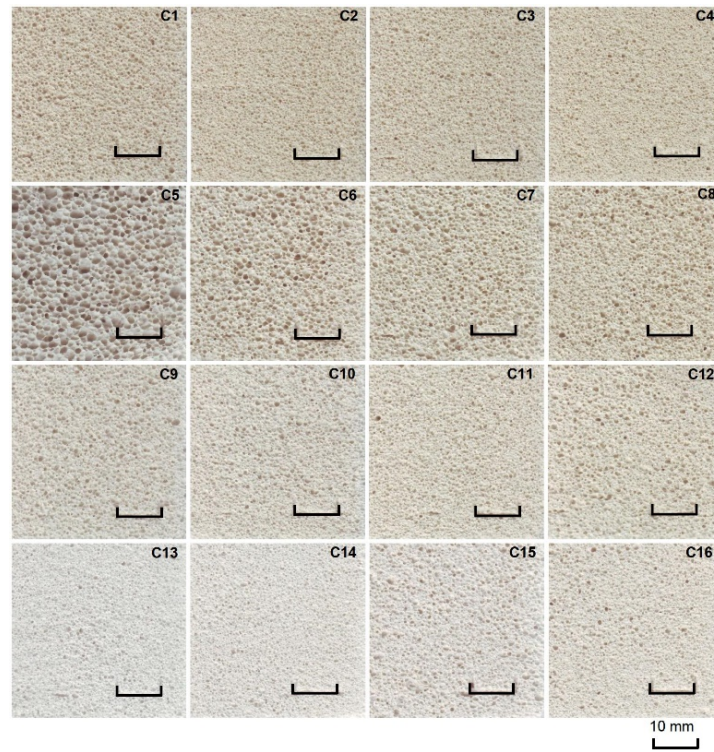


**Figure 5. A scan of the surface of porous glass ceramic samples.**

All samples of porous glass ceramic materials have a cellular (finely porous) structure (Fig. 5.). The porosity over the entire surface area of the samples is uniform. The pore size does not exceed 1.5 mm (except for samples C5). The maximum pore size in samples C5  $\approx$  4 mm. With the increase of calcite in the charge mixture composition, the surface color of the annealed samples becomes lighter. And vice versa, it darkens with the increase of  $\text{Al}_2\text{O}_3$ . The different color of the surface can be attributed to a change in the phase composition of the samples. According to Fig. 4, the crystalline phase of light samples consists mainly of wollastonite and devitrite, and dark ones – anorthoclase, quartz and nepheline. The color of the samples surface can also be affected by the pore structure [8]. The results of the study into the microstructure of the samples are given below.

### 3.5. SEM images of samples

The effect of calcite in the charge composition on the microstructure of porous glass ceramics samples is shown in Fig. 6. The results were obtained by using the SEM. Samples of compositions C1, C9 and C13 were exposed to testing.

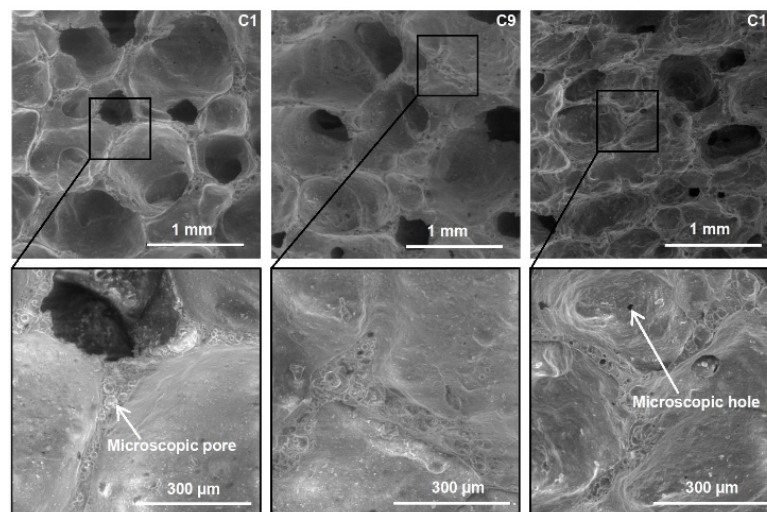


**Figure 6. SEM images of samples.**

The SEM images of sample C1 (Fig. 6) show pores with a diameter of  $\leq$  1 mm. The pores are in the shape of a ball, closed. Some of them are connected to each other. There are many closed micropores with a diameter of  $<$  30  $\mu\text{m}$  in the pore walls. The surface of the walls is smooth. The sample was obtained

from a calcite-free rock. The SEM images of sample C9 display pores with a diameter of  $< 1.5$  mm. The shape is stretched. The individual pores are connected to each other by wide channels. The pore walls consist of closed micropores. Sample C9 was obtained from a rock containing 7 % of calcite. The pores in sample C13 have different diameters and shapes. Pore diameter is  $< 1$  mm. The surface of the walls is uneven. There is a great deal of through microscopic holes with a diameter of  $< 30$   $\mu\text{m}$  between the pores. There are many closed and open micropores with a diameter of  $< 20$   $\mu\text{m}$  in the walls of large pores. It is known that open pores in glass ceramics are formed during intensive crystallization [6]. According to Fig. 3, with the increase of calcite content in siliceous rock up to 10.5 % (Sample C13), crystallization in glass ceramics begins at a lower temperature ( $\approx 770$   $^{\circ}\text{C}$ ). The exothermic effect of crystallization is more intense in comparison with the calcite-free composition. As a result, more open pores appear.

### 3.6. Micro-CT of samples

To study the macro- and microstructure inside porous glass ceramics, a Micro-CT of samples was carried out. Samples C1, C9 and C13 were tested. The samples were obtained from rocks with different calcite content. The test results are shown in Fig. 7.

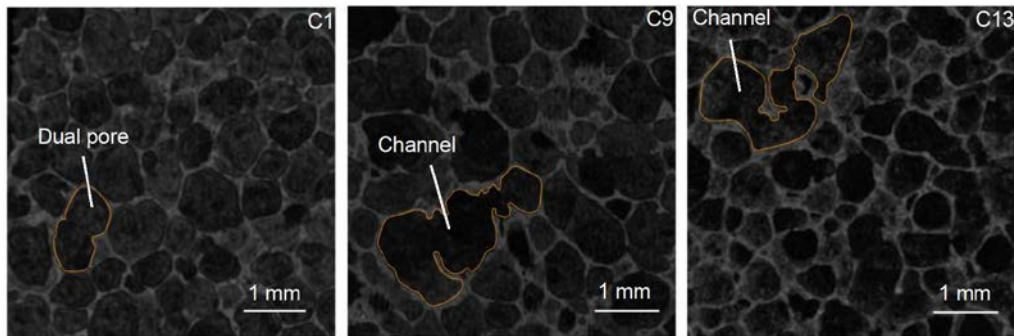


Figure 7. Micro-CT of samples.

The results of the Micro-CT samples (Fig. 7.) complement the SEM findings. The Micro-CT image inside the sample C1 shows pores with a diameter of  $< 1$  mm. Some adjacent pores are merged. With the increase of calcite in the siliceous rock composition to 7 % (Sample C9), the number of merged pores increased. The image of C9 clearly shows a channel that connects more than 3 adjacent pores in one section of the sample. The diameter of select pores increased to 1.5 mm. With the 10.5 % calcite in the composition (Sample C13), the length of channels in porous glass ceramics increased. The image of C13 shows a channel that connects more than 5 adjacent pores in one section of the sample. There are no ruptured walls inside the channel. The diameter of the pores decreased to 1mm or less. There are many bright dots in the walls of the pores. This indicates a large number of micropores in the sample.

Based on the analysis of the SEM and Micro-CT images, it was found that the macro- and microstructure of porous glass ceramics from siliceous rocks is significantly influenced by the amount of calcite in the charge mixture. The increase of  $\text{CaCO}_3$  changes the size and shape of pores. Channels are formed inside the material, which consist of connected adjacent pores. Microscopic holes appear in the pores' walls.

### 3.7. Samples' density and porosity

Fig. 8 shows dependency graphs of the apparent density and porosity of glass ceramic samples on the amount of  $\text{CaCO}_3$  and  $\text{Al}_2\text{O}_3$  in the charge mixture composition.

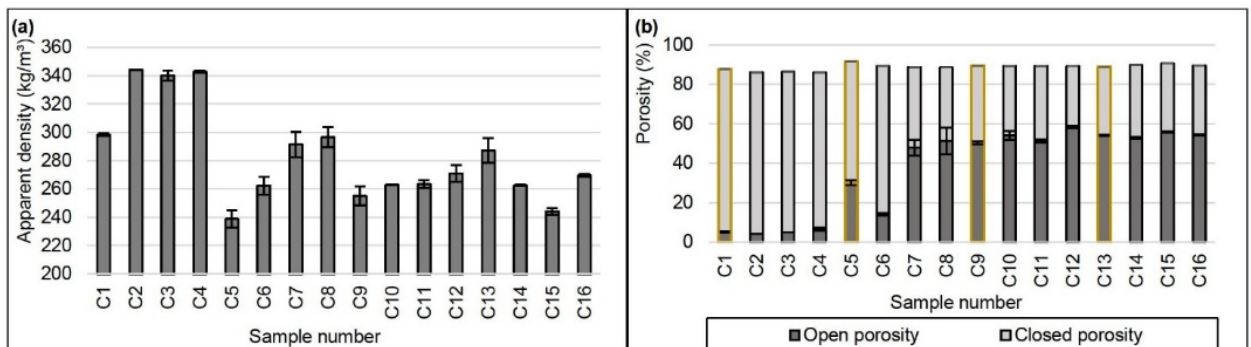


Figure 8. Apparent density (a) and porosity (b) of samples.

The effect of calcite in the siliceous rock composition on the apparent density of porous glass ceramic samples is as follows (Fig. 8a, samples C1, C5, C9, C13). The apparent density of the samples decreased from  $\approx 300 \text{ kg/m}^3$  to  $\approx 240 \text{ kg/m}^3$  in response to a 3.5 % increase of  $\text{CaCO}_3$  in the rock. A further increase of calcite in the rock to 10.5 %, increased the apparent density of the samples linearly to  $\approx 285 \text{ kg/m}^3$  (Sample C13). The obtained dependencies are similar to the findings of other authors. The effect of CaO on the apparent density of samples of porous glass ceramics from fly ash is similar [26, 27].

Dependencies of changes in the samples' apparent density on the amount of  $\text{Al}_2\text{O}_3$  additive have been obtained. Depending on the amount of calcite in the rock, the addition of  $\text{Al}_2\text{O}_3$  affects the apparent density of glass ceramics in different ways. The samples density increased if  $\text{CaCO}_3$  content in the rock amounted to  $\leq 3.5 \%$  and the introduction of  $\text{Al}_2\text{O}_3$  additive was up to 6.11 % (Samples C1–C8). The addition of  $\text{Al}_2\text{O}_3$  in an amount of  $\leq 8.14 \%$  caused the decrease in the apparent density of samples from  $\approx 285 \text{ kg/m}^3$  to  $\approx 244 \text{ kg/m}^3$  with a 10.5 % calcite content in the rock (Samples C13–C15). The increase of  $\text{Al}_2\text{O}_3$  additive to more than 8.14 % in the charge mixture raised the apparent density of the samples (Sample C16).

Based on the findings obtained (Fig. 8b), the total porosity of the samples of glass ceramic materials is in the range from 85.70 to 91.54 %. The lowest values of the total porosity demonstrate the samples from the calcite-free charge mixture (C1–C4). In given samples > 79 % of the pores are closed. It is easy to trace the characteristic dependence between the increase in the number of open pores in the material and the increase in the amount of calcite in the charge mixture composition. For sample C13, the open porosity is > 54 %. The addition of  $\text{Al}_2\text{O}_3$  also increases the number of open pores in the material. The findings obtained confirm the results of TA, SEM and Micro-CT.

### 3.8. Strength

Fig. 9 shows the strength values of porous glass ceramic samples from siliceous rocks.

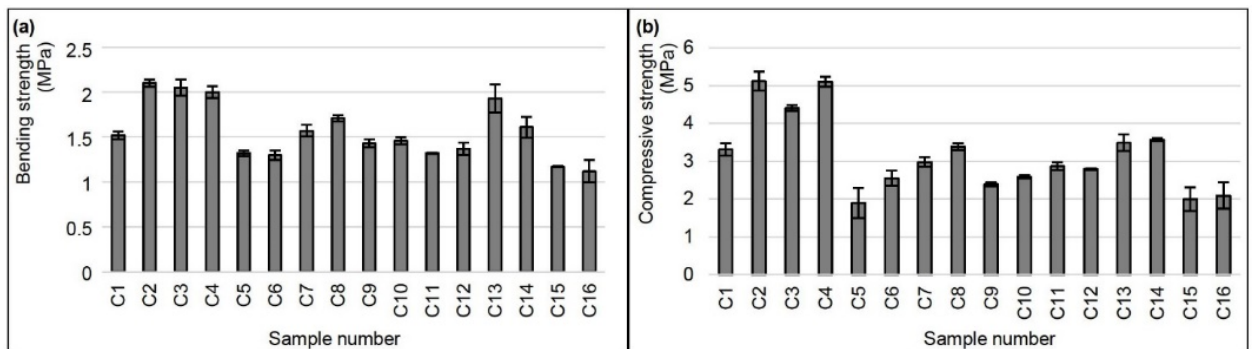


**Figure 9. Bending (a) and compressive strength (b) of samples.**

According to the conducted research (Fig. 9), the obtained porous glass ceramic materials have a bending strength in the range from 1.12 to 2.1 MPa. The compressive strength is in the range of 1.9–5.1 MPa. The following relationship is traced between the phase composition of the material and the bending strength of the samples (Fig. 9a). With the increase of the wollastonite mineral in the material, the bending strength increased. Thus, for samples C9, bending strength  $\approx 1.5 \text{ MPa}$ . The strength is similar for samples of composition C1. However, the average density of samples C1 is  $40 \text{ kg/m}^3$  higher than that of samples C9. The bending strength of samples C13 is  $1.93 \text{ MPa}$  at a density  $\approx 285 \text{ kg/m}^3$ . The value is commensurate with the test results of samples C4, which density is  $\approx 340 \text{ kg/m}^3$ . There is evidence in the scholarly literature on the positive effect of the wollastonite mineral on the bending strength of glass ceramic materials [32].

The negative influence of the mineral nepheline in porous glass ceramics samples on their bending strength has been revealed. The crystalline phase of sample C16 consists mainly of this mineral. The samples have the lowest bending strength (1.12 MPa). The effect of the  $\text{Al}_2\text{O}_3$  content in the composition of glass ceramics on its strength characteristics has been explored in the works of other authors [28, 29]. The authors have established the maximum concentration of aluminum oxide in the composition of glass ceramics.

According to the research findings (Fig. 9b), the compressive strength of samples of porous glass ceramic materials is linearly related to the apparent density. The highest compressive strength ( $\approx 5 \text{ MPa}$ ) was in samples C2 and C4. The apparent density of samples is slightly more than  $340 \text{ kg/m}^3$ . The lowest compressive strength of samples C5, C15, C16 ( $\approx 2 \text{ MPa}$ ). Samples of compositions C5, C15 have the lowest density ( $\approx 240 \text{ kg/m}^3$ ). Probably, the samples C16 are less durable due to the nepheline content. According to Fig. 4, the main crystalline phase of the sample is nepheline. It was not possible to find other

relationships between the phase composition and compressive strength of the samples. The obtained porous glass ceramics with an equal apparent density are superior in strength to foam glass and glass ceramics from industrial waste [1, 7, 11–16].

### 3.9. Thermal conductivity

Fig. 10 shows the results of thermal conductivity testing of porous glass ceramic samples. The results are shown in relation to the apparent density of the samples.

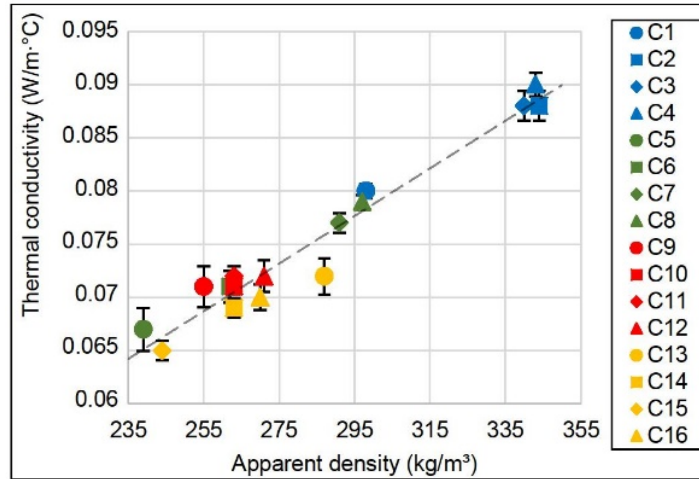


**Figure 10. Thermal conductivity of samples.**

The findings presented in Fig. 9 underwent a thorough analysis. The dependence of the thermal conductivity of porous glass ceramic samples on their apparent density was established. The dependence is linear. It refers to samples with a density from 235 to 355 kg/m<sup>3</sup>. The dependence of thermal conductivity on the density of samples is expressed by the formula (6):

$$\lambda = 21.7 \cdot 10^{-5} \cdot \rho + 0.014, \quad (6)$$

where  $\lambda$  is thermal conductivity (W/(m·°C));  $\rho$  is apparent density of the material dry basis (kg/m<sup>3</sup>).

The validity coefficient of the approximation ( $R^2$ ) is equal to 0.971.

The thermal conductivity values of all samples from siliceous rock with a 10.5 % calcite (C13–C16) are below the regression line (Fig. 9). It is known that thermal conductivity depends largely on the conductivity in the solid phase [6]. According to the SEM and Micro-CT findings, the increase in the amount of CaCO<sub>3</sub> in the charge mixture raised the number of micropores in the pore walls of the samples. Probably, owing to this, the thermal conductivity of porous glass ceramics has decreased.

Following the results of the experiment, it was found that dry samples C15 of porous glass ceramics have the lowest thermal conductivity (0.065 W/(m·°C)). The apparent density of the samples is 244 kg/m<sup>3</sup>. Highest thermal conductivity (0.09 W/(m·°C)) belongs to samples of composition C3 (apparent density is 340 kg/m<sup>3</sup>). The influence of the phase composition of samples of porous glass ceramic materials on their thermal conductivity has not been revealed. The results obtained correlate with the findings supplied by other authors [6].

### 3.10. Limiting operating temperature

The main goal of our work is to obtain porous glass ceramic materials with an operating temperature of more than 900 °C. The effect of the phase composition of porous glass ceramics on the limiting operating temperature of materials is shown in Fig. 11. The limiting temperature was estimated by the size of the samples after holding for 2 hours at a given temperature.

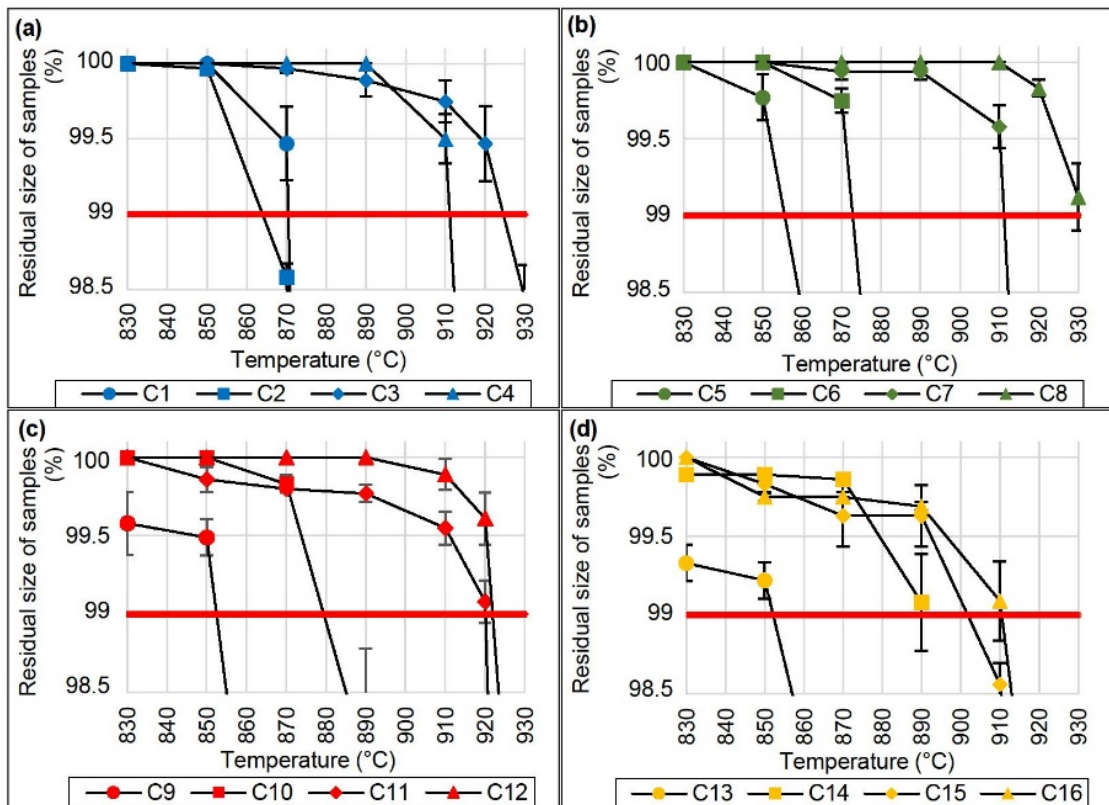


**Figure 11. Residual size of samples after holding for 2 hours at a given temperature. (Samples from siliceous rock with calcite content equal to: a – 0%; b – 3,5%; c – 7%; d – 10,5%; C1–C16 – numbers of compositions)**

During the experiment, it was found that the compositions C3, C4, C7, C8, C11, C12, C16 can be operated at a temperature  $> 900$  °C. The residual sizes of the samples after holding for 2 hours at a temperature of more than  $900$  °C are larger than 99 % of the control values (Fig. 11). All compositions were obtained by modifying the charge mixture with aluminum oxide. The positive effect of  $Al_2O_3$  in the composition of ceramic materials on their resistance to a lasting exposure to high temperatures have been explored in the scholarly literature [28, 29]. Following the analysis of findings in Fig.11 we have found that the amount of  $Al_2O_3$  additive must be adjusted depending on the amount of calcite in the charge mixture. The amount of  $Al_2O_3$  must be increased with reference to  $CaCO_3$  increase. To achieve the limiting operating temperature of porous glass ceramics  $> 900$  °C is possible if we modify the charge mixture with a 2.04 % or more  $Al_2O_3$ . Calcite-free charge mixture (Samples C3, C4). The phase composition of the samples consists of anorthoclase, nepheline and quartz (Fig. 4). With a 10.5 % amount of calcite in the rock, it was also possible to obtain glass ceramics with an operating temperature  $> 900$  °C. The amount of  $Al_2O_3$  in the charge should be equal 12.21 % (Sample C16). According to Fig. 4, the main crystalline phase of the samples is anorthoclase, nepheline, quartz and wollastonite.

Samples C5, C9, C13 can be operated at a temperature of no more than  $850$  °C. The crystal phase of these samples contains a lot of devitrite. This compound has a low melting point [33]. The effect of devitrite on the limiting operating temperature is negative.

The developed porous glass ceramic materials significantly exceed foam glass and porous glass ceramics from siliceous rocks based on charge mixture exposed to alkaline activation in terms of the limiting operating temperature [17–19]. The glass-ceramic materials from siliceous rock can be used as thermal insulation of melting furnaces, boiler equipment, etc.

### 3.11. Thermal shock resistance

Thermal insulation materials used in the insulation of industrial equipment should have high thermal shock resistance [2, 28, 29]. Thermal shock resistance is the ability of material not to break down when exposed to sudden temperature changes. Fig. 12 shows the results of testing the thermal shock resistance of porous glass ceramic samples.

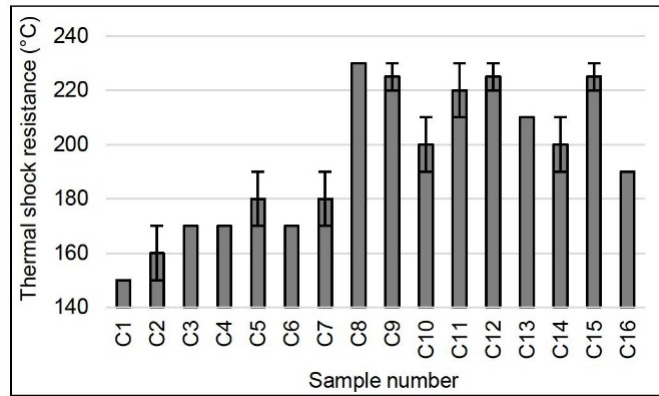


**Figure 12. Thermal shock resistance.**

Based on obtained findings (Fig. 12), the thermal shock resistance of porous glass ceramic samples varies depending on the composition. The lowest values of thermal shock resistance have samples from the calcite-free charge mixture. The values are in the range of 150–170 °C. Owing to the increase of the aluminum oxide in the charge mixture composition to 2.04 % or more, a linear increase in the thermal shock resistance of the samples from 150 to 170 °C occurs. There is a linear relationship between the values of thermal shock resistance of samples of glass-ceramic materials and their porosity. The more closed pores in the material, the less stability. The thermal shock resistance of samples C1–C4 and C6 does not exceed 170 °C. More than 75 % of the pores in these samples are closed (Fig. 8b). During the experiment, heated samples were immersed in water. Owing to the pores' structure, water did not penetrate into the material. The sample surface cooled faster. The sample was destroying due to the large temperature difference on the surface and inside of it. Consequently, the increase in the number of open pores in the material raised the thermal shock resistance of the samples. Maximum thermal shock resistance (225–230 °C) belongs to the samples C8, C9, C12 and C15. The number of open pores in the material is > 50 % (Fig. 8b). The assumption about the relationship between thermal shock resistance and porosity of the material is confirmed. Similar conclusions can be found in [6].

After analyzing the values in Fig. 12, the negative effect of nepheline on the thermal shock resistance of the samples was established. Sample C16 failed at a temperature drop of 190 °C. This is 35 °C less in comparison with the sample C15. According to Fig. 8b, the number of open pores in both samples is almost equal (> 54 %). The main difference is in the phase composition. There is more nepheline in the sample C16.

The thermal shock resistance of the developed porous glass ceramic materials is almost equal to that of foam glass and porous glass ceramics derived from industrial waste [28, 29].

### 3.12. Chemical stability

The influence of the chemical and mineralogical composition of porous glass ceramic materials on the chemical stability of samples is shown in Table 4. Chemical stability was determined by the loss of weight of powdered samples (fraction 0.315–0.63 mm) after boiling for 3 hours in aggressive chemical media.

**Table 4. Change in the samples' weight after boiling in chemical media for 3 hours.**

Sample number	Change in the samples' weight after boiling in chemical media for 3 hours (%)*		
	H <sub>2</sub> O	6N HCl solution	1N Na <sub>2</sub> CO <sub>3</sub> solution + 1N NaOH solution (1:1)
C1	0.82	1.37	6.95
C2	0.17	0.63	6.75
C3	0.67	1.47	7.05
C4	0.37	1.10	7.12
C5	0.39	0.59	6.93
C6	0.34	1.60	7.31
C7	0.54	1.99	6.71
C8	0.63	2.20	6.68
C9	0.47	1.91	7.17
C10	0.41	3.13	7.20

Sample number	Change in the samples' weight after boiling in chemical media for 3 hours (%)*		
	H <sub>2</sub> O	6N HCl solution	1N Na <sub>2</sub> CO <sub>3</sub> solution + 1N NaOH solution (1:1)
C11	0.97	4.44	6.80
C12	0.56	7.13	6.69
C13	0.99	4.80	7.94
C14	0.57	5.42	7.45
C15	0.73	7.81	7.46
C16	0.56	17.89	6.99

\* – The differences in the test results of the samples of each composition did not exceed 5% of the average value.

After the analysis of the experimental findings (Table 4), the following ensues. After boiling samples of glass ceramic materials (fraction 0.315–0.63 mm) for 3 hours in water, all samples lost less than 1 % in weight. This result confirms the ability of glass ceramic materials not to be destroyed by the action of water. The material can be operated in wet conditions without restrictions.

The influence of the phase composition of glass ceramic samples on their chemical stability in an aqueous solution of HCl (6N) has been established. The stability decreases in response to the increase in the amount of wollastonite, devitrite and nepheline in the material. After 3 hours of boiling the sample C16, the color of the solution turned bright yellow. The sample weight decreased by 17.89 %. Sample C16 contains the largest amount of wollastonite and nepheline (Fig. 4). Samples in which the main crystalline phase is anorthoclase and quartz (C1–C5) are almost unsusceptible to chemical corrosion in an aqueous solution of HCl (6N). The mass loss does not exceed 1.5 %. There is a great deal of evidence in the scholarly literature on the dissolution of nepheline and wollastonite minerals in aqueous solutions of hydrochloric acid [34].

The effect of the phase composition of glass-ceramic samples on the resistance to alkaline solutions (Na<sub>2</sub>CO<sub>3</sub> (1N) + NaOH (1N)) has not been detected. The chemical stability of the samples deteriorates slightly after the increase of CaO in their compositions. The weight loss increased from 6.95 % (Sample C1) to 7.94 % (Sample C13). There is evidence in the scholarly literature about the negative effect of CaO in the composition of glass ceramics on its chemical stability [35]. The effect of addition of Al<sub>2</sub>O<sub>3</sub> in the amount of up to 12.21 % to the charge mixture composition on the resistance of glass ceramic samples in alkalis is insignificant.

The completed experimental studies of samples of glass ceramic materials allowed to reveal their high chemical stability in water, HCl aqueous solution and alkalis. With reference to some indicators, porous glass-ceramic materials from siliceous rocks surpassed foam glass [35]. It is recommended to use the developed materials as insulation for pipelines, industrial installations, etc.

## 4. Conclusions

Porous glass-ceramic materials were obtained from siliceous rocks with different amounts of calcite in their composition. To raise the limiting operating temperature of the samples, aluminum oxide was added to the charge mixture. A joint mechanochemical activation of components (siliceous rocks, Na<sub>2</sub>CO<sub>3</sub>, Al<sub>2</sub>O<sub>3</sub> and KCl) was carried out in a planetary ball mill. The resulting charge was annealed at a temperature of 850 °C. The influence of the calcite and aluminum oxide content in the charge mixture composition on the properties of porous glass-ceramics samples has been revealed.

Main conclusions:

- The main crystalline phase of glass ceramics from a calcite-free charge mixture is anorthoclase and quartz. The calcite-containing charge mixture samples additionally contain wollastonite and devitrite. After increasing the amount of Al<sub>2</sub>O<sub>3</sub> additive in the composition of the charge mixture, nepheline appears in glass ceramics. The influence of the phase composition of glass ceramics on the properties of samples has been examined.
- Glass-ceramic materials from siliceous rocks have a finely porous structure. The pore size of most samples is less than 1.5 mm. The increase in the calcite and aluminum oxide amount in the charge mixture composition had a significant impact on the glass ceramics microstructure. The size and shape of the pores have changed. The number of open pores in the material increased from ≈ 5 % to > 50 %.

- The developed porous glass ceramics has an apparent density of 239–344 kg/m<sup>3</sup>, bending and compressive strength up to 2.1 MPa and 5.1 MPa, respectively.
- The developed porous glass ceramics has a thermal conductivity is 0.065–0.09 W/(m<sup>2</sup>·C), thermal shock resistance up to 230 °C, limiting operating temperature up to 920 °C. The limiting operating temperature of the samples was increased to 920 °C owing to the introduction of Al<sub>2</sub>O<sub>3</sub> additive into the charge mixture. The amount of the additive depends on the amount of calcite in the siliceous rock. With the increase in the CaCO<sub>3</sub> amount it is necessary to increase Al<sub>2</sub>O<sub>3</sub> content. The 10.5 % content of calcite in the siliceous rock allowed to obtain porous glass ceramics with an operating temperature over 900 °C. The additive of Al<sub>2</sub>O<sub>3</sub> in the amount of > 8.14 % was dispensed into the charge mixture composition.
- The completed experimental studies of samples of glass ceramic materials allowed to reveal their high chemical stability in water, HCl aqueous solution and alkalis.
- Porous glass-ceramic materials from siliceous rocks are superior in many respects to foam glass and porous glass ceramics from industrial waste. This material can be used in the construction and repair of industrial and civil facilities (for heat and sound insulation, as a refractory lining of furnaces, for protection of structures from corrosion, etc.).

## References

1. Fernandes, H.R., Tulyaganov, D.U., Ferreira, J.M.F. Preparation and characterization of foams from sheet glass and fly ash using carbonates as foaming agents. *Ceramics International*. 2009. 35 (1). Pp. 229–235. DOI: 10.1016/j.ceramint.2007.10.019
2. Guo, H., Ye, F., Li, W., Song, X., Xie, G. Preparation and characterization of foamed microporous mullite ceramics based on kyanite. *Ceramics International*. 2015. 41 (10). Pp. 14645–14651. DOI: 10.1016/j.ceramint.2015.07.186
3. Bessmertnyi, V.S., Lesovik, V.S., Krokhin, V.P., Puchka, O.V., Nikiforova E.P. The Reducing Effect of Argon in the Plasma Treatment of High-Melting Nonmetallic Materials (A Review). *Glass and Ceramics*. 2001. Vol. 58. Pp. 362–364. DOI: 10.1023/A:1013963916418
4. Jabir, H.A., Abid, S.R., Murali, G., Ali, S.H., Klyuev, S., Fediuk, R., Vatin, N., Promakhov, V., Vasilev, Y. Experimental Tests and Reliability Analysis of the Cracking Impact Resistance of UHPFRC. *Fibers*. 2020. 8 (12). Article No. 74. DOI: 10.3390/fib8120074
5. Smirnova, O.M., Potyomkin, D.A. Influence of ground granulated blast furnace slag properties on the superplasticizers effect. *International Journal of Civil Engineering and Technology*. 2018. 9 (7). Pp. 874–880.
6. König, J., Lopez-Gil, A., Cimavilla-Roman, P., Rodriguez-Perez, M.A., Petersen, R.R., Østergaard, M.B., Iversen, N., Yue, Y., Spreitzer, M. Synthesis and properties of open- and closed-porous foamed glass with a low density. *Construction and Building Materials*. 2020. Vol. 247. Article No. 118574. DOI: 10.1016/j.conbuildmat.2020.118574
7. Zhu, M., Ji, R., Li, Z., Wang, H., Liu, L., Zhang, Z. Preparation of glass ceramic foams for thermal insulation applications from coal fly ash and waste glass. *Construction and Building Materials*. 2016. Vol. 112. Pp. 398–405. DOI: 10.1016/j.conbuildmat.2016.02.183
8. Cao, J., Lu, J., Jiang, L., Wang, Z. Sinterability, microstructure and compressive strength of porous glass-ceramics from metallurgical silicon slag and waste glass. *Ceramics International*. 2016. 42 (8). Pp. 10079–10084. DOI: 10.1016/j.ceramint.2016.03.113
9. Kyaw Oo D'Amore, G., Caniato, M., Travan, A., Turco, G., Marsich, L., Ferluga, A., Schmid, C. Innovative thermal and acoustic insulation foam from recycled waste glass powder. *Journal of Cleaner Production*. 2017. Vol. 165. Pp. 1306–1315. DOI: 10.1016/j.jclepro.2017.07.214
10. Yatsenko, E.A., Ryabova, A.V., Goltsman, B.M. Development of fiber-glass composite coatings for protection of steel oil pipelines from internal and external corrosion. *Chernye Metally*. 2019. Vol. 12. Pp. 46–51.
11. Yatsenko, E.A., Gol'tsman, B.M., Kosarev, A.S., Karandashova, N.S., Smolii, V.A., Yatsenko, L.A. Synthesis of Foamed Glass Based on Slag and a Glycerol Pore-Forming Mixture. *Glass Physics and Chemistry*. 2018. 44 (2). Pp 152–155. DOI: 10.1134/S1087659618020177
12. Ji, R., Zheng, Y., Zou, Z., Chen, Z., Wei, S., Jin, X., Zhang, M. Utilization of mineral wool waste and waste glass for synthesis of foam glass at low temperature. *Construction and Building Materials*. 2019. Vol. 215. Pp. 623–632. DOI: 10.1016/j.conbuildmat.2019.04.226
13. Jia, R., Deng, L., Yun, F., Li, H., Zhang, X., Jia, X. Effects of SiO<sub>2</sub>/CaO ratio on viscosity, structure, and mechanical properties of blast furnace slag glass ceramics. *Materials Chemistry and Physics*. 2019. Vol. 233. Pp. 155–162. DOI: 10.1016/j.matchemphys.2019.05.065
14. Hisham, N.A.N., Zaid, M.H.M., Aziz, S.H.A., Muhammad, F.D. Comparison of foam glass-ceramics with different composition derived from ark clamshell (ACS) and soda lime silica (SLS) glass bottles sintered at various temperatures. *Materials*. 2021. 14(3). Article No. 570. DOI: 10.3390/ma14030570
15. Zeng, L., Sun, H., Peng, T., Zheng, W. Preparation of porous glass-ceramics from coal fly ash and asbestos tailings by high-temperature pore-forming. *Waste Management*. 2020. Vol. 106. Pp. 184–192. DOI: 10.1016/j.wasman.2020.03.008
16. Romero, A.R., Toniolo, N., Boccaccini, A.R., Bernardo, E. Glass-ceramic foams from 'weak alkali activation' and gel-casting of waste glass/fly ash mixtures. *Materials*. 2019. 12 (4). Article No. 588. DOI: 10.3390/ma12040588
17. Ivanov, K.S. Optimization of the structure and properties of foam-glass ceramics. *Magazine of Civil Engineering*. 2019. 89 (5). Pp. 52–60. DOI: 10.18720/MCE.89.5
18. Kazantseva, L.K., Rashchenko, S.V. Optimization of porous heat-insulating ceramics manufacturing from zeolitic rocks. *Ceramics International*. 2016. 42 (16). Pp. 19250–19256. DOI: 10.1016/j.ceramint.2016.09.091
19. Yatsenko, E.A., Goltsman, B.M., Klimova, L.V., Yatsenko, L.A. Peculiarities of foam glass synthesis from natural silica-containing raw materials. *Journal of Thermal Analysis and Calorimetry*. 2020. 142 (1). Pp. 119–127. DOI: 10.1007/s10973-020-10015-3

20. Zhimalov, A.A., Bondareva, L.N., Igitkhanyan, Y.G., Ivashchenko, Y.G. Use of Amorphous Siliceous Rocks – Opokas to Obtain Foam Glass with Low Foaming Temperature. *Steklo i Keramika (Glass and Ceramics)*. 2017. 74 (1–2). Pp. 13–15. DOI: 10.1007/s10717-017-9916-1
21. Kruszewski, Ł., Palchik, V., Vapnik, Y., Nowak, K., Banasik, K., Galuskina, I. Mineralogical, geochemical, and rock mechanic characteristics of zeolite-bearing rocks of the hatrurim basin, Israel. *Minerals*. 2021. 11(10). Article No. 1062. DOI: 10.3390/min11101062
22. Erofeev, V., Rodin, A., Bochkina, V., Ermakov, A. The formation mechanism of the porous structure of glass ceramics from siliceous rock. *Magazine of Civil Engineering*. 2020. 100 (8). Article No.10006. DOI: 10.18720/MCE.100.6
23. Erofeev, V.T., Rodin, A.I., Bochkina, V.S., Ermakov, A.A. Properties of porous glass ceramics based on siliceous rocks. *Magazine of Civil Engineering*. 2021. 102 (2). Article No. 10202. DOI: 10.34910/MCE.102.2
24. Kazantseva, L.K., Rashchenko, S.V. Chemical processes during energy-saving preparation of lightweight ceramics. *Journal of the American Ceramic Society*. 2014. 97 (6). Pp. 1743–1749. DOI: 10.1111/jace.12980
25. Li, Y., Zhao, L.-H., Wang, Y.-K., Cang, D.-Q. Effects of Fe<sub>2</sub>O<sub>3</sub> on the properties of ceramics from steel slag. *International Journal of Minerals, Metallurgy and Materials*. 2018. 25 (4). Pp. 413–419. DOI: 10.1007/s12613-018-1586-7
26. Zhou, M., Ge, X., Wang, H., Chen, L., Chen, X. Effect of the CaO content and decomposition of calcium-containing minerals on properties and microstructure of ceramic foams from fly ash. *Ceramics International*. 2017. 43 (12). Pp. 9451–9457. DOI: 10.1016/j.ceramint.2017.04.122
27. Liu, Z.B., Zong, Y.B., Ma, H.Y., Dai, W.B., Li, S.H. Effect of (CaO+MgO)/SiO<sub>2</sub> ratio on crystallisation and properties of slag glass-ceramics. *Advances in Applied Ceramics*. 2014. 113 (7). Pp. 411–418. DOI: 10.1179/1743676114Y.0000000187
28. Costa, F.P.D., Morais, C.R.D.S., Pinto, H.C., Rodrigues, A.M. Microstructure and physico-mechanical properties of Al<sub>2</sub>O<sub>3</sub>-doped sustainable glass-ceramic foams. *Materials Chemistry and Physics*. 2020. Vol. 256. Article No. 123612. DOI: 10.1016/j.matchemphys.2020.123612
29. Keyvani, N., Marghussian, V.K., Rezaie, H.R., Kord, M. Effect of Al<sub>2</sub>O<sub>3</sub> content on crystallization behavior, microstructure, and mechanical properties of SiO<sub>2</sub>-Al<sub>2</sub>O<sub>3</sub>-CaO-MgO glass-ceramics. *International Journal of Applied Ceramic Technology*. 2011. 8(1). Pp. 203–213. DOI: 10.1111/j.1744-7402.2009.02428.x
30. Kazantseva, L.K., Lygina, T.Z., Rashchenko, S.V., Tsyplakov, D.S. Preparation of Sound-Insulating Lightweight Ceramics from Aluminosilicate Rocks with High CaCO<sub>3</sub> Content. *Journal of the American Ceramic Society*. 2015. 98 (7). Pp. 2047–2051. DOI: 10.1111/jace.13581
31. McClane, D.L., Amoroso, J.W., Fox, K.M., Hsieh, M.C., Kesterson, M.R., Kruger, A.A. Nepheline crystallization and the residual glass composition: Understanding waste glass durability. *International Journal of Applied Glass Science*. 2020. 11 (4). Pp. 649–659. DOI: 10.1111/ijag.15418
32. Almasri, K.A., Sidek, H.A.A., Matori, K.A., Zaid, M.H.M. Effect of sintering temperature on physical, structural and optical properties of wollastonite based glass-ceramic derived from waste soda lime silica glasses. *Results in Physics*. 2017. Vol. 7. Pp. 2242–2247. DOI: 10.1016/j.rinp.2017.04.022
33. Yang, S., Lu, J.-X., Poon, C.S. Recycling of waste glass in cement mortars: Mechanical properties under high temperature loading. *Resources Conservation and Recycling*. 2021. Vol. 174. Article No. 105831. DOI: 10.1016/j.resconrec.2021.105831
34. Bagani, M., Balomenos, E., Papias, D. Nepheline Syenite as an Alternative Source for Aluminum Production. *Minerals*. 2021. 11 (7). Article No. 734. DOI: 10.3390/min11070734
35. Abdel-Hameed, S.A.M., El-kheshen, A.A. Thermal and chemical properties of diopside-wollastonite glass-ceramics in the SiO<sub>2</sub>-CaO-MgO system from raw materials. *Ceramics International*. 2013. 29(3). Pp. 265–269. DOI: 10.1016/S0272-8842(02)00114-1

#### **Information about authors:**

**Alexander Rodin**, PhD in Technical Science

ORCID: <https://orcid.org/0000-0002-8080-9808>

E-mail: [al\\_rodin@mail.ru](mailto:al_rodin@mail.ru)

**Anatolij Ermakov**,

ORCID: <https://orcid.org/0000-0002-2560-0948>

E-mail: [anatoly.ermakov97@mail.ru](mailto:anatoly.ermakov97@mail.ru)

**Vladimir Kyashkin**, PhD in Physical and Mathematical Science

ORCID: <https://orcid.org/0000-0002-3413-247X>

E-mail: [kyashkin@mail.ru](mailto:kyashkin@mail.ru)

**Natalya Rodina**,

ORCID: <https://orcid.org/0000-0002-4709-4847>

E-mail: [rodina.ng@list.ru](mailto:rodina.ng@list.ru)

**Vladimir Erofeev**, Doctor of Technical Science

ORCID: <https://orcid.org/0000-0001-8407-8144>

E-mail: [verofeevvt@mail.ru](mailto:verofeevvt@mail.ru)

